

ISI

bilimi ve tekniği
dergisi

Journal of Thermal Science and Technology

2020 Cilt/Volume 40 Sayı/Number 1
ISSN 1300-3615

Türk Isı Bilimi ve Tekniği Derneği tarafından yılda iki kez
Nisan ve Ekim aylarında yayınlanır.

*A publication of the Turkish Society for Thermal Sciences and
Technology, published twice a year, in April and October.*

TIBTD Adına Yayın Sahibi Sorumlu Yayımcı/Publisher:
Prof. Dr. Atilla BIYIKOĞLU, Gazi Üniversitesi

Sorumlu Yazı İşleri Müdürü-Editör/Editor-in-Chief:
Prof. Dr. Zafer DURSUNKAYA
Orta Doğu Teknik Üniversitesi Makina Mühendisliği Bölümü
06800 ANKARA Tel: 312 210 5232
editor@tibtd.org.tr

Yayın Türü: Yaygın, süreli

Editörler Kurulu/Editorial Board:

Prof. Dr. Tuba OKUTUCU ÖZYURT, Orta Doğu Teknik
Üniversitesi

Prof. Dr. Almıla GÜVENÇ YAZICIOĞLU, Orta Doğu
Teknik Üniversitesi

Doç. Dr. Cüneyt SERT, Orta Doğu Teknik Üniversitesi

Doç. Dr. Barbaros ÇETİN, İhsan Doğramacı Bilkent
Üniversitesi

Teknik Danışman/Technical Advisor

Dr. Öğr. Üyesi Nureddin DİNLER, Gazi Üniversitesi

Baskı/Printed at: KALKAN Matbaacılık San. Tic. Ltd.
Büyük Sanayi 1. Cadde, Alibey İş Hanı No: 99/32 İskitler,
ANKARA 312 342 16 56

TIBTD

Türk Isı Bilimi ve Tekniği Derneği: Dernek ve bu dergi,
Türkiye'de ısı bilimi ve tekniğini geliştirmek amacıyla 1976
yılında Prof. Dr. Yalçın A. GÖĞÜŞ tarafından kurulmuştur.

Turkish Society of Thermal Sciences and Technology: The
association and the journal was founded by Prof. Dr. Yalçın
A. GÖĞÜŞ in 1976 to improve thermal sciences and
technology in Turkey.

Adresi/Address: TIBTD, Mühendislik Fakültesi, Zemin Kat
No.22 Gazi Üniversitesi, 06570 ANKARA

http://www.tibtd.org.tr
tibtd@tibtd.org.tr

Üyelik aidatları için: İş Bankası Maltepe Şubesi Hesap No:
42120867567 IBAN: TR08 0006 4000 0014 2120 8675 67

Yönetim Kurulu/Executive Board:

Prof. Dr. Atilla BIYIKOĞLU (Bşk.), Prof. Dr. Nuri YÜCEL
(Bşk. Yard.), Prof. Dr. Oğuz TURGUT (Genel Sek.), Prof.
Dr. İlhami HORUZ (Muhasip Üye), Prof. Dr. Zafer
DURSUNKAYA, Prof. Dr. L. Berrin ERBAY, Prof. Dr. Tuba
OKUTUCU ÖZYURT

İÇİNDEKİLER / CONTENTS

Sayfa / Page

| | |
|--|-----|
| A Life Cycle Costing Approach to Determine the Optimum Insulation Thickness of Existing Buildings <i>Yaşam Dönemi Maliyetlemesi Yaklaşımı İle Mevcut Binalarda Optimum Yalıtım Kalınlığının Belirlenmesi</i> Semih ÇAĞLAYAN, Beliz OZORHON, Gülbin ÖZCAN-DENİZ and Sadık YİĞİT | 1 |
| The Effects of CO₂, H₂O, and N₂ Dilutions on Pollutants of Shale Gas Combustion <i>Şeyl Gaz Yanmasının Kirleticileri Üzerinde CO₂, H₂O ve N₂ Dilüsyonlarının Etkileri</i> Suat ÖZTÜRK | 15 |
| Prediction of the Annual Heat Load of an Articulated Electric Urban Bus <i>Bir Elektrikli Körüklü Şehir İçi Otobüsün Yıllık Isı Yükü Kestirimi</i> M. Nicem TANYERİ and S. Çağlar BAŞLAMİŞLİ | 27 |
| Improving Performance and Thermoeconomic Optimization of an Existing Binary Geothermal Power Plant: A Case Study <i>Mevcut Bir Binary Jeotermal Santralin Performans Geliştirmesi ve Termodinamik Optimizasyonu: Bir Vaka Çalışması</i> Ceyhan YILMAZ | 37 |
| Validation of Aerodynamic Heating Prediction Tool <i>Aerodinamik Isınma Kestirim Aracının Doğrulanması</i> Buğra ŞİMŞEK, Sıtkı USLU and Mehmet Ali AK | 53 |
| Performance Evaluation for Thermal Architectures of Flue-Gas Assisted Organic Rankine Cycle Systems <i>Baca Gazı Destekli Organik Rankine Çevrimlerinin Termal Mimarileri İçin Performans Değerlendirmesi</i> Burak TURKAN and Akın Burak ETEMOĞLU | 65 |
| CFD Investigation of the Near-Surface Streamline Topology On a Simple Nonslender Delta Wing <i>Hesaplamalı Akışkanlar Dinamiği Kullanılarak Basit Üçgen Kanat Modelinde Yakın Yüzey Akış Yapısının İncelenmesi</i> Hacı SOGUKPINAR, Serkan CAG and Bulent YANIKTEPE | 77 |
| Yapay Sinir Ağları ve Uyarlamalı Sinirsel Bulanık Çıkarım Sistemi ile Francis Tipi Türbinler İçin Verim Tahminlemesi <i>ANN and ANFIS Performance Prediction Models For Francis Type Turbines</i> Ece AYLI ve Oğuzhan ULUCAK | 87 |
| Flow and Forced Heat Transfer from Tandem Square Cylinders Near a Wall <i>Duvar Yakınında Art Arada Yerleştirilmiş Kare Kesitli Silindirel Etrafında Akış ve Zorlanmış Taşınım İle Isı Geçişi</i> Özge YETİK and Necati MAHIR | 99 |
| A Novel Thermal Analysis for Cooking Process in Bulgur Production: Design Considerations, Energy Efficiency and Wastewater Diminution for Industrial Processes <i>Bulgur Üretiminde Pişirme İşlemine Yönelik Özgün Bir Isıl Analizi: Endüstriyel Süreçler İçin Tasarım Önerileri, Enerji Verimliliği ve Atıksu Azaltımı</i> İbrahim Halil YILMAZ and Mehmet Sait SÖYLEMEZ | 113 |
| Investigating the Effects of Plasma Actuator On the Flow Control Around NACA2415 Airfoil <i>Plazma Aktivatörün NACA2415 Airfoil Etrafında Akış Kontrolüne Etkilerinin Araştırılması</i> Aytaç SANLISOY and Yahya Erkan AKANSU | 131 |
| Theoretical Analysis of a Cascade Refrigeration System with Natural and Synthetic Working Fluid Pairs for Ultra Low Temperature Applications <i>Doğal ve Sentetik Soğutucu Akışkan Çiftleri Kullanılan Bir Kaskad Soğutma Sisteminin Ultra Düşük Sıcaklık Uygulamaları İçin Teorik Analizi</i> Barış YILMAZ, Ebru MANÇUHAN and Deniz YILMAZ | 141 |
| A Comparison of the Thermal Performance of a Conventional Fin Block and Partially Copper and Aluminum Foam Embedded Heat Sinks <i>Geleneksel Kanatçıklı Blok ve Kısmi Alüminyum ve Bakır Metal Köpük Yerleştirilmiş Isı Alıcıların Isıl Performanslarının Karşılaştırılması</i> S. Kaançan ATAER, Cemil YAMALI and Kahraman ALBAYRAK | 155 |
| Radiofrequency Ablation for Spherically-Shaped Hepatic Tumors <i>Küresel Şekilli Karaciğer Tümörleri İçin Radyofrekans Ablasyonu</i> Güven Hasret YILMAZ, Uğur Tuna YAY, Oğuz TURGUT, Burak TİĞLİ and Nuri Eren TÜRKÖĞLU | 167 |
| Enhancement of Heat Transfer by Heat Pipes with Piecewise Uniform Longitudinal Wick Profiles <i>Parçalı Ünitiform Boylamasına Fıtil Profilli Isı Boruları ile Isı Transferinin Arttırılması</i> Mehmed Akif PAKSOY and Salih Özen ÜNVERDİ | 177 |

Amaç/Objective

Isı bilimi ve tekniğinin geliştirilmesini teşvik etmek, ısı bilimi ve tekniği alanında özgün, teorik, sayısal ve deneysel çalışmaların yayınlanmasına olanak sağlamaktır. *To contribute to the improvement of thermal sciences and technology and publication of original, theoretical, numerical and experimental studies in thermal sciences and technology.*

İçerik/Content

Isı bilimi ve tekniği alanındaki özgün ve derleme makaleler. *Original and review articles in thermal sciences and technology.*

Değerlendirme/Evaluation

Dergi hakemli bir dergi olup, her bir makale konusunda uzman en az iki hakem tarafından değerlendirilir.

Each article published in this journal is evaluated by at least two referees.

Dergimiz Science Citation Index Expanded (SCIE), Engineering Index (EI), EBSCO ve Mühendislik ve Temel Bilimler Veri Tabanı (TÜBİTAK-ULAKBİM) tarafından taranmaktadır.
Indexed by Science Citation Index Expanded (SCIE), Engineering Index (EI), EBSCO and Engineering and Natural Sciences Data Base (TÜBİTAK-ULAKBİM).



A LIFE CYCLE COSTING APPROACH TO DETERMINE THE OPTIMUM INSULATION THICKNESS OF EXISTING BUILDINGS

Semih ÇAĞLAYAN*, Beliz ÖZORHON**, Gülbin ÖZCAN-DENİZ*** and Sadık YİĞİT****

*** Boğaziçi University, Department of Civil Engineering
Bebek 34342 Istanbul, Turkey,

*semih.caglayan@boun.edu.tr, **beliz.ozorhon@boun.edu.tr

*** Thomas Jefferson University, College of Architecture and the Built Environment
Philadelphia, PA 19144, USA, gulbin.deniz@jefferson.edu

**** The University of Sydney, School of Civil Engineering
NSW 2006 Australia, sadik.yigit@sydney.edu.au

(Geliş Tarihi: 17.12.2018, Kabul Tarihi: 13.11.2019)

Abstract: The ongoing global increase of energy prices and energy use has directed many researchers to study energy conservation strategies as an instrument of sustainable development. A common yet effective strategy is to insulate the exterior envelope of existing buildings in an attempt to improve energy efficiency. While an insulation application requires an initial investment, it helps the building to spend less energy during its operation. In order to sustain feasibility, it is crucial to find an insulation thickness that is cost-effective and especially applicable in developing countries. The objective of this study is to determine the optimum insulation thickness for existing buildings by using a representative building approach. For this purpose, insulation alternatives including 15 cm stone wool on ceilings and expanded polystyrene (EPS) on exterior walls at varying thicknesses were applied on a representative existing building. A variety of EPS thicknesses (from 1 cm to 20 cm) were analyzed as alternatives for the insulation application. Annual energy requirement of the building was calculated by the heat balance method by conducting a dynamic analysis. Life cycle costing (LCC) analysis was performed to find out which alternative results in the best economical outcome. The optimum insulation thicknesses were obtained for various climate regions by considering a number of scenarios with different discount and inflation rates. The results demonstrated the inadequacy of the national regulation's current insulation limits, as it was observed that the optimum insulation thicknesses were significantly greater than the limiting values in the national standard. To overcome this inadequacy, it is suggested to effectively improve energy efficiency by lowering the limiting heat transfer coefficients in the standard.

Keywords: Optimum insulation thickness, thermal insulation requirements, energy efficiency of existing buildings, life cycle costing.

YAŞAM DÖNEMİ MALİYETLEMESİ YAKLAŞIMI İLE MEVCUT BİNALARDA OPTİMUM YALITIM KALINLIĞININ BELİRLENMESİ

Özet: Enerji kullanımının ve enerji fiyatlarının devamlı bir şekilde artması birçok araştırmacıyı bir sürdürülebilir kalkınma aracı olan enerji tasarrufu stratejilerine yönlendirmiştir. Mevcut binaların dış cephelerinin yalıtımı enerji verimliliğinin artırılması için yaygın ve etkin bir yöntemdir. Yalıtım uygulamaları bir ilk yatırım maliyeti gerektirmesine karşın binanın gelecek senelerde daha az enerji harcamasını sağlar. Bu açıdan, özellikle gelişmekte olan ülkelerde, mali açıdan uygun bir yalıtım kalınlığının bulunması önem arz etmektedir. Bu çalışmanın amacı bir temsili bina yaklaşımı kullanarak mevcut binalar için optimum yalıtım kalınlığının belirlenmesidir. Bu amaçla, temsili bir mevcut bina için tavana 15 cm taş yünü ve dış duvarlara değişen kalınlıklarda genleşmiş polistiren (EPS) yalıtımı uygulanmıştır. Çeşitli EPS kalınlıkları (1 cm'den 20 cm'e) yalıtım alternatifleri olarak analiz edilmiştir. Binanın yıllık enerji gereksinimi dinamik analiz yapan ısı dengesi yöntemi ile belirlenmiştir. Yaşam dönemi maliyetlemesi analizi gerçekleştirilerek hangi alternatifin en iyi ekonomik sonucu verdiği belirlenmiştir. Optimum yalıtım kalınlıkları çeşitli iklim bölgeleri için farklı iskonto ve enflasyon oranlarını içeren birtakım senaryolar göz önünde bulundurularak elde edilmiştir. Sonuçlar ulusal standardın mevcut yalıtım limitlerinin yetersiz olduğunu göstermektedir. Optimum yalıtım kalınlıklarının ulusal standartta belirtilen sınırlayıcı değerlerden bariz bir şekilde daha büyük oldukları anlaşılmıştır. Bu verimsizliğin giderilmesi amacıyla standarttaki sınırlayıcı ısı transfer katsayılarının azaltılarak enerji verimliliğinin artırılması önerilmektedir.

Anahtar Kelimeler: Optimum yalıtım kalınlığı, ısı yalıtımı gereksinimleri, mevcut binaların enerji verimliliği, yaşam dönemi maliyetlemesi.

NOMENCLATURE

| | |
|--------------|--|
| d | Discount rate [%] |
| e | Inflation rate [%] |
| IRR | Internal rate of return [%] |
| h_{ci} | Inside convection coefficient [$W/m^2 \cdot ^\circ C$] |
| h_{co} | Outside convection coefficient [$W/m^2 \cdot ^\circ C$] |
| NS | Net savings [\$] |
| PBP | Payback period [years] |
| q_{CE} | Convective part of the internal loads [W] |
| q_{conv} | Convection heat transfer from walls to zone air [W] |
| q''_{conv} | Convection flux exchange with outdoor air [W/m^2] |
| q_{IV} | Sensible load due to ventilation and infiltration [W] |
| q''_{ki} | Conduction heat flux on inside face [W/m^2] |
| q''_{ko} | Conduction heat flux on outside face [W/m^2] |
| q''_{LWR} | Net long-wave-length radiation flux exchange with the air and surroundings [W/m^2] |
| q''_{LWS} | Long-wave radiation flux from equipment in the zone [W/m^2] |
| q''_{LWX} | Long-wave radiant exchange flux between zone surfaces [W/m^2] |
| q''_{sol} | Transmitted solar radiation from windows to inside surface [W/m^2] |
| q''_{sw} | Net short-wave radiation flux from lights to surface [W/m^2] |
| q_{SYS} | Heat transfer from heating system [W] |
| q''_{sol} | Absorbed direct and diffuse solar radiation heat flux (shortwave) [W/m^2] |
| SIR | Saving-to-investment ratio |
| T_a | Zone air temperature [$^\circ C$] |
| T_i | Inside surface temperature [$^\circ C$] |
| T_o | Outside surface temperature [$^\circ C$] |
| U | Heat transfer coefficient [$W/m^2 K$] |
| X_j | Outside conduction transfer function |
| Y_j | Cross conduction transfer function |
| Z_j | Inside conduction transfer function |
| Φ_j | Flux conduction transfer function |

INTRODUCTION

Sustainability of the planet depends mainly on three components including energy efficiency, using renewable energy, and energy savings (Morales et al. 2016). Conservation of energy has become an essential part of the national energy strategies since the energy crises in 1973. This is of extreme importance for developing countries, as they import energy mostly from abroad in order to meet their energy needs. The increase in population and urbanization of cities result in a rapid escalation of energy consumption. Building and construction industry is majorly responsible for the total primary energy consumption globally and it has had a continuous growth since 1960s (Maleviti et al. 2013). The industry is accountable for more than 20% of global energy consumption of delivered energy and about 10% of global greenhouse gas emissions, both in developing and developed countries. The potential for reducing

greenhouse gas emissions is the largest in the construction sector (IEO 2013).

There is an increasing trend in energy users, from individual home owners to corporations and even nations, to pursue energy efficiency (Nikoofard et al. 2015). Although the issue has been widely acknowledged since the 1970s, it is getting more important with the concern on climate change (Miguel et al. 2015). Energy efficiency has been mentioned as the best approach to keep energy demand under control and to facilitate a smooth transition towards a low-carbon future. This suggestion emphasizes the key role of residential sector due to having the highest cost-efficient potential to reduce CO₂ emissions (Ramos et al. 2015). In addition to reducing the energy consumption in buildings, there are alternative ways to save energy. An approach to reduce heat loss includes the application of optimum insulation thicknesses to external walls. Wall and roof insulation are known for providing an increased amount of energy savings in buildings compared to traditional methods.

In terms of building insulation, various studies have also been performed to establish the optimum insulation thickness. The optimum insulation thicknesses were determined for different wall structures in Palestine (Hasan 1999), for four cities in China (Yu et al. 2009), for Tunisian buildings (Daouas 2011), for different types of building walls in India (Mishra et al. 2012), for hot regions of India (Sundaram and Bhaskaran 2014), for external walls on different orientations in Greece (Axaopoulou et al. 2014), and in Cameroon as a wet and hot tropical climate (Nematchoua et al. 2015). In all of the prementioned studies, the optimum insulation thicknesses were determined according to a theoretically derived net saving/cost formula, which did not consider the building as a whole. The insulation thickness, which made the derivative of the net saving formula equal to zero, was considered as the optimum thickness.

In this study, a representative building approach is proposed to determine the optimum insulation thickness for existing buildings in four different climate regions. There has not been any study specifically done for existing buildings, where the optimum insulation thickness calculations and the limitations in national standards can be representative for energy efficiency in developing countries. Additionally, the proposed approach enables not only determining the optimum insulation option, but also generating the cash flow diagram for each insulation alternative. Therefore, financial parameters such as net savings (NS), internal rate of return (IRR), savings-to-investment ratio (SIR), and payback period (PBP) can be effectively calculated for each insulation alternative. Previously applied methods have only provided NS and PBP, whereas other parameters were missing. This study fills this gap by questioning the optimality of the limitations in the

national standard, which can be adapted to other developing countries based on their own standards.

The representative building is selected as a traditional five-story building. The cost of insulation is determined by taking the average of the offers obtained from three different general contracting companies to make sure fair and feasible cost data is used. The annual energy savings are calculated by considering the annual energy requirements of the uninsulated and insulated building. The annual energy requirement is calculated according to a heat balance based software developed by Yigit and Ozorhon (2018) for four climate regions defined in the national standard. The cost of insulation application and future savings resulting from decreased energy requirements are reflected in the life cycle costing (LCC) analysis. Optimization is performed to determine the optimum insulation thickness on the exterior walls that would be the most feasible alternative economically.

RESEARCH BACKGROUND

A number of studies have been performed to investigate energy consumption and thermal insulation in buildings from various perspectives. Dylewski and Adamczyk (2011) studied both the environmental and economic benefits of thermal insulation on the exterior walls. The benefits were obtained for several versions of thermal insulation. It was concluded that thermal insulation made of polystyrene foam or ecofibre provided the best results. Briga-Sa et al. (2013) suggested using woven fabric waste (WFW) and woven fabric subwaste (WFS) for thermal insulation in buildings. The results of the study showed that implementation of WFW and WFS in exterior double walls could improve the thermal behavior 56% and 30%, respectively. Yildiz et al. (2014) investigated the impacts of energy efficiency measures on energy consumption in Eskisehir, Turkey. Highest energy savings (37%) were obtained by applying insulation on exterior walls, roof floor, and basement and replacing the windows. Asdrubali et al. (2015) reported a state of art of sustainable building insulation materials that are made of natural or recycled content. A recycled cotton insulator was shown to exhibit thermal insulation features comparable to EPS, extruded polystyrene (XPS), and sheep wool. Kaya et al. (2016) analyzed energy savings of thermal insulation for buildings in Erzincan, Turkey. Annual energy savings were observed to go up to 43.8% with the application of 4 cm XPS. Cristina et al. (2017) compared two different refurbishment scenarios, high investment and low investment, for an Italian vernacular building. The high investment scenario with greater insulation materials and glazing systems was realized to result in a higher income, despite its higher initial investment cost. Lucchi et al. (2017) assessed the economic benefits of energy retrofitting in historic buildings with a particular focus on the insulation materials. They identified EPS, XPS, mineral and flexible wood fibers, glass mineral wool,

and rock wool as the cost-effective materials. It was also reported that PBP of an insulation system of 0.20 m changes between 5 and 18 years. Serrano et al. (2017) conducted a study to assess the residential energy consumption (heating and cooling) trends and drivers for Europe. Even though a consistent trend was detected for the drivers during the studied time period, heating and cooling energy consumption was observed to follow different trends when considered globally or at a country level.

Several studies have focused specifically on determining the optimum insulation thickness. For instance, Yu et al. (2009) studied the optimum insulation thickness for four cities in China. Both the heating and cooling energies were considered in the study. The optimum insulation thicknesses varied between 5.3 and 23.6 cm. Daouas (2011) calculated the optimum insulation thickness of walls in Tunisian buildings. Electricity and natural gas were considered as energy sources for cooling and heating, respectively. The optimum insulation thicknesses varied between 10.1 and 11.7 cm. In another study, Mishra et al. (2012) determined the optimum insulation thickness in India for different types of building walls. The optimum insulation thicknesses varied between 5.2 and 7.4 cm. Kaynakli (2013) determined the optimum insulation thickness and payback periods for the building walls in Turkey. The results showed that the optimum insulation thickness can go up to 16.6 cm depending on the city. Cuce et al. (2014) focused on the optimum insulation thickness and the environmental impacts of aerogel-based thermal superinsulation for the climate conditions of Nottingham. Sundaram and Bhaskaran (2014) studied the optimum insulation thickness of walls in hot regions of India. Only cooling energy was considered as the heating energy is zero in these regions. Electricity was used as the only energy source. Nematchoua et al. (2015) detected the optimal thermal insulation thickness in Cameroon as a wet and hot tropical climate. The optimum insulation thickness values were found to be higher than 9 cm and approximately 80% energy saving was obtained for the south-oriented wall. A higher optimum insulation thickness was observed in the concrete block wall than in compressed stabilized earth block wall. Kon and Yuksel (2016) calculated the optimum insulation thickness for an exemplary building in Balikesir. The optimum insulation thicknesses were calculated for exterior walls, basement, and roof floor. Ashouri et al. (2016) used exergetic life cycle assessment method to specify the optimum insulation thickness in a building wall. Optimal thicknesses for rockwool and glasswool were respectively specified as 9.8 cm and 21.9 cm based on environmental impact analysis; and 1.2 cm and 1.8 cm based on exergetic life cycle cost analysis. Nematchoua et al. (2017) studied the optimum insulation thickness of walls for buildings in Yaounde (equatorial region) and Garoua (tropical region) cities in Cameroon. The optimum insulation thickness and corresponding energy savings were

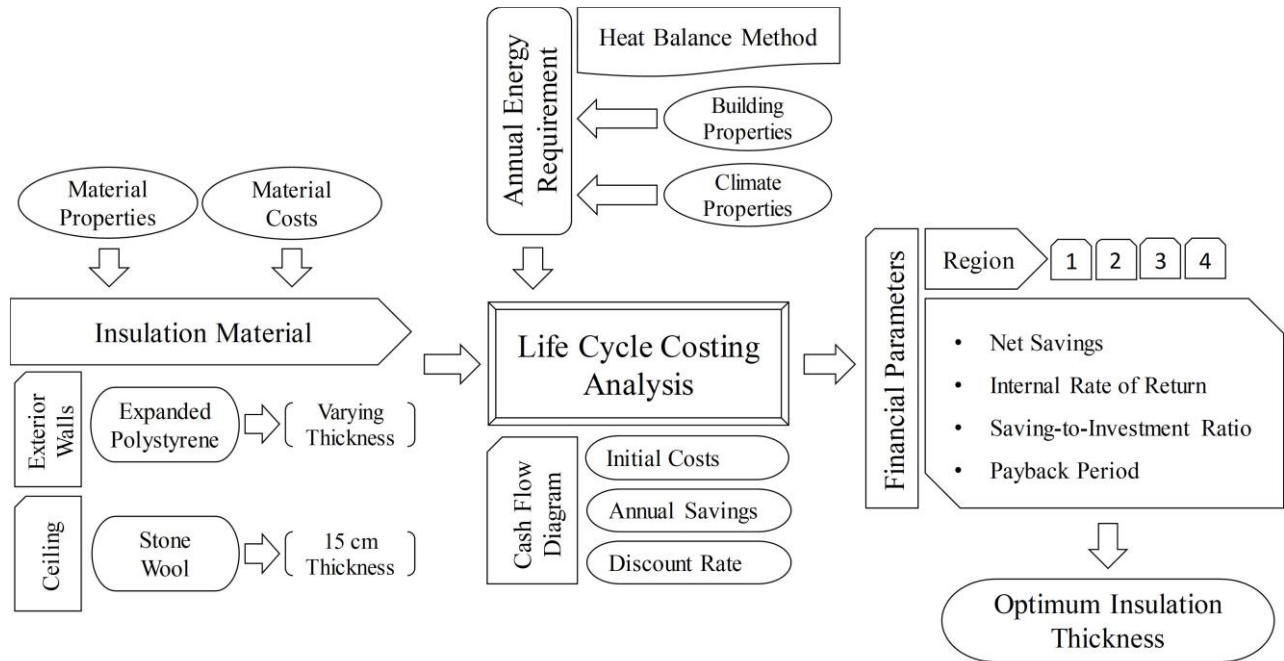


Figure 1. Flowchart of methodology

determined as 8 cm and 51.69 \$/m² in Yaounde; and 11 cm and 97.82 \$/m² in Garoua. Considering the approaches of the previous studies, this study adopts LCC to evaluate the insulation options on a typical existing building. This paper aims to define the optimum insulation thickness of buildings in the four different climate regions stated in the national standard. The optimum EPS thicknesses are determined for each climate region by using LCC, as described in the following sections.

RESEARCH METHODOLOGY

The flowchart of the representative building approach methodology is shown in Figure 1. Through this method, insulation alternatives are applied to a representative existing building. The methodology starts with the selection of insulation material based on material properties and costs. EPS is used for exterior walls, while stone wool is used for the ceiling. Meanwhile, annual energy requirements are derived from a heat balance based software developed by Yigit and Ozorhon (2018) based on building properties and various climate zones. Both information is used to perform LCC, which initiates cash flow diagrams and finally the financial parameters such as NS, IRR, SIR, and PBP. The aim is to determine the optimum EPS thickness that results in the best economic outcomes. The financial parameters and LCC results are used to determine the optimum insulation thicknesses for each climate region.

Annual energy requirements are calculated for uninsulated and insulated versions of a typical existing building and annual energy savings are obtained by taking the difference. Annual energy saving values are

calculated for each insulation alternative (1 cm to 20 cm EPS application), separately. Considering the initial insulation cost and the following annual energy savings, cash flow diagrams are generated and net savings are calculated for each insulation thickness. The insulation thickness resulting in the highest net saving value is regarded as the optimum insulation thickness.

Building Properties

LCC is applied on insulation applications for a typical five-story existing building. The uninsulated building has a length of 25 m, a width of 20 m and each floor has a height of 3 m. Net height of each floor is 2.6 m and gross volume (V_{gross}) of the building is 7,500 m³. The areas of the windows are 50 m², 20 m², 40 m² and 20 m² for south, north, east and west directions, respectively. It is assumed that natural ventilation is used for air-conditioning.

The building envelope cross sections are shown for the uninsulated and insulated cases in Figure 2 and Figure 3, respectively. While no change is considered for the basement (as practically this is the case for insulation application in existing buildings), the ceiling is insulated with stone wool at a thickness of 15 cm. The exterior walls, both infilled and reinforced, are insulated with EPS at varying thicknesses.

Calculation of Annual Energy Requirements

The annual energy requirement of the building was calculated by using a heat balance based software developed by Yigit and Ozorhon (2018). The heat balance method is based on hourly dynamic thermodynamic calculations. In this method, the solar

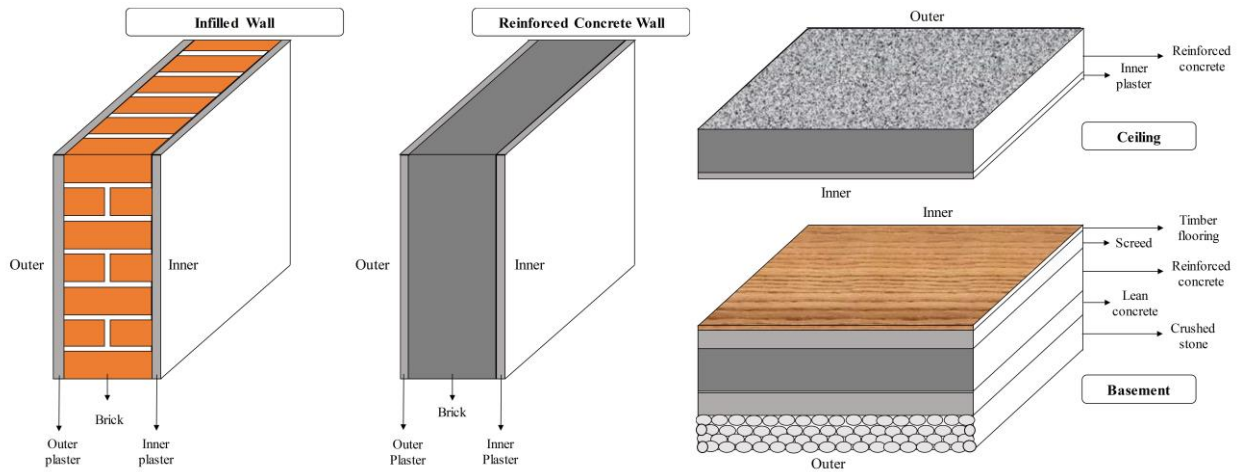


Figure 2. Building envelope cross section for the uninsulated case

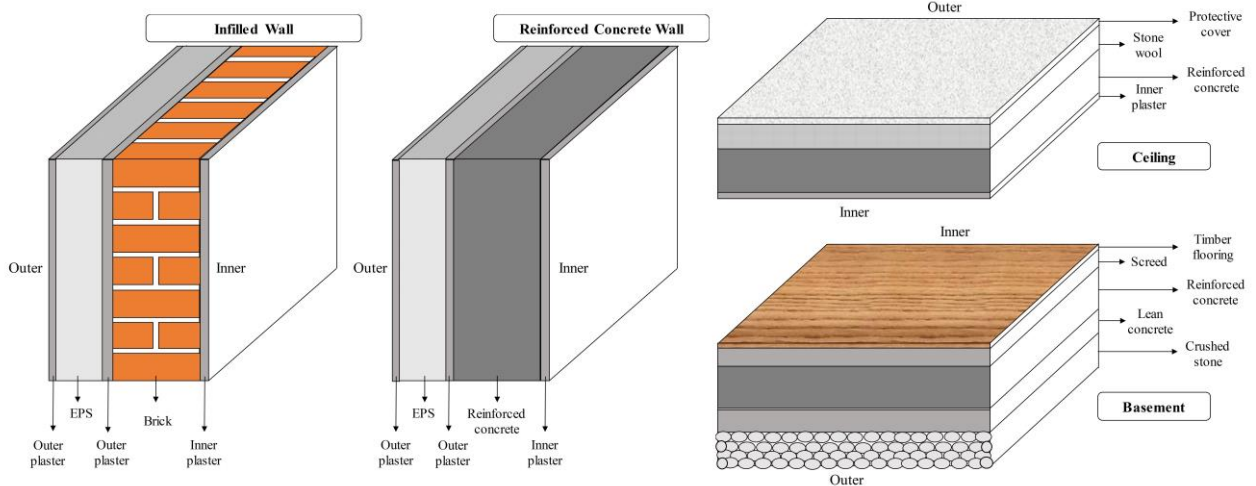


Figure 3. Building envelope cross section for the insulated case

heat gains and internal loads that are caused by occupants, appliances, and lightings are calculated in detail. The internal surface temperatures of the buildings are calculated separately. The heat balance method reduces the number of assumptions and its models are closest to real physical buildings. The method takes its name from the first law of thermodynamics. "Energy is conserved" in the inner and outer surfaces and the zone air of the buildings (ASHRAE 2013). The formulation of the heat balance method for cooling load calculations was published in 1997 and accepted to be the most scientifically rigorous method (Pedersen et al. 1997). Designers use the heat balance method to calculate instantaneous heating and cooling loads (ASHRAE 1997).

The procedure of heat balance method calculations consists following processes (Spitler 2013);

- Outside face heat balance
- Wall conduction process
- Inside face heat balance
- Air heat balance

Outside Face Heat Balance

There are four heat exchange processes between outside zone air and outside surface of the walls and the heat balance of the exterior surface can be formulated as:

$$q''_{\alpha sol} + q''_{LWR} + q''_{conv} - q''_{ko} = 0 \quad (1)$$

Wall Conduction Process

Wall conduction process can be conducted in various ways (Spitler 2013):

- Numerical finite difference
- Numerical finite element
- Transform Methods
- Time Series Methods

To make simultaneous calculations for both surfaces of the walls, conduction transfer function coefficients are utilized. Conduction transfer function procedures

provide a faster calculation than numerical methods with a little loss of generality.

The general form for inside heat flux:

$$q_{ki}''(t) = -Z_0 T_{i,t} - \sum_{j=1}^{nz} Z_j T_{i,t-j\delta} + Y_0 T_{o,t} + \sum_{j=1}^{nz} Y_j T_{o,t-j\delta} + \sum_{j=1}^{nq} \Phi_j q_{ki,i,t-j\delta}'' \quad (2)$$

The general form for outside heat flux is:

$$q_{ko}''(t) = -Y_0 T_{i,t} - \sum_{j=1}^{nz} Z_j T_{i,t-j\delta} + X_0 T_{o,t} + \sum_{j=1}^{nz} X_j T_{o,t-j\delta} + \sum_{j=1}^{nq} \Phi_j q_{ko,i,t-j\delta}'' \quad (3)$$

Inside Face Heat Balance

Inside face heat balance is generally modeled by four coupled heat transfer components (ASHRAE 1997):

- Conduction through the building walls
- Convection from walls to zone air
- Short-wave radiant absorption and reflection
- Long-wave radiant interchange

Long-wave radiation includes the emittance from people and equipment while shortwave radiation consist the radiation enters the zone through windows and emitted from internal sources such as lights.

The general form of inside face heat balance can be formulated as:

$$q_{LWX}'' + q_{SW}'' + q_{LWS}'' + q_{ki}'' + q_{sol}'' + q_{conv}'' = 0 \quad (4)$$

Air Heat Balance

The components contributing to the heat balance equation are: convection from inside surface of the walls, infiltration and ventilation, convective part of internal loads and heating, ventilation, and air conditioning (HVAC) system.

$$q_{conv} + q_{CE} + q_{IV} + q_{sys} = 0 \quad (5)$$

Heat Balance Procedure

The general zone for a heat balance procedure has 12 inside surfaces and 12 outside surfaces; four wall surfaces, five window surfaces (for walls and the roof), slab surface and roof surface. The heat balance method consists for each element's inside and outside face and HVAC system as variables for 24 hours. This makes a total of about 600 variables. Therefore, a routine needed to iterate all these variables for 24 hours in a day. In the following part of the study, the mathematical procedure

of heat balance calculation for generalized zone will be described.

The variables of the procedure are 12 inside face and 12 outside face for each 24 hours of the day. Subscript "i" is assigned as the surface index subscript and "j" is assigned as the hour index.

The heat balance equation for outside surfaces:

$$T_{soi,j} = \frac{\sum_{k=1}^{nz} T_{si,j-k} Y_{i,k}}{Z_{i,0} + h_{coi,j}} - \frac{\sum_{k=1}^{nz} T_{soi,j-k} Z_{i,k} + \sum_{k=1}^{nq} \Phi_{i,k} q_{ko,i,j-k}''}{Z_{i,0} + h_{coi,j}} + \frac{q_{\alpha sol,i,j}'' + q_{LWR,i,j}'' + T_{si,j} Y_{i,0} + T_o j h_{coi,j}}{Z_{i,0} + h_{coi,j}} \quad (6)$$

The heat balance equation for inside surfaces:

$$T_{sii,j} = \frac{T_{soi,j} Y_{i,0} + \sum_{k=1}^{nz} T_{soi,j-k} Y_{i,k}}{Z_{i,0} + h_{ci,j}} - \frac{\sum_{k=1}^{nz} T_{si,j-k} Z_{i,k} - \sum_{k=1}^{nq} \Phi_{i,k} q_{ki,i,j-k}''}{Z_{i,0} + h_{ci,j}} + \frac{T_a j h_{ci,j} + q_{LWS}'' + q_{LWX,i,j}'' + q_{SW}'' + q_{sol}''}{Z_{i,0} + h_{ci,j}} \quad (7)$$

The remaining equation for the heat balance method is derived from air heat balance equation:

$$q_{sys,j} = \sum_{i=1}^{12} A_i h_{c,i} (T_{sii,j} - T_a j) + q_{CE} + q_{IV} \quad (8)$$

Heat Balance Iterative Solution Procedure

- The steps of heat balance calculations are listed below:
1. Identify the area properties, face temperatures for surfaces and other properties, for all 24 hours.
 2. Incident and transmitted solar fluxes for the building surfaces calculated.
 3. The calculated transmitted solar energy is distributed to all surfaces inside (incident transmitted solar radiation is intercepted by floor).
 4. Internal load quantities, for all 24 hours (people, lighting, machines etc.).
 5. Long-wave, short-wave, and convective energy from internal loads to all surfaces for all 24 hours is calculated.
 6. Infiltration and ventilation loads are calculated for all 24 hours.

7. Iteration is utilized for heat balance equations according to following pseudo-code scheme (Pedersen et al. 1997):

For Day = 1 to Maxdays
 For j = 1 to 24 (Hours in a day)
 For SurfaceIteration = 1 to MaxIter
 For i=1 to 12 (Number of Zone Surfaces)
 Evaluate Equation of T_{si} and T_{so}
 Next Surface "i"
 Next SurfaceIteration
 Evaluation Equation of q_{sys}
 Next "j"
 If not converged, Next Day
 Display Results

8. Present the results.

Limitations of the National Standard

In the national standard, it is stated that "when substantial repair, amendment and additions are made to the whole or independent sections of the existing buildings, the limiting heat transfer coefficient values should be observed in terms of providing the values equal or smaller than these for the section in which applications are made" (TSI 2008). The limiting values are shown in Table 1, where U_{ew} , U_{ce} , U_{bs} , and U_{gl} represent the heat transfer coefficients of exterior walls, ceiling, basement, and glazing, respectively.

Table 1. The limiting values for existing buildings (TSI 2008)

| Region | U_{ew} (W/m ² K) | U_{ce} (W/m ² K) | U_{bs} (W/m ² K) | U_{gl} (W/m ² K) |
|----------|----------------------------------|----------------------------------|----------------------------------|----------------------------------|
| Region 1 | 0.70 | 0.45 | 0.70 | 2.4 |
| Region 2 | 0.60 | 0.40 | 0.60 | 2.4 |
| Region 3 | 0.50 | 0.30 | 0.45 | 2.4 |
| Region 4 | 0.40 | 0.25 | 0.40 | 2.4 |

Life Cycle Costing Analysis

An insulation application possesses an initial cost and annual savings in the following years. The initial or the capital cost is the cost of insulation application. It includes the material cost, the auxiliary items cost and the application cost. It is obtained by taking offers from companies and taking the average of them. Annual savings are the savings achieved by the reductions in the operational cost of buildings. The operational cost represents the annual energy requirement of buildings. After an insulation application, the annual energy requirement decreases. As a consequence, annual savings are achieved due to the decrease in operational costs.

LCC method predicts savings based on the initial cost of insulations and the annual savings due to decreased operational costs. Annual savings occur over a certain period of time, which is assumed to be 20 years. Previous studies have assumed lifetimes between 10 to 30 years (Yu et al. 2009; Daouas 2011; Mishra et al. 2012; Sundaram and Bhaskaran 2014; Cuce et al. 2014). After determining the initial cost and savings over 20

years, the cash flow diagram is generated. The savings are discounted back to present with an appropriate discount rate in order to find net savings (NS), internal rate of return (IRR), savings-to-investment ratio (SIR) and payback period (PBP).

RESULTS AND DISCUSSION

In this study, different types of insulation are applied on the building envelope, specifically on the ceilings and exterior walls. The ceiling is insulated with stone wool that has a thickness of 15 cm. The resultant conductance is 0.219. This value satisfies the requirements for all the regions as shown in the column U_{ce} of the Table 1. The exterior walls are insulated with EPS with varying thicknesses. The resultant heat transfer coefficient values must be lower than the values stated in the column U_{ew} . The shaded values in Table 2 indicate that these insulation thicknesses satisfy the minimum conditions as defined by the standard. The limiting values in the national standard are identified as 4 cm, 5 cm, 6 cm, and 8 cm in Region 1, Region 2, Region 3, and Region 4, respectively.

Table 2. Heat transfer coefficient values of insulation applications

| U_{ew} values (W/m ² K) | Region 1 $U_{ew}'=0.7$ | Region 2 $U_{ew}'=0.6$ | Region 3 $U_{ew}'=0.5$ | Region 4 $U_{ew}'=0.4$ |
|---|---------------------------|---------------------------|---------------------------|---------------------------|
| None | 3.24 | 3.24 | 3.24 | 3.24 |
| 1 | 1.62 | 1.62 | 1.62 | 1.62 |
| 2 | 1.11 | 1.11 | 1.11 | 1.11 |
| 3 | 0.84 | 0.84 | 0.84 | 0.84 |
| 4 | 0.68 | 0.68 | 0.68 | 0.68 |
| 5 | 0.57 | 0.57 | 0.57 | 0.57 |
| 6 | 0.49 | 0.49 | 0.49 | 0.49 |
| 7 | 0.43 | 0.43 | 0.43 | 0.43 |
| 8 | 0.38 | 0.38 | 0.38 | 0.38 |
| 9 | 0.34 | 0.34 | 0.34 | 0.34 |
| 10 | 0.31 | 0.31 | 0.31 | 0.31 |
| 11 | 0.29 | 0.29 | 0.29 | 0.29 |
| 12 | 0.27 | 0.27 | 0.27 | 0.27 |
| 13 | 0.25 | 0.25 | 0.25 | 0.25 |
| 14 | 0.23 | 0.23 | 0.23 | 0.23 |
| 15 | 0.22 | 0.22 | 0.22 | 0.22 |
| 16 | 0.20 | 0.20 | 0.20 | 0.20 |
| 17 | 0.19 | 0.19 | 0.19 | 0.19 |
| 18 | 0.18 | 0.18 | 0.18 | 0.18 |
| 19 | 0.17 | 0.17 | 0.17 | 0.17 |
| 20 | 0.17 | 0.17 | 0.17 | 0.17 |

Annual Energy Requirements & Savings

Table 3 and Figure 4 show the annual energy requirements calculated for 4 climate regions. It is observed that a considerable difference exists in the energy consumption values of the building in different climate regions. Heating energy consumption of the uninsulated building in Region 4 is roughly 9-10 times greater than its energy consumption in Region 1. On the other hand, cooling energy consumption in Region 1 is about 7 times higher than Region 4. Consequently, different optimum thickness values are expected to be

Table 3. Annual energy requirements (kWh/year)

| Annual Energy Requirements | | Heating Energy Requirement | | | | Cooling Energy Requirement | | | |
|----------------------------|-------|----------------------------|----------|----------|----------|----------------------------|----------|----------|----------|
| | | Region 1 | Region 2 | Region 3 | Region 4 | Region 1 | Region 2 | Region 3 | Region 4 |
| Insulation Thickness (cm) | None | 37,193 | 134,880 | 211,900 | 356,650 | 178,830 | 76,368 | 45,913 | 25,531 |
| | 1 | 26,461 | 105,073 | 167,520 | 285,590 | 153,290 | 66,461 | 40,496 | 25,459 |
| | 2 | 12,924 | 64,060 | 108,910 | 190,630 | 140,930 | 66,175 | 40,430 | 25,382 |
| | 3 | 11,991 | 58,860 | 101,210 | 178,030 | 139,150 | 66,101 | 40,362 | 25,294 |
| | 4 | 11,265 | 55,240 | 96,051 | 169,580 | 137,700 | 66,024 | 40,283 | 25,200 |
| | 5 | 10,669 | 52,690 | 92,403 | 163,550 | 136,530 | 65,933 | 40,198 | 25,094 |
| | 6 | 10,235 | 50,780 | 89,730 | 159,080 | 135,560 | 65,838 | 40,103 | 24,973 |
| | 7 | 9,847 | 49,220 | 87,711 | 155,630 | 134,760 | 65,735 | 39,993 | 24,838 |
| | 8 | 9,488 | 48,040 | 86,139 | 152,930 | 134,130 | 65,662 | 39,671 | 24,483 |
| | 9 | 9,140 | 46,920 | 84,905 | 150,690 | 133,590 | 65,618 | 39,130 | 24,106 |
| | 10 | 8,808 | 45,810 | 83,699 | 148,700 | 133,340 | 65,587 | 38,272 | 23,453 |
| | 11 | 8,492 | 44,780 | 82,553 | 146,720 | 133,170 | 65,557 | 37,459 | 22,768 |
| | 12 | 8,188 | 43,850 | 81,477 | 144,760 | 133,070 | 65,491 | 36,875 | 22,271 |
| | 13 | 7,966 | 43,310 | 80,421 | 142,820 | 133,050 | 65,461 | 36,340 | 21,951 |
| | 14 | 7,831 | 42,810 | 79,415 | 140,940 | 133,030 | 65,382 | 36,197 | 21,849 |
| | 15 | 7,711 | 42,310 | 78,559 | 139,230 | 133,020 | 65,342 | 36,028 | 21,713 |
| | 16 | 7,601 | 41,790 | 77,925 | 137,870 | 133,020 | 65,262 | 35,950 | 21,548 |
| | 17 | 7,508 | 41,360 | 77,352 | 136,870 | 133,020 | 65,198 | 35,832 | 21,339 |
| | 18 | 7,424 | 40,967 | 76,804 | 136,070 | 133,020 | 65,139 | 35,637 | 21,027 |
| | 19 | 7,349 | 40,611 | 76,300 | 135,350 | 133,010 | 65,088 | 35,347 | 20,508 |
| 20 | 7,289 | 40,284 | 75,834 | 134,680 | 133,010 | 65,075 | 34,880 | 20,508 | |

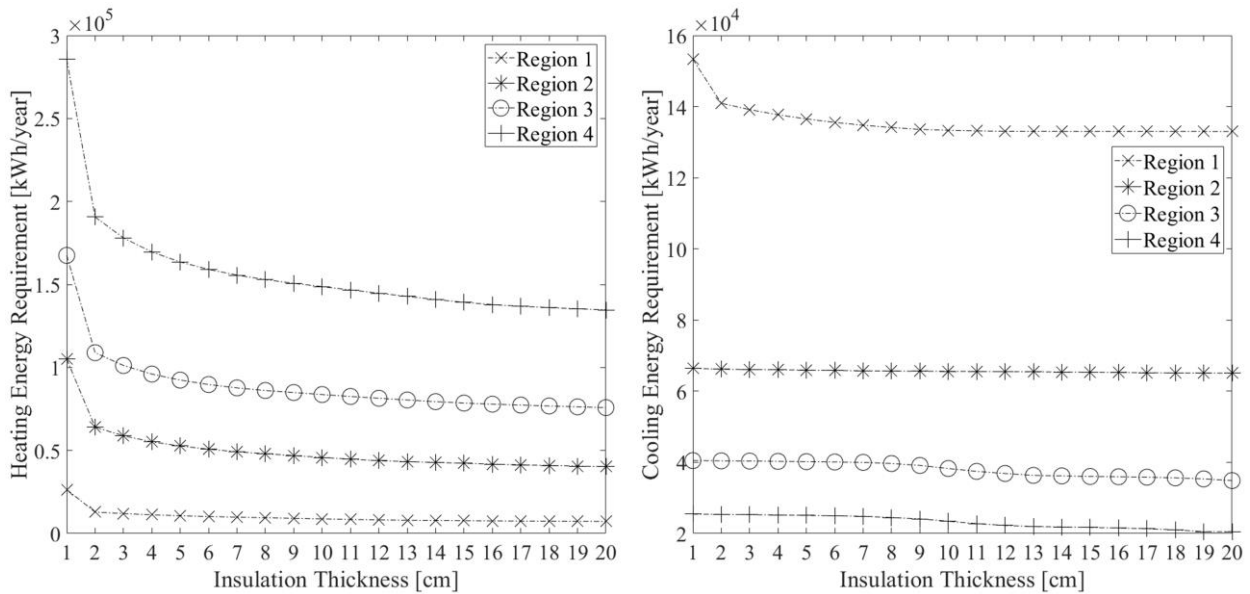


Figure 4. Annual energy requirements

determined for each region. It can also be inferred that insulation implementation in existing buildings can theoretically decrease the heating and cooling energy consumptions up to 60-80% and 15-25%, respectively. However, it does not imply that the insulation thickness, which provides the maximum energy conservation, is the optimum one. Considering the fact that increasing insulation thicknesses would bring additional costs, the optimum insulation thickness can be described as the one that provides maximum net benefit, which is obtained by subtracting the cost from the benefits obtained.

Table 4 and Figure 5 present the annual energy savings. It is noticed that the minimum insulation thicknesses that satisfy the conditions in the standard can provide heating energy savings between 26 kWh/year and 204 kWh/year in different climate regions. However, it is possible to obtain an additional heating energy saving up to 15%, which indicates that there is still room for achieving better economic outcomes by implementing thicker insulations.

Table 4. Annual energy savings (kWh/year)

| Annual Energy Savings | | Heating Energy Savings | | | | Cooling Energy Savings | | | |
|---------------------------|--------|------------------------|----------|----------|----------|------------------------|----------|----------|----------|
| | | Region 1 | Region 2 | Region 3 | Region 4 | Region 1 | Region 2 | Region 3 | Region 4 |
| Insulation Thickness (cm) | None | 0 | 0 | 0 | 0 | 0 | 0 | 0 | 0 |
| | 1 | 10,732 | 29,807 | 44,380 | 71,060 | 25,540 | 9,907 | 5,417 | 72 |
| | 2 | 24,269 | 70,820 | 102,990 | 166,020 | 37,900 | 10,193 | 5,483 | 149 |
| | 3 | 25,202 | 76,020 | 110,690 | 178,620 | 39,680 | 10,267 | 5,551 | 237 |
| | 4 | 25,928 | 79,640 | 115,849 | 187,070 | 41,130 | 10,344 | 5,630 | 331 |
| | 5 | 26,524 | 82,190 | 119,497 | 193,100 | 42,300 | 10,435 | 5,715 | 437 |
| | 6 | 26,958 | 84,100 | 122,170 | 197,570 | 43,270 | 10,530 | 5,810 | 558 |
| | 7 | 27,346 | 85,660 | 124,189 | 201,020 | 44,070 | 10,633 | 5,920 | 693 |
| | 8 | 27,705 | 86,840 | 125,761 | 203,720 | 44,700 | 10,706 | 6,242 | 1,048 |
| | 9 | 28,053 | 87,960 | 126,995 | 205,960 | 45,240 | 10,750 | 6,783 | 1,425 |
| | 10 | 28,385 | 89,070 | 128,201 | 207,950 | 45,490 | 10,781 | 7,641 | 2,078 |
| | 11 | 28,701 | 90,100 | 129,347 | 209,930 | 45,660 | 10,811 | 8,454 | 2,763 |
| | 12 | 29,005 | 91,030 | 130,423 | 211,890 | 45,760 | 10,877 | 9,038 | 3,260 |
| | 13 | 29,227 | 91,570 | 131,479 | 213,830 | 45,780 | 10,907 | 9,573 | 3,580 |
| | 14 | 29,362 | 92,070 | 132,485 | 215,710 | 45,800 | 10,986 | 9,716 | 3,682 |
| | 15 | 29,482 | 92,570 | 133,341 | 217,420 | 45,810 | 11,026 | 9,885 | 3,818 |
| | 16 | 29,592 | 93,090 | 133,975 | 218,780 | 45,810 | 11,106 | 9,963 | 3,983 |
| | 17 | 29,685 | 93,520 | 134,548 | 219,780 | 45,810 | 11,170 | 10,081 | 4,192 |
| | 18 | 29,769 | 93,913 | 135,096 | 220,580 | 45,810 | 11,229 | 10,276 | 4,504 |
| | 19 | 29,844 | 94,269 | 135,600 | 221,300 | 45,820 | 11,280 | 10,566 | 5,023 |
| 20 | 29,904 | 94,596 | 136,066 | 221,970 | 45,820 | 11,293 | 11,033 | 5,023 | |

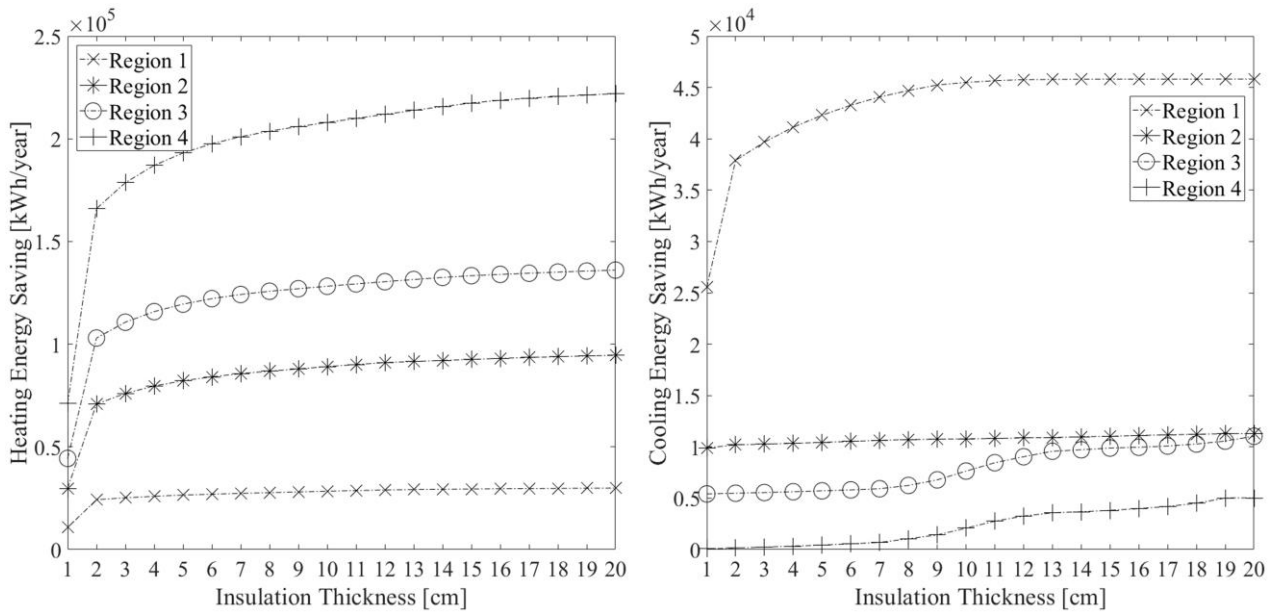


Figure 5. Annual energy savings

Cost of Insulation

The cost of insulation is determined by taking offers from three general contracting companies. The offers are received in the same format so that they can be compared and their averages can be taken in order to determine the cost of insulation. The total cost of insulation, as shown in Table 5, is determined by taking

the average of the three offers. It should be noted that the costs are presented in United States (U.S.) Dollars (\$). As it can be seen from the table that for EPS, the material and installation costs increase, as the insulation thickness increases. There is one average cost for stone wool insulation, as only one insulation thickness is used.

Table 5. The total cost of insulation applications

| EPS Insulation Thickness | Material Cost (\$/m ²) | Auxiliary Items Cost (\$/m ²) | Installation Cost (\$/m ²) | Total Unit Cost (\$/m ²) | Total Cost (\$) |
|--------------------------|------------------------------------|---|--|--------------------------------------|-----------------|
| 1 cm | 0.71 | 4.41 | 7.00 | 12.12 | 14,727.74 |
| 2 cm | 1.18 | 4.41 | 7.00 | 12.59 | 15,300.71 |
| 3 cm | 1.91 | 4.41 | 7.00 | 13.31 | 16,177.56 |
| 4 cm | 2.63 | 4.41 | 7.00 | 14.04 | 17,054.41 |
| 5 cm | 3.35 | 4.52 | 7.00 | 14.86 | 18,057.43 |
| 6 cm | 4.07 | 4.52 | 7.00 | 15.58 | 18,934.28 |
| 7 cm | 4.79 | 4.59 | 7.09 | 16.47 | 20,010.47 |
| 8 cm | 5.51 | 4.59 | 7.18 | 17.28 | 20,997.72 |
| 9 cm | 6.24 | 4.67 | 7.18 | 18.08 | 21,969.82 |
| 10 cm | 6.96 | 4.67 | 7.18 | 18.80 | 22,846.67 |
| 11 cm | 7.79 | 5.01 | 7.27 | 20.07 | 24,389.04 |
| 12 cm | 8.53 | 5.09 | 7.27 | 20.88 | 25,373.13 |
| 13 cm | 9.26 | 5.15 | 7.27 | 21.68 | 26,338.30 |
| 14 cm | 9.99 | 5.15 | 7.45 | 22.59 | 27,448.55 |
| 15 cm | 10.72 | 5.29 | 7.45 | 23.46 | 28,508.34 |
| 16 cm | 11.58 | 5.29 | 7.45 | 24.32 | 29,549.21 |
| 17 cm | 12.23 | 5.35 | 7.63 | 25.22 | 30,637.39 |
| 18 cm | 12.96 | 5.46 | 7.63 | 26.05 | 31,656.17 |
| 19 cm | 13.70 | 5.52 | 7.81 | 27.03 | 32,845.28 |
| 20 cm | 14.43 | 5.52 | 7.81 | 27.77 | 33,737.90 |
| EPS Insulation Thickness | Material Cost (\$/m ²) | Auxiliary Items Cost (\$/m ²) | Installation Cost (\$/m ²) | Total Unit Cost (\$/m ²) | Total Cost (\$) |
| 15 cm | 16.87 | 5.94 | 9.14 | 31.96 | 15,979.66 |

Optimum Insulation Thicknesses

Cash flow diagram is generated using the initial cost and the operational savings over 20 years. The initial cost is the cost of insulation, which is calculated by adding the cost of 15 cm stone wool insulation on the ceiling to the cost of EPS insulation at various thicknesses on the exterior walls. The operational savings are the savings resulted from the decrease in annual energy requirements of the building. An operational saving in a specific year is determined by multiplying the annual energy saving amount (kWh) by the average energy price in this year, which is the average of the prices (\$/kWh) at the beginning and at the end of the corresponding year. The energy prices in the following years are determined by the following formula:

$$EnergyPrice(n) = EnergyPrice(0) * (1+e)^n \quad (9)$$

where Energy Price (n) is the energy price in year n, e is the inflation rate, and n is the year. Here, Energy Price (0) is the energy price in the base year, which is 0.038 \$/kWh and 0.161 \$/kWh for natural gas and electricity, respectively.

The operational saving in year “n” can be formulated as follows:

$$OperationalSaving(n) = \frac{AnnualEnergySaving(kWh) * EnergyPrice(n-1) + EnergyPrice(n)}{2} \quad (10)$$

Operational savings include both the heating and cooling energy savings. Therefore, operational savings in a specific year are obtained by adding up the natural gas and electricity savings multiplied by the corresponding year’s average energy prices.

The two variables in the cash flow diagram are the inflation and discount rates. Due to the fluctuations in those rates, more than one value is assigned to each of the inflation and discount rates and then, optimized thicknesses are determined for each combination. 7%, 9% and 11% are the values assigned to the discount and inflation rates. NS, IRR, SIR and PBP are calculated for each combination. The option having the highest net saving value is considered as the optimized option.

Table 6 shows the cash flow diagram in Region 1 for discount and inflation rates of 9% and 11%, respectively. As it can be observed from the table, insulation at a thickness of 9 cm results in the highest net saving amount, which is \$60,278. Also, it is observed that this optimum option has an IRR, SIR, and PBP values of 20.53%, 2.59, and 8-9 years, respectively. Table 7 summarizes the optimized insulation thicknesses for the stated discount and

Table 6. Cash flow diagram for discount rate 9% and inflation rate %11 in Region 1

| Thickness | Years | | | | | | | NS (\$) | IRR (%) | SIR (-) | PBP (years) |
|-----------|---------|-------|-------|-------|--------|--------|--------|---------|---------|---------|-------------|
| | 0 | 1 | 2 | 5 | 10 | 15 | 20 | | | | |
| 1 cm | -30,707 | 2,273 | 2,523 | 3,451 | 5,815 | 9,798 | 16,510 | 19,137 | 14.24 | 1.62 | 13-14 |
| 2 cm | -31,280 | 3,791 | 4,208 | 5,755 | 9,698 | 16,342 | 27,537 | 51,854 | 20.94 | 2.66 | 8-9 |
| 3 cm | -32,157 | 3,959 | 4,394 | 6,010 | 10,127 | 17,064 | 28,755 | 54,654 | 21.18 | 2.70 | 8-9 |
| 4 cm | -33,034 | 4,094 | 4,544 | 6,215 | 10,472 | 17,646 | 29,734 | 56,735 | 21.29 | 2.72 | 8-9 |
| 5 cm | -34,037 | 4,203 | 4,665 | 6,381 | 10,752 | 18,117 | 30,529 | 58,130 | 21.23 | 2.71 | 8-9 |
| 6 cm | -34,914 | 4,291 | 4,763 | 6,514 | 10,976 | 18,495 | 31,165 | 59,176 | 21.16 | 2.69 | 8-9 |
| 7 cm | -35,990 | 4,365 | 4,845 | 6,626 | 11,165 | 18,813 | 31,701 | 59,718 | 20.95 | 2.66 | 8-9 |
| 8 cm | -36,977 | 4,425 | 4,912 | 6,718 | 11,320 | 19,075 | 32,143 | 60,063 | 20.74 | 2.62 | 8-9 |
| 9 cm | -37,949 | 4,480 | 4,972 | 6,800 | 11,459 | 19,309 | 32,536 | 60,278 | 20.53 | 2.59 | 8-9 |
| 10 cm | -38,826 | 4,513 | 5,010 | 6,851 | 11,545 | 19,454 | 32,780 | 60,139 | 20.30 | 2.55 | 8-9 |
| 11 cm | -40,369 | 4,541 | 5,040 | 6,893 | 11,615 | 19,572 | 32,979 | 59,197 | 19.80 | 2.47 | 9-10 |
| 12 cm | -41,353 | 4,563 | 5,064 | 6,926 | 11,671 | 19,667 | 33,139 | 58,696 | 19.52 | 2.42 | 9-10 |
| 13 cm | -42,318 | 4,575 | 5,078 | 6,945 | 11,703 | 19,720 | 33,230 | 58,004 | 19.22 | 2.37 | 9-10 |
| 14 cm | -43,428 | 4,583 | 5,087 | 6,958 | 11,724 | 19,755 | 33,289 | 57,072 | 18.87 | 2.31 | 9-10 |
| 15 cm | -44,488 | 4,590 | 5,095 | 6,968 | 11,741 | 19,784 | 33,338 | 56,159 | 18.55 | 2.26 | 9-10 |
| 16 cm | -45,529 | 4,595 | 5,101 | 6,976 | 11,755 | 19,808 | 33,378 | 55,239 | 18.24 | 2.21 | 9-10 |
| 17 cm | -46,617 | 4,600 | 5,106 | 6,983 | 11,767 | 19,828 | 33,411 | 54,253 | 17.93 | 2.16 | 10-11 |
| 18 cm | -47,636 | 4,604 | 5,111 | 6,990 | 11,778 | 19,846 | 33,442 | 53,327 | 17.64 | 2.12 | 10-11 |
| 19 cm | -48,825 | 4,609 | 5,116 | 6,996 | 11,789 | 19,865 | 33,474 | 52,235 | 17.32 | 2.07 | 10-11 |
| 20 cm | -49,718 | 4,612 | 5,119 | 7,001 | 11,797 | 19,878 | 33,496 | 51,408 | 17.09 | 2.03 | 10-11 |

Table 7. Optimized insulation thicknesses for discount rate 9% and inflation rate %11

| Option | NS (\$) | IRR (%) | SIR (-) | PBP (years) |
|-----------------|---------|---------|---------|-------------|
| Region 1, 9 cm | 60,278 | 20.53 | 2.59 | 8-9 |
| Region 2, 10 cm | 75,113 | 22.53 | 2.93 | 7-8 |
| Region 3, 15 cm | 116,765 | 26.28 | 3.62 | 6-7 |
| Region 4, 19 cm | 201,841 | 33.86 | 5.13 | 4-5 |

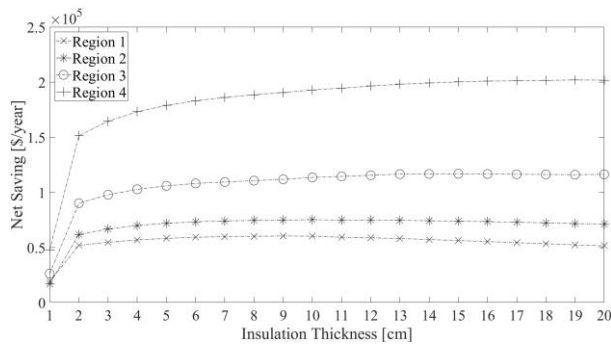


Figure 6. NS values for discount rate 9% and inflation rate 11%

inflation rates. Figure 6 shows the NS values for the same discount and inflation rates as an example. Table 8 shows the optimum insulation thickness corresponding to all 9 combinations of discount rates and inflation rates. There are notable variations in the optimum insulation thickness values of all climate regions. The optimized thicknesses change between 6-10 cm, 7-12 cm, 13-20 cm, and 15-20 cm in the first, second, third, and fourth regions, respectively. The optimized thicknesses are observed to be significantly greater than the limiting insulation thicknesses, which are 4 cm, 5 cm, 6 cm, and 8 cm in the first, second, third, and fourth

regions, respectively. Therefore, it can be concluded that the national regulation's current insulation limits are by no means at the optimum level.

Table 8. Optimum insulation thicknesses for all combinations

| No | Disc. Rate | Inf. Rate | Reg.1 | Reg.2 | Reg.3 | Reg.4 |
|----|------------|-----------|-------|-------|-------|-------|
| 1 | 7% | 7% | 9 cm | 10 cm | 13 cm | 19 cm |
| 2 | 7% | 9% | 9 cm | 10 cm | 15 cm | 19 cm |
| 3 | 7% | 11% | 10 cm | 12 cm | 20 cm | 20 cm |
| 4 | 9% | 7% | 7 cm | 7 cm | 13 cm | 16 cm |
| 5 | 9% | 9% | 9 cm | 10 cm | 13 cm | 19 cm |
| 6 | 9% | 11% | 9 cm | 10 cm | 15 cm | 19 cm |
| 7 | 11% | 7% | 6 cm | 7 cm | 13 cm | 15 cm |
| 8 | 11% | 9% | 7 cm | 7 cm | 13 cm | 16 cm |
| 9 | 11% | 11% | 9 cm | 10 cm | 13 cm | 19 cm |

Table 9 shows U_{ew} values for the optimized thicknesses in four climate regions. Considering the limiting U_{ew} ' values which are 0.70 W/m²K, 0.60 W/m²K, 0.50 W/m²K, and 0.40 W/m²K for the first, second, third and fourth regions, respectively; it can be stated that the optimized U_{ew} values are far less than the limiting values.

Table 9. Corresponding U_{ew} values for the optimized thicknesses (W/m²K)

| Option | Optimized Thicknesses | Corresponding U_{ew} Values |
|----------|-----------------------|-------------------------------|
| Region 1 | 6 - 10 cm | 0.31 - 0.49 |
| Region 2 | 7 - 12 cm | 0.27 - 0.43 |
| Region 3 | 13 - 20 cm | 0.17 - 0.25 |
| Region 4 | 15 - 20 cm | 0.17 - 0.22 |

In literature, there are several studies that have utilized the LCC approach to determine the optimum insulation thickness. Even though this study uses the same LCC approach to the previous ones, there are significant differences in the objective, methodology, and findings. First of all, the objective of this study is to determine the optimum insulation thickness specifically for existing buildings. Previous studies have not distinguished whether the building is an existing or a new building. For a symbolic wall cross section, they considered the insulation thickness value that made the derivative of the net saving formula equal to zero as the optimum insulation thickness. However, in existing buildings, insulation is applied on the exterior walls and ceiling in practice. It is not common to see insulation applications on the basement. Therefore, determining the optimum insulation thickness for existing buildings requires an approach that takes the whole building into account rather than a single cross section. The methodology employed in this study assumes fixed insulation on the ceiling and insulation at varying thickness on the exterior walls. The insulation thickness resulting in the best economic outcomes is regarded as the optimum insulation thickness. The methodology adopted in previous studies was not suitable for existing buildings. Furthermore, findings obtained in this study enable evaluating and questioning the limitations stated in the national standard for insulation applications in existing buildings. The study paves the way for discussion on the sufficiency of the limitations, whether they should be increased or decreased. It is expected to guide the potential modifications to be done in the standard.

CONCLUSIONS

This paper contributes to the body of knowledge by proposing an improved and effective way to calculate the optimum insulation thickness of existing buildings in developing countries. In previous studies, optimum insulation thicknesses were calculated by making derivative of the net saving formula equal to zero. As opposed to those studies, in this study, the optimized thicknesses were calculated by adopting a representative building approach. The cost of insulation implementation and operational savings resulting from the decreases in annual energy requirements were reflected on the LCC analysis. Annual energy requirements were determined according to a heat balance based software. Optimized thicknesses were determined for four climate regions defined in the national standard.

The findings suggested that optimum thicknesses and U_{ew} values were quite different than the limiting values stated in the national standard. The optimized thicknesses were found to be far greater than the requirements, which were established as 4 cm, 5 cm, 6 cm, and 8 cm for the first, second, third, and fourth regions, respectively. The same could be stated for the U_{ew} values. The optimized U_{ew} values were far less than

the requirements, which were 0.70 W/m²K, 0.60 W/m²K, 0.50 W/m²K, and 0.40 W/m²K for the first, second, third and fourth regions, respectively. It can be interpreted that the minimum requirements for existing buildings were not at the optimum levels in the standard. Based on the findings, it is possible to come up with some recommendations for the government and the owners of the existing buildings.

First of all, the governments are advised to lower the limiting heat transfer coefficients in the standard. This advice is applicable to all countries where the standard limitations are insufficient. Scholars in various regions and countries should conduct similar studies to observe the sufficiency of the national standards. It is clearly shown in this study that it would economically be more feasible to apply thicker insulations than the limits stated in the standard. Considering the environmental concerns, it is obvious that the thicker the insulation is, the less the environment impact of the building would be.

Secondly, the home owners are strongly recommended to apply the optimum insulation thicknesses rather than the minimum insulation thicknesses that satisfy the limiting conditions in the standards. The increasing initial costs most of the time make the home owners reluctant to apply thicker insulations and pay more money. However, they should appreciate the future operational savings. They must be aware of the fact that as clearly demonstrated in this study, the minimum insulation thicknesses satisfying the conditions in the standards are not the most economically feasible ones and there is still room for economically better outcomes with the application of optimum insulation thickness.

This study questions the optimality of thermal insulation requirements applicable in a developing country. It presents a novel approach by calculating the optimum insulation thicknesses for a typical existing building. In this respect, it goes beyond the previous studies adopting a single formula. The methodology employed in previous studies can be used neither to determine the optimum insulation thickness specifically for existing buildings nor to question the sufficiency of the corresponding standard, while the methodology proposed in this study can fulfill both needs and fill this gap in the literature. By repeating the methodology, similar studies can be performed in other countries to compare their results to the national standards. This would allow to decide on the applicability and appropriateness of these standards in terms of LCC and economically viable construction values.

REFERENCES

Asdrubali, F., D'Alessandro, F. and Schiavoni, S., 2015, A Review of Unconventional Sustainable Building Insulation Materials, *Sustainable Mater. Technol.*, 4, 1-17.

- Ashouri, M., Astaraei, F. R., Ghasempour, R., Ahmadi, M. H. and Feidt, M., 2016, Optimum Insulation Thickness Determination of a Building Wall Using Exergetic Life Cycle Assessment, *Appl. Therm. Eng.*, 106, 307-315.
- ASHRAE, 2013, 2013 ASHRAE Handbook Fundamentals, American Society of Heating, Refrigerating and Air-Conditioning Engineers, ISBN: 978-1-936504-46-6, Atlanta, GA 30329.
- ASHRAE, 1997, 1997 ASHRAE Handbook Fundamentals, American Society of Heating, Refrigerating and Air-Conditioning Engineers, ISBN: 188-3-413443, Atlanta, GA 30329.
- Axaopoulos, I., Axaopoulos, P. and Gelegenis, J., 2014, Optimum Insulation Thickness for External Walls on Different Orientations Considering the Speed and Direction of the Wind, *Appl. Energy*, 117, 167-175.
- Briga-Sa, A., Nascimento, D., Teixeira, N., Pinto, J., Caldeira, F., Varum, H. and Paiva, A., 2013, Textile Waste as an Alternative Thermal Insulation Building Material Solution, *Constr. Build. Mater.*, 38, 155-160.
- Cristina, B., Paolo, C. S. and Spigliantini, G., 2017, Evaluation of Refurbishment Alternatives for an Italian Vernacular Building Considering Architectural Heritage, Energy Efficiency and Costs, *Energy Procedia*, 133, 401-411.
- Cuce, E., Cuce, P. M., Wood, C. J. and Riffat, S. B., 2014, Optimizing Insulation Thickness and Analysing Environmental Impacts of Aerogel-Based Thermal Superinsulation in Buildings, *Energy Build.*, 77, 28-39.
- Daouas, N., 2011, A Study on Optimum Insulation Thickness in Walls and Energy Savings in Tunisian Buildings Based on Analytical Calculation of Cooling and Heating Transmission Loads, *Appl. Energy*, 88, 156-164.
- Dylewski, R. and Adamczyk, J., 2011, Economic and Environmental Benefits of Thermal Insulation of Building External Walls, *Build. Environ.*, 46, 2615-2623.
- Hasan, A., 1999, Optimizing Insulation Thickness for Buildings Using Life Cycle Cost, *Appl. Energy*, 63, 115-124.
- IEO, 2013, International Energy Outlook, Technical Report, U.S. Energy Information Administration.
- Kaya, M., Firat, I. and Comakli, O., 2016, Economic Analysis of Effect on Energy Saving of Thermal Insulation at Buildings in Erzincan Province, *J. Therm. Sci. Technol.*, 36(1), 47-55.
- Kaynakli, O., 2013, Optimum Thermal Insulation Thicknesses and Payback Periods for Building Walls in Turkey, *J. Therm. Sci. Technol.*, 33(2), 45-55.
- Kon, O. and Yuksel, B., 2016, Optimum Insulation Thickness Calculated by Measuring of Roof Floor and Exterior Walls in Buildings Used for Different Purposes, *J. Therm. Sci. Technol.*, 36(1), 17-27.
- Lucchi, E., Tabak, M. and Troi, A., 2017, The "Cost Optimality" Approach for the Internal Insulation of Historic Buildings, *Energy Procedia*, 133, 412-423.
- Maleviti, E., Wehrmeyer, W. and Mulugetta, Y., 2013, An Empirical Assessment to Express the Variability of Buildings' Energy Consumption, *Int. J. Energy Optim. Eng.*, 2(3), 55-67.
- Miguel, C., Labandeira, X. and Löschel, A., 2015, Frontiers in the Economics of Energy Efficiency, *Energy Econ.*, 52, S1-S4.
- Mishra, S., Usmani, J. A. and Varshney, S., 2012, Energy Saving Analysis in Building Walls Through Thermal Insulation System, *Int. J. Eng. Res. Appl.*, 2(5), 128-135.
- Morales, S. P., Munoz, P., Juarez, M. C., Mendivil, M. A. and Munoz, L., 2016, Energy Efficiency in Buildings: Study of Single-Leaf Walls Made with Clay Bricks, *J. Energy Eng.*, 142(1), 04015011.
- Nematchoua, M. K., Raminoso, C. R., Mamiharijaona, R., René, T., Orosa, J. A., Elvis, W. and Meukam, P., 2015, Study of the Economical and Optimum Thermal Insulation Thickness for Buildings in a Wet and Hot Tropical Climate: Case of Cameroon, *Renewable Sustainable Energy Rev.*, 50, 1192-1202.
- Nematchoua, M. K., Ricciardi, P., Reiter, S. and Yvon, A., 2017, A Comparative Study on Optimum Insulation Thickness of Walls and Energy Savings in Equatorial and Tropical Climate, *Int. J. Sustainable Built Environ.*, 6(1), 170-182.
- Nikoofard, S., Ugursal, I. and Beauseleil-Morrison, I., 2015, Economic Analysis of Energy Upgrades Based on Tolerable Capital Cost, *J. Energy Eng.*, 141(3), 06014002.
- Pedersen, C. O., Fisher, D. E. and Liesen, R. J., 1997, Development of a Heat Balance Procedure for Calculating Cooling Loads, *ASHRAE Trans.*, 103(2), 459-468.
- Ramos, A., Gago, A., Labandiera, X. and Linares, P., 2015, The Role of Information for Energy Efficiency in the Residential Sector, *Energy Econ.*, 52, S17-S29.

Serrano, S., Urge-Vorsatz, D., Barreneche, C., Palacios, A. and Cabeza, L. F., 2017, Heating and Cooling Energy Trends and Drivers in Europe, *Energy*, 119, 425-434.

Spitler Jeffrey D., 2013, Load Calculation Application Manual, ASHRAE and Oklahoma State University, Atalanta.

Sundaram, A. S. and Bhaskaran, A., 2014, Optimum Insulation Thickness of Walls for Energy-Saving in Hot Regions of India, *Int. J. Sustainable Energy*, 33(1), 213-226.

Turkish Standards Institution, 2008, Thermal Insulation Requirements for Buildings, Turkish Standard 825, Official Gazette Number 27019, (In Turkish).

Yigit, S. and Ozorhon, B., 2018, A Simulation-Based Optimization Method for Designing Energy Efficient Buildings, *Energy Build.*, 178, 216-227.

Yildiz, Y., Ozbalta, T. G. and Eltez, A., 2014, Energy-Saving Retrofitting of Houses in Cold Climates, *J. Therm. Eng.*, 34(1), 53-61.

Yu, J., Yang, C., Tian, L. and Liao, D., 2009, A Study on Optimum Insulation Thicknesses of External Walls in Hot Summer and Cold Winter Zone of China, *Appl. Energy*, 86, 2520-2529.



THE EFFECTS OF CO₂, H₂O, AND N₂ DILUTIONS ON POLLUTANTS OF SHALE GAS COMBUSTION

Suat ÖZTÜRK

Zonguldak Bülent Ecevit University, Zonguldak Vocational School, Department of Electronic and Automation
67100 Merkez, Zonguldak, suatozturk@beun.edu.tr

(Geliş Tarihi: 19.03.2019, Kabul Tarihi: 03.12.2019)

Abstract: Increase in demands for energy and discovered huge reserves of shale gas in the world cause countries and researchers to focus on it progressively. The amount of shale gas production has begun to rise by developing the techniques of gas extraction from shale rocks recently. In this paper, the non-premixed combustion characteristic and emissions of shale gas and humid air with dilution effects are numerically investigated under different equivalence ratio, pressure and temperature. A two dimension model of cylindrical combustor is considered. It is concluded that NO_x for New Albany and Haynesville come to the maximum value at 1.025 and 1.02 of equivalence ratio and the maximum reaction temperatures are 2027 and 2014 K in turn. The rising equivalence ratio raises CO mass fractions. The increasing dilution rates decrease NO_x and uplift CO mass fractions. The enhancing pressure rears NO_x and diminishes CO fractions. The ascending wall temperature boosts NO_x, CO and reaction temperatures. NO_x and CO from environmental pollutants emerging at the end of shale gas combustion can be lowered by decreasing equivalence ratio, wall temperature, and pressure. The use of H₂O dilution steps forward in compared with CO₂ and N₂ because of its opposite effects on NO_x and CO pollutants.

Keywords: Shale gas, Non-premixed combustion, Turbulent, Nitrogen oxides.

ŞEYL GAZ YANMASININ KİRLETİCİLERİ ÜZERİNDE CO₂, H₂O VE N₂ DİLÜSYONLARININ ETKİLERİ

Özet: Dünyada şeyl gazın keşfedilmiş büyük rezervleri ve enerji taleplerindeki artış, ülkelerin ve araştırmacıların artan bir şekilde şeyl gaz üzerine odaklanmasına sebep olmaktadır. Şeyl gazın üretim miktarı, son zamanlarda şeyl kayalarından gazın çıkartılması tekniklerinin geliştirilmesi ile artmaya başladı. Bu çalışmada, dilüsyon etkileri ile birlikte şeyl gaz ve nemli havanın ön karışimsız yanma karakteristikleri ve emisyonları, farklı ekivalans oranları, basınç ve sıcaklıklar altında sayısal olarak araştırılmıştır. Silindirik yakıcının iki boyutlu bir modeli düşünülmüştür. New Albany ve Haynesville için NO_x'lerin, 1.025 ve 1.02 ekivalans oranında maksimum değere ulaştığı ve maksimum reaksiyon sıcaklıklarının sırasıyla 2027 ve 2014 K olduğu sonucuna varılmıştır. Artan ekivalans oranı CO kütle kesitlerini yükseltmektedir. Yükselen dilüsyon oranları NO_x'i düşürmekte ve CO kütle kesitlerini artırmaktadır. Artan basınç NO_x'i yükseltmekte ve CO kesitlerini azaltmaktadır. Yükselen duvar sıcaklığı NO_x, CO ve reaksiyon sıcaklıklarını artırmaktadır. Şeyl gaz yanmasının sonunda ortaya çıkan çevresel kirleticilerden NO_x ve CO, ekivalans oranı, duvar sıcaklığı ve basıncı düşürerek azaltılabilir. CO₂ ve N₂ ile karşılaştırıldığında, NO_x ve CO kirleticileri üzerindeki zıt etkilerinden dolayı H₂O dilüsyonunun kullanımı bir adım öne çıkmaktadır.

Anahtar Kelimeler: Şeyl gazı, Ön karışimsız yanma, Türbülans, Nitrojen oksitler.

NOMENCLATURE

| | | | |
|-------------------------------|--------------------------------|--------------------|---|
| CFD | Computational fluid dynamics | K | Thermal conductivity [W/m.K] |
| CH ₄ | Methane | MM | Molecular mass [kg/mol] |
| C ₂ H ₆ | Ethane | Pr | Prandtl number [=μ.c _p /k] |
| C ₃ H ₈ | Propane | R | Gas constant [J/mol.K] |
| CO | Carbon monoxide | S_{rea}, S_{rad} | Thermal energy causing by chemical reactions and radiative transfer [J] |
| CO ₂ | Carbon dioxide | T_{wall} | Wall temperature [K] |
| N ₂ | Nitrogen | c_p | Specific heat [J/kg.K] |
| NO _x | Nitrogen oxides | f_x | Mass fraction [kg x/kg] |
| NO | Nitrogen monoxide | h | Enthalpy [J/mol] |
| NO ₂ | Nitrogen dioxide | k, ϵ | Turbulent kinetic energy and its dissipation |
| A_k | Surface area [m ²] | u, v | Axial and radial velocities [m/s] |
| | | σ | Stefan-Boltzman constant |

| | |
|--------|------------------------------------|
| ρ | Specific mass [kg/m ³] |
| μ | Dynamic viscosity [kg.m/s] |

INTRODUCTION

Hydro carbon based fuels still take an important place at the electricity and energy production for the purposes of heating and cooling, lighting, transporting, communication, sanitation, etc. Many countries seek out alternatives emitting lower greenhouse gases for differentiating energy sources. Shale gas as a new energy source comes forward with the confirmed potential of countries in the last years (Cohen and Winkler, 2014; Chang et al., 2015). The total shale gas reserve in the world is 214.5 trillion cubic meters by 1.4 times of natural gas. China, Argentina, Algeria, USA, Canada, Mexico, Australia, South Africa are among countries possessing crucial shale gas reserves (Lan et al., 2019).

Shale gas reservoirs have organic-rich deposition, low matrix permeability, and mineral-filled nature fracture clusters. It has a better production cycle and long mining life according to natural gas as well (Bilgen and Sarıkaya, 2016; Wang et al., 2019). United States firstly extracted by horizontal drilling and hydraulic fracturing procedures and currently sells it commercially. The water pollution and earthquakes caused by hydraulic fracturing process and greenhouse gases emitted by fugitive methane seem as environmental issues to be solved at shale gas extraction (Wang et al., 2014).

Electricity production from shale gas is realized by the combustion process in energy plants. Shale gas burned by air emits various hazardous emissions. Nitrogen oxides (NO_x) and carbon monoxide (CO) are seen as the most unfavorable and obtrusive environmental pollutants emerging at the end of shale gas combustion because of fuel and oxide ingredients, high reaction temperature, and incomplete combustion. NO_x causes for respiratory illness, acid rains, and smog. CO is a toxic gas poisoning the living things (Akça et al., 2017; Alberts, 1994). NO_x comes to exist by the oxidation of nitrogen and oxygen in three ways called thermal, prompt, and fuel NO_x depending on stoichiometry, reaction temperature, and nitrogen concentration in fuel and air. Thermal way transcends more at the reaction temperatures above 1300 °C. CO occurs by the reaction of carbon and oxygen during the incomplete combustion (Ozturk, 2018).

The combustion case of gas and other fuels in various types of combustors are both numerically and experimentally examined under different conditions as turbulent, laminar, adiabatic, non-adiabatic, premixed, non-premixed, partially premixed, and etc. Studies for shale gases in literature have mostly focused on the environmental effects of the extracting process of shale gas. It is seen that there is a gap for the combustion process, characteristics, and emissions of shale gas.

Cohen and Winkler (2014) concluded shale gas have lower greenhouse gas emissions with respect to coal for the electricity generation. Chang et al. (2015) determined the greenhouse gas emissions of shale gas fired electricity are lower than those of coal. Ozturk (2018) detected that rising inlet pressure increases NO_x, accruing humidity ratio decreases NO_x, and growing flow rate diminishes NO_x for non-premixed shale gas combustion. Vargas et al. (2016) detected the shale gas consisting of 58% CH₄ - 20% C₂H₆ - 12% C₃H₈ - 10% CO₂ indicates higher laminar burning velocity than the others. Zahedi and Yousefi (2014) indicated the addition of N₂ or CO₂ to the mixture reduces NO and the rising initial pressure arises NO in pre-mixed laminar methane-air combustion. McTaggart-Cowan et al. (2009) found that nitrogen addition lowers NO_x emissions and ethane addition enhances it in high-pressure non-premixed natural gas combustion. Jerzak et al. (2014) proved that CO₂ addition to natural gas increases CO and causes to NO_x and the combustion temperature to decrease. Silva et al. (2007) studied on CO and CO₂ emissions and temperature distributions for turbulent non-premixed combustion of natural gas in a cylindrical chamber. Hayashi et al. (1998) determined NO_x rises with pressure and temperature increment in non-premixed gas combustion.

In this study, the temperature and emission characteristics of turbulent, non-premixed and non-adiabatic combustion of shale gas and humid air in a cylindrical combustor are computationally investigated under the dilutive effects of CO₂, H₂O, and N₂ added in the burning air by ANSYS software.

MATHEMATICAL FORMULATION

The CFD simulation of shale gas and humid air combustion in a cylindrical burner is the calculations of heat and mass transfer, chemical species concentration and velocities, temperatures, and thermal radiation equations defining the combustion process with finite rates chemical reactions.

Mass Conservation

The continuity equation for cylindrical coordinates is given by

$$\frac{\partial}{\partial x} \rho \bar{u} + \frac{\partial}{\partial r} \rho \bar{v} + \frac{\rho \bar{v}}{r} = 0 \quad (1)$$

where \bar{u} and \bar{v} are time averaged velocities, ρ is the specific mass of the mixture, and x and r are the axial and radial coordinates.

Momentum Conservation

The flow equations in axial and radial directions can be written by

$$\bar{u} \frac{\partial}{\partial x} (\rho \bar{u}) + \bar{v} \frac{\partial}{\partial r} (\rho \bar{u}) = -\frac{\partial p^*}{\partial x} + \bar{\nabla} \cdot ((\mu + \mu_t) \bar{\nabla} \bar{u}) + \frac{\partial}{\partial x} \left(\mu_t \frac{\partial \bar{u}}{\partial x} \right) + \frac{1}{r} \frac{\partial}{\partial r} \left(r \mu_t \frac{\partial \bar{v}}{\partial x} \right) \quad (2)$$

$$\bar{u} \frac{\partial}{\partial x} (\rho \bar{v}) + \bar{v} \frac{\partial}{\partial r} (\rho \bar{v}) = -\frac{\partial p^*}{\partial r} + \bar{\nabla} \cdot ((\mu + \mu_t) \bar{\nabla} \bar{v}) + \frac{\partial}{\partial x} \left(r \mu_t \frac{\partial \bar{u}}{\partial r} \right) + \frac{1}{r} \frac{\partial}{\partial r} \left(r \mu_t \frac{\partial \bar{v}}{\partial r} \right) - \frac{(\mu + \mu_t) \bar{v}}{r^2} + \frac{\rho \bar{v}^2}{r} \quad (3)$$

$$\mu_t = C_\mu \rho \frac{k^2}{\varepsilon} \quad (4)$$

$$p^* = \bar{p} - \left(\frac{2}{3} \right) k \quad (5)$$

where μ and μ_t are mixture dynamic and turbulent viscosity, p and p^* is time averaged and modified pressures, and C_μ , k and ε are an empirical constant for the turbulent model, the turbulent kinetic energy and its dissipation respectively.

The k- ε Turbulence Model

The equations for k and ε where σ_k , σ_ε , $C_{1,\varepsilon}$, $C_{2,\varepsilon}$ and P_k are Prandtl numbers for kinetic energy and dissipation, empirical constants of turbulent model and the destruction or production of turbulent kinetic energy is given as

$$\bar{u} \frac{\partial}{\partial x} (\rho k) + \bar{v} \frac{\partial}{\partial r} (\rho k) = \bar{\nabla} \cdot \left(\left(\mu + \frac{\mu_t}{\sigma_k} \right) \bar{\nabla} k \right) + P_k - \rho \varepsilon \quad (6)$$

$$\bar{u} \frac{\partial}{\partial x} (\rho \varepsilon) + \bar{v} \frac{\partial}{\partial r} (\rho \varepsilon) = \bar{\nabla} \cdot \left(\left(\mu + \frac{\mu_t}{\sigma_\varepsilon} \right) \bar{\nabla} \varepsilon \right) + C_{1,\varepsilon} \frac{\varepsilon}{k} P_k - C_{2,\varepsilon} \frac{\varepsilon^2}{k} \quad (7)$$

$$P_k = \mu_t \left(2 \left(\frac{\partial \bar{u}}{\partial x} \right)^2 + \left(\frac{\partial \bar{u}}{\partial r} + \frac{\partial \bar{v}}{\partial x} \right)^2 \right) + \mu_t \left(2 \left(\frac{\partial \bar{v}}{\partial r} \right)^2 + 2 \left(\frac{\bar{v}}{r} \right)^2 \right) \quad (8)$$

Energy Conservation

The energy equation by neglecting the transport of energy can be written as

$$\bar{u} \frac{\partial}{\partial x} (\rho \bar{h}) + \bar{v} \frac{\partial}{\partial r} (\rho \bar{h}) = \bar{\nabla} \cdot \left(\left(\frac{K}{c_p} + \frac{\mu_t}{Pr_t} \right) \bar{\nabla} \bar{h} \right) + \bar{S}_{rad} + \bar{S}_{rea} \quad (9)$$

$$c_p = \sum_x \bar{f}_x c_{p,x} \quad (10)$$

$$\bar{S}_{rea} = \sum_x \left(\frac{h_x^o}{MM_x} + \int_{T_{ref,x}}^{\bar{T}} c_{p,x} d\bar{T} \right) \bar{R}_x \quad (11)$$

$$\bar{S}_{rad,k} = \frac{1}{A_k} \left(\sum_{\gamma=1}^{\Gamma} \bar{g}_\gamma \bar{s}_k \sigma \bar{T}_\gamma^4 + \sum_{j=1}^J \bar{s}_j \bar{s}_k q_{o,j} \right) - q_{o,k} \quad (12)$$

where h and c_p are average enthalpy and specific heat, $c_{p,x}$, f_x , MM_x , Pr_t , K and are specific heat, average mass fraction, and mixture molecular mass of x-th chemical specie, turbulent Prandtl number, and thermal conductivity of mixture, S_{rea} and S_{rad} are the sources of thermal energy causing by chemical reactions and radiative transfer, A_k is surface area, σ are Stefan-Boltzman constant, and $g_{\gamma s_k}$ and $s_{j s_k}$ are directed-flux areas (Silva et al., 2007).

MATERIALS AND METHODS

The combustion issue is a complex process based on fluid mechanics, heat and mass transfer, chemical kinetics, thermodynamics, radiation, and etc. Researchers mostly prefer numerical solution being close to the experimental results because the experiments are hard to handle with, expensive, and need more time. The computational fluid dynamics (CFD) as a numerical method is used at the solution of combustion problems by computing temperatures, rates, mass fractions, products, and emissions under the given conditions. CFD software utilized for calculations in this study is Fluid Flow (Fluent) of ANSYS solving the equations of combustion defined by mathematical models under the selected solution methods, controls, and boundary conditions over meshed geometry of a burner chamber (Ozturk, 2018).

In ANSYS's non-premixed combustion that fuel (shale gas) and oxidizer (humid air) enter the reaction zone as separate streams, the thermochemistry is degraded to a single parameter called the mixture fraction, f . The mixture fraction is the local mass fraction of elements (C, H, O, N, etc.) of burnt and unburnt fuel stream in all the species (N_2 , CO_2 , H_2O , O_2 , CO , etc.) and the atomic elements are conserved in chemical reactions. In this approach, the governing transport equation of mixture fraction does not include a source term because it is a conserved scalar quantity. Thus, the case of gas combustion is reduced to a mixing problem and removes the difficulties including non-linear mean reaction rates. As a result, the chemistry is modeled as being in chemical equilibrium once mixed (ANSYS, 2009).

A 2D model of the cylindrical chamber is devised to simplify and accelerate CFD solutions. Grid independence test for the model are realized at numbers of different elements for Haynesville shale gas as given

in Figure 1. The mesh of 12000 elements and 12261 nodes for combustion field is decided to use for the computations because it provides fast solution and requires less time and energy for CFD at considering of enormous size of the cylindrical combustor. The percentage differences for reaction temperatures and mass fractions of NO_x and CO between element numbers of 12000 and 40500 are 0.8 and 6.4% respectively in acceptable limits. The meshed combustor chamber under Mesh section in ANSYS software is given in Figure 2.

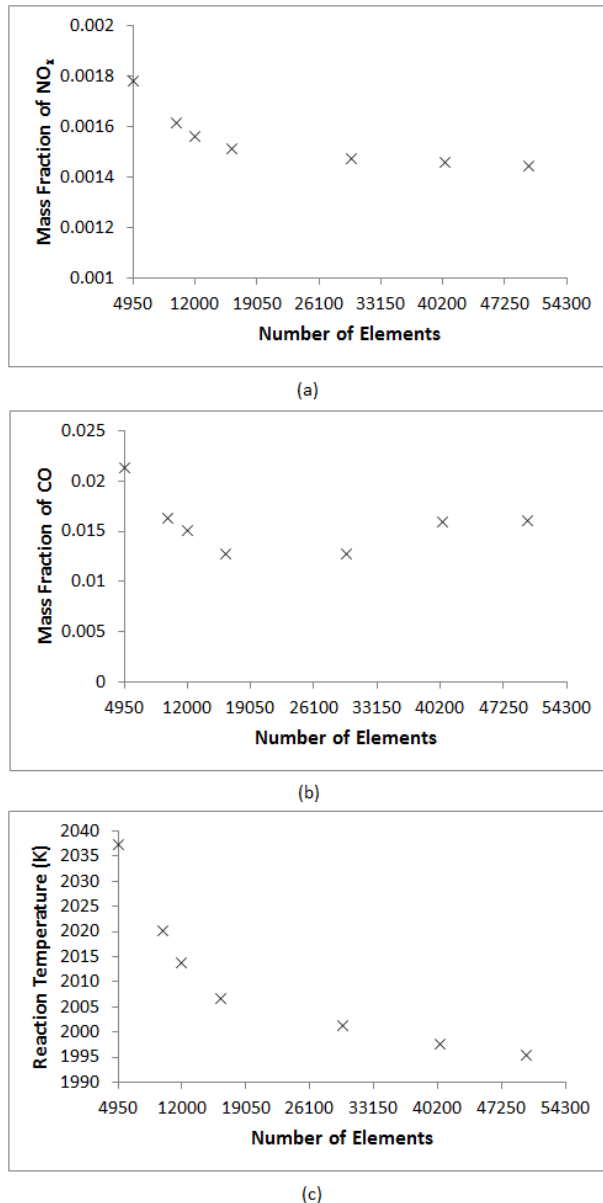


Figure 1. Grid independence test at different element numbers.

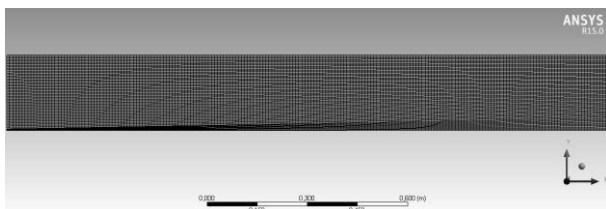


Figure 2. The meshed field of the cylindrical combustor.

The inlet flow rates, temperatures, and the dimensions of the cylindrical combustor are illustrated in Figure 3. The burning air includes onset humidity at the rate of 1.5%, the pressure is 1 Atm, the wall, inlet fuel and air temperatures are 300 K and equivalence ratio is 1 if not mentioned else in the study. The diluents of CO_2 , H_2O , and N_2 to investigate the dilutive effects on the combustion characteristics are added to the burning air at different ratios between 0 and 30%.

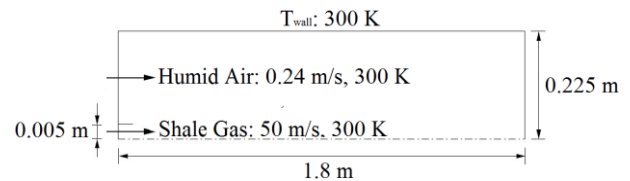


Figure 3. The temperatures and rates of fuel and oxide entering the combustor (Ozturk, 2018; ANSYS, 2009).

Shale gases used in the calculations are extracted from New Albany and Haynesville regions of United States. The average values of the compositions of the gases obtained from the fields in these regions are given in Table 1. It is seen that the compositions of shale gases aggregate around two different types because compositions of shale gases extracted at other countries generally resemble to the compositions of New Albany and Haynesville shale gases.

Table 1. The shale gas compositions (Bullin et al., 2008).

| Regions | CH_4 | C_2H_6 | C_3H_8 | CO_2 | N_2 |
|-------------|---------------|------------------------|------------------------|---------------|--------------|
| Haynesville | 95 | 0.1 | 0 | 4.8 | 0.1 |
| New Albany | 89.875 | 1.125 | 1.125 | 7.875 | 0 |

To solve the equations of energy, k-epsilon, radiation, etc. defining the present case of gas combustion in CFD simulation needs to be assigned setup parameters in ANSYS Fluent software. Moreover, the models of turbulent, non-premixed, non-adiabatic, and NO_x also needs to be selected. Thermal and prompt NO_x formation and N_2O intermediate steps are crucial for NO_x production in gas combustion. P1 model works reasonably for radiation in combustion, facilitates radiative transfer equations, and also includes scattering effects of particles, droplets, and soot. Standard k-epsilon (2 eqn.) model generally presents enough solution for turbulent cases and decreases computational costs per iteration. Standard wall functions are widely used for mean velocity in turbulent boundary layer of industrial flows.

The following models and properties are selected from under Setup section: Energy–On, Viscous Model–k-epsilon (2 eqn.) and k-epsilon model–standard, Near-Wall Treatment–Standard Wall Functions, Radiation Model–P1, Species Model–Non-Premixed Combustion (Inlet Diffusion, Chemical Equilibrium, Non-Adiabatic are selected), NO_x Model–On (Thermal, Prompt and N_2O Intermediate are selected). The compositions of

fuel and air for the complete combustion and others at several equivalence ratios are entered under Fuel and Oxide at Boundary tab of PDF Table.

RESULTS AND DISCUSSION

Mass fractions of CH₄ and CO₂ along symmetry line are represented in Figure 4a, b. The results indicate that computed mass concentrations of combustion products have trends that are similar to those of numerical simulation (Silva et al., 2007) and experimental data (Garreton and Simonin, 1994). The fuel and air begin to combust after a certain distance because there is a dividing wall between air and fuel at the entrance of the cylindrical combustor in the present study. Mass fraction of CO₂ begins at 0.12 because Haynesville shale gas includes 4.8% CO₂.

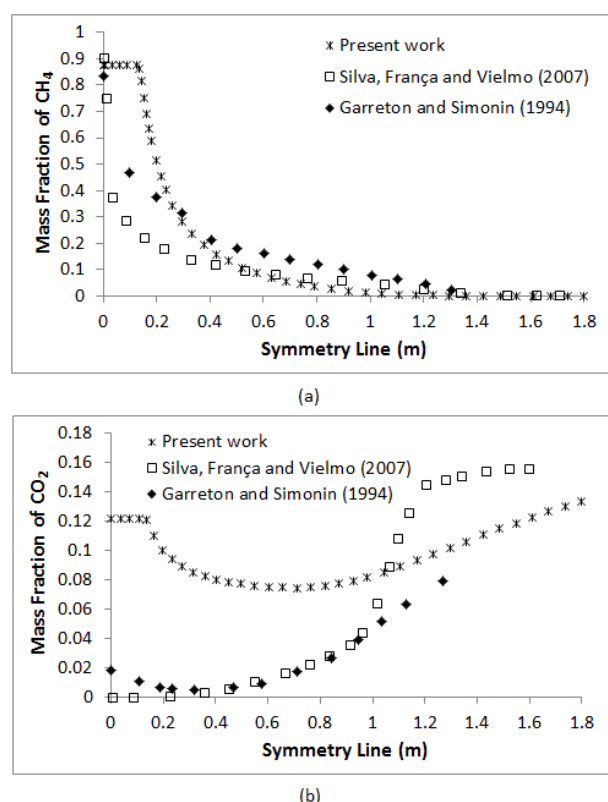


Figure 4. Mass fractions of CH₄ and CO₂ along symmetry line with numerical simulation (Silva et al., 2007) and experimental data (Garreton and Simonin, 1994).

The mass fractions of NO_x emerging at the end of non-premixed combustions of shale gases at various equivalence ratios (ER) are given in Figure 5a. NO_x reach to the maximum at 1.025 of ER as 0.0021 kg NO_x/kg for New Albany and 1.02 of ER as 0.00158 kg NO_x/kg for Haynesville. New Albany has the higher NO_x values because of its high C₂H₆ and C₃H₈ components. The difference between NO_x of gases at ER=1 is 25%. The burning air rate in the combustion chamber decreases by rising equivalence ratio and it causes the incomplete combustion. The incomplete burning leads to the fall of NO_x and reaction temperatures and the increment of CO mass fraction by

enhancing carbon and hydro carbon compounds in the chamber as illustrated in Figure 5b. The difference between CO mass fractions is 24.5% at ER=1. The reaction temperatures are depicted in Figure 5c. The maximum reaction temperatures are 2027 and 2014 K for New Albany and Haynesville. It is seen that NO_x follows the reaction temperature because thermal NO_x is especially more effective than prompt and fuel NO_x at reaction temperatures above 1300 °C.

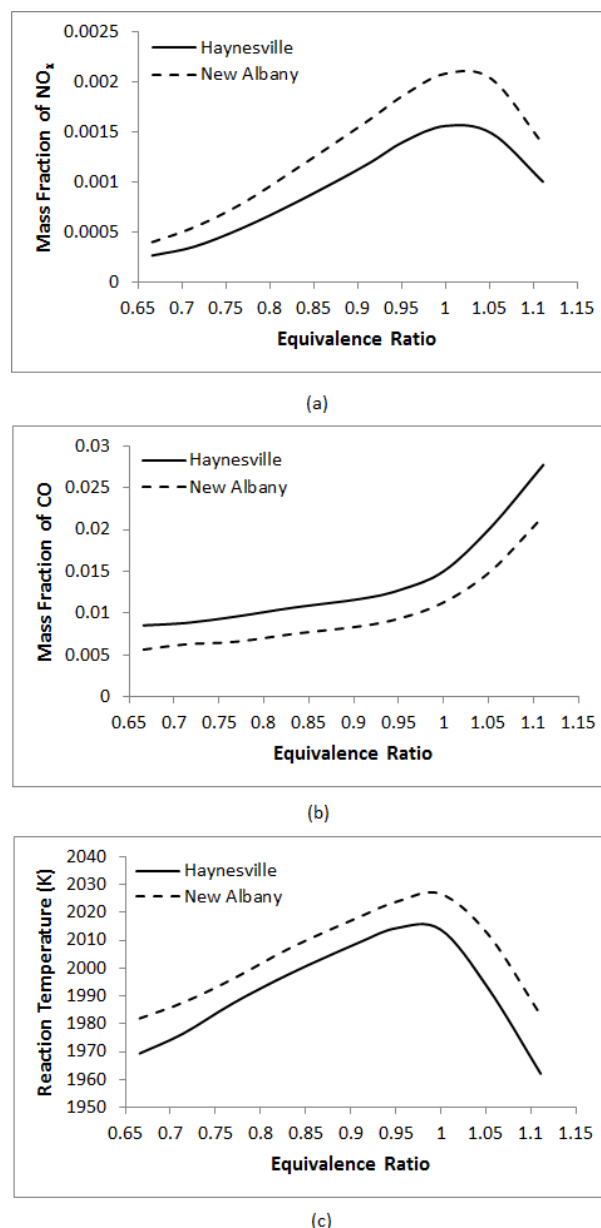


Figure 5. The reaction temperatures, NO_x and CO mass fractions of shale gases at different equivalence ratios.

The mass fractions of NO_x under the dilutive effects of CO₂, H₂O, and N₂ additions into the burning air are depicted in Figure 6a, b. The enhancing dilution rates diminish NO_x values for both shale gases. NO_x is decreased at the furthest by H₂O addition following by CO₂ and N₂. The high heat hold capacity of H₂O cushions the reaction temperature and fades NO_x. The addition of CO₂ into the air reduces the reaction temperature by dropping reaction rates, species

concentrations, and flame speed during the combustion and the decreasing flame temperature lowers NO_x (Hraiech et al., 2015). N_2 dilution causes NO to fall down because it decreases the temperature by altering the temperature based kinetic pathways (Sabia et al., 2015). 5% dilution of H_2O , CO_2 , and N_2 abates NO_x 59.1, 51.3, and 51.2% for Haynesville and 57.2, 49.3, and 49.1% for New Albany respectively.

The dilution additions cause CO mass fractions to increase for all the shale gas as given in Figure 6c, d. As expected, CO_2 addition enhances CO mass fraction at the highest rate by raising carbon atoms in the burning chamber. H_2O dilution has the least effect for CO emissions to rise. 5% addition of H_2O , N_2 , and CO_2 increases CO mass fractions 30.1, 45.2, and 61.9% for Haynesville and 32.8, 50.3, and 62.4% for New Albany.

The reaction temperatures are represented in Figure 6e, f. The excessive decrease in reaction temperature is an unfavorable situation from the view point of system output. The rank from highest to the lowest for dilutions to reduce the reaction temperature is CO_2 , H_2O , and N_2 respectively. 5% addition of CO_2 , H_2O , and N_2 into the air falls the temperatures down 5.1, 4.2, and 3.6% for Haynesville and 4.8, 3.8, and 3.25% for New Albany. It can be interpreted that H_2O dilution indicates the best effects under the evaluations of NO_x , CO emissions and reaction temperatures.

Figure 7a and b illustrates NO_x mass fractions for Haynesville and New Albany shale gases at 10% dilutions of CO_2 , H_2O , and N_2 under different pressures.

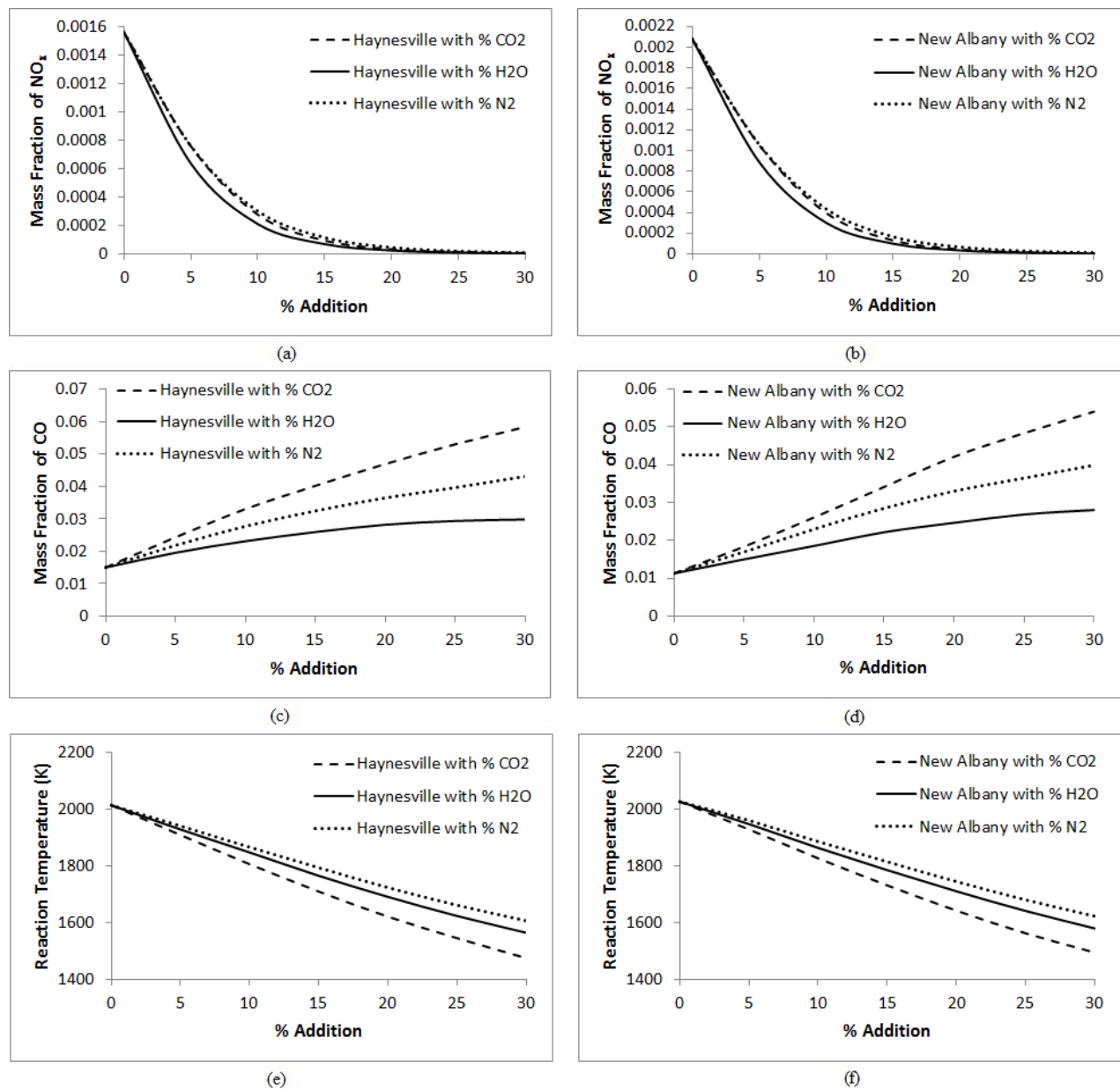


Figure 6. The mass fraction and reaction temperatures of shale gases at various dilution rates: (a) NO_x mass fractions for Haynesville, (b) NO_x mass fractions for New Albany, (c) CO mass fractions for Haynesville, (d) CO mass fractions for New Albany, (e) Reaction temperatures for Haynesville, and (f) Reaction temperatures for New Albany shale gas.

The pressure is absolute. The rising pressure raises NO_x values for both gases. The highest values for NO_x occur with N_2 dilution followed by CO_2 and H_2O in the decreasing range. The variances between 0 and 10 Atm with N_2 , CO_2 , and H_2O additions are 317, 258, and 327% for Haynesville and 292, 239, and 302% for New Albany. The highest increment of NO_x at the interval of 0-10 Atm belongs to H_2O dilution.

CO emissions are depicted in Figure 7c and d. CO mass fractions reduce up to 2 Atm and stay constant between 2 and 10 Atm. The high pressure reduces CO because the necessary time for the reaction of carbon and oxygen atoms is not available (Muharam et al., 2015). The highest CO values arise with CO_2 dilution pursued by N_2 and H_2O additions. The decrease rates for CO between 0 and 2 Atm in the rank of CO_2 , N_2 , and H_2O are 12.9,

11.9, and 10.1% for Haynesville and 14.9, 17.3, and 14.1% for New Albany.

The enhancing pressure increases the reaction temperatures as shown in Figure 7d and e. The rising pressure shortens the flame length, the reactions occur in a micro area, and the fuel is depleted faster. It also rears the reaction temperature (Ziani and Chaker, 2016). The highest vales belong to the shale gases with N_2 dilution followed by H_2O and CO_2 . The total increment rates between 0 and 10 Atm for N_2 , H_2O , and CO_2 dilutions are 5.5, 5.3, and 5.3% for Haynesville and 5.6, 5.6, and 5.4% for New Albany in sequence. H_2O addition in the burning air entering into the combustion chamber can be preferred for high operating pressures as well.

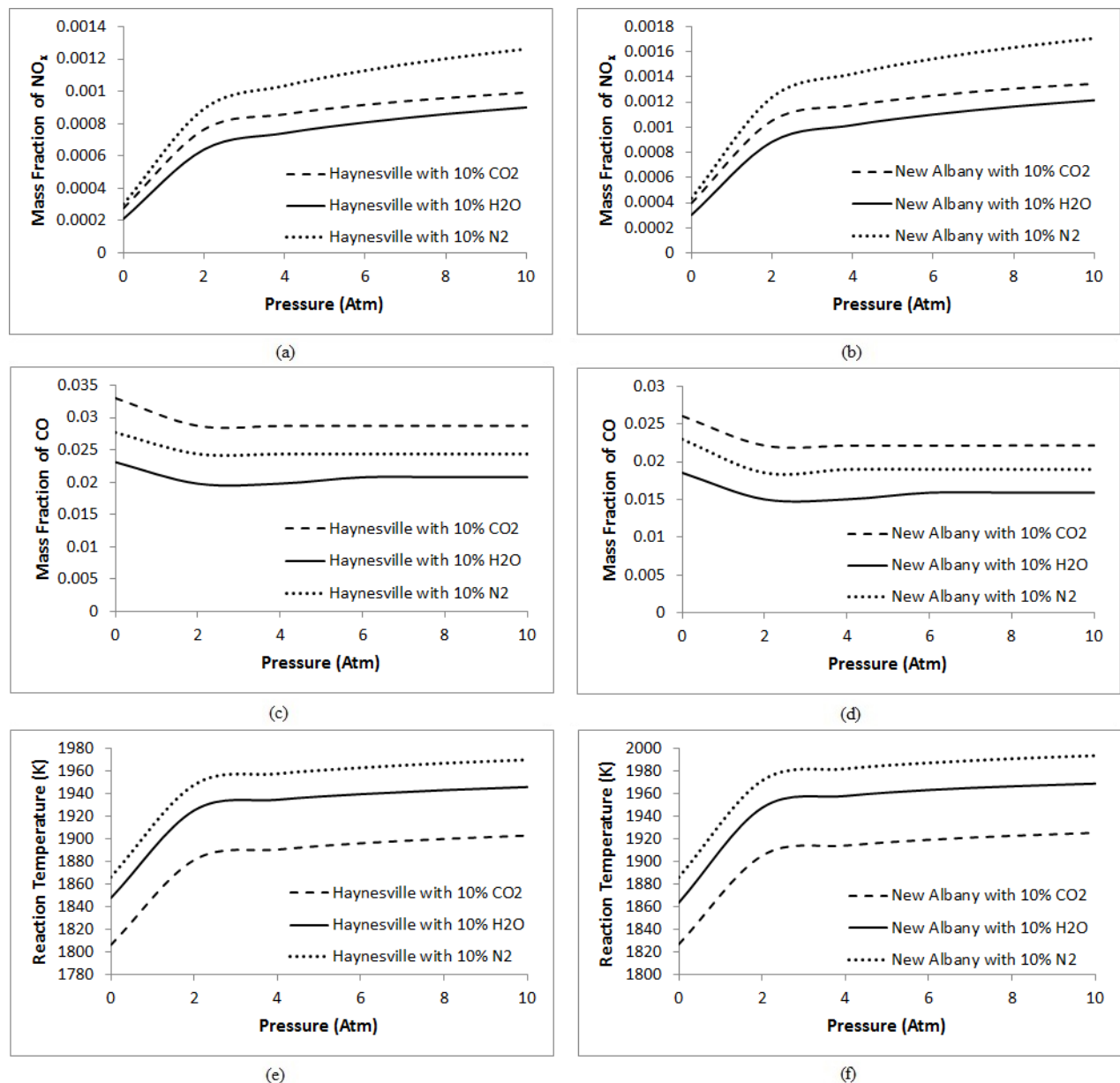


Figure 7. The mass fraction and reaction temperatures of shale gases at different pressures with 10% dilution rates: (a) NO_x mass fractions for Haynesville, (b) NO_x mass fractions for New Albany, (c) CO mass fractions for Haynesville, (d) CO mass fractions for New Albany, (e) Reaction temperatures for Haynesville, and (f) Reaction temperatures for New Albany shale gas.

NO_x mass fractions for Haynesville and New Albany gases with and without additions increases by the rising

wall temperature as represented in Figure 8a, b and c. The enhancing wall temperature reduces heat transfer from the reaction field to outside and advances both the reaction temperature and NO_x. The difference among NO_x values of the combustions with H₂O and the other diluent added airs rises with the lifting wall temperature. The increment rates for NO_x between 300 and 1200 K of the wall temperature with 10% N₂, CO₂, and H₂O dilutions are 235, 259, and 235% for Haynesville and 224, 243, and 226% for New Albany shale gas in turn.

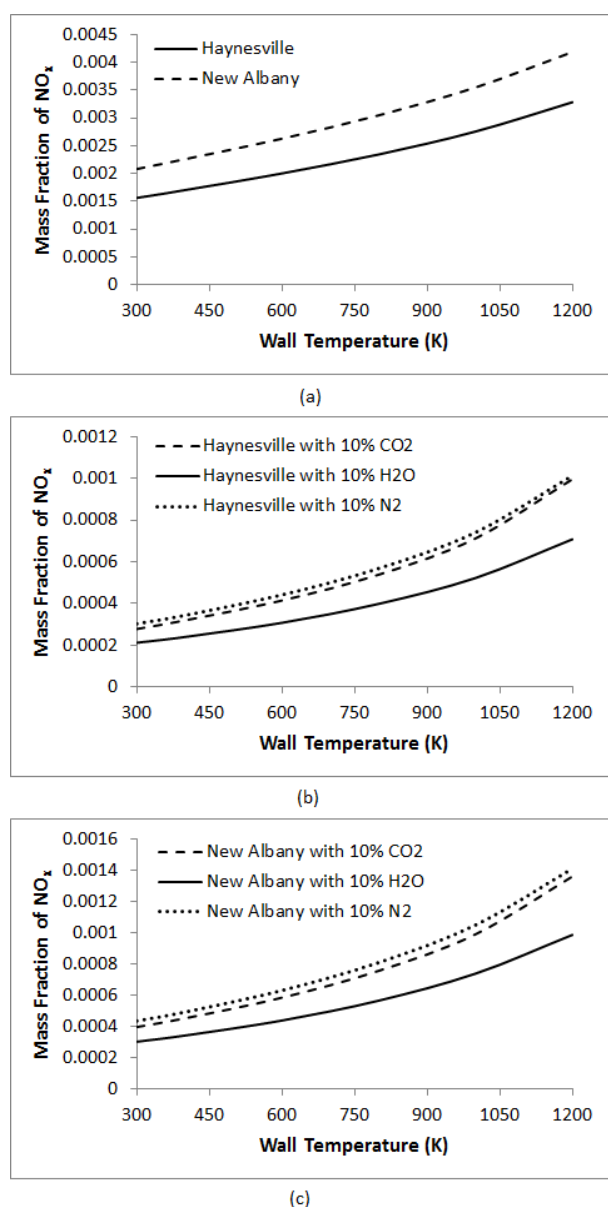


Figure 8. NO_x mass fractions of shale gases at various wall temperatures: (a) NO_x mass fractions for Haynesville and New Albany without dilution, (b) NO_x mass fraction for Haynesville with 10% dilution rates, (c) NO_x mass fractions for New Albany with 10% dilution rates.

Figure 9a, b, and c present CO mass fractions with and without dilutions at various wall temperatures. The increasing wall temperature raises CO emissions too.

The higher temperatures urge CO formation between carbon and oxygen atoms. The rising rates for CO mass fractions between 300 and 1200 K of the wall temperature with 10% CO₂, N₂, and H₂O dilutions are 8.7, 10.9, and 12.4% for Haynesville and 15, 13.1, and 17% for New Albany respectively. The difference among CO emissions of combustions with diluent added airs is constant at the enhancing wall temperature for both gases.

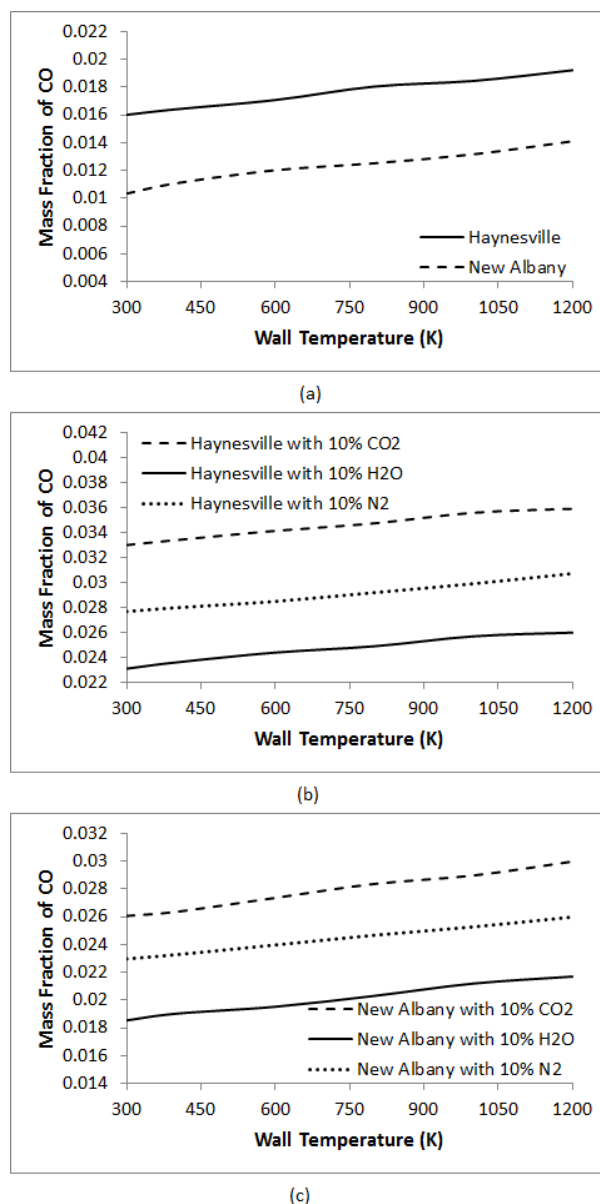


Figure 9. CO mass fractions of shale gases at various wall temperatures: (a) CO mass fractions for Haynesville and New Albany without dilution, (b) CO mass fraction for Haynesville with 10% dilution rates, (c) CO mass fractions for New Albany with 10% dilution rates.

The rearing wall temperature also uplifts the reaction temperatures for all the shale gases with and without dilutions as depicted in Figure 10a, b, and c. The increasing ratios for the reaction temperatures between 300 and 1200 K of the wall temperature with 10% N₂, H₂O, and CO₂ dilutions are 5.5, 5.4, and 5.8% for Haynesville and 5.5, 5.6, and 5.8% for New Albany in

sequence. The difference among reaction temperatures of the combustions with diluent added airs stays stationary at the enhancing wall temperature for both gases.

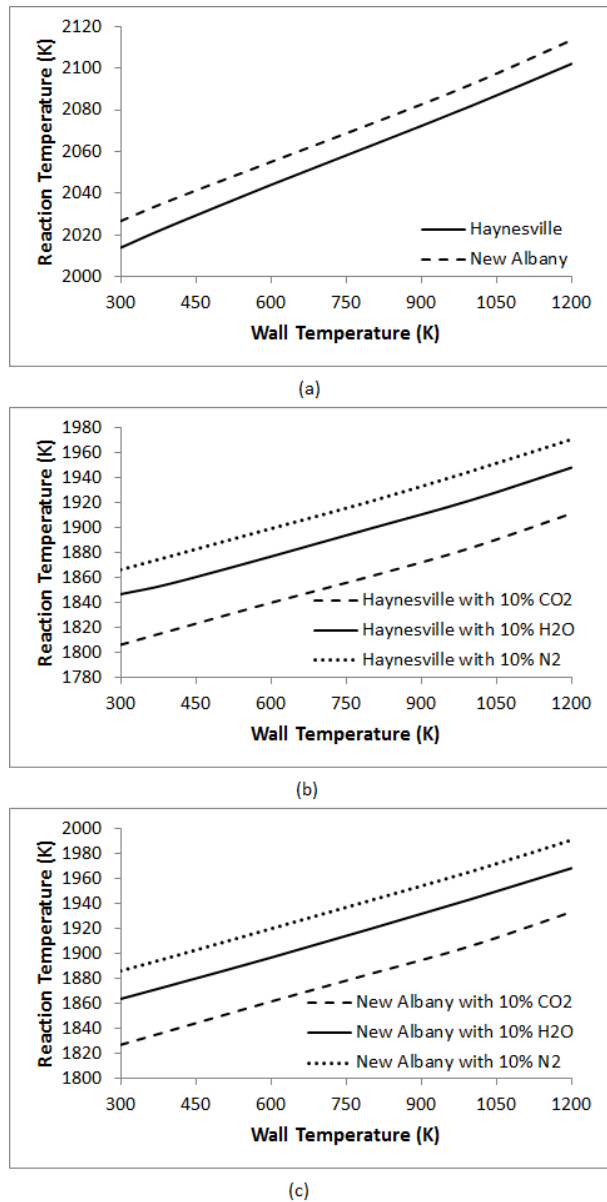


Figure 10. Reaction temperatures of shale gases at various wall temperatures: (a) Reaction temperatures for Haynesville and New Albany without dilution, (b) Reaction temperature for Haynesville with 10% dilution rates, (c) Reaction temperature for New Albany with 10% dilution rates.

In industrial systems, to reduce the exhaust emissions of environmental pollutants as NO_x , CO, soot, etc. producing at the end of combustion process is used both the procedure of CO_2 and H_2O addition to reactants and pre-heat technique of reactants by exhausted gases (Sabia et al., 2015). Generally, it is seen that the addition of CO_2 , H_2O , and N_2 to reactants reduces NO_x with reaction temperature (Zahedi and Yousefi, 2014) and increases CO in exhaust emissions. Moreover, H_2O addition shows the best performance in taking care of NO_x , CO, and reaction temperature as a whole. The increase of pressure raises NO_x (Zahedi and Yousefi,

2014) and reduces CO as expected (Muharam et al., 2015). The rise in wall temperature enhances pollutants emissions and reaction temperature.

CONCLUSION

The characteristics and hazardous emissions of turbulent, non-adiabatic, non-premixed combustions of moist air and shale gases extracted from New Albany and Haynesville fields of United State are numerically investigated in this study. Furthermore, the reaction temperatures and mass fractions of nitrogen oxides and carbon monoxide are determined for various equivalence ratios, pressures, and wall temperatures under the effects of CO_2 , H_2O , and N_2 diluents added in the burning air. The following results are obtained:

- The maximum values of mass fractions of NO_x for New Albany and Haynesville shale gas combustion are 0.0021 kg NO_x/kg at $\text{ER}=1.025$ and 0.00158 kg NO_x/kg at $\text{ER}=1.02$ in turn. The difference between NO_x of both shale gas combustions at $\text{ER}=1$ is 25%. The mass fractions of CO rise by raising equivalence ratio. The difference between CO mass fractions is 24.5% at $\text{ER}=1$. The maximum reaction temperatures for New Albany and Haynesville shale gases are 2027 and 2014 K.
- The rising dilution rates generally decrease NO_x values for both shale gases. H_2O dilution is more effective over NO_x to be reduced because of its high heat hold capacity especially. 5% dilution additions of H_2O , CO_2 , and N_2 diminish NO_x mass fractions at the rate of 59.1, 51.3, and 51.2% for Haynesville and 57.2, 49.3, and 49.1% for New Albany respectively. The dilution additions increase CO mass fractions for all the shale gas. H_2O dilution has the least effect over CO fractions to enhance. CO_2 has the biggest effect on the reaction temperature to decrease.
- The rearing pressure increases NO_x values for both gases. The highest values for NO_x occur with N_2 dilution followed by CO_2 and H_2O in the decreasing range. On the contrary, the escalating pressure fades CO mass fractions. The advancing pressure causes the reaction temperatures to upsurge. The increment ratios between 0 and 10 Atm for N_2 , H_2O , and CO_2 dilutions are 5.5, 5.3, and 5.3% for Haynesville and 5.6, 5.6, and 5.4% for New Albany respectively.
- The ascending wall temperature elevates NO_x values for both gases because of thermal NO_x increment at high reaction temperature. It also boosts both the reaction temperatures and CO mass fractions. The rising rates for the reaction temperatures between 300 and 1200 K of the wall temperature with 10% N_2 , H_2O , and CO_2 additions are 5.5, 5.4, and 5.8% for Haynesville and 5.5, 5.6, and 5.8% for New Albany.

ACKNOWLEDGEMENT

The present work is not financially supported by any funding agency.

REFERENCES

Akça H., Ürel G., Karacan C. D., Tuygun N., and Polat E., 2017, The Effect of Carbon Monoxide Poisoning on Platelet Volume in Children, *J Pediatr Emerg Intensive Care Med*, 4, 13-16.

Alberts W. M., 1994, Indoor Air Pollution: NO, NO₂, CO, and CO₂, *J Allergy Clin Immunol*, 94, 289-95.

ANSYS Release 12.0. Tutorial 14. Modeling Species Transport and Gaseous Combustion. 1-46, ANSYS, Inc, 2009.

Bilgen, S., and Sarıkaya, İ., 2016, New Horizon in Energy: Shale Gas, *Journal of Natural Gas Science and Engineering*, 35, 637-645.

Bullin K., Krouskop P., and Bryan Research and Engineering Inc. Bryan, Tex., 2008, Composition Variety Complicates Processing Plans for US Shale Gas, *E-book, Based on: Annual Forum, Gas Processors Association, Houston Chapter*, Houston.

Chang Y., Huang R., Ries R. J., and Masanet E., 2015, Life-Cycle Comparison of Greenhouse Gas Emissions and Water Consumption for Coal and Shale Gas Fired Power Generation in China, *Energy*, 86, 335-343.

Cohen B, and Winkler H., 2014, Greenhouse Gas Emissions from Shale Gas and Coal for Electricity Generation in South Africa, *S Afr J Sci.*, 110 (3/4), 1-5.
Garreton D. and Simonin O., 1994, Aerodynamics of Steady State Combustion Chambers and Furnaces, *In ASCF Ercoftac Cfd Workshop*, Org: EDF Chatou, France.

Hayashi S., Yamada H., Shimodaira K., and Machida T., 1998, NO_x Emissions from Non-Premixed, Direct Fuel Injection Methane Burners at High-Temperature and Elevated Pressure Conditions, *Twenty-Seventh Symposium (International) on Combustion/The Combustion Institute*, 1833-1839.

Hraiech, I., Sautet, J. C., Yon, S., and Mhimid, A., 2015, Combustion of Hythane Diluted with CO₂, *Thermal Science*, 19 (1), 1-10.

Jerzak W., Kuzniaa M., Zajemska M., 2014, The Effect of Adding CO₂ to The Axis of Natural Gas Combustion Flames on CO and NO_x Concentrations in The Combustion Chamber, *Journal of Power Technologies*, 94 (3), 202-210.

McTaggart-Cowan G. P., Wu N., Jin B., Rogak S. N., Davy M. H. and Bushe W. K., 2009, Effects of Fuel Composition on High-Pressure Non-Premixed Natural Gas Combustion, *Combust. Sci. and Tech.*, 181, 397-416.

Muharam, Y., Mahendra, M., Giffari, F., and Kartohardjono, S., 2015, Effects of Injection Temperature and Pressure on Combustion in An Existing Otto Engine using CNG Fuel, *Journal of Environmental Science and Technology*, 8 (1), 25-34.

Lan, Y., Yang, Z., Wang, P., Yan, Y., Zhang, L., and Ran, J., 2019, A Review of Microscopic Seepage Mechanism for Shale Gas Extracted by Supercritical CO₂ Flooding, *Fuel*, 238, 412-424.

Ozturk, S., 2018, A Computational Evaluation for Hazardous Emissions of Non-Premixed Shale Gas Combustion, *Journal of Scientific and Engineering Research*, 5 (11), 256-264.

Sabia, P., Lavadera M. L., Giudicianni P., Sorrentino G., Ragucci, R., and Joannon, M., 2015, CO₂ and H₂O Effect on Propane Auto-Ignition Delay Times under Mild Combustion Operative Conditions, *Combustion and Flame*, 162 (3), 533-543.

Silva C. V., Franca F. H. R, and Vielmo H. A., 2007, Analysis of The Turbulent, Non-Premixed Combustion of Natural Gas in A Cylindrical Chamber with and without Thermal Radiation, *Combust. Sci. and Tech.*, 179, 1605-1630.

Vargas A. C., Arrieta A. A., and Arrieta C. E., 2016, Combustion Characteristics of Several Typical Shale Gas Mixtures, *Journal of Natural Gas Science and Engineering*, 33, 296-304.

Wang Q., Chen X., Jha A. N., and Rogers H., 2014, Natural Gas from Shale Formation - The Revolution, Evidences and Challenges of Shale Gas Revolution in United States, *Renewable and Sustainable Energy Reviews*, 30, 1-28.

Wang, Y., Liao, B., Qiu, L., Wang, D., Xue, Q., 2019, Numerical Simulation of Enhancing Shale Gas Recovery Using Electrical Resistance Heating Method, *International Journal of Heat and Mass Transfer*, 128, 1218-1228.

Zahedi P., and Yousefi K., 2014, Effects of Pressure and Carbon Dioxide, Hydrogen and Nitrogen Concentration on Laminar Burning Velocities and NO Formation of Methane-Air Mixtures, *Journal of Mechanical Science and Technology*, 28 (1), 377-386.

Ziani, L. and Chaker, A., 2016, Ambient Pressure Effect on Non-Premixed Turbulent Combustion of CH₄-H₂ Mixture, *International Journal of Hydrogen Energy*, 41, 11842-11847.



Suat OZTURK received his B. Sc. degree in mechanical engineering in 1996 from Hacettepe University, Turkey. He completed his M. Sc. in electrical and computer engineering at University of Florida in 2001, USA and mechanical engineering at Zonguldak Bülent Ecevit University in 2008, Turkey. He obtained his Ph. D. degree in mechanical engineering at Zonguldak Bülent Ecevit University in 2017, Turkey. He is working as doctor in Department of Electronic and Automation at Zonguldak Vocational School, Zonguldak Bülent Ecevit University, Turkey. His research interests include energy, combustion, computational fluid dynamics, forecasting, economic analysis, composites and mechanical properties.



PREDICTION OF THE ANNUAL HEAT LOAD OF AN ARTICULATED ELECTRIC URBAN BUS

M. Nicem TANYERİ* and S. Çağlar BAŞLAMIŞLI**

*ASELSAN Inc., 06172 Ankara, Turkey, mntanyeri@aselsan.com.tr

** Hacettepe University Department of Mechanical Engineering,
06800 Ankara, Turkey, scaglarb@hacettepe.edu.tr

(Geliş Tarihi: 25.03.2019, Kabul Tarihi: 19.12.2019)

Abstract: This study presents a detailed method to estimate the thermal load of an articulated electric urban bus. Thermal load, which consists of solar, metabolic, ambient and ventilation heat loads, is estimated hourly for a one year period. A mathematical model takes into account the hourly passenger occupancy rate, hourly weather condition of the line and hourly solar loads as input and predicts the heat load accordingly. In order to determine the importance and contribution of each thermal load, all loads are calculated individually. Calculations are made for each hour of a year in order to observe the change of the contribution of each load in time. With the proposed method, the thermal load of an electric bus can be predicted in the system design phase and the HVAC system of the bus can be selected accordingly.
Keywords: Thermal loads, HVAC, Electric bus, Electromobility, Electrification.

BİR ELEKTRİKLİ KÖRÜKLÜ ŞEHİR İÇİ OTOBÜSÜN YILLIK ISI YÜKÜ KESTİRİMİ

Özet: Bu çalışma, körüklü elektrikli şehir içi otobüsünün ısı yükünü tahmin etmek için ayrıntılı bir yöntem sunmaktadır. Güneş, metabolik, ortam ve havalandırma ısı yüklerinden oluşan termal yük, bir yıllık bir süre için saatlik olarak tahmin edilmiştir. Kullanılan model, saatlik yolcu doluluk oranını, hattın bulunduğu bölgedeki saatlik hava durumunu ve saatlik güneş yüklerini girdi olarak alır ve ısı yükünü buna göre tahmin eder. Her termal yükün önemini ve katkısını belirlemek için tüm yükler ayrı ayrı hesaplanmıştır. Her yükün zaman içindeki katkısının değişimini gözlemlemek için yılın her saati için hesaplamalar yapılmıştır. Önerilen yöntemle, bir elektrik otobüsün termal yükü sistem tasarım aşamasında tahmin edilebilir ve elektrikli otobüsün HVAC sistemi buna göre seçilebilir.

Anahtar Kelimeler: Isı yükleri, HVAC, Elektrikli otobüs, Elektromobilite, Elektrifikasyon.

INTRODUCTION

Global warming probably is the one of the biggest environmental problems of today's world. Over the last fifteen years, environmental foundations and organizations have invested hundreds of millions of dollars into combating global warming (Shellenberger et al. 2004). Global warming is partly due to transportation activities which produce substantial amounts of carbon dioxide emissions. In addition, these have side effects like noise pollution and traffic congestion. It is believed that the transportation sector, which consumes the quarter of the world's energy production, should be made more environmentally sensitive for a sustainable growth (Juan et al. 2016). Use of electric buses for public transportation may be an alternative solution in order to decrease urban noise and air pollutions (Pihlatie et al. 2015). As a matter of fact, due to ecological and economic concerns, there is an increasing interest in electric buses. Bus producers are observed to invest increasingly in the production of electric and hybrid buses (Graurs et al. 2015).

As far as fuel and electrical energy consumptions calculated for the SORT 2 (Standardised On-Road Test)

driving cycle for 12-meter buses are concerned, it is proven that electrical buses perform better than buses with conventional engines powered with CNG (Compress Natural Gas) or diesel fuel. Energy consumptions per km of CNG, diesel fuel and electric buses are 4.98 kWh, 3.90 kWh and 0.95kWh, respectively (Gis et al. 2017).

For bus operators, it may sometimes make sense to pick up a ready-made electric bus; however, for large bus lines that carry thousands of passengers daily by a populous bus fleet, it may be more efficient to use a bus that is designed especially for the specific line. In order to design an efficient electric bus for a specific line, design requirements should be carefully determined. Special care should be given to requirements imposed by energy consuming sub-systems, such as the HVAC (Heating, ventilation air conditioning) system, which is the main focus of the present study. To design and select elements of a bus HVAC system, it is crucial to accurately determine the heating and cooling loads (Aktacir et al. 2008). Energy consumption of the HVAC system accounts for about 20% of the total energy consumption of a bus (Kamiya 2006). Underestimated HVAC energy consumption may lead to thermal comfort problems,

while an oversized HVAC system may increase manufacturing and operating costs.

In this paper, we propose a calculation model for the determination of the energy requirements of a HVAC system. More specifically, the HVAC power requirement of a specific route of the Istanbul Metrobus network is calculated in detail by taking into account the annual hourly passenger density, the hourly position of the sun, the location of the bus line and the bus working hours. In the present case, Istanbul Metrobus network is operated by Metrobus vehicles (Figure 1) with internal combustion engines. The present 18-meter articulated ICE (Internal Combustion Engine) driven bus design is taken as a reference to design a HVAC system to be installed in an electrified version of the bus.



Figure 1. A photo of Metrobus

A system design of an electric bus is presented in the study of Göhlich et al. (2018). The researcher concludes that HVAC system is the most energy consuming auxiliary system and therefore must be given special attention in electric bus system design. Additionally, the heating case is considered as the most critical condition if zero-emission operation is required. Exergy analysis was implemented to improve the intercity bus air-conditioning system design by Tosun et al. (2016). In this study hourly cooling capacity was determined in detail. In the study of Ünal (2016), the cooling load of a fully loaded bus at steady state was obtained as 22 kW. In the study of Göhlich et al. (2018) assumed a constant 24 kW load for heating in their study. The power required to cool the vehicle in summer at an outdoor temperature of 35 °C is assumed to be 24 kW. As a matter of fact these 24kW loads increases vehicle consumption by 1.3 kWh/km for an average velocity 18 km/h and 2 kWh/km for an average velocity of 12 km/h. Javani et al. (2012) studied the role of design parameters on the cooling capacity of hybrid and electric vehicles and energy and exergy analyses were presented. Ružić et al. (2011) investigated thermal interaction between a human body and a tractor cab. In this study a model is developed to calculate solar thermal loads of a tractor cab that has windows on its four surfaces. In the study of Stancato et al. (1992) a mathematical model was developed to simulate cooling loads in a cab and the results of the simulation were

compared with experimental results. Fayazbakhsh et al. (2013) developed a model to calculate the head load of an internal combustion engine car. Ding and Zito (2001) presented a differential equation for the cabin that relates the heat transfer coefficient, discharge panel temperature and discharge volumetric air flow to the interior and the solution of the corresponding transient heat transfer differential equation was presented.

In the proposed study, loads are calculated for continuous working condition and heat loads that are required to be reached at first start of the bus are neglected. For calculations and model development, previous work accomplished by Fayazbakhsh et al. (2013) and the ASHRAE standard (2001) are taken into account. In the study of Fayazbakhsh et al. (2013) heat load is calculated for a passenger vehicle with internal combustion engine. In the case presented in our study, the heat generation of the electric motor is negligible compared to the internal combustion engine. Therefore, heat loads of exhaust system and internal combustion are omitted. Moreover, in the case of an urban bus, the number of passenger is large and very changeable. The bus has a very specific line and work schedule compared to a passenger car; and therefore this allows calculating HVAC energy consumption with higher accuracy. Furthermore, the geometry (a bus is very similar to a cuboid) and window/body ratio are different, which increases the solar heat load.

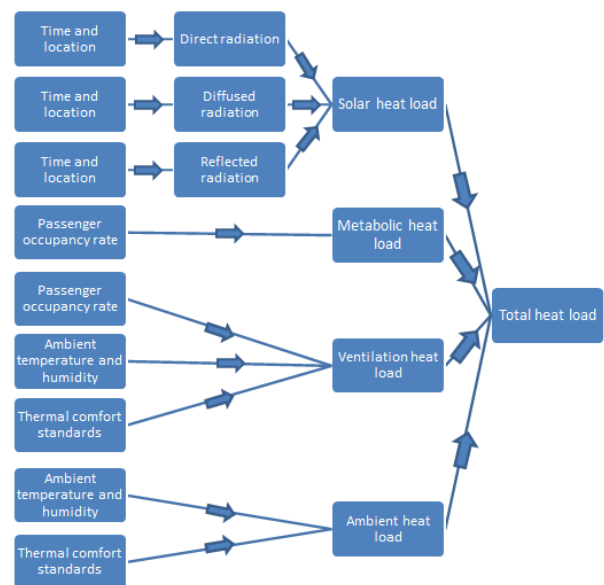


Figure 2. Flow chart of the calculation

In the first section, metabolic, solar, ambient and ventilation heat models are introduced and thermal comfort standards are presented. In the second section, firstly, thermal properties of the vehicle, the location and operation system of the line are presented. After that, the total heat load of the Metrobus for a period of one year is predicted according to the model by considering the weather condition, bus schedule and passenger occupancy rates. Finally the required HVAC system is selected according to the results of the calculations.

The details of the calculations and the flow sequence are summarized in Figure 2.

BACKGROUND

Heat Model

Heat gain refers to the transfer of heat into or out of the bus cabin through a variety of components. There are nine main components of heat gain of an internal combustion bus. These components can support the HVAC system (for example, radiation that heats up the bus in a cold winter day) or can work against the HVAC system (for example, metabolic heat of passenger that heats up the bus in a hot summer day). In order to determine the HVAC requirements of a bus, the heat load is calculated by an inductive method. Here, the model developed by Fayazbakhsh et al. (2013) for a typical internal combustion car cabin is adapted for the electric bus. The heat load model developed for a typical car cabin is given in equation (1).

$$\begin{aligned} \dot{Q}_{Total} = \dot{Q}_{Met} + \dot{Q}_{Dir} + \dot{Q}_{Dif} + \dot{Q}_{Ref} & \quad (1) \\ + \dot{Q}_{Amb} + \dot{Q}_{Exh} + \dot{Q}_{Eng} & \\ + \dot{Q}_{Ven} + \dot{Q}_{AC} & \end{aligned}$$

\dot{Q}_{Total} refers to the net total heat flow into bus cabin, \dot{Q}_{Met} is the metabolic heat flow generated by passengers, \dot{Q}_{Dir} is the heat flow of direct radiation, \dot{Q}_{Dif} is the heat flow caused by diffused radiation, \dot{Q}_{Ref} is the heat flow of reflected radiation, \dot{Q}_{Amb} is the heat exchange between ambient and bus cabin, \dot{Q}_{Exh} is the heat flow due to exhaust system, \dot{Q}_{Eng} is the heat flow of the engine, \dot{Q}_{Ven} is the heat flow generated by the air that is blown by HVAC system into bus cabin so as to supply fresh air for passengers and \dot{Q}_{AC} is the thermal load created by the air conditioning system to reach the comfort temperature. Since, there is no exhaust system, \dot{Q}_{Exh} is omitted and since the heat generation of the electric motor is negligible compared to the internal combustion engine \dot{Q}_{Eng} is also assumed to be zero. Thus, equation (1) becomes;

$$\begin{aligned} \dot{Q}_{Total} = \dot{Q}_{Met} + \dot{Q}_{Dir} + \dot{Q}_{Dif} + \dot{Q}_{Ref} & \quad (2) \\ + \dot{Q}_{Amb} + \dot{Q}_{Ven} + \dot{Q}_{AC} & \end{aligned}$$

Hence, in order to calculate total heat flow into an electric bus cabin equation (2) can be used.

In Figure 3, thermal loads acting on an articulated bus are illustrated. In the following sections each component is explained in detail.

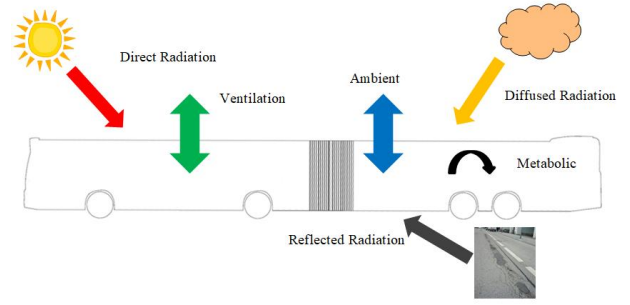


Figure 3. Representation of thermal loads

Metabolic Heat Load

Passengers in the bus cabin create heat load because of their metabolic activities. For the calculation of metabolic load of passengers, they are separated into three different groups; driver, sitting passenger and standing passengers. Therefore, the metabolic load can be calculated from equation (3);

$$\begin{aligned} \dot{Q}_{Met} = \dot{Q}_{Driver} + n_{sitting}\dot{Q}_{sitting} & \quad (3) \\ + n_{Standing}\dot{Q}_{Standing} & \end{aligned}$$

where \dot{Q}_{Driver} refers to the metabolic load of driver and $\dot{Q}_{sitting}$ and $\dot{Q}_{Standing}$ are the metabolic loads of sitting passengers and standing passengers, respectively. Number of passenger is represented with $n_{sitting}$ and number of standing passenger is represented with $n_{standing}$. Metabolic load of a person can be calculated from equation (4);

$$\dot{Q}_{Met\ one\ Person} = MA_{DU} \quad (4)$$

where metabolic heat production rate, M , of a sitting passenger and standing passenger are defined as 60 W/m² and 70 W/m², respectively (ASHRAE 2001). Metabolic heat production rate of a heavy vehicle driver is 185 W/m² while this value ranges between 60 W/m² and 115 W/m² for a car driver so for an articulated bus it is assumed as 120 W/m² (ASHRAE 2001).

A_{DU} refers to the DuBois area which estimates the surface area of a person from the mass and height of one person. (5) (Lee et al. 2008)

$$A_{DU} = 0.202 \times Weight^{0.425} \times Height^{0.725} \quad (5)$$

$Weight$ and $Height$ refer to mass in kilogram and height in meter of a person, respectively.

Solar Heat Loads

Solar heat load is divided into three components; direct radiation, diffused radiation and reflected radiation. Total solar heat load is the summation of these three components. The solar gain model assumes clear sky conditions for sizing purposes.

Geometry of a bus is assumed to be a rectangular prism. Solar angle of a surface is given in Figure 4 (Goswami et al. 2015).

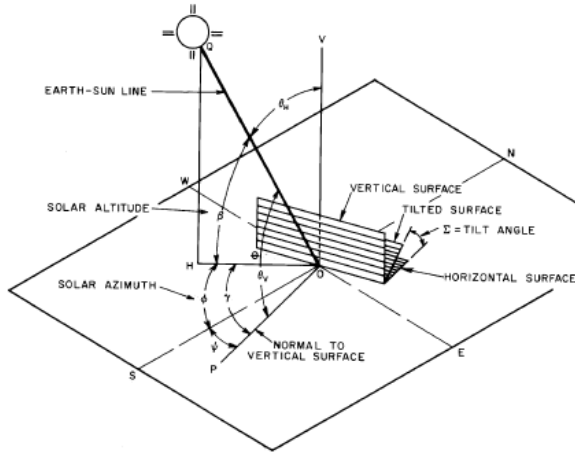


Figure 4. Solar angle of a surface (Goswami et al. 2015)

For any surface, the angle between the surface normal and the position of the sun which is the incident angle, θ , can be found from equation (6).

$$\theta = \cos^{-1}(\sin \beta \times \cos \Sigma + \cos \gamma \times \cos \beta \times \sin \Sigma) \quad (6)$$

where, γ is the azimuth angle, β is the altitude angle and Σ is the surface tilt angle. β can be calculated from equation (7)

$$\beta = \sin^{-1}(\sin L \times \sin \delta + \cos L \times \cos \delta \times \cos H) \quad (7)$$

where, δ is the solar declination, L is the latitude and H is the hour angle, where

$$H = 15(\text{Atlantic Standard Time} - 12) \quad (8)$$

Solar declination, δ , can be calculated from equation (9).

$$\delta = 23.45 \sin([360(284 + n)]/365) \quad (9)$$

where, n represents the day of the year.

Direct Radiation

Direct solar radiation (I) is the proportion of the almost rectilinear solar radiation, which reaches the Earth's surface from an angle with a distance of 0.25° to the center of the sun and reaches a normal area, which is oriented perpendicularly to the direction of the radiation.

Direct radiation load can be calculated from equation (10) (Fayazbakhsh et al. 2013);

$$\dot{Q}_{Dir} = S\tau I_{Dir} \cos(\theta) \quad (10)$$

where, S is the area of the surface, τ is the transmissivity of the surface, I_{Dir} is the direct normal irradiance and \dot{Q}_{Dir} is the heat gain due to direct radiation.

Irradiance of the direct radiation can be calculated from equation (11) (ASHRAE 2001).

$$I_{Dir} = \frac{A}{e^{\left(\frac{B}{\sin(\beta)}\right)}} \quad (11)$$

A and B are constants that change with monthly. Values of A and B that are obtained from ASHRAE Handbook of Fundamentals (2001) are given in Table 1. Data are for 21st day of each month (ASHRAE 2001). To increase the resolution of calculation A , B and C values are interpolated to their daily values.

Table 1. Extraterrestrial Solar Irradiance and Related Data

| Month | A [$\frac{W}{m^2}$] | B [$\frac{1}{airmass}$] | C |
|-----------|-----------------------|---------------------------|-------|
| January | 1230 | 0.142 | 0.058 |
| February | 1215 | 0.144 | 0.060 |
| March | 1186 | 0.156 | 0.071 |
| April | 1136 | 0.180 | 0.097 |
| May | 1104 | 0.196 | 0.121 |
| June | 1088 | 0.205 | 0.134 |
| July | 1085 | 0.207 | 0.136 |
| August | 1107 | 0.201 | 0.122 |
| September | 1151 | 0.177 | 0.092 |
| October | 1192 | 0.160 | 0.073 |
| November | 1221 | 0.149 | 0.063 |
| December | 1233 | 0.142 | 0.057 |

Diffused Radiation

Diffused radiation is the portion of solar radiation which arrives on the surface of the Earth after single or repeated dispersion in the atmosphere (Goswami 2015). The diffused radiation heat gain can be calculated from equation (12) (Fayazbakhsh et al. 2013).

$$\dot{Q}_{Dif} = S\tau I_{Dif} \quad (12)$$

where, I_{Dif} is given in equations (13a) and (13b) (ASHRAE 2001). Equation (13a) is for surfaces other than vertical and equation (13b) is for vertical surfaces.

$$I_{Dif} = CI_{Dir} \frac{1 + \cos(\Sigma)}{2} \quad (13a)$$

$$I_{Dif} = CI_{Dir} (0.55 + 0.437 \cos(\theta) + 0.313 \cos^2(\theta)) \quad (13b)$$

For vertical surfaces of the bus such as front, back, left and right surfaces equation (13b) is utilized.

Reflected Radiation

Reflected radiation refers to the part of radiation heat gain that is reflected from the ground and with strikes the body surfaces of the vehicle (Fayazbakhsh et al. 2013). Heat gain due to reflected radiation can be calculated from equation (14).

$$\dot{Q}_{Ref} = S\tau I_{Ref} \quad (14)$$

where, I_{Ref} is defined in equation (15) for all surface orientation (ASHRAE 2001).

$$I_{Ref} = I_{Dir}(C + \sin(\beta))\rho_g \frac{1 - \cos(\Sigma)}{2} \quad (15)$$

where, ρ_g is the reflectivity coefficient of the ground.

Ambient Heat Load

There may be difference between outside temperature and inside temperature. This temperature difference causes heat transfer through surfaces from outside into bus cabin on hot days and heat transfer from bus cabin to outside on cold days. The heat transfer can be calculated from equation (16) (ASHRAE 2001).

$$\dot{Q}_{Amb} = SU(T_s - T_i) \quad (16)$$

Here, S is the area of the surface, U is the overall heat transfer coefficient of the surface, T_s and T_i refer to outer surface temperature and cabin temperature of the bus, respectively. U is composed of three parts; conduction of the body, convection of inner and outer surfaces, respectively. U can be calculated from equation (17).

$$\frac{1}{U} = \frac{1}{h_o} + \frac{\lambda}{k} + \frac{1}{h_i} \quad (17)$$

where λ is the thickness of the material, k is the conduction coefficient of the body, h_o and h_i are the convection coefficients of the outer and inner surfaces, respectively. h_i and h_o are assumed only convective and calculated from equation (18a) and equation (18b) (Li et al. 2013).

$$h_i = 9 + 3.5v^{0.66} \quad (18a)$$

$$h_o = 9 + 3.5v^{0.66} \quad (18b)$$

where, v is the relative speed of the air in m/s with respect to corresponding surface. Since the air in the bus cabin assumed to be stationary, from equation (18a) h_i becomes 9 W/m²K and h_o is calculated according to velocity data obtained from the driving cycle test.

Ventilation Heat Load

Passengers in the bus consume oxygen for breathing. Since the volume of the bus cabin is limited for the long-term O₂ needs of passengers, fresh air must be supplied into the bus cabin. According to ASHRAE Standard 62 it is recommended to supply 8L of fresh air per second for one passenger (ASHRAE 1999). The heat load because of air exchange between outside and bus cabin can be calculated from equation (18a) and equation (18b). The first part of the equation is for the calculation of sensible heat load, while the second part is for the calculation of latent heat load.

$$\dot{Q}_{Ven} = \dot{V}_{ven}\rho c_p \Delta T + \dot{V}_{ven} \Delta W (4775 + 1.998 \Delta T) \quad (19)$$

where, \dot{V}_{ven} is the air flow rate, ρ is the air density (1.2 kg/m³), c_p is the specific heat of air (1000 J/(kgK)) and ΔT and ΔW are the temperature difference and humidity ratio difference, respectively.

Thermal Comfort Requirements

Acceptable ranges of operative temperature and humidity for people in typical summer and winter clothing during primarily sedentary activity are defined in Table 2. For the design of the HVAC system of the bus, temperature and relative humidity range that is shown in blue in Figure 5 is selected (ASHRAE 1999).

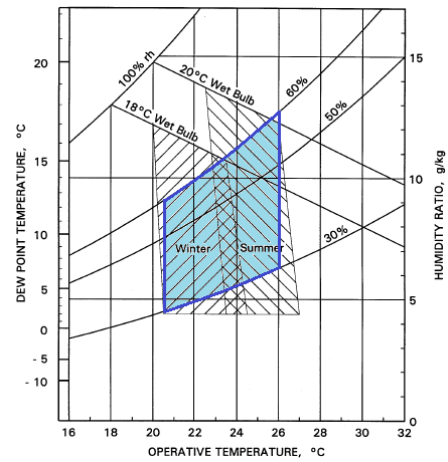


Figure 5. Thermal comfort range of temperature and humidity (adapted from ASHRAE standard 62 (1999))

Temperatures and humidity ratios that are selected as design requirements for HVAC system for different season of year are represented in Table 2.

Table 2. Design temperatures and humidity ratio

| Season | Temperature range (°C) | Humidity range (%) |
|--------|------------------------|--------------------|
| Winter | 20.5-23 | 30-60 |
| Spring | 22-24.5 | 30-60 |
| Summer | 23.5-26 | 30-60 |
| Fall | 22-24.5 | 30-60 |

DETERMINATION OF HVAC REQUIREMENTS

Location and Weather

In this part of the study, Metrobus Line of Istanbul is analyzed to determine the HVAC heat load requirements of a bus line. Latitude and longitude of Istanbul are 41.015° and 28.979°, respectively. For the calculations, hourly outside temperature and relative humidity data are obtained from Turkish State Meteorological Service. The Metrobus network is mainly established on the East-West axis. Metrobus line is shown in Figure 6.



Figure 6. Map of the Metrobus Line

Operation System of the Bus Line

The Metrobus line has one route. However, on the same route there are separate lines with different start and end stations. In addition, these different lines have different working hours and time tables but, working hours are usually between 06:00 and 24:00. However, there is one line that is only active at night passing through all 44 stations. For HVAC calculation only lines that are active from 06:00 to 24:00 are considered.

Passenger Compartment

Passenger capacity of the 18-m articulated Metrobus is 160. Number of seats is 43+1 (one for driver). Surface areas, S , that are obtained from the technical drawings of the Metrobus and transmissivity, τ , of the surfaces are shown in Table 3. According to the safety regulation, the transmittance of visible light through the window should be at least 70% in the US and 75% in Europe. Transmissivity of the windows of the Metrobus is assumed to be 0.75 according to J.W.Lee et al (2014).

Table 3. Transmissivity and surface area of each bus surface

| Surface | Part | Material | Area | Transmissivity |
|----------------|-------------------|----------|--------------------|----------------|
| Front | Wind-shield | Glass | 3.3m ² | 0.75 |
| | Body | Al | 4.2m ² | 0 |
| Rear | Windows and doors | Glass | 1.9m ² | 0.75 |
| | Body | Al | 5.2m ² | 0 |
| Left | Windows | Glass | 17.1m ² | 0.75 |
| | Body | Al | 39.6m ² | 0 |
| Right | Windows | Glass | 17.6m ² | 0.75 |
| | Body | Al | 39.1m ² | 0 |
| Top and bottom | Body | Al | 45.9m ² | 0 |

In the analysis, It is accepted that surfaces remove the solar radiative heat load that is absorbed through convection because there is always air flow around the body. Thus, it is assumed that there is no heat gain from aluminum surfaces.

Analysis

Since the passenger occupancy rate, which affects the thermal load most, is similar in both directions, HVAC power requirement is calculated for one direction.

Metabolic Heat Load

Hourly passenger density data for one year between each station of the Metrobus line was obtained from the bus service operator. That is an important data to calculate heat loads related to occupancy rate. Heat map of passenger occupancy rate is shown in Figure 7. Horizontal axes shows hours, vertical axis shows the station number and the color indicates the occupancy rate, occupancy rate of 1 means full bus while 0 means empty bus.

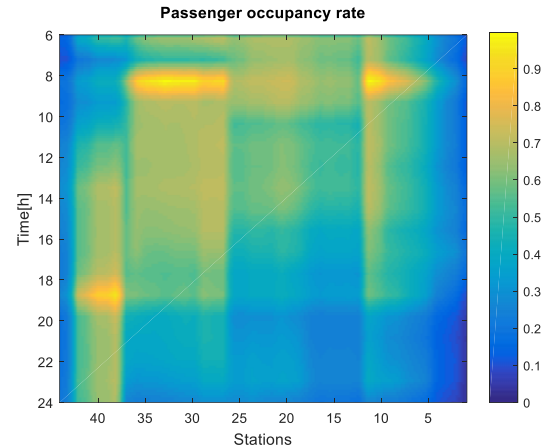


Figure 7. Heat map of passenger occupancy rate

According to Turkish Statistical Institute Health Survey (2010), average height and average weight of Turkish people are 1.67 m and 71.5 kg, respectively. Thus, from equation (20) A_{DU} of an average Turkish person is calculated as follows.

$$A_{DU} = 0.202 \times 71.5^{0.425} \times 1.672^{0.725} \quad (20)$$

$$= 1.80 \text{ m}^2$$

With the help of equation (4) and (20) metabolic heat generation rate of a driver, sitting passenger and a standing passenger is calculated as 216 W, 108 W and 126 W, respectively.

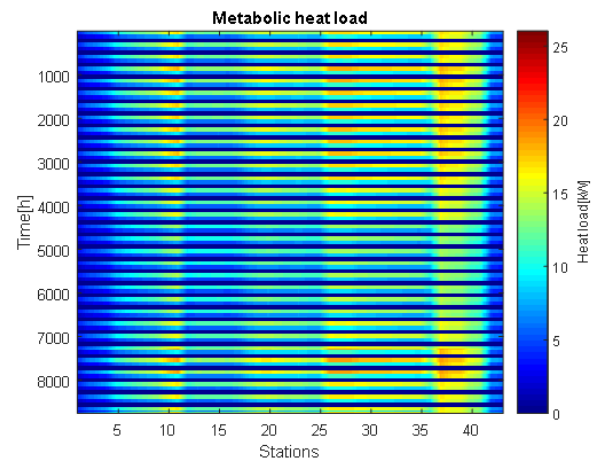


Figure 8. Heat map of metabolic heat load

It is assumed that passengers prefer to sit in the bus when there is empty space. There are only 43 seats in the Metrobus but the passenger capacity is 181. Accordingly, heat map of metabolic heat load is shown in Figure 8.

Solar Heat Loads

As can be seen in Figure 6, the Metrobus line is mainly established on the East-West direction thus, solar heat load is calculated for East-West direction.

Hourly incidence angle of each surface for one year, which are calculated from equation (6), are shown in Figure 9.

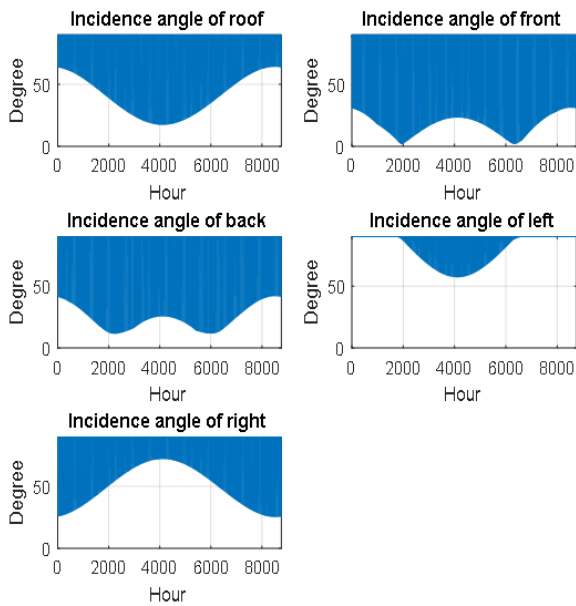


Figure 9. Incidence angle of all surfaces

Hourly altitude angles of all surfaces for a one year period, which are calculated from equation (7), are shown in Figure 10.

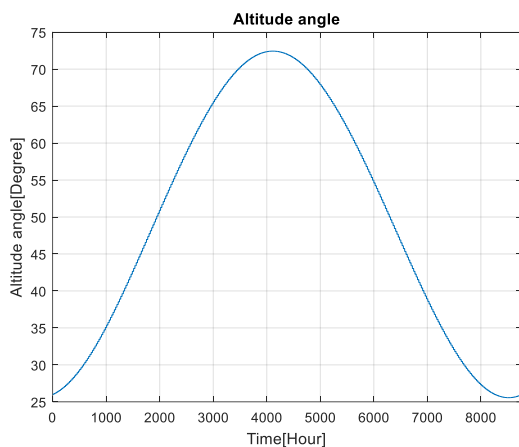


Figure 10. Altitude angles

Sunset and sunrise hours for a one year period are shown in Figure 11.

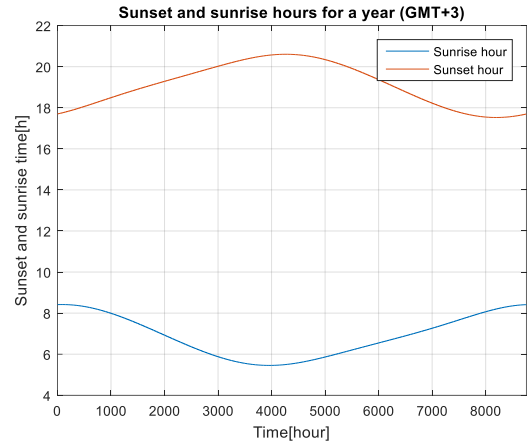


Figure 11. Sunset and sunrise hours

Direct Radiation Heat Load

Direct radiation heat loads for each hour are calculated from equation (10). Transmissivity values and surface areas, which are required in order to calculate direct radiations, are obtained from Table 3. Results of calculation are shown in Figure 12.

Diffused Radiation Heat Load

Heat loads of diffused radiation are obtained from equation (13a) and equation (13b). Heat load that is generated by diffused radiation for each hour of a year are shown in Figure 12.

Reflected Radiation Heat Load

Heat load due to reflected radiation is calculated from equation (14). It is assumed that sunlight is reflected only from the ground (asphalt) and, reflectivity coefficient of the ground (asphalt), ρ_g , is 0.2 according to Tran et al. (2009). Results are shown in Figure 12.

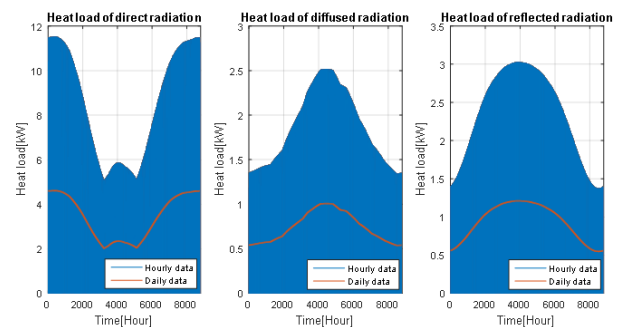


Figure 12. Direct, Diffused and Reflected radiation heat load

Ambient Heat Load

Thickness of the body and glass, λ , may vary from vehicle to vehicle and is easy to measure. In the present case vehicle body thickness is measured as 17mm and glass thickness is measured as 4.8mm. Thermal conductivity of the glass is 1.05 W/mK and thermal conductivity of the body is 0.2 W/mK. (Fayazbakhsh et al. 2013).

For the calculation of ambient heat load, inner temperature of the Metrobus is required. For practical reasons, inner temperature of the bus is assumed to be always in comfortable ranges. Comfortable inner temperature and relative humidity ranges were tabulated in Table 2.

In addition to inner temperature, outer temperatures are also required. Hourly outside temperature data are obtained from Turkish State Meteorological Service. Temperature difference between outside and inside of the Metrobus in a one year period are given in Figure 13.

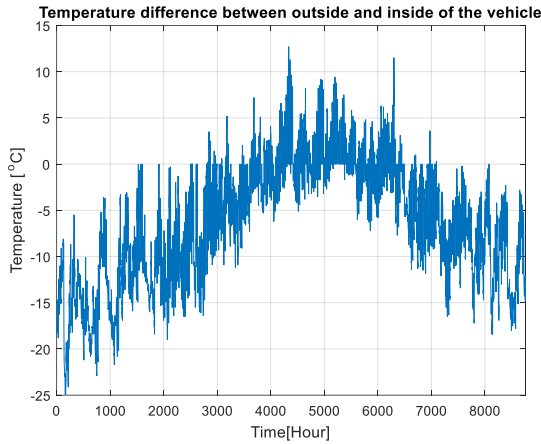


Figure 13. Hourly temperature difference between outside and inside of the vehicle

Convection coefficient of the outer, h_o , and inner, h_i , surfaces are calculated from equation (18a) and equation (18b). Velocity of the inside air is assumed to be zero and the velocity air on the outer surface of the Metrobus is assumed to be 11.33 m/s which is the average velocity of the Metrobus according the driving cycle obtained by tests with zero wind speed assumption.

Ambient heat load due to conductive and convective heat transfer through body and windows for each hour of a year is calculated from equation (17) and result are shown in Figure 14.

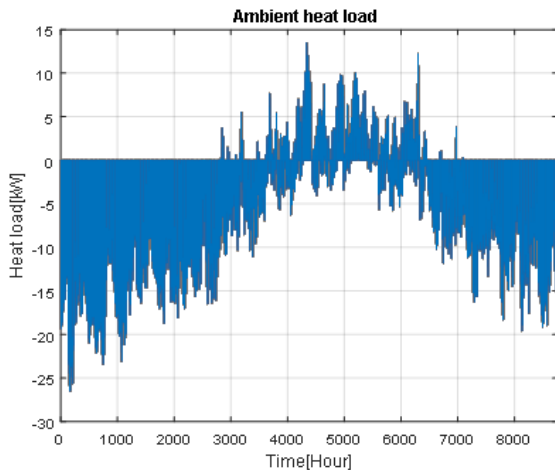


Figure 14. Ambient heat load

Ventilation Heat Load

The temperature and relative humidity must be changed according to thermal comfort requirements so as to keep the interior of the bus comfortable. Target inner temperature and relative humidity ranges are tabulated in Table 2. For the calculation of ventilation load, hourly outside temperature and humidity data that are obtained from Turkish State Meteorological Service are used. In addition to outdoor temperature and target inside temperature, another important data for thermal comfort, target relative humidity and inside relative humidity are shown in Figure 15.

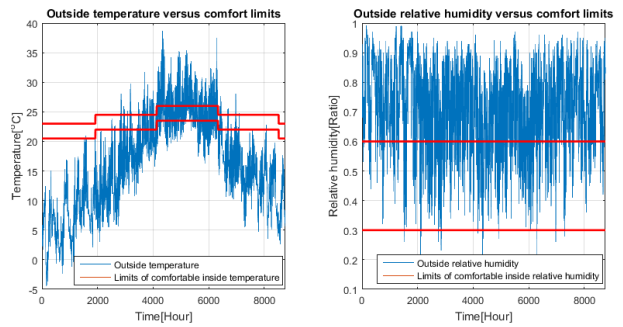


Figure 15. Outside temperature and target temperature (left), Outside relative humidity and target relative humidity (right)

Since the ventilation requirements are directly dependent on the number of passenger, hourly passenger occupancy rate of each station for one year are used in this calculation. Ventilation heat load of the Metrobus are calculated for each hour of the year by using equation (19). Results of the calculation are shown in Figure 16.

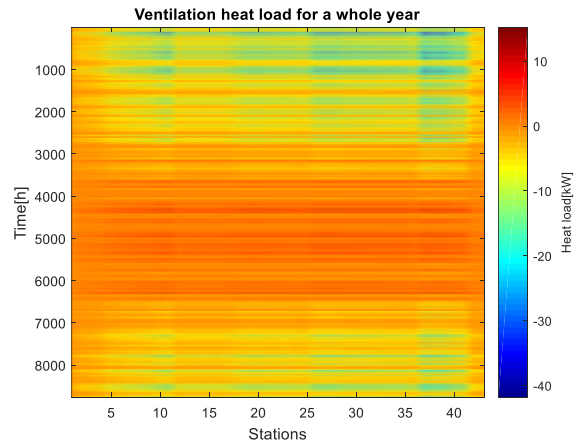


Figure 16. Ventilation heat load

Results

Total heat load of the Metrobus for each hour for one year and for each station is shown in Figure 17.

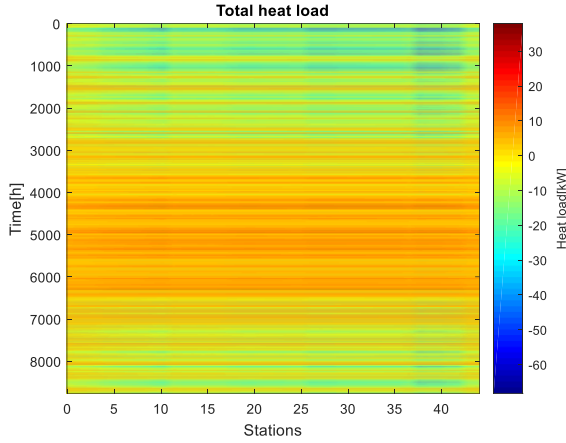


Figure 17. Total heat load

Total heat load of the Metrobus for each service hour for one year is shown in Figure 18. The heat load that is shown in Figure 18 is the average heat load of all stations.

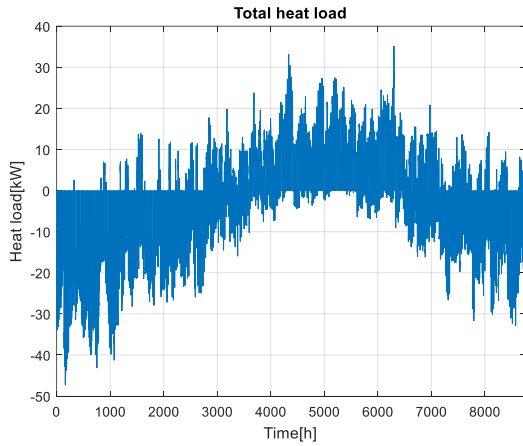


Figure 18. Hourly total heat load

Daily average and monthly average heat load of the Metrobus are shown in Figure 19.

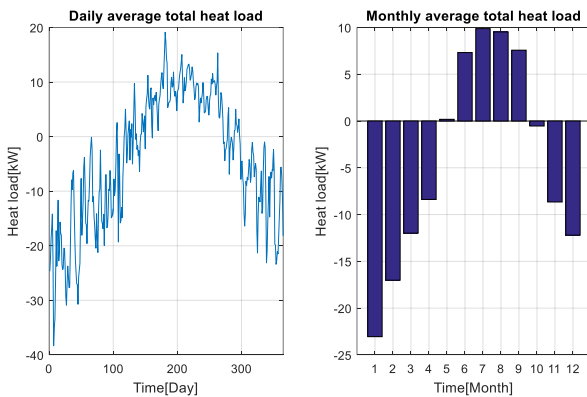


Figure 19. Daily and monthly total heat load

Power requirement of HVAC System

The energy-based efficiency measure of the refrigeration unit, COP (Coefficient of performance) can be defined as follows;

$$COP_{cooling} = \frac{\dot{Q}_{HVAC\ cooling}}{W_{Comp}} \quad (21a)$$

$$COP_{heating} = \frac{\dot{Q}_{HVAC\ heating}}{W_{Comp}} \quad (21b)$$

$$= \frac{\dot{Q}_{HVAC\ cooling} + W_{Comp}}{W_{Comp}}$$

$$= COP_{cooling} + 1$$

$\dot{Q}_{HVAC\ cooling}$ and $\dot{Q}_{HVAC\ heating}$ are the heat loads during cooling and heating, respectively and W_{Comp} is the minimum power that is needed to be supplied to the compressor. COP may vary according to different months, temperature and air mixture ratios. Average coefficient of performance of an air conditioning system of a bus is 3 for cooling and is 4 for heating (Tosun et al. 2016). Thus, according to Figure 19 it can be said that the maximum power needed to heat up the Metrobus is about 12 kW and the maximum power to cool down the Metrobus is about 11 kW. The total energy consumption of the AC system for one year can be calculated from equation (26).

$$W_{average\ day} = \int W dt \quad (22)$$

From equation (21a), (21b) and (22) average HVAC power for one day, $W_{average\ day}$, is calculated. Figure 20 shows the change of average HVAC power by day.

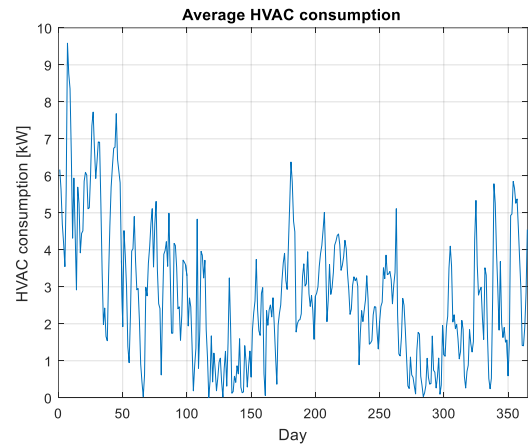


Figure 20. Daily change of HVAC power requirement

CONCLUSION

Accurate calculation of the thermal load of an urban bus in the design phase is crucial for the assessment of the comfort and cost of the bus to be produced. In this study, the thermal load of the Istanbul Metrobus has been estimated by a method that takes into account the annual weather and passenger density with an hourly resolution. Owing to these detailed inputs, short-term fluctuations could be observed and thus an appropriate HVAC system could be selected. Furthermore, average and overall HVAC consumptions have been estimated with higher resolution which is a valuable input for the feasibility of bus electrification projects.

It can be observed that, from the Metrobus line analyzed in this study, the HVAC loads are higher in winter time. The reason for this is that the heating demand is higher due to lower outdoor temperatures. In vehicles with internal combustion engine, heat may be supplied from the waste heat of the internal combustion engine. Meanwhile, in electric vehicles there is no waste heat, and therefore heat must be supplied by the HVAC system.

The ventilation requirement of the vehicle has been observed to depend on the number of passengers in the vehicle; in fact, the number of passenger is the most important input of the HVAC power consumption model. Daily average power consumption of HVAC system varies between 1 kW and 9 kW for HVAC system with COP equal to 3 for cooling and 4 for heating. The yearly average of the HVAC energy consumption is 0.11 kWh/km which represents around 8 % of the total energy consumption of the vehicle, but in winter the average consumption can increase up to 0.27 kWh/km, which is about 25% of the total consumption of the vehicle.

Automatic HVAC controllers used in today's buses activate the HVAC system according to the temperature and humidity of the current air in the vehicle. However, these controllers cannot predict the need of rising thermal loads due to solar radiation, passenger number or outdoor temperature. Finally, as a prospective application, a HVAC controller designed based on the proposed model may be developed to provide necessary pre-heating and pre-cooling in order to keep the bus cabinet in a comfortable temperature range in face of varying thermal load.

REFERENCES

Aktacir M. A., Büyükalaca O., Bulut H. and Yilmaz T., 2008, Influence of different outdoor design conditions on design cooling load and design capacities of air conditioning equipments, *Energy Conversion and Management*, 49(6), 1766–1773.

Anna Laura P., Veronica Lucia C., Cristina P., Claudia F., Ilaria P., Gloria P., 2016, Calculation of Direct Solar and Diffuse Radiation in Israel Stefan, 1576, 1–202.

ASHRAE Handbook of Fundamental, American Society of Heating, Refrigerating, and Air Conditioning, 2001. ASHRAE Standard, “Ventilation for Acceptable Indoor Air Quality,” *ASHRAE Standard 62*, 1999

Fayazbakhsh, M. A. and Bahrami M., 2013, Comprehensive Modeling of Vehicle Air Conditioning Loads Using Heat Balance Method.

Gis W., Kruczynski S., Taubert S., Wierzejski A., 2017, Studies of energy use by electric buses in SORT tests Goswami D. Y., 2007, *Solar Energy Resources*

Graurs I., Laizans A., Rajeckis P. and Rubenis A., 2015, Public bus energy consumption investigation for

transition to electric power and semi-dynamic charging, *Engineering for Rural Development*, 14, 366–371.

Juan A. A., Mendez C. A., Faulin J., De Armas J. and Grasman S. E., 2016, Electric vehicles in logistics and transportation: A survey on emerging environmental, strategic, and operational challenges, *Energies*, 9(2), 1–21.

Kamiya Y., Daisho Y., Takahashi S. and Narusawa K., 2006, Development and performance evaluation of an advanced electric micro bus transportation system - Part 1: Waseda Advanced Electric Micro Bus, *22nd International Electric Vehicle Symposium (EVS)*, 7, 836–847.

Lee J. W., Jang E. Y., Lee S. H., Ryou H. S., Choi S., Kim Y., 2014, Influence of the spectral solar radiation on the air flow and temperature distributions in a passenger compartment, *International Journal of Thermal Sciences*, 75, 36–44.

Lee J-Y., Choi J-W. and Kim H., 2008, Determination of Body Surface Area and Formulas to Estimate Body Surface Area Using the Alginate Method, *Journal of Physiological Anthropology*

Li W., Sun J., 2013, Numerical simulation and analysis of transport air conditioning system integrated with passenger compartment, *Applied Thermal Engineering*, 50(1), 37–45.

Pihlatie M., Kukkonen S., Halmeaho T., Karvonen V. and Nylund N. O., 2015, Fully electric city buses - The viable option, *2014 IEEE International Electric Vehicle Conference*, IEVC 2014.

Shellenberger M. and Nordhaus T., 2004, The death of environmentalism

Tosun E., Bilgili M., Tuccar G., Yasar A., Aydin K., 2016, Exergy analysis of an inter-city bus air-conditioning system, *International Journal of Exergy*, 20(4), 445.

Tran N., Powell B., Marks H., West R., Kvasnak A., 2009, Strategies for Design and Construction of High-Reflectance Asphalt Pavements, *Transportation Research Record: Journal of the Transportation Research Board*, 2098(1), 124–130.

Turkish Statistical Institute, 2010, Health Survey, 3654 Ankara

Ünal Ş., 2016, An experimental study on a bus air conditioner to determine its conformity to design and comfort conditions, *Journal of Thermal Engineering*, 3(1), 1089-1101.

www.otobussaatleri.net, 2019, Retrieved from <https://www.otobussaatleri.net/istanbul-metrobus-hatlari-haritasi/>



IMPROVING PERFORMANCE AND THERMOECONOMIC OPTIMIZATION OF AN EXISTING BINARY GEOTHERMAL POWER PLANT: A CASE STUDY

Ceyhun YILMAZ*

*Afyon Kocatepe Üniversitesi Teknoloji Fakültesi Makina Mühendisliği Bölümü
03200 Merkez, Afyonkarahisar, ceyhunyilmaz@aku.edu.tr

(Geliş Tarihi: 05.02.2019, Kabul Tarihi: 16.01.2020)

Abstract: Geothermal power plants have been in operation for decades in many parts of the world. Different thermodynamic cycles can be used for producing power from geothermal resources. Binary cycle plants use the geothermal water from liquid-dominated resources at relatively low temperatures. These plants operate on a Rankine cycle with a binary working fluid (isobutane, pentane, isopentane, R-114, etc.) that has a low boiling temperature. A case study on an existing binary geothermal power plant is available in this study. Thermoeconomic performance evaluation and optimization of 2.7 MW binary organic Rankine cycle (ORC) design geothermal power plant in western Turkey is conducted using actual plant operating data, and potential improvements are identified. Afyon Geothermal Power Plant (AFJES) is thermodynamically modeled in a computer environment using current working parameters in a comprehensive way for the use of geothermal energy in electricity generation. Geothermal water temperature and mass flow rate of the plant are 110°C, and 150 kg/s, respectively. Energy and exergy efficiencies of the plant are calculated as 10.4% and 29.7%. The potential annual revenue of geothermal electricity is calculated to be 2,880,277 \$/yr with a simple payback period of 3.36 years. The exergetic cost of the electricity from the plant is calculated as 0.0233 \$/kWh. The optimized simple payback period and exergy cost of the electricity generated in the plant is calculated as 2.87 years and 0.0176 \$/kWh, respectively.

Keywords: Geothermal power plant, thermodynamic analysis, thermoeconomic analysis, optimization.

MEVCUT BİR BİNARY JEOTERMAL SANTRALİN PERFORMANS GELİŞTİRMESİ VE TERMOEKONOMİK OPTİMİZASYONU: BİR VAKA ÇALIŞMASI

Özet: Jeotermal güç santralleri dünyanın birçok yerinde yıllardır kullanılmaktadır. Jeotermal kaynaklardan güç üretmek için farklı termodinamik çevrimler kullanılabilir. Binary çevrim santralleri, nispeten düşük sıcaklıklarda sıvı yoğunluklu kaynaklardan gelen jeotermal suyu kullanır. Bu santraller, düşük kaynama sıcaklığına sahip bir binary iş akışkanı (izobütan, pentan, izopentan, R-114, vb.) ile Rankin çevrimiyle çalışır. Bu çalışmada, mevcut bir binary jeotermal güç santrali ile ilgili bir vaka çalışması yapılmıştır. Türkiye'nin batısındaki 2.7 MW'lık Binary Organik Rankine çevrimi (ORC) tasarımı bir jeotermal santralin termoekonomik performans değerlendirmesi ve optimizasyonu, gerçek santral çalışma verileri kullanılarak yapılmış ve geliştirme potansiyeli tespit edilmiştir. Afyon Jeotermal Enerji Santrali (AFJES), elektrik üretiminde jeotermal enerjinin kullanımı için mevcut çalışma parametreleri kapsamlı bir şekilde kullanılarak bilgisayar ortamında termodinamik olarak modellenmiştir. Santralin jeotermal su sıcaklığı ve kütleli debisi sırasıyla 110 °C ve 150 kg/s'dir. Santralin enerji ve ekserji verimliliği % 10.4 ve % 29.7 olarak hesaplanmıştır. Jeotermal elektrikten elde edilen gelir 2.880.277 \$/yıl ve basit bir geri ödeme süresi ise 3.36 yıl olarak hesaplanmıştır. Santralden üretilen elektriğin ekserjetik maliyeti 0.0233 \$/kWh olarak hesaplanmıştır. Santralden üretilen elektriğin optimize edilmiş basit geri ödeme süresi ve ekserji maliyeti sırasıyla 2.87 yıl ve 0.0176 \$/kWh olarak hesaplanmıştır.

Anahtar Kelimeler: Jeotermal güç santrali, termodinamik analiz, termoekonomik analiz, optimizasyon.

NOMENCLATURE

| | |
|-------------|--|
| β | specific energy consumption, kg/kJ |
| c | specific exergy cost, \$/kJ |
| C | cost associated with exergy flow, \$ |
| CRF | capital recovery factor |
| \dot{C} | cost rate associated with exergy, \$/h |
| \dot{E}_x | exergy rate, kW |
| ex | specific exergy, kJ/kg |

| | |
|-----------|------------------------------|
| f | exergoeconomic factor, % |
| h | enthalpy, kJ/kg |
| i | interest rate, % |
| \dot{m} | mass flow rate, kg/s |
| PEC | purchased equipment cost, \$ |
| PWF | present worth factor |
| r | relative cost difference, % |
| s | entropy, kJ/kg K |
| S | salvage value, \$ |
| SPP | simple payback period, year |

| | |
|-----------|--|
| t | time |
| T | temperature, °C |
| \dot{W} | power, kW |
| y | exergy destruction over total exergy destruction |
| \dot{Z} | equipment cost rate, \$/h |

Greek symbols

| | |
|---------------|----------------------------|
| η | energy efficiency |
| ε | exergy efficiency |
| τ | capacity factor of system |
| $\$$ | United State Dollars, US\$ |

Subscripts

| | |
|-------------|------------------------|
| 0 | dead states |
| <i>act</i> | actual |
| BHE | binary heat exchanger |
| BT | binary turbine |
| <i>dest</i> | exergy destruction |
| <i>e</i> | exit state |
| <i>elec</i> | electricity |
| <i>f</i> | fluid |
| <i>F</i> | exergy of fuel |
| geo | geothermal |
| IC | investment cost |
| <i>i</i> | inlet state |
| <i>k</i> | <i>k</i> -th equipment |
| pp | pinch point |
| <i>P</i> | exergy of product |
| rev | reversible |
| <i>turb</i> | turbine |
| <i>T</i> | total |
| WCC | water cooled condenser |

Superscripts

| | |
|-----------|------------------------|
| \bullet | time rate |
| CI | investment cost |
| OMC | operation maintenance |
| <i>n</i> | operating period, year |

INTRODUCTION

Geothermal energy is within the earth's thermal energy that is transferred to the underground water. This thermal energy trapped beneath and within the earth. This energy exists in the form of steam and hot or liquid water. It is released naturally or drilling operations. The utilization of geothermal energy is not a new technology, as the first geothermal steam well was drilled at Larderello, Italy, in 1904 (Kasaei et al., 2017). The present installed energy capacity of the plants is now around 1,144 MW, which has 40 power plants in Turkey (Balcilar et al., 2018). Turkey's geothermal resources mainly consist of low-grade energy sources. However, this is not a disadvantage because the recent progress of technological developments, Organic Rankine cycles (ORC) are preferred to produce electricity for low enthalpy type of geothermal sources. The most common cycle is the binary cycle that allows electricity generation from low-temperature geothermal energy sources (Yilmaz, 2017). The binary plants developed for the use of working fluids at low boiling points enable the generation of electricity

from low-temperature geothermal water. Geothermal binary plant technology was developed primarily to produce electricity from low-temperature resources and to increase utilization of thermal resources by conversion waste heat (Korkmaz et al., 2014).

The binary plant at Chena Hot Springs uses a geothermal resource at 80°C in Alaska (Zheng et al., 2015). The binary system uses a secondary working fluid, typically n-pentane, n-butane, and R144 which, compared with steam, have a low boiling point and high vapor pressure at low temperatures. This secondary fluid is operated through a conventional Rankine Cycle. By selecting the appropriate working fluid, binary plants can be designed to operate with inlet temperatures in the range 80 to 150°C. The upper-temperature limit is selected by the thermophysical condition of organic binary fluids. The lower temperature limit is primarily selected by useful and economic considerations, as the required heat exchanger size for a given capacity becomes impractical. Heat is transferred from geothermal water to the binary fluid via heat exchangers, where the binary fluid is heated and vaporized before being expanded through a turbine (Cengel and Boles, 2015).

In the open literature, some relevant studies have been conducted on geothermal energy for electricity production. Kanoglu (2002), performed an exergy analysis of 12.4 MW existing binary geothermal power plant. The exergetic efficiency of the plant was found to be 29.1% based on the exergy of the geothermal water at the inlet state, and 34.2% based on the exergy loss of the preheater system. The corresponding thermal efficiencies for the plant were calculated to be 5.8 and 8.9%, respectively. DiPippo (2007), reviewed as to its appropriateness to serve as the ideal model for geothermal binary power plants. He showed that the Carnot cycle sets a theoretical upper limit on the thermal efficiency of these plants. He found that actual binary plants can achieve relative efficiencies as high as 85%. Yari (2010), proposed an exergetic analysis of various types of geothermal power plants. The maximum thermal efficiency was found to be related to the binary cycle with R123 as the working fluid and was calculated to be 7.65%. Karadas et al. (2015), conducted a regression analysis of 7.35 MW existing binary geothermal power plant using actual plant data to assess the plant performance. According to their analyses, since 2009, the plant performance was started to decline with 270 kW electricity capacities. Wang et al. (2015), performed a thermodynamic analysis and optimization of a flash-binary geothermal plant. The effects of some thermodynamic parameters on system performance were examined. A parametric optimization was performed to obtain the optimum system performance. Hanbury and Vasquez (2018), performed a life cycle analysis of geothermal energy for power and transportation with a stochastic approach. They showed that geothermal energy extraction is not without environmental cost. Aksoy (2014), provided an information on power generation via geothermal resources and sector development. He

considered by a power plant at Kızıldere in Denizli, whereas the first private sector investment was the Dora-I power plant, commissioned in 2006. Koroneos et al. (2017), studied an exergy analysis for a proposed binary geothermal power plant in Nisyros Island, Greece. According to their study, a system exergetic efficiency of 41% and a thermal one of 12.8% have been resulted in supporting the technical feasibility of the proposed geothermal plant. Kolahi et al. (2018), presented a novel approach for optimizing and also improving a flash binary geothermal power plant. They have shown an investigation on flash chamber pressure effect on the system performance was accomplished. Shokati et al. (2015), compared a basic, dual-pressure, and dual-fluid ORCs and Kalina cycle for power generation from the geothermal fluid reservoir from energy, exergy, and exergoeconomic viewpoints. Heberle et al. (2017), investigated a techno-economic analysis of a solar thermal retrofit for an air-cooled geothermal Organic Rankine Cycle power plant. Their analysis results indicated that the detailed simulations throughout one year show up to 7.8% more electricity, a solar-to-electric efficiency of 10% and a significant power gain during summer. Coskun et al. (2014), considered a geothermal resource in Kutahya-Simav region in Turkey. Economic analysis of four cycles was considered to indicate that the cost of producing a unit amount of electricity is 0.0116 \$/kW h for double flash and Kalina cycles, 0.0165 \$/kW h for combined cycle, and 0.0202 \$/kW h for the binary cycle. Karimi and Mansouri (2018), presented a comparative profitability study of geothermal electricity production in developing countries. They are considered an exergoeconomic analysis and optimization of different cycle configurations. According to the results, the maximum and minimum values of the levelized cost of electricity are obtained as 0.1474 and 0.0493 \$/kWh, respectively. Kahraman et al. (2019), investigated the thermodynamic and thermoeconomic performances of a 21 MW geothermal plant. The results showed that ambient temperature affects efficiencies. The energy efficiency decreased from 13.7% to 9.2%, while exergy efficiency decreased from 54.9% to 36.7. The unit cost of products the plant increased from nearly 230 \$/GJ to 330 \$/GJ, respectively.

The study presents a thermoeconomic evaluation and optimization of an existing Afyon Geothermal Power Plant. Thermoeconomic approach was developed and

used to determine the optimum working conditions in the plant. In this context, a thermoeconomic analysis of the plant was carried out, and the performance values were determined and optimized. As can be seen in the open literature, there is no thermodynamic and economic analysis for the plant. Thermodynamic and thermoeconomic analysis of this plant has not been done before in the current status of the literature. Therefore this study is almost original and new for this plant. The novelty of the study is performance analysis of an existing Afyon Geothermal Power Plant (AFJES), which is currently installed and operating. The plant is performed and optimized the economics of thermodynamically modeled in a computer environment using the thermoeconomic cost method in a comprehensive way for the use of geothermal energy in power generation. This study was performed by (1) thermodynamic analysis under current working conditions of the plant, (2) conducting exergy and exergetic cost analyses for each component of the plant, and (3) the optimum working conditions and costs concerning the thermoeconomic analysis. Moreover, the simple payback period of the current situation of the plant has been investigated with parametric studies for different working conditions.

EXISTING PLANT DESCRIPTION AND OPERATION

Figure 1 shows the general overview of Afyon Geothermal Power Plant (AFJES). It is an existing geothermal plant located at 10 km north side of the city center of Afyonkarahisar in western of Turkey. Geothermal liquid water at 115°C is extracted from two resource wells (AF-23 and R-260) at a rate of 150 kg/s. The production wells AF-23 and R-260, built between 2012 and 2014, are 800 m and 1800 m in depth, respectively. Opened on 13 July 2017, the plant started to produce electricity on 16 August 2017. This water is pumped to the energy conversion heat exchanger of the thermodynamic cycle. The wells are a liquid form of geothermal water resource at a relatively low temperature and a binary cycle is best suited for electricity power generation. The installed capacity of Afyon Geothermal Power Plant located in Afyonkarahisar is 2.76 MW and it provides energy requirements of an average 4762 dwellings. A natural landscape of the Afyon Geothermal Power Plant is given in Fig. 1 (Sahin, 2016).



Figure 1. A general overview of Afyon Geothermal Power Plant (AFJES) (Sahin, 2016).

The AFJES ORC plant consists of three parts. These are the cycle of the geothermal water, the cycle of the ORC (R134a), and the cycle of cooling water. In order to convert the vapor form of R134a that reaches high pressure with the cooling water cycle to the geothermal water at the turbine outlet, the working fluid is supplied to the condenser at the correct flow and temperature, and it is necessary for efficient energy conversion of

geothermal water. For this reason, when the average monthly air temperatures in Afyonkarahisar province are examined, it will help us to predict the cooling fluid temperature and performance graphs regarding the approach to the design values of cooling water. Afyon Geothermal Power Plant (AFJES) system modeling and SCADE view are given below in Fig. 2 (Sahin, 2016).

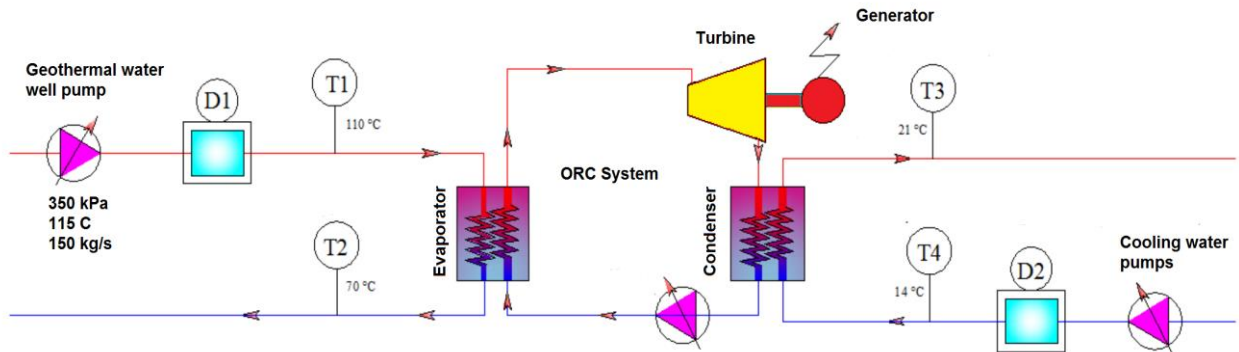


Figure 2. Afyon Geothermal Power Plant (AFJES) System Modeling and SCADA (Sahin, 2016).

WORKING PRINCIPLE OF PLANT

Fig. 3 shows the water cooled binary geothermal cycle. R134a was assumed for the working fluid which is the most efficient working fluid in the low-temperature binary cycle power plants. The thermodynamic details of the working fluid selection are given in comparison to the results and discussion section. Hot geothermal water passes through a series of heat exchangers, where the working fluid vaporizes. Then the vaporized working fluid is expanded through a binary turbine to generate electricity. The expanded working fluid in the turbine is subsequently condensed in a water cooler and returned to the heat exchangers to be heated by hot geothermal water again. Generally, an air-cooled condenser is used, but water-cooled condenser is used in this plant. The reason for this is that it is a river basin suitable for cooling near the power plant. Therefore, more efficient cooling can be achieved. The geothermal water is often reinjected into the reservoir via the reinjection well. When the binary cycle is used in the geothermal power plants are insensitive to the presence of non-condensable gases and produce nearly no environmental emissions. The binary geothermal power plant is a heat engine that converts energy in geothermal water into shaft work of turbine, usually made available on a steam turbine shaft. The Afyon geothermal plant uses geothermal water at 110°C as the heat source of the binary cycle. The plant has a power capacity of 2622 kW and operates on the simple Rankine cycle with R134a as the working fluid. Geothermal water energy is transferred to the binary cycle by a heat exchanger in which geothermal liquid water enters at 110°C at a rate of 150 kg/s and leaves about at 70°C. The geothermal water passes through a heat exchanger is reinjected into the ground about at 70°C. Binary cycle working fluid of R134a enters the turbine 2800 kPa and 100°C and leaves at 500 kPa. R-134a has condensed in a water-cooled condenser and pumped to the heat exchanger pressure.

The isentropic efficiencies of the turbine and pump are assumed to be 85 percent. For the design of heat exchanger of the binary cycle is called pinch point temperature difference ΔT_{pp} . The value of ΔT_{pp} is usually taken between 5°C and 10°C (Sahin, 2016).

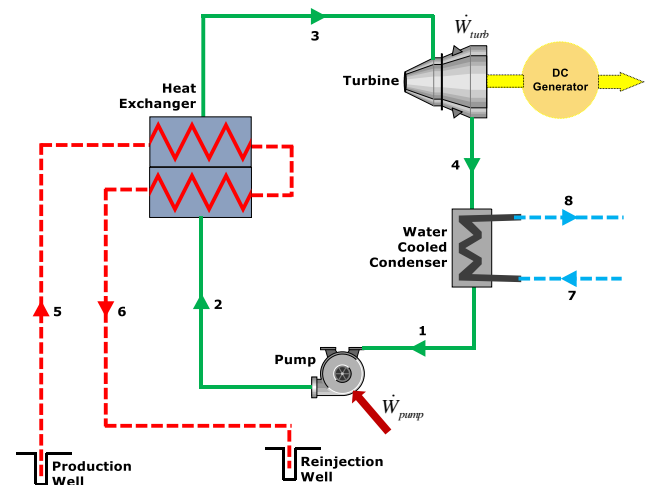


Figure 3. Schematic configuration of Afyon Geothermal Power Plant (AFJES).

The power input to the production and circulation pumps is usually small compared to turbine power. However, the power consumed by the cooling fans in the condenser can be up to 20 percent or more of the turbine power. Ambient temperature has a considerable effect on the power production of air-cooled binary geothermal power plants. As a result of reduced turbine power and increased fan power at higher ambient temperatures, the power output from such a plant decreases by up to 50 percent from winter to summer (Kanoglu and Bolatturk, 2008).

THERMODYNAMIC MODELING OF PLANT

Afyon Binary Geothermal Power Plant operates on a steady state and steady flow condition. For thermodynamic analysis, we use properties of water for geothermal water. Control volume has been conserved mass, energy, entropy, and exergy. The equation equilibriums for the plant are as follows (Abusoglu and Kanoglu, 2008).

$$\sum \dot{m}_i = \sum \dot{m}_e \quad (1)$$

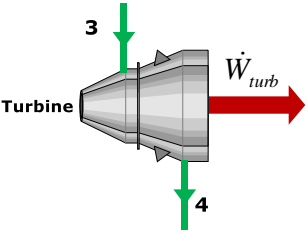
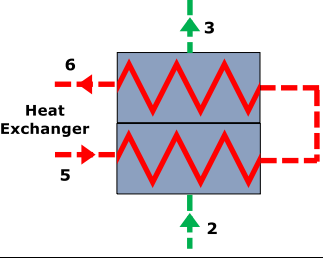
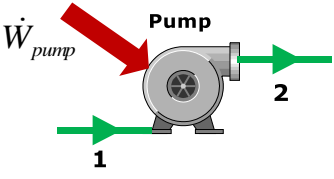
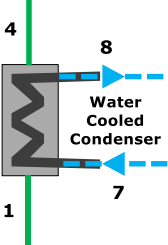
$$\dot{Q} + \dot{W} = \sum \dot{m}_e h_e - \sum \dot{m}_i h_i \quad (2)$$

$$\sum \frac{\dot{Q}}{T_s} + \dot{S}_{gen} = \sum \dot{m}_e s_e - \sum \dot{m}_i s_i \quad (3)$$

$$\dot{E}x_{heat} - \dot{W} = \sum \dot{m}_e ex_e - \sum \dot{m}_i ex_i + \dot{E}x_{dest} \quad (4)$$

where ex is the specific flow exergy, \dot{W} and \dot{Q} are the net work and heat transfer, the mass flow rate is denoted by \dot{m} , enthalpy is represented by h , $\dot{E}x_{dest}$ is the amount of exergy destruction and $\dot{E}x_{heat}$ is the amount of exergy transfer by heat. Although we will select real operation values for the geothermal water and the cycle parameters, the results will be almost realistic. Here are assumed parameters: geothermal water temperature, $T_5 = 110$ °C. Geothermal water mass flow rate, $\dot{m}_{geo} = 150$ kg/s. Dead state temperature, $T_0 = 14$ °C. Optimum flash process pressure, $P_5 = 143.4$ kPa. Binary turbine inlet pressure, $P_3 = 2800$ kPa. Turbine isentropic efficiencies, $\eta_{turb} = 90\%$. Analysis environment dead state pressure, $P_0 = 89.4$ kPa, respectively. Mass, energy and exergy balance equations applied to the all components are expressed in the Table 1, according to the above thermodynamic considerations and assumptions.

Table 1. Thermodynamic balance equations applied to the all system components.

| System component | Mass, energy and exergy equations |
|---|--|
|  | $\dot{m}_3 = \dot{m}_4$ $\dot{W}_{turb,act} = \dot{m}_3(h_3 - h_4)$ $\dot{W}_{turb,rev} = \dot{m}_3(ex_3 - ex_4)$ $\dot{E}x_{turb,dest} = \dot{W}_{turb,rev} - \dot{W}_{turb,act}$ $\varepsilon = \frac{\dot{W}_{turb,act}}{\dot{W}_{turb,rev}}, \quad \eta_{turb} = \frac{h_3 - h_4}{h_3 - h_{4s}}$ |
|  | $\dot{m}_3 = \dot{m}_2 \quad \dot{m}_6 = \dot{m}_5$ $\dot{m}_2(h_3 - h_2) = \dot{m}_5(h_5 - h_6)$ $\dot{E}x_{BHE,dest} = \dot{m}_5(ex_5 - ex_6) - \dot{m}_2(ex_3 - ex_2)$ $\varepsilon = \frac{\dot{m}_2(ex_3 - ex_2)}{\dot{m}_5(ex_5 - ex_6)}$ |
|  | $\dot{m}_2 = \dot{m}_1$ $\dot{W}_{pump,act} = \dot{m}_2(h_2 - h_1)$ $\dot{W}_{pump,rev} = \dot{m}_2(ex_2 - ex_1), \quad \varepsilon = \frac{\dot{W}_{pump,rev}}{\dot{W}_{pump,act}}$ $\dot{E}x_{pump,dest} = \dot{W}_{turb,act} - \dot{W}_{turb,rev}$ |
|  | $\dot{m}_4 = \dot{m}_1 \quad \dot{m}_8 = \dot{m}_7$ $\dot{m}_4(h_4 - h_1) = \dot{m}_7(h_8 - h_7)$ $\dot{E}x_{WCC,dest} = \dot{m}_4(ex_4 - ex_1) - \dot{m}_7(ex_8 - ex_7)$ $\varepsilon = \frac{\dot{m}_7(ex_8 - ex_7)}{\dot{m}_4(ex_4 - ex_1)}$ |

The energy input to the binary geothermal power plant can be written from the Fig. 1 as:

$$\dot{E}_{geo} = \dot{m}_{geo}(h_5 - h_6) \quad (5)$$

The power outputs from the binary cycle can be written as:

$$\dot{W}_{turb} = \dot{m}_R(h_3 - h_4) \quad (6)$$

$$\dot{W}_{pump} = \dot{m}_R(h_2 - h_1) \quad (7)$$

$$\dot{W}_{net,binary} = \dot{W}_{turb} - \dot{W}_{pump} \quad (8)$$

The energy efficiency of the binary geothermal power plant can be written according to the above equations as:

$$\eta = \frac{\dot{W}_{net,geo}}{\dot{E}_{geo}} = \frac{\dot{W}_{net,binary} - \dot{W}_{parasitic}}{\dot{m}_{geo}(h_{geo} - h_0)} \quad (9)$$

The exergy efficiency of the combined geothermal power plant can be written using exergy of the geothermal water at well head as:

$$\varepsilon = \frac{\dot{W}_{net,geo}}{\dot{E}x_{geo}} = \frac{\dot{W}_{net,binary} - \dot{W}_{parasitic}}{\dot{m}_{geo}(h_{geo} - h_0 - T_0(s_{geo} - s_0))} \quad (10)$$

The binary working fluid is pumped to the binary heat exchanger for energy conversion with geothermal water to finish the thermodynamic cycle. Fig. 4 shows the binary working fluid of R134a operation on a temperature entropy diagram. This is an important decision parameter for R134a, because it is a proper thermodynamic fluid in the binary geothermal power plant. So there is no moisture in the binary turbine under these current conditions.

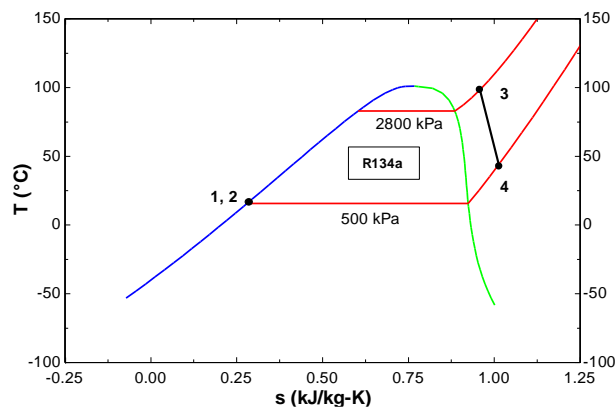


Figure 4. Temperature entropy (T - s) diagram of binary cycle.

Binary heat exchanger pinch analysis is performed as the design consideration of the binary plant. The power consumption to the production and pumps is usually small compared to the turbine power. However, the power consumed by the cooling fans in the condenser can be up to 20 % of the turbine power (Kanoglu and Dincer, 2009). The energy efficiency of the binary plant can be expressed on the geothermal water heat input to binary plant. The heat transfer process between the geothermal water and binary working fluid is shown in

Fig. 5. The state points refer to Fig. 3. Binary working fluid should be vaporized completely (state h_{pp} to $h_{f,binary}$) and superheated by the geothermal water (state $h_{f,binary}$ to 3) as the water temperature is decreased from T_5 to T_{pp} . Binary working fluid is heated from T_2 to T_{vap} as the temperature of geothermal water is decreased from T_{pp} to T_6 . To achieve this heat transfer, there must be a temperature difference between the vaporization temperature of the binary working fluid (state h_{pp}) and temperature of geothermal water at state pp. this temperature differences is called pinch point temperature difference ΔT_{pp} . The state “pp” is called pinch point of geothermal water. An application of the energy conversion principle on this binary heat exchanger gives the following equations (Kanoglu and Bolatturk, 2008):

$$\dot{m}_{geo}(h_5 - h_{pp}) = \dot{m}_{binary}(h_3 - h_{f,binary}) \quad (11)$$

$$\dot{m}_{geo}(h_{pp} - h_6) = \dot{m}_{binary}(h_{f,binary} - h_2) \quad (12)$$

Here \dot{m}_{geo} and \dot{m}_{binary} are the mass flow rates of geothermal water and binary working fluid, respectively, and h is the state enthalpy of fluid flow. Solving these equations simultaneously gives the mass flow rate of binary working fluid and exit the exit temperature of geothermal water when the initial temperature of geothermal water and binary working fluid, the exit temperature of binary working fluid and the pinch point temperature differences ΔT_{pp} are known. The value of ΔT_{pp} is usually taken between 5°C and 10°C, respectively (Kanoglu and Bolatturk, 2008). The vaporization temperature and the pinch point temperature of this plant are calculated to be 82.86°C and 87.86°C, respectively. Also, these design considerations and calculations give an exit temperature of geothermal water of 70°C at the binary heat exchanger outlet state.

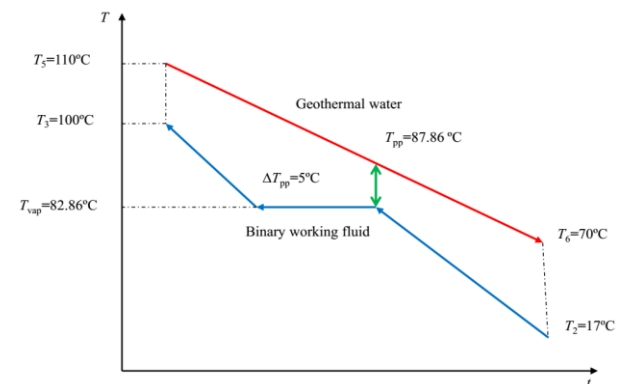


Figure 5. Plant heat transfer process in the binary heat exchanger.

Energy and exergy characteristics for each state of the system in Fig. 3 are calculated in Table 2. The thermodynamic properties of the liquid and gaseous phases of the geothermal water and of the selected working fluid of R134a in the binary cycle are calculated by computer software program EES (F-Chart Software, 2019).

Table 2. Calculated thermodynamic properties of binary power plant.

| State | Fluid | P (kPa) | T (°C) | \dot{m} (kg/s) | h (kJ/kg) | s (kJ/kg°C) | ex (kJ/kg) | \dot{E}_x (kW) |
|-------|------------------|-----------|----------|------------------|-------------|---------------|--------------|------------------|
| 0 | Geothermal water | 89.4 | 11.3 | - | 47.56 | 0.1703 | - | - |
| 0' | R-134a | 89.4 | 11.3 | - | 265.1 | 1.076 | - | - |
| 0'' | Water | 89.4 | 11.3 | - | 47.52 | 0.1701 | - | - |
| 1 | R-134a | 6501 | 15.7 | 108 | 73.33 | 0.2802 | 34.54 | 3731 |
| 2 | R-134a | 120 | 17.0 | 108 | 75.51 | 0.2814 | 36.39 | 3931 |
| 3 | R-134a | 120 | 100 | 108 | 309 | 0.9644 | 75.74 | 8182 |
| 4 | R-134a | 1650 | 34.1 | 108 | 276.9 | 0.9831 | 38.29 | 4137 |
| 5 | Geothermal water | 1650 | 110 | 150 | 461.4 | 1.419 | 58.9 | 8835 |
| 6 | Geothermal water | 720 | 70 | 150 | 293.1 | 0.9552 | 22.38 | 3357 |
| 7 | Water | 100 | 11.3 | 541.9 | 47.52 | 0.1701 | 0 | 0 |
| 8 | Water | 100 | 21 | 541.9 | 88.1 | 0.3104 | 0.6976 | 378 |

The thermodynamic analysis is critical because it forms the basis of thermoeconomic analysis. For this reason, the thermodynamic analysis must be done correctly. In Table 2, exergy values of all states in the plant are calculated and are given in detail. These values are calculated taking into account the actual operating conditions of the plant as mentioned before

THERMOECONOMIC MODELING OF PLANT

Thermoeconomic analysis is a highly realistic method of assessing the cost of a thermal system that inevitably interacts with the environment. Since the available thermodynamic values of mass, heat, and work in the systems can be determined by exergy, it is significant that the exergy is used when cost allocation is made in thermal systems. We refer to this approach as exergy costing. Thus, the cost of power and heat flow associated with exergy entering and leaving the system can be expressed by the following equations. The purchase equipment costs and the operating maintenance costs of the plant equipment are considered as the fundamental part of the system costs. These two

main cost parameters include all other cost parameters of the plant. Thus, the cost balance for system equipment can be written as (Bejan et al., 1996):

$$\sum_{in} \dot{C}_{k,in} + \dot{Z}_k^T + \dot{C}_k^Q = \sum_{out} \dot{C}_{k,out} + \dot{C}_k^W \quad (13)$$

Here

$$\dot{C} = c \times \dot{E}_x \quad (14)$$

For any k component, the exergy rates of inlet and exit are calculated by using exergy relations. \dot{Z}^T is the cost ratio for a component in \$/h. The general equation of the cost ratio associated with initial cost and operating-maintenance costs for a component can be expressed as (Bejan et al., 1996):

$$\dot{Z}_k^T = \dot{Z}_k^{IC} + \dot{Z}_k^{OMC} \quad (15)$$

The economic analysis results of the power plant and equipments with Aspen Plus program in the computer environment are given in Table 3 (Aspen Plus, 2014).

Table 3. The cost rates associated with the components of the plant (Aspen Plus, 2015).

| System components | PEC (\$) | \dot{Z}_k^{IC} (\$/h) | \dot{Z}_k^{OMC} (\$/h) | \dot{Z}_k^T (\$/h) |
|--------------------------------------|-----------|-------------------------|--------------------------|----------------------|
| Binary Heat Exchanger | 300,000 | 4.233 | 3.488 | 7.722 |
| Binary Turbine | 750,000 | 10.584 | 8.722 | 19.306 |
| Water cooled condenser | 300,000 | 4.233 | 3.488 | 7.722 |
| Binary pump | 100,000 | 1.411 | 1.162 | 2.574 |
| Other system outlays | 100,000 | 1.411 | 1.162 | 2.574 |
| Total purchase equipment cost (PEC) | 1,550,000 | 21.872 | 18.022 | 39.894 |
| Operating and maintenance cost (OMC) | 150,000 | | | |

THERMOECONOMIC COST RELATIONS OF PLANT

The cost of power and heat flow associated with exergy entering and leaving the system can be expressed by the following equations. Thermo-economic cost balance equations can be expressed as (Bejan et al., 1996):

$$\dot{C}_i = c_i \dot{E}x_i = c_i (\dot{m}_i e_i) \quad (16)$$

$$\dot{C}_e = c_e \dot{E}x_e = c_e (\dot{m}_e e_e) \quad (17)$$

$$\dot{C}_w = c_w \dot{W} \quad (18)$$

$$\dot{C}_q = c_q \dot{E}x_q \quad (19)$$

From here, the exergetic cost balance due to the heat generated and power for a system component can be written as:

$$\sum_e (c_e \dot{E}x_e)_k + c_{w,k} \dot{W}_k = c_{q,k} \dot{E}x_{q,k} + \sum_i (c_i \dot{E}x_i)_k + \dot{Z}_k^T + \sum_i (c_i \dot{E}x_i) \quad (20)$$

The above equation states that the total cost of the exergy flow from the system for a system component is equal to all the expenditure required to calculate this cost: the cost of the incoming exergy flow plus the initial investment and other costs. All equipment of the plant exergy costing are expressed as in Table 4. The cost rates associated with the fuel (\dot{C}_F) and product (\dot{C}_P) of a component are obtained simply by replacing the exergy rates ($\dot{E}x$) given in Table 2 by cost rates (\dot{C}). Table 4 defines the expressions of cost rates associated with fuel and product of the components contained in Table 2. The cost rate associated with fuel or product of a component contains the cost rates of the same streams used in the same order and with the same sign as in the definition of the exergy of fuel or product.

Table 4. Cost balance equations and auxiliary equations for the exergy costing of system.

| Component | Exergetic cost rate balance equation | Auxiliary Equations |
|------------------------|---|---|
| Binary Heat Exchanger | $\dot{C}_5 + \dot{C}_2 + \dot{Z}_{BHE} = \dot{C}_6 + \dot{C}_3$ | $c_5 = c_6$ c_3 (variable) |
| Binary Turbine | $\dot{C}_3 + \dot{Z}_{BT} = \dot{C}_{W_{BT}} + \dot{C}_4$ | $c_3 = c_4$ $c_{electricity}$ (variable) |
| Water cooled condenser | $\dot{C}_4 + \dot{C}_7 + \dot{Z}_{WCC} = \dot{C}_8 + \dot{C}_1$ | $c_8 = c_7$ $c_7 = 0$ |
| Binary pump | $\dot{C}_1 + \dot{C}_{W_p} + \dot{Z}_{BP} = \dot{C}_2$ | c_1 (known) c_2 (variable) |

THERMOECONOMIC OPTIMIZATION OF PLANT

Thermal system optimization is the process to find the conditions that give maximum and minimum values of the plant efficiency and electricity cost. The plant manufacturer does not try to design the system to provide the minimum total cost to the consumer during the economic life of the equipment. Optimization of the plant is a complicated procedure generally involving many thermodynamic and economic variables. Reducing the difficulties of this process breaking up the procedure into many relatively simple optimization processes is usually helpful. One aspect of the overall problem which can be often treated separately before the main thermo-economic optimization is optimization of the thermodynamic variables of the plant components with the thermodynamic and economic boundary conditions. In this study, thermo-economic optimization was performed using the genetic algorithm method which is a subprogram of EES software. As given below Fig. 6 shows the base procedure of a genetic algorithm optimization (Leiva-Illanes et al., 2018).

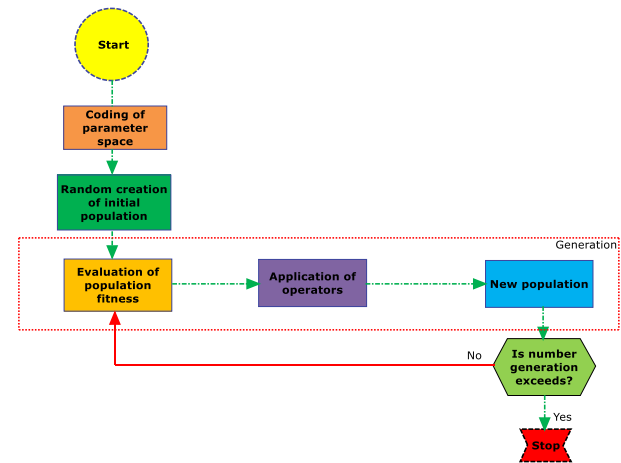


Figure 6. Optimization procedure of a genetic algorithm method (Leiva-Illanes et al., 2018).

The system has two objective functions for the optimization as shown in Fig. 7. These are the exergy efficiency and the cost of electricity generated by the plant. Optimization has been performed by analyzing how all components of the system response due to thermo-economic analysis. For this purpose, economic cost analyzes were made with Aspen Plus program, and optimization calculations were coded with EES program. Because EES is a thermodynamically based analysis program, it provides a thermodynamic choice of design variables for thermal systems and convenience in monitoring the thermodynamic response of the system. Thermodynamic boundary conditions can be considered account by optimizing the EES program. In this study, optimization method with genetic algorithm was selected from the sub-library of EES software. The entire system is coded and optimized by design variables and thermodynamic boundary conditions. The genetic algorithm optimization is a search and

optimization method that works in a similar way to the change process observed in the universe. According to the principle of finding the best in a complex multi-dimensional search space, it is the best solution for the system. The parameter \dot{C}_{elec} must provide the energy corresponding to the primary parameter values in Fig. 7 so that the maximum energy output and minimum electricity cost values can be obtained from the plant.

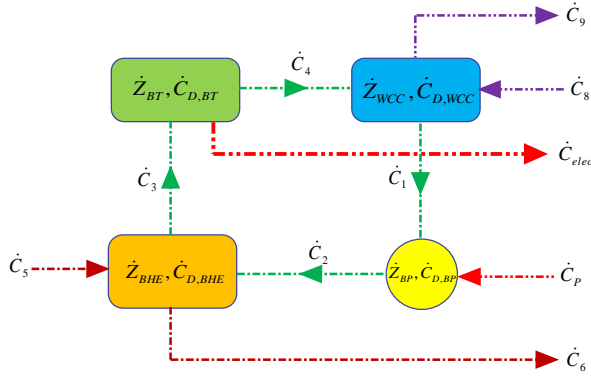


Figure 7. Thermoeconomic optimization flow diagram of the plant.

In the plant, the number of individuals in the population, the number of generations to explore, and the maximum mutation rate were considered as 1000, 0.317, and 16 in the EES program, respectively. Thermodynamically boundary conditions of the variables considered for this system are: $100 \leq P_1 \leq 1000$ kPa, $5 \leq \Delta T_{pp} \leq 30$ °C, $1000 \leq P_2 \leq 3000$ kPa, and $6 \leq i \leq 10$ %, respectively. The decision variables are randomly generated for the above acceptable ranges.

RESULTS AND DISCUSSION

Thermodynamic Analysis

As a result of the thermodynamic analysis, the energy efficiency of the Afyon Geothermal binary power plant was calculated as 10.4% based on the energy input to the R134a binary cycles, according to the states at 7 and 8. Approximately 90% of the geothermal water energy in the reservoir means that it cannot be used and is rejected as heat or reinjected back to the ground. The exergy rate input the plant was calculated as 8835 kW by approaching the approximate value of the exergy transferred from the geothermal water to the binary plant supported by the secondary working fluid (R134a). The net power production from the binary plant was calculated as 2622 kW. The exergy change of geothermal water is thought to be the additional exergy input to the cycle in the well state. According to these conditions, the exergy efficiency of the dual geothermal power plant was calculated to be 29.7%.

The exergy rates and distributions of the components exergy destruction of the Afyon Geothermal Power Plant is given in Figures 8 and 9. After using in the plant, geothermal water is reinjected

into the underground. The geothermal water reinjection exergy loss of geothermal water is calculated to be 3357 kW. In geothermal power plants, reinjection is the most loss of exergy destruction. The large part of the energy from the geothermal water is rejected from the plant without being used. The most destructive components are the binary heat exchanger and water cooled condenser, representing 1227 kW and 1021.2 kW of the total exergy destruction in the cycle, respectively. The causes of exergy destruction in the plant included heat exchanger loss, turbine and pump losses, the exergy of the reinjected geothermal water, and the exergy of the R134a lost in the water-cooled condenser. This power plant is used Akarçay river water as cooling water in the condenser unit (Sahin, 2016). The average temperature will not change as the river water temperature constant throughout the year. Therefore, the water-cooled condensing unit will be more efficient for the plant.

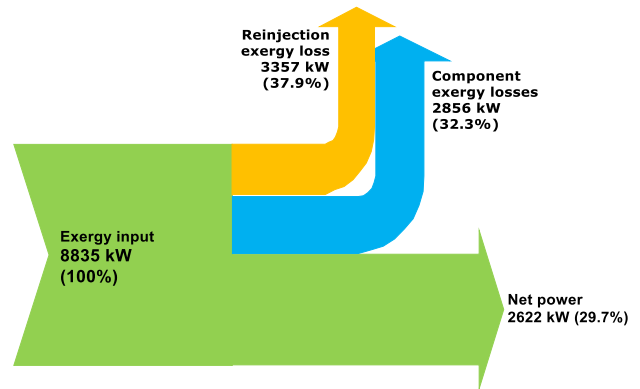


Figure 8. Exergy rate diagram of Afyon Geothermal Power Plant (AFJES).

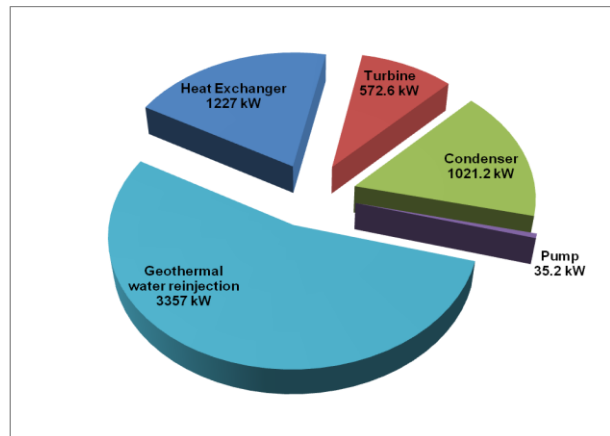


Figure 9. Exergy destructions in the components of the plant.

Thermoeconomic analysis

The total purchase and equipment costs and exergetic cost rates of the plant components are given in Table 3. The unit cost of the geothermal water as a fuel input to the plant is calculated to be 1.372 \$/GJ and the exergetic cost of binary working fluid R134a is 3 \$/kg and the exergetic cost of the working fluid R134a is calculated to be 2.86 \$/GJ (Ergun et al., 2017). According to the thermoeconomic method, a sufficient number of

auxiliary equations have been developed with the help of Fuel and Product principles for the system components and the cost equilibrium equations related to these equations are given in Table 4. The results in Table 5 are obtained when the exergy cost equations are written in the EES program and simultaneously solved in the computer environment. From this analysis, the exergy cost ratio of the R134a working fluid is evaluated to be 49.7 \$/h at the exit state of the binary system pump. The unit exergy cost of the produced electricity by making technical assumptions and solving with auxiliary equations from the plant is calculated to be 6.47 \$/GJ or 0.0233 \$/kWh, respectively.

Table 5. Thermo-economic results of the Afyon Geothermal Power Plant (AFJES).

| State | \dot{E}_x (kW) | C (\$/GJ) | \dot{C} (\$/h) |
|-------------------------|------------------|-------------|------------------|
| 1 | 3731 | 3.099 | 41.62 |
| 2 | 3931 | 3.51 | 49.68 |
| 3 | 8182 | 2.867 | 84.46 |
| 4 | 4137 | 2.867 | 42.7 |
| 5 | 8835 | 1.372 | 43.64 |
| 6 | 3357 | 1.372 | 16.58 |
| 7 | 0 | 6.47 | 0 |
| 8 | 378 | 6.47 | 8.803 |
| $\dot{W}_{Turbine}$ | 3473 | 6.47 | 80.88 |
| \dot{W}_{Pump} | 235.6 | 6.47 | 5.486 |
| $\dot{W}_{Parasitic}^2$ | 615.1 | 6.47 | 14.32 |
| \dot{W}_{Plant} | 2622 | 6.47 | 61.07 |

Fig.10 shows the exergy cost destruction under real operating conditions for the plant components. The binary heat exchanger is the higher exergy cost destructive component compared to the other plant components. The way of the reducing the cost of electricity generated in the power plant is to reduce the exergy cost destruction of the plant. In order to reduce the exergetic cost of electricity production, it is also considered to increase plant efficiency, to reduce exergy losses and to optimize operating conditions of the plant.

In this section, we also investigated how the results changed if different working fluids are used. Currently, installed plant is started with R134a binary fluid and we have also investigated for the most commonly used working fluids, Isobutane and n pentane. Another important parameter of the classification of the working fluid performance is the unit work versus to specific geothermal water consumption that is mass flow rate of

geothermal water to the net work output to the plant. The parameter is defined as β

$$\beta = \frac{\dot{m}_{geo}}{\dot{W}_{net}} \quad (21)$$

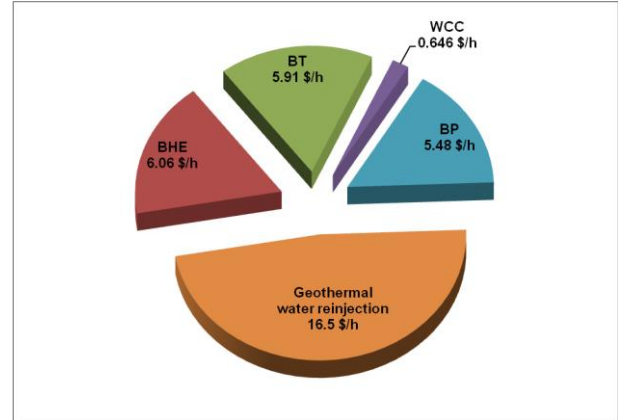


Figure 10. Distribution of exergetic cost destruction rate diagram of the plant.

Some basic results of the plant are given in Table 6. The results are obtained for the same value of the working conditions in the plant as $T_{geo,in} = 110^\circ\text{C}$ and $T_{geo,out} = 70^\circ\text{C}$.

Different working fluids cost comparisons of electricity production from the plant are evaluated in Table 6. At the same time, this comparison shows the optimum working fluid selection for the binary geothermal plant according to the operating conditions of the plant. The optimization is showed that R134a is caused to be the most efficient power production, and also has the lowest cost of the electricity production from the plant. The difference in the production costs evaluated with R134a and Isobutane is about 4.9%. The difference between the R134a and n-pentane working fluids is about 65.4%, whereas the difference between the Isobutane and n-pentane as to be used working fluid is about 63.6%. The electricity cost production of the binary geothermal plant is the lowest when the working fluid R134a is used.

Table 6. Different working fluids cost comparisons of electricity production.

| Fluids | β (kg/kJ) | \dot{W}_{net} (kW) | η (%) | ε (%) | $C_{electricity}$ (\$/kWh) |
|-----------|-----------------|----------------------|------------|-------------------|----------------------------|
| R134a | 0.05721 | 2622 | 10.4 | 29.7 | 0.0233 |
| Isobutane | 0.06381 | 2351 | 9.3 | 26.6 | 0.0245 |
| n-pentane | 0.1282 | 1170 | 4.6 | 13.24 | 0.0674 |

Table 7 illustrates the use of the thermo-economic variables introduced thus far for the evaluation of the geothermal plant. First, the design evaluation of the plant is presented, and then the performance evaluation of an existing plant is described. When applying the thermo-economic methodology, recognize that the values of all thermo-economic variables depend on the components (binary heat exchanger, turbine, pump,.

Table 7. Energetic and exergetic analyses results for the subsystems in the plant.

| Components | $\dot{E}x_F$ (kW) | $\dot{E}x_P$ (kW) | $\dot{E}x_D$ (kW) | y^* (%) | ε (%) | $c_{F,k}$ (\$/GJ) | $c_{P,k}$ (\$/GJ) | \dot{C}_D (\$/h) | r (%) | f (%) |
|------------------------------|----------------------|----------------------|----------------------|--------------|----------------------|----------------------|----------------------|-----------------------|------------|------------|
| Binary heat exchanger | 5478 | 4251 | 1227 | 23.5 | 77.6 | 1.372 | 2.867 | 6.06 | 65.6 | 56.0 |
| Binary turbine | 4045 | 3473 | 572.6 | 10.9 | 85.8 | 2.867 | 6.470 | 5.91 | 70.3 | 59.1 |
| Water cooled condenser | 405.7 | 378 | 27.73 | 0.5 | 93.1 | 6.469 | 3.099 | 0.646 | 89.0 | 92.2 |
| Binary pump | 235.6 | 200.4 | 35.2 | 0.67 | 85.0 | 6.469 | 3.510 | 5.486 | 72.7 | 75.8 |
| Geothermal water reinjection | 8835 | 2622 | 3357 | - | - | - | - | 16.58 | - | - |
| Overall System | 10,164 | 8302 | 5219 | 35.7 | 81.6 | 1.372 | 6.470 | 13.44 | 297.6 | 283.1 |

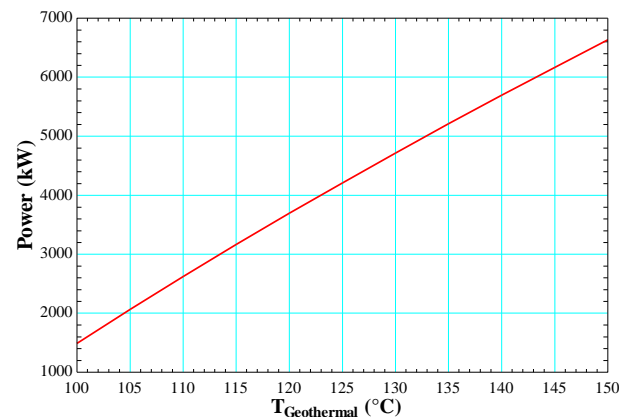
water-cooled condenser). The accompanying Table 7 summarizes the thermoeconomic parameters calculated for each component of the binary geothermal power plant using data from Fig. 2., and definitions from Tables 4 and 5. The parameters include the exergy efficiency ε , exergy destruction rate, exergy destruction ratio y^* , average cost per unit of fuel exergy and product exergy, cost rate of exergy destruction, investment Z , the relative cost of difference r , and exergoeconomic factor f . The average exergy cost of geothermal water as a fuel input from the plant is calculated to be 1.372 \$/GJ, and then, the corresponding exergy cost rate is calculated to be 43.6 \$/h, respectively

Thermoeconomic optimization

In this study, the optimization process was applied to the plant by genetic algorithm, and the obtained results were examined. Proper operation conditions will be defined by optimization, and the plant will work more efficiently. Therefore, the plant will operate more efficiently, so that more power will be generated and the unit cost of the generated electricity will be reduced. For this reason optimization process is an essential tool for energy systems. The current power capacity of the Afyon Geothermal Power plant is 2622 kW, while this optimization capacity is 3461 kW. However, the cost of the electricity produced from the plant is 0.0233 \$/kWh, while the optimization process result is 0.0176 \$/kWh. Therefore, the unit cost of electricity from the plant is reduced by 24.3% with the optimization process. Due to this cost change, the plant's payback period has decreased from 3.36 to 2.87 years. This decrease also has a seriously positive effect on the annual profit and benefit-cost ratio. This value has a great proposition for energy project investments. Energy systems are directly related to investment and product costs. In this respect, optimization process will be very beneficial regarding thermodynamic performance and cost analysis of the plant.

Parametric study of the plant

In the system, the unit kJ is the amount of energy generated from the geothermal water. In the system, the amount of unit kJ energy is increased with increasing geothermal water temperature from the unit kg of geothermal water. In this context, parametric studies have been performed to observe how some critical parameters of the system variation with the temperature of the geothermal source. In particular, the power obtained from the plant and the exergy cost of electricity generated by the geothermal water temperature was investigated. The power generation from the plant increases almost linearly with the geothermal water temperature as shown in Fig. 8. The parametric study showing the power output was performed at temperatures between 100 and 150°C. Fig. 8 shows that the geothermal water temperature directly affects the net power output of the system. The net power production from the plant increased from 2622 kW at 110°C to 6633 kW at 150°C, respectively.

**Figure 11.** Power production of plant with geothermal water temperature

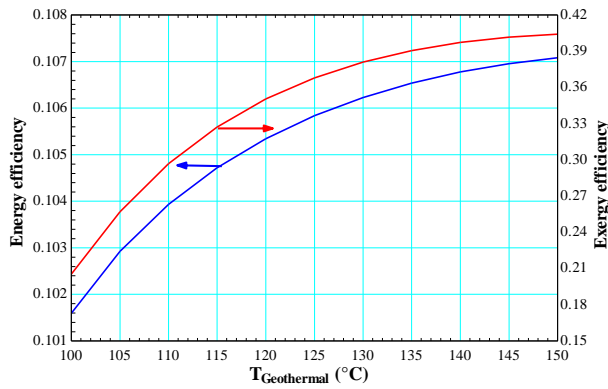


Figure 12. Thermodynamic performance evaluation of the plant.

Fig. 12 shows the variation of energy and exergy efficiencies with respect to the geothermal water temperature. The plant energy and exergy efficiencies simultaneously increase with the geothermal water temperature increases. The reason for the increase in efficiencies is that the unit mass flow rate of geothermal water has more intensive energy. The efficiencies will decrease at a point logarithmically, because plant working conditions must be optimized and reorganized according to the new geothermal water temperature of the plant.

The variation of electricity cost concerning the geothermal water temperature is shown in Fig. 13. The unit exergetic cost of electricity decreases with the geothermal temperature increases. In the current working condition of the plant, the unit exergetic cost of electricity is 0.0233 \$/kWh at 110°C.

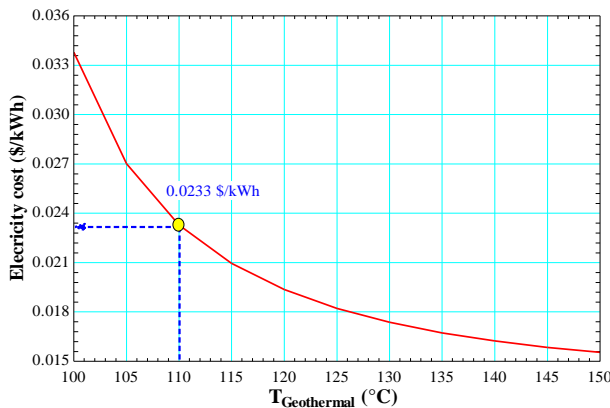


Figure 13. Electricity cost with geothermal water temperature.

The variation of plant power and destruction cost rate for the different geothermal water temperatures of the different conditions are shown in Fig. 14. The electricity cost as linearly increased with the increase of the geothermal water temperature because more energy can be used and obtained from the same amount of geothermal water. However, the exergy destruction cost rate of the plant increases with geothermal water increases. The evaluation is suitable because the exergy destruction cost rate is rather than low to the production cost rate of the plant.

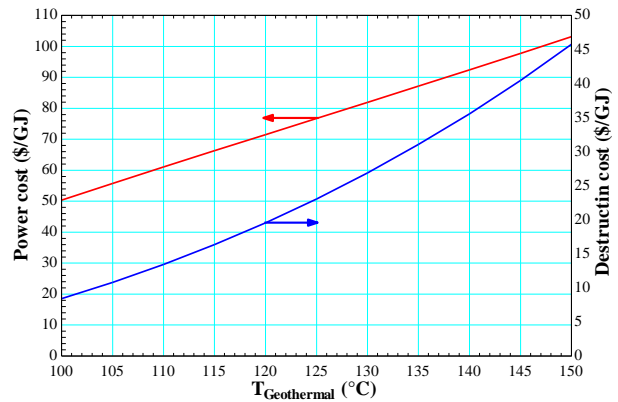


Figure 14. Variation of plant power and destruction cost rate with respect to the geothermal water temperature.

Fig. 15 shows the variation of plant power and destruction cost rate with respect to the geothermal water temperature. Geothermal water exergetic energy cost value as a fuel input to the plant increases with geothermal water temperature increases because energy quality of the water is higher than at low temperatures states. But reinjection geothermal water cost value inversely decreases with geothermal water temperature increase. And also, differences of the destruction values are very low and that can be neglected range of the destruction cost rate.

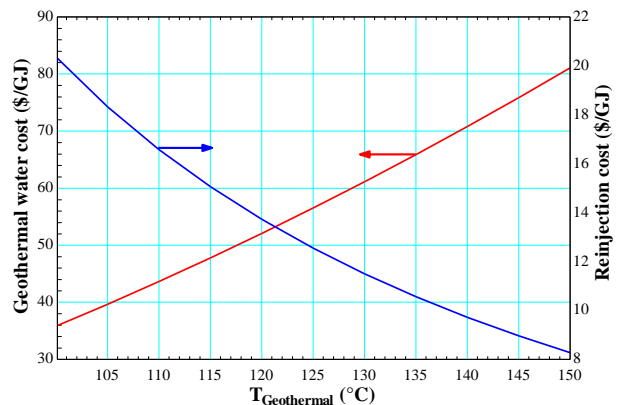


Figure 15. Variation of plant power and destruction cost rate with respect to the geothermal water temperature.

The annual total revenue for the plant is collected in given year through the market cost of electricity to supply the plant operating for all expenses incurred in the same year and to supply reliable economic plant operation. If the plant produces one product, its unit cost can be calculated directly from the total annual revenue cost. The annual revenue of the plant electricity production cost is calculated as (Dhillon, 2009):

$$\begin{aligned} \text{Annual electricity production} &= (\text{Net power output}) \times (\text{Operating time}) \\ &= (2622 \text{ kW}) \times (8322) = 21,820,284 \text{ kWh/year} \end{aligned}$$

$$\begin{aligned} \text{Total cost of investment} &= (3500 \text{ \$/kW}) \times (2622 \text{ kW}) \\ &= 9,177,000 \text{ \$} \end{aligned}$$

The plant payback period is defined as the length of time required for the cash inflows received from the

plant to recover the original cash outlays required by the initial cost of investment. The purchase cost guaranteed of geothermal electricity is 0.132 \$/kWh by the government (EPDK, 2017). Calculation of the plant simple payback period is relatively simple. The following relations are expressed:

$$\text{Simple payback period (SPP)} = (\text{Total cost of investment}) / (\text{Potential Annual Revenue} - \text{OMC})$$

$$\begin{aligned} \text{Annual Potential Revenue} &= (\text{Annual electricity production}) \times (\text{Electricity market cost}) \\ &= (21,820,284 \text{ kWh/year}) \times (0.132 \text{ \$/kWh}) \\ &= 2,880,277 \text{ \$/yr} \\ \text{SPP} &= 9,177,000 \text{ \$} / (2,880,277 - 150,000 \text{ \$/yr}) \\ &= 3.36 \text{ years.} \end{aligned}$$

Fig. 16 shows the variation of plant power and destruction cost rate with respect to the geothermal water temperature. The plant payback period logarithmically decreases with geothermal water temperature linearly increases. When the market cost of the electricity is 0.132 \$/kWh and geothermal water temperature is 110°C, according to the current working condition of the plant, the simple payback period of the plant is calculated to be 3.36 years.

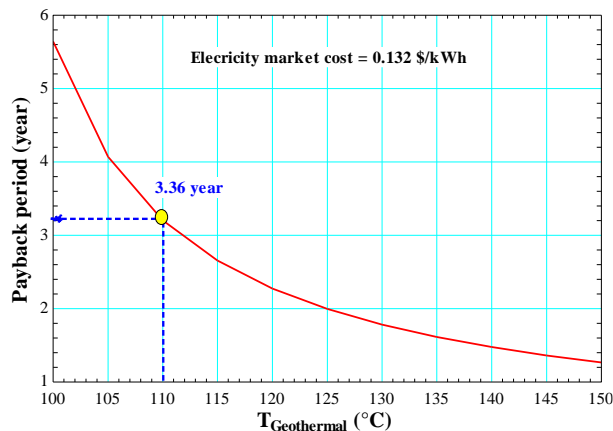


Figure 16. Plant payback period with respect to the geothermal water temperature.

CONCLUSIONS

Each geothermal power plant may have differences in design according to the application areas. The responses of the system based on exergoeconomic design values can be calculated in advance with this study. If the system does not provide the design values in the actual parameters, the reasons for loss of efficiency will be investigated, and studies can be made to improve the system efficiency. The high cost of the heat transmission line and the application difficulties are significant problems when geothermal resources are far from the settlements. In these cases, generating electricity using binary cycle by the direct or indirect heating method according to geothermal source temperature and capacity is a more advantageous and profitable investment compared to district heating.

Therefore, this study will guide the determination of optimum power plant installed capacity in low temperature and capacity geothermal fields. In this study, the performance evaluation of the geothermal power plant, which became operational in Afyonkarahisar province in July 2017, was performed by using actual plant data. The optimum operating conditions of the system and the optimum value of the electricity cost were investigated. In this context, the study has been presented to the authorities, and it has been an innovative and useful research to increase the feasibility and energy efficiency of the existing plant. Some important results obtained are summarized from the plant as follows:

Geothermal power plants are cyclic systems that receive heat from a geothermal source, convert some of it to work, and reject the rest to the ground. So, in this plant, the exergy input by this power plant is 8835 kW and the rate of heat rejection is to be determined as 3357 kW and this value correspond to 37.9 % of totally exergy input by the geothermal water. Energy and exergy values inputs from the geothermal water are evaluated with the base assumptions to be 62,079 kW and 8835 kW, respectively. According to the evaluated geothermal input energy values, the optimized net power generation from the plant is calculated to be 3461 kW. The energy and exergy efficiencies were evaluated as 10.4% and 29.7% for Afyon Geothermal Power Plant (AFJES). The energy production of a binary plant can be increased by good conservation measures such as operating parameters of plant longest time possible and for optimum longest duration, and it is important to clean the condenser coils.

The optimized exergetic cost of electricity produced of the plant are calculated to be 0.01763 \$/kWh with the thermoeconomic method respectively. The plant exergy cost rate of product (net electricity) and exergy destruction cost rate by thermoeconomic analysis is calculated to be 61.7 \$/h and 13.44 \$/h, respectively. The exergy cost rate of geothermal water as a fuel and reinjection of the plant are determined as 43.64 \$/h and 16.58 \$/h, respectively. Internal and external destruction rate of cost allocation is determined as 30.0 \$/h. The annual potential revenue of the plant is estimated to be 2,880,277 \$/yr with simple payback period of 2.87 years. It has been observed that the current performance of the system can be improved significantly with the optimization process. This improvement is 24.2% in net power generation and 24.3% in electricity cost.

ACKNOWLEDGMENT

This study is sponsored by The Scientific and Technological Research Council of Turkey (TUBITAK) under the project 218M739. This support is greatly appreciated.

REFERENCES

- Abusoglu, A. and Kanoglu, M., 2008, First and second law analysis of diesel engine powered cogeneration systems, *Energy Conversion and Management*, 49(8), 2026-2031.
- Aksoy, N., 2014, Power generation from geothermal resources in Turkey, *Renewable Energy*, 68, 595-601.
- Aspen Plus Software, 2015, Aspen Technology Incorporated., Ten Canal Park, Cambridge, MA, USA. www.aspentech.com.
- Balcilar, M., Ozdemir, Z. A., Ozdemir, H. and Shahbaz, M., 2018, The renewable energy consumption and growth in the G-7 countries: Evidence from historical decomposition method, *Renewable Energy*, 126, 594-604.
- Bejan, A., Tsatsaronis, G. and Moran, M.J., 1996, *Thermal Design And Optimization*. (First Ed.), John Wiley & Sons.
- Cengel, Y. A. and Boles, M.A., 2015, *Thermodynamics: An Engineering Approach*, (Seventh Ed.) McGraw-Hill.
- Coskun, A., Bolatturk, A. and Kanoglu, M., 2014, Thermodynamic and economic analysis and optimization of power cycles for a medium temperature geothermal resource, *Energy conversion and management*, 78, 39-49.
- Dhillon, B.S., 2009, *Life cycle costing for engineer*, (First Ed.), Crc Press.
- DiPippo, R., 2007, Ideal thermal efficiency for geothermal binary plants, *Geothermics*, 36(3), 276-285.
- Yari, M., 2010, Exergetic analysis of various types of geothermal power plants, *Renewable Energy*, 35(1), 112-121.
- Ergun, A., Ozkaymak, M., Aksoy Koc, G., Ozkan, S. and Kaya, D., 2017, Exergoeconomic analysis of a geothermal organic Rankine cycle power plant using the SPECO method, *Environmental Progress & Sustainable Energy*, 36(3), 936-942.
- F-Chart Software, EES, engineering equation solver. In: F-Chart Software (2019), Internet Website, www.fchart.com/ees/ees.shtml
- Hanbury, O. and Vasquez, V.R., 2018, Life cycle analysis of geothermal energy for power and transportation: A stochastic approach, *Renewable Energy*, 115, 371-381.
- Heberle, F., Hofer, M., Ürlings, N., Schröder, H., Anderlohr, T. and Brüggemann, D., 2017, Techno-economic analysis of a solar thermal retrofit for an air-cooled geothermal Organic Rankine Cycle power plant, *Renewable Energy*, 113, 494-502.
- Internet, 2017, www.epdk.org.tr/tr/Dokumanlar/elektrik/yekdem/2017.
- Kahraman, M., Olcay, A.B. and Sorgüven, E., 2019, Thermodynamic and thermoeconomic analysis of a 21 MW binary type air-cooled geothermal power plant and determination of the effect of ambient temperature variation on the plant performance, *Energy Conversion and Management*, 192, 308-320.
- Kanoglu, M., 2002, Exergy analysis of a dual-level binary geothermal power plant, *Geothermics*, 31(6), 709-724.
- Kanoglu, M. and Bolatturk, A., 2008, Performance and parametric investigation of a binary geothermal power plant by exergy, *Renewable Energy*, 33(11), 2366-2374.
- Kanoglu, M. and Dincer, I., 2009, Performance assessment of cogeneration plants, *Energy conversion and management*, 50(1), 76-81.
- Karadas, M., Celik, H. M., Serpen, U. and Toksoy, M., 2015, Multiple regression analysis of performance parameters of a binary cycle geothermal power plant, *Geothermics*, 54, 68-75.
- Karimi, S. and Mansouri, S., 2018, A comparative profitability study of geothermal electricity production in developed and developing countries: Exergoeconomic analysis and optimization of different ORC configurations, *Renewable Energy*, 115, 600-619.
- Kasaei, M. J., Gandomkar, M. and Nikoukar, J., 2017, Optimal management of renewable energy sources by virtual power plant, *Renewable Energy*, 114, 1180-1188.
- Korkmaz, E. D., Serpen, U. and Satman, A., 2014, Geothermal boom in Turkey: Growth in identified capacities and potentials, *Renewable Energy*, 68, 314-325.
- Kolahi, M. R., Nemati, A. and Yari, M., 2018, Performance optimization and improvement of a flash-binary geothermal power plant using zeotropic mixtures with PSO algorithm, *Geothermics*, 74, 45-56.
- Koroneos, C., Polyzakis, A., Xydis, G., Stylos, N. and Nanaki, E., 2017, Exergy analysis for a proposed binary geothermal power plant in Nisyros Island, Greece, *Geothermics*, 70, 38-46.
- Leiva-Illanes, R., Escobar, R., Cardemil, J. M. and Alarcón-Padilla, D. C., 2018, Comparison of the levelized cost and thermoeconomic methodologies—Cost allocation in a solar polygeneration plant to produce

power, desalted water, cooling and process heat, *Energy Conversion and Management*, 168, 215-229.

Sahin, C., 2016, *Electricity Generation With Organic Rankine Cycle (ORC) In Low Temperature Geothermal Field And Modeling Of Afyon Geothermal Electric Production Co.*, M.S. Thesis, Electrical and Electronics Engineering, Kütahya Dumlupınar University, Turkey.

Shokati, N., Ranjbar, F. and Yari, M., 2015, Exergoeconomic analysis and optimization of basic, dual-pressure and dual-fluid ORCs and Kalina geothermal power plants: A comparative study, *Renewable Energy*, 83, 527-542.

Wang, J., Wang, J., Dai, Y. and Zhao, P., 2015, Thermodynamic analysis and optimization of a flash-binary geothermal power generation system, *Geothermics*, 55, 69-77.

Yilmaz, C., 2017, Thermodynamic and economic investigation of geothermal powered absorption cooling system for buildings, *Geothermics*, 70, 239-248.

Zheng, B., Xu, J., Ni, T. and Li, M., 2015, Geothermal energy utilization trends from a technological paradigm perspective, *Renewable Energy*, 77, 430-441.



VALIDATION OF AERODYNAMIC HEATING PREDICTION TOOL

Buğra ŞİMŞEK*, Sıtkı USLU** and Mehmet Ali AK***

***TOBB Ekonomi ve Teknoloji Üniversitesi, Söğütözü Caddesi No:43, 06560, Ankara,

*bsimsek@etu.edu.tr, **suslu@etu.edu.tr

*** ROKETSAN AŞ., Kemalpaşa Mah. Şehit Yüzbaşı Adem Kutlu Sk. No:21, 06780, Ankara, mehmetali.ak@roketan.com.tr

(Geliş Tarihi: 03.02.2019, Kabul Tarihi: 22.01.2020)

Abstract: Validation of one-dimensional aerodynamic heating and ablation prediction program, *AeroheataBS* to calculate transient skin temperatures and heat fluxes for high-speed vehicles has been performed. In the tool shock relations, flat plate convective heating expressions, Eckert's reference temperature method and modified Newtonian flow theory are utilized to compute local heat transfer coefficients. Corresponding governing equations are discretized explicitly and numerically solved. Time varying flight conditions including velocity, altitude and angle of attack serve as input to the program. In order to examine the accuracy of aerodynamic heating capabilities of *AeroheataBS*, calculated temperature histories are compared with flight data of the X-15 research vehicle, a modified von-Karman nose shaped body, cone-cylinder-flare configuration and results of conjugate computational fluid dynamics studies. Comparative studies show that computed values are in good agreement with the reference data and prove that methodology established in *AeroheataBS* is appropriate for estimating aerodynamic heating and structural thermal response.

Keywords: Aerodynamic heating, thermal design of missiles, thermal protection systems.

AERODİNAMİK ISINMA KESTİRİM ARACININ DOĞRULANMASI

Özet: Yüksek hızlı hava araçlarının gövde sıcaklıklarını ve aerodinamik ısı akılarını hesaplama yazılımı olan, bir boyutlu aerodinamik ısınma ve ısıl aşınma kestirim yazılımı, *AeroheataBS*'in doğrulama çalışmaları yürütülmüştür. Şok denklemleri, düz plaka üzeri taşınım ısı transferi yaklaşımları, Eckert'in referans sıcaklık yöntemi ve değiştirilmiş Newton yasası aerodinamik ısınmanın hesaplanmasında kullanılmıştır. Denklemler açık olarak ayrılaştırılmış ve sayısal olarak çözülmüştür. Işınım ile olan ısı transferi de dikkate alınmıştır. Uçuş hızı, uçuş irtifası ve hücum açısı zamana bağlı olarak tanımlanmıştır. Hesaplamaların doğruluğu literatürde bulunan uçuş verileriyle ve hesaplamalı akışkanlar dinamiği çalışmalarının sonuçlarıyla kıyaslanarak değerlendirilmiştir. Kıyaslamalarda gözlemlenen uyumlu sonuçlar *AeroheataBS* yazılımında kullanılan yöntemin aerodinamik ısınmanın ve gövde sıcaklıklarının kestiriminde kullanılabileceğini göstermiştir.

Anahtar kelimeler: Aerodinamik ısınma, füzelerin ısıl tasarımı, ısıl koruma sistemleri.

NOMENCLATURE

| | | | |
|------------|--|---------------|---|
| c_p | Specific heat [J/kgK] | T_0 | Total temperature [K] |
| h | Heat transfer coefficient [W/m ² K] | T_∞ | Free stream temperature [K] |
| k | Thermal conductivity [W/mK] | V_1 | Local velocity [m/s] |
| M_L | Local Mach number [-] | v | Volume [m ³] |
| M_∞ | Free stream Mach number [-] | y | Distance along thickness direction [m] |
| Nu_x | Nusselt number at point x [=hx/k] | α | Thermal diffusivity [m ² /s] |
| P_L | Local pressure [Pa] | γ | Specific heat ratio [-] |
| Pr | Prandtl number [= $\mu c_p/k$] | Δy | Mesh size [m] |
| P_{0L} | Local stagnation pressure [Pa] | Δt | Time step size [s] |
| q_{hw}'' | Hot wall heat flux [W/m ²] | δ | Thickness [m] |
| Re_x | Reynolds number at point x [= $V\rho x/\mu$] | ε | Emissivity [-] |
| r | Recovery factor | η | Blowing coefficient [-] |
| \dot{s} | Surface recession rate [m/s] | μ | Viscosity [Pa s] |
| St | Stanton number [$h/\rho c_p V$] | ρ | Density [kg/m ³] |
| t | Time [s] | σ | Stefan-Boltzman constant [W/m ² K ⁴] |
| T | Temperature [K] | | |
| T_L | Local temperature [K] | | |
| T_r | Recovery temperature [K] | | |
| T_w | Wall temperature [K] | | |
| T^* | Eckert's reference temperature [K] | | |

INTRODUCTION

Aerodynamic heating is conversion of kinetic energy into heat energy due to relative motion between a body and flow and the subsequent transfer of this energy to the skin and the interior of the body. Some portion of heat is

produced by compression of fluid across the shock near the stagnation regions and additional heat results from viscous dissipation inside the boundary layer.

Aerodynamic heating is one of the major concerns in the design of high-speed vehicles since success of mission strongly depends on surviving in harsh thermal environment. Thermal protection systems are used to maintain the underlying structure and avionics within allowable temperature limits. Selection of an appropriate thermal protection system is highly bound to accuracy of the thermal environment estimation since poor estimation leads poor design and mission failure. Therefore preliminary thermal design of high speed vehicles requires precisely and reliably predicting the convective heating over the vehicle. Detailed reviews about the advances made within the past 50 years of aerodynamic heating and thermal protection systems can be found in Bertin and Cummings (2003). Analytical calculations for aerodynamic heating are available under certain conditions and assumptions. The work (Liu and Cao, 2017) deals with how to use suitable equations of convective heat transfer coefficient to compute aerodynamic heating in high speed laminar flow over a flat plate under incoming flow Mach numbers 1 to 10. Another detailed analytical study of the aerodynamic heating problem for both laminar and turbulent flow regimes is given in Arnas et al., (2010). In that study by use of Newton's second law of motion, continuity equation, first law of thermodynamics and the equation of state, governing equations are derived and appropriate aerodynamic heat transfer equations are developed. Additional methods of predicting aerodynamic heating to blunt-nosed bodies, flat plates and sharp cones through the hypersonic speed range for laminar, transitional or turbulent boundary layers are described in Crabtree et al., (1970). Comparisons of some engineering correlations to predict aerodynamic heating with CFD results and experimental data are published in Higgins (2005). Good agreement was observed between the results obtained from laminar correlations, CFD simulations and experimental data. Comparisons of turbulent correlation results with CFD and experimental data produced reasonable agreement in most cases. Aerodynamic heating can be estimated by following three different ways which are ground testing, numerical simulation and approximate engineering methods (Yang et al., 2014). One of the major difficulties with ground testing is to generate exact flight conditions and to determine the suitable testing configuration. Verification of the test facility, providing the required test conditions, is also challenging (Mazaheri et al., 2014). Therefore, it is hard to determine exactly which parameters must be reproduced and how the ground to flight connection must be done. In addition, ground testings are generally costly compared to other methods.

Developments in Computational Fluid Dynamics, CFD make numerical computations the best to predict aerodynamic heating. Computer power makes it possible

to solve the most of the complex equations numerically for many different types of designs and flight trajectories of interest; unfortunately, complicated methodologies of CFD include some difficulties. Intense modeling efforts should be made to improve the level of accuracy and too much computational time may be required to calculate complete time histories of transient temperature and heat flux. It is not appropriate for the early phases of design, which requires for predictions and design iterations to provide proof of concept for new vehicles. There are many studies reported in the literature for the calculation of aerodynamic heating using CFD simulations. In Barth (2007), aerothermodynamic analysis of the flight of SHEFEX 1 is presented. By use of in-house CFD solver, Navier-Stokes computations have been performed to compare the numerical results with the experimental data. Well agreement between the numerical and experimental data is seen for selected altitudes of the trajectory. CFD analysis of HYFLEX (Hypersonic Flight Experiment) is published in Murakami et al., (2004). In this study temperature history of the nose cap is evaluated and compared with the available flight data. CFD analysis of the post flight wind tunnel experiments are also conducted for the comparison studies.

Approximate engineering methods can be followed to obtain rapid predictions with their reasonable accuracy and much less running times compared to multi-dimensional numerical simulations. These estimations are performed to determine the seriousness of the problem and identify the most critical conditions of flight. Many engineering estimation tools have been developed to compute aerodynamic heating such as AEROHEAT (Quinn and Gong, 1990), MINIVER (Louderback, 2013), TPATH (Quinn and Gong, 2000), INCHES (Hamilton et al., 1993), LATCH (Hamilton et al., 1994), HABP (Smyth and Loo, 1981), CBAERO (Kinney, 2004) and HATLAP (Jain and Hayes, 2004).

Each of these codes uses different types of methods for aerodynamic heating. Unfortunately, tools are allowed for in-house use only and most of them are subject to export control regulations and are not commercially available.

Aerodynamic heating and ablation simulation software, *AeroheataBS* has been developed to compute transient structural thermal response. Flight parameters including velocity, height and angle of attack are utilized to find the convective boundary conditions. Both laminar and turbulent flows have been considered. Compressibility effects are taken into account by reference temperature method. Material properties are used as a function of temperature. All of the input parameters are defined by developed graphical user interface, GUI of the software.

In the present work, verification studies for aerodynamic heating capabilities of *AeroheataBS* are presented. Verification of ablation, remeshing capabilities and numerical approaches of the code is out of scope and can be found in Simsek and Uslu (2019).

MATHEMATICAL BACKGROUND

Governing Equations

Insulation and underlying structure have been divided by a network of nodes and governing equations are derived from rate based general form of conservation of energy given in Eq. (1) for each element about the assigned node.

$$\dot{E}_{in} - \dot{E}_{out} = \dot{E}_{st} \quad (1)$$

The energy inflow, \dot{E}_{in} and outflow term, \dot{E}_{out} for the element boundaries are substituted with conduction rate equations given in Eq. (2). Energy storage term, \dot{E}_{st} is calculated as given in Eq. (3).

$$q'' = -k \left(\frac{\partial T}{\partial y} \right) \quad (2)$$

$$\dot{E}_{st} = \nu \rho c_p \left(\frac{\partial T}{\partial t} \right) \quad (3)$$

Points away from the stagnation regions are exposed to aerodynamic heating due to viscous dissipation inside the boundary layer. Computation of temperature response of the structure has been carried out setting incident heat flux as given in Eq. (4). Equation (4) shows that aerodynamic heating is directly proportional to the difference between the recovery temperature and the wall temperature.

$$q''_{hw} = -k \left(\frac{\partial T}{\partial y} \right)_{y=\delta} = \eta h (T_r - T_w) - \sigma \varepsilon (T_w^4 - T_\infty^4) \quad (4)$$

In Eqn (4), η is the blowing coefficient that accounts the ablation effects on heat transfer coefficient. Recovery temperature, also known as adiabatic wall temperature, is calculated as given in Eq. (5). The recovery temperature is the upper limit for the surface temperature and when it is reached, no exchange of heat takes place between the flow and the wall. The adiabatic wall temperature is higher than the freestream temperature and "drives" the convective aerodynamic heating.

$$T_r = T_L \left(1 + r \frac{\gamma - 1}{2} M_L^2 \right) \quad (5)$$

The recovery factor, r depends on flow type. It is estimated as $\sqrt{\text{Pr}}$ and $\sqrt[3]{\text{Pr}}$ for laminar and turbulent flows, respectively (Bertin, 1994). For viscous flow over a body, the local Mach number and the local temperature can be predicted using inviscid isentropic relations. The relationship between the local Mach number and the local static pressure is given in Eq. (6). Isentropic formulation for the local temperature as a function of the local Mach number and the total temperature is given in Eq. (7).

$$M_L = \sqrt{\left[\left(\frac{P_{0L}}{P_L} \right)^{\frac{\gamma-1}{\gamma}} - 1 \right] \frac{2}{\gamma-1}} \quad (6)$$

$$T_L = T_0 / \left(1 + \frac{\gamma-1}{2} M_L^2 \right) \quad (7)$$

For subsonic speeds, the local stagnation pressure can be calculated using a simple isentropic relation. For supersonic speeds, it is found using normal shock wave equations with the assumption of bow shock behaving similar to a normal shock at the center in the transverse direction. The total temperature is constant across a normal shock wave for the adiabatic flow of a perfect gas and it is found by Eq. (8).

$$T_0 = T_\infty \left(1 + \frac{\gamma-1}{2} M_\infty^2 \right) \quad (8)$$

Local static pressure is calculated by use of Modified Newtonian theory. The Newtonian theory assumes that when flow strikes a surface, the normal component of momentum to that surface diminishes and the freestream flow moves along the surface with its tangential component of momentum unchanged (Hankey, 1988). This theory is valid for the estimation of local static pressure over all surfaces experiencing non-separated flows. In modified theory, pressure coefficient is corrected by use of the maximum value of the pressure coefficient, evaluated at a stagnation point behind a normal shock wave. For the prediction of pressure distribution over blunt-nosed bodies, Modified Newtonian theory yields in considerably more accurate results than does the straight Newtonian theory (Anderson, 2006). Modified Newtonian theory is also attractive because it requires only the angle between the freestream velocity vector and the inward normal to the surface. Theoretical background of the modified Newtonian theory is published in Lees (1955). Flow phenomena which give rise to significant differences between the actual pressures and those predicted using modified Newtonian flow are described in Bertin (1994). Examples of where such differences seen are (Bertin 1994):

- In the flow behind the shock-wave of a truncated blunt body.
- In the rapid overexpansion and recompression of the flow around the nose region of a sphere.
- On the control surfaces/wings where additional shock waves are seen within the shock layer.

In general, Newtonian theory provides satisfactory results when Mach number is large and/or the flow deflection angle is large (Bertin, 1994). Its use at subsonic and low supersonic speeds is justified by the continuity and simplicity it provides in the lower Mach number regions where aerodynamic heating rates are negligible. Effects of the angle of attack and surface conical angle on the aerodynamic heating are taken into account by the modified Newtonian theory since angle between the flow direction and surface normal is used to find its tangential and normal components.

Free stream properties are estimated by interpolating the 1976 U.S. Standard Atmosphere model versus the altitude. Nusselt numbers for laminar and turbulent flows are expressed below, respectively (Arnas et al., 2010).

$$Nu_x = 0.332\sqrt{Re_x}(Pr)^{\frac{1}{3}} \quad (9)$$

$$Nu_x = 0.0291(Re_x)^{\frac{4}{5}}(Pr)^{\frac{1}{3}} \quad (10)$$

Three-dimensional relieving effects make the boundary layer thinner for the cone. This in turn results in larger velocity and temperature gradient in the boundary layer and hence causes a higher heat transfer and skin friction than in the two-dimensional boundary layer over a flat plate (Anderson, 2006). For the conical side of the body, heat transfer coefficient, h is multiplied by the Mangler fraction $\sqrt{3}$ and then computation is made as for a flat plate (Crabtree et al., 1970). Derivation of the factor $\sqrt{3}$ can be found in both Anderson (2006), Hantzsche and Wendt (1947). By use of this factor, relation between the Nusselt number for conical and planar regions is given in Eq. (11) for laminar flows.

$$Nu_{x,conical} = \sqrt{3}Nu_{x,planar} \quad (11)$$

Thermodynamic and transport properties are found at Eckert's reference temperature, T^* which is given in Eq. (12). Eckert's reference temperature method is used to add compressibility effects into the convective heat transfer equations. The reference temperature method provides a simple engineering approach to calculating the surface skin-friction and aerodynamic heating for compressible boundary layers using classic results from incompressible flow (Anderson, 2006). Recently, Meador and Smart (2005) suggested improved equations for the calculation of the reference temperature for laminar and turbulent flows.

$$T^* = T_L + 0.5(T_w - T_L) + 0.22(T_r - T_L) \quad (12)$$

Thermal conductivity, density, dynamic viscosity and specific heat of air are computed at reference temperature. Sutherland equations which are given in Eq. (13) and Eq. (14) are used to determine the dynamic viscosity and the thermal conductivity, respectively. In these equations temperature is given in K, viscosity in kg/m.s and thermal conductivity in W/m K.

$$\mu = 1.458 \times 10^{-6} \frac{T^{1.5}}{T + 110.4} \quad (13)$$

$$k = 1.993 \times 10^{-3} \frac{T^{1.5}}{T + 112} \quad (14)$$

Finally, Nusselt number for laminar and turbulent flow conditions can now be written as in Eq. (15) and Eq. (16), respectively. Heat transfer coefficient, h is then evaluated from the given Nusselt number correlations. In the equations, superscript (*) indicates that corresponding property is calculated at the reference temperature.

$$Nu_x^* = \frac{hx}{k^*} = 0.332 \sqrt{\frac{\rho^* V_{lx}}{\mu^*}} \left(\frac{\mu^* c_p^*}{k^*} \right)^{\frac{1}{3}} \quad (15)$$

$$Nu_x^* = \frac{hx}{k^*} = 0.0291 \left(\frac{\rho^* V_{lx}}{\mu^*} \right)^{\frac{4}{5}} \left(\frac{\mu^* c_p^*}{k^*} \right)^{\frac{1}{3}} \quad (16)$$

Following the calculation of heat transfer coefficient, convective heat flux is evaluated at each time step by use of Eq. (4). Temperature distribution along the wall is then determined by use of boundary conditions and explicit finite difference equations derived for interior nodes.

In Eq. (4) η is the reduction of the heating due to mass injection into boundary layer. This phenomenon thickens the boundary layer and causes a decrease in aerodynamic heating (Bianchi, 2007). Reduction rate is estimated by a simple relation expressed in Eq. (17).

$$\eta = \frac{\Phi}{e^{\Phi} - 1} \quad (17)$$

In Eqn. (17), Φ is a function of mass injection rate, local flow density, local velocity and unblown Stanton number. Pyrolysis gas flux is calculated by use of conservation of mass for each node by considering density change due to decomposition. Mass loss rate due to ablation is approximated by use of surface recession. Decomposition of insulation is modeled by Arrhenius relation and steady state ablation approach employing heat of ablation is performed to predict surface recession.

In previous work, verification of finite difference computations are made by use of analytical solutions of transient conduction, transient conduction with convection and transient conduction with temperature dependent material properties. It was shown that 0.1 mm mesh size and 0.001 s time step size are appropriate to attain the required accuracy. In Simsek and Uslu, (2019) code-to-code comparison is also performed using MSC MARC for an ablation problem with specified surface recession. It is showed that newly developed prediction tool can also be used for problems where the surface recession is known. Thermochemical ablation model is verified using arcjet test results of a low-density phenolic impregnated carbon ablator (PICA). The computed and experimental surface temperatures show reasonable agreement with a maximum discrepancy of approximately 10%. Details of the decomposition and surface recession are out of scope of this study and details can be found in Simsek and Uslu, (2019).

Laminar to turbulent transition criteria recommended by Quinn and Gong (2000) is implemented into the tool. In the criteria, transition Reynolds number is a function of local Reynolds number and local Mach number. Different types of transition models are also implemented into tool and selection of the model is left to the user. Fully turbulent and laminar computations without transition are also possible.

Developed methodology has the following limitations.

- In *AeroHeataBS*, aerodynamic heating due to skin friction is computed. Locations close to the stagnation regions such as leading edges of wings and tips of nose cones cannot be computed by this methodology. Work to develop a methodology for stagnation point heating is currently going on.
- In the current methodology, perfect gas assumption is made. At hypersonic speeds dissociation and ionization of air takes place and specific heat ratio of air cannot be assumed as constant any longer. Implementation of real gas effects into *AeroheataBS* is being studied.
- Due to one-dimensional computation, complex geometries and longitudinal conduction effects are not considered. Shock/boundary-layer interaction cannot be simulated by *AeroheataBS*.
- Several problems in which flow separation occur. A consequence of flow separation is to increase significantly the local aerodynamic heating.

FINITE DIFFERENCE APPROACH

Thickness of the missile wall is divided into elements by nodal network with constant mesh size, Δy normal to flow direction. Each of the interior nodes is centered at the elements. Surface and back-face nodes are assigned a thickness that is one-half that of the interior nodes. Longitudinal conduction in the missile wall is neglected since temperature gradients in that direction are much smaller than in the normal radial direction except near the leading edge nose. Circumferential velocity and pressure gradients are also neglected in the *AeroheataBS*. Detailed 3-D CFD simulations are required to capture these effects on the aerodynamic heating especially in the cases with high yaw angles.

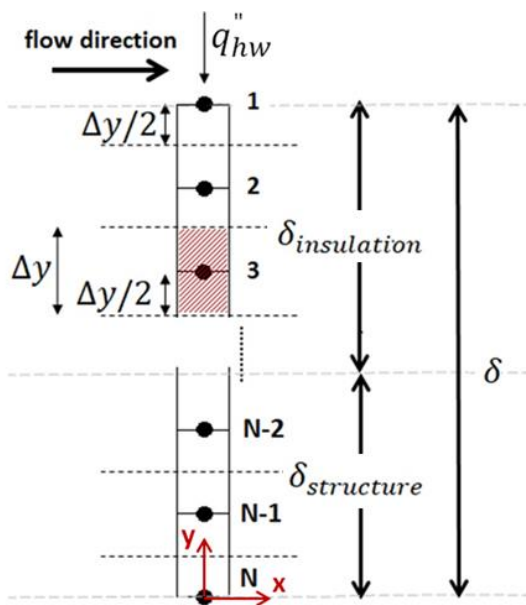


Figure 1. Schematic representation of solution domain

In the preliminary design phase, neglecting 3-D effects are acceptable for rapid predictions. Representation of the discretized wall is illustrated in Fig.1.

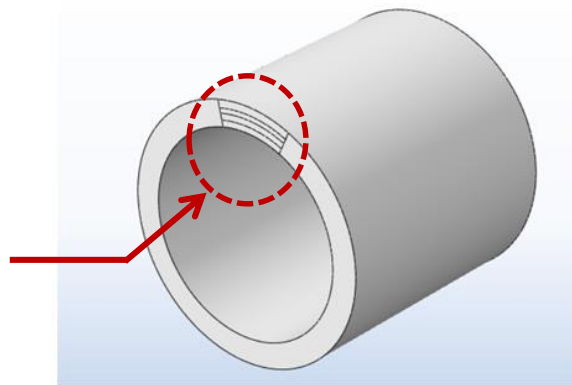
Governing equations are discretized explicitly for each node assigned to each element. Explicit means that temperature computations at each node for a future time are based on the present values at the node and its neighbors. If the temperature distribution at an initial time is known, the distribution at a future time can be computed (Chapra and Canale, 2015). To illustrate the methodology, discretized governing equation for $i=3$ is given in Eq. (18) which is obtained from the energy balance equation. The first term represents the energy flux from the 2nd element to the 3rd element by conduction. Similarly, the second term in the equation shows the energy flux from the 3rd element to the 4th element by conduction. Term on the right hand side is the energy storage in the third element. For each grid point, governing equations are derived and solved explicitly to calculate nodal temperatures for each instant of time. For the surface node, energy inlet term is calculated by convection and radiation which is given in Eq. (4).

$$[k_2(T_2^n)] \frac{T_2^n - T_3^n}{\Delta y^n} - [k_3(T_3^n)] \frac{T_3^n - T_4^n}{\Delta y^n} = \Delta y^n [\rho_3(T_3^n)] [c_{P3}(T_3^n)] \frac{T_3^{n+1} - T_3^n}{\Delta t} \quad (18)$$

Insulation thickness and mesh size are updated as shown in Eq. (19) and Eq. (20) respectively for each time step. In Eqn. (20), N is the total number of nodes.

$$\delta^{n+1} = \delta^n - \dot{\delta}^n \Delta t \quad (19)$$

$$\Delta y^{n+1} = \frac{\delta^{n+1}}{N - 1} \quad (20)$$



Explicit discretization is ‘conditionally’ stable. Solution may present numerically induced oscillations, which are physically impossible. These oscillations may cause divergence. To avoid divergence, time step size should be less than a certain limit. By use of stability criteria which is given in Eq. (21), certain limit value for the time step size can be calculated by Eq. (22).

$$\left(1 - 2 \frac{\alpha \Delta t}{\Delta y^2}\right) \geq 0 \quad (21)$$

$$\Delta t \leq \frac{1}{2} \frac{\Delta y^2}{\alpha} \quad (22)$$

During computations, if the stability criterion is not satisfied, computation is terminated with an error message. In Simsek and Uslu (2019), detailed comparison studies for different mesh and time step sizes are investigated and as a rule of thumb a time step size of 0.001 seconds is recommended for missile applications.

Due to stability concerns recommended minimum mesh sizes for some material types are given in Table 1 for $\Delta t=0.001$ s. In general, in order to increase the accuracy, mesh and time step sizes should be as small as possible.

Table 1. Recommended minimum mesh sizes for different material types.

| Material Type | k (W/mK) | c_p (J/kgK) | ρ (kg/m ³) | Δx (mm) |
|---------------|----------|---------------|-----------------------------|-----------------|
| Inconel | 12 | 431 | 8280 | 0.082 |
| Aluminum | 167 | 896 | 2700 | 0.371 |
| Steel | 42 | 473 | 7700 | 0.152 |
| Insulation | 0.2 | 1500 | 1200 | 0.015 |

STRUCTURE OF *AeroheataBS*

AeroheataBS can be divided into several major sections. In the first section, input files including flight trajectory, material properties, standard atmosphere data, initial conditions and geometric properties are imported from external files. Total number of nodes and time step size are also defined in this section. In the second section, free stream properties are calculated by use of standard atmosphere model. Recovery temperature, dynamic pressure and local flow properties are also computed. In the third section, Eckert’s reference temperature and corresponding Reynolds number are calculated. Type of flow regime is determined in this section. Temperature distribution along the thickness is calculated in the fourth section. Ablation parameters including surface recession and blowing ratio are computed in the next section. Thickness of the insulation is updated for the following time step. Calculations continue until the total flight duration is reached. In the last section, all of requested parameters are written in text file and surface temperature histories are plotted. The flow logic used in the *AeroheataBS* is illustrated in Fig.2.

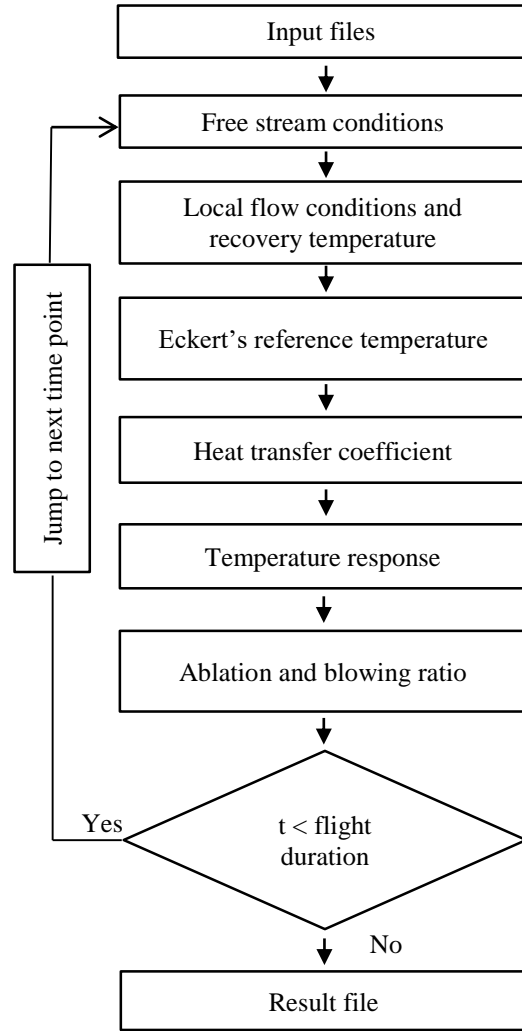


Figure 2. Flowchart of *AeroheataBS*

VALIDATION OF THE TOOL

In order to validate the accuracy of the *AeroheataBS*, four different cases are examined. The following assumptions are made in all of the cases:

- Air is assumed to be a perfect gas; γ is constant and equal to 1.4.
- Properties of the structural material are constant and used as given in corresponding reference study.
- Time step size is 0.001 s. for all cases. For the first and second case, mesh size is 0.1 mm, for the third and fourth case mesh size is 0.5 mm.
- An adiabatic condition is applied to the bottom wall, not exposed to the aerodynamic heating.
- Longitudinal heat conduction is neglected since thermal gradient is larger in radial direction compared to longitudinal direction.

The first data belongs to a modified Von-Karman nose shaped body. The body which consisted of a modified fineness ratio 5, von Karman nose shape, a fineness ratio 5 cylinder and a frustum of a cone is shown as a sketch in Fig.3 (William and Katherine, 1961).

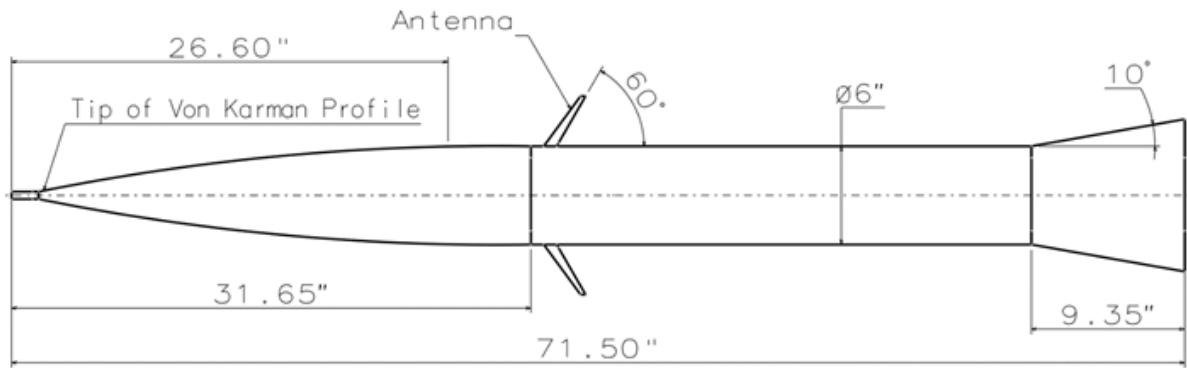


Figure 3. Sketch of model with dimensions (inches) (William and Katherine, 1961).

Mathematically, fineness ratio is the ratio of the length of a body to its maximum diameter. The body is 0.8128-mm-thick (0.032 inches) Inconel. Temperature measurement point is 675.6 mm (26.6 inches) behind the nose tip. Flight trajectory is digitized from William and Katherine (1961) and is given in Fig.4. As can be seen from the velocity profile, system has four stages. After nearly 15 s. the first stage burns out and the second stage is ignited. Third stage is ignited at 22 seconds and the fourth stage is ignited at 31 seconds. Two different cases, fully turbulent and transitional with specified Reynolds number are computed with *AeroheataBS* and results are compared in Fig.5. Prediction of Wing (1971) is also included in comparison.

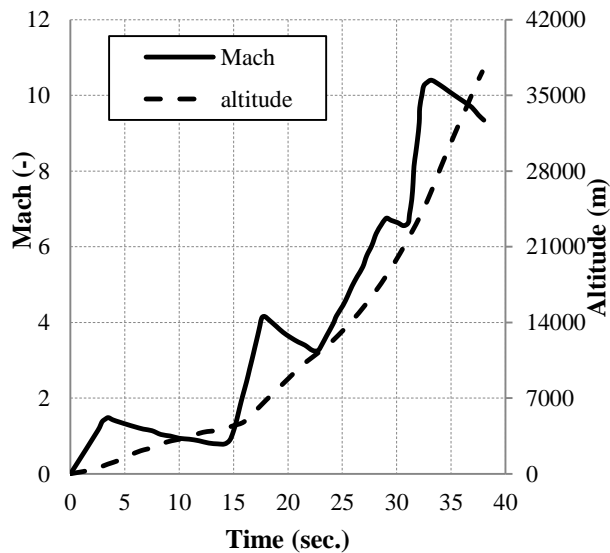


Figure 4. The histories of the velocity and altitude (William and Katherine, 1961).

As seen in Fig.5, the calculated results are followed the experimental data and predictions done by Wing (1970) closely during the first 30 s. From this point on, agreement between *AeroheataBS*, referenced prediction and flight data agreed best when transition local Reynolds number of ten million; indicating relaminarization from turbulent to laminar flow probably occurred at this local Reynolds number.

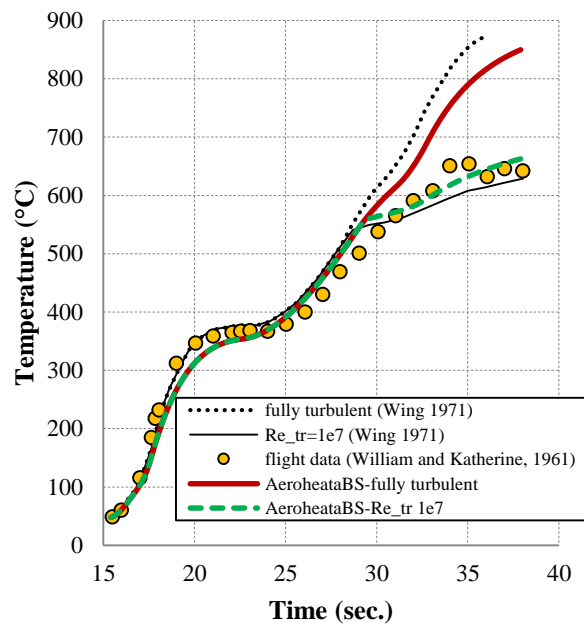


Figure 5. Comparison of *AeroheataBS* with flight data and another code prediction.

Numerous flow field parameters, including surface roughness, wall temperature, mass injection into boundary layer due to ablation, gas chemistry etc. affect transition from laminar to turbulent flow. Premature transition may occur due to unpredictable events and increase heat loads. For a safe-side estimation of aerodynamic heating, it is desirable to consider the fully turbulent flow in thermal design. Fully turbulent solution of *AeroheataBS* also agrees well with the fully turbulent solution of the Wing (1970) and the maximum discrepancy is less than 7%.

The second part of the comparative study includes aerodynamic heating data of a 15° cone-cylinder-flare configuration in flight up to 4.7 Mach (Rumsey and Lee, 1958). The conical nose has a total angle of 15° and is 31 inches long. The cylindrical section was 8.5 inches in diameter and 35 inches long. The flare skirt, which provides aerodynamic stability, had a 10° half-angle and a base diameter of 15.55 inches. Total length of the model was 86 inches. Temperature history for a point which is

0.3556 m (14 inches) behind the nose tip, is calculated with *AeroheataBS* and results are compared with flight measured data and CFD studies presented by Charubhun and Chusilp (2017). Material of the skin is Inconel and thickness is 0.762 mm (0.03 inch). Reader is referred to Ramsey & Lee (1958) for model dimensions, parameters and measurement locations. Time histories of velocity and altitude are shown in Fig.6.

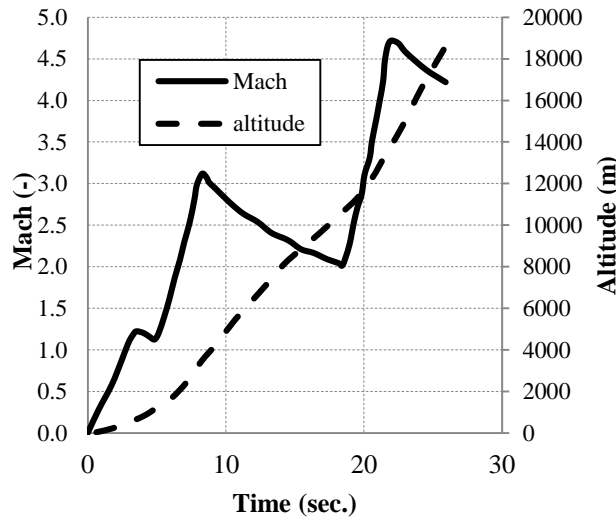


Figure 6. Digitized flight profile from reference (Rumsey and Lee, 1958).

Results of *AeroheataBS* are compared with the flight data and results of the two-dimensional CFD simulations in which five turbulent models were utilized and effects of time step size on the results were investigated (Charubhun and Chusilp, 2017). Results of SST turbulence model are used for comparison as it showed best agreement with the flight data (Charubhun and Chusilp, 2017). As seen in Fig.7, predicted temperature histories agreed satisfactorily especially in the first 22 seconds of flight. Up to this point, computations overestimated the temperatures by about 30 °C. Discrepancy seen in the last three seconds may be the boundary layer transition. Near 22 seconds, an abrupt reduction in skin temperature of the flight data suggests relaminarization of the boundary-layer flow.

Temperature history predicted by *AeroheataBS* and by CFD simulations (Charubhun and Chusilp, 2017) show good agreement. According to Charubhun and Chusilp, (2017), total run time of a CFD analysis is 130 hours, however, run time of *AeroheataBS* for one benchmark point is less than 2 minutes. Although *AeroheataBS* calculates only for one point in a single simulation, timesaving advantage of *AeroheataBS* compared to CFD analysis is quite significant especially in early design stages in which complicated numerical computations may not be mandatory where computation for relatively small number of points seems to be sufficient. The striking advantage of the present approach would be lost if it is necessary to calculate the temperature for too many points which is in fact often not the case.

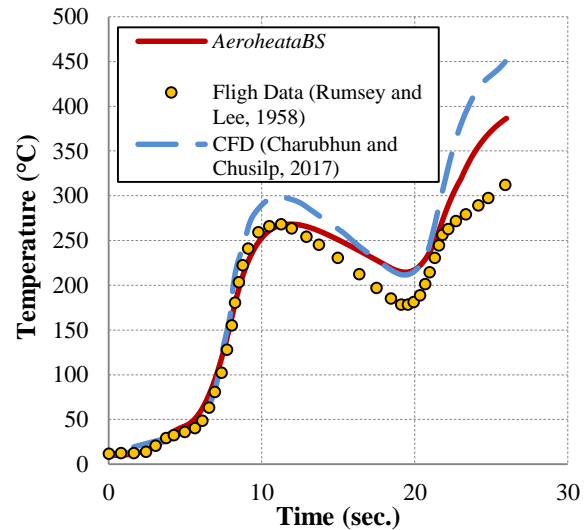


Figure 7. Comparison of the results and measured data.

Comparative studies are also performed with temperatures measured on the wing mid semi-span portion of X-15 plane at high-altitude flight and temperatures calculated by CFD studies presented in Hussain and Qureshi (2013). The flight trajectory is given in Fig.8. Angle of attack is digitized from same reference.

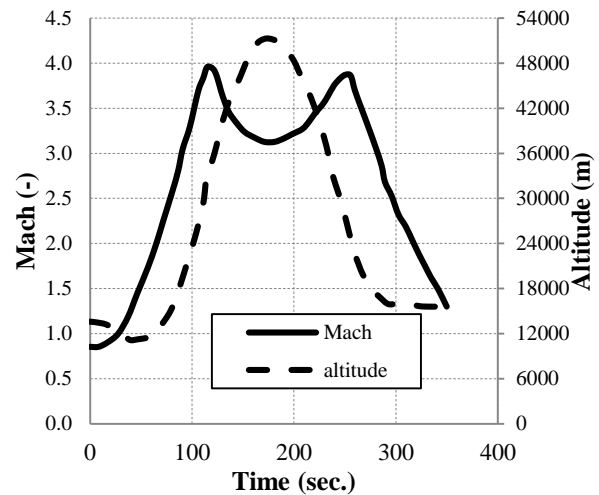


Figure 8. High-altitude flight profile.

Comparisons are made for two locations, at 4% and 20% windward side chord length. Thickness of the wing at points of interest is 1.44 mm (0.057 inch) and material is Inconel. Wing dimensions are obtained from Jenkins (2017). Two computations are made with *AeroheataBS* with different flow regime assumptions, fully turbulent and transition model recommended by Quinn and Gong (2000). Comparison of the results for the point located at %4 chord is given in Fig.9. As can be seen in Fig.9, a reasonably good agreement is captured between the CFD results and *AeroheataBS* predictions when no transition model is used. But when the laminar to turbulent transition is accounted for then an excellent agreement is obtained between the *AeroheataBS* predictions and the flight data. It is clear that flow in some parts of the flight is laminar since fully turbulent computations overestimate the measured flight data. Total run time of the

AeroheataBS simulation is 7 minutes. Fig.10 shows comparisons of measured and calculated temperatures on the point at 20% mid-span chord.

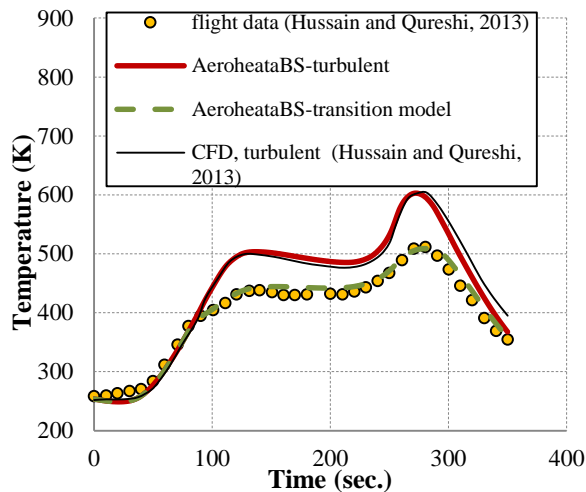


Figure 9. Comparison of measured and calculated temperatures, 4% chord.

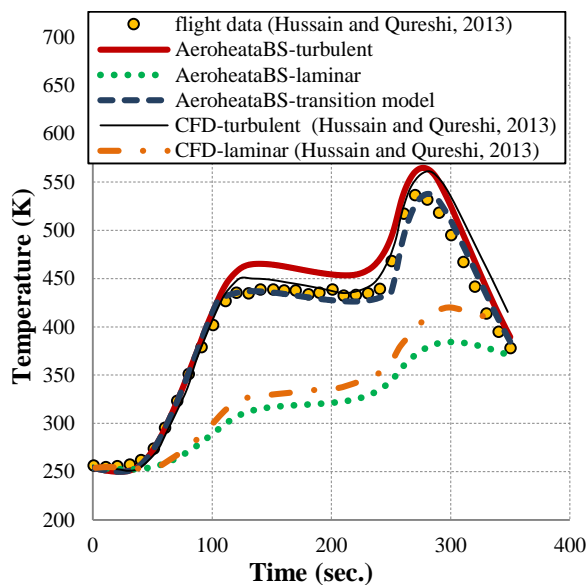


Figure 10. Comparison of measured and calculated surface temperatures at 20% chord.

Predicted temperature histories for turbulent and laminar conditions agree well with the CFD results as shown in Fig.10. The maximum discrepancies between the *AeroheataBS* and CFD results are 3% and 9% for turbulent and laminar flow regimes, respectively. Transition model of the *AeroheataBS* agrees excellent with the flight data. Fully laminar predictions underestimate the flight data, proving that turbulence is occurred during flight.

CONCLUSIONS

Validation studies of aerodynamic heating prediction tool, *AeroheataBS* to calculate transient in-depth temperature response have been described. Mathematical background and the working methodology of the tool are presented.

Predicted transient surface temperatures are compared with the measured flight data and other available numerical results, which are published in the open literature. These comparisons show that the values predicted using the *AeroheataBS* are in good agreement with measured surface temperatures and CFD studies.

Different combinations of insulation and underlying material can be modeled over wide range of flight conditions. Fast prediction of aerodynamic heating under different flight conditions may help engineer to evaluate the alternatives of the options and to make the optimum design. Computed boundary conditions may also be exported to finite element solvers for detailed thermal analyses. Work to enhance capabilities of the *AeroheataBS* is going on.

REFERENCES

- Anderson, J. D. Jr., 2006, *Hypersonic And High Temperature Gas Dynamics*, AIAA, Reston, VA, USA.
- Arnas, A. Ö., D. D. Boettner, G. Tamm, S. A. Norberg, J. R. Whipple, M. J. Benson, and B. P. VanPoppel. 2010. On The Analysis Of The Aerodynamic Heating Problem. *J. Heat Transfer* 132 (12): 124501.
- Barth T., 2007, Aero-Thermodynamic Analysis To SHEFEX I, *Engineering Applications of Computational Fluid Mechanics* Vol.1, No. 1.
- Bertin, J. J., 1994, *Hypersonic Aerothermodynamics*, AIAA Education Series, AIAA, Reston, VA, USA.
- Bertin, J. J., and R. M. Cummings, 2003. Fifty Years Of Hypersonics: Where We've Been, Where We're Going. *Prog. Aerosp. Sci.* 39 (6-7): 511-536.
- Bianchi, D. , 2007, *Modeling Of Ablation Phenomena In Space Applications*, Ph.D. dissertation, Dept. of Mechanics and Aeronautics, The Sapienza University of Rome, Italy.
- Chapra, S. C., and Canale R. P., 2015, *Numerical Methods For Engineers*, New York: McGraw-Hill Education.
- Charubhun, W., and Chusilp P., 2017, Aerodynamic Heat Prediction On A 15 Degree Cone-Cylinder-Flare Configuration Using 2D Axisymmetric Viscous Transient CFD, *In Proc., 3rd Asian Conf. on Defense Technology*, Piscataway, NJ: IEEE.
- Crabtree, L. F., Woodley, J. G., and Dommett, R. L., 1970, Estimation of Heat Transfer to Flat Plates, Cones and Blunt Bodies, *Ministry of Technology, Aeronautical Research Council, Rept. and Memoranda* No. 3637, London.
- Hamilton H. H., Greene F. A. and Dejarnette F. R., 1993, An Approximate Method For Calculating Heating Rates On Three-Dimensional Vehicles, AIAA paper 93-2881.

- Hamilton, H. H., Greene, F. A., and DeJarnette, F. R., 1994, Approximate Method for Calculating Heating Rates on Three Dimensional Vehicles, *Journal of Spacecraft and Rockets*, Vol. 31, No. 3, 345-354.
- Hankey W. L., 1988, *Re-Entry Aerodynamics*, AIAA Education Series, AIAA, Reston, VA, USA.
- Hantzsche, W., and Wendt, H., 1947, The Laminar Boundary Layer on a Cone in a Supersonic Air Stream at Zero Angle of Attack, *Jahrbuch 1941 der Deutschen Luftfahrtforschung*. Also available as Translation No. RAT-6, Project RAND.
- Higgins K., 2008, Comparison of Engineering Correlations for Predicting Heat Transfer in Zero-pressure-gradient Compressible Boundary Layers with CFD and Experimental Data, *Australia Defense Science and Technology Organization*, DSTO-TR-2159.
- Hussain M., Qureshi M.N., 2013, Prediction Of Transient Skin Temperature Of High Speed Vehicles Through CFD, *6th International Conference on Recent Advances in Space Technologies*, Istanbul, Turkey.
- Jain, A.C., Hayes, J.R., 2004, Hypersonic Pressure, Skin-Friction, and Heat Transfer Distributions on Space Vehicles: Planar Bodies”, *AIAA Journal* Vol. 42 No. 10, 2060-2068.
- Jenkins D.R., 2017, *X-15: Extending the Frontiers of Flight*, NASA.
- Kinney, D. J., 2004, Aero-Thermodynamics for Conceptual Design, *42nd AIAA Aerospace Sciences Meeting and Exhibit*, Reno, NV, USA.
- Lees, L., 1955, Hypersonic Flow, *5th International Aeronautical Conference*, Los Angeles, Inst. of Aeronautical Sciences, New York, 241-276.
- Louderback P.M., 2013, *A Software Upgrade Of The NASA Aeroheating Code “MINIVER”*, MSC Thesis, Florida Institute of Technology, USA.
- Liu C., Cao W., 2017, Study Of Predicting Aerodynamic Heating For Hypersonic Boundary Layer Flow Over A Flat Plate, *International Journal of Heat and Mass Transfer* 111, 1079-1086.
- Mazaheri A., Bruce W.E., Mesick N.J. Sutton K., 2014, Methodology For Flight-Relevant Arc-Jet Testing Of Flexible Thermal Protection Systems, *Journal of Spacecraft and Rockets*, Vol.51 No.3.
- Meador, W. E., and Smart, M. K., 2005, Reference Enthalpy Method Developed from Solutions of the Boundary Layer Equations, *AIAA Journal*, Vol. 43, No. 1, 135-139.
- Murakami K., Yamamoto Y., Rouzand O., 2004, CFD Analysis Of Aerodynamic Heating For Hyflex High Enthalpy Flow Tests And Flight Conditions, *24th International Congress of the Aeronautical Sciences*, Yokohama, Japan.
- Quinn R.D., Gong L., 1990, Real Time Aerodynamic Heating And Surface Temperature Calculations For Hypersonic Flight Simulation, *NASA Technical Memorandum 4222*.
- Quinn, R. D., and Gong L., 2000, A Method For Calculating Transient Surface Temperatures And Surface Heating Rates For High-Speed Aircraft, *NASA/TP-2000-209034*, Washington, DC: NASA.
- Rumsey C.B., Lee D.B., 1958, Measurements of aerodynamic heat transfer on a 15° cone-cylinder-flare configuration in free flight at Mach numbers up to 4.7., *NACA RM LJ57J10*.
- Smyth, D. N. and Loo, H. C., 1981, Analysis of Static Pressure Data from 1/12-scale Model of the YF-12A. Volume 3: The MARK IVS Supersonic-Hypersonic Arbitrary Body Program, User's Manual, NASA-CR-151940.
- Simsek B., Uslu S., 2019, One-Dimensional Aerodynamic Heating and Ablation Prediction, *Journal of Aerospace Engineering*, Vol.32 Issue 4.
- William M.B. Jr., Katherine A.C., 1961, Free-flight aerodynamic heating data to Mach number 10.4 for a modified von Karman nosed body, *NASA TN D-889*.
- Wing L.D., 1971, Tangent ogive nose aerodynamic heating program: NQLDW019T, NASA-TM-X-65540.
- Yang G., Duan Y., Liu C., Cai J., 2014, Approximate Prediction for Aerodynamic Heating and Design for Leading-edge Bluntness on Hypersonic Vehicles. *AIAA Paper 2014-1393*, AIAA, Reston, VA.



Dr. Buğra ŞİMŞEK is currently a lead engineer at ROKETSAN A.Ş. He received his major and minor BSc degrees in Mechanical Engineering and Materials and Metallurgical Engineering from Middle East Technical University in 2009, respectively. He obtained his MSc degree from the Mechanical Engineering Department of Middle East Technical University in 2013. His MSc thesis involved research on missile nose heating and ablation. He received his PhD degree from TOBB University of Economics and Technology under the supervision of Assistant Professor Sıtkı USLU in December 2019. His PhD studies are related to aerodynamic heating and ablation including investigation of effects of transition from laminar to turbulent and relaminarization of the flow. Dr. ŞİMŞEK works in thermal and structural design of missiles at ROKETSAN A.Ş. since 2009. Main research areas; aerodynamic heating, thermal protection systems, nose cone ablation and thermal management.



Dr. Sıtkı USLU is assistant professor in the Department of Mechanical Engineering at TOBB University of Economics and Technology (TOBB ETU), Ankara, Turkey. Dr. USLU has obtained his first degree in mechanical engineering at Uludağ University in 1983, Bursa - Turkey. He then received his MSc degree in mechanical engineering in 1986 from Middle East Technical University, Ankara. Dr. USLU did his PhD at Imperial College London in 1993. He worked as a postdoc researcher at Imperial College in a EU Project and another year at Computational Dynamics (STAR-CD) before moving to Germany in 1995 to work in the Internal Combustion Engines research lab at Daimler Benz AG, Stuttgart - Germany. He worked as a senior CFD and combustion research engineer at Daimler Benz between 1995 to 2001. After that he moved to MTU Aero Engines in Munich and worked in the Combustion Chamber Design Group as an R&D engineer between 2001-2008. Dr. USLU has been working as a faculty staff in the Department of Mechanical Engineering at TOBB ETU since 2008 teaching Thermo-Fluid Sciences and doing research in Propulsion Systems. Dr. USLU leads the CSL (Combustion Systems Lab) at TOBB ETU that is mainly involved in research on Gas Turbine Combustion Chamber and Internal Combustion Engines. The CSL lab has participated in several national research projects and as well as EU technology projects also.



Dr. Mehmet Ali AK is a manager in ROKETSAN. He is graduated from Mechanical Engineering Department of Middle East Technical University in 1993. He obtained his MSc and PhD degrees from the same department in 1995 and 2001, respectively. He worked as lead researcher in TUBITAK SAGE for 19 years and executive designer in TUSAŞ TEI for a year. He is working in ROKETSAN A.Ş. since 2012 and today he is manager of Department of Space Systems. His main research areas; computational fluid dynamics, turbulent reactive flows, heat transfer, aerothermodynamics, numerical gas dynamics, propulsion systems and system engineering.



PERFORMANCE EVALUATION FOR THERMAL ARCHITECTURES OF FLUE-GAS ASSISTED ORGANIC RANKINE CYCLE SYSTEMS

Burak TÜRKAN* and Akın Burak ETEMOĞLU**

*Bursa Uludağ University, Faculty of Engineering, Department of Mechanical Engineering,
16059, Bursa, Turkey, burakt@uludag.edu.tr

**Corresponding author, Bursa Uludağ University, Faculty of Engineering, Department of Mechanical Engineering,
16059, Bursa, Turkey, aetem@uludag.edu.tr

(Geliş Tarihi: 15.01.2019, Kabul Tarihi: 05.02.2020)

Abstract: Effective use of waste heat at low and medium temperatures is considered as one of the solutions to alleviate energy shortages and environmental pollution problems. Due to its feasibility and reliability, the organic Rankine cycle is continued to attract widespread interest from researchers and/or manufacturers. This paper presents thermodynamic and economic analyses on flue-gas assisted organic Rankine cycles (FGA-ORCs) based on both energy and exergy concepts. The heat source of the FGA-ORC system is the exhaust flue-gas of a stenter-frame which is highly used in textile finishing process. In this study, to convert thermal energy into electrical and/or mechanical energy on a small scale, an optimization study was performed using five different cycle architectures. Parametric studies were also carried out to investigate the effect of operating parameters on performance indicators such as efficiency, economical profit and performance ratio. Finally, under specified operating conditions, the thermal architecture was identified that reduces exergy destruction and increases economic profit due to increased net-work output. For analyzed cases in this study, Scenario-4 (i.e., thermal architecture 4) shows the best system performance with 69% exergetic efficiency within the thermodynamic and practical limits.

Keywords: Organic Rankine cycle, Waste-heat recovery, Flue-gas, Energy analysis, Exergy analysis.

BACA GAZI DESTEKLİ ORGANİK RANKİNE ÇEVİRİMLERİNİN TERMAL MİMARİLERİ İÇİN PERFORMANS DEĞERLENDİRMESİ

Özet: Düşük ve orta sıcaklıklarda atık ısının etkin kullanımı, enerji sıkıntısı ve çevre kirliliği sorunlarını hafifletmek için çözümlerden biri olarak kabul edilir. Uygulanabilirliği ve güvenilirliği nedeniyle, organik Rankine çevrimi, araştırmacıların ve/veya üreticilerin ilgisini yaygın olarak çekmeye devam etmektedir. Bu makalede, hem enerji hem de ekserji kavramlarına dayanan baca-gazı destekli organik Rankine döngüleri (FGA-ORCs) üzerinde termodinamik ve ekonomik analizler sunulmaktadır. FGA-ORC sisteminin ısı kaynağı, tekstil bitim işleminde çok kullanılan bir ramöz makinasının egzoz baca gazıdır. Bu çalışmada, termal enerjiyi küçük ölçekte elektrik ve/veya mekanik enerjiye dönüştürmek için beş farklı çevrim yapısı kullanılarak optimizasyon çalışması yapılmıştır. İşletme şartlarının verimlilik, ekonomik kar ve performans oranı gibi performans göstergeleri üzerindeki etkisini araştırmak için parametrik çalışmalar yapılmıştır. Son olarak, belli çalışma koşulları altında, ekserji yıkımını azaltan ve artan net iş çıkışı nedeniyle ekonomik karı artıran termal mimari tespit edilmiştir. Bu çalışmada analiz edilen vakalarda, Senaryo - 4 (yani termal yapı 4), termodinamik ve pratik sınırlar içinde %69 ekserji verimliliği ile en iyi sistem performansını göstermektedir.

Anahtar Kelimeler: Organik Rankine çevrimi, Atık ısı geri kazanımı, Baca gazı, Enerji analizi, Ekserji analizi.

NOMENCLATURE

| | |
|-----------|-----------------------------|
| e | specific exergy (kJ/kg) |
| \dot{E} | exergy rate (kW) |
| h | specific enthalpy (kJ/kg) |
| H | enthalpy (kJ) |
| \dot{I} | exergy destruction (kW) |
| \dot{m} | mass flow rate (kg/s) |
| P | pressure (kPa) |
| PC | percentage ratio (%) |
| PR | performance ratio (%) |
| Q | the heat transfer rate (kW) |
| s | specific entropy (kJ/kgK) |
| T | temperature (°C or K) |
| W | work (kW) |

η efficiency (%)

Subscription

| | |
|------|-----------------------|
| o | dead state conditions |
| II | second law |
| evap | evaporator |
| hex | heat exchanger |
| in | inlet |
| out | outlet |
| OF | organic fluid |

Superscript

quantity per unit time

INTRODUCTION

Due to increased energy consumption and rapid industrialization, mankind is faced with negative environmental and economic effects. In order to meet future energy demand while reducing greenhouse gas emissions and dependence on fossil fuels, development of energy production and/or conversion systems is unavoidable. A tremendous amount of heat is wasted. Forman et al. (2016) stated that 72% of the primary energy consumption is dissipated and 63% of the considered waste heat streams have temperature below 100°C (Forman et al., 2016). However, conventional energy production/conversion systems are not suitable for efficient production/conversion of low to medium grade heat sources. The Organic Rankine Cycle (ORC), which is a heat recovery technology, converts waste heat into power, using a low-boiling organic material as the working-fluid. The advantages such as adoptability to different operation conditions, construction simplicity, equipment sizes, automatic control and power generation ability make Organic Rankine Cycle (ORC) technology an ideal choice for heat and/or power production from low to medium temperature waste heat sources (Velez et al., 2012; Quoilin et al., 2013; Sun et al., 2017).

To guide the future researches, many review articles covering different aspects of ORC systems have been published (Chen et al., 2010; Tchanche et al., 2011; Bao and Zhao, 2013; Fu et al., 2014; Imran et al., 2018; Garcia et al., 2018). An important feature of ORC, which proposed by different authors, is the possibility of using different low grade heat sources and temperature ranges for power generation such as geothermal energy (Heberle and Brüggemann, 2010; El-Emam and Dincer, 2013), solar (Delgado-Torres and Garcia-Rodriguez, 2010), biomass (Al-Sulaiman et al., 2012), industrial waste heat (Etemoglu, 2013). So, the ORC systems emerge as a promising and powerful technique for the conversion of low to medium temperature heat sources (Tchanche et al., 2014; Zhai et al., 2016).

Organic working fluids significantly affect the efficiency of ORC systems, so selection of appropriate working fluids is important for system performance (Agromayor and Nord, 2017; Gyorke et al., 2018). According to Cengel (2007), a process with a lower entropy generation or higher second-law efficiency requires less energy input for a specified output (Cengel, 2007). Therefore, such a process conserves energy and energy resources. For this reason, the performance of the Organic Rankine cycle was analysed by many researchers from the perspective of energy conversion and exergy destruction theoretically (Mago et al., 2008; Safarian and Aramoun, 2015; Braimakis and Karellas, 2018) and experimentally (Fu et al., 2015).

Research on ORC systems is very active because it provides more efficient energy utilization for the needs of specific operating conditions. Some of these studies have concentrated on the new cycle designs and optimization of the system performance, which was

committed to maximising the efficiency. Panesar et al. (2017) presented a heat recovery and working fluid test-rig to investigate a wide range of realistic gaseous sources such as the direct utilization of the High-Temperature (HT) exhaust gases. Optimal integration of ORCs with industrial processes is still a challenging task. To get optimal thermal architecture, operating conditions, and working fluids, an optimization technique was presented by Kermani et al. (2018).

Among these researches in the literature, investigations of the alternative thermodynamic cycles for ORC systems are essential in order to assure the cost-effective and optimal operation scheme. In this work, a parametric investigation is conducted to determine the effects of parameters which affect the performance of ORC-based combined cycles (FGA-ORCs) driven by flue-gas of stenter-frames. For this, five different thermal architectures, which is the novel aspect of the study, have been examined to show the direction for improvement possibility of FGA-ORCs. Furthermore, the present study describes an easy-to-follow procedure for calculation of the performance and exergy destruction of FGA-ORCs by an appropriate mathematical model which is based on the first and second-law of thermodynamics. Finally, the investigated five different cycles are compared in terms of economic profit, net power output and appropriate operating conditions.

THEORETICAL ANALYSIS

Stenter-frames are continuous dryers which are highly used in textile finishing operations. At the end of the mentioned textile process, the high volume of flue-gas is discharged into the environment. So, low-temperature flue-gas, which is suitable to recovery, is considered as a candidate for a new energy source.

The work potential of the energy contained in a system at a specified state is simply the maximum useful work that can be obtained from the system. This situation is described with the exergy term. Exergy represents quantitatively the useful energy, or the ability to do or receive work-the work content-of the great variety of streams (mass, heat, work etc.) that flow through the system (Cengel and Boles, 1989; Cengel et al., 2002; Bejan, 2002). So, the exergy analysis is a powerful tool for the design, analysis and classification of thermal systems. Disregarding kinetic and potential energy changes, the specific flow exergy of fluid at any state, e , can be calculated from Eq. (1).

$$e = h - h_o - T_o(s - s_o) \quad (1)$$

where h is the specific enthalpy (kJ/kg), s is the specific entropy (kJ/kgK), T is the temperature (K) and o is the dead state conditions. Multiplying specific exergy, e , by the mass flow rate of the fluid, \dot{m} , gives the exergy rate, \dot{E} , as

$$\dot{E} = \dot{m}e \quad (2)$$

The rate form of the entropy balance can be expressed by

$$\underbrace{\dot{S}_{in} - \dot{S}_{out}}_{\text{Net entropy transfer rate}} = \underbrace{\dot{S}_{gen}}_{\text{Entropy generation rate}} \quad (3)$$

and the entropy generation rate, \dot{S}_{gen} , for a steady-flow process can be calculated from the following equation:

$$\dot{S}_{gen} = \sum \dot{m}_{out} s_{out} - \sum \dot{m}_{in} s_{in} - \sum \frac{\dot{Q}}{T} \quad (4)$$

where \dot{Q} is the heat transfer rate. Rate of exergy destruction (or the rate of irreversibility), \dot{I} , can be obtained based on the general exergy rate balance for steady-state open system could be expressed by means of the following equation:

$$\dot{I} = T_0 \dot{S}_{gen} \quad (5)$$

where T_0 is the temperature of dead state. The total exergy destruction, \dot{I}_{TOTAL} , of the system is calculated that the sum of the exergy destructions of each system components and the performance ratio of i_{th} device of the system, PR_i ,

$$PR_i = \dot{I}_i / \dot{I}_{TOTAL} \quad (6)$$

The schematic illustrations of the investigated FGA-ORC systems (i.e. investigated scenarios) can be seen in Figure 1.

Compared to a simple ORC system, five thermal architectures were designed to improve the net-work output of FGA-ORC systems. In the first thermal architecture (see Figure 1a), the effects of the turbine-to-heater mass flow rate and the internal heat exchanger on the system performance parameters were investigated. In the second thermal architecture shown in Figure 1b, the internal heat exchanger was used to improve the evaporator inlet conditions. In Figure 1c, before the turbine, a certain amount of organic fluid was separated from the main flow direction of the cycle and sent directly to the heat exchanger. Thus, the system efficiency was improved by increasing the temperature of the organic fluid entering the evaporator. A complex thermal architecture was shown in Figure 1d for better system efficiency. Having two turbines in the cycle provides a primary advantage for net-work output for the designed thermal architecture. Furthermore, the hot organic fluid from the throttling valve I improves the turbine II inlet conditions with the positive effect of the mixing chamber. Finally, the overall system efficiency was increased by increasing the temperature of the organic fluid entering the evaporator with the heat exchanger and pre-heater. The fifth thermal architecture has an internal heat exchanger and the mixing chamber

before evaporator (see Figure 1e). At the turbine outlet, some amount of organic fluid was sent directly to the heat exchanger and then combined with the organic fluid from the condenser by the mixing chamber. Due to the change in the T-s diagram in the fifth cycle, a definite improvement in ORC system parameters was expected.

Second law efficiency, η_{II} (or exergetic efficiency) is expressed as the ratio of the performance of a device to the performance under reversible conditions for the same final states.

$$\eta_{II} = \eta / \eta_{rev} \quad (7)$$

where η is the actual thermal efficiency of FGA-ORC and η_{rev} is the maximum possible thermal efficiency at same conditions. Heat transfer rate and/or work-output can be easily calculated for steady-flow engineering devices such as turbine, pump, evaporator, condenser, throttling valve, mixing chamber and heat exchanger based on the first law of thermodynamics. For i_{th} device of the system,

$$\dot{Q}_i - \dot{W}_i = \sum H_{i,outlet} - \sum H_{i,inlet} \quad (8)$$

and

$$\sum \dot{m}_{i,inlet} = \sum \dot{m}_{i,outlet} \quad (9)$$

Economical profit of the FGA-ORC can be expressed as the sum of the price of the equivalent natural-gas rate to the recovered, if any, heat transfer and the produced electricity in the system. The price of natural-gas and electricity were taken as 0.2194 \$/m³ and 0.0664 \$/kWh respectively.

The following several assumptions are adopted for the first and second law analyses of FGA-ORC (Safarian and Aramoun, 2015; Sun et al., 2017; Braimakis and Karellas, 2018).

1. All processes are steady state and steady flow with negligible potential and kinetic energy effects and no chemical or nuclear reactions.
2. The directions of heat transfer to the system and work output from the system are positive.
3. The turbine operation has an adiabatic efficiency of 80%.
4. Adiabatic efficiencies of the circulating pumps are 85%.
5. Pressure drops are ignored.
6. Outlet temperature of the condenser is 25°C and the quality is 0.
7. The dead state condition is taken as $T_0=20^\circ\text{C}$ and $P_0=100$

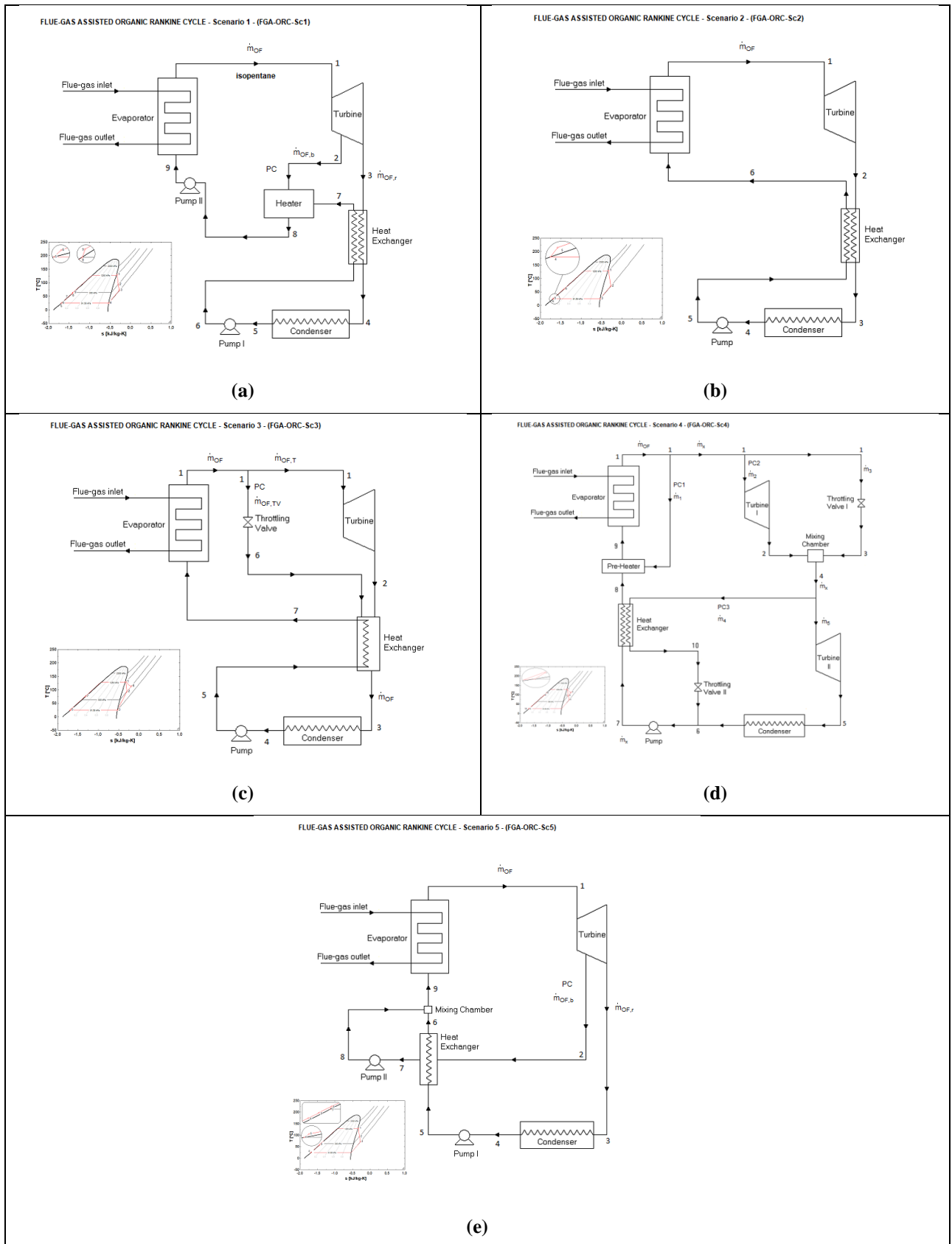


Figure 1. Schematic illustrations of FGA-ORCs.

RESULTS AND DISCUSSION

The optimization process for each thermal architecture is based on our codes on Engineering Equation Solver, EES. Performance of FGA-ORCs strongly depends on

the thermo-physical conditions of the heat source and organic working-fluid. Among a lot of options, it may be challenging to find suitable working conditions for a specified waste-heat source, i.e. stenter-frame flue-gas, to maximize the efficiency and economic profit. So, the

present study can be used to predict the effects of many parameters such as temperature, pressure, mass flow rate and dead state conditions on the performance of FGA-ORCs.

Characteristics of the examined heat source, flue-gas, are as follows: Volumetric flow rate was 20000 m³/h and inlet temperature was 140°C. These values are the typical results of flue-gas measurement of a stenter-frame drying process.

The working-fluid of ORC should satisfy several criteria, such as environmentally friendly, safe, non-corrosive, low-cost, compatible for material contact, stability for certain temperature and pressure values. Moreover, critical point, latent heat, density, specific heat, curve of T-s diagram should also be considered for the selection of suitable working-fluid for ORC systems. So, isopentane was selected as the working fluid of the FGA-ORC because of its thermodynamics performance (Etemoglu, 2013). Table 1 summarizes the thermophysical properties of isopentane (Jang and Lee, 2018).

The evaporator capacity i.e. heat transfer rate from source to working fluid was kept constant as 255.6 kW for all the analysis for investigated thermal architectures. For this reason, the mass flow rate was recalculated for each different scenarios from the energy balance of the evaporator. Turbine inlet pressure and turbine inlet temperature were selected as 1250 kPa and $T_{turbine,inlet}=T_1=T_{gas,in}-10^{\circ}C$, respectively.

Comparison of Thermal Architectures

The most important stage for calculation of the system efficiency is definitely the correct choice of both working

organic fluid and cycle thermal architecture. Making the wrong choice entails a poor cycle performance. Figures 2, 3 and 4 are presented to compare different scenarios (i.e. different FGA-ORCs). Figure 2 shows the comparison of thermal efficiency, η_I , exergy efficiency, η_{II} , total exergy destruction, \dot{I}_{TOTAL} , and economical value of equivalence electricity, Profit_E, of the different FGA-ORC systems. It is clearly observed from Figure 2 that Scenario 4 is more effective and more exergetic than the other scenarios for low pressure and temperature values.

Figure 3 also shows another comparison for different FGA-ORCs to determine the performance of main equipments such as evaporator, turbine, condenser. The relation between the thermal architecture of the cycle and the main system equipments can be easily seen from Figure 3. For example, in Scenario-1, 45% of the total exergy destruction is in the evaporator, while in Scenario-4 this value is about 11%. Thus, it is possible to determine the FGA-ORCs system equipments that needs to be improved for a given thermal architecture.

Table 1. Thermophysical properties and some characteristics of isopentane.

| Fluid Type | Dry |
|-----------------------------|-------|
| Molecular Weight (g/mol) | 72.1 |
| T _{boiling} (°C) | 27.82 |
| T _{critical} (°C) | 187.2 |
| P _{critical} (kPa) | 3378 |
| GWP | 5 |
| ODP | 0 |

GWP : Global warming potential
ODP : Ozone depletion potential

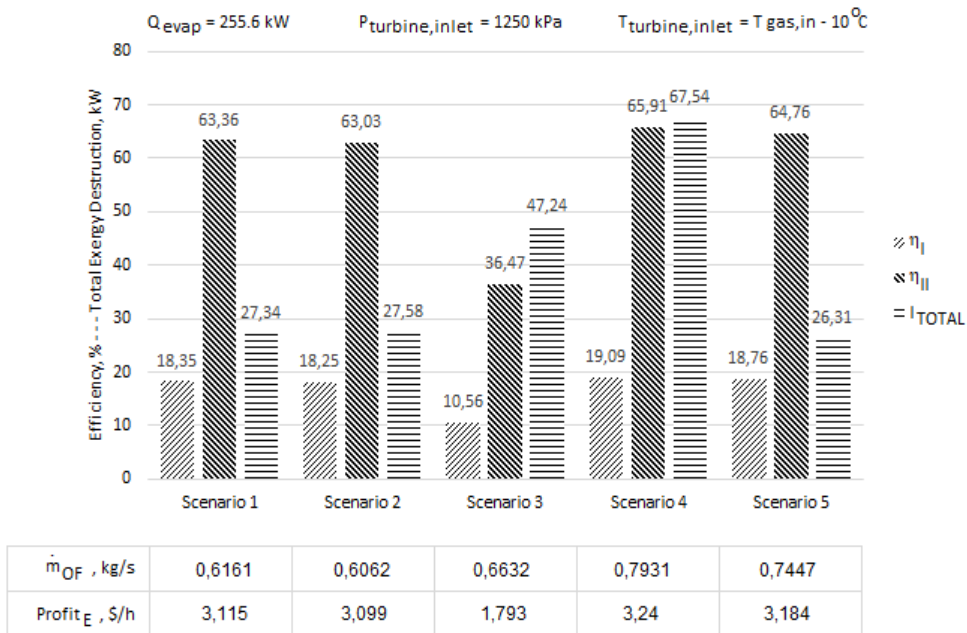


Figure 2. Comparison of different scenarios.

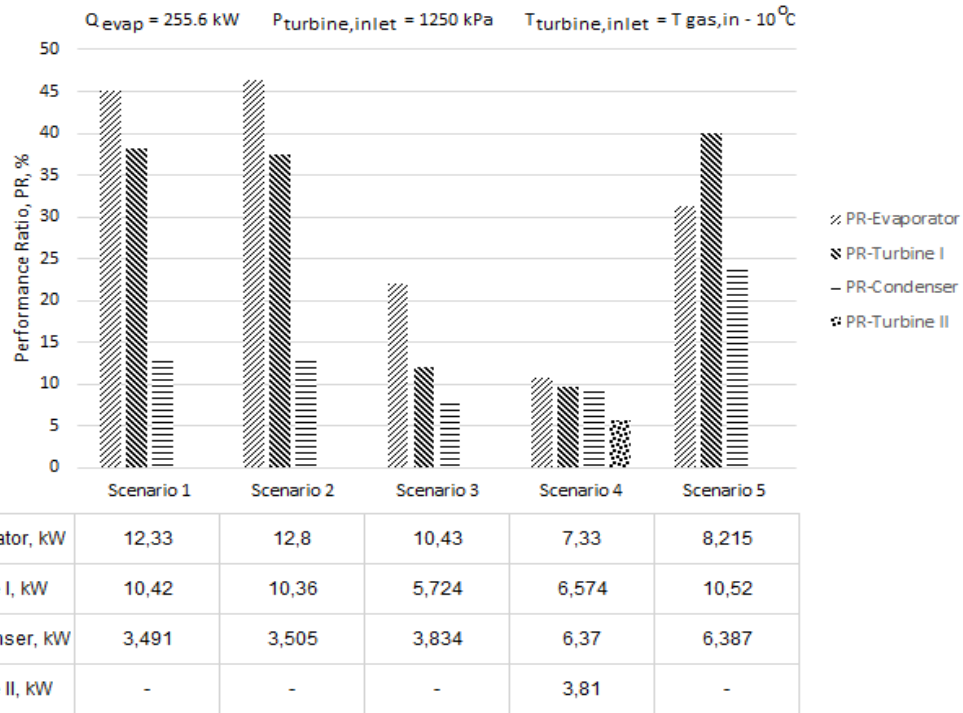


Figure 3. Exergy destruction and performance rates for main equipments of different scenarios.

Figure 4 shows the effect of turbine (turbine-I for Scenario-4) inlet pressure on the thermal and exergetic efficiencies for different FGA-ORCs while the operation conditions was kept constant. It was observed that the highest efficiency values were obtained in Scenario-4 for investigated turbine inlet pressure values. It should be noted that the exergy destruction rates should be a positive quantity ($I > 0$) for any actual thermal processes and that is valid for all the equipments of the thermal architectures of FGA-ORCs. As the exergy destruction rate of the heat exchangers in Scenario-1 and Scenario-2 were negative, these cycles could not be operated at $P=3000 \text{ kPa}$ due to the thermodynamic principles.

The various selection of thermal architectures is usually investigated with a search method type approach to limit the number of discontinuities in the objective function and to obtain more reliable results. This exhaustive approach is the strategy used in the researches about ORC applications. Technical limits, thermodynamic constraints and environmental and safety issues should be taken into account to exclude some thermal architectures or to fix some design parameters of ORCs. Therefore, the optimization process is carried out by examining the operating parameters of ORCs.

Optimization with Working Parameters for Best Thermal Architecture

Astolfi et al. (2017) stated that, the objective function for an optimization problem is the figure that is maximized or minimized during the optimization process. Therefore, for ORCs, two main classes of objective functions could

be defined. (1) Maximizing the plant performance or (2) Minimizing the cost of the produced electrical power.

The search-method-type optimization process, which is performed step by step depending on the operating parameters, was presented to obtain maximum efficiency. The search methods generally fall into two categories, elimination, and hill-climbing techniques. In both, there is a progressive improvement throughout the course of the search (Stoecker, 1989).

Figures 2, 3 and 4 were used to identify the best thermal architecture that the research should focus on to determine the optimum operating conditions. For all the next cases in the present work, Scenario-4 which has the best thermodynamic performance was selected and investigated as the thermal architecture for FGA-ORC. In other words, Scenario-4 provides the highest thermal efficiency and exergetic efficiency in each case examined. Then, the optimization process in our study has been progressed step by step to find the best value of each parameter within the thermodynamic and practical limits for FGA-ORC.

Turbine-I inlet pressure

Figure 5 shows the effect of the turbine-I inlet pressure on the FGA-ORC performance indicators such as η_I , η_{II} , \dot{I} , and Profite . The highest thermal and exergetic efficiencies were calculated at 1311 kPa for investigated pressure range. Increasing the turbine-I inlet pressure from 800 kPa to 1311 kPa, within the thermodynamics limits, the total work output of the turbines increases by

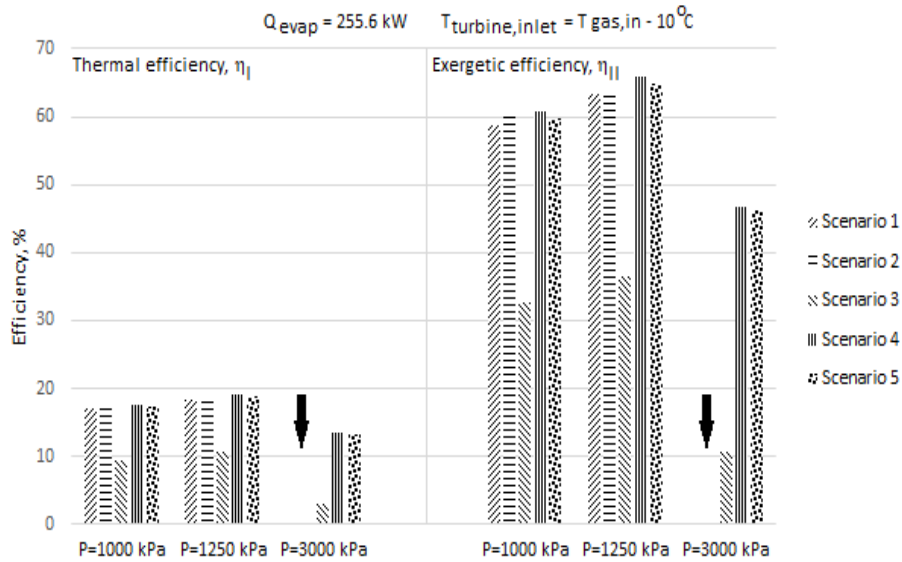
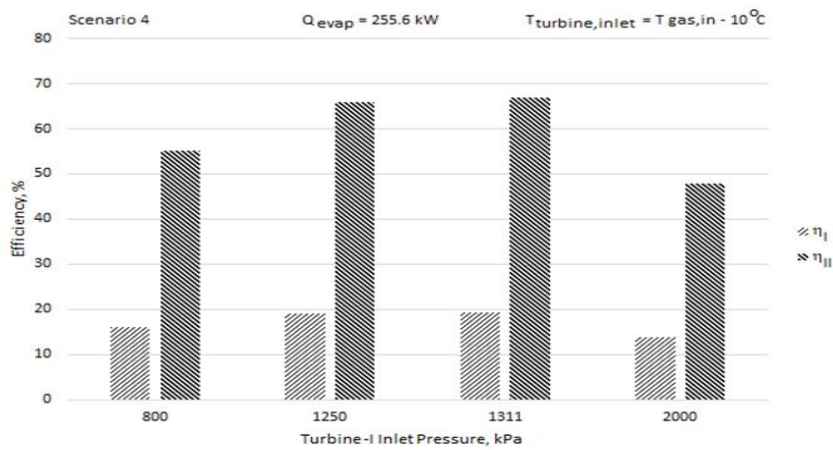


Figure 4. Efficiency values for different scenarios.



| | | | | |
|---------------------------|--------|--------|--------|-------|
| \dot{m}_{OF} , kg/s | 0,7736 | 0,7931 | 0,7975 | 1,523 |
| Profit _E , S/h | 2,711 | 3,24 | 3,289 | 2,355 |
| I-Evaporator, kW | 15,74 | 7,33 | 6,541 | 19,72 |
| I-Turbine I, kW | 4,571 | 6,574 | 6,787 | 4,895 |
| I-Condenser, kW | 8,406 | 6,37 | 6,126 | 3,691 |
| I-Turbine II, kW | 3,733 | 3,81 | 3,829 | 4,527 |
| PR-Evaporator, % | 24,74 | 10,85 | 9,531 | 6,913 |
| PR-Turbine I, % | 7,184 | 9,733 | 9,888 | 1,716 |
| PR-Condenser, % | 13,21 | 9,432 | 8,925 | 1,294 |
| PR-Turbine II, % | 5,868 | 5,642 | 5,578 | 1,587 |

Figure 5. Effect of turbine-I inlet pressure for Scenario-4.

about 23% and the evaporator exergy destruction rate decreases by about 58%. At above 1311 kPa, mass flow rate and total exergy destruction rate of FGA-ORC increase and, as expected, thermal and exergetic efficiencies significantly decrease.

Turbine-I outlet pressure (i.e. cycle mid-pressure)

Turbine-I outlet pressure, i.e. cycle mid-pressure, is a significant factor affecting the efficiency of FGA-ORC. In order to predict the effect of outlet pressure of turbine-I on the efficiency values of FGA-ORC, the cycle mid-pressure values were varied from 200 kPa to 400 kPa (see Figure 6). The highest thermal and exergetic efficiencies were obtained when the turbine-I inlet pressure was 1311

kPa and the turbine-I outlet pressure was 300 kPa. As can be seen from Figure 6, FGA-ORC is not operated due to the exergy destruction value of the heat exchanger at low mid-pressures of the cycle, and moreover the efficiency values are decreased when the turbine-I inlet pressure was 2000 kPa.

Percentage ratio (PC)

The thermodynamic simulation developed in this study was designed in order to maximize the performance indicators such as η_I , η_{II} and Profit_E. Dependence of the investigated performance indicators on mass flow rate was also incorporated in the simulation. The magnitude of the performance indicators and exergy destruction rates clearly depend on mass flow rate through the components of FGA-ORC and characteristics of working fluids as well. Therefore, percentage ratio, PC, was defined to calculate the mass flow rate of the next component of the cycle, i.e. $\dot{m}_4 = PC3 \times \dot{m}_x$ (see Figure 1-d).

In Figure 7, the comparison of the effect of the mass flow rate percentage of the organic fluid which sent to the heat exchanger was shown based on data obtained from the present thermodynamic analysis. Increasing of PC3 from 30% to 38%, within the practical limits, the total exergy destruction rate decreases about 5% and, as expected, efficiency and profit values increase about 6.4%. Moreover, at same PC3 value range, it was also calculated that the heat exchanger capacity was increased by 41%. So, optimised FGA-ORC processes mean not only higher profits but also more efficient process in terms of lower environmental impacts.

Temperature difference (ΔT)

ΔT is the difference between the flue-gas inlet temperature of the evaporator and the turbine-I inlet temperature of the organic fluid. Plots of the exergy destruction rate and efficiency values versus ΔT are shown in Figure 8. It can be seen from Figure 8 that the total exergy destruction rate is increased by increasing ΔT , and, the efficiency values are decreased as expected. Exergy is consumed during the process due to irreversibilities, so, the increased ΔT is proved to produce bigger exergy destruction. It was also concluded that, in general, the exergy destruction rate of the evaporator was higher than those of the exergy destruction rates of the other components of FGA-ORC due to thermodynamics conditions.

Dead-state temperature

The dead-state is a state in which the system is equilibrium with its surroundings. Maximum possible work of a system at a specified state depends on dead-state conditions as well as the thermo-physical properties of the system. In other words, exergy is a property of the combination of the system and its surroundings. So, the calculated performance indicators of FGA-ORC as the results of energy and exergy analyses are sensitive to variations above mentioned properties. With the increase of dead state temperature, results obtained from the analysis represent that the exergy destruction rate decreases and the exergetic efficiency increases (see Figure 9). But, thermodynamic limits should always be considered, because Scenario-4 cannot be operated over the dead-state temperature of 29°C due to $I_{\text{condenser}} < 0$.

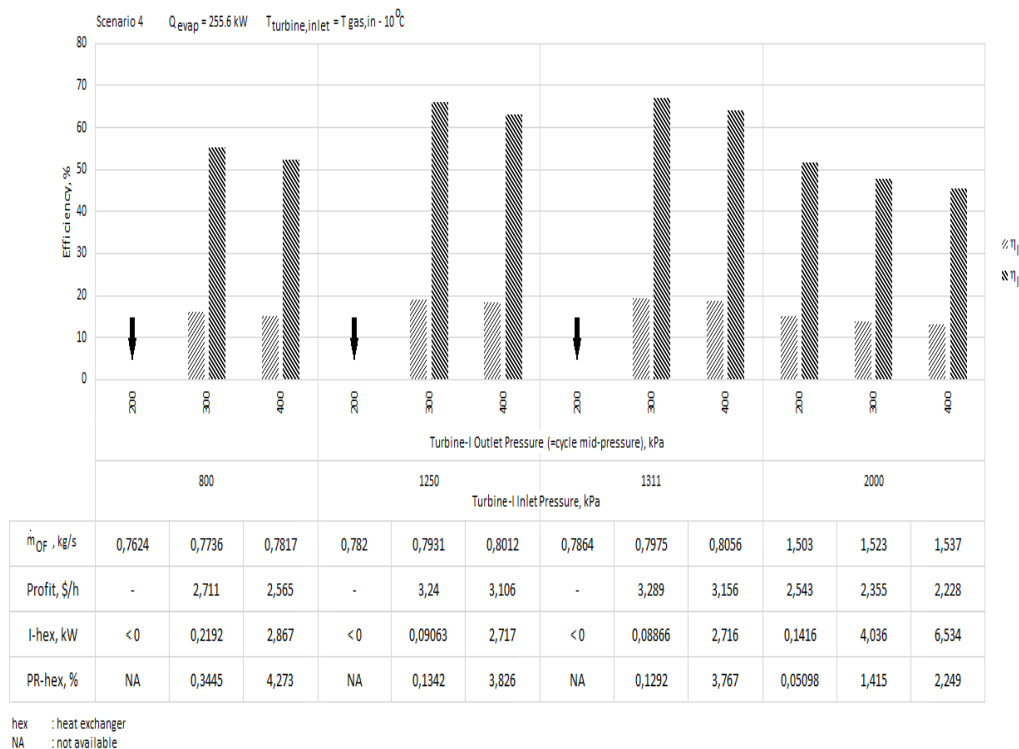
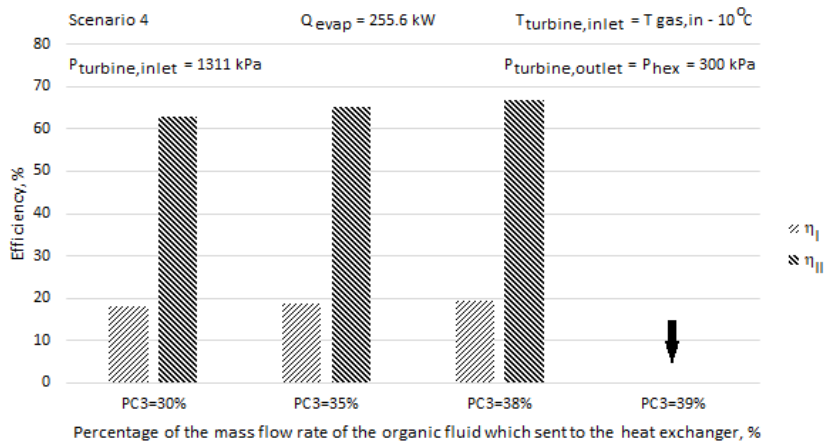


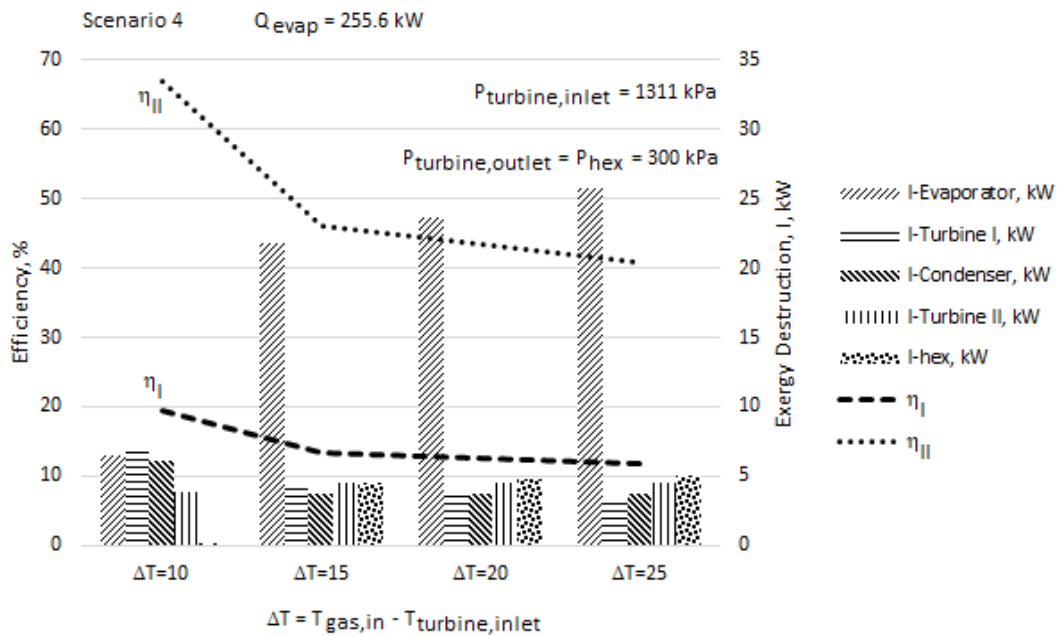
Figure 6. Effect of turbine-I outlet pressure for Scenario-4.



| | | | | |
|-----------------------|--------|--------|---------|--------|
| \dot{m}_{OF} , kg/s | 0,7165 | 0,7651 | 0,7975 | 0,8089 |
| Profit, \$/h | 3,092 | 3,211 | 3,289 | - |
| I-hex, kW | 1,87 | 0,9021 | 0,08866 | < 0 |
| PR-hex, % | 2,589 | 1,287 | 0,1292 | NA |

hex : heat exchanger
 NA : not available

Figure 7. Effect of PC3 on performance parameters for Scenario-4.



| | | | | |
|-----------------------|--------|-------|-------|-------|
| \dot{m}_{OF} , kg/s | 0,7975 | 1,605 | 1,708 | 1,823 |
| Profit, \$/h | 3,289 | 2,263 | 2,133 | 2,003 |
| I-TOTAL, kW | 68,64 | 310 | 341 | 375,6 |

Figure 8. Effect of ΔT on performance parameters for Scenario-4.

CONCLUSIONS

Due to the facts of high production costs of the primary energy production as well as more and more stringent environmental legislation, the waste-heat recovery is expected to gain increasing importance depending on the

global sustainable development goals. The design and optimization process for a generic ORC has three different stages: (1) analysis of the problem, (2) working fluid and cycle configuration selection, and (3) system optimization. In this study, a systematic roadmap with the

steps mentioned above was presented for academic and industrial users.

ORCs are promising technology that is feasible and economical while minimizing the risk to human health and the environment. Energy and exergy based thermodynamics analysis were carried out for FGA-ORCs to provide a better guidance for system improvement. And, in this study, to assure high flexibility and efficiency for waste-heat recovery from low to medium grade heat sources, five different thermal architectures were investigated using isopentane as organic fluid. Based on the present analysis, the following results are concluded:

1. Exergetic optimization is a useful method for determining the optimal design of different thermal architectures for given thermodynamic constraints. So, the results of the analysis show that optimum values of pressure, temperature and mass flow rate can be obtained for different FGA-ORCs.
2. The presented thermodynamic analysis is a powerful tool for the evaluation of thermal system performance. For analyzed cases in this study, Scenario-4 shows the best system performance by an exergy point of view. From the results of the analysis for Scenario-4, the maximum value of the exergetic efficiency is

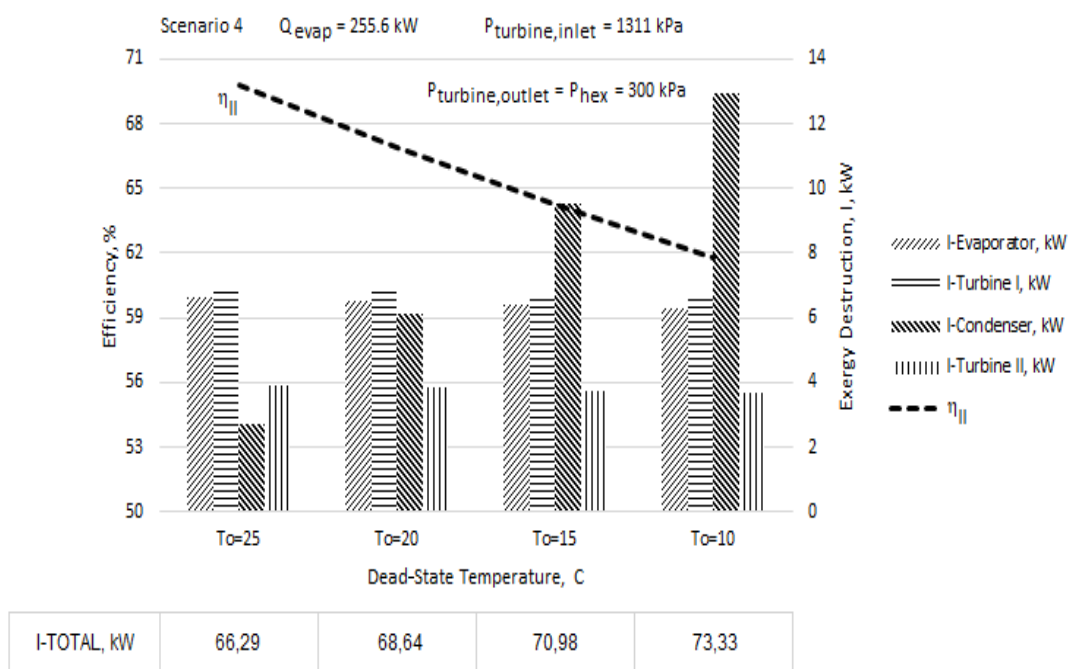


Figure 9. Evaluation of the effect of dead-state temperature for Scenario-4.

found to be 69% at $P_1=1311$ kPa, $P_4=300$ kPa, $\Delta T=10^\circ\text{C}$, $PC_3=38\%$, $T_0=25^\circ\text{C}$.

3. Organic fluid mass flow rate which sent to heat exchanger from turbine-I, and, the mid-pressure of the cycle should not be underestimated in the performance calculations of Scenario-4. As can be seen from the results of the analyses, depending on thermodynamic principles and the concept of exergy destruction, the maximum results for FGA-ORC efficiency could be provided by the optimum values of the mentioned parameters.
4. While the total exergy destruction decreases, the turbine work-output and economic profit increase, in general. Finally, obtained results represent that the decrease of the total exergy destruction rate with the increase of dead state temperature.

In order to avoid serious environmental and economic threats, the written reports of the Intergovernmental Panel on Climate Change (IPCC) have strongly recommended that the increase in global temperature should be limited. So, ORC systems will contribute to reducing the carbon footprint and waste energy in industrial facilities in accordance with the above recommendation. Thus, it is hoped that the results obtained in this study would be provided a better understanding of optimal control and operation strategy for FGA-ORCs with constant evaporator capacity.

ACKNOWLEDGEMENTS

The authors would like to express their gratitude to Mr. M.Gumus and Mr. B.Kula for the discussions about the textile sector processes.

REFERENCES

- Agromayor R. and Nord L.O., 2017, Fluid Selection and Thermodynamic Optimization of Organic Rankine Cycles for Waste Heat Recovery Applications, *Energy Procedia*, 129, 527-534.
- Al-Sulaiman F.A., Dincer I. and Hamdullahpur F., 2012, Energy and Exergy Analyses of a Biomass Trigeration System Using an Organic Rankine Cycle, *Energy*, 45, 975-985.
- Astolfi M., Martelli E., Pierobon L., 2017, Section 7. Thermodynamic and Technoeconomic Optimization of Organic Rankine Cycle Systems, *Organic Rankine Cycle (ORC) Power Systems Technologies and Applications*, edited by Macchi E and Astolfi M., Elsevier, United Kingdom.
- Bao J. and Zhao L., 2013, A Review of Working Fluid and Expander Selections for Organic Rankine Cycle, *Renewable and Sustainable Energy Reviews*, 24, 325-342.
- Bejan A., 2002, Fundamentals of Exergy Analysis, Entropy Generation Minimization, and the Generation of Flow Architecture, *International Journal of Energy Research*, 26, 545-565.
- Braimakis K. and Karellas S., 2018, Energetic Optimization of Regenerative Organic Rankine Cycle (ORC), *Energy Conversion and Management*, 159, 353-370.
- Cengel Y.A and Boles M.A., 1989, *Thermodynamics : An Engineering Approach*, McGraw Hill Book Co., Singapore.
- Cengel Y.A., Wood B. and Dincer I., 2002, Is Bigger Thermodynamically Better? *Exergy*, 2, 62-68.
- Cengel Y.A., 2007, Green Thermodynamics, *International Journal of Energy Research*, 31, 1088-1104.
- Chen H., Goswami D.Y. and Stefanakos, E.K., 2010, A Review of Thermodynamic Cycles and Working Fluids for the Conversion of Low-Grade Heat, *Renewable and Sustainable Energy Reviews*, 14, 3059-3067.
- Delgado-Torres A.M. and García-Rodríguez L., 2010, Analysis and Optimization of the Low-Temperature Solar Organic Rankine Cycle (ORC), *Energy Conversion and Management*, 51, 2846-2856.
- El-Emam R.S. and Dincer I., 2013, Exergy and Exergoeconomic Analyses and Optimization of Geothermal Organic Rankine Cycle, *Applied Thermal Engineering*, 59,435-444.
- Etemoglu A.B., 2013, Thermodynamic Investigation of Low-Temperature Industrial Waste-Heat Recovery in Combined Heat and Power Generation Systems, *International Communications in Heat and Mass Transfer*, 42, 82-88.
- Forman C., Muritala I.K., Pardemann R. and Meyer B., 2016, Estimating the Global Waste Heat Potential, *Renewable and Sustainable Energy Reviews*, 57, 1568-1579.
- Fu B.R., Hsu S.W. and Liu C.H., 2014, Trends in Patent Applications Relating to Organic Rankine Cycle, *Procedia Engineering*, 79, 249-257.
- Fu B.R., Lee Y.R. and Hsieh J.C., 2015, Design, Construction, and Preliminary Results of a 250-kW Organic Rankine Cycle System, *Applied Thermal Engineering*, 80, 339-346.
- Garcia S.I., Garcia R.F., Carril J.C. and Garcia D.I., 2018, A Review of Thermodynamic Cycles Used in Low Temperature Recovery Systems over the Last Two Years, *Renewable and Sustainable Energy Reviews*, 81, 760-767.
- Gyorke G., Deiters U.K., Groniewsky A., Lassu I. and Imre A.R., 2018, Novel Classification of Pure Working Fluids for Organic Rankine Cycle, *Energy*, 145, 288-300.
- Heberle F. and Brüggemann D., 2010, Exergy Based Fluid Selection for a Geothermal Organic Rankine Cycle for Combined Heat and Power Generation, *Applied Thermal Engineering*, 30, 1326-1332.
- Imran M., Haglind F., Asim M. and Alvi J.Z., 2018, Recent Research Trends in Organic Rankine Cycle Technology - A Bibliometric Approach, *Renewable and Sustainable Energy Reviews*, 81, 552-562.
- Jang Y., and Lee J.. 2018. Influence of Superheat and Expansion Ratio on Performance of Organic Rankine Cycle-Based Combined Heat and Power (CHP) System. *Energy Conversion and Management* 171:82-97.
- Kermani M., Wallerand A.S., Kantor I.D. and Maréchal F., 2018, Generic Superstructure Synthesis of Organic Rankine Cycles for Waste Heat Recovery in Industrial Processes, *Applied Energy*, 212, 1203-1225.
- Mago P.J., Srinivasan K.K., Chamra L.M. and Somayaji C., 2008, An Examination of Exergy Destruction in Organic Rankine Cycles, *International Journal of Energy Research*, 32, 926-938.
- Panesar A., Morgan R. and Kennaird D., 2017, Organic Rankine Cycle Thermal Architecture - From Concept to Demonstration, *Applied Thermal Engineering*, 126, 419-428.
- Quoilin S., Broek M.V.D., Declaye S., Dewallef P. and Lemort, V., 2013, Techno-Economic Survey of Organic Rankine Cycle (ORC) Systems, *Renewable and Sustainable Energy Reviews*, 22, 168-186.

Safarian S. and Aramoun F., 2015, Energy and Exergy Assessments of Modified Organic Rankine Cycles (ORCs), *Energy Reports*, 1, 1–7.

Stoecker W.F., 1989, *Design of Thermal Systems*, McGraw Hill Book Co., Singapore.

Sun W., Yue X. and Wang Y., 2017, Exergy Efficiency Analysis of ORC (Organic Rankine Cycle) and ORC-Based Combined Cycles Driven by Low-Temperature Waste Heat, *Energy Conversion and Management*, 135, 63–73.

Tchanche B.F., Lambrinos G., Frangoudakis A. and Papadakis G., 2011, Low-Grade Heat Conversion into Power Using Organic Rankine Cycles – A Review of Various Applications, *Renewable and Sustainable Energy Reviews*, 15, 3963–3979.

Tchanche B.F., Pétrissans M. and Papadakis G., 2014, Heat Resources and Organic Rankine Cycle Machines, *Renewable and Sustainable Energy Reviews*, 39, 1185–1199.

Vélez F., Segovia J.J., Martín M.C., Antolín G., Chejne F. and Quijano A., 2012, A Technical, Economical and Market Review of Organic Rankine Cycles for the Conversion of Low-Grade Heat for Power Generation, *Renewable and Sustainable Energy Reviews*, 16, 4175–4189.

Zhai H., An Q., Shi L., Lemort V. and Quoilin S., 2016, Categorization and Analysis of Heat Sources for Organic Rankine Cycle Systems, *Renewable and Sustainable Energy Reviews*, 64, 790–805.



Burak TURKAN graduated from the Mechanical Engineering Department of Bursa Uludag University in 2009. In 2010, he was appointed as the OYP to Mechanical Engineering Department of Bayburt University. Then, in 2011, he was appointed to the Mechanical Engineering Department of Bursa Uludag University to do MSc and Ph.D. He received his MSc degree from the same university in 2014. He is currently a Ph.D student and research assistant at Bursa Uludag University. His main research interests are drying, heat and mass transfer, thermal insulation, energy and exergy analysis.



Akin Burak ETEMOGLU graduated from Mechanical Engineering Department at Uludag University in 1994. He received MSc and Ph.D. degrees in energy area at the same department in 1996 and 2003 respectively. He is currently a professor in the Mechanical Engineering Department at Bursa Uludag University. His research interests are simultaneous heat and mass transfer operations, waste-heat recovery, ORC systems, geothermal energy, and exergy.



CFD INVESTIGATION OF THE NEAR-SURFACE STREAMLINE TOPOLOGY ON A SIMPLE NONSLENDER DELTA WING

Haci SOĞUKPINAR*, Serkan ÇAĞ** and Bülent YANIKTEPE***

* University of Adıyaman, Department of Electric and Energy, Vocational School, Adıyaman 02040, Turkey hsogukpinar@adiyaman.edu.tr

** University of Adıyaman, Department of Machinery and Metal Technology Vocational School,02040, Turkey, scag@adiyaman.edu.tr

*** Korkut Ata University, Department of Energy Systems Engineering, Faculty of Engineering, Osmaniye, 80000, Turkey, byaniktepe@osmaniye.edu.tr

(Geliş Tarihi: 27.02.2019, Kabul Tarihi: 18.02.2020)

Abstract: In this study, a non-slender simple delta wing was investigated numerically by using RANS with SST $k - \omega$ turbulence model and the results were compared with experimental data to validate the simulation accuracy of the Computational Fluid Dynamics (CFD) approach. The delta wing configuration has a straight wing, with thickness 3 mm, chord length 101.6 mm, wingspan 254 mm, 30° beveled angle, and 40° sweep leading edge. Effect of angle of attack on the near-surface patterns of the delta wing was interpreted in terms of streamline topology, particularly bifurcation lines, as well as contours of streamwise and transverse velocity components, and also vorticity contours on the surface at the angle of attack starting from 5° to 17° with Reynolds number of 1×10^4 . The leading-edge vortices (LEV) developed at the angle of 5°, the vortex breakdown happened first time at the angle of 7° and moved upstream direction and reached around $x=0.5c$ at 10°. With the increasing angle of attack further, vortex breakdown moved to upstream a substantial distance and finally, the stall occurred at an angle of attack at 17°.

Keywords: LEV, CFD, SST, delta wing, vorticity, leading-edge vortices.

HESAPLAMALI AKIŞKANLAR DİNAMİĞİ KULLANILARAK BASİT ÜÇGEN KANAT MODELİNDE YAKIN YÜZEY AKIŞ YAPISININ İNCELENMESİ

Özet: Bu çalışmada, düşük süpürme açısına sahip basit üçgen kanat modeli RANS denklemleri kullanılarak SST $k-\omega$ türbülans modeli ile incelenmiş, elde edilen bulgular daha önceden yapılmış deneysel verilerle kıyaslanarak Hesaplamalı Akışkanlar Dinamiğinin (HAD) tutarlılığı doğrulanmaya çalışılmıştır. Bu çalışma için, giriş uzunluğu 101,6 mm, kanat genişliği 254 mm, et kalınlığı 3 mm, pah açısı 30°, ve süpürme açısı 40° olan üçgen kanat modellenmiştir. Hücum açısının (5 dereceden 17 dereceye kadar) kanat yüzeyi üzerindeki akış yapısına etkisi ve girdap çökmesi, hem üst plan hem de arka plan görüntüsü açısından Reynolds sayısı 10.000’de sabit tutularak incelenmiştir. Kıvrımlı, hücum kenar yanal girdap oluşumu 5 derecede başlamış, girdap çökmesi ilk defa 7 derecelik hücum açısında kanadın arka kısmında oluşmuş ve 10 derecede kanadın ön tarafına ($x/c=0.5$) doğru ilerlemiştir. Hücum açısı arttıkça girdap çökmesi kanadın ön uç kısmına ilerlemiş, yaklaşık 17 derecede akış stol olmuştur.

Anahtar kelimeler: LEV, CFD, SST, üçgen kanat, girdap, hücum kenar yanal girdap.

INTRODUCTION

Unmanned aerial vehicles (UCAV) were developed as reconnaissance vehicles, and even as tactical weapons mostly in military applications but nowadays, commercial usage has been expanding to scientific, agricultural, and other applications such as policing, peacekeeping, agriculture, and smuggling. Therefore a non-slender or

‘low sweep’ ($\Lambda < 60$) delta wings has become a very important topic to investigate in the last 3 decades. The typical and well-known delta wing flow is the formation of Leading-Edge Vortices (LEV) which has determined across a wide range of Reynolds numbers and varying angle of attacks. This flow separates at a low angle of attack and the separated layer rolls up to form a large-scale

vortex on each half of the wing. Flow regime on a non-slender delta wing was investigated experimentally and numerically then primary characteristics of the flow structure and the potential for their control were summarized. It is difficult to observe vortex breakdown at high Reynolds numbers (10^6) (Wentz and Kohlman, 1971) but the well defined vortical flow was clearly visible at low Reynolds numbers of 7000 (Ol and Gharib, 2003). Experimental evidence suggests that as the increasing Reynolds number, vortex breakdown moves apex (Elkhoury *et al.*, 2005) even at a small angle of incidence. The location of vortex breakdown also depends on the angle of incidence therefore with the increasing angle of attack, the onset of vortex breakdown moves up the apex and separated shear layers become the dominant feature of the flow (Gursul *et al.*, 2005). As the increasing angle of attack further, primary attachment occurs outboard of the symmetry plane and this attachment line moves in-board towards the wing centerline where vortex breakdown and stall occur and the identification of buffeting mechanisms in these regions (Yaniktepe and Rockwell, 2004). An experimental study showed that at low Reynolds number or at low angle of attack, there is an elongated separated flow region exists which lies very close to the upper surface of the wing (Taylor *et al.*, 2003) and velocity profile in numerical studies showed similar property with those experiments (Gordnier and Visbal, 2003). Numerical results indicate a broad wake-like flow that is coherent with the experiment. Flow field over a yawed simple delta wing was investigated experimentally and study indicated that there was a symmetrical flow on the delta wing in the case of zero yaw angle but with changing the angle, vortex breakdown occurs earlier on the windward side of the delta wing and vortex breakdown location moves further downstream on the leeward side of the delta wing (Canpolat *et al.*, 2009; Yayla *et al.*, 2010). They observed high-scale Kelvin-Helmholtz vortex structure at side view which was emanating from the leading edge to rolls up periodically into discrete sub-structures especially at the angle of 13° and 17° . Another experiment shows the presence of a co-rotating form of small scale vorticity and this was noticeable in sudden images of the flow (Yavuz *et al.*, 2004). Numerical prediction and wind tunnel experiment for a pitching unmanned combat air vehicle were conducted for a modified delta wing up to the angle of attack 25° (Cummings *et al.*, 2008) with various frequencies of pitch oscillation. For the numerical part Reynolds Average Navier-Stokes equations (RANS) were implemented for compressible flow and vorticity patterns were figured out. Vortex breakdown was calculated in the middle of the wing surface at the angle of 15° . Vortex breakdown was

simulated like streamline rotating and enlarging by spiral motion. Another numerical study investigated the flow field structure by using Computational Fluid Dynamic approaches (CFD) with the Shear Stress Transport (SST) model (Saha and Majumdar, 2012). Vortex breakdown phenomenon above a delta wing at high angles of attack for the cases with and without a symmetric trailing-edge jet flap was investigated by using RANS Low Reynolds Launder-Sharma $k-\epsilon$ turbulence model (Kyriakou *et al.*, 2010) but in the figures, the onset of vortex breakdown was not clearly presented. Detached-Eddy Simulation of the vortical flow field about the VFE-2 delta wing was investigated (Cummings and Schütte, 2013) and compared with available experimental data. CFD calculation was conducted with unstructured Cobalt code by using RANS, DES (Detached-Eddy Simulation), and DDES (Delayed Detached-Eddy Simulation) turbulence models. Mostly Lift, drag and pressure coefficients were calculated and compared with available experiment but the figures show only LEV structure. Vortex breakdown behind a delta wing was investigated by using a Large Eddy Simulation (LES) method and compared with wind tunnel experiments (Mary, 2003). In the paper, only numerical data were presented but plan and end view visual presentations were rarely considered. Effect of thickness-to-chord ratio on flow structure of a low swept delta wing was investigated in a low-speed wind tunnel using laser-illuminated smoke visualization, particle image velocimetry, and surface pressure measurements (Gülsaçan *et al.*, 2018). The thickness of the wing was changed and its effect on the flow structure was investigated then plan and end view smoke visualization and pressure coefficient on the surface were presented and discussed. Several other experimental (Canpolat *et al.*, 2011) studies were conducted to investigate the flow field regime of delta wing but the tremendous cost involved in building up of the experimental system like a wind tunnel, PIV, etc. For instance, the wind tunnel has the advantage of dealing with a “real” fluid and can produce global data over a far greater range of the flight envelope than CFD can (Johnson *et al.*, 2005). However, CFD accelerates the design process and saves time and millions of money. Today CFD has joined the experimental process to provide significant value in vehicle design. Therefore in this study flow field characteristics of simple delta wing were investigated by using RANS with SST $k-\omega$ turbulence model and plan and end view streamline and streamwise velocity and vorticity field were investigated and location and shape of LEV and vortex breakdown were clearly presented and obtained data were compared with available experiments.

NUMERICAL APPROACH

The flow solver PARDISO (a commercial version built-in COMSOL) was chosen because of its performance, robust, memory efficient and easy to use software for solving large sparse symmetric and unsymmetrical linear systems of equations on shared-memory and distributed-memory multiprocessors (Internet, 2019). For the current study direct solver, PARDISO with nested dissection multithreaded preordering algorithm was set. Constant (Newton) nonlinear method was used for the method then iterations options were specified for termination technics. PARDISO solves the RANS equation for the SST $k-\omega$ turbulence model. This model combines the superior behavior of the $k-\omega$ model in the near-wall region with the robustness of the $k-\epsilon$ model (Menter, 1994). Detailed information about numerical calculation and modeling is available at (Sogukpinar, 2019, 2018, Internet, 2019). The PARDISO solved RANS equations with two turbulence equations for the incompressible flow along the simple delta wing. For the equations, gravity was included and no-slip condition was applied on the wing surface. The upstream, top and bottom border of computational domains are situated at least 10 mean aerodynamic chords away to minimize the effect of the applied boundary circumstances. The boundary conditions were set to velocity inlet and open boundary and other parts stay as a wall. Not half but the full model was simulated under wind speed of 5.6 cm/s. For the delta wing surface, the triangular mesh type was applied and the minimum mesh size was set to 0.0001 m, and 0.0005 m for the maximum. Then the model was fully enclosed in a thin ellipsoid and tetrahedral mesh type was preferred with a maximum growth rate of 1.2 and 5 million mesh elements were created in the ellipsoid. For the outer part of the domain, the minimum element size was set 0.001 and 0.05 for

maximum and 1 million extra mesh elements were created. Mesh distribution is given in Fig. 1.

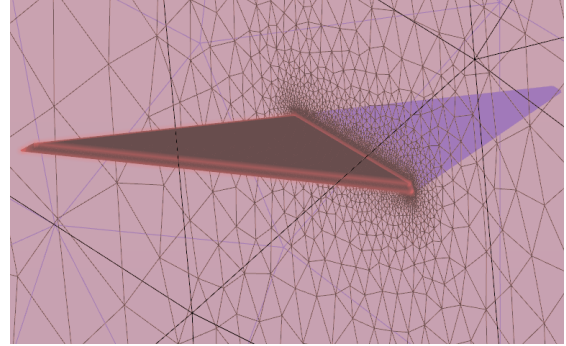


Figure 1. Delta wing for 6 million mesh.

RESULTS AND DISCUSSION

Simple delta wing with thickness 3 mm, chord length 101.6 mm, wingspan 254 mm, 30° beveled angle, and 40° sweep leading edge was numerically investigated by using SST $k-\omega$ turbulence model. The numerical calculation was performed with a server with 64 GB RAM and 32 processors. Fig.2 shows dye visualization experiment (Canpolat *et al.*, 2009) the same configuration with the current study, which was conducted before at the angle of attack $\alpha=7^\circ, 10^\circ, 13^\circ, 17^\circ$. LEV and vortex breakdown are clearly visible at the angle of attack at 7° . When the angle of attack is increased to $\alpha = 10^\circ$, the location of the vortex breakdown moves upstream direction and reaches around $x=0.5c$. By the time $\alpha = 13^\circ$, the location of vortex breakdown moves toward the apex of the delta wing rapidly and flow shows significant fluctuations in the streamwise direction. At $\alpha = 17^\circ$, a large scale flow separation develops over the entire surface and flow passes to the stall stage completely (Canpolat *et al.*, 2009).

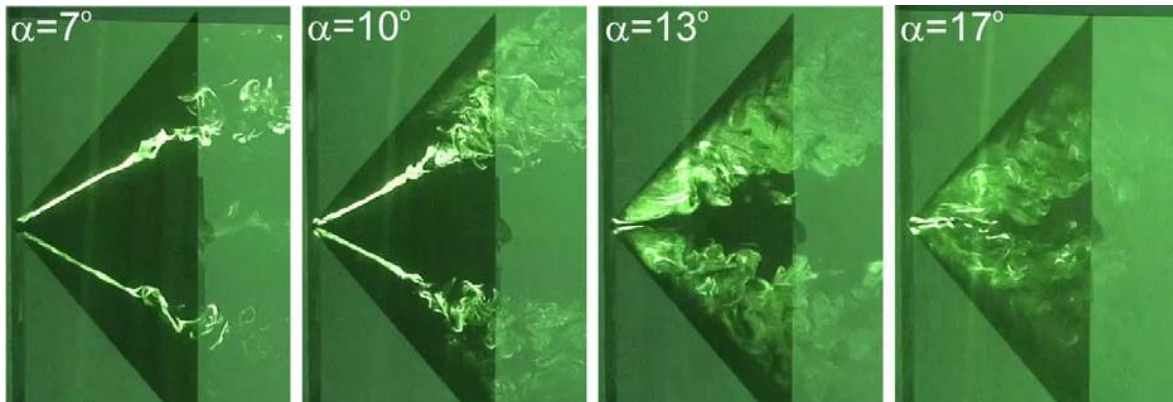


Figure 2. Dye visualization, development and formation of LEV, vortex breakdown (Canpolat *et al.*, 2009)

Fig. 3 shows the streamline velocity field for the formation and development of LEV, the vortex breakdown, and the separated flow as a function of angle of attack angle from 5° to 17° . The LEV is clearly visible at the angle of 5° which is small in size and circulates along the downstream trajectory. When the angle of attack is increased to $\alpha = 7^\circ$, streamlines began to move away from each other and enlarge the rotating flow at the trailing edge side, indicating the onset of vortex breakdown. By the time $\alpha = 10^\circ$ is reached (Fig. 3c), the flow continues to expand and rotate in the downstream trajectory and the location of the vortex breakdown moves to around $x=0.5c$. The dye visualization experiment in Fig.2 and Ref. (Yaniktepe and Rockwell, 2004) also confirm this numerical part (Fig. 3c) because, in the experiment, vortex breakdown starts at $\alpha=7^\circ$ and moves to around $x=0.5c$ at the angle 10° and other numerical studies (Cummings *et al.*, 2008; Saha and Majumdar, 2012) confirm the streamline shape of the

vortex breakdown. In the reported paper (Cummings *et al.*, 2008) vortex breakdown happens like streamlines are enlarging like a rotating cone. At $\alpha = 13^\circ$, the LEV system increases in size and strength with increased α and location of vortex breakdown moved to around apex, flow shows significant fluctuations in the streamwise direction, radius of rotation increased considerably but even if the flow structure is fluctuating, there is still continuing flow in the downstream and this implies that leading-edge vortex provides additional lift. The reported experiment in Fig. 3 (Canpolat *et al.*, 2009 ; Yaniktepe and Rockwell, 2004) show that flow is not completely stalled at the angle of 13° and they correlate numerical results in Fig. 3(d). By the time the angle of attack reaches from $\alpha = 15^\circ$ to 17° , downstream streamline structure deteriorates completely, location of vortex breakdown reaches to the apex and the flow passes to the stall phase as indicated in Fig. 2 (Canpolat *et al.*, 2009).

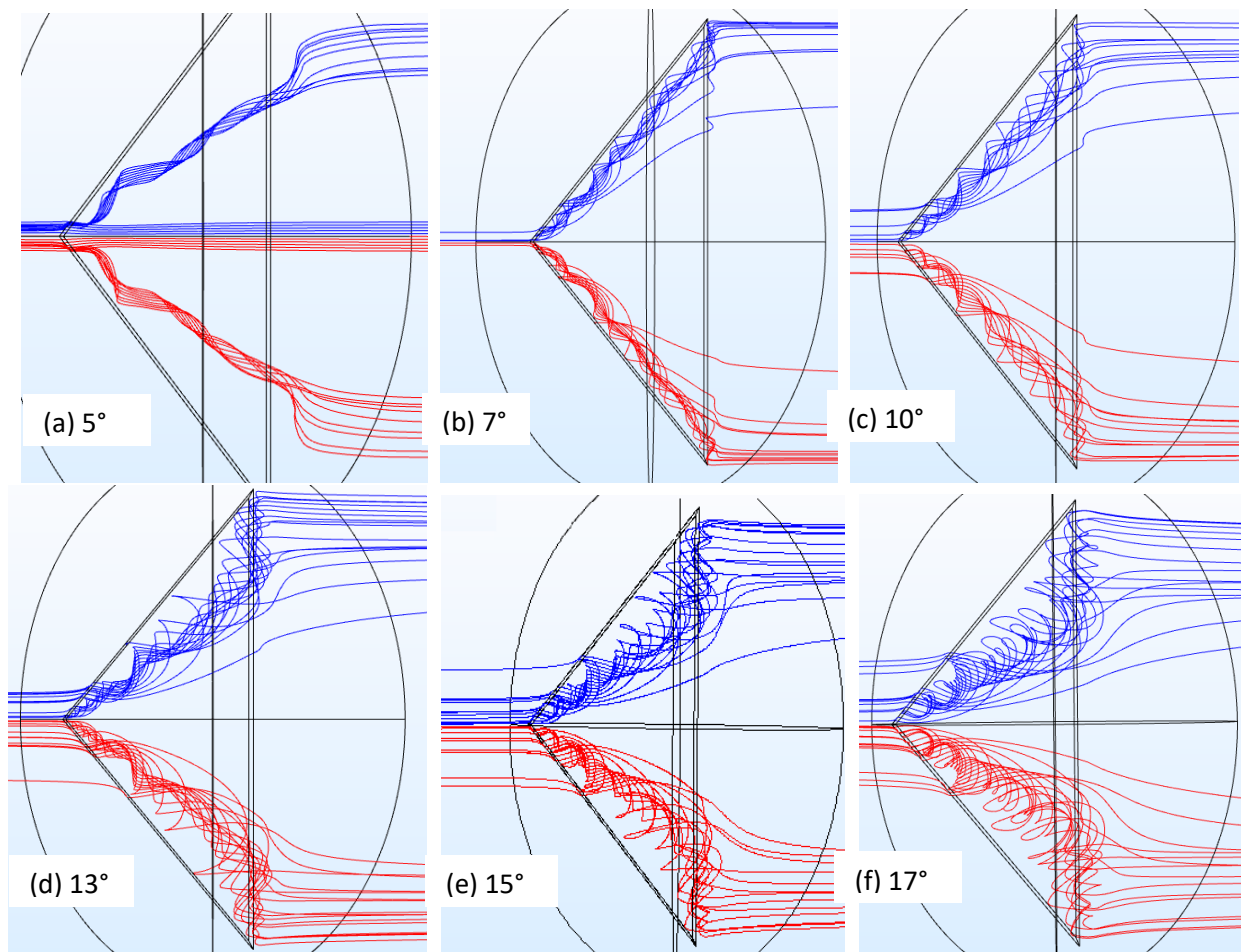


Figure 3. Lower surface plan view streamline velocity field (m/s)

Fig. 4 shows the vorticity magnitude contours of a delta wing at the angle of attack from 5° to 17° . Fig. 4a shows the development of small scale vorticity patterns. When the angle of attack is increased to 7° , there are three separate vorticity patterns as primary (PV), secondary (SV), and the third (VB). The primary rotating vortices occur in the inner side of the leading edge vortices which is close to the central axis of the delta wing and the secondary vortices develop between main vortex and side edges of the delta wing. It was reported in the previous experiment (Muir *et al.*, 2017), if the secondary vortex is significantly weaker, which suggests breakdown. The development of a third stronger vortex indicates the onset of vortex breakdown (VB) at the middle backside of the

wing. At $\alpha = 10^\circ$, the secondary vortex significantly disappears and the primary vortex increases in size and prolongs to the upstream direction. The area of vortex breakdown expands in all directions and flow shows significant fluctuations. At the angle of 13° , the vortex breakdown area increases and moves further upstream direction. Circulation of LEV is visible close to the apex but in other parts, the vortex breakdown prevails. By the time $\alpha = 15^\circ$ is reached, the location of vortex breakdown moves further upstream but the flow hasn't completely stalled yet because there is circulation flow at the apex. Finally, by the time the angle of attack reaches $\alpha = 17^\circ$, the location of the vortex breakdown reaches the apex and the burst vortex slowly gives away to a largely stalled lower surface.

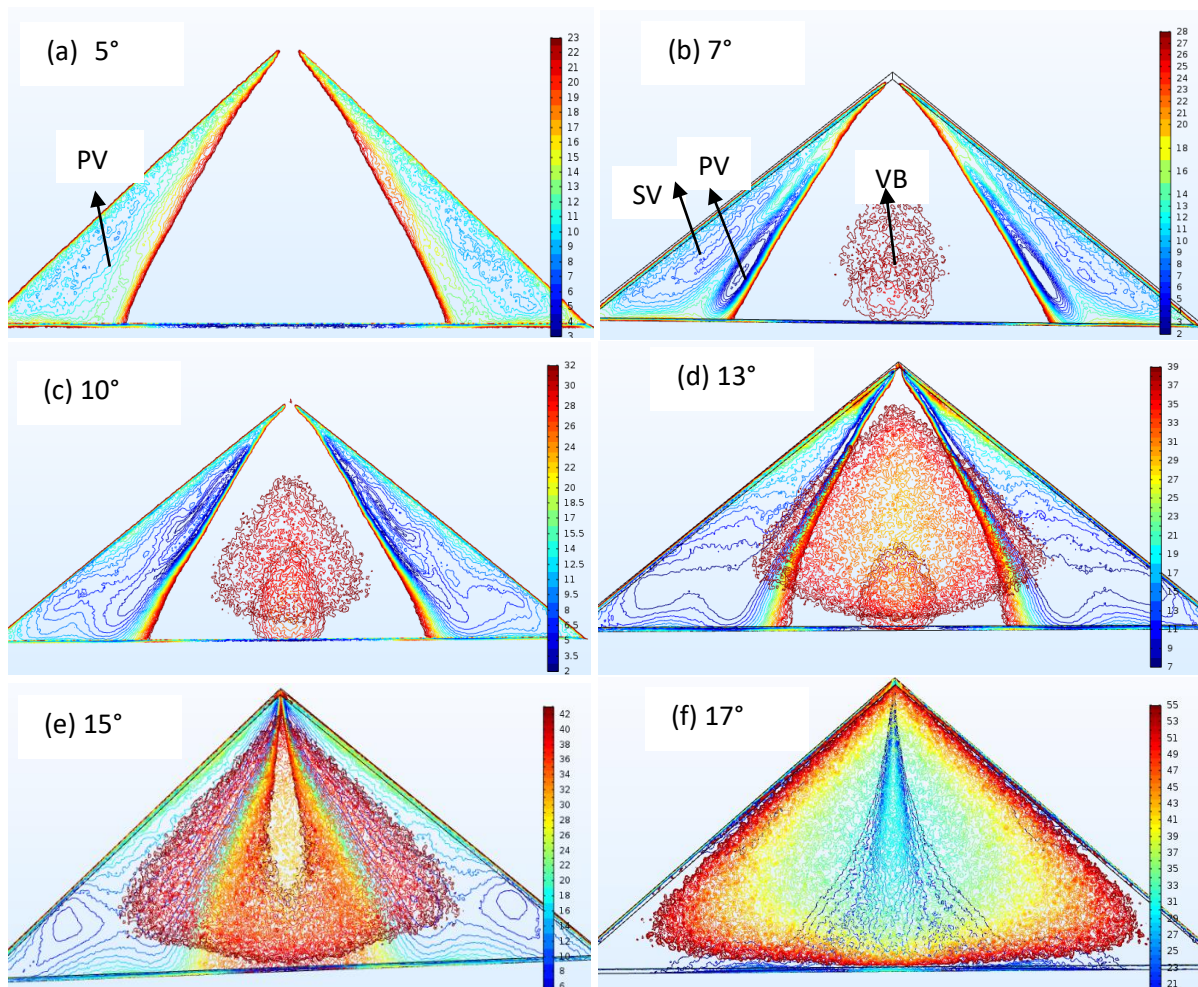


Figure 4. Plan view vorticity magnitude contour on the delta wing surface (1/s)

Fig. 5 shows PIV data (Yaniktepe and Rockwell, 2004) of the delta wing the same configuration with the current study. LEV starts to form very close to the lower surface by covering a larger area near the side edge at the angle of

7° . When the angle of attack increased to 13° , LEV becomes more pronounced, moves further down from the surface and approaches the centerline of the wing in the lateral direction. Finally, by the time angle of attack.

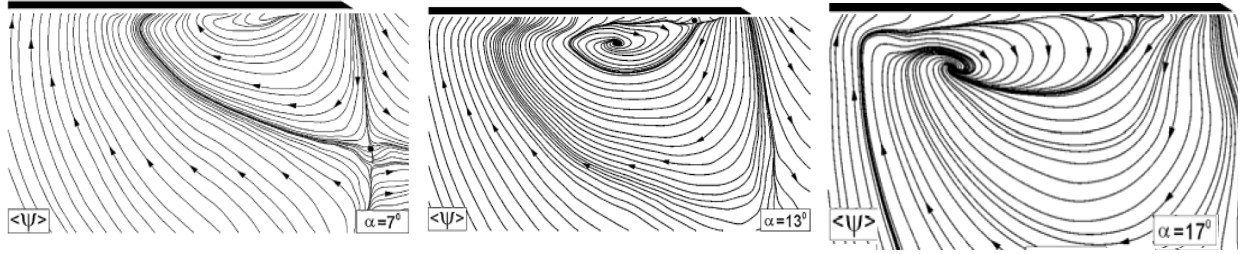


Figure 5. End view streamline velocity pattern ($x/c=0.8$) at the angle of attack at $\alpha=7^\circ$, 13° , 17° (Yaniktepe and Rockwell, 2004)

reaches $\alpha = 17^\circ$, LEV increases its intensity and continues its lateral and downward movement Fig. 6 shows the end view streamline topology at $x=0.8C$ at the angle of attack from 5° to 17° . LEV formation starts very close to the lower surface at the angle of 5° . When the angle of attack increased, LEV becomes more pronounced, moves further down from the lower surface and also approaches the centerline of the wing in the lateral direction as indicated in the experiment (Fig. 5) (Yaniktepe and Rockwell, 2004). In contrast to the experimental measurements, the secondary vortex (SV) area was calculated. Secondary

LEV is clearly visible at the angle of 7° and their size seems to become equal and tends to fade away at the angle of 10° . In line with the experiment (Muir *et al.*, 2017) the secondary LEV shows the greatest reduction incoherence and this is an early indication of vortex breakdown. The presence of the secondary vortex was also confirmed for these two-angle cases (7° and 10°) in Fig. 4(b) and vortex core shifted down from the surface and also gets close to the centerline as the increasing angle of incidence.

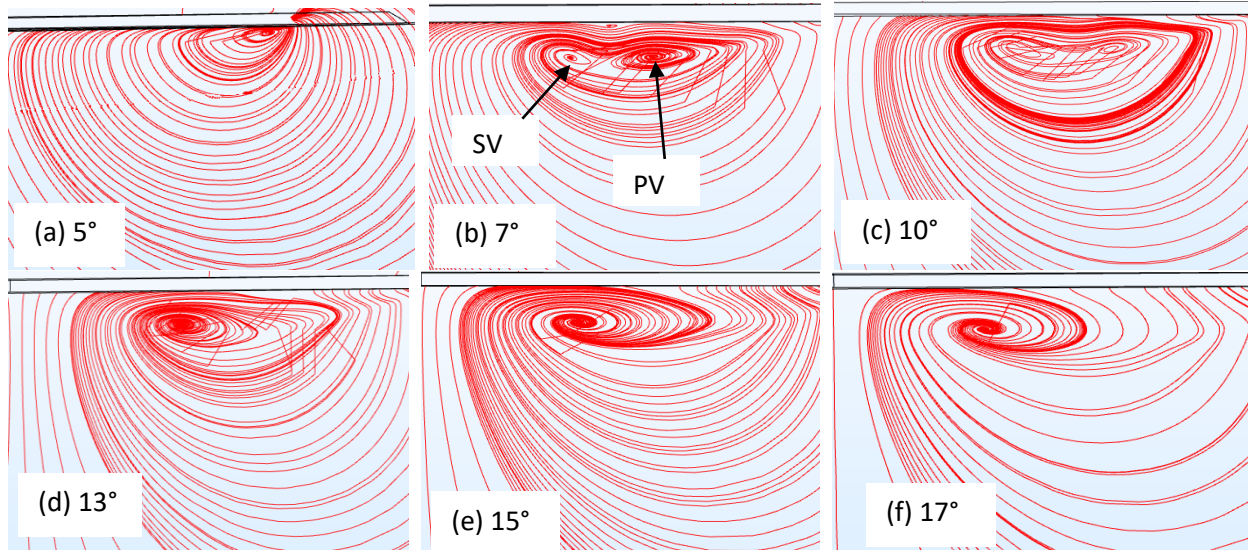


Figure 6. End view streamlines velocity field (m/s) at $x/C=0.8$ when the angle of attack changes from 5° to 17° .

Fig.7 shows the end view velocity field magnitude with arrow and color range representation of the delta wing at the angle of attack from 5° to 17° . At the angle of 5° , a small size leading-edge vortex formation starts very close to the lower surface and lateral edge. As the increasing angle of attack, the size of LEV increases and moves close to the centerline. Secondary vortex is visible at the angle

of 7° and 10° . By the time angle of attack reaches 13° , the severity of LEV increases and the core of cyclic vortex became more pronounced. When the angle of attack increased further up to 15° , vortex becomes more violent and vortices on both sides merged into a single vortex at the angle starting from 17° .

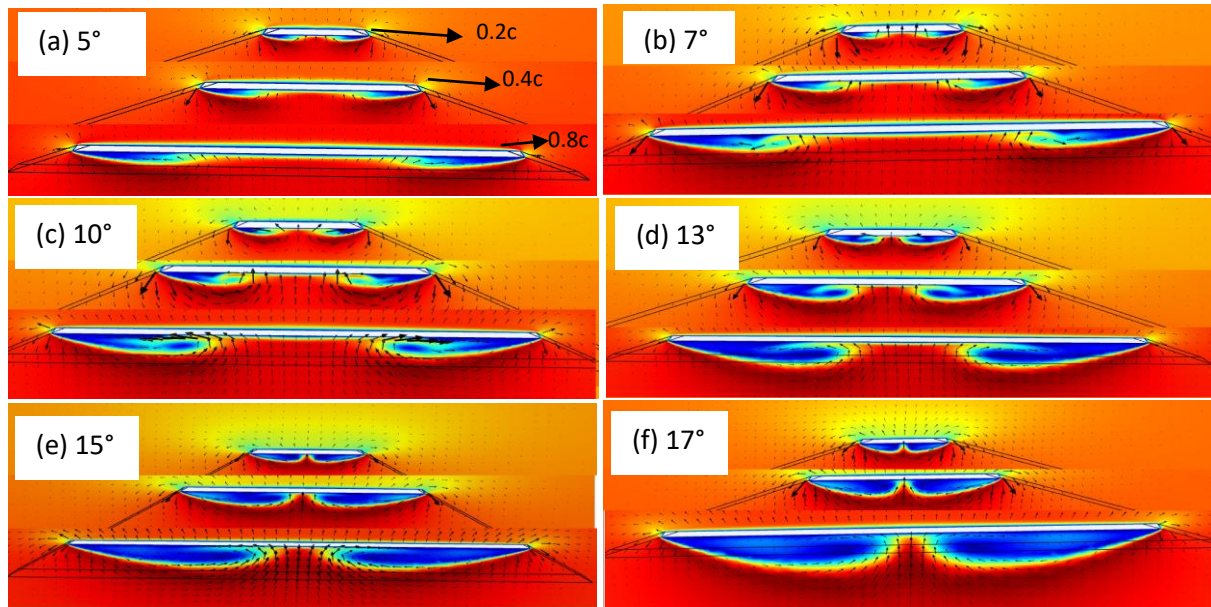


Figure 7. End view velocity field magnitude (m/s) with arrow and color representation; In the figure upper to lower $x/C=0.2$, $x/C=0.4$, $x/C=0.8$, when the angle of attack changes from 5° to 17° .

Fig. 8 shows the end view vorticity contour magnitude at $x/C=0.8$, where there are two vorticity patterns at $\alpha=5^\circ$. The smaller vortex is secondary LEV (SV) and it is very close to the bottom surface and the larger one is primary LEV (PV), located just below the small one, which spreads over the half surface of the wing. As the increasing angle of attack to 7° and 10° , secondary LEV lost its prominence and merged with the primary vortex and disappeared completely at 13° . Several small-scale vortex areas start to form within the primary vortex starting at the angle of 7° and numbers of them increase with the increasing angle.

This was also reported in a previous experimental study (Muir *et al.*, 2017). An increasing number of small scale vorticity regions (SSVR) indicates the onset of vortex breakdown, because after breakdown numbers of small scale vorticity regions increases (Muir *et al.*, 2017). Vortex breakdown location moves to upstream direction as the increasing angle of incidence and this increases turbulence at the backside of the wing. The numbers of small vortex regions increase up to the angle of 13° then start to decrease and finally they merge to become a single huge rotation core at $\alpha=17^\circ$.

CONCLUSION

This paper numerically investigates the effect of angle of attack on the aerodynamic performance of a simple delta wing by using CFD with the SST $k-\omega$ turbulence model and findings were compared with experimental observation to assess simulation accuracy of the

Computational Fluid Dynamics (CFD) approach. Streamline velocity field and vorticity magnitude contour for plan and end view cases were investigated at the angle of attack from 5° to 17° , and the simulation results were compared with those obtained water channel experiment and comparison showed good agreement. First, the streamline velocity field was simulated for the plan view case. Leading-edge vortex developed at the angle of 5° , vortex breakdown started in the back lower side of the wing at $\alpha=7^\circ$. As the increasing angle of attack from 7° to 10° , the location of the vortex breakdown moved toward $x=0.5c$. The location of the vortex breakdown reached closed to the apex of the delta wing rapidly when the angle of attack increased to 13° and this was confirmed by reported experiment. There is no complete vortex breakdown at 13° because LEV is visible at very close to the apex but after 15° , the flow regime shows a complete deterioration and passed to the stall stage at the angle of 17° . Next, plan view vorticity magnitude contour on the delta wing was investigated and location and evolution of primary and secondary LEV and also vortex breakdown were analyzed for the angle of attack from 5° to 17° and compared with experimental observations. The secondary vortex system was identified at the angle of 7° and disappeared after 10° . Finally, end view streamlines velocity and vorticity field were investigated and discussed.

The application of CFD has accelerated the design process of the aerodynamic vehicle. Aerodynamicists could predict the flow properties of aircraft only by doing an experiment

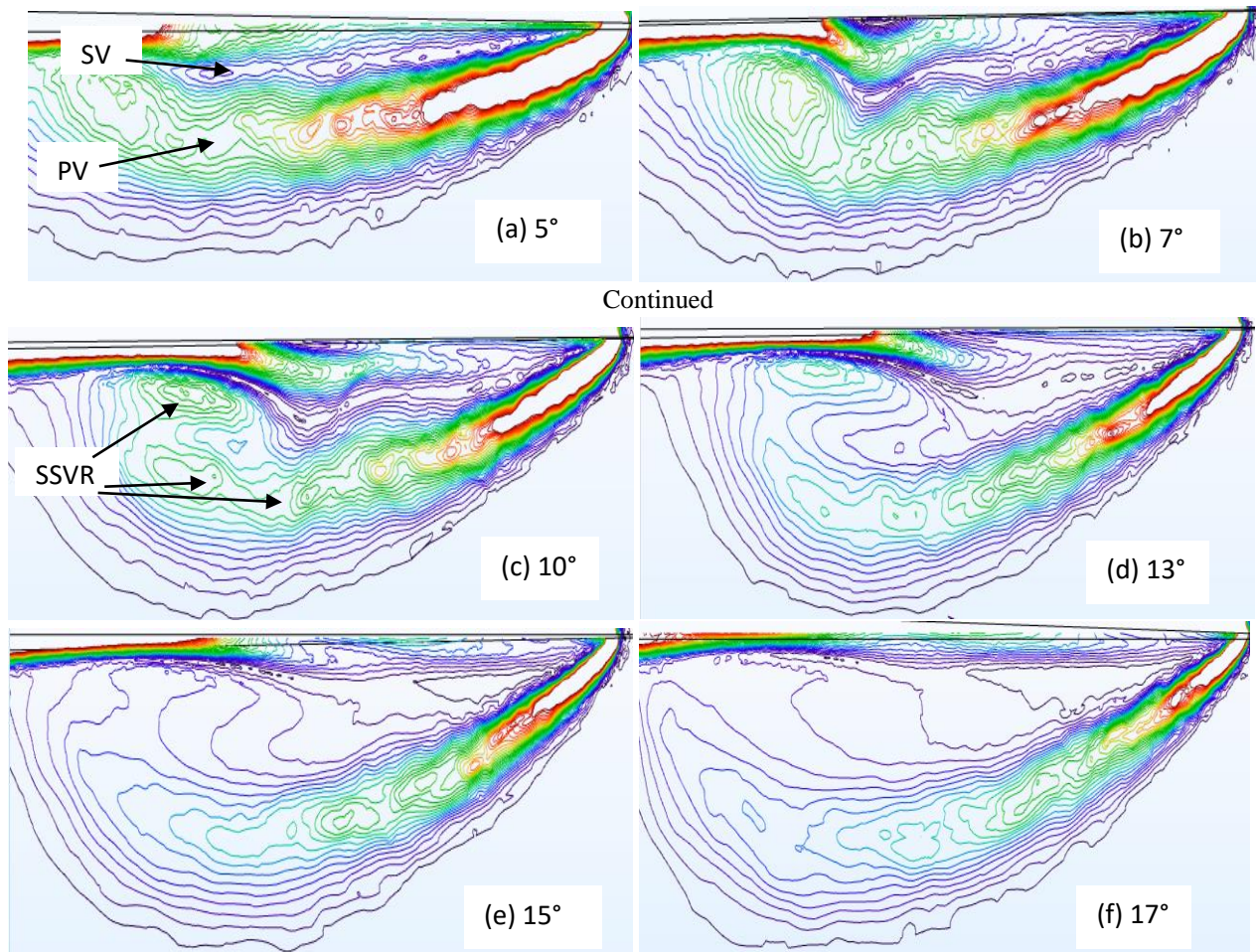


Figure 8. End view vorticity magnitude (1/s) contour lines at $x/C=0.8$ when the angle of attack changes from 5° to 17° .

or by using an analytic method in a long time ago. However in the last 40 years, with the development of sophisticated computers, CFD has become a main supplementing tool to experiment. Because CFD is a cost-effective and critical tool to predict accurately and confirm flight characteristics of an object in any flow condition.

ACKNOWLEDGMENT

Many thanks to Middle East Technical University and Adiyaman University for technical support. This work was supported by Adiyaman University Scientific Research Project (Project no: TEBMYOMAP/2018-0001).

REFERENCES

Canpolat C., Yayla S., Sahin B., Akilli H., 2011, Observation of the vortical flow over a yawed delta wing, *Journal of Aerospace Engineering*, 25(4), 613-626.

Canpolat C., Yayla S., Sahin B., Akilli H., 2009, Dye visualization of the flow structure over a yawed nonslender delta wing. *Journal of Aircraft*, 46(5), 1818-1822.

Cummings R.M., Morton S.A., Siegel S.G., 2008, Numerical prediction and wind tunnel experiment for a pitching unmanned combat air vehicle, *Aerospace Science and Technology* 12(5), 355-364.

Cummings R.M., Schütte, A., 2013, Detached-Eddy Simulation of the vortical flow field about the VFE-2 delta wing, *Aerospace Science and Technology*, 24(1), 66-76.

Elkhoury M., Yavuz M.M., and Rockwell D., 2005, Near-surface topology of unmanned combat air vehicle platform: Reynolds number dependence, *Journal of aircraft* 42(5), 1318-1330.

Gordnier R.E., Visbal M.R., 2003, Higher-order compact difference scheme applied to the simulation of a low sweep delta wing flow, 41st AIAA Aerospace Sciences Meeting and Exhibit, 6-9 January, Reno, NV. AIAA 0620.

- Gursul I., Gordnier R., Visbal M., 2005, Unsteady aerodynamics of nonslender delta wings, *Progress in Aerospace Sciences*, 41(7), 515-557.
- Gülsağan B., Şencan G., Yavuz, M.M., 2018, Effect of Thickness-to-Chord Ratio on Flow Structure of a Low Swept Delta Wing, *AIAA Journal*, 56(12), 4657-4668.
- Johnson F. T., Tinoco E. N., Yu, N. J., 2005, Thirty years of development and application of CFD at Boeing Commercial Airplanes, *Computers & Fluids*, 34(10), 1115-1151.
- Kyriakou M., Missirlis D., Yakinthos K., 2010, Numerical modeling of the vortex breakdown phenomenon on a delta wing with trailing-edge jet-flap, *International Journal of Heat and Fluid Flow*, 31(6), 1087-1095.
- Mary I., 2003, Large eddy simulation of vortex breakdown behind a delta wing. *International journal of heat and fluid flow*, 24(4), 596-605.
- Menter F.R., 1994, Two-Equation Eddy-Viscosity Turbulence Models for Engineering Applications, *AIAA Journal*, 32, 1598-1605.
- Muir R. E., Arredondo-Galeana A., Viola I.M., 2017, The leading-edge vortex of swift wing-shaped delta wings, *Royal Society open science*, 4(8), 1-14.
- OL M.V., Gharib M., 2003, Leading-edge vortex structure of nonslender delta wings at low Reynolds number, *AIAA Journal*, 41(1), 16–26.
- Saha S., and Majumdar B., 2012, Flow visualization and CFD simulation on 65 delta wing at subsonic condition, *Procedia engineering*, 38, 3086-3096.
- Sogukpinar H., 2019, Numerical Investigation of Influence of Diverse Winglet Configuration on Induced Drag, *Iranian Journal of Science and Technology, Transactions of Mechanical Engineering*, 44, 203-215.
- Sogukpinar H., 2018, Low Speed Numerical Aerodynamic Analysis of New Designed 3D Transport Aircraft, *International Journal of Engineering Technologies*, 4(4), 153-160.
- Taylor G.S., Schnorbus T., Gursul I., 2003, An investigation of vortex flows over low sweep delta wings, *AIAA Fluid Dynamics Conference*, 23–26 June, Orlando FL, AIAA 4021, 1-13
- Wentz W.H., Kohlman D.L., 1971, Vortex breakdown on slender sharp-edged wings. *Journal of Aircraft*, 8(3), 156–61.
- Yayla S., Canpolat C., Sahin B., Akilli H., 2010, Elmas Kanat Modelinde Oluşan Girdap Cokmesine Sapma Acisinin Etkisi, *Isi Bilimi ve Teknigi Dergisi/Journal of Thermal Science & Technology*, 30(1),79-89.
- Yaniktepe B., and Rockwell D., 2004, Flow structure on a delta wing of low sweep angle, *AIAA journal*, 42(3), 513-523.
- Yavuz M., Elkhoury M., and Rockwell D., 2004, Near-Surface Topology and Flow Structure on a Delta Wing, *IAA Journal*, 42(2), 332–340.
- Internet, 2019, Pardiso Parallel Sparse Direct and Multi - Recursive Iterative Linear Solvers, User Guide Version 6.0, <https://pardiso-project.org> [accessed 20 February 2019].
- Internet, 2019, COMSOL CFD module user guide <http://www.comsol.com>, [accessed 20 February 2019].



Hacı SOGUKPINAR is an assistant professor at Adiyaman University, Department of Electric and Energy in Vocational School. He received his B.Sc. (2001) in Physics at Middle East Technical University, Ankara, Turkey, and his PhD (2013) in the Department of Physics at Eskisehir Osmangazi University. His research field is about computational fluid dynamics (CFD), heat transfer and also experiment related to fluid flow in the water channel. He has two books, one is related to the application of the COMSOL simulation technics and second book is related to industrial design with SOLIDWORKS and its applications and both books are available online sales.



SERKAN CAG is a teaching assistant at Adiyaman University, Department of Machinery and Metal Technology in Vocational School. He received his B.Sc. (2012) in Energy System Engineering and M.Sc. (2015) in Mechanical Engineering Department at Osmaniye Korkut Ata University, Osmaniye, Turkey. His research field: Flow Visualization and Control, Flow Topology, Flow Structure on Delta Wings, Vortex Breakdown.



BULENT YANIKTEPE is an associate professor in the Mechanical Engineering Department at Osmaniye Korkut Ata University. He received his B.Sc. (1998), M.Sc. (2000) and also his PhD (2006) in Department of Mechanical Engineering at Cukurova University Adana, Turkey. His research field: Flow Visualization and Control, Flow Topology, Flow Structure on Delta Wings, Vortex Breakdown.



YAPAY SINIR AĞLARI VE UYARLAMALI SINİRSEL BULANIK ÇIKARIM SİSTEMİ İLE FRANCİS TİPİ TÜRBİNLER İÇİN VERİM TAHMİNLEMESİ

Ece AYLI* ve Oğuzhan ULUCAK**

***Çankaya Üniversitesi Mühendislik Fakültesi Makina Mühendisliği Bölümü
06790 Etimesgut, Ankara, *eayli@cankaya.edu.tr

(Geliş Tarihi: 06.09.2019, Kabul Tarihi: 18.02.2020)

Özet: Türbinler tasarım noktaları dışında mevsimsel yağış dalgalanmaları, zamana bağlı elektrik ihtiyacı farklılıkları sebebiyle kısmi yükleme şartlarında çalıştırılabilmektedir. Bu noktada tasarımcılar tepe diyagramları oluşturmakta ve farklı debi ve düşüleri altında sistem verimini tahminlemektedir. Tepe diyagramı çalışması bir çok farklı ayar kanadı açıklığında ve düşüde test gerektirdiğinden oldukça maliyetli bir çalışmadır. Bu çalışmada Yapay Sinir Ağları (YSA) ve Uyarlamalı Sinirsel Bulanık Çıkarım Sistemi (ANFIS) metodu ile farklı çalışma koşullarında Francis tipi türbin verim tahminlemesi gerçekleştirilmiştir. Elde edilen sonuçlar Hesaplamalı Akışkanlar Dinamiği (HAD) yöntemi ile elde edilmiş verim değerleri ile kıyaslanmıştır. Sonuçlara göre, maliyetli bir test veya sayısal süreç yerine ANFIS metodu kullanarak tepe diyagramı oluşturmak mümkündür. Sayısal veriler %25'i test ve %75'i modeli eğitmek için kullanılmak üzere ikiye ayrılmıştır. Geliştirilen YSA ve ANFIS modelleri ile verim tahminleri yapılmış ve elde edilen sonuçlar karşılaştırılmıştır. Çıktılar ortalama hata, maksimum hata ve regresyon katsayısı olmak üzere 3 farklı istatistiksel kriter ile test edilmiş ve ANFIS'in tepe diyagramı uygulamasında YSA'ya göre daha iyi sonuç verdiği tespit edilmiştir. ANFIS parametrelerinin optimize edilmesi ile ortalama hata %1.41, R^2 değeri ise 0.999 olarak hesaplanmıştır. Yazarların bilgisine göre YSA ve ANFIS uygulamasının türbinlere uygulandığı ilk literatür araştırması bu çalışmadır.

Anahtar Kelimeler: YSA, ANFIS, türbin, HES, Francis tipi türbin, tepe diyagramı

ANN AND ANFIS PERFORMANCE PREDICTION MODELS FOR FRANCIS TYPE TURBINES

Abstract: Turbines can be operated under partial loading conditions due to the seasonal precipitation fluctuations and due to the needed electrical demand over time. According to this partial working need, designers generate hill chart diagrams to observe the system behavior under different flow rates and head values. In order to generate a hill chart, several numerical or experimental studies have been performed at different guide vane openings and head values which are very time consuming and expensive. In this study, the efficiency prediction of Francis turbines has been performed with ANN and ANFIS methods under different operating conditions and compared with simulation results. The obtained results indicate that it is possible to obtain a hill chart using ANFIS method instead of a costly experimental or numerical tests. ANN and ANFIS parameters which effect the output, have been optimized with trying 100 different cases. 75% of the numerical data set is used for training and 25 % is used for validation as testing data. To asses and compare the performance of multiple ANN and ANFIS models several statistical indicators have been used. Insight to the performance evaluation, it is seen that ANFIS can predict the efficiency distribution with higher accuracy than the ANN model. The developed ANFIS model predicts the efficiency with 1.41% mean average percentage error and 0.999 R^2 value. To the best of the author's knowledge, this is the first study in the literature that ANN and ANFIS are used in order to predict the efficiency distribution of the turbines at different loading conditions.

Keywords: ANN, ANFIS, turbine, HEPP, Francis type turbine, Hill chart

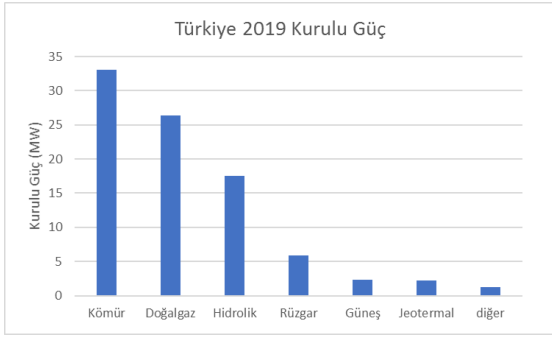
NOMENCLATURE

| | |
|---------------|---|
| YSA | Yapay Sinir Ağları |
| ANFIS Sistemi | Uyarlamalı Sinirsel Bulanık Çıkarım Sistemi |
| H | Düşü (m) |
| mf | Üyelik Fonksiyonu |
| MSE | Ortalama Hata (%) |
| Q | Debi [m^3/s] |
| X_i | YSA Girdileri |
| Y_i | YSA Çıktıları |
| w | Ağırlık Fonksiyonu |

GİRİŞ

Günümüzde enerji ihtiyacının her geçen gün artması, enerji kaynaklarının hızla tükenmesi ve fosil yakıtların kullanımına bağlı olarak oluşan atmosfer kirliliği sürdürülebilir ve yenilenebilir kaynaklara olan ilgiyi arttırmıştır. Ülkemizde yerli ve yenilenebilir bir kaynak olması, işletme, çevre ve stratejik açılarından da avantajları bulunması sebebi ile hidroelektrik enerjiden faydalanmak teşvik edilmektedir.

2016 yılı itibarıyla Dünya’da tüm enerji kaynakları içerisinde hidrolik enerjinin kurulu gücü 1064 GW ile tüm enerji kaynaklarının kurulu gücüne oranı %16.4’tür. Yenilenebilir enerji kaynakları içerisinde ise hidrolik enerjinin oranı %71’dir (International Energy Agency,2018). 2018 yılında Çin var olan hidroelektrik santral kapasitesini 35% arttırarak dünyada birinci sırada yer alırken, Türkiye 1 GW’den fazla kapasite ilave ederek üçüncü sırada yer almıştır. Türkiye’de ki enerji kaynaklarına göre kurulu güç dağılımı Şekil 1’de verilmiştir. Türkiye de 2018 yılında Hidrolik enerjinin toplam enerji üretime oranı %19.8’dir (Türkiye Cumhuriyeti Enerji ve Tabii Kaynaklar Bakanlığı). Ayrıca yenilenebilir enerji kaynakları içinde en büyük paya yine %66.6 ile hidroelektrik enerji sahiptir.



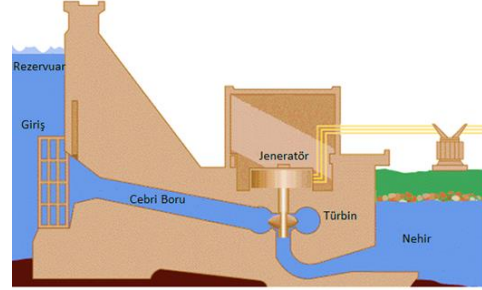
Şekil 1. Enerji kaynaklarına göre Türkiye’de kurulu güç (Türkiye Cumhuriyeti Enerji ve Tabii Kaynaklar Bakanlığı web sayfasından uyarlanmıştır)

2016 yılı verilerine göre, hidrolik enerji tüm enerji üretim kaynakları arasında dünya genelinde Watt başına en düşük yatırım maliyeti gereken enerji kaynağıdır. KW saat başına hidrolik enerji 0.05 dolar iken, rüzgâr enerjisi 0.06 dolar, biyoenerji 0.07 dolar jeotermal 0.10 dolar maliyet gerektirmektedir (Irena, 2018). Bunun yanı sıra, hidroelektrik santrallerin yüksek verim ile çalışabiliyor olması (%85-%97), uzun ömre sahip olması, tehlikeli atık oluşturmaması ve güvenilir olması hidrolik enerjiyi tercih sebebi haline getirmektedir. Türkiye, 2023 yılında toplam kurulu gücü %20 arttırarak 34 GW’a çıkarmayı hedeflemektedir.

Hidroelektrik sistemlerde suyun akım enerjisinden faydalanılmaktadır. Su bir boru sistemi ile (cebri boru) yüksek bir yerden türbine verilmektedir ve potansiyel enerji kinetik enerjiye çevrilmektedir. Yüksek basınçlı su türbinin kanatlarını döndürmekte ve kinetik enerji mekanik enerjiye dönüşmektedir. Türbinin tahrik ettiği jeneratörün dönmesi ile de elektrik enerjisi elde edilmektedir (Şekil 2). Türbinden elde edilen güç, suyun düşüşüne ve debisine bağlıdır (Ayli,2016).

Günümüz teknolojisinde türbin bileşenlerinin tasarımı için özellikle Hesaplamalı Akışkanlar Dinamiğinden (HAD) yararlanılmaktadır. Shukla ve diğerleri (Shukla,2011), deneysel olarak test edilmiş bir Francis tipi türbini sayısal olarak modellemişlerdir. Elde ettikleri sonuçları deneysel sonuçlar ile kıyaslamış ve hidrolik türbinlerde HAD yöntemlerinin güvenilir bir yöntem olduğunu ve maliyetten kazanç sağladığını öne

sürmüşlerdir. Anup vd.(2014), 70 kW güç ve 0.5 m³/s debiye sahip Francis tipi türbin için üç boyutlu Reynolds Ortalamalı Navier Stokes (RANS) çözümlemesi yapmıştır. Ayli (2016), üç boyutlu zamandan bağımsız sayısal çözümleme ile Türkiye, Bursa ilinde kurulmakta olan Francis tipi HES’in temel bileşenlerinin tasarımını gerçekleştirmiştir. Tasarlanan türbin geniş bir debi-düşü aralığında %90 üstü verim ile çalışabilmektedir.



Şekil 2. Hidroelektrik sistemlerinin çalışma prensibi

Okyay (2010), Francis tipi türbinler için tasarım metodolojisi geliştirmiştir ve izlenen yöntem ile tasarlanan türbin enerji üretimi için kurulmuştur. Ayancık (2014), Francis tipi türbin çarkları tasarımı için optimizasyon metodolojisi geliştirmiştir. Geliştirilen optimizasyon metodolojisi çark tasarımında harcanan süreyi 8.8 kat azaltmıştır.

Türbin tasarımlarında sadece tam yükleme durumu değil, kısmi yükleme durumlarında da yüksek performans sağlanması önem teşkil etmektedir. Bu bağlamda yapılan tasarımın farklı ayar kanadı açıklıklarında ve düşülerde de test edilmesi gerekmektedir. Deneysel yöntemler maliyetli olduğundan ötürü farklı debi ve düşülerde birçok deney gerçekleştirmek yerine sayısal yöntemler yardımı ile türbin performansının araştırılması birçok araştırmacı tarafından tercih edilmiştir. Gohil vd. (2014), farklı yükleme durumları için Francis tipi türbinlerde HAD çalışmaları gerçekleştirmiştir. Elde ettikleri sonuçları model testler ile kıyaslamış ve maksimum hatayı %1 mertebesinde bulmuşlardır. Patel vd. (2011) %25 ile %130 yükleme arasında farklı debilerde Francis tipi türbin performansını irdelemiş ve kısmi yükleme durumlarında kayıpların arttığını ortaya koymuştur. Celebioglu vd. (2018), farklı ayar kanadı açıklıklarında farklı yükleme durumları için (%20-%130) toplamda 52 HAD analizi gerçekleştirmiş ve türbinin davranışını geniş bir debi düşü aralığında irdelemiştir. Her bir türbin analizi 36 milyon eleman içermektedir.

Her ne kadar farklı debi düşü aralıklarında türbin performansı irdelemek gerekli bir tasarım süreci olsa da bu çalışma bilgisayar maliyetlerini ve tasarım zamanını çok arttırmaktadır. Bu noktada farklı debi ve düşü durumlarında verim tahminlemesini daha az maliyet ve kısa sürede yüksek doğruluk ile gerçekleştirebilmek önem arz etmektedir.

YSA’nın insan beynine benzer bir biçimde çalışması, verilen veriyi öğrenip tahmin yapabiliyor olması, YSA yöntemine geniş bir kullanım alanı yaratmaktadır. Bu

yaklaşım ile mühendislik uygulamalarında hem akademik hem pratik birçok problem çözümlenebilmektedir. Yenilenebilir enerji alanında konum optimizasyonu verim tahmini gibi uygulamaları mevcuttur (Mensour v.d, 2017). YSA bir dizi algoritmanın birbiri ile iletişimi ile verilen girdi ve çıktılar arasındaki doğrusal olmayan ilişkileri çözebilmekte ve bu karmaşık ilişkileri-fonksiyonları kullanarak daha önce tanımadığı girdiler üzerinden başarılı tahminler-çıktılar verebilmektedir.

ANFIS, Takagi-Sugeno fuzzy çıkarım sistemini kullanan bir tür melez (hibrid) YSA sistemidir. Bir dizi eğer-sonra (if-then) kurallarını kullanarak doğrusal olmayan fonksiyonlar öğrenebilmektedir. ANFIS hem sinir ağları hem de bulanık mantığı birbirleriyle uyumlu bir şekilde kullanabildiği için, her iki teknolojinin de güçlü yanlarından faydalanır (Raju, 2011).

Literatürde, yenilenebilir enerji alanında, ANFIS ve YSA kullanılarak gerçekleştirilmiş birçok çalışma bulunmaktadır. Antonopoulos vd.(2019), günlük hava durumu, hava sıcaklığı, nem ve rüzgâr hızı verilerini kullanarak toplam potansiyel radyasyon tahmin eden bir YSA modeli geliştirmiştir. Elde ettikleri sonuçların değerlendirilmesinde R^2 ve ortalama hata üzerinden performans irdelemesi yapmışlardır. Elde edilen regresyon sonuçları ve YSA sonuçları birbirleri ile tutarlı bulunmuştur. Ghosh ve Majumder (2019), YSA ve ANFIS kullanarak dalga enerjisine etki eden dalga boyu ve dalga periyodu dışındaki parametrelerin ağırlıklarını belirlemiştir. Terzi vd (2011), YSA ve ANFIS yöntemi ile rüzgâr hızı tahminlemesi yapmışlar ve iki yöntemi birbirleri ile ve gerçek hızlar ile kıyaslamışlardır. Elde edilen sonuçlara göre ANFIS, YSA metoduna oranla daha iyi bir yaklaşım sağlamaktadır. Kurtgöz vd (2017), YSA metodu kullanarak biyogaz tesisinde kullanılan bir gaz motorunun değişik koşullarda verimini tahmin etmiştir. Literatürde birçok yenilenebilir enerji kaynağı verim tahminlemesi üzerine çalışma bulunmakta olup yazarların bilgisine göre, hidroelektrik santral verim tespitinde bu metotlardan hiç faydalanılmamıştır.

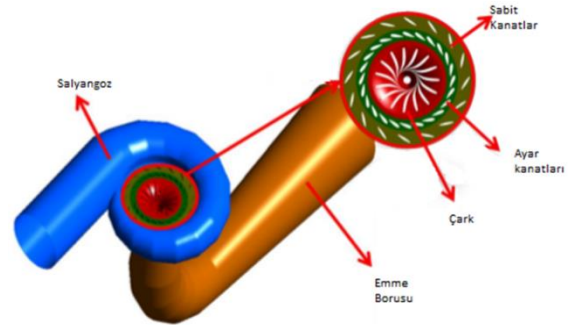
Bu çalışmada ANN ve ANFIS metotlarının farklı yüklenme durumlarında verim tahminleme becerisi üzerine çalışılmıştır. Bu bağlamda bir önceki çalışmada (Ayli, 2014) tasarımı gerçekleştirilmiş ve farklı debi ve düşülerdeki davranışı tepe diyagramı ile irdelenmiş olan çalışmadan faydalanılmıştır. ANN ve ANFIS performansı değerlendirilmesi için farklı öğrenme fonksiyonları, gizli katman sayıları ve üyelik fonksiyonları denenmiş ve en iyi sonucu veren mimariler seçilmiştir. Toplamda 100 farklı mimari oluşturulmuş ve sonuçları birbirleri ile kıyaslanmıştır.

METODOLOJİ

Francis tipi türbinler 60 m ile 700 m düşü aralığında, 2 m³/s ile 1000 m³/s debi aralığında çalışabilmektedir. Bu türbinler ile 500 MW'a kadar güç elde edilebilmektedir. Bu avantajlar Francis türbinlerine geniş bir uygulama alanı yaratmaktadır. Francis tipi türbinler salyangoz, sabit kanat, ayar kanatları, çark ve emme borusundan

oluşmaktadır. Su, akış boyunca sırasıyla salyangoz, sabit kanatlar, ayar kanatları ve çarktan geçmekte son olarak emme borusundan tahliye olmaktadır. Salyangoz ve sabit kanadın amacı, akışı düzenlemek ve ayar kanatlarına uygun açı ile suyu yönlendirmektir. Ayar kanatları servo motorlar ile kendi ekseninde sağa veya sola dönebilmekte böylece çarka ulaşan su debisi ayarlanabilmektedir. Su çarka ulaştıktan sonra sahip olduğu enerjiyi çarka vermekte ve emme borusundan tahliye olmaktadır.

Ayli (2014), çalışmasında 2 m³/s debi 78 m düşü ve 1.4 MW güç isterleri olan BUSKİ HES için beş temel bileşenin tasarımını ANSYS-CFX yazılımı ile gerçekleştirmiştir. Tasarım süreci boyunca maksimum verim, minimum kaviteasyon hedeflenmiştir. Çark kanatlarında X-blade geometrisi seçilmiş bu sayede daha dengeli bir basınç dağılımı elde edilmiştir. Tüm bileşenlerin tasarımı minimum kayıp ve maksimum verim ile tek tek gerçekleştirildikten sonra tam yüklenme durumunda tüm türbin analizi gerçekleştirilmiştir. Tasarım noktasında verim % 93.835 olarak hesaplanmıştır. Şekil 3'de Buski HES için tasarlanan bileşenler verilmiştir.



Şekil 3. Buski HES bileşenleri

Sayısal Metodoloji

BUSKİ HES için tasarım süreci tamamlandıktan sonra 48-108 m arasında 10 m aralıklı düşü değerleri için 6 farklı ayar kanadı açıklığında toplamda 42 tüm türbin analizi gerçekleştirilerek tepe diyagramı elde edilmiştir. Tepe diyagramı çalışmasında basınç giriş-basınç çıkış sınır koşulları kullanılmıştır. Bu sayede sistemden geçen debi hesaplanmıştır. Üç boyutlu türbülanslı sıkıştırılmaz akış koşulları için Navier-Stokes denklemleri kullanılarak hesaplama yapılmıştır. Korunum denklemleri Denklem (1) ve Denklem (2)'de verilmiştir.

$$\frac{\partial \rho}{\partial t} + \frac{\partial (\rho u_i)}{\partial x_i} = 0 \quad (1)$$

$$\frac{D(u_i)}{Dt} = \frac{\partial u_i}{\partial t} + u_j \frac{\partial u_i}{\partial x_j} = -\frac{1}{\rho} \frac{\partial P}{\partial x_i} + \nu \frac{\partial^2 u_i}{\partial x_j^2} + F_i \quad (2)$$

Denklem (3)'e göre salyangoza giriş ve çıkıştaki toplam basınçlar hesaplanmıştır ve sınır koşulları tanımlanarak denklemler çözülmüştür.

$$P = \rho gH + P_{atm} \quad (3)$$

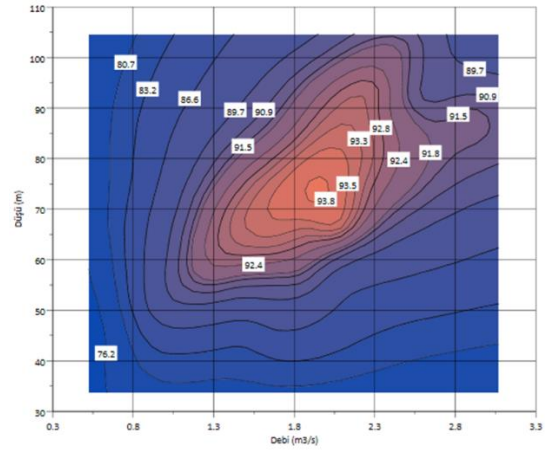
42 farklı düşü ve debide yapılan analizler sonucu debi, düşü ve verim eğrisi çizilmiştir. Buski Francis türbini tepe diyagramı Şekil 4’de verilmiştir. Sistemin tasarım noktası en yüksek verim aralığına denk gelmektedir. Maksimum verim 93.8 m olarak elde edilmiştir. Kısmi yüklemelerde sistem kayıplarının artmasına bağlı olarak verim ve güç düşmektedir.

Akış karakteristiklerinin gözlemlenebilmesi ve yakalanabilmesi için ağ yapısının yeterli nokta sayısına sahip olması gerekmektedir. Ayar kanadı, sabit kanat ve çark kanatları H,J,C ve L ağ topolojileri kullanılarak hazırlanmıştır. Salyangoz ve emme borusunda ise karmaşık geometriden ötürü yapısal olmayan ağ yapısı kullanılmıştır. Çözümün eleman sayısının artması ile değişmediği nokta yeterli eleman sayısı olarak kabul edilmiştir. Salyangoz için çıkış yüzeyindeki ortalama akış açısı, emme borusu için geri kazanım katsayısı, sabit ve ayar kanadı için çıkış yüzeylerindeki ortalama hızlar ve çark için güç, verimlilik değerleri incelenmiştir.

Ayli’nin (2016) çalışmasında ayrıntıları verildiği üzere ağ yapısından bağımsızlaşma çalışması sonrasında tüm türbin bileşenlerinin sahip olduğu eleman sayısı 14×10^6 olarak hesaplanmıştır. Tüm türbin için gerçekleştirilen türbülans modeli çalışması sonucunda k-ε türbülans modeli seçilmiştir. Tüm türbin analizleri TOBB ETU Hidro Laboratuvarına ait 108 çekirdekli öbek bilgisayar sistemi ile gerçekleştirilmiştir. Bu çalışmada her bir analiz ortalama olarak 8 saat sürmüştür. ANN ve ANFIS yöntemi ile verim tahminlemesinin yüksek doğrulukla yapılabilmesi durumunda ciddi bir zaman ve bilgisayar maliyeti minimize edilmiş olacaktır.

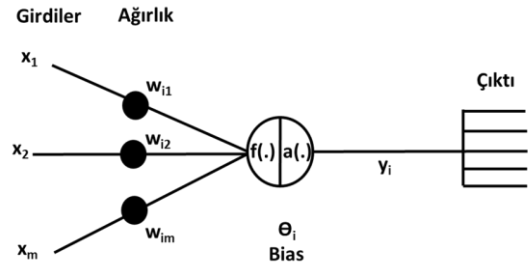
Yapay Sinir Ağları Metodu

YSA biyolojik sinir sisteminden esinlenerek geliştirilmiş deneme yolu ile öğrenme ve genelleştirme yapabilen bir matematiksel metottür. YSA, sayısız doğrusal olmayan nöronlardan ve bu nöronlar arası bağlantılardan oluşmaktadır. Temel olarak tüm YSA’lar; girdi, gizli ve çıktı katmanları olarak üç katmandan oluşur. İlk katman, giriş katmanı olarak adlandırılır ve girdi verilerinden oluşur. Bu katman dış ortamdan verilen girdileri alarak gizli katmana iletir. Gizli katman ise girdi katmanından gelen bilgileri işlemekte ve çıkış katmanına yollamaktadır, bu katman çok sayıda yapay sinir hücresi barındırmaktadır. Şekil 5’de YSA mimarisi gösterilmektedir.



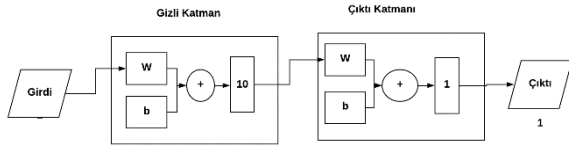
Şekil 4. Buski Hes tepe diyagramı

YSA’da optimize edilmesi gereken parametrelerden bir tanesi gizli katmandaki katman sayısıdır. Gizli katman sayısının performansa olan etkisi üzerine genelleştirilmiş bir sonuç bulunmamaktadır. Bazı problemlerde katman sayısını arttırmak tahminleme performansını artırırken bazı problemlerde ise istenmeyen kararsızlıklara sebep olmaktadır (Vuraş, 2007 ve Ataseven, 2013) Dolayısı ile deneme yanılma yolu ile katman sayısı belirlenmesi gerekmektedir.



Şekil 5. YSA mimarisi

YSA mimarileri sinirler arası bağlantılara göre ileri veya geri beslemeli ağlar olarak tanımlanırlar. İleri beslemeli ağlarda geri besleme hiçbir zaman yoktur ve her bir katmandaki nöron bir sonraki katmana ağırlıklar üzerinden iletilir. Bu çalışmada ileri beslemeli ağlarda en çok kullanılan çok katmanlı algılayıcı (MLP) kullanılmaktadır. Tek katmanlı algılayıcılar sadece doğrusal problemleri çözümlenebilmekte çok katmanlılar ise doğrusal olmayan problemlerde de kullanıldığı için sıklıkla tercih edilmektedir (Ataseven, 2013). İleri beslemeli ağlar Giriş ve çıkış katmanları arasında gizli katmanlara sahip olduğundan ötürü tek katmanlı algılayıcıların karşılaştıkları sınırlamalara sahip değildir, bu sebepten ötürü bu çalışmada çok katmanlı algılayıcılar kullanılmıştır. Bu uygulamada girdi olarak debi ve düşü verilmekte çıktı olarak ise verim alınmaktadır. Gizli katmandaki eleman sayısı ise deneme yanılma yolu ile tespit edilecektir. 2 giriş 1 çıkışlı bir YSA mimarisi Şekil 6’da verilmiştir.



Şekil 6. YSA şematik gösterimi

Eğitim, bilinen bir çıktı setinin, girdi seti kullanılmasıyla yapılmaktadır. Girdi seti ağırlık fonksiyonları ile çarpılarak toplanır. Gizli katmanda bulunan herhangi bir nöronun yapısı Şekil 5’de gösterilmiştir. X, girdi değerini, y çıktı değerini ve w girdinin yoğunluğunu ifade etmektedir. Herhangi bir girdinin çıktıya olan etkisini ifade eden w, giriş parametreleri ile Denklem (4)’de verildiği şekilde çarpılır ve toplanır.

$$S_i = \sum_{i=1}^n w_{ij} x_i \quad (4)$$

Bu toplam ve bilinen çıktı değeri kullanılarak transfer fonksiyonu çözülür ve b değeri tespit edilir. Böylece giriş değeri ve çıkış değeri arasındaki lineer olmayan ilişki kurulmuş olur. Unit step, sigmoid-tanh, piecewise linear,

gaussian gibi birçok farklı transfer fonksiyonları olsa da çok katmanlı YSA’da tan-sigmoid fonksiyonu tercih edilmektedir (Xie,2009). Sigmoid fonksiyonu Denklem (5)’de verilmiştir. Bu işlem her defasında epoch denilen iteratif bir süreç ile her katman için tekrarlanır. Bu çalışmada eğitilen modeller için epoch sayısı 100 olarak sınırlandırılmıştır.

$$f(S_i) = \frac{1}{1 + e^{-\beta(S_i)}} \quad (5)$$

Bu çalışmada YSA ve ANFIS uygulaması için MATLAB yazılımı kullanılmıştır. Doğruluğu arttırmak için girdi verileri normalize edilmiştir. Normalizasyon, bir veri setindeki verilerin en büyük değere bölünerek normalleştirilmesi işlemidir. Bu işlem sonucunda veriler [0,1] aralığında yer almaktadır. Denklem (6)’da ifade edildiği üzere YSA modeline girilecek verilerin tamamı normalize edilmiştir. Normalize edilmiş veri seti Tablo 1’de verilmiştir.

$$X_{normalize} = \frac{X - X_{Minimum}}{X_{Maksimum} - X_{Minimum}} \quad (6)$$

Tablo 1. Normalize Edilmiş Simülasyon girdileri ve verim değerleri

| Buski Hes Normalize Edilmiş Veriler | | | | | | | |
|-------------------------------------|----------|----------|----------|----|----------|----------|----------|
| | Debi | Düşü | Verim | | Debi | Düşü | Verim |
| 1 | 0 | 0 | 0 | 22 | 0.585837 | 0.589748 | 1 |
| 2 | 0.115471 | 0.078328 | 0.31823 | 23 | 0.681945 | 0.579421 | 0.954025 |
| 3 | 0.231452 | 0.126038 | 0.494809 | 24 | 0.787008 | 0.557007 | 0.891132 |
| 4 | 0.377451 | 0.156019 | 0.510779 | 25 | 0.107733 | 0.610866 | 0.461348 |
| 5 | 0.452818 | 0.162181 | 0.605628 | 26 | 0.293783 | 0.689567 | 0.798807 |
| 6 | 0.53166 | 0.162462 | 0.594868 | 27 | 0.467499 | 0.722654 | 0.916626 |
| 7 | 0.029732 | 0.160795 | 0.052998 | 28 | 0.664703 | 0.718333 | 0.969354 |
| 8 | 0.16433 | 0.238845 | 0.700729 | 29 | 0.749971 | 0.706546 | 0.930698 |
| 9 | 0.298967 | 0.278751 | 0.852013 | 30 | 0.861278 | 0.678419 | 0.888748 |
| 10 | 0.460441 | 0.30563 | 0.861897 | 31 | 0.13177 | 0.753605 | 0.483018 |
| 11 | 0.530851 | 0.310477 | 0.849747 | 32 | 0.331252 | 0.834614 | 0.725583 |
| 12 | 0.62201 | 0.302831 | 0.69155 | 33 | 0.515691 | 0.864567 | 0.877961 |
| 13 | 0.057618 | 0.32313 | 0.302708 | 34 | 0.724035 | 0.847113 | 0.938843 |
| 14 | 0.209968 | 0.391435 | 0.829931 | 35 | 0.814893 | 0.830991 | 0.845057 |
| 15 | 0.35953 | 0.432852 | 0.962219 | 36 | 0.931935 | 0.796369 | 0.880775 |
| 16 | 0.534488 | 0.450147 | 0.965918 | 37 | 0.153765 | 0.89367 | 0.4482 |
| 17 | 0.610463 | 0.449315 | 0.967229 | 38 | 0.366286 | 0.981297 | 0.657405 |
| 18 | 0.708731 | 0.432795 | 0.845185 | 39 | 0.559405 | 1 | 0.788672 |
| 19 | 0.083029 | 0.468253 | 0.44341 | 40 | 0.779771 | 0.974124 | 0.881208 |
| 20 | 0.253172 | 0.54083 | 0.847961 | 41 | 0.87691 | 0.953624 | 0.792215 |
| 21 | 0.414752 | 0.577581 | 0.966484 | 42 | 1 | 0.912696 | 0.769346 |

Normalize edilmiş veriler, sırasıyla eğitim ve test olmak üzere %75 ve %25 olarak ikiye ayrılmıştır. Uygun YSA modeli tespiti için toplamda 75 model eğitimi yapılmıştır. Bayesian Regularization (BR), Scaled Conjugate

Gradient (SCG) ve Levenberg-Marquardt (LM) olarak 3 farklı eğitim algoritması kullanılmıştır. Her bir algoritma için gizli katman sayısı değiştirilerek test edilmiştir. MLP tipi YSA geri yayılım algoritması kullanarak eğitilmiştir

Toplamda 75 adet model geliştirilmiş ve üç farklı eğitim modeli için her bir modelde gizli katman sayısı 1'den 25'e kadar değiştirilmiştir. Tablo 2'de geliştirilen tüm mimariler verilmiştir. Alınan çıktılar ile R² ve OH kriterine göre çıktılar değerlendirilmiştir.

Tablo 2. Geliştirilen YSA mimarileri

| | Gizli Katman Sayısı | Eğitim Modeli |
|-------------|---------------------|---------------------------|
| Model 1-25 | 1,2,3,4,...25 | Levenberg-Marquardt |
| Model 26-50 | 1,2,3,4,...25 | Bayesian Regularization |
| Model 51-75 | 1,2,3,4,...25 | Scaled Conjugate Gradient |

Sinirsel Bulanık Çıkarım Sistemi (ANFIS) Metodu

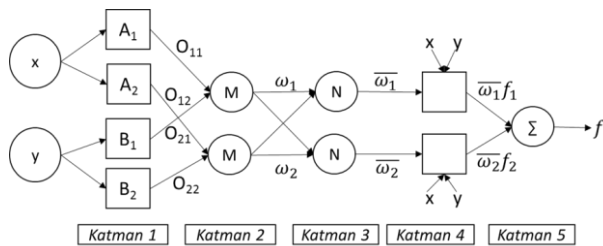
ANFIS, Bulanık mantığın (Fuzzy Logic) YSA modeline uygulanmasıyla oluşan melez bir sistemdir. Böylece her iki sistemin avantajlı olan yönlerini birleştirmekte ve dezavantajlı yönlerini de törpülemektedir. Bulanık mantığın en önemli avantajı belirsizlik problemlerini çözümedeki başarısıdır. Simgesel mantık, doğru veya yanlış gibi bir başka ifade ile bir ve sıfırlardan oluşurken, bulanık mantık, üyelik fonksiyonları ile birlikte girdileri ve çıktıları derecelendirebilir. Örneğin; bir bardak su, simgesel mantık kurgusu ile sıcak veya sıcak değil olarak tanımlanmakta iken, bulanık mantık ile bir bardak su, %10 yüksek sıcaklık, %30 orta sıcaklık, %40 normal sıcaklık ve %20 düşük sıcaklık olarak tanımlanabilir. ANFIS, bu esnek matematiksel yapısı sebebiyle mühendislik problemlerini daha gerçekçi modelleyebilmektedir (Kurtgöz,2017)

Şekil 7'de gösterilen, 2 giriş ve bir çıkıştan oluşan, Sugeno tipi bir çıkarılma sistemi için aşağıdaki kurallar tanımlanır.

Kural 1: Eğer (x is A₁) ve (y is B₁) ise f₁=p₁x+q₁y+r₁ (7)

Kural 2: Eğer (x is A₂) ve (y is B₂) ise f₂=p₂x+q₂y+r₂(8)

A_i ve B_i bulanık kümeleri f_i ise çıktıyı temsil etmektedir. Eğitim sırasında amaç, p_i, q_i ve r_i ile ifade edilen tasarım parametrelerini hesaplamaktır.



Şekil 7. ANFIS metodunun şematik yapısı

ANFIS, giriş ve çıkış parametreleri arasında 5 katman bulundurulur. 2 giriş parametresi ve bir çıktı içeren ANFIS yapısı Şekil 7'de gösterilmiştir. Şekil'de x, y giriş parametreleri, f ise çıkış parametresini ifade etmektedir.

1. Katmanda her bir düğüm, giriş değişkenlerinin üyelik fonksiyonları düğüm fonksiyonlarını oluşturur. Her bir düğüm çıkışı Denklem 9'da verildiği şekilde hesaplanır.

$$O_{1,i} = \mu_{A_i}(x) \quad i = 1,2 \text{ veya } O_{1,i} = \mu_{B_{i-2}}(y) \quad i = 3,4 \quad (9)$$

İlk katman aldığı x ve y girdilerini üyelik fonksiyonları ile bulanıklaştırmaktadır. Üyelik derecelerinin değişimi üyelik fonksiyonları ile belirlenmektedir. Uygulama alanına göre üyelik fonksiyonun şekli değişiklik göstermektedir. Uygun üyelik fonksiyonu literatürde genelde deneme yanılma yöntemi ile tespit edilmektedir. ANFIS elde bulunan girdi setine göre farklı üyelik fonksiyonları sunmaktadır. Bunların başlıcaları üçgen, yamuk, gauss dağılımı veya çan eğrisi ve sigmoid'lerdir. Seçilen üyelik fonksiyonları ayrı ayrı test verisinde kullanılarak en küçük hata değerine sahip fonksiyon tipi kurulan modelin eğitilmesi için seçilir (Bisen, 2011).

Üçgensel (triangular) ve Gauss dağılımı (Gaussian) tipi üyelik fonksiyonları sırasıyla Denklem 9 ve Denklem 10'da verilmiştir.

$$\mu_A(x) = \frac{1}{1 + \left| \frac{x-c_i}{a_i} \right|^{2b_i}} \quad (9)$$

$$\mu_A(x) = \exp \left[- \left(\frac{x-c_i}{a_i} \right)^2 \right] \quad (10)$$

2. katmanda, tanımlanan kurallar kullanılarak, bulanık çıkarsama yapılır ve YSA sistemine benzer ağırlık fonksiyonları uygulanır. Düğüm çıkışı Denklem 11'de verildiği gibi hesaplanır.

$$O_{2,i} = w_i = \mu_{A_i}(x) \mu_{B_i}(y) \quad i = 1,2 \quad (11)$$

3. Katmanda, bulanıklaştırılmış girdi değerlerinin ağırlık fonksiyonlarıyla çarpılıp toplanmış büyüklükleri aşağıdaki gibi normalize edilmektedir:

$$O_{3,i} = \bar{w}_i = \frac{w_i}{w_1 + w_2} \quad i = 1,2 \quad (12)$$

4. katmanda, her bir düğümün model çıktısı üzerindeki katkısı Denklem 13'de gösterildiği şekilde hesaplanır.

$$O_{4,i} = \bar{w}_i f_i = \bar{w}_i (p_i x + q_i y + r_i) \quad (13)$$

4. Katmanda tekrar ağırlık fonksiyonuyla çarpılıp toplanan normalize edilmiş değerler 5. Katmanda basitçe toplanır ve çıktıya ulaşılır. YSA de olduğu gibi geri yayılım metodu kullanılarak ağırlık fonksiyonları optimize edilir ve ANFIS öğrenme yeteneğini kazanmış olur.

$$O_{5,i} = \sum_i \bar{w}_i f_i = \frac{\sum_i w_i f_i}{\sum_i w_i} \quad (14)$$

ANFIS performansı, üyelik fonksiyonlarının çeşidine, yapısına, sayısına ve tanımlanan kural sayısına bağlıdır. Bu çalışmada her bir parametre değiştirilerek toplamda 25 model eğitilmiştir. YSA ile aynı eğitim koşullarını sağlamak amacı ile veriler, sırasıyla eğitim ve test olmak üzere %75 ve %25 olarak ikiye ayrılmıştır. Tablo 3'de hazırlanan her bir ANFIS mimarisi özellikleri verilmiştir. Giriş ve çıkış üyelik fonksiyon tipleri ve üyelik fonksiyon

sayıları optimize edilmiş ve en iyi yaklaşımı sağlayan mimari belirlenmiştir.

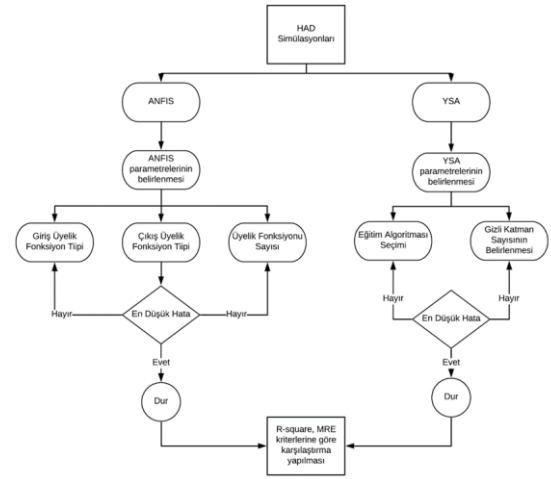
Tablo 3. ANFIS Modeli Mimarileri

| | Giriş Üyelik Fonksiyon tipi | Çıkış Üyelik Fonksiyon Tipi | Üyelik Fonksiyon sayısı |
|----------|-----------------------------|-----------------------------|-------------------------|
| Model 1 | trimf | Sabit | 3 |
| Model 2 | trapmf | Sabit | 3 |
| Model 3 | gbellmf | Sabit | 3 |
| Model 4 | gaussmf | Sabit | 3 |
| Model 5 | gauss2mf | Sabit | 3 |
| Model 6 | pimf | Sabit | 3 |
| Model 7 | dsigmf | Sabit | 3 |
| Model 8 | psigmf | Sabit | 3 |
| Model 9 | trimf | Doğrusal | 3 |
| Model 10 | trapmf | Doğrusal | 3 |
| Model 11 | gbellmf | Doğrusal | 3 |
| Model 12 | gaussmf | Doğrusal | 3 |
| Model 13 | gauss2mf | Doğrusal | 3 |
| Model 14 | pimf | Doğrusal | 3 |
| Model 15 | dsigmf | Doğrusal | 3 |
| Model 16 | psigmf | Doğrusal | 3 |
| Model 17 | trimf | Doğrusal | 2 |
| Model 18 | trimf | Doğrusal | 3 |
| Model 19 | trimf | Doğrusal | 4 |
| Model 20 | trimf | Doğrusal | 5 |
| Model 21 | trimf | Doğrusal | 6 |
| Model 22 | trimf | Doğrusal | 7 |
| Model 23 | trimf | Doğrusal | 8 |
| Model 24 | trimf | Doğrusal | 9 |
| Model 25 | trimf | Doğrusal | 10 |

Performans Değerlendirilmesi

Bu çalışmada Francis tipi türbinlerin tepe diyagramı oluşturulmasında verim tahminlemesi yapmak amacı ile YSA ve ANFIS modelleri birbirleri ile ve sayısal sonuçlar ile kıyaslanmıştır. Çalışma sırasında izlenen metodoloji Şekil 8’de verilmiştir.

42 adet HAD analizi sonucunda elde edilen sayısal sonuçlarla YSA ve ANFIS çıktıları kıyaslaması istatistiksel kıyaslama yapılarak gerçekleştirilmiştir. Bu bağlamda Denklem (15) ve (16)’da verilen ortalama hata (OH) ve regresyon kat sayısı (R^2) hesaplamaları yapılarak kıyaslamalar gerçekleştirilmiştir.



Şekil 8. Çalışma metodolojisi

$$OKH = \frac{1}{N} \frac{|X_{Gerçek,i} - X_{tahmin,i}|}{|X_{Gerçek,i}|} \quad (15)$$

$$R^2 = 1 - \frac{\sum_i^N (X_{Gerçek,i} - X_{tahmin,i})^2}{\sum_i^N (X_{Gerçek,i})^2} \quad (16)$$

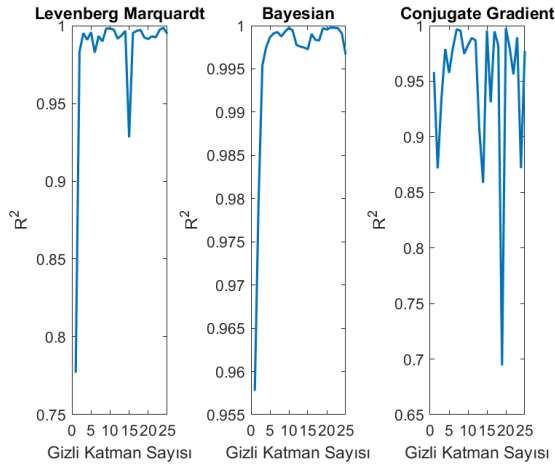
Denklem (16)’da verilen regresyon kat sayısı (R^2) değeri 0-1 aralığında değişim göstermektedir. Bu değer 1’e yaklaşması sayısal ve tahminlenen veri arasında doğruluğun arttığı anlamını taşımaktadır.

SONUÇLAR VE TARTIŞMALAR

Bu bölümde önceki çalışmada (Ayli,2014 ve Ayli,2015) elde edilmiş sayısal sonuçlar sırası ile YSA ve ANFIS yaklaşımı ile elde edilen sonuçlarla performans değerlendirme kriterlerine göre kıyaslanmıştır.

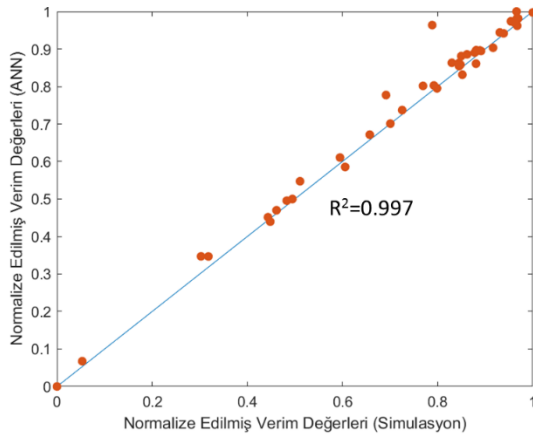
YSA Yaklaşımı ile Elde Edilen Sonuçların İrdelenmesi

Tablo 2’de verildiği üzere 75 farklı YSA mimari hazırlanmış ve probleme uygulanarak verim tahminlemesi yaptırılmıştır. Şekil 9’da katman sayısının farklı eğitim algoritmaları için etkisi gösterilmektedir. Elde edilen sonuçlara göre eğitim algoritması modelin başarısını doğrudan etkilemektedir. Bunun yanı sıra modelin içerdiği gizli katman sayısı da performansı etkileyen bir diğer faktör olarak karşımıza çıkmaktadır. Katman sayısının etkisi SCG modelinde diğer modellere göre daha baskın olarak gözlemlenmektedir. Gizli katman sayısının artışına bağlı olarak R^2 değişimi ortak bir davranış sergilememektedir. Bu durum katman sayısının optimize edilmesi gereken bir parametre olduğunu ve deneme-yanılma yolu ile ilgili problem için uygun değer bulunacağını göstermektedir. İstatistiksel kıyaslamaya göre SCG metodu en düşük R^2 değerleri ve en yüksek ortalama hataya sahip iken, en iyi sonuç veren eğitim algoritması 10 adet gizli katman içeren BR olarak hesaplanmıştır.



Şekil 9. Gizli katman sayısı ve eğitim algoritmasının performans üzerindeki etkisi

Şekil 10'da en iyi yaklaşımı sağlayan 10 gizli katmana sahip BR eğitim algoritması için sayısal ve tahminlenmiş verilerin kıyaslanması normalize edilmiş veriler cinsinden hem eğitim hem test seti için gösterilmiştir. Sadece deney seti verileri kullanıldığında 0.9987 olan R^2 değeri test verilerinin de katılması ile 0.997 değerine düşmektedir.



Şekil 10. Simülasyon verisi ve YSA tahmin değerleri karşılaştırması

ANFIS Yaklaşımı ile Elde Edilen Sonuçların İrdelenmesi

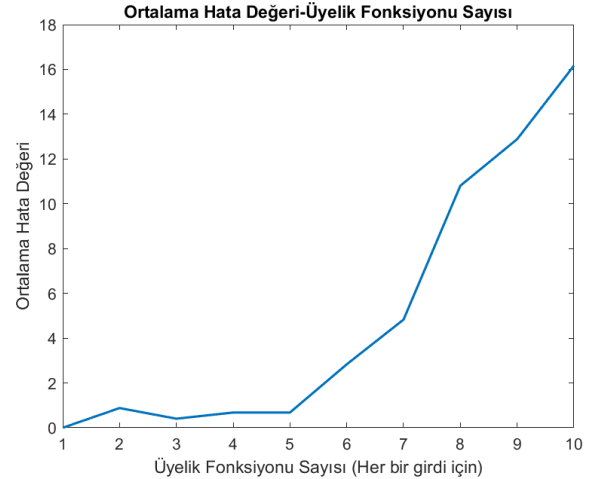
En uygun ANFIS modelini elde etmek için Tablo 3'de verildiği üzere toplamda 25 farklı senaryo için eğitim yapılmıştır. Bu eğitimlerin 16 tanesi üyelik fonksiyonunu belirlemek geri kalan 9 tanesi üyelik fonksiyonu sayısının modele olan etkisini gözlemlemeyi amaçlamaktadır. Sonuçlar OH kriterine göre değerlendirilmiştir. ANFIS modeli eğitilirken normalizasyon yapılmamıştır. Bunun sebebi ANFIS ve YSA katmanları arasında zaten bu işlemin yapılıyor olmasıdır. Girdileri 0 ve 1 arasında normalize etmek tahminlemeyi negatif yönde etkilemiştir. Tablo 4'te her bir giriş için tanımlanan 3x3 üyelik fonksiyonlar ile çıkış üyelik fonksiyonuna bağlı olarak yapılan tahmin çıktıları ve bunların arasında hata değerleri ortalaması hesaplanmıştır. Elde edilen sonuçlara göre en iyi sonuç Trimf modeli doğrusal çıktı üyelik fonksiyonu kullanıldığında elde edilmiştir. En iyi üyelik

fonksiyonunun (MF) seçilmesinin ardından üyelik fonksiyonu sayısının sonuçlara olan etkisi istatistiksel olarak irdelenmiştir.

Tablo 4. Üyelik fonksiyon çeşitlerinin hata değerleri

| | Ortalama Hata | | R ² |
|----------|---------------|----------|----------------|
| | Sabit | Doğrusal | Doğrusal |
| Trimf | 3.164 | 1.418 | 0.9992 |
| Trapmf | 9.873 | 5.583 | 0.9928 |
| Gbellmf | 9.209 | 2.281 | 0.9959 |
| Gaussmf | 8.733 | 2.096 | 0.9944 |
| Gauss2mf | 7.750 | 6.264 | 0.9731 |
| Pimf | 13.320 | 24.354 | 0.9602 |
| Dsigmf | 9.014 | 55.775 | 0.8771 |
| Psigmf | 9.012 | 55.749 | 0.8871 |

Şekil 11'de ortalama hata değerinin üyelik fonksiyonu sayısına göre değişimi gösterilmiştir. Her bir girdi için 3 üyelik fonksiyonun tanımlanması durumunda ortalama hata minimize olmuştur. Üyelik fonksiyonun artması ile tanımlanan kural sayısı da artmaktadır. Mimarideki karmaşıklığın artmasına bağlı olarak ortalama hata değerleri üyelik fonksiyonun artışı ile artış göstermiştir. Ayrıca, üyelik fonksiyonu artışı yakınsama kriterine ulaşma süresini uzatmaktadır. Dolayısı ile hem zaman maliyetini hem de hatayı minimize etmek için üyeli fonksiyonu sayısı düşük tutulmalıdır. 3x3 kurallı doğrusal çıkışlı ANFIS modelinin, simülasyon verisine göre ortalama hata değeri %2'nin altına düşmektedir.

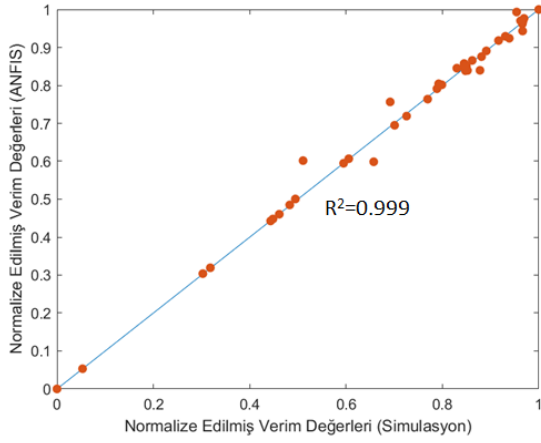


Şekil 11. Ortalama hata değerinin üyelik fonksiyonu sayısına oranı

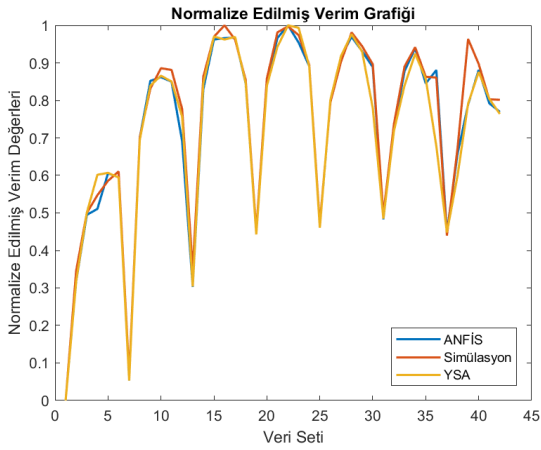
Şekil 12'de optimize edilen ANFIS mimarisi çıktıları ile simülasyon verileri hem eğitim hem test verileri için karşılaştırılmıştır. R^2 değeri 0.999, ortalama hata ise %1.41 olarak hesaplanmıştır.

ANFIS ve YSA Sonuçlarının Kıyaslanması

Şekil 13'de Simülasyon verim eğrisi ile birlikte YSA ve ANFIS verim tahminlemesi değerleri verilmiştir. Her iki yaklaşım ile de verim değişimi gözlemlenebilmekte beraber YSA metodu düşük ya da yüksek tahminleme yaparken ANFIS ile verim dağılım davranışı sayısal sonuçlara daha uyumlu gözlemlenmektedir.



Şekil 12. Simülasyon verisi ve ANFIS tahmin değerleri karşılaştırılması

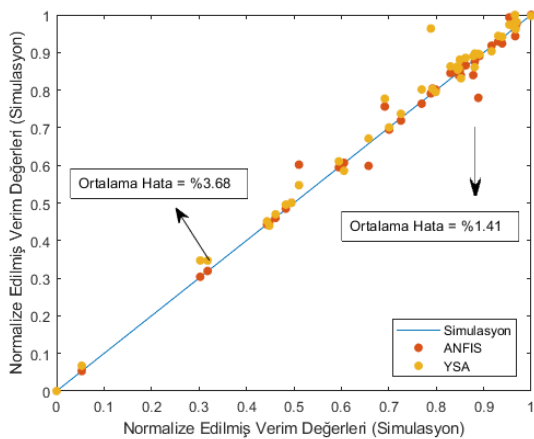


Şekil 13. Normalize edilmiş Verim eğrileri

ANFIS ve YSA modellerinin istatistiksel kıyaslamaları Tablo 5’de gösterilmektedir. Hesaplanan hata değerlerine ve R^2 değerlerine göre ANFIS modelinin daha iyi sonuç verdiği görülmektedir.

Tablo 5. YSA ve ANFIS metodlarının performans kıyaslaması

| | YSA | ANFIS |
|-----------------------------|--------|--------|
| Ortalama Hata Değeri | 3.77 | 1.41 |
| Maksimum Hata Değeri | 27.28 | 16.98 |
| R^2 | 0.9971 | 0.9992 |



Şekil 14. YSA ve ANFIS metodu ile elde edilen normalize verilerin sayısal veriler ile kıyaslanması

Şekil 14’de her iki metot ile de elde edilen normalize edilmiş veriler sayısal veriler üzerinde gösterilmektedir. ANFIS yaklaşımı ile verilerdeki sapmanın daha az olduğu ve sayısal veriler ile daha uyumlu olduğu gözlemlenmektedir.

BULGULAR

Su türbinleri tasarım debi ve düşüsü esas alınarak tasarlansalar dahi; mevsimsel yağış dalgalanmaları, zaman bağlı elektrik ihtiyacı farklılıkları sebebiyle tasarım noktası dışında da kısmi yüklemeler şartlarında çalıştırılabilmektedir. Beklendiği üzere türbinlerin farklı çalışma koşullarında verimleri ve güç üretimleri değişiklik göstermektedir. Bu sebep ile türbin tasarımı yapılırken kısmi yüklemeler koşullarındaki türbin performansı irdelenmekte ve kısmi performansı olabildiğince tasarım noktasına yakın güç ve verim değerlerinde tasarlamak hedeflenmektedir. Bu amaç doğrultusunda tasarımcılar tepe diyagramları oluşturmakta ve türbinin farklı debi ve düşü altındaki davranışını bu grafik üzerinden irdelemektedir. Tepe diyagramı oluşturulması deneysel ve sayısal olarak oldukça maliyetli bir süreçtir. Bu çalışma da tepe diyagramı elde etme sürecini kısaltmak ve deneysel ve sayısal sonuçlarla elde edilen verim değerleri ile tutarlı verimi değerleri elde etmek amacı ile YSA ve ANFIS metodları kullanılmıştır. YSA ve ANFIS metodları arasında yapılan kıyaslamaya göre parametre optimizasyonu yapıldığında ANFIS metodu YSA’ya göre daha yüksek doğrulukta yaklaşım sağlamaktadır. Ancak optimizasyon sürecinin iyi yönetilememesi durumunda (uygun üyelik fonksiyonu ve fonksiyon sayısının seçilememesi gibi) YSA metodunun daha yüksek doğrulukta sonuçlar vermesi mümkündür. Dolayısı ile parametre optimizasyonu yapmak gerekli bir çalışma olarak karşımıza çıkmaktadır.

YSA metodunda öğrenme algoritması, gizli katman sayısı, ANFIS metodunda ise üyelik fonksiyonu ve üyelik fonksiyonu sayısının çıktı üzerindeki etkileri irdelenmiştir. En hızlı yakınsama Bayesian Regulation eğitim algoritması ile elde edilmiştir. Sayısal sonuçlara yakın sonuçlara ise yine bu algoritma ile ulaşılmıştır. Ortalama hata oranı bu algoritma ile %3.77 değerine kadar düşürülmüştür. ANFIS metodunda sayısal çalışma ile en tutarlı sonuçlar Trimf üyelik fonksiyonu ile elde edilmiştir. Literatür irdelendiğinde ANFIS uygulamalarında en yaygın olarak bu üyelik fonksiyonunun kullanıldığı gözlemlenmiştir. Bu üyelik fonksiyonu ile ortalama hata % 1.41 değerine düşürülmüş R^2 değeri ise 0.999 olarak hesaplanmıştır. Yazarların bilgisine göre YSA ve ANFIS uygulamasının Francis tipi türbinlere uygulandığı ilk literatür araştırması bu çalışmadır. Elde edilen sonuçlar doğrultusunda ANFIS metodunun 1.41% ortalama hata ile sayısal sonuçlar ile tatmin edici tutarlılıkta verim tahminlemesi yaptığı görülmektedir. Dolayısıyla, yüksek zaman ve maliyetten kurtulmak ve yüksek mertebe doğrulukta bir tepe diyagramı oluşturmak ANFIS metodu ile sağlanabilmektedir.

REFERANSLAR

- Antonopoulos, V. Z., Papamichail, D. M., Aschonitis, V. G., & Antonopoulos, A. V. 2019, Solar radiation estimation methods using ANN and empirical models. *Computers and Electronics in Agriculture*, 160(March), 160–167.
- Ataseven, B. 2013, Yapay Sinir Ağları İle Öngörü Modellemesi. *Öneri Dergisi*, 10(39), 101-115–115. <https://doi.org/10.14783/od.v10i39.1012000311>.
- Anup, K. C., Bhola Thapa, and Young-Ho Lee.,2014, Transient Numerical Analysis of Rotor–Stator İnteraction in a Francis Turbine. *Renewable Energy*, cilt 65, Sf: 227-235.
- Ayancik F.,2014,Hesaplamalı Akışkanlar *Dinamiği Yardımıyla Su Türbini Çarkı Tasarımı Ve Eniyilemesi*, Yüksek Lisans Tezi, TOBB Fen Bilimleri Enstitüsü, Ankara, Türkiye
- Ayli, E., Kaplan, A., Cetinturk, H., Demirel, G., Celebioglu, K., Aradag, S., CFD Analysis of 3D flow for 1.4 MW Francis turbine and model turbine manufacturing, *35th Computers and Information in Engineering Conference*, August 2015,America.
- Ayli, E., 2016. Francis Tipi Türbinlerin Sayisal Yöntemler İle Tasarımı, Parametre Optimizasyonu Ve Model Testlerinin Sayisal Alt Yapısının Geliştirilmesi, *Doktora Tezi*, TOBB Fen Bilimleri Enstitüsü, Ankara, Türkiye
- Bisen, Ö., 2011 Üst Yapı İnşaat Projelerinde Öngörülme Endirekt Maliyetlerin Belirlenmesine Yönelik Bir Karar Destek Sistemi Oluşturulması, *Doktora Tezi*, İstanbul Kültür Üniversitesi Fen Bilimleri Enstitüsü, İstanbul, Türkiye.
- Celebioglu, K., Aradag, S., Ayli, E., Altintas, B. 2018. Rehabilitation of Francis Turbines of Power Plants with Computational Methods. *Hittite Journal of Science & Engineering*, 5(1), 37–48. <https://doi.org/10.17350/hjse19030000076>
- Ghosh, S., & Majumder, M. 2019, Prediction of Wave Energy Potential in India: A Fuzzy-ANN Approach. *Metaheuristics in Bioenergy Supply*, IntechOpen. DOI: 10.5772/intechopen.84676
- Gohil PP, Saini RP.2014, CFD: Numerical analysis and performance prediction in Francis turbine. *IEEE 1st International Conference on Non-Conventional Energy (ICONCE)*, pp:94-97.
- International Renewable Energy Agency. (2018). Renewable capacity statistics 2018 *Statistiques de capacité renouvelable Estadísticas de capacidad renovable 2018*.
- IRENA 2018. Renewable Power Generation Costs in 2017. In *International Renewable Energy Agency*. https://doi.org/10.1007/SpringerReference_7300
- Kurtgoz, Y., Karagoz, M., Deniz, E. 2017. Biogas engine performance estimation using ANN. *Engineering Science and Technology, an International Journal*, 20(6), 1563–1570. <https://doi.org/10.1016/j.jestch.2017.12.010>.
- Mensour, O. N., El Ghazzani, B., Hlimi, B., & Ihlal, A. 2017. Modeling of solar energy potential in Souss-Massa area-Morocco, using intelligence Artificial Neural Networks (ANNs). *Energy Procedia*, 139, 778–784. <https://doi.org/10.1016/j.egypro.2017.11.287>
- Okuy, G., 2010. *Utilization of CFD Tools in the Design Process of a Francis Turbine*, Yüksek Lisans Tezi, ODTÜ Fen Bilimleri Enstitüsü, Ankara, Türkiye
- Patel, K., Desai, J., Chauhan, V., Charnia, S. 2011, Development of Francis Turbine using Computational Fluid Dynamics. In *11st Asian International Conference on Fluid Machinery and 3rd Fluid Power Technology Exhibition* pp. 1-3.,
- Raju, D., Sumalatha,M. Ramani,Lakshmi, K.V. 2011 Solving Uncertain Problems using ANFIS. *International Journal of Computer Applications*, 29(11), 14–21. <https://doi.org/10.5120/3690-5152>
- Shukla, M. K., Jain, R., Prasad, V., Shukla, S. 2011. CFD Analysis of 3D Flow for Francis Turbine. *MIT International Journal of Mechancial Engineering*, Cilt:1, sf: 93-100.
- Terzi, Ü. K., Onat, N., & At, S. 2011. New Hybrid Method Proposal for Wind Speed Prediction : a Case Study of Lüleburgaz, *Environmental Research, Engineering and Management*, 1(1), 23–28.
- Türkiye Cumhuriyeti Enerji ve Tabii Kaynaklar Bakanlığı, “Enerji: Elektrik”, <https://www.enerji.gov.tr/tr-TR/Sayfalar/Elektrik>
- Vuraş, B.B., 2007, Yapay Sinir Ağları ile Finansal Tahmin,*Yüksek Lisans Tezi*, Ankaya Üniversitesi Sosyal Bilimler Enstitüsü, Ankara, Türkiye.
- Xie,G., Sunden, G., Wang, Q., Tang,L., 2009, Performance Predictions of Laminar and Turbulent Heat Transfer and Fluid Flow of Heat Exchangers Having Large Tube-Diameter and Large Tube-Row by Artificial Neural Networks, *International Journal of Heat and Mass Transfer*, vol:52,pp: 2484-2497.



Ece Aylı 1989 yılında Ankara'da doğdu. TOBB ETU Üniversitesi Mühendislik Fakültesi Makine Mühendisliği Bölümünden 2010 yılında mezun oldu. 2012 yılında TOBB ETU Üniversitesi Fen Bilimleri Enstitüsünde Yüksek Lisans, 2016 yılında aynı üniversiteden Doktora Derecesi aldı. 2018 yılından bu yana Dr. Öğretim Üyesi olarak Çankaya Üniversitesi Mühendislik Fakültesi Makine Mühendisliği Bölümünde çalışmaktadır. İlgili alanları, yenilenebilir enerji, Hesaplamalı Akışkanlar Dinamiği, Süpersonik akışlardır.



Oğuzhan Ulucak 1993 yılında Ankara'da doğdu. Selçuk Üniversitesi Mühendislik Fakültesi Makine Mühendisliği Bölümü'nden 2017 yılında mezun oldu. Halen Çankaya Üniversitesi Fen Bilimleri Enstitüsü Makine Mühendisliği alanında yüksek lisansını yapmaktadır. Akışkanlar mekaniği, Yenilenebilir enerji alanında çalışmalarına devam etmektedir.



FLOW AND FORCED HEAT TRANSFER FROM TANDEM SQUARE CYLINDERS NEAR A WALL

Özge YETİK* and Necati MAHİR**

***Eskişehir Osmangazi Üniversitesi, Mühendislik Mimarlık Fakültesi Makine Mühendisliği Bölümü
26480 Batımeşelik, Eskişehir
*oyetik@ogu.edu.tr, **nmahir@ogu.edu.tr

(Geliş Tarihi: 04.07.2019, Kabul Tarihi: 21.02.2020)

Abstract: In this study, the flow and heat transfer characteristics of two heated square cylinders in a tandem arrangement near a wall is investigated. The numerical computations are carried out by solving the unsteady two dimensional Navier-Stokes and energy equations. A fractional step method with Crank-Nicholson schema was employed to the convective and the viscous terms of the equations. At the inlet, fully developed laminar boundary layer is employed for longitudinal velocity over the plane wall while transverse velocity set to zero. The simulations are performed for Prandtl number (Pr) of 0.71 and Reynolds number (Re) of 150 where the flow is considered two dimensional. The flow field characteristics and heat transfer depend not only on the ratio of the space between the cylinders (L/D) but also on the distance between the cylinder center and the wall (G/D). The vorticity and isotherm curves are generated and discussed for various L/D and G/D ratios to clarify the connection with flow and heat transfer characteristics. When the cylinders are within the boundary layer formed on the plane wall, the large difference between the velocities at the upper and lower side of the cylinders leads to noticeable variation at the flow and heat transfer characteristics.

Keywords: Heat Transfer, Numerical Simulation, Tandem square cylinders, Wall effect.

DUVAR YAKININDA ART ARADA YERLEŞTİRİLMİŞ KARE KESİTLİ SİLİNDİRLER ETRAFINDA AKIŞ VE ZORLANMIŞ TAŞINIM İLE ISI GEÇİŞİ

Özet: Bu çalışmada bir duvar yakınında arka arkaya yerleştirilmiş ısıtılmış kare kesitli silindirler etrafındaki akışın karakteristiklerini ve ısı geçişi incelenmiştir. Hesaplamalar zamana bağlı 2-boyutlu Navier Stokes ve enerji denklemlerinin çözümü ile gerçekleştirilmiştir. Denklemlerin viskoz ve taşınım terimleri için Crank-Nicholson şeması ile birlikte kısmi adımlar metodu kullanılmıştır. Girişte duvara paralel hız bileşeni için tam gelişmiş laminar sınır tabaka kullanılmış, akışa dik yönde hız bileşeni sıfır olarak alınmıştır. Simulasyonlar 0.71 Prandtl (Pr) sayısı ve akışın iki boyutlu olduğu Reynolds (Re) sayısının 150 değeri için gerçekleştirilmiştir. Akış karakteristikleri ve ısı geçişi yalnızca silindirler arasındaki uzaklık (L/D) ye değil aynı zamanda silindirlerin merkezi ile duvar arasındaki uzaklığa da (G/D) bağlıdır. Akış ve ısı geçişi arasındaki bağlantıyı ortaya çıkarmak için değişik L/D ve G/D oranları için çevrinti ve eş sıcaklık eğrileri elde edilmiş ve tartışılmıştır. Silindirler duvardan oluşan sınır tabakanın içerisinde kaldığında, silindirlerin üst ve alt yüzeyindeki hızlar arasındaki büyük fark akış ve ısı geçiş parametrelerinde önemli değişimlere neden olmuştur.

Anahtar Kelimeler: Isı geçiş, sayısal simulasyon, art arda kare kesitli silindirler, duvar etkisi.

NOMENCLATURE

| | | | |
|-------|--|-----|--|
| C_D | drag coefficient | L | distance between cylinders [m] |
| C_L | lift coefficient | Lap | laplacian |
| D | cylinder length [m] | n | time step |
| f | vortex shedding frequency [Hz] | Nu | Nusselt number [= hD/k] |
| F_D | drag force [N] | P | dimensionless pressure [= $P^*/\rho U^2$] |
| F_L | lift force [N] | Pr | Prandtl number [= ν/α] |
| G | gap between cylinder center and the plane wall [m] | r | normal direction |
| Grad | gradient | Re | Reynolds number [= UD/ν] |
| H | advection | St | Strouhal number [= fD/U] |
| h | local heat transfer coefficient [W/m^2K] | T | dimensionless temperature [$(T^* - T_\infty^*) / (T_w^* - T_\infty^*)$] |
| k | conductivity [W/mK] | t | dimensionless time [= t^*U/D] |
| | | U | average velocity (m/s) |

| | |
|-------|--|
| u | dimensionless axial velocity component [= u^*/U] |
| u_c | average velocity [m/s] |
| V | dimensionless velocity [= V/U] |
| v | dimensionless normal velocity component [v^*/U] |
| x | dimensionless axial coordinate [= x^*/D] |
| y | dimensionless normal coordinate [= y^*/D] |

Greek symbols

| | |
|----------|---|
| α | thermal diffusivity [m^2/s] |
| δ | boundary layer thickness [m] |
| Φ | pressure correction |
| ϕ | intermediate velocity and pressure correction |
| ν | kinematic viscosity [m^2/s] |
| ρ | density [kg/m^3] |
| τ | shear stress [Pa] |

Subscripts

| | |
|----------|---------------------|
| b | back surface |
| f | front surface |
| rms | root mean square |
| tp | top surface |
| w | wall |
| 1 | upstream cylinder |
| 2 | downstream cylinder |
| ∞ | free stream |

INTRODUCTION

Unsteady flow around the bluff bodies are extensively studied in the past because of their many practical applications. Heat exchangers, offshore pipelines in close proximity to the seabed, electronic cooling are some of the application areas encountered as tandem or side by side in arrangement. The succession of the two cylinders complicates the flow in the downstream region. Existence of the wall near these cylinders also leads the flow to become more complex. The heat transfer from the cylinders is also affected by the complex structure between the cylinders and in the downstream region. Much of the studies related to the flow around the bluff bodies are about a single cylinder located in a free stream. Robichaux et al. (1999), Franke et al. (1990), Shimizu and Tanida (1978), Sohankar et al. (1998) are studied 2-D and 3-D flow structures and the variation of flow parameters for the Reynolds number ranging from 100 to 250. Sharma and Eswaran (2004) studied flow structure from a square cylinder and the study also includes forced heat transfer for both uniform heat flux and constant cylinder temperature. The effects of the Reynolds and Prandtl number on the heat transfer from a square cylinder also investigated by Sahu et al. (2009) for constant cylinder temperature and heat flux.

The flow characteristics behind the cylinder placed near a plane wall have been studied by many researchers (Bhattacharyya and Maiti (2004), Malavasi and Trabucchi (2008), Samani and Bergstrom (2015), Wang and Tan (2008), Mahir (2009)). Studies focus mainly on interactions of shear layers formed from both cylinder

and wall when the cylinders placed near the wall. Wang and Tan (2008) investigated flow characteristics behind a circular cylinder placed close to wall at the difference boundary layer thicknesses (δ) for Reynolds number (Re) of 1.2×10^4 . They observed Karman-like vortex shedding for the distances between the cylinder and wall (G/D) is larger than 0.3, however the wake is asymmetric about the cylinder centerline for $G/D \leq 0.6$. Mahir (2009) focused on the 3-D flow and investigated the vortex structure and unsteady forces on the square cylinder placed close to the plane wall. In this study the Reynolds number range was 155-250 where between the transition from 2-D to 3-D flow takes place. Wang et al. (2014) studied flow around a square cylinder near a plane wall for $Re = 6300$. They categorized flow structure relating to cylinder-wall spacing.

For tandem arrangements, the flow structures are more complicated than the single one due to the unsteady flow between the cylinders and in the gap region of cylinders-wall. The studies on the tandem cylinders mostly focus on the identification of flow structures. Chatterjee and Mondal (2012) performed numerical simulations to investigate forced convective heat transfer from isothermal tandem cylinders in the free stream of air. In their study Reynolds number ranges from 50 to 150 while the gap between the cylinder varies from 1D to 10D. They observed a discontinuous jump at the drag coefficient on the downstream cylinder at the critical cylinder spacing where vortex formed between cylinder. Time average drag coefficients and Nusselt numbers have higher values on the upstream cylinder than that on downstream. Sohankar and Etmnan (2009) performed numerical simulation on the flow characteristics and heat transfer over isothermal tandem square cylinders. They ranged the Reynolds number from 1 to 200 while keeping the cylinder spacing and the Prandtl number (Pr) constant as 5D and 0.71, respectively. They found that the heat transfer is higher from the front surface while is the lowest on the back surface. At the given cylinder spacing, heat transfer from upstream cylinder was relatively similar to that from the single cylinder. Mahir and Altaç (2008) performed numerical simulation to study convective heat transfer from isothermal tandem cylinders. They changed the distance between the cylinders in the range of 2D-10D while keeping the Reynolds number as 100 and 200. They provide variation of local nusselt number on the cylinders during one period of vortex formation in the downstream region. Chatterjee and Amiroudine (2010) studied numerically mixed convection heat transfer from isothermal tandem cylinders. In the study, the cylinders were confined with the blockage ratio of 10% and the Reynolds number was in the range of $1 \leq Re \leq 30$. They also changed Prandtl and Richardson number (Ri) in the range of $0.7 \leq Pr \leq 100$ and $0 \leq Ri \leq 1$ respectively.

There are very few investigations on the tandem cylinders near the wall. The numerical studies were performed with uniform flow or a uniform shear assumption at the inlet of computational domain. Tang et al. (2015) investigated flow structure behind the tandem

circular cylinders near the wall. In the study, they changed the gap between the wall and cylinders in the range of 0.25D-2.0D, and the distance between the cylinders as 1.0D- 4.0D while keeping the Reynolds number fixed at 200. They classified the vortex structures as no shedding mode, one-wake mode and two-wake mode. Harichandan and Roy (2012) performed a numerical study to investigate the behavior of the vertical wake behind a single and tandem cylinders placed in the boundary layer of a wall for Reynolds number of 100 and 200. They changed the gap between the wall and cylinders in the range of 0.2D-2.0D by maintaining the gap between the cylinders as 2D and 5D. They compared their result with a single cylinder near the wall and observed that flow structure in the downstream region of the tandem cylinders in the vicinity of a plane wall shows a stronger dependence on Reynolds number than gap ratio compared to that of a single cylinder. Raiola et al. (2016) experimentally investigated the near wake of two circular tandem cylinders near the wall for Reynolds number of 4.9×10^3 . They chose the distance between the cylinders as 1.5D, 3D and 6D, and the cylinder-wall gap as 0.3D, 1D and 3D. For 1D wall-to-cylinder distance, the ground has strong effect on the flow field with introducing Von Kármán type wake. For the gap 0.3D, a flapping jet-type like structure forms from the gap between the cylinders and wall.

Foregoing studies deal with mainly the heat transfer from tandem cylinders in a uniform flow field and/or the flow around a single cylinder near a plane wall. The boundary layer formed on the wall close to the tandem cylinders also contributes the complexity of flow around the cylinders and convective heat transfer from them. To the best of our knowledge, we have not come across publications on the heat transfer from the cylinders in a tandem arrangement near a wall. Thus, the influence of wall proximity on heat transfer from the tandem cylinders in conjunction with the flow needs to be investigated. For this purpose; in this study the flow and convective heat transfer from tandem cylinders within and outside of an oncoming boundary layer are studied for air flow. The flow and heat transfer characteristic are computed and analyzed for the cylinder spacing (L/D) 1.5, 2.5, and 4, and cylinder center to wall distances (G/D) 0.7, 1, 1.5, 2, 2.5, 3, 3.5, 4 and 6.

GOVERNING EQUATIONS AND NUMERICAL METHOD

The transition from 2-D to 3-D takes place at the Reynolds number of about 165 (Mahir, 2009) for flow around a single cylinder. Therefore, in this study Reynolds number kept constant at 150 where the flow is 2-D. The unsteady dimensionless form of the 2-D Navier-Stokes and the energy equations are given as:

$$\frac{\partial u}{\partial x} + \frac{\partial v}{\partial y} = 0 \quad (1)$$

$$\frac{\partial u}{\partial t} + u \frac{\partial u}{\partial x} + v \frac{\partial u}{\partial y} = -\frac{\partial p}{\partial x} + \frac{1}{\text{Re}} \left(\frac{\partial^2 u}{\partial x^2} + \frac{\partial^2 u}{\partial y^2} \right) \quad (2)$$

$$\frac{\partial v}{\partial t} + u \frac{\partial v}{\partial x} + v \frac{\partial v}{\partial y} = -\frac{\partial p}{\partial y} + \frac{1}{\text{Re}} \left(\frac{\partial^2 v}{\partial x^2} + \frac{\partial^2 v}{\partial y^2} \right) \quad (3)$$

$$\frac{\partial T}{\partial t} + u \frac{\partial T}{\partial x} + v \frac{\partial T}{\partial y} = \frac{1}{\text{RePr}} \left(\frac{\partial^2 T}{\partial x^2} + \frac{\partial^2 T}{\partial y^2} \right) \quad (4)$$

where u and v are the dimensionless velocity components, T and p is the dimensionless temperature and pressure in the fluid respectively, t presents the dimensionless time. Prandtl number defined as $\text{Pr} = \nu/\alpha$, where ν is kinematic viscosity and α is thermal diffusivity. Re defined with respect to cylinder length D . Nondimensional form of the variables defined as

$$u = \frac{u^*}{U}, \quad v = \frac{v^*}{U}, \quad p = \frac{p^*}{\rho U^2}, \quad t = \frac{t^* U}{D}, \quad x = \frac{x^*}{D}, \quad y = \frac{y^*}{D},$$

$$T = \frac{T^* - T_\infty^*}{T_w^* - T_\infty^*}$$

where U is the average velocity and ρ is the density.

The numerical method presented here was used by one of the authors (Mahir, 2009) before for simulation of a single cylinder near a wall. In this study, the method is modified for tandem cylinders in proximity of a wall. Eqs. (1)-(4) were solved applying a fractional step method (Armfield and Street, 2000) including Crank-Nicolson scheme at the discretization of the convective and viscous terms in the momentum equation. The intermediate velocities are expressed as

$$\frac{V^{n+1/2} - V^n}{\Delta t} + \left[\frac{1}{2} H(V^{n+1/2}) + \frac{1}{2} H(V^n) \right] =$$

$$-Grad(p^n) + \frac{1}{\text{Re}} \left[\frac{1}{2} Lap(V^{n+1/2}) + \frac{1}{2} Lap(V^n) \right] \quad (5)$$

where H is the advection, $Grad$ is the gradient, Lap diffusion operator and n is the time step. The nonlinear convective terms are linearized as

$$H(V^{n+1/2}) \cong (V^n \nabla) V^{n+1/2} \quad (6)$$

The Poisson equation for the pressure correction, Φ , is expressed as

$$Lap \Phi = \frac{1}{\Delta t} \Delta V^{n+1/2} \quad (7)$$

At the next time step, the velocity and the pressure are evaluated as

$$V^{n+1} = V^{n+1/2} - \Delta t Grad \Phi \quad (8)$$

$$p^{(n+1)} = p^n + \Phi \quad (9)$$

Staggered grid has been used for solving pressure, velocity and temperature components in the equations. In both momentum and energy equations, a third order upwind scheme was applied to discretize the first order derivatives in the convective terms, whereas the central-difference formula was employed for the second-order derivatives in the viscous terms. Poisson-type equations were solved using the Jacobi method with Chebyshev acceleration procedure (Mahir, 2009).

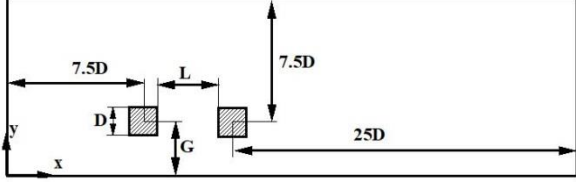


Figure 1. Computational domain and boundary locations.

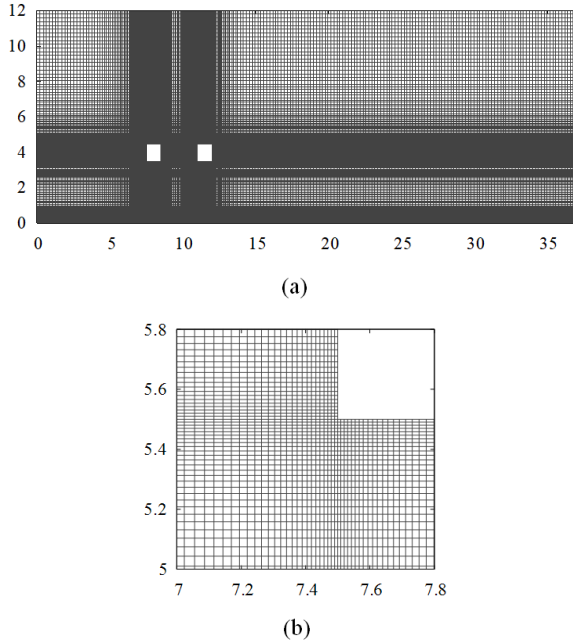


Figure 2. Grid distribution in the computation domain (a), and close-up the upstream cylinder (b).

The inflow, lateral and outflow boundaries were determined according to the Lei et al. (2000) suggestions, so that they have negligible effects on the calculated flow and heat transfer characteristics. While the upstream cylinder is placed $7.5D$ far from the inlet, out plane is located $25D$ away from the downstream one (Figure 1). The grid distribution in the computation area with the close-up view of a near corner of the upstream cylinder is presented in Figure 2. Near the cylinder walls as well as over the plane wall, dense grids are used and grid is generated in the flow field as follows. The distance of the two consecutive grid lines was determined from a geometric series. The stretching ratio ($\Delta x_i / \Delta x_{i-1}$, $\Delta y_i / \Delta y_{i-1}$) at front and bottom of the cylinders was 0.9, while it was 1.1 at behind and over the cylinders. Grid over the plane wall is also generated with the stretching ratio of 1.1 (Mahir, 2009).

For each time step, the convergence of the iterations were determined as

$$\sum_{i,j} \frac{(\phi_{i,j}^n - \phi_{i,j}^{n-1})^2}{(\phi_{i,j}^n)^2} < 5 \times 10^{-5} \quad (10)$$

where n is time step and ϕ is the intermediate velocity and pressure correction.

At the inlet, fully developed laminar boundary layer with a third order Blasius velocity profile (Schlichting, 1979) is employed for longitudinal velocity over the plane wall. Besides, dimensionless transverse velocity and temperature also set to zero. Other boundary conditions are stated as:

No-slip condition and constant temperature on the cylinders surfaces $u = 0$, $v = 0$, $T = 1$.

No-slip condition on adiabatic plane wall (at $y = 0$)

$$u = 0, v = 0, \partial T / \partial y = 0.$$

Free slip on top boundary

$$\partial u / \partial y = \partial T / \partial y = 0, v = 0.$$

To minimize the distortion of the vortices at the exit, the outflow velocity is set to $\partial u / \partial t + u_c \partial u_i / \partial x_i = 0$,

where u_c is average velocity. The boundary condition

for the temperature is $\partial T / \partial x = 0$.

Drag and Lift force coefficients are obtained from the following expressions respectively

$$C_D = \frac{F_D}{\frac{1}{2} \rho U^2 D} \quad (11)$$

$$C_L = \frac{F_L}{\frac{1}{2} \rho U^2 D} \quad (12)$$

where both drag (F_D) and lift forces (F_L) are calculated by integrating the pressure and shear stresses on the cylinder surfaces.

$$F_D = \int_0^D (\tau_{tp}(x) + \tau_b(x)) dx + \int_0^D (P_f(y) + P_r(y)) dy \quad (13)$$

$$F_L = \int_0^D (\tau_f(y) + \tau_r(y)) dy + \int_0^D (P_{tp}(x) + P_b(x)) dx \quad (14)$$

At the equations; f , r , tp and b indicate the front, back, top and bottom surface of the cylinder. Mean values are calculated by taking average of the time history of drag, lift coefficient and Nusselt number.

The local Nusselt number (Nu) based on the cylinder length is given as

$$Nu = \frac{hD}{k} = -\frac{\partial T}{\partial r} \quad (15)$$

where r is the direction normal to the cylinder surface, h is the local heat transfer coefficient and k is the thermal conductivity of fluid. The Strouhal number is expressed as follows:

$$St = \frac{fD}{U} \quad (16)$$

where f is the vortex shedding frequency.

The accuracy of the current program was verified by simulating a single cylinder and tandem cylinders in a free stream. First, the flow and heat transfer over the tandem cylinders were simulated. To determine the effects of different grid structures on the calculated values, the distance between the cylinders was taken as $0.5D$ at which no vortex formed, and $7D$ at which the vortex formed between them. The variation of the mean force coefficients, Nusselt and Strouhal numbers (St) with minimum grid spacing over the walls is presented in table 1 (Yetik, 2013) where the subscripts 1 and 2

correspond to upstream and downstream cylinders respectively. For both gap ratios, the smaller differences were obtained between the cases B and C. For $L/D = 0.5$, the mean values of C_{D1} and C_{D2} were 0.005 and 0.001 respectively while they were 0.003 for $L/D = 7$. Similarly, the differences at the Nu_{mean1} and Nu_{mean2} observed as 0 and 0.004, respectively, for $L/D = 0.5$. These values were 0.004 and 0.002, respectively, for $L/D = 7$. Therefore, case B is preferred at the simulations for accuracy with a convenient grid structure. Time step of $\Delta t = 0.05$ was determined to be optimum value and employed at the rest of the simulations.

The flow and heat transfer characteristics over a square cylinder were also obtained by using the same grid structure referred for tandem cylinders and the results were compared with some the existing literature values (Tables 2-4). It is observed that the computed flow and heat transfer characteristics were in the range of the values given in the literature.

Table 1. Grid independence test for tandem cylinders in uniform flow at $Re = 150$.

| Grid | L/D | Minimum grid interval | Grid | C_{Dmean1} | C_{Dmean2} | CL_{mean1} | CL_{mean2} | Nu_{mean1} | Nu_{mean2} | St |
|------|-----|-----------------------|----------|--------------|--------------|--------------|--------------|--------------|--------------|-------|
| A | 0.5 | 0.020 | 235× 153 | 1.382 | -0.177 | 0.0239 | -0.00040 | 4.139 | 1.831 | 0.152 |
| B | | 0.010 | 340× 205 | 1.375 | -0.169 | 0.0196 | -0.00016 | 4.151 | 1.837 | 0.154 |
| C | | 0.008 | 486× 265 | 1.380 | -0.170 | 0.0174 | -0.00021 | 4.151 | 1.833 | 0.153 |
| A | 7 | 0.020 | 309× 153 | 1.467 | 0.957 | 0.0245 | 0.0184 | 4.766 | 4.463 | 0.158 |
| B | | 0.010 | 426× 205 | 1.463 | 0.931 | 0.0205 | 0.0166 | 4.790 | 4.409 | 0.162 |
| C | | 0.008 | 582× 265 | 1.466 | 0.928 | 0.0187 | 0.0154 | 4.794 | 4.407 | 0.159 |

Table 2. Comparison of C_{Dmean} values for single cylinder in uniform flow.

| Re | Present study | Franke et al. (1990) | Shimizu et al.(1978) | Sharma et al. (2004) | Sohankar et al. (2009) | Sohankar et al. (1998) | Sohankar et al. (1995) | Chatterjee et al. (2009) | Sahu et al. (2009) |
|-----|---------------|----------------------|----------------------|----------------------|------------------------|------------------------|------------------------|--------------------------|--------------------|
| 100 | 1.51 | 1.62 | 1.58 | 1.5 | 1.48 | 1.48 | 1.48 | 1.52 | 1.49 |
| 120 | 1.48 | 1.59 | 1.54 | 1.45 | 1.45 | 1.45 | 1.42 | 1.47 | |
| 140 | 1.48 | 1.57 | 1.51 | 1.46 | 1.44 | 1.44 | 1.42 | 1.48 | |
| 150 | | 1.56 | 1.5 | 1.47 | | 1.44 | 1.41 | | |
| 160 | 1.48 | | | 1.47 | 1.45 | | | 1.5 | 1.46 |

Table 3. Comparison of Strouhal number values for single cylinder in uniform flow.

| Re | Present study | Luo et al. (2003) | Sharma et al. (2004) | Sohankar et al. (2009) | Sohankar et al. (1997) | Chatterjee et al. (2009) | Sahu et al. (2009) |
|-----|---------------|-------------------|----------------------|------------------------|------------------------|--------------------------|--------------------|
| 100 | 0.151 | 0.147 | 0.149 | 0.146 | 0.143 | 0.145 | 0.148 |
| 120 | 0.155 | 0.155 | 0.155 | 0.154 | 0.149 | 0.151 | |
| 140 | 0.159 | 0.159 | 0.158 | 0.158 | 0.154 | 0.156 | |
| 160 | 0.162 | 0.157 | 0.159 | 0.161 | 0.156 | 0.159 | 0.16 |

Table 4. Comparison of mean Nu values for single cylinder in uniform flow.

| Re | Present study | Sharma et al. (2004) | Sohankar et al. (2009) | Chatterjee et al. (2009) | Sahu et al. (2009) |
|-----|---------------|----------------------|------------------------|--------------------------|--------------------|
| 100 | 4.02 | 4 | 4.2 | 4.05 | 4.3 |
| 120 | 4.36 | 4.4 | 4.5 | 4.45 | 4.7 |
| 140 | 4.66 | 4.75 | 4.75 | 4.75 | 5 |
| 160 | 4.93 | 5 | 5 | 5 | 5.3 |

RESULT AND DISCUSSION

To correlate flow structure with convective heat transfer from cylinders, the flow structure and isotherms around tandem cylinders near a wall were obtained. At the simulations, the variation of the lift and drag coefficients were provided for both cylinders. In addition to mean values, local Nusselt numbers on the cylinder surfaces also obtained.

Flow Structure and Isotherms:

In Figures 3 and 4, isovorticity curves and corresponding isotherms for various gaps (G/D) were given at the

cylinder to cylinder distances of (L/D) 1.5 and 4. These cylinder to cylinder spacing were selected such that the vortex forms between the cylinders and does not form. Left and right columns present the isovorticities and the isotherms respectively for the same instances. For $G/D = 0.7$ and 1.0, both cylinders were inside of the boundary layer formed on the plane wall surface (Figures 3a, b). For these cases, negative vorticities are observed to be dominant in the downstream region. For $G/D = 1$, weak vorticities form from down surface of the both cylinders and shear layer curls at the top side of downstream region. For $G/D = 1.5$, the cylinders are partially inside of the boundary layer. Again, the weak positive vortex forms from down surface of the cylinders. While positive shear layer rolls between the cylinders, it loses its strength in the downstream region and negative vortex becomes dominant. For larger cylinder wall spacing ($G/D \geq 2$), the cylinders are outside of the boundary layer formed on the plane wall and positive vorticities also appear in the wake region while boundary layer formed on the plane wall merges with the vorticities in the downstream region. The appearance of the isotherms behind the cylinders (right column) resemble to the isovorticity curves.

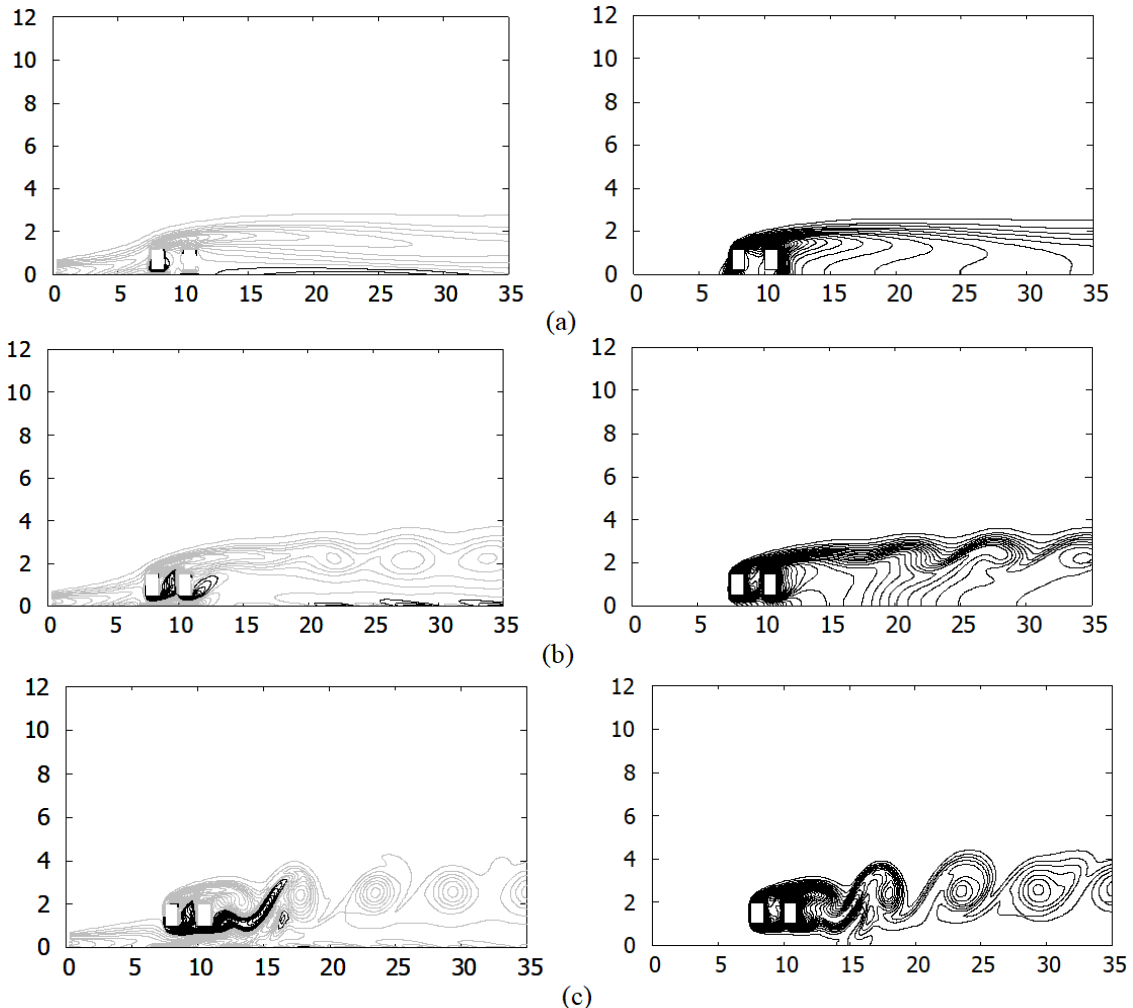
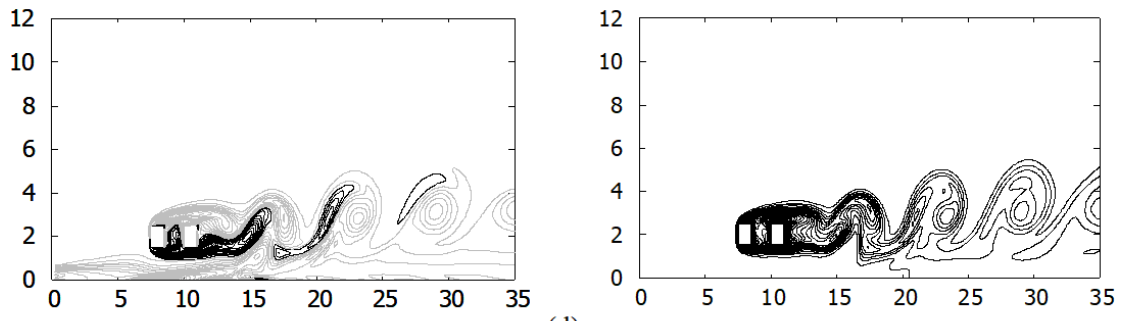
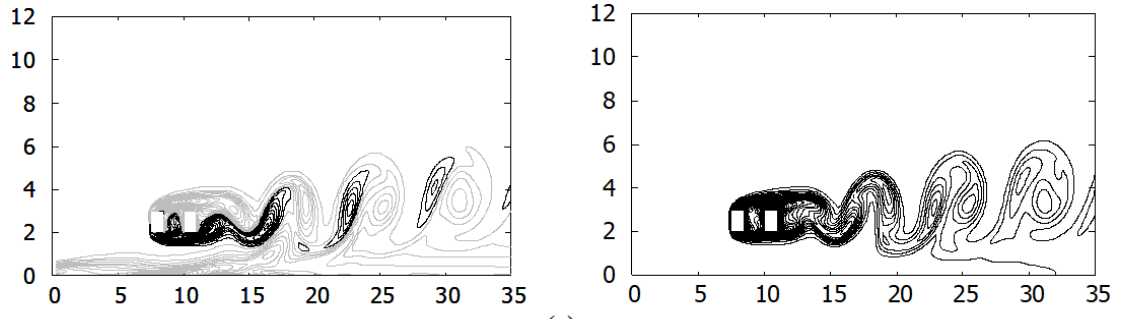


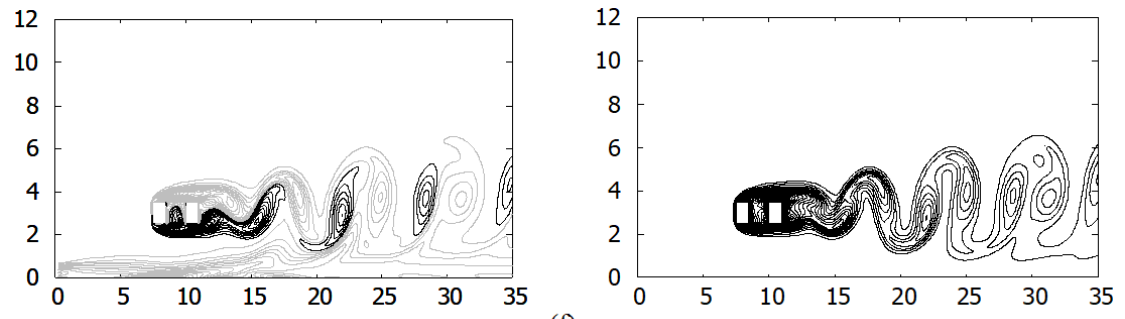
Figure 3. (cont.)



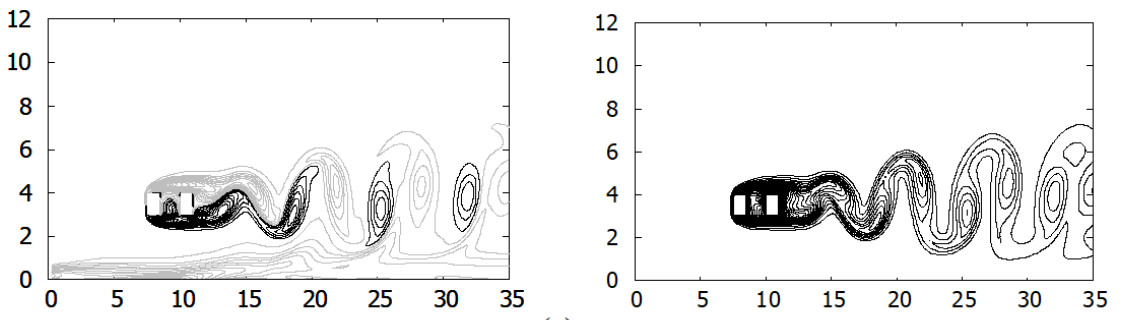
(d)



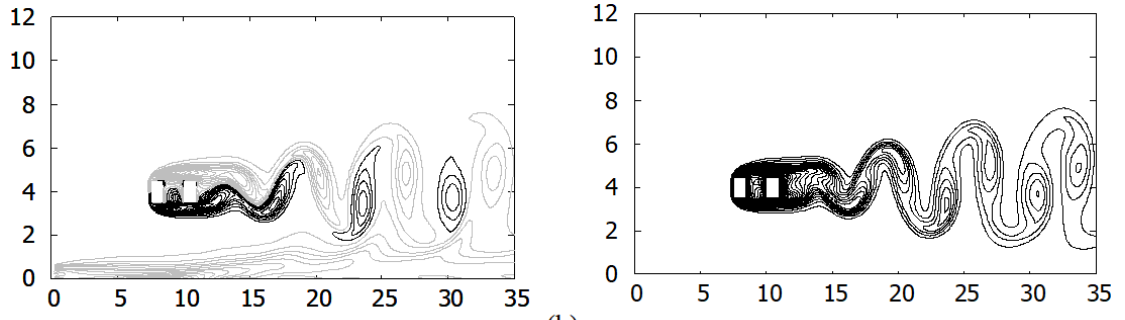
(e)



(f)

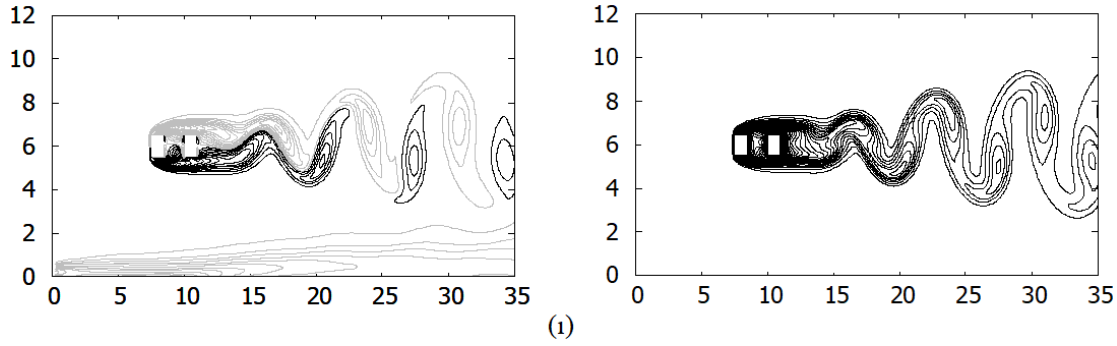


(g)

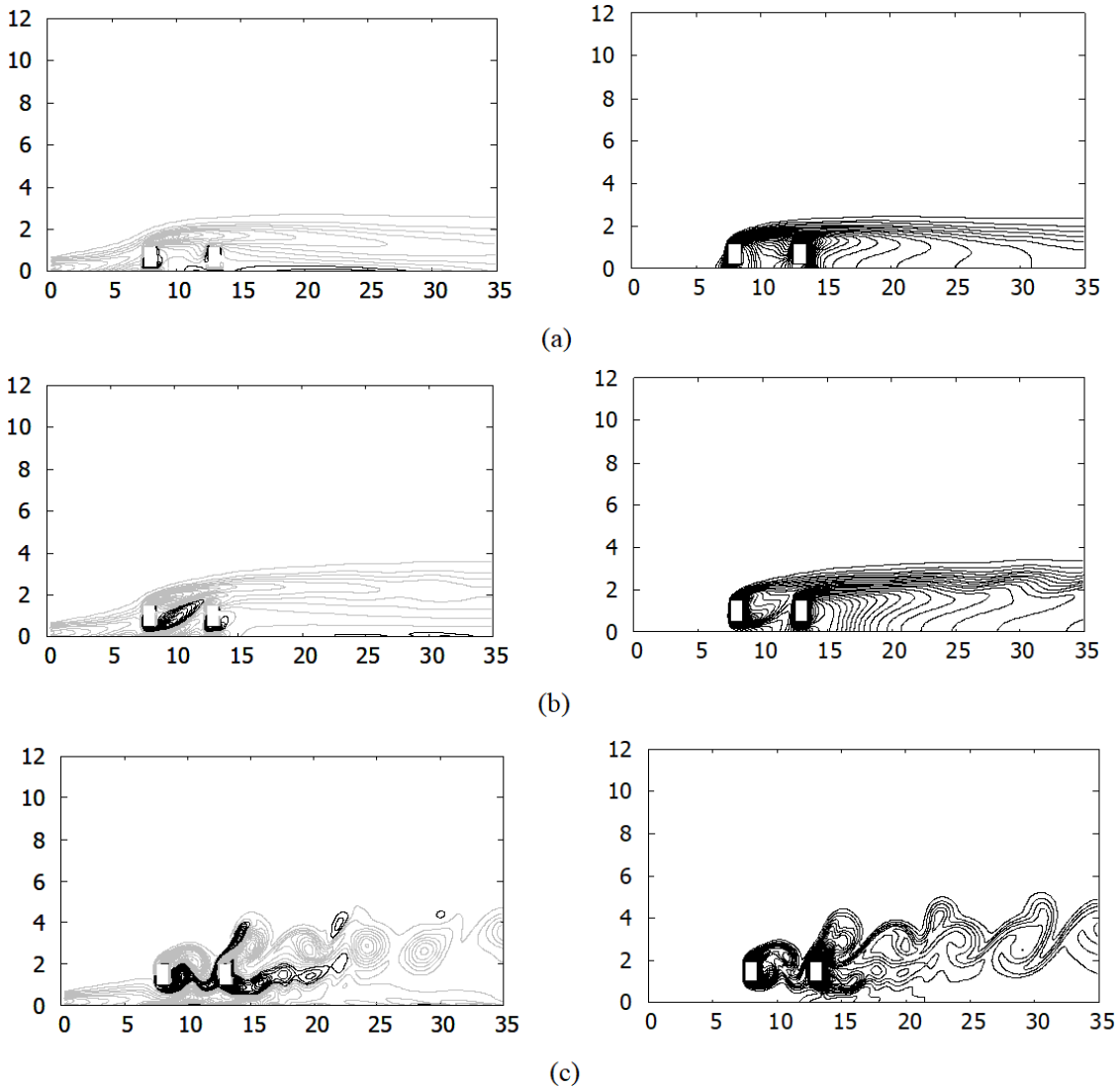


(h)

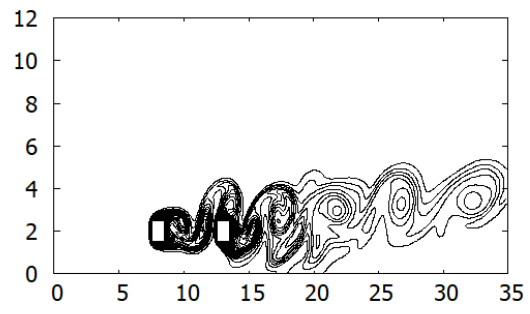
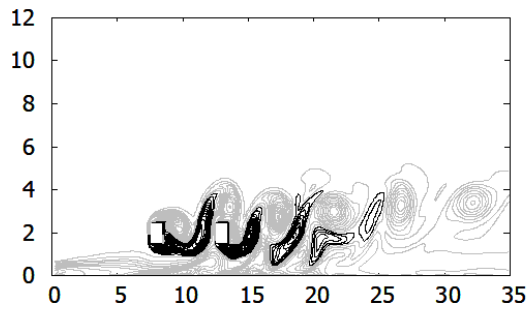
Figure 3. (cont.)



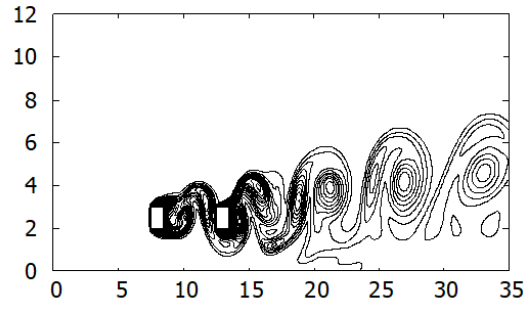
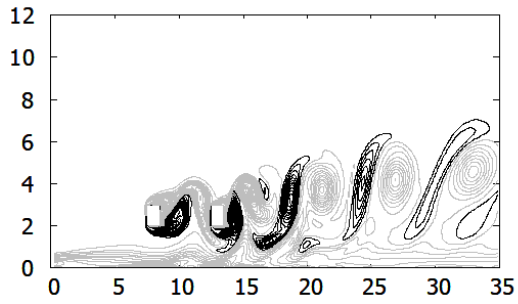
(1)
Figure 3. Vorticity for tandem arrangement of two cylinders with the wall ($L = 1.5 D$): a) $G/D = 0.7$, b) $G/D = 1$, c) $G/D = 1.5$, d) $G/D = 2$, e) $G/D = 2.5$, f) $G/D = 3$, g) $G/D = 3.5$, h) $G/D = 4$, i) $G/D = 6$. Gray and black lines present the negative and positive vorticities respectively. (Left and right columns present the isovorticities and the isotherms respectively. Axial and normal coordinates corresponds to x and y respectively.)



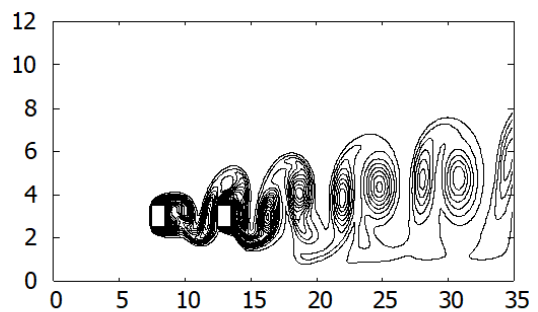
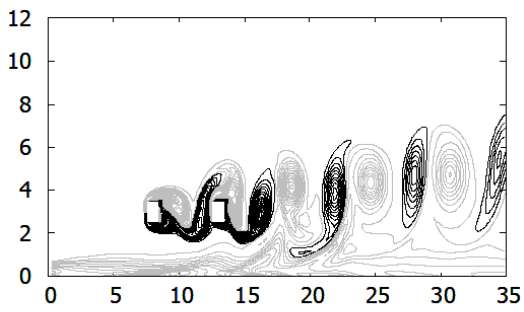
(a)
(b)
(c)
Figure 4. (cont.)



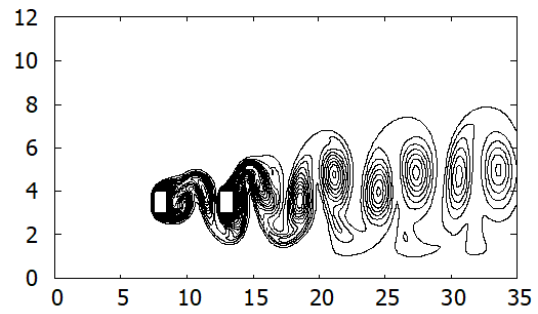
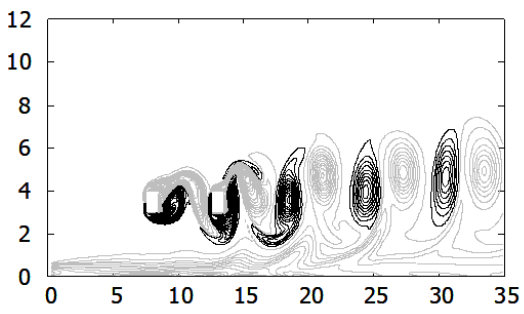
(d)



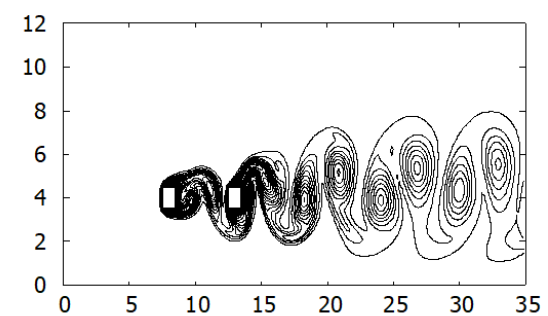
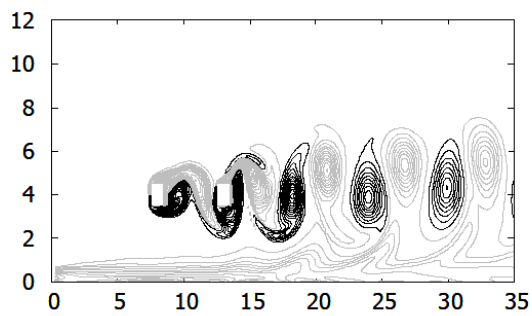
(e)



(f)



(g)



(h)

Figure 4. (cont.)

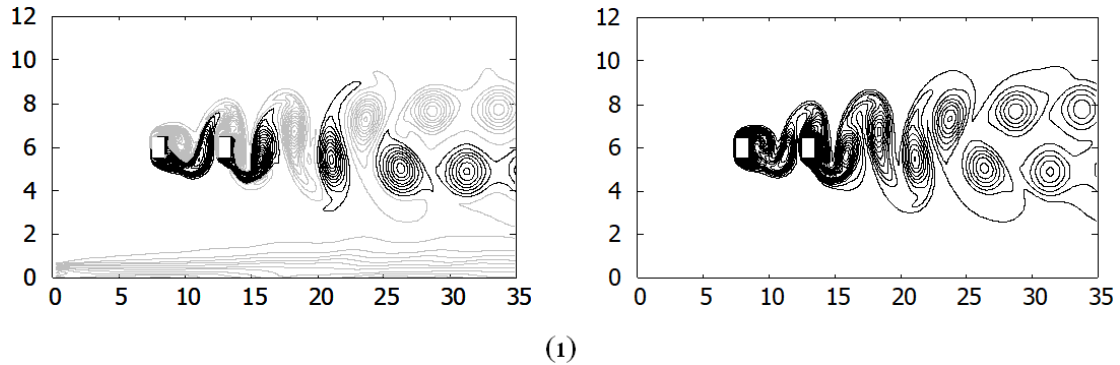


Figure 4. Vorticity for tandem arrangement of two cylinders with the wall ($L = 4D$): a) $G/D = 0.7$, b) $G/D = 1$, c) $G/D = 1.5$, d) $G/D = 2$, e) $G/D = 2.5$, f) $G/D = 3$, g) $G/D = 3.5$, h) $G/D = 4$, i) $G/D = 6$. Gray and black lines present the negative and positive vorticities respectively. (Left and right columns present the isovorticities and the isotherms respectively. Axial and normal coordinates corresponds to x and y respectively.)

In Figure 4, instantaneous vortex structure and isotherms were provided for larger spacing of the cylinders ($L/D = 4$). In small gaps ($G/D = 0.7$ and 1), the cylinders were within the oncoming boundary layer, and this leads to flow with smaller velocities around the cylinders, resulting suppression of vortex formation between the cylinders (Figures 4a, b).

For $G/D = 1.5$, although cylinders were partially inside of the oncoming boundary layer, the velocities around the cylinders were high enough to produce vortices in the gap of cylinders (Figure 4c) while positive vorticities formed from down edge of the cylinders disappear in the wake region where negative ones become dominant. For larger distances ($G/D \geq 2$), the positive vorticities diffuse further downstream region. It is evident that the weaker wall effect yields stronger positive vortex in the downstream of cylinders (Figures 4e-i). While regular type Karman vortex street formed in the wake of cylinder at $G/D = 2.5$ - 4 (Figures 4e-h), a pair of row with a positive and negative vortex lines observed at $G/D = 6$ (Figure 4i). At this cylinder to cylinder spacing, the isotherms between the cylinders and in the wake region similar to the isovorticity contours (Figure 4 left column).

Unsteady Forces

In Figure 5, mean and root mean square values of C_L on the both cylinders were provided for the range of cylinder spacing $L/D = 1.5, 2.5, 4$ and cylinder wall gap ratio of $G/D = 0.7$ - 6 . On the upstream cylinder, the mean lift coefficients reach their maximum values at $G/D = 0.7$ (Figure 5a), where the cylinders are inside the boundary layer formed on the plane wall (Yetik, 2013). Large differences between the velocities upper and lower side of the upstream cylinder lead to large deviations at $G/D = 0.7$. As G/D increases, the mean lift coefficient drops sharply. For $G/D \geq 2$, the cylinders were outside of the plane wall boundary layer so that the differences between the velocities upper and lower side of the cylinders were small and the mean lift coefficients on the upstream

cylinders takes small values. The lift coefficient reaches maximum values at $G/D = 1$ on the downstream cylinder. Large value of the mean lift coefficient observed on the downstream cylinder for $L/D = 1.5$ where boundary layer separated from upstream cylinder overshoot the downstream one (Figure 3). The root mean square values of the lift coefficients are more sensitive to cylinder-wall distances when cylinders are in boundary layer or partially in it (Figure 5b). For $G/D < 2$, C_{Lrms} values increase more rapidly with increasing G/D . For $G/D \geq 2$, these values are affected by the distance between the cylinders rather than the plane wall. The shear layer separated from upstream cylinder provides more oscillatory velocities and pressures on the upper and lower side of the downstream cylinder, resulting in larger C_{Lrms} values on the downstream cylinder.

The C_{Dmean} and C_{Drms} values obtained at different wall to cylinder distances are depicted in Figure 6 for $L/D = 1.5, 2.5$ and 4 . For upstream cylinders (Figure 6a), the variation of the C_{Dmean} value greatly depends on whether cylinder is inside or outside of the coming boundary layer. When the cylinder is within the boundary layer ($G/D \leq 1.5$), C_{Dmean} value increases with increasing G/D , while slightly decreases for $G/D > 1.5$. The C_{Dmean} value on the upstream cylinder slightly changes with L/D indicating that the flow structure between the cylinders has weak upstream effect on drag force. C_{Dmean} values on the downstream are more sensitive to flow between the cylinders. For $L/D \geq 2.5$, vortex forms between the cylinders and formed vortices strikes the front surface of downstream cylinder yielding larger C_{Dmean} mean values. The root mean square value of the drag force on the upstream cylinder is also slightly influenced by the flow between the cylinders while it take largest values at $L/D = 2.5$. C_{Drms} values on the downstream cylinder yields the largest values at $L/D = 2.5$ and 4 at which vortex street forms between the cylinders. When the cylinders are within the boundary layer, C_{Drms} value on the downstream cylinder increases rapidly as G/D increases (Figure 6b)

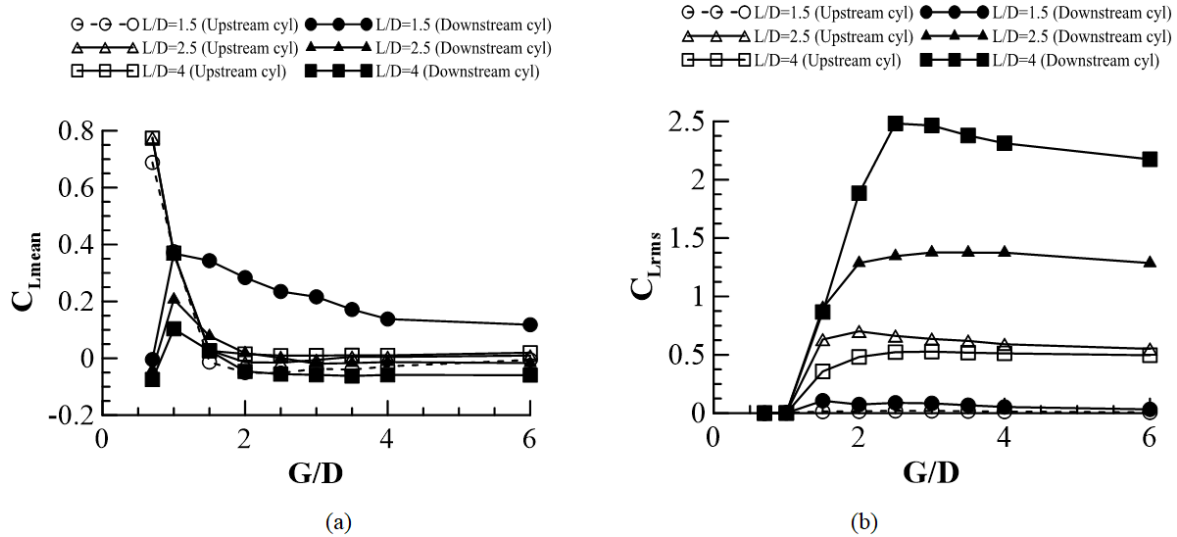


Figure 5. Variation of the mean lift coefficient (a), the root mean square value of lift coefficient (b) with the G/D values.

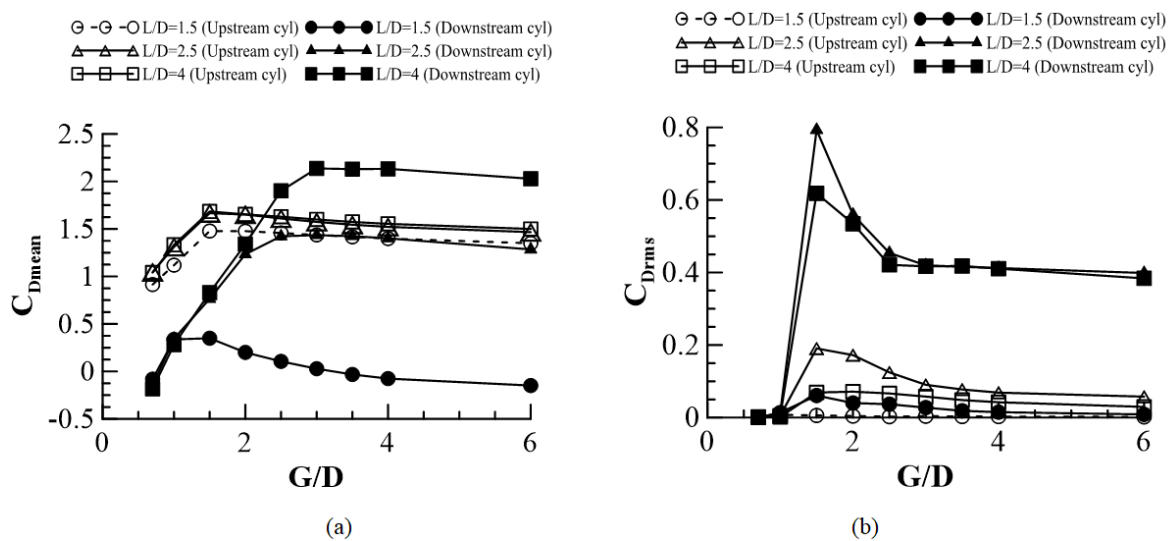


Figure 6. Variation of the mean drag coefficient (a), mean square value of drag coefficient (b) with the G/D values.

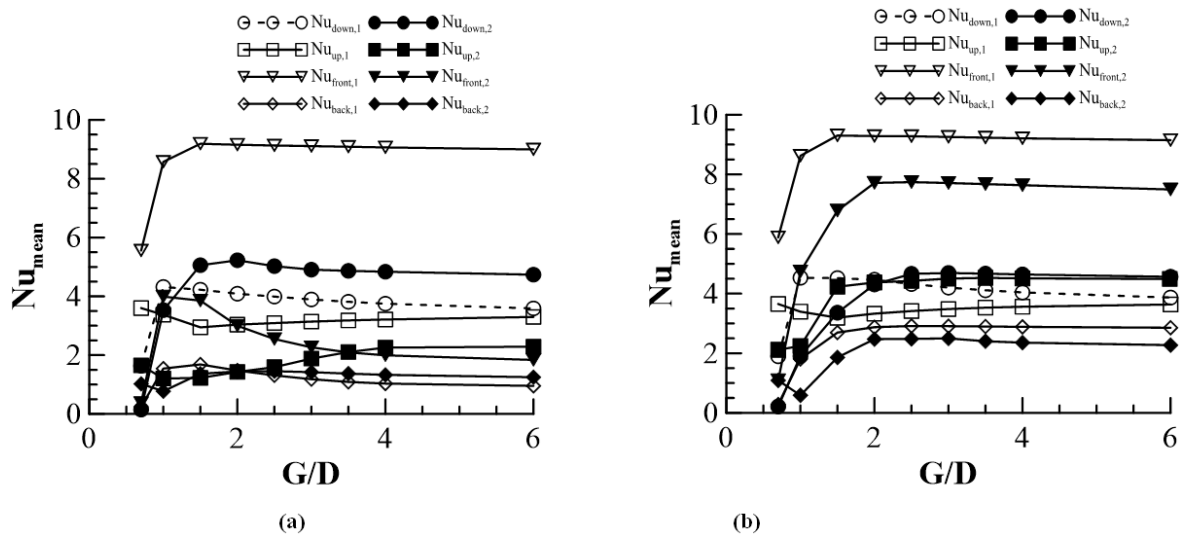


Figure 7. Variation of the Nusselt number for each of cylinder faces for $L/D = 1.5$ (a) and for $L/D = 4$ (b).

Variation of Mean Nusselt Number On The Cylinder Surfaces

Variation of the mean Nusselt number on the surfaces of up and downstream cylinders were provided in Figure 7 for $L/D = 1.5$ and 4. The heat transfer from cylinder surfaces sensitive to cylinder-plane wall distances. For $G/D \geq 2$ the mean Nusselt numbers on the back, up and down surface of the upstream cylinders are approximately same at both L/D ratios, indicating that when the cylinders are outside of the oncoming boundary layer, the distance between the cylinders do not have distinct effect on the heat transfer from these surfaces whereas the heat transfer from front surface is higher for $L/D = 4$. For both L/D ratios, the Nusselt number on the down surface of upstream cylinder is larger than that on the up one due to jet like flow between plane wall and cylinders. As the cylinder plane wall distance increases, the mean Nusselt values on the up surface of the upstream cylinder approximate those of the down surface. For downstream cylinders, the heat transfer from surfaces is largely dependent on the flow between the cylinders at $G/D \geq 2$. For $L/D = 1.5$, the Nusselt number on the front surface has relatively smaller values due to over shooting or reattachment flow between the cylinders (Figure 3), while it takes larger values for $L/D = 4$ where vortex forms between cylinders (Figure 4).

Local Nusselt Numbers On The Cylinder Surfaces

The convective heat transfer from cylinder surfaces also depends on the flow around the cylinders and between the cylinder-plane wall. Figures 8 and 9 present the variation of the mean Local Nusselt numbers on both cylinders with the plane wall distances for $L/D = 1.5$.

On the upstream cylinder, smaller values of Nusselt numbers were observed when the cylinders were inside the boundary layer formed on the plane wall $G/D = 0.7$ (Figure 8). On the down surface, it takes larger values at $G/D = 1$ due to jet like flow between cylinder and wall. At $G/D = 2$ and 4, the cylinders were outside the oncoming boundary layer, and the flow hits the front surface and deflects up and down, causing greater heat transfer near the corners of this surface.

For $G/D = 0.7$, the heat transfer from front and down surface of the downstream cylinder is approximately zero (Figure 9) due to very low flow velocities in the gap of downstream cylinder - plane wall. The Nusselt numbers take the maximum values on the front surface when the cylinders are still inside the oncoming boundary layer at $G/D = 1$. Further distance to plane wall leads to drop on the Nusselt number on this surface. For $G/D = 1, 2$ and 4; the greatest values of the Nusselt numbers were observed at the common edges of the front and bottom surface since the jet flow formed between the upstream cylinder and the plane wall directed to these surfaces (Figure 9). At the back and up surfaces Nusselt numbers are relatively small.

Figures 10 and 11 provide local Nusselt number variations on the cylinder surfaces for $L/D = 4$ where the vortex formed between the cylinders (Figure 4). For $L/D = 1.5$ and 4 cases, the comparison of Nusselt number variations on the upstream cylinder shows that the flow structure between the cylinders has negligible effect on the heat transfer from the front, bottom and top surfaces (Figures 8 and 10).

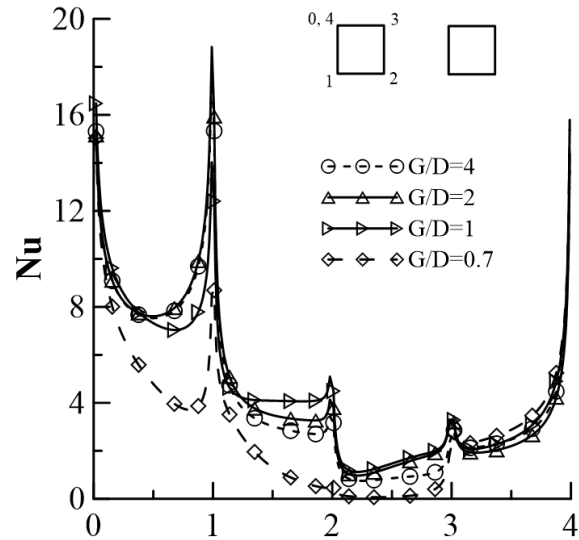


Figure 8. Local Nu values on the surfaces of upstream cylinder at $L/D = 1.5$, $G/D = 0.7, 1, 2,$ and 4.

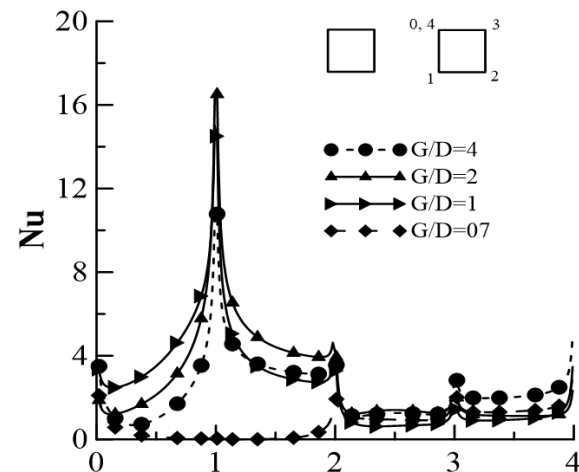


Figure 9. Local Nu values on the surfaces of downstream cylinder at $L/D = 1.5$, $G/D = 0.7, 1, 2,$ and 4.

For $G/D = 0.7$, the Nusselt numbers variation on back surface are approximately same for both cases. For $L/D = 4$, while the cylinders are within the coming boundary layer, the Nu number increases as the G/D increases on the back surface of the upstream cylinder and becomes approximately twice that for $L/D = 1.5$ when the cylinder is just outside the boundary layer ($G/D = 1$) (Figure 10). The variation of Nusselt number on the downstream cylinder surfaces is given in Figure 11 for $L/D = 4$. While the cylinders are outside the oncoming boundary layer ($G/D = 2, 4$), the variation of the Nusselt number on the front surface of the upstream cylinder is somewhat unaffected by the cylinder plane wall distances, but on the other surfaces it slightly varies. When the cylinders

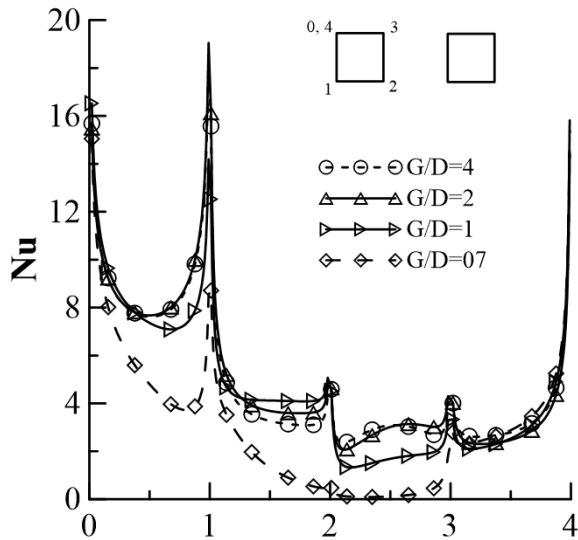


Figure 10. Local Nu values on the surfaces of upstream cylinder at $L/D = 4$, $G/D = 0.7, 1, 2,$ and 4 .

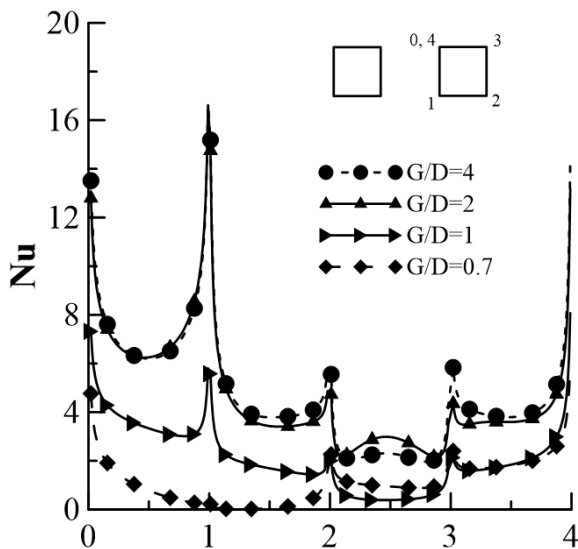


Figure 11. Local Nu values on the surfaces of downstream cylinder at $L/D = 4$, $G/D = 0.7, 1, 2,$ and 4 .

are in the boundary layer, the Nusselt numbers take lower values for the front and top surfaces at $G/D = 0.7$, for which flow velocities have relatively smaller values. On the downstream cylinders, Nusselt numbers is less sensitive to the distance between the cylinders (Figures 9 and 11) for $G/D = 0.7$, due to fact that both upstream and downstream cylinders are inside of the oncoming boundary layer. Other noticeable difference appears at the variation of Nusselt number on the front surfaces of downstream cylinders at $G/D = 4$ (Figures 9 and 11). At this G/D ratio, flow between the cylinders differs depending on the distance between the cylinders (Figure 3h and Figure 4h). For $L/D = 4$, shedding vortices from upstream cylinder pass through up and down side of the downstream cylinder alternately and leads nearly symmetrical Nu variation about the centerline although it is non symmetrical for $L/D = 1.5$. At the same time, vortex shedding between the cylinders also leads Nu

values become larger on the surfaces of downstream cylinders for $L/D = 4$ than that for $L/D = 1.5$.

CONCLUSION

In this study, the flow around two heated tandem cylinders near a plane wall and the convective heat transfer from these cylinders were investigated numerically for $Re = 150$ and $Pr = 0.71$. The distance between the cylinders are selected as $L/D = 1.5, 2.5$ and 4 while the gap ratios between the cylinders varied as $G/D = 0.7, 1, 1.5, 2, 2.5, 3, 3.5, 4$ and 6 . The vorticity and coincident temperature curves are obtained to understand and interpret flow and heat transfer. It is possible to separate the distance between the plane wall and cylinders to three regions as close proximity, moderate proximity and far proximity regions.

At close proximity region, the gap between the cylinder and wall is small ($G/D \leq 1$), the cylinders inside of the coming boundary layer and around the cylinder, the flow velocities are relatively low. There are approximately no oscillations in the drag and lift coefficients of the upstream and downstream cylinders, and values of approximately zero C_{Lrms} and C_{Drms} occur. In the close proximity region, mean values of the lift coefficients on the upstream cylinder takes their largest values and decrease by the increasing G/D ratio, while these values are very low on the downstream one and increase by the increasing G/D (Figure 5a). In this region ($G/D \leq 1$), the mean Nusselt numbers on the left and down surfaces also sharply increased with increasing G/D while it slightly varies on the up surfaces of both cylinders (Figure 7a). At moderate proximity region, cylinders are still inside of the approaching boundary layer. For both cylinders, the C_{Dmean} values increases while C_{Lmean} values continuous to drop until $G/D = 1.5$. At far proximity region, variations of flow and heat transfer characteristics on the both cylinders are less sensitive to the cylinder plane wall distances especially for $G/D > 2.5$.

REFERENCES

- Armfield, S. W and Street, 2000, Fractional step methods for the Navier-Stokes equations on non-staggered grids, *ANZIAM journal*, Vol. 42, pp. C134-C156.
- Bhattacharyya, S. and Maiti, D. K., 2004, Shear flow past a square cylinder near a wall, *International Journal of Engineering Science*, 42, 2119-2134.
- Chatterjee, D. and Amiroudine, S., 2010, Two-dimensional mixed convection heat transfer from confined tandem square cylinders in cross-flow at low Reynolds numbers, *International Communications in Heat and Mass Transfer*, 37, 7-16.
- Chatterjee, D., Biswas, G. and Amiroudine, S., 2009, Numerical investigation of forced convection heat transfer in unsteady flow past a row of square cylinders, *International Journal of Heat and Fluid Flow*, 30, 1114-1128.

- Chatterjee, D., and Mondal, B., 2012, Forced convection heat transfer from tandem square cylinders for various spacing ratios, *Numerical Heat Transfer, Part A: Applications*, 61, 381-400.
- Franke, R., Rodi, W. and Schönung B., 1990, Numerical calculation of laminar vortex shedding flow past cylinders, *Journal of Wind Engineering and Industrial Aerodynamics*, 35, 237-257.
- Harichandan, A. B., and Roy, A., 2012, Numerical investigation of flow past single and tandem cylindrical bodies in the vicinity of a plane wall, *Journal of Fluids and Structures*, 33, 19-43.
- Lei, C., Cheng, L., Armfield, S.W.K., Kavanagh, K., 2000. Vortex shedding suppression for flow over a circular cylinder near a plane boundary. *Ocean Engineering* Vol. 27, pp. 1109–1127.
- Luo, S. C., Chew, Y. T. and Ng, T. T., 2003, Hysteresis phenomenon in the galloping oscillation of a square cylinder, *Journal of Fluids and Structures*, 18, 103-118.
- Mahir, N., 2009, Three-dimensional flow around a square cylinder near a wall, *Ocean Engineering*, 36, 357-367.
- Mahir, N. and Altaç, Z., 2008, Numerical investigation of convective heat transfer in unsteady flow past two cylinders in tandem arrangements, *International Journal of Heat and Fluid Flow*, 29, 1309-1318.
- Malavasi, S. and Trabucchi, N., 2008, Numerical investigation of the flow around a rectangular cylinder near a solid wall, *BBAV. VI International Colloquium on: Bluff Bodies Aerodynamics & Applications* Milano, Italy, July, 20-24 2008.
- Raiola, M., Ianiro, A. and Discetti, S., 2016, Wake of tandem cylinder near a wall, *Experimental Thermal and Fluid Science*, 8, 354-369.
- Robichaux, J., Balachandar, S. and Vanka, S. P., 1999, Three-dimensional Floquet instability of the wake of square cylinder, *Physics of Fluids*, 11, 560–578.
- Sahu, A. K., Chhabra, R. P. and Eswaran, V., 2009, Effects of Reynolds and Prandtl number on heat transfer from a square cylinder in the unsteady flow regime, *International Journal of Heat and Mass Transfer*, 52, 839-850.
- Samani, M. and Bergstrom, D. J., 2015, Effect of a wall on the wake dynamics of an infinite square cylinder, *International journal of Heat and Fluid Flow*, 55, 158-166.
- Schlichting, H., *Boundary layer theory*, 1979, Seventy ed. Mc Graw-Hill Book Company, NewYork.
- Sharma, A. and Eswaran, V., 2004, Heat and fluid flow across a square cylinder in the two-dimensional laminar flow regime, *Numerical Heat Transfer, Part A: Applications*, 45, 247–269.
- Shimizu, Y. and Tanida, Y., 1978, Fluid forces acting on cylinders of rectangular cross section, *Transc JSME B* 44, 2699–2706.
- Sohankar, A., Davidson, L. and Norberg, C., 1995, Numerical simulation of unsteady flow around a square two-dimensional cylinder, *Twelfth Australasian Fluid Mechanics Conference, The University of Sydney, Australia*, 517-520.
- Sohankar, A. and Etminan, A., 2009, Forced-convection heat transfer from tandem square cylinders in cross flow at low Reynolds numbers, *International Journal For Numerical Methods in Fluids*, 60, 733-751.
- Sohankar, A., Norberg, C. and Davidson, L., 1997, Numerical simulation of unsteady low-Reynolds number flow around rectangular cylinders at incidence, *Journal of Wind Engineering and Industrial Aerodynamics*, 69, 189-201.
- Sohankar, A., Norberg, C. and Davidson, L., 1998, Low-Reynolds-number flow around a square cylinder at incidence: study of blockage, onset of vortex shedding and outlet boundary condition, *International Journal for Numerical Methods in Fluids*, 26, 39–56.
- Tang, G., Chen, C., Zhao, M. and Lu, L., 2015, Numerical simulation of flow past twin near-wall circular cylinders in tandem arrangement at low Reynolds number, *Water Science and Engineering*, 8, 315-325.
- Wang, X. K., Hao, Z., Zhang, J. X. and Tan, S. K., 2014, Flow around two tandem square cylinders near a plane wall, *Experiments in Fluids*, pp. 55:1818.
- Wang, X. K. and Tan, S. K., 2008, Near-wake flow characteristics of a circular cylinder close to wall, *Journal of Fluids and Structures*, 24, 605-627.
- Yetik, O., 2013, Flow and heat transfer from two square cylinders, MSc Dissertation, Eskisehir Osmangazi University, Eskisehir, Turkey.



A NOVEL THERMAL ANALYSIS FOR COOKING PROCESS IN BULGUR PRODUCTION: DESIGN CONSIDERATIONS, ENERGY EFFICIENCY AND WASTEWATER DIMINUTION FOR INDUSTRIAL PROCESSES

İbrahim Halil YILMAZ* and Mehmet Sait SÖYLEMEZ**

*Department of Mechanical Engineering, Adana Alparslan Türkeş Science and Technology University,
Adana, iyilmaz@atu.edu.tr

**Department of Mechanical Engineering, Gaziantep University, Gaziantep, sait@gantep.edu.tr

(Geliş Tarihi: 24.07.2019, Kabul Tarihi: 24.02.2020)

Abstract: The main contribution of this study is to present a novel thermal model for analyzing the wheat cooking process and to propose a design procedure for an energy-efficient cooking pot. A small-scale cooking pot was designed and an experimental setup was installed to verify the model under various operating conditions. The developed model was solved using the Engineering Equation Solver software. Results were compared with those of the experiments and good agreement was obtained. Additionally, a computational fluid dynamics model was developed to verify the thermal model and have a useful design tool for large-scale cooking pots. It was found that the energy efficiency of the cooking process can be enhanced by initiating nucleate boiling (at ~ 5 °C minimum temperature difference between the heating element surface and saturation) which will supply the minimum heat flux on the helicoidal heat exchanger of the cooking pot. Lessening the energy demand but preserving the final product quality has decreased the 5-day biological oxygen demand of wastewater at least 50%. It is proposed that the wheat to water ratio can be reduced to 1.0–1.2 once the energy optimization and water recovery practices are satisfied. The estimated average specific energy consumption rate lies between 400–475 $\pm 5\%$ W/kg (thermal power supplied for one kilogram of wheat) which can be reduced $\sim 25\%$ further by reducing the wheat to water ratio to 1.0. The results reported in the present study are expected to guide thermal and food engineers for the design applications of industrial cooking pots, energy optimization with less harmful wastewater and process control strategies for cooking of wheat.

Keywords: Wheat cooking; bulgur; cooking model; energy analysis; cooker design; wastewater

BULGUR ÜRETİMİNDE PİŞİRME İŞLEMİNE YÖNELİK ÖZGÜN BİR ISIL ANALİZİ: ENDÜSTRİYEL SÜREÇLER İÇİN TASARIM ÖNERİLERİ, ENERJİ VERİMLİLİĞİ VE ATIKSU AZALTIMI

Özet: Bu çalışmanın ana katkısı, buğday pişirme işlemini özgün bir ısıl modelle izah ederek sunmak ve enerji-verimli bir pişirme kazanı için tasarım yöntemi önermektir. Küçük-ölçekli bir pişirme kazanı tasarlanmış ve modelin çeşitli çalışma şartları altında doğrulanması için bir deney düzeneği kurulmuştur. Geliştirilen model Engineering Equation Solver yazılımı kullanılarak çözülmüştür. Sonuçlar deneylerle kıyaslanmış ve iyi bir uyum elde edilmiştir. Isıl modelin doğrulanması ve büyük-ölçekli pişirme kazanlarına yönelik kullanışlı bir tasarım aracı olması için ayrıca bir hesaplamalı akışkanlar dinamiği modeli geliştirilmiştir. Pişirme işleminin enerji verimliliğinin, pişirme kazanının sarmal ısı değiştiricisi üzerindeki minimum ısı akısının çekirdekli kaynamayı (ısıtma elemanı yüzeyi ve doyma sıcaklığı arasında minimum ~ 5 °C farkla) karşılayacak şekilde başlatılmasıyla artırılabilirliği bulunmuştur. Enerji talebini azaltarak fakat nihai ürün kalitesini koruyarak, atıksuyun 5-günlük biyolojik oksijen ihtiyacı en az %50 oranında azaltılmıştır. Enerji optimizasyonu ve su geri kazanımı teknikleri yerine getirildiği takdirde buğday-su oranının 1,0–1,2'ye düşürülebileceği önerilmektedir. Tahmini ortalama özgül enerji tüketim hızının 400–475 $\pm 5\%$ W/kg (bir kilogram buğday için gerekli olan ısıl güç) arasında yer almakta, bu değer buğday-su oranının 1,0'a düşürülmesiyle ilaveten $\sim 25\%$ oranında azaltılabilmektedir. Çalışmadan elde edilen sonuçların ısı ve gıda mühendisleri için endüstriyel pişirme kazanlarının tasarım uygulamalarında, daha az zararlı atıksu ile enerji optimizasyonunda ve buğdayın pişirilmesi için süreç kontrol stratejilerinde kılavuzluk edeceği düşünülmektedir.

Anahtar Kelimeler: Buğday pişirme; bulgur; pişirme modeli; enerji analizi; kazan tasarımı; atıksu

NOMENCLATURE

| | |
|-----------|---|
| a | radius of the coiled pipe [m] |
| A | cross-sectional area [m ²] |
| b | coil pitch [m] |
| BOD_5 | 5-day biological oxygen demand [mg/L] |
| c_p | specific heat capacity [J/kg°C] |
| D | diameter [m]; diffusion coefficient [m ² /s] |
| De | Dean number [= $Re(a/R)^{1/2}$] |
| g | gravitational acceleration [m/s ²] |
| Gr | Grashof number [= $g(\rho_s - \rho_\infty)L_c^3/\rho\nu^2$] |
| h | convective heat transfer coefficient [W/m ² °C] |
| H | height [m] |
| He | Helical number [= $De(1 + (b/2\pi R)^2)^{1/2}$] |
| h_{fg} | enthalpy of vaporization [J/kg] |
| k | thermal conductivity [W/m°C] |
| L_c | characteristic length [m] |
| m | mass [kg] |
| \dot{m} | mass flowrate [kg/s] |
| M_w | molecular weight of water [kg/mol] |
| Nu | Nusselt number [= hD/k] |
| P | pressure [Pa] |
| Pr | Prandtl number [= $\mu c_p/k$] |
| \dot{q} | heat flux [W/m ²] |
| Q | heat transfer [J] |
| \dot{Q} | heat transfer rate [W] |
| R | coil radius [m]; universal gas const. [J/K mol] |
| Ra | Rayleigh number [= $g\beta(T_s - T_\infty)L_c^3 Pr/\nu^2$] |
| Re | Reynolds number [= $u_m D/\nu$] |
| Sh | Sherwood number [$Sh = hL_c/D$] |
| t | thickness [m]; time [s] |
| T | temperature [°C] |
| u_m | mean velocity [m/s] |
| U | overall heat transfer coefficient [W/m ² °C] |
| W | moisture content [%] |
| x_a | air mass fraction [= $m_{air}/(m_{air} + m_v)$] |

Greek letters

| | |
|---------------------|----------------------------|
| α | inclination angle [°] |
| ΔT_{excess} | excess temperature [°C] |
| μ | dynamic viscosity [kg/m·s] |

INTRODUCTION

Cooking is the initial step for the production of certain cereal products. Typically, grains are heated firstly with water at elevated temperatures and pressures in this process. After cooking, the grains become soft enough to be worked into the final product. During this process, it is essential to obtain a product at the desired quality and the lowest cost since it requires a significant amount of thermal energy. The cooking process of cereal products involves both the diffusion of water into grains and the subsequent conversion (reaction) of starch within them i.e., gelatinization. The literature on the cooking model of wheat is limited and largely focused on the effects of

| | |
|----------|---|
| ν | kinematic viscosity [m ² /s] |
| ρ | density [kg/m ³] |
| σ | surface tension [N/m] |
| ϕ | relative humidity [= P_v/P_g] |

Subscripts

| | |
|--------|------------------------------------|
| a | absorbed |
| air | air |
| ave | average |
| b | boiling |
| $bulk$ | bulk fluid |
| c | critical; condensation |
| cp | cooking pot |
| d | dry basis |
| e | equivalent water of metallic parts |
| ev | evaporated water |
| f | film; flash |
| g | grain; gas |
| htf | heat transfer fluid |
| i | inner |
| in | inlet |
| ins | insulation |
| m | mixture |
| l | liquid |
| $loss$ | loss |
| o | outer |
| out | outlet |
| p | pipe; preheating |
| r | residual |
| s | surface; sensible |
| sat | saturation |
| v | vapor |
| w | water; wall |

Abbreviations

| | |
|------|--|
| CFD | computational fluid dynamics |
| CHE | coiled heat exchanger |
| CP | cooking pot |
| EES | Engineering Equation Solver |
| GP | gear pump |
| HTF | heat transfer fluid |
| ONB | onset of nucleate boiling |
| TCEH | temperature controlled electric heater |
| TET | thermal expansion tank |
| WPT | water preheating tank |

cooking time, temperature and starch gelatinization. Stapley *et al.* (1998) studied the diffusion and reaction behaviors of wheat grains during boiling. They developed a diffusion model using the finite-element method and tested certain model scenarios to compare the simulation results with the experimental data for moisture distribution across the central section of grains at 100 °C and 120 °C. Watanabe *et al.* (2001) proposed a new mathematical model to describe the moisture profile in starchy food during cooking. Bayram (2005) determined the cooking degree of wheat kernels by using three different gelatinization measuring methods. The optimum cooking time was specified to be 40 min at 97 °C in case of maintaining 100% gelatinization without

any deformation on wheat kernels. Lately, Balcı and Bayram (2020) investigated the possibility of cooking wastewater reuse for the subsequent cooking operation obtained from the former process. It was indicated that the energy requirement might be reduced by 57% at the expense of increasing 5-day biological oxygen demand (BOD₅) and filtering cost.

Physically, cooking is a type of thermal process which involves boiling that occurs at the solid-liquid interface when a liquid is brought into contact with the solid surface of heating material maintained at a temperature sufficiently above the saturation temperature of the liquid. Unlike ordinary cooking pot (CP), a pressure cooker is an appliance that is used to cook foods at high pressure and temperature to reduce the cooking time. The use of saturated steam and reduction in cooking time are the two methods of preserving vitamins (Rocca-Poliméni *et al.*, 2011). Pressure cookers have many nutritional, organoleptic and sanitary advantages however the literature does not have sufficient studies to explain these traits (Koca and Aml, 1996; Rocca-Poliméni *et al.*, 2011). Rocca-Poliméni *et al.* (2011) developed a model which includes the physical and thermal characteristics of a commercial pressure cooker and of the food cooked in it based on the energy balance and heat and mass transfer relations.

In this study, the physical insight of cooking phenomena was described in detail and a novel thermal model was proposed for a small-scale industrial wheat CP. The developed model was coded in EES (Engineering Equation Solver) and the model results were compared with those of the experiments done. Additionally, a computational fluid dynamics (CFD) analysis was conducted to verify the thermal model and to present a design procedure for large-scale CPs. The prediction of specific energy demand for the cooking process was made by the methodology proposed for the first time. The wastewater properties after the cooking process were investigated to enhance energy efficiency and water recovery. As a result, a guide for the design applications of industrial CPs, energy optimization with less harmful wastewater and process control strategies for cooking of wheat has been presented.

DESCRIPTION OF COOKING MECHANISM

In industrial processes, process-water is firstly preheated to the temperature of 90 °C and then discharged into the CP. The temperature of the preheated water falls down when it is mixed with the unsoaked wheat grains (initially at about ambient temperature) inside the CP. After the discharging process, the mixture is heated up until the cooking temperature reaches the boiling temperature. The degree of cooking temperature is adjusted according to the condition of starch gelatinization since the degree of gelatinization of hard wheat starch depends strongly on cooking temperature. The rate of the gelatinization increases with increasing cooking temperature (Bakshi and Singh, 1980) and it is never completed 100% at a cooking temperature lower than 90 °C (Turhan and

Gunasekaran, 2002). The amount of energy supply during the boiling process is regulated to keep the central region of the CP (charged with bulky wheat) at the cooking temperature.

THERMAL MODELING OF COOKING PROCESS

The detailed drawing of the CP used in the experimental setup is demonstrated in Figure 1. The CP was custom-designed (Yılmaz, 2018) and suited for industrial applications and its specifications are introduced in Table 1. A metal screen made of the perforated sheet was placed into the CP to prevent the direct contact between the wheat grains and the coiled pipe (i.e., coiled heat exchanger, CHE). Thus, the wheat grains will not adhere to the surface of the CHE whose temperature is high due to the heat transfer fluid (HTF) flowing inside it. The outer surface of the CP was well insulated to minimize the heat loss to the surroundings.

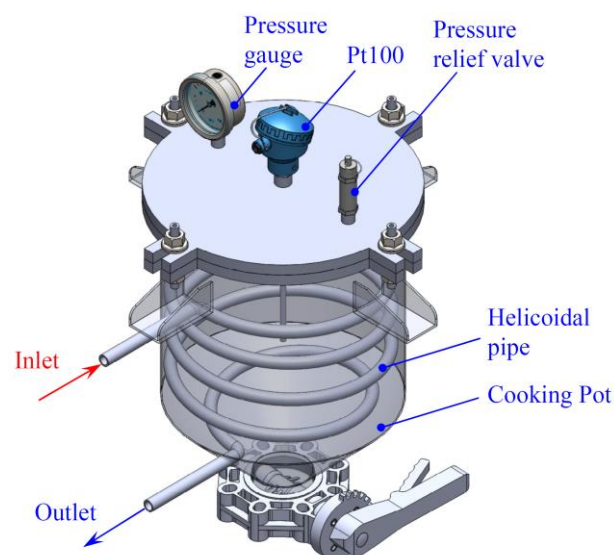


Figure 1. CP design used in the experimental setup.

Table 1. Specifications of the CP.

| | |
|--------------------------------------|----------------------|
| Sheet material | 316L SS |
| Inner diameter of CP, $D_{i,cp}$ | 0.4 m |
| Material thickness of CP, t | 0.002 m |
| CHE material | 304L SS |
| CHE pipe diameter, $D_{i,p}/D_{o,p}$ | 0.0157/0.0213 m |
| Coil pitch, b | 0.085 m |
| Coil radius, R | 0.175 m |
| CHE effective surface area, A_s | 0.288 m ² |
| Volume of CP | 0.06 m ³ |
| Insulated material | Stone wool |

Heating Process of Water-grain Mixture (Sensible Heat Gain)

After the preheated water is discharged onto wheat grains, it is heated from the mixture temperature, T_m to the boiling temperature, T_b . This heating process is named as subcooled or local boiling since the main body

of the liquid temperature is below the saturation temperature, T_{sat} . At the early stages of boiling, the bubbles are confined to a narrow region near the hot surface. This is because the liquid adjacent to the hot surface vaporizes as a result of being heated above its saturation temperature. However, these bubbles disappear soon before reaching the liquid-gas interface as a result of heat transfer from the bubbles to the cooler liquid surrounding them. In this case, only sensible heat gain is considered for the heating process and the final temperature of the mixture can be calculated by using energy balance:

$$m_g c_{p,g} (T_m - T_g) = (m_w + m_e) c_{p,w} (T_w - T_m) \quad (1)$$

The sensible energy demand of the mixture to reach the boiling temperature can be defined by

$$Q_s = (m_w + m_e) c_{p,w} (T_b - T_m) + m_g c_{p,g} (T_b - T_m) \quad (2)$$

During the preheating process, some water will penetrate into the grains so that the amount of process-water will decrease and the moisture within the grains will increase with time. Thus, the specific heat of the grain samples will change through the temperature rise from T_m to T_b . The value of $c_{p,g}$ is estimated by the relation (Bruce and Giner, 1993):

$$c_{p,g} = c_{p,d} + c_{p,w} W \quad (3)$$

Mass transfer by evaporation

During the transition from subcooled boiling to saturated boiling, mass transfer by evaporation takes place at the liquid-gas interface as a result of water molecules diffusing into the air confined in the CP. This process continues until the phase equilibrium is maintained at boiling temperature since the vapor pressure at the mixing temperature is less than the saturation pressure of the liquid. The basic theory for estimating the evaporated water is presented in detail (Yılmaz, 2014).

$$\frac{dm_{ev}}{dt} = \frac{-A_{cp} D_{w-air}}{H_w - H_{cp}} \left(\frac{M_w P_v}{R T_v} \right) (1 - \phi) \quad (4)$$

Energy transfer to process-water

The constant mass flow inside the CHE is stated by forced circulation due to the pumping of the HTF (Yılmaz *et al.*, 2018). The dynamical state of the single-stream steady pipe flow shown in Figure 2 is determined by the flow parameter, Reynolds number (Re).

Curved or helicoidal pipes are widely used in engineering applications such as food processing. Contrary to straight pipes, the following dimensionless parameters are used in flow and heat transfer calculations of helicoidal pipes:

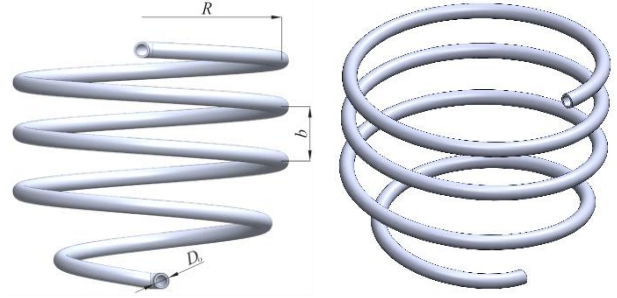


Figure 2. Geometry of the CHE.

$$De = Re \left(\frac{a}{R} \right)^{1/2} \quad (5)$$

$$He = De \left[1 + \left(\frac{b}{2\pi R} \right)^2 \right]^{1/2} \quad (6)$$

$$R_c = R \left[1 + \left(\frac{b}{2\pi R} \right) \right] \quad (7)$$

where De is the Dean number, He is the Helical number, a denotes the radius of the circular pipe (i.e., $D_o/2$ in this study), b represents the coil pitch, R is the radius of the coil and the effective radius of curvature, R_c .

The estimation of the critical Re, which is used to identify the transition from the laminar to the turbulent regime in curved or helicoidal pipes, has been recommended by (Srinivasan *et al.*, 1970) for design purposes:

$$Re_c = 2100 \left[1 + 12 \left(\frac{R}{a} \right)^{-0.5} \right] \quad (8)$$

The fully developed Nusselt number (Nu) relation for the laminar regime in helicoidal pipes subjected to uniform wall temperature was derived theoretically and experimentally by many researchers (Rohsenow *et al.*, 1998). For the corresponding thermal boundary condition, the Nu relation has been proposed by (Manlapaz and Churchill, 1981).

$$Nu_i = \left[\left(3.657 + \frac{4.343}{\left(1 + \frac{957}{Pr_{hff} De^2} \right)^2} \right)^3 + 1.158 \left(\frac{De}{1 + \frac{0.477}{Pr_{hff}}} \right)^{3/2} \right]^{1/3} \quad (9)$$

The flow inside the CHE shows turbulent behavior although the Re is close to the critical Re of the transitional regime. Hogg (1969) has indicated that

turbulent entrance length in coils with circular cross-sections much shorter than that of laminar flow. Turbulent flow can be fully developed within the first half-turn of the CHE. Therefore, most of the turbulent flow and heat transfer analyses concentrate on the fully developed region in CHEs. The fully developed Nu relation for turbulent flow in helicoidal pipes subjected to constant wall temperature was recommended by the Pratt (1947) equation which was modified by Orlov and Tselishchev (1964) for the influence of temperature-dependent properties as below:

$$\text{Nu}_i = \text{Nu}_p \left(1 + 3.54 \frac{a}{R} \right) \left(\frac{\text{Pr}_{bulk}}{\text{Pr}_w} \right)^{0.25} \quad 5 < R/a < 84$$

$$1500 < \text{Re} < 2 \times 10^4 \quad (10)$$

where Nu_p is the Nusselt number for plain tubes which is estimated using the Dittus-Boelter equation (Çengel and Ghajar, 2011):

$$\text{Nu}_p = 0.023 \text{Re}_{hf}^{0.8} \text{Pr}_i^{0.3} \quad (11)$$

The convection heat transfer coefficient of the HTF is calculated using (Yılmaz and Söylemez, 2014)

$$h_i = \text{Nu}_i \frac{k_{hf}}{D_{i,p}} \quad (12)$$

All fluid properties inside the pipe were evaluated at the bulk fluid temperature, i.e., $T_{bulk} = (T_{in} + T_{ex})/2$. The thermophysical properties of the HTF (Renolin therm 320 thermal oil) as a function of temperature were fitted to polynomial functions from the manufacturer's supplied data (Fuchs, 2013) as below:

$$\rho = 1058.108 - 0.6507T \quad (13)$$

$$c_p = 692.37 + 4.2887T \quad (14)$$

$$k = 0.15399 - 7.1764 \times 10^{-5}T \quad (15)$$

$$\mu = 0.3345 - 2.15348 \times 10^{-3}T + 4.66657 \times 10^{-6}T^2 - 3.39167 \times 10^{-9}T^3 \quad (16)$$

where ρ , c_p and k are valid in the temperature range of $273 \text{ K} \leq T < 473 \text{ K}$ while μ is valid in $373 \text{ K} \leq T < 473 \text{ K}$. For any given temperature during iterations, Eqs. (13)–(16) were used without any problem.

Cooking Process of Mixture (Latent Heat Gain)

Transition from subcooled boiling to saturated boiling

Boiling is classified as pool boiling or flow boiling, depending on the presence of bulk fluid motion. It is called pool boiling in the absence of bulk fluid flow or called flow boiling (or forced convection boiling) in the presence of it. In this study, it is dealt with pool boiling rather than flow boiling. Four different boiling regimes are observed in pool boiling: natural convection, nucleate, transition and film boiling as illustrated in Figure 3. The specific shape of the curve depends on the fluid-heating surface material combination and the fluid pressure however it is practically independent of the geometry of the heating surface and its orientation (Çengel and Ghajar, 2011).

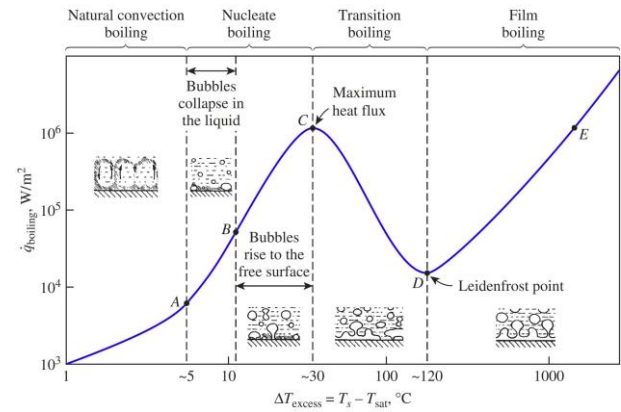


Figure 3. Typical boiling curve for water at 1 atm pressure. Adapted from (Çengel and Ghajar, 2011).

In the natural convection regime, the heat transfer takes place from the heater surface (only a few degrees above the saturation temperature i.e., towards point A or ONB (onset of nucleate boiling)) to the saturated liquid. The fluid motion in this mode of boiling is governed primarily by natural convection currents. If the temperature of the heating surface becomes higher than the saturation temperature, the regime is replaced from free convection to nucleate boiling. In the nucleate boiling regime, the bubbles start to form at various preferential sites on the heating surface. They are detached from the surface and dissipated in the liquid as receiving high heat fluxes. The nucleation sites form at an increasing rate so that the continuous columns of vapor appear as moved along the boiling curve from B to point C. As a result, very high heat fluxes are obtainable in this region. The nucleate boiling region ends and the unstable region (existence of partially both nucleate and film boiling) begins after the maximum (critical) is reached. As the heater temperature is increased past point C, the heat flux decreases as shown in Figure 3 since a large fraction of the heater surface is covered by a vapor layer which acts as an insulation due to its low thermal conductivity. Thus, operation in the transition boiling regime is generally avoided in practice when high temperatures involved. Nucleate boiling at point C is completely replaced by film boiling at point D. Beyond point D, the heater surface is completely covered by a continuous stable vapor layer. The presence of the vapor layer is responsible for the low heat transfer rates in the film boiling region. The heat transfer rate increases with increasing ΔT_{excess} as a result of heat transfer from the

heated surface to the liquid through the vapor film by radiation, which becomes significant at high temperatures.

Numerous experimental investigations have been reported in the literature for characterizing the heat transfer behavior in the nucleate boiling region (Cornwell and Houston, 1994). However, the derivation of heat transfer correlations for nucleate pool boiling is accompanied by difficulty (Rohsenow *et al.*, 1998). Any designer is faced with the problem of calculating the heat transfer coefficient for the nucleate boiling region where the use of correlations is inevitable although the designer should be aware of the uncertainties involved. Based on the problem physics, these correlations may yield different predictions for the estimation of the heat transfer coefficient. For nucleate pool boiling on horizontal tubes, the following correlation gives reasonable results (Cornwell and Houston, 1994):

$$\text{Nu}_o = 9.7P_c^{0.5}F''\text{Re}_b^{2/3}\text{Pr}_b^{0.4} \quad (17)$$

where P_c is the critical pressure in bar and F'' is given by Eq. (17)

$$F'' = 1.8(P_{sat}/P_c)^{0.17} + 4(P_{sat}/P_c)^{1.2} + 10(P_{sat}/P_c)^{10} \quad (18)$$

Under saturated pool boiling conditions, the boiling Re becomes

$$\text{Re}_b = \frac{\dot{q}_b D_{o,p}}{\mu_l h_{fg}} \quad (19)$$

Average heat transfer coefficient on the tube is defined as

$$h_o = \text{Nu}_o \frac{k_w}{D_{o,p}} \quad (20)$$

Mass diffusion into wheat grains

The moisture content of wheat grains varies with time due to water diffusion until the wheat grains are not able to accept moisture uptake anymore. Absorbed water throughout the cooking process can be estimated by summing up water absorbed by wheat grains in both preheating and boiling processes.

$$m_a = m_g \frac{[(W_p - W_d) - (W_b - W_p)]}{100} \quad (21)$$

Condensation heat transfer

Water condensation takes place on the inner surfaces of the CP (cover plate and lateral wall) when the surface temperature falls below the dew point temperature of the evaporated water. Heat transfer rates for laminar film condensation on the horizontal and inclined downward-facing surfaces are predicted by assuming the condensate flow to be quasi-steady. This assumption makes it possible to determine the final shape of the liquid-vapor

interface and thus to predict the average heat transfer coefficient. Gerstmann and Griffith (1967) studied the film condensation on the underside of horizontal and inclined surfaces. A slight inclination angles ($\alpha < 7.5^\circ$), various wave patterns were observed. At moderate inclination angles ($\alpha > 20^\circ$), roll waves appeared. The net effect of the roll waves increases and remains nearly constant up to 20° from the horizontal. However, the interfacial waves appear to be unchanged between 20° – 90° .

For a horizontal surface, they developed the modified Rayleigh number (Ra_c) to estimate Nu:

$$\text{Ra}_c = \frac{g\rho_l(\rho_l - \rho_g)h_{fg}}{\mu_l \Delta T k_l} \left(\frac{\sigma}{g(\rho_l - \rho_g)} \right)^{3/2} \quad (22)$$

The Nu relation for laminar film condensation is recommended to be

$$\text{Nu}_c = \begin{cases} 0.69\text{Ra}_c^{0.20} & 10^6 < \text{Ra}_c < 10^8 \\ 0.81\text{Ra}_c^{0.193} & 10^8 < \text{Ra}_c < 10^{10} \end{cases} \quad (23)$$

For slightly inclined surfaces i.e., $\alpha < 20^\circ$, Nu_c and Ra_c are modified in the above equations by replacing g by $g\cos\alpha$.

The presence of air (non-condensable gas) in the CP hinders the condensation heat transfer. Minkowycz and Sparrow (1966) investigated the effects of non-condensable gas, interfacial resistance, superheating, free convection, mass, and thermal diffusions and variable properties of liquid and gas-vapor regions on laminar film condensation. It was demonstrated that small concentrations of non-condensable gases can have a decisive effect on the heat transfer rate. Chin (1995) performed a numerical study for the influence of air-mass fraction ($x_a = m_{air}/(m_{air}+m_v)$) on condensation rate over a vertical plate with respect to stagnant or moving steam–air mixtures and compared their results with the experimental values obtained by Minkowycz and Sparrow (1966).

Figure 4 shows the agreement between these two models. The ratio between the condensation rate of the mixture and pure steam (K_{air}) depends mainly on x_a and slightly on the temperature difference between the gas and the wall. The variation of K_{air} obtained by (Chin, 1995) was proposed in order to predict the heat transfer coefficient due to condensation as a function of x_a for the temperature range of $(T_b - T_w)$. Here, T_b is the boiling temperature and T_w is the wall temperature which will be estimated from the heat loss analysis of the CP.

Accordingly, the mass of condensed steam is predicted by

$$m_c = \frac{K_{air} h_c (T_b - T_w)}{h_{fg @ T_b}} \quad (24)$$

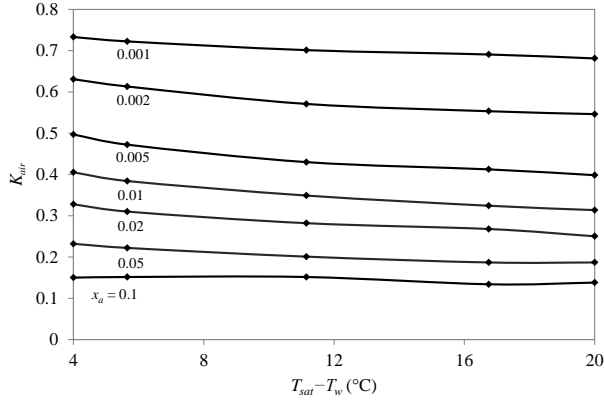


Figure 4. Condensation heat transfer in the presence of a non-condensable gas in quiescent mixture at $T_{sat} = 100$ °C. Adapted from (Chin, 1995).

Heat loss to surroundings

Heat loss from the outer surface of the CP (the lateral sides and cover plate) is estimated using the following relations:

For the lateral side in a cylindrical shape, the average Nu relation for an isothermal vertical plate can be evaluated using the relation proposed by (Churchill and Chu, 1975):

$$Nu_{air} = \left[0.825 + \frac{0.387Ra_{air}^{1/6}}{\left[1 + (0.492/Pr_{air})^{9/16} \right]^{8/27}} \right]^2 \quad (25)$$

For the lateral side in a conical shape, Ra_{air} is modified in Eq. (25) replacing g by $g \cos \alpha$.

For the cover plate, the average Nu relation can be determined using power-law relations proposed by (Fujii and Imura, 1972) for horizontal surface facing upwards.

$$Nu_{air} = \begin{cases} 0.16Ra_{air}^{1/3} & 2 \times 10^8 < Ra_{air} \\ 0.13Ra_{air}^{1/3} & 5 \times 10^8 < Ra_{air} \end{cases} \quad (26)$$

Noting that all fluid properties were evaluated at the film temperature, $T_f = (T_{s,cp} + T_{air})/2$.

Through the analysis of heat loss from the CP, the thermal resistance approach presented in (Çengel and Ghajar, 2011) was used where the heat flow from the boiling water to the ambient air combined into a single resistance $(UA)_{cp}$ as

$$\frac{1}{(UA)_{cp}} = \frac{1}{h_o A_{i,cp}} + \frac{\ln(D_{o,cp}/D_{i,cp})}{2\pi L k_{cp}} + \frac{\ln(D_{o,ins}/D_{i,ins})}{2\pi L k_{ins}} + \frac{1}{h_{air} A_{o,cp}} \quad (27)$$

The total heat loss from the CP is found to be

$$\dot{Q}_{loss} = (UA)_{cp} (T_b - T_{air}) \quad (28)$$

Mass transfer by flash evaporation

At the end of the cooking process, the energy transfer to the mixture is finished and the butterfly valve at the bottom side of the CP is opened for a while. The water in the CP evaporates due to flash boiling as a result of the concentration differences between the saturated water and ambient air. The diffusion of water vapor in the air was estimated by the empirical equations below (Marrero and Mason, 1972):

$$D_{w-air} = 1.87 \times 10^{-10} \frac{T^{2.072}}{P} \quad 280 \text{ K} < T < 450 \text{ K} \quad (29)$$

Utilizing the analogy between heat and mass convection, the mass transfer coefficient is determined by

$$h_f = \frac{Sh D_{w-air}}{L_c} \quad (30)$$

The Sherwood number (Sh) and the mass transfer coefficients were determined for the case of a horizontal surface:

$$Sh = \begin{cases} 0.54(Gr Sc)^{1/4} & 10^4 < Gr Sc < 10^7 \\ 0.15(Gr Sc)^{1/3} & 10^7 < Gr Sc < 10^{11} \end{cases} \quad (31)$$

where $Gr = g(\rho_s - \rho_\infty)L_c^3/\rho v^2$ and $Sc = \nu/D_{w-air}$ is the Schmidt number.

The evaporation heat transfer rate is estimated from

$$\dot{m}_f = h_f A_w (\rho_{v,s} - \rho_{v,\infty}) \quad (32)$$

Mass balance of water

During cooking operation, the total mass of water is conserved. This can be defined by the following equation:

$$m_i - \int_0^{\Delta t_1} \dot{m}_{ev} dt - \int_0^{\Delta t_2} (\dot{m}_b - \dot{m}_c) dt - \int_0^{\Delta t_3} \dot{m}_f dt - m_{loss} - (m_r - m_l) - m_a = 0 \quad (33)$$

where m_i is the total amount of process-water charged into the CP at the beginning of the cooking process, \dot{m}_{ev} is the total evaporated water during Δt_1 (the preheating process of the water-wheat mixture), $\dot{m}_b - \dot{m}_c$ is the difference between the total amount of water boiled and condensed during Δt_2 (boiling process), \dot{m}_f is the total amount of flashed water along Δt_3 (opening the cover plate to ambient air), m_{loss} is the flashing and evaporating water losses from the CP and bulgur respectively during

the depressurizing the CP with opening the butterfly valve, $m_r - m_l$ is the difference between the amount of residual water, m_r , obtained at the end of cooking process and the leached substances, m_l existing in the residual water, m_a is the amount of water absorbed by wheat grains during cooking operation.

Cooking load

The outlet temperature of the HTF is estimated by using energy balance and the heat transfer equations derived in the previous sections. In this estimation, the radiation heat transfer among the lateral walls, food, and the CHE was considered negligible as compared to the condensation heat transfer since the surfaces have a low emissivity (stainless steel) and small temperature difference with their surroundings and the water vapor absorbs infrared radiation, as well. Only the energy supplied to the CP was taken into consideration to launch nucleate boiling and compensate for the heat loss.

As a form of convection heat transfer, the boiling heat flux from a solid surface to the fluid is expressed from Newton's law of cooling as

$$\dot{q}_b = h_o \Delta T_{excess} \quad (34)$$

where $\Delta T_{excess} = T_s - T_{sat}$ which represents the temperature excess of the surface above the saturation temperature of the fluid.

The energy transferred to the mixture during boiling can be written under the steady-state condition as

$$\begin{aligned} \dot{Q}_{cp} &= \dot{m}_{hf} c_{p,ave} (T_{in} - T_{ex}) \\ &= h_i A_s \Delta T_{lm} = \dot{q}_b A_s = \dot{m}_b h_{fg@T_b} \end{aligned} \quad (35)$$

where $\Delta T_{lm} = \frac{\Delta T_1 - \Delta T_2}{\ln(\Delta T_1/\Delta T_2)}$ and here $\Delta T_1 = T_{h,in} - T_s$,

$\Delta T_2 = T_{h,out} - T_s$, respectively.

The exit temperature of the HTF can be predicted by

$$T_{ex} = T_s + (T_s - T_{in}) e^{\frac{-h_i A_s}{(\dot{m} c_p)_{hf}}} \quad (36)$$

The governing equations were modeled in EES and solved simultaneously.

NUMERICAL ANALYSIS

CFD is a useful tool for simulating the flow field (Mwesigye *et al.*, 2018) and reproducing data during the design cycle (Yilmaz and Mwesigye, 2018). The design can be improved using this tool for optimization purposes. A CFD analysis was conducted to verify the thermal model and to extend it as a design procedure for large-scale CPs and improving the design by subsequent

parametric analyses. For the numerical simulations, ANSYS Fluent v17.2 was used to solve the governing equations (the conservation equations for mass, momentum and energy) along with the boundary conditions applied. The flow inside the CHE was considered steady-state and fully developed turbulent. These considerations are reasonable since the experimental measurements were taken under steady conditions and the flow is fully developed due to the negligible entrance effect compared to the coil length.

Mesh Structure

The mesh structure of the CHE is shown in Figure 5. Mesh dependency studies were applied for each run considered in the study. The solution was considered grid-independent when the maximum changes in the outlet temperature were less than 1% based on the change of mesh element size. The numbers of mesh elements with 3,685,776; 7,100,622 and 11,217,391 were applied for mesh refinement, respectively however the 7,100,622 mesh element case was used in the analyses.

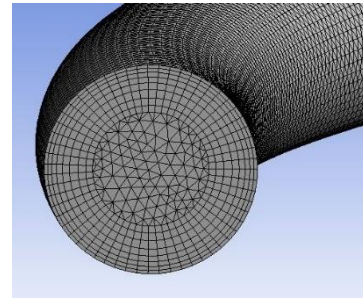


Figure 5. Sample mesh for the CHE.

Boundary Conditions

The boundary conditions include i) no-slip and no-penetration conditions exist on the coil wall, ii) constant temperature and velocity inlet conditions were used in the CHE inlet, iii) the convection heat transfer coefficient and temperature subjected to the CHE surface were determined using the analytical approach presented in the previous section, iv) the turbulence intensity was assumed to be 5% at the inlet.

Numerical Solution

The computational domain was discretized using tetrahedron elements with structured elements in the wall-normal direction. The k- ω turbulence model was used to evaluate the fluid domain of the curved pipe. The coupling of pressure and velocity was made with the SIMPLE algorithm. Second-order upwind schemes were employed for integrating the governing equations with the boundary conditions over the computational domain. The y+ value was ensured ~ 1 for all simulations to obtain the high resolution of gradients in the near-wall regions. The solution convergence was satisfied when the scaled residuals of continuity, momentum, turbulence kinetic energy, turbulent dissipation rate, and energy ceased after about 800 successive iterations. The values of the scaled

residuals were in the order of less than 10^{-4} for continuity, less than 10^{-5} for velocity components, turbulent kinetic energy, and turbulent dissipation rate and less than 10^{-7} for energy.

EXPERIMENTAL ANALYSIS

An experimental setup was installed for verifying the presented model as shown in Figure 6. The setup basically consists of a temperature-controlled electric heater (TCEH), a cooking pot (CP), water preheating tanks (WPTs), a thermal expansion tank (TET), a gear pump (GP) and measuring instruments. The HTF used in the system was selected to be Renolin therm 320 thermal oil –whose thermo-physical properties given in Eqs. (13)–(16) (Yılmaz and Göksu, 2016; Yılmaz *et al.*, 2017; Yılmaz *et al.*, 2018)– to easily control the process-temperature and make the energy analyses precisely. A frequency-controlled gear pump (Yildizpompa, 2019) was used to adjust the flow rate of the HTF. The outer surface of the CP was insulated with a 40 mm-thick rock wool covered with an aluminum sheet (Izocam, 2019). The TCEH was specially designed heat exchanger (coiled square duct enclosed by an electric heater) which was used to supply thermal power to the HTF. The effective power of the TCEH was 6 kW which was controlled by a PID (Proportional Integral Derivative) controller. When the operating temperature of the system fell below the load-temperature, the TCEH was activated automatically to increase the return-temperature of the HTF to the load-temperature. The role of the WPT was preheating the process-water up to 90 °C. The TET was used to provide additional space for the thermally expanded HTF.

The temperature measurements in the experimental setup were performed by the resistance temperature detectors (Pt100, Class A) connected with two leads (Ordel, 2019). The temperature-dependent uncertainty of the detectors was designated by the relation of $\pm(0.15 + 0.002T)$ °C and calibrated according to the standard of IEC751:1983 (BS EN 60751:1996) by the manufacturer. The surface temperature of the CP was measured from several points using a portable device (Mastech MS8217 with K-type thermocouple) and averaged to use it the analytical model. The operating pressure measurements for the CP were realized by pressure gauges (Pakkens, 2019). In order to measure the pressure at high temperatures, the gauges were connected to the CP by a pigtail siphon. The mass flow rate of the HTF was measured by a Coriolis flow meter having an accuracy of $\pm 0.1\%$ with a repeatability of less than 0.05% (Krohne, 2019). During the experimental tests, the signal data of the measurement devices were collected by the 24-bit USB-2416 and USB-TEMP data acquisition (DAQ) devices for further analyses. For this task, highly-accurate voltage and temperature processing DAQ devices (Mccdaq, 2019a, 2019b) were selected and managed by an interface software program (TracerDAQ Pro) to process data by virtual graphing and data logging.



Figure 6. Experimental setup.

Error Analysis

The uncertainty in experimental measurements describes the factors that are to be taken into consideration such as instrument accuracy etc. A precise method for estimating uncertainty in experimental results has been presented by (Kline and McClintock, 1953).

The surface area of the CHE can be calculated using Eq. (35). Thus, the uncertainty is given by the expression as

$$w_R = \left[\left(\frac{\partial R}{\partial x_1} w_1 \right)^2 + \left(\frac{\partial R}{\partial x_2} w_2 \right)^2 + \dots + \left(\frac{\partial R}{\partial x_n} w_n \right)^2 \right]^{1/2} \quad (37)$$

where w_R is the standard uncertainty in the result and $w_1, w_2, \dots, w_x, \dots, w_n$ are the standard uncertainties of the independent variables.

$$w_{\dot{Q}} = \left[\left(\frac{c_p (T_{in} - T_{ex})}{h_i \Delta T_{lm}} w_m \right)^2 + \left(\frac{\dot{m} (T_{in} - T_{ex})}{h_i \Delta T_{lm}} w_{c_p} \right)^2 + \left(\frac{\dot{m} c_p}{h_i \Delta T_{lm}} w_{\Delta T} \right)^2 + \left(-\frac{\dot{m} c_p (T_{in} - T_{ex})}{h_i \Delta T_{lm}^2} w_{\Delta T_{lm}} \right)^2 \right]^{1/2} \quad (38)$$

The temperature-dependent error of the temperature detectors is designated by the relation of $\pm(0.15 + 0.002\Delta T)$ °C and calibrated according to the standard of IEC751:1983 by the manufacturer (Ordel, 2019). The temperature-dependent uncertainty for the specific heat capacity of the HTF was included as a function of temperature given in Eq. (14). The flow meter has an accuracy of $\pm 0.1\%$ with a repeatability of less than 0.05%. The USB-TEMP Daq device contributes additional error except the error of the sensor itself. Typically, the maximum error is ± 0.11 °C for the temperature range of 0–150 °C.

Preparation of Materials

For the cooking facility, sample to water ratio of 1:2 was used to satisfy a high degree of starch gelatinization in wheat grains since the transition temperatures for

gelatinization depend on the availability of water (Münzing, 1991). As the moisture levels of starch are reduced, the starch transition temperature increases to higher levels.

The wheat used in the experiments was received from a regional wheat producer as cleaned i.e. separated from dust, foreign materials, and broken wheat. The test results of the wheat properties are given in Table 2. For the statistical analysis, ANOVA was performed for the predicted data to determine the significant differences ($P < 0.05$). Duncan's multiple range tests were carried out. The experiments were replicated and the measurements were duplicated. Note that the mass of the wheat and the corresponding mass of water used in cooking were specified as 13 kg and 26 kg, respectively.

Table 2. Properties of wheat used in experiments.

| Properties | Values | SD (n = 4) | |
|--------------------------|--------|------------|--------|
| Type | Hard | – | |
| Color | L^* | 51.45 | 0.0568 |
| | a^* | 9.6 | 0.2998 |
| | b^* | 26.51 | 0.2968 |
| | YI | 77.81 | 0.0734 |
| Moisture content, | 6.00 | 0.0046 | |
| Protein (% d.b.) | 9.01 | 0.0146 | |
| Ash (% d.b.) | 1.48 | 0.0017 | |
| Specific heat, $c_{p,d}$ | 1975 | 25.0545 | |

Table 3. Variation in the grain moisture content.

| During preheating | | | | | | |
|-----------------------------------|--------------|-----------|--------------|-------|-------|-------|
| Initial moisture content (% d.b.) | | 6.00 | | | | |
| Grain | °C | T_m | 85 | 90 | 95 | 100 |
| moisture content | (% d.b.) | 12.01 | 16.07 | 33.21 | 37.36 | 39.33 |
| During boiling | | | | | | |
| t (min) | W (% d.b.) | t (min) | W (% d.b.) | | | |
| 5 | 42.73 | 30 | 77.62 | | | |
| 10 | 49.23 | 35 | 83.58 | | | |
| 15 | 59.73 | 40 | 90.74 | | | |
| 20 | 68.98 | 45 | 94.74 | | | |
| 25 | 71.6 | 50 | 100.3 | | | |

The color of the wheat samples was measured by HunterLab Colorimeter (Hunterlab, 2019). The moisture content of wheat was measured at 105 °C using oven method (AOAC, 1990). The Kjeldahl method was used to determine the protein contents of wheat using the methodology presented in (AOAC, 1990). The ash contents of wheat were measured at 900 °C according to (AOAC, 1990). The specific heat of the dry wheat grains was measured by using energy balance applied in Eq. (1). Additionally, the variation in grain moisture content during preheating and boiling processes was measured as indicated in Table 3. This dataset is significant to predict the specific heat of wheat grains during preheating and the time period of cooking process for complete gelatinization. The measurement procedure for this dataset is as follows: grain samples were extracted from the CP (open to the atmosphere) at each 5 °C temperature-interval during the

preheating process. Through the boiling process, grain samples were taken out of each 5-min time interval and then quenched in cold water. After removing the surface moisture, grains were wrapped and sheltered at 4 °C to prevent moisture loss before measuring the moisture content of grains for each batch.

Each cooking process was operated in a total time period of 50 min of which 5 min time period was specified to be the resting for boiled wheat grains and the complete discharging of the vapor inside the CP at the end of the cooking process. During the cooking operation, the boiled water was directed to a double pipe heat exchanger connected to the pressure relief valve. It was designed for condensing the water with an effective heat transfer area of $5 \times 10^{-2} \text{ m}^2$. The water being boiled was cooled by the water circulating through the double pipe heat exchanger. At the end of the cooking operation, the total condensed water was measured by a sensitive balance. Thus, the amount of heat rejected or the boiling loss was basically estimated for the entire cooking process:

$$Q_r = m_v h_{fg} = m_w c_{p,w} (T_p - T_w) \quad (39)$$

RESULTS AND DISCUSSION

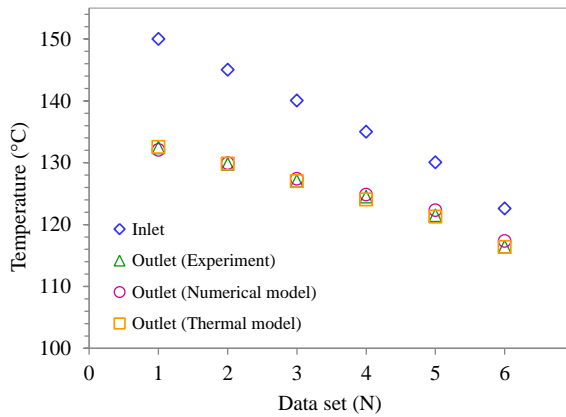
The results of the developed thermal model were compared with those of the numerical model and the experiments. The model outputs for the CP were obtained for different cooking parameters given in Table 4. It is seen that the model yields pretty good results for the prediction of the heat transfer area of the CHE and the exit temperature of the HTF even at saturation (i.e. boiling) temperature higher than 100 °C. This validation is very significant for describing the most effective parameters of the cooking process in terms of energy efficiency. Besides, it can be useful in the design stage of large-scale CPs and their efficient energy control.

Figure 7 shows the results obtained from the experimental analyses and the numerical and thermal models. The numerical and analytical results were compared with the experimental results and good agreement was obtained. While the maximum deviation of the outlet temperature is 1.12% for the numerical analysis, it is around 0.38% for the analytical approach.

Although the thermal model provides the advantage of solution simplicity, it gives limited information about the flow properties of HTF but is sufficient to make a CP design. On the contrary, making a numerical analysis is tedious and time-consuming; it provides better insight into fluid dynamics properties. The developed thermal model which estimates the outlet temperature of the designed CHE favorably will ensure to calculate the energy transferred to the mixture in the CP. This knowledge is significant both in the stage of CP design, energy optimization and system control. In Turkey, all CP producers make their designs using trial and error or by experience. However, this does not constantly give satisfying results when the CP capacity and the operating

Table 4. Predictions of the analytical model for sample experiments.

| N | Experimental | | | | | | | Model | | | | | | |
|---|-------------------------|----------------|----------------|-----------------|-----------------|-----------------|---------------------|------------------------------|------|------------------------------|-------------|----------------|-------------------------|--------------------------|
| | \dot{m}_{htf} kg/s | T_{in} °C | T_{ex} °C | T_{sat} °C | T_{ins} °C | T_{air} °C | Δt_2 sec | h_i W/m ² °C | Re | h_o W/m ² °C | T_s °C | T_{ex} °C | A_s m ² | Uncertainty $A_s, \%$ |
| 1 | 0.0847 | 150.0 | 132.4 | 100.0 | 52.1 | 40.0 | 2,700 | 360 | 3184 | 2,371 | 105.4 | 132.6 | 0.290 | 1.93 |
| 2 | 0.0916 | 145.0 | 129.8 | 100.1 | 52.3 | 39.5 | 2,700 | 377 | 3253 | 2,265 | 105.4 | 129.8 | 0.289 | 2.17 |
| 3 | 0.1000 | 140.0 | 127.0 | 100.2 | 53.7 | 37.1 | 2,700 | 397 | 3341 | 2,152 | 105.3 | 127.0 | 0.287 | 2.48 |
| 4 | 0.1111 | 135.0 | 124.5 | 100.0 | 53.5 | 37.7 | 2,700 | 424 | 3494 | 1,995 | 104.9 | 124.0 | 0.272 | 2.96 |
| 5 | 0.1378 | 130.1 | 121.5 | 100.0 | 53.6 | 37.2 | 2,700 | 494 | 4060 | 1,996 | 104.9 | 121.3 | 0.279 | 3.55 |
| 6 | 0.1380 | 122.6 | 116.4 | 100.1 | 53.1 | 37.8 | 2,700 | 478 | 3642 | 1,597 | 104.4 | 116.4 | 0.286 | 4.81 |
| 7 | 0.1904 | 130.9 | 125.4 | 110.2 | 56.2 | 36.0 | 2,220 | 674 | 5835 | 2,070 | 114.5 | 125.3 | 0.280 | 5.33 |
| 8 | 0.2258 | 130.8 | 128.2 | 120.2 | 56.0 | 36.2 | 1,400 | 805 | 7072 | 1,564 | 123.4 | 128.3 | 0.299 | 10.99 |

**Figure 7.** Comparison between the theories and practice.

conditions change. Moreover, this would not result in energy-efficient CP and lead to having a systematic approach for waste heat recovery. When the system parameters vary with design or operation, the system control would not be able to sustain energy optimization anymore. For this reason, the developed models will provide benefits from various aspects.

Temperature contours at the outlet of the CHE are illustrated in Figure 8 for each case given in Figure 7. The flow pattern is quite different relative to a straight tube since the most prominent characteristic of flow in helicoidal pipes is the secondary flow induced by centrifugal force which causes the fluid particles inner side of the CHE to move faster than the outer and thus provides benefit to enhance the heat transfer rate. The degree of secondary flow lowers gradually as moving from Figure 8a to 8f. This is related to the balance between the inlet temperature of the CHE and the corresponding mass flow rate of the HTF demanded by the cooking process. As the inlet temperature increases, the mass flow rate is reduced to adjust the sufficient heat load that needs to be transferred to the mixture in the CP. At high inlet temperatures, the average HTF velocity is relatively low thus it is probably earlier the secondary flow at the pipe outlet to develop. This means that increasing the HTF velocity in the CHE results in less chance to develop the secondary flow. Therefore, the inlet temperature, HTF properties and velocity, and pipe

length are important design parameters that need to be specified properly so that the convection heat transfer coefficient in the CHE is enhanced.

During the cooking process, the minimization of the thermal energy supply accompanied by preserving the final product quality is essential and can be improved. The heat flux transferred to the mixture, \dot{q}_b should be adjusted as initiating the ONB since bubbles during nucleate boiling serve as energy movers and provide upside-down movement of the mixture. Bayram (2006) also proposed that the cooking temperature is to be at boiling temperature to benefit from the mixing effect of water bubbles. Thus, the regime of boiling is a decisive parameter for enhancing the convective heat transfer coefficient and effective cooking. Increasing the convection heat transfer coefficient will increase the mass transfer to wheat kernels and quicken the gelatinization. However, as the ONB point is over exceeded, the boiling loss and accordingly the energy consumption will increase. Furthermore, the disruption of wheat kernels and leaching of the starch during cooking operation are affected by the strength of nucleate bubbles. This may cause lots of problems such as stickiness, size deformation, nutrient loss, etc. (Bayram *et al.*, 2004). Using a mechanical mixer inside the CP can satisfy homogeneous mixing and cooking enhancement but this will cause deformation of wheat grains. Therefore, cooking conditions should be well arranged for product quality to ensure complete gelatinization without deforming, darkening and making the product so, sticky. On the other hand, increasing the heat flux on the CHE strengthens the boiling which, in turn, increases the organic and coloring compounds leached into the water and changes the watercolor to dark. Additionally as the level of the leaching intensifies, the water becomes much denser and its viscosity increases during boiling due to water absorption by the wheat grains and water unavailability with time. This partially prevents the bubble movements and causes to lessen nucleate mixing toward the end of the cooking process. Thus, it is supplied more energy to the mixture in practical applications for this problem to obtain complete gelatinization at the bottom side (conical part) of the CP. An increasing mass of wheat grains at the upper part

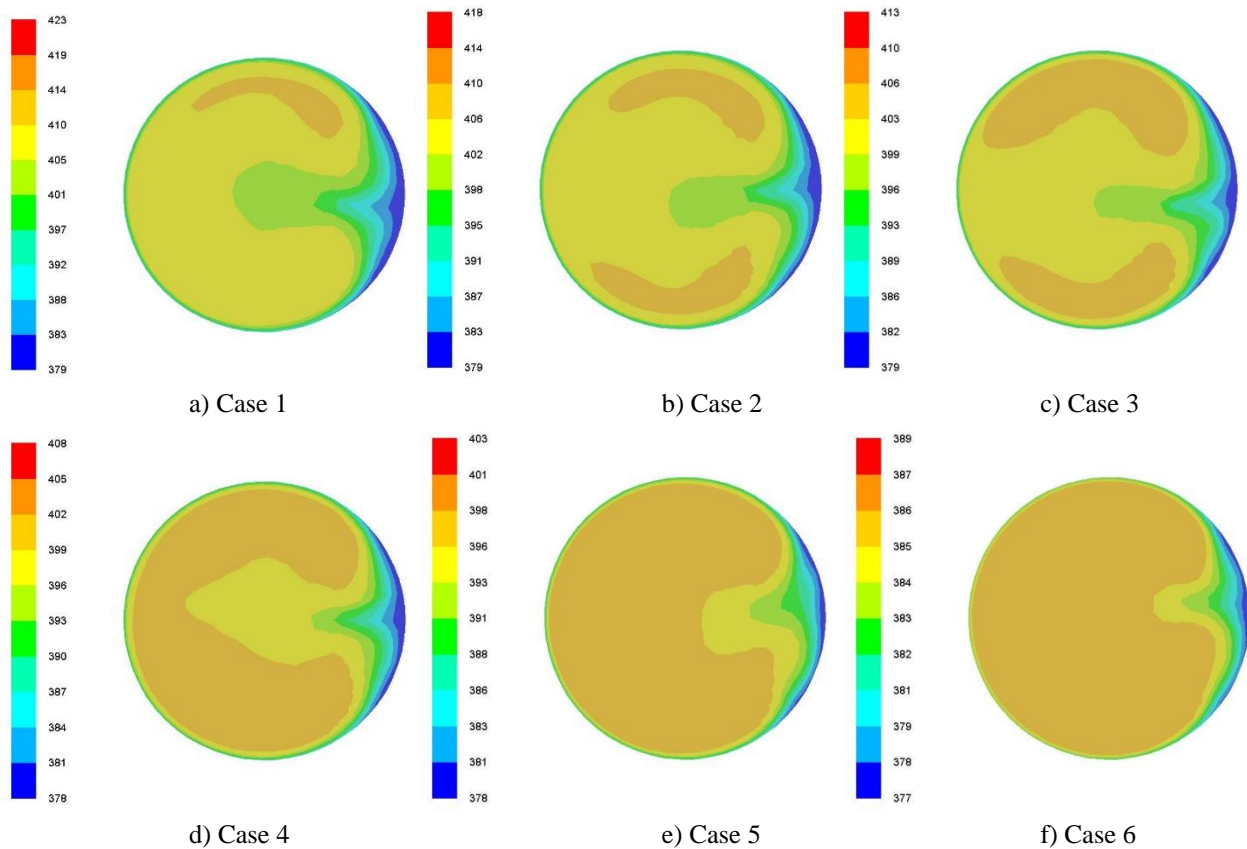


Figure 8. Temperature contours at the CHE outlet (as Kelvin) for the specified cases.

makes cushion effect to the bottom or applies pressure which degrades the gelatinization of grains in that region. Another factor causing ineffective energy transfer to that part is the reduced HTF temperature at the downstream of the CHE. Thus, the minimization of the energy consumption results in many problems which should be considered thoroughly.

Table 5 shows the cooking parameters of boiled wheat obtained from different batches. The results reveal that the inner structure of wheat grains, their initial moisture content and thermo-physical properties affect cooking quality and cooking time for complete gelatinization. The complete gelatinization depends strongly on wheat properties, cooking time, boiling temperature and regime. Water absorption of wheat samples (i.e., moisture uptake) during the cooking process can give information about the level of gelatinization. The minimum moisture content of boiled wheat on dry basis (d.b.) must be at the level of 100%. In this study, the cutting method to examine the gelatinization was used where 100 cooked kernels were cut into two equal pieces and then the endosperms were examined for the opaque white center. As seen from Table 5, the yellowness index is inversely affected by increasing the boiling temperature but this is not desired for the final product quality. For the calculation of BOD_5 , the method presented by Balcı and Bayram (2020) was used. Most of the BOD_5 values are lower than half of the results presented by Balcı and Bayram (2020) who obtained 429.5 mg/L under controlled experimental conditions. One of the followed methods in this study is the minimization of energy demand for cooking which results in reduced BOD_5

values due to decreasing leaching substances with reducing energy supply during the boiling process. Wastewater of a bulgur plant is disposed to the environment however it has a high value of BOD_5 (about 450 mg/L Balcı and Bayram (2020)) which can lead to environmental diseases.

Minimization of the energy need to obtain gelatinized wheat was also investigated in this study. The minimum energy transfer to the mixture was adjusted by keeping the central region of the CP at the boiling temperature. This was accomplished by simultaneously monitoring the measured temperature of the central region on the DAQ interface program and adjusting the flow rate of the HTF using a frequency-controlled pump. The diffusion of convective currents from the CHE to the central part of the CP was effective on this phenomenon. For this reason, the heat flux on the CHE was regulated enough to initiate the nucleate boiling. However, the ONB depends on the fluid–heating material combination and the fluid pressure. Thus, the ONB point specified in Figure 3 is able to change with operating conditions. There is no available correlation in the literature to estimate the ONB point for different combinations. In this study, \dot{q}_b and ΔT_{excess} were calculated and the results presented in Table 4 were obtained. The measurements and the calculations showed that \dot{q}_b ranged from 7,000 W/m² to 10,000 W/m² at $\Delta T_{excess} \approx 5$ °C. This range is in accord with the region of nucleate boiling presented in Figure 3. Lowering the \dot{q}_b more causes to lessen the bubble density and mixing effect, particularly in large-scale industrial CPs.

Table 5. Properties of wheat for sample cooking operations.

| Sample | T_b °C | Color | | | | Protein % d.b. | Ash % d.b. | BOD_5 mg/L | W % d.b. |
|--------|-------------|-------|-------|-------|-------|-------------------|---------------|-----------------|---------------|
| | | L^* | a^* | b^* | YI | | | | |
| 1 | 100 | 51.50 | 8.88 | 31.78 | 85.43 | 10.94 | 1.26 | 215.0 | 103.3 |
| 2 | 100 | 50.36 | 8.55 | 30.49 | 83.99 | 10.40 | 1.32 | 212.5 | 108.7 |
| 3 | 100 | 51.33 | 9.22 | 30.39 | 86.51 | 10.85 | 1.32 | 222.7 | 114.0 |
| 4 | 100 | 51.09 | 8.85 | 31.71 | 85.64 | 11.57 | 1.21 | 220.5 | 108.3 |
| 5 | 100 | 50.71 | 9.06 | 31.96 | 84.83 | 11.03 | 1.22 | 182.5 | 103.7 |
| 6 | 100 | 50.73 | 9.15 | 31.36 | 85.59 | 10.65 | 1.25 | 200.2 | 104.3 |
| 7 | 110 | 52.98 | 7.00 | 26.40 | 72.95 | 9.52 | 1.58 | 228.0 | 100.8 |
| 8 | 110 | 53.44 | 7.32 | 30.99 | 80.15 | 9.13 | 1.08 | 197.5 | 98.5 |
| 9 | 120 | 52.60 | 7.59 | 30.27 | 80.50 | 9.48 | 1.10 | 194.7 | 101.2 |
| 10 | 120 | 50.39 | 7.46 | 28.00 | 77.22 | 10.37 | 1.24 | 216.3 | 111.0 |

Conventional bulgur plants have operated CPs supplying high energy to wheat grains in order to gelatinize them as much as possible. The cooking state is controlled by the use of centre cutting method, the color of evaporated water from the CP or smell of this water (Bayram, 2006). These simple methods are useful to be able to control the cooking operation during bulgur production due to low labor however these sensory methods are not developed and rely on experience and qualified staff. Recently, this step has left its place to new automated CPs in modern bulgur plants.

In the automated CP, preheating temperature/time, cooking temperature/time, water amount, resting and discharging times are adjusted by the operator who makes these data entry to the control panel of the CP. The energy demand for industrial cooking is supplied indirectly by a steam generator which is generally operated under certain temperature levels and specified thermal loads. The cooking load is adjusted by an operator who manipulates the cooking time until the gelatinization of the grains' structure is maintained. However, this procedure requires operational experience based on the variation in the operational parameters mentioned above. Noting that the properties of raw material and the mixing of the reddish wheat with durum wheat during harvesting and storing also affect the cooking process and final product since finding pure or homogeneous raw material is nearly impossible for bulgur production in undeveloped and developing countries (Bayram and Öner, 2006). Thus, the energy supplied to the mixture in the CP is adjusted by an experienced operator who observes the cooking degree of bulgur at the end of the cooking process. During the cooking process, the geometry of the CP (shape,

capacity, etc.) and the properties of the heating element affect the cooking quality. For example, the latest automated CP consumes 1.5 tons of saturated steam at 4.5–5 bar gauge pressure with a steam trap for the cooking process utilizing 5:4 of tons wheat to water ratio. The double-stage cooking operation is used in this system. The CP in the first-stage preheats the water-wheat mixture to a preset temperature of 80–85 °C. The heating element is composed of a CHE in which steam is used. After preheating, the mixture is unloaded into the second-stage which cooks the wheat grains about 25–28 min until the preheating temperature reaches the maximum temperature of 108 °C at the end of cooking. Then, the mixture in this stage is rested about 15 min. The moisture content of the wheat grains reaches 50–52% w.b. (wet basis) at the end of the cooking process. The residual water amount changes between 1–1.2 tons for such a process. The CP in the second-stage has two individual CHEs to enhance the degree of cooking. One of them is used for heating the upper region (cylindrical in shape) of the CP and the other is used for the conical part heating. The use of single-piece CHE requires much energy to keep the HTF temperature at the conical part not lower. Lowering of the steam temperature will lead to ineffective heat transfer at this part of the CP. Moreover, circulation pumps are used to circulate the process-water from the bottom side to the upper. The steam expelled out during the cooking process is used in the first stage of the cooking system for energy efficiency. As a result, the average rate of specific energy consumption is estimated at around 400–500 W/kg (thermal power supplied for one kilogram of wheat) for a modern industrial bulgur plant to produce bulgur. This rate would increase to 800 W/kg for conventional bulgur plants having a single-stage non-automated CP.

Table 6. Water balance for sample cooking operations*.

| Sample | m_{ev} | $m_b - m_c$ | m_f | m_{loss} | m_r | m_l | m_a | m_t |
|--------|----------|-------------|-------|------------|--------|-------|--------|--------|
| 1 | 3 | 903 | 483 | 518 | 12,460 | 137 | 11,770 | 26,000 |
| 2 | 3 | 1,501 | 447 | 565 | 12,150 | 140 | 11,474 | 26,000 |
| 3 | 3 | 1,626 | 406 | 530 | 12,200 | 134 | 11,369 | 26,000 |
| 4 | 3 | 2,001 | 525 | 648 | 11,965 | 122 | 10,980 | 26,000 |
| 5 | 3 | 2,014 | 511 | 583 | 12,240 | 124 | 10,773 | 26,000 |
| 6 | 3 | 3,500 | 436 | 645 | 10,453 | 145 | 11,108 | 26,000 |

*All units in gram.

The experimental findings show that the minimum rate of specific energy consumption is around 325–375 ±5% W/kg in case of preheating the process-water with boiling losses, but it could reach 400–475 ±5% W/kg without using waste heat. When the wheat to water ratio is reduced to 1, the energy supply for preheating could be reduced ~25%. As concluded, the energy need in large-scale CPs can be improved by enhancing the overall convection heat transfer coefficient inside the CP and by lowering the water amount. However, even the energy demand can be reduced as a result of the mentioned improvements; it cannot be lowered any more. Since the average Re in the CHE must be higher than 2,300. Under most practical conditions, the flow in a pipe is laminar for $Re < 2,300$ which results in low \dot{q}_b to reject heat for a certain pipe length. Otherwise, the pipe length extends too much and it becomes unsuitable for CP design. A conservative approach for fully turbulent is taken as $Re > 4,000$ in many cases (Çengel and Ghajar, 2011). Thus, the mass flow rate through the CHE is adjusted based on this critical value and the coil length is specified as a function of convection heat transfer coefficient and critical heat flux. Besides, as the coil radius is increased in large-scale applications, the effect of coil curvature on flow decreases and thus the domination of centrifugal forces will be lesser (Jayakumar *et al.*, 2010). In other words, the curved pipe would behave a straight pipe which, in turn, lowers the convection heat transfer coefficient inside the CHE.

The mass balance of water during the cooking process is considered to be significant for energy consumption. Table 6 shows the mass balance for the water utilized during the cooking process. In many conventional bulgur plants, the process-water amount is used 1.4 times of the wheat amount. As a rule of thumb, ~43% of the process-water is absorbed by wheat kernels at the end of the cooking process and ~28% of the process-water is rejected as wastewater and 2.5% of the cooked wheat amount is leached into the wastewater in industrial practices. The water uptake (m_a) calculated in this study is coherent with the industrial data and the wastewater amount (m_r) is higher relative to the practice since the energy optimization has yielded lower water evaporation. It is noted that 1.4-ratio corresponds to 2.0-ratio in our experimental study. Based on 2.0-ratio, the percentage of wastewater will increase from 28% to 40%. While m_r obtained from this study was around 12,000 gr, it would have been ~10,400 gr (26,000×40%) based on the data of industrial practice. Sample 2 in Table 6 shows that the wastewater amount is close to the practice since the energy supplied to the mixture was high and more water was accordingly evaporated during boiling. The total amount of leached substances was measured by evaporating the sample residual water. The percentage of leached substance was about half of the industrial practice which is pretty consistent with the practice since BOD_5 which is a measure of leached substance amount in the wastewater was reduced to less than half as compared to the practice.

At the end of the cooking process, the butterfly valve of the CP is opened and the residual water is discharged into a collecting vessel. Some part of this water which flashed and evaporated into ambient air constitutes ~4% of the process-water amount. The amount of water flashed depends strongly on atmospheric conditions such as atmospheric pressure, the relative humidity of a location. The instantly measured values by the Turkish State Meteorological Service (MGM, 2019) were used in the calculations. As seen, the estimated m_{ev} values are negligible to consider it in the water balance.

CONCLUSION

Turkey is the biggest bulgur producer (1,230,766 tons per annum as of 2018 (TMO, 2019)) in the world and exports annually above 120 million \$ to other countries. In Turkey, there are a great number of manufacturers producing CPs at different types and performance. The designs of these systems are generally made by trial and error or experience however this is not an effective method of getting these systems better without prior theoretical analyses. This study presents the details of the wheat cooking process and a novel thermal model for designing CP (having CHE as an energy supplier or heating element) which is widely used in bulgur plants. The effect of the heating element and its design properties have been discussed from the views of energy efficiency and bulgur quality. The findings of this study which would guide CP producers and bulgur plants positively are as follows:

- The ONB serves as an energy mover and provides upside-down movement of the mixture via nucleate bubbles. It depends upon the critical heat flux on the CHE which corresponds to $\Delta T_{excess} \approx 5$ °C. This value is significant to estimate the critical heat flux and the surface area of the CHE for regulating energy efficiency. Increasing the critical heat flux which, in turn, causes more water to be evaporated during cooking increases the water unavailability in the CP. As a result, this may result in producing ungelatinized wheat kernels if wheat to water ratio is around 1.
- Changing the coil pitch has a negligible effect on the Nu inside the CHE whereas the effect of coil radius decreases it. Increasing the diameter of the coil requires having a lengthy pipe to attain a fully developed flow. The proper sizing of CHE is very essential for both the volume in the CP and the heat transfer properties of flow to accomplish the task.
- The minimum energy supplied to the mixture is related to the degree of wheat kernels being completely gelatinized at the end of the cooking process. This can be performed by accelerating the nucleate bubble formations, i.e. initiating the nucleate boiling. Only supplying energy during the cooking process to meet the heat loss of the CP does not accomplish the complete gelatinization and extends the gelatinization time since the diffusion of

water into starch is related to the enhancement of boiling convection heat transfer coefficient.

- The estimated average rate of specific energy consumption lies between 400–500 W/kg (thermal power supplied for one kilogram of wheat) for a modern industrial bulgur plant whereas it would increase to 800 W/kg for conventional bulgur plants having single-stage CP. The experimental findings have indicated that the corresponding range could be between 325–375 \pm 5% W/kg with waste heat recovery (otherwise it would reach to 400–475 \pm 5% W/kg) and doubled process-water amount. The estimated range can be reduced both by reducing the water amount (this minimizes only the energy consumption through the preheating of the mixture ~25%) and enhancing the convection heat transfer coefficient of the HTF inside the CHE using steam instead of thermal oil.
- The minimization of energy supply for cooking has a positive effect on BOD_5 . BOD_5 which is about 450 mg/L in the wastewater of a bulgur plant has been reduced less than half of that value by the energy optimization strategies.
- The process-water can be reduced to half by water recovery, i.e. decreasing wheat to water ratio to 1:1–1:1.2 as the study clearly indicates. This knowledge is also supported based on the applications of a modern bulgur plant. Reducing water amount will have a positive effect on the energy demand minimization.
- Insulating the outer side of the CP is essential to minimize the heat loss to the surroundings up to 3–4 based on the operating conditions. As seen in Table 4, the insulation material prevents the CP outer surface to increase higher levels i.e. boiling temperature. This is not a common application in Turkish bulgur plants. The inclination angle of the cover plate is to be adjusted lower than 20° if the evaporated water is used in the second stage of the CP and it would be higher than 20° if the evaporated water is to be condensed in the CP. The latter case benefits water recovery. A non-insulated cover plate of the CP will also cause to increase the condensation on the plate.

ACKNOWLEDGEMENT

This study was funded by the Scientific Research Projects Governing Unit of Gaziantep University with grant no. MF.11.13. Authors also appreciate Dr. Fatih Balcı (Food Engineer), Günmak Milling Machinery Co. (Manufacturer of cooking and drying systems for bulgur) and Arbel Group (Making production and processing of bulgur) for their cooperation in part of the study. Any opinions, findings and conclusions or recommendations expressed in this study are those of the authors and do not necessarily reflect the views of the cooperators.

REFERENCES

- AOAC, 1990, *Official Methods of Analysis of the Association of Official Analytical Chemists*, (Fifteenth Ed.), Washigton, DC.
- Bakshi A. S. and Singh R. P., 1980, Kinetics of water diffusion and starch gelatinization during rice parboiling, *J. Food Sci.*, 45(5), 1387-1392.
- Balcı F. and Bayram M., 2020, Bulgur cooking process: Recovery of energy and wastewater, *J. Food Eng.*, 269, 109734.
- Bayram M., 2005, Modelling of cooking of wheat to produce bulgur, *J. Food Eng.*, 71(2), 179-186.
- Bayram M., 2006, Determination of the cooking degree for bulgur production using amylose/iodine, centre cutting and light scattering methods, *Food Control*, 17(5), 331-335.
- Bayram M. and Öner M. D., 2006, Determination of applicability and effects of colour sorting system in bulgur production line, *J. Food Eng.*, 74(2), 232-239.
- Bayram M., Öner M. D. and Eren S., 2004, Effect of cooking time and temperature on the dimensions and crease of the wheat kernel during bulgur production, *J. Food Eng.*, 64(1), 43-51.
- Bruce D. and Giner S., 1993, Mathematical modelling of grain drying in counter-flow beds: investigation of crossover of air and grain temperatures, *J. Agr. Eng. Res.*, 55(2), 143-161.
- Chin Y.-S. S., 1995, *Numerical solution of the complete two-phase model for laminar film condensation with a noncondensable gas*, Ph.D. Thesis, Manitoba University, Canada.
- Churchill S. W. and Chu H. H., 1975, Correlating equations for laminar and turbulent free convection from a vertical plate, *Int. J. Heat Mass Tran.*, 18(11), 1323-1329.
- Cornwell K. and Houston S., 1994, Nucleate pool boiling on horizontal tubes: a convection-based correlation, *Int. J. Heat Mass Tran.*, 37, 303-309.
- Çengel Y. A. and Ghajar A. J., 2011, *Heat and mass transfer: Fundamentals & Applications* (Fourth Ed.), McGraw-Hill, New York.
- Fuchs, 2013, Opet Fuchs Mineral Oil Industry and Trade Inc., Izmir, Turkey, *Renolin Therm 320 Product Information*.
- Fujii T. and Imura H., 1972, Natural-convection heat transfer from a plate with arbitrary inclination, *Int. J. Heat Mass Tran.*, 15(4), 755-767.

- Gerstmann J. and Griffith P., 1967, Laminar film condensation on the underside of horizontal and inclined surfaces, *Int. J. Heat Mass Tran.*, 10(5), 567-580.
- Hogg G. W., 1969, *The effect of secondary flow on point heat transfer coefficients for turbulent flow inside curved tubes*, Ph.D. Thesis, Idaho University, Moscow.
- Hunterlab, 2019, *Colorflex specifications*, <https://www.hunterlab.com/colorflex-ez-specifications.pdf>.
- Izocam, 2019, *Technical datasheet of Izocam industrial blanket*, <http://www.izocam.com.tr/p157-industrial-blanket.html>.
- Jayakumar J., Mahajani S., Mandal J., Iyer K. N. and Vijayan P., 2010, CFD analysis of single-phase flows inside helically coiled tubes, *Comput. Chem. Eng.*, 34(4), 430-446.
- Kline S. and McClintock F., 1953, Describing uncertainties in single-sample experiments, *ASME Mech. Eng.*, 75(1), 3-8.
- Koca A. F. and Anil M., 1996, Farklı buğday çeşitleri ve pişirme yöntemlerinin bulgur kalitesine etkisi, *Gıda Dergisi*, 21(5).
- Krohne, 2019, *Optimass 6000 technical datasheet*, https://cdn.krohne.com/fileadmin/media-lounge/files-marine/Downloads_pdf/TD_OPTIMASS_6000.pdf.
- Manlapaz R. L. and Churchill S. W., 1981, Fully developed laminar convection from a helical coil, *Chem. Eng. Commun.*, 9(1-6), 185-200.
- Marrero T. R. and Mason E. A., 1972, Gaseous diffusion coefficients, *J. Phy. Chem. Ref. Data*, 1(1), 113-118.
- Mccdaq, 2019a, *USB-2416 User's Guide*, <https://www.mccdaq.com/pdfs/manuals/USB-2416.pdf>.
- Mccdaq, 2019b, *USB-TEMP User's Guide*, <https://www.mccdaq.com/pdfs/manuals/USB-TEMP.pdf>.
- MGM, 2019, *Weather forecast for Gaziantep*, <https://www.mgm.gov.tr/tahmin/il-ve-ilceler.aspx?il=Gaziantep&ilce=%C5%9Eehitkamil>.
- Minkowycz W. and Sparrow E., 1966, Condensation heat transfer in the presence of noncondensables, interfacial resistance, superheating, variable properties, and diffusion, *Int. J. Heat Mass Tran.*, 9(10), 1125-1144.
- Münzing K., 1991, DSC studies of starch in cereal and cereal products, *Thermochim. Acta*, 193, 441-448.
- Mwesigye A., Yılmaz İ. H. and Meyer J. P., 2018, Numerical analysis of the thermal and thermodynamic performance of a parabolic trough solar collector using SWCNTs-Therminol® VP-1 nanofluid, *Renew. Energ.*, 119, 844-862.
- Ordel, 2019, *Resistance thermometer*, <http://www.ordel.com.tr/en/urun/or60>.
- Orlov V. and Tselishchev P., 1964, Heat exchange in spiral coils with turbulent flow of water, *Therm. Eng.* (Translated from Teploenergetika), 11(12), 97.
- Pakkens, 2019, *Accurate pressure gauges*, <http://www.pakkens.com.tr/products/basinc-olcerler-1/hassas-manometre-6/?lang=en>.
- Pratt N. H., 1947, The heat transfer in a reaction tank cooled by means of a coil, *T. I. Chem. Eng.-Lond.*, 25, 163-180.
- Rocca-Poliméni R., Flick D. and Vasseur J., 2011, A model of heat and mass transfer inside a pressure cooker, *J. Food Eng.*, 107(3-4), 393-404.
- Rohsenow W. M., Hartnett J. P. and Cho Y. I., 1998, *Handbook of Heat Transfer* (Third Ed.), McGraw-Hill, New York.
- Srinivasan P., Nandapurkar S. and Holland F., 1970, Friction factors for coils, *Trans. Inst. Chem. Eng.*, 48(4-6), T156-T161.
- Stapley A., Fryer P. and Gladden L., 1998, Diffusion and reaction in whole wheat grains during boiling, *AIChE J.*, 44(8), 1777-1789.
- TMO, 2019, *Turkish grain board*, <http://www.tmo.gov.tr/Upload/Document/hububatsektor-raporu2018.pdf>.
- Turhan M. and Gunasekaran S., 2002, Kinetics of in situ and in vitro gelatinization of hard and soft wheat starches during cooking in water, *J. Food Eng.*, 52(1), 1-7.
- Watanabe H., Fukuoka M., Tomiya A. and Mihori T., 2001, A new non-Fickian diffusion model for water migration in starchy food during cooking, *J. Food Eng.*, 49(1), 1-6.
- Yildizpompa, 2019, *Technical properties of YKF-1" internal eccentric gear pump*, <http://www.yildizpompa.com/wp-content/uploads/2017/11/YKF-1%C2%BD.pdf>.
- Yılmaz İ. H. and Söylemez M. S., 2014, Thermomathematical modeling of parabolic trough collector. *Energ. Convers. Manage.*, 88, 768-784.
- Yılmaz İ. H., 2014, *A theoretical and experimental study on solar-assisted cooking system to produce bulgur by using parabolic trough solar collector*, Ph.D. Thesis, Gaziantep University, Turkey.

Yılmaz İ. H., 2018, *Energy efficient cooking pot* (In Turkish: Enerji verimli pişirme kazanı), Patent No: TR 2015 13024 B, Turkish Patent and Trademark Office, Turkey.

Yılmaz İ. H. and Göksu T. T., 2016, Experimental and CFD analyses of a helicoidal heat exchanger, *International Energy Engineering Congress 2016*, Gaziantep, Turkey, 638-646.

Yılmaz İ. H., Göksu T. T., Kılıç M. and Söylemez M. S., 2017, Performance comparison of circular and square cross-sectioned helicoidal heat exchangers using experimental and CFD analyses, *International*

Conference on Advances and Innovations in Engineering, Elazığ, Turkey, 487-490.

Yılmaz İ. H., Hayta H., Yumrutaş R. and Söylemez M. S., 2018, Performance testing of a parabolic trough collector array for a small-scale process heat application, *ISI BILIM TEK DERG* (Journal of Thermal Science and Technology), 38(1), 43-53.

Yılmaz İ. H. and Mwesigye A., 2018, Modeling, simulation and performance analysis of parabolic trough solar collectors: A comprehensive review, *Appl. Energ.*, 225, 135-174.



İbrahim Halil YILMAZ is an associate professor at the Mechanical Engineering Department of AAT Science and Technology University, Adana, Turkey. He received his B.Sc. (2005), M.Sc. (2009) and Ph.D. (2014) degrees in Mechanical Engineering Department of Gaziantep University. He worked in several positions including Gaziantep University (2007–2016), Zurich Technopark (2009), and German recycling sector (2009). He is the author or co-author of more than 50 scientific papers in the international prestigious journals or conferences. His main research interests include green energy systems, thermal system design and modeling, analytical and numerical heat transfer/fluid flow, refrigeration systems, biomass to power, and machine learning for renewables.



Mehmet Sait SÖYLEMEZ is a professor at the Mechanical Engineering Department of Gaziantep University, Gaziantep, Turkey. He obtained his B.Sc. (1985) and M.Sc. (1988) degrees from the Mechanical Engineering Department of Middle East Technical University, and his Ph.D. (1992) in the Mechanical Engineering Department of Gaziantep University. He has published more than 50 scientific papers in various international journals and conferences. His main research areas are refrigeration, heat pumps, solar energy, heat transfer and thermo-economic optimization.



INVESTIGATING THE EFFECTS OF PLASMA ACTUATOR ON THE FLOW CONTROL AROUND NACA2415 AIRFOIL

Aytaç ŞANLISOY* and Yahya Erkan AKANSU**

*Department of Mechanical Engineering, Faculty of Engineering, Yalova University, Yalova, Turkey, aytacsanlisoy@gmail.com

** Department of Mechanical Engineering, Faculty of Engineering, Niğde Ömer Halisdemir University, Niğde, Turkey, akansu@ohu.edu.tr

(Geliş Tarihi: 03.05.2019, Kabul Tarihi: 27.02.2020)

Abstract: In this study, the effects of the plasma actuator on flow control at varied Reynolds numbers and attack angles are examined. Plasma actuator is placed on the NACA2415 airfoil at $x/C = 0.1$. The effect of the actuator to active flow control is examined at Reynolds number between 8×10^3 and 9×10^4 in the wind tunnel. The lift force which acted on the airfoil was measured by using a force balance system. The velocity measurements were done by the hot-wire probe, located at the wake region, and the flow around model was visualized by the smoke wire method. When the plasma was active, an increased lift force and a narrowed wake region are observed. The stall angle shifted to the higher attack angle by the effective active flow control at low Reynolds numbers. Prevent of the flow separation was enhanced up to 18° angle of attack and the maximum lift force occurred at the 14° angle of attack which is doubled when the plasma actuator is on.

Keywords: airfoil, flow control, lift force, plasma actuator

PLAZMA AKTÜATÖRÜN NACA2415 AIRFOIL ETRAFINDA AKIŞ KONTROLÜNE ETKİLERİNİN ARAŞTIRILMASI

Özet: Bu çalışmada, değişen Reynolds sayılarında ve hücum açılarında plazma aktüatörlerin akış kontrolüne etkisi incelenmiştir. Plazma aktüatör NACA2415 airfoil üzerinde $x/C=0.1$ konumuna yerleştirilmiştir. Aktüatörün aktif akış kontrolüne etkisi Reynolds sayısının 8×10^3 ile 9×10^4 aralığında rüzgar tüneline incelenmiştir. NACA2015 tipi uçak kanat profiline etki eden kaldırma kuvveti, kuvvet balans sistemi kullanılarak ölçülmüştür. Hız ölçümleri, iz bölgesine konumlandırılan kızgın tel probu ile ölçülmüş ve model etrafındaki akış duman tel yöntemi ile görselleştirilmiştir. Plazmanın aktif olduğu durumda, kaldırma katsayısında artış ve iz bölgesinde daralma gözlemlenmiştir. Düşük Reynolds sayılarında etkili aktif akış kontrolü ile akış ayrılması daha yüksek hücum açılara kaydırılmıştır. Akış ayrılması önlenmesi 18° hücum açısına kadar artırılmıştır ve 14° de gerçekleşen en yüksek kaldırma kuvveti plazma aktüatörün çalıştırılması ile iki katına çıkmıştır.

Anahtar Kelimeler: airfoil, akış kontrolü, kaldırma kuvveti, plazma aktüatör

NOMENCLATURE

| | |
|------------|---------------------------------|
| Re | Reynolds number |
| C_L | Lift coefficient |
| α | Attack angle |
| f | Frequency |
| V | Voltage |
| C | Chord length |
| x | Location of actuator on airfoil |
| AR | Aspect ratio |
| pp | Peak to peak |
| U_∞ | Free stream velocity |
| U | Local velocity |

INTRODUCTION

In many engineering applications, the fluid acting on bodies caused design and control problems. In recent years, optimum design and control have been desired in the aeronautic industry to produce lightweight and compact air vehicles. Many control strategies are developed to control flow around bodies. These methods can be classified as a passive control such as trip wires, geometrical modification, control rod, splitter plates and active control such as synthetic jets, suction or blowing channels, plasma actuators etc (Firat et al. 2013). In this study, the plasma actuators are investigated because of the promising solutions they provide to the flow control. The plasma actuators convert surrounding air to ionized air and generate a surface plasma which drives the bulk motion of molecules in the plasma region. The bulk motion creates

an induced flow on the bodies (Sanlisoy 2013). The advantages of the plasma actuators could be as follows: transfer of electrical energy to the flow without any moving parts and high response time. The flow control characteristics, such as aerodynamic force coefficients, flow separation and the stall angle could be enhanced by plasma actuators at low Reynolds numbers (Akansu and Karakaya 2013; Akansu et al. 2013; Akbıyık et al. 2017). Basically, plasma actuators consist of two electrodes, dielectric material, and a power supply which provides the energy. The plasma actuators can be

classified as a DC corona discharge plasma actuators and the dielectric barrier discharge actuators. Preliminary researches were done by using the DC corona discharge which consists of two electrodes located on the geometry and then activated by the power supply. This method has limited use because of glow to spark transition occurrence at high voltages. Roth et al. (2004) designed the dielectric barrier discharge actuator which has electrodes located on the upper and lower surface of dielectric material to prevent this transition.

Table 1. The studied topics in the literature.

| Research team | Studied topics | Required properties |
|---|---|---|
| Zito et al. (2012), Thomas et al. (2009), Ryan and Subrata (2012) | Dielectric materials | -high dielectric strength, -low dielectric constant (quartz-like materials) -increased thickness of dielectric material -flexible to mount on curved bodies, thin and nonfragile |
| Debien et al. (2012), Erfani et al. (2015), Thomas et al. (2009) | Electrode geometry | The embedded electrode should be sufficiently wide to obtain optimum body forces. There are a variety of exposed electrode geometry in the literature which has been investigated. |
| Thomas et al. (2009), Roth et al. (2004) | Multi actuator arrays | the body forces increase with the number of actuators. the enhancements are not proportional to the number of actuators. Paraelectric and peristaltic actuation mechanisms are introduced to enhance body forces. |
| Benard and Moreau (2010), Little and Samimy (2010), Guler et al. (2018) | Signal modulation | Duty cycles, burst modulation, and amplitude modulation signals were used in the literature. |
| Roth et al. (2004), Song et al. (2012) | Plasma discharge mechanism | Corona discharge, dielectric barrier discharge, nanosecond pulse discharge. |
| Abdollahzadeh et al. (2018), Feng et al. (2012), Taleghani et al. (2012), Meng et al. (2018) | The effect of plasma applicator on the flow control | The effects of plasma applicator on the lift coefficient, the drag coefficient and stall angle delaying are examined. |
| Jolibois et al. (2008), Sosa and Artana (2006) | Plasma actuator position | Optimum position is near separation edge. |
| Feng et al. (2012) | Wake region characteristics | The effects of the plasma applicator on the wake region of airfoils are drifted to downward and the recirculation region narrowed and shortened |

The studies in the literature are carried out in the stationary medium to investigate the generated flow with the plasma actuator (wall jet velocity) or in controlled flow field to examine the effect of plasma actuator on the flow control. There are electrical parameters which are effective in the plasma actuator characteristics whereas there are flow control parameters which are affected by the electrical properties of the plasma actuator. The effective parameters are the voltage, frequency, plasma power, dielectric material properties, electrode design while the flow control parameters such as the plasma-induced velocity, velocity distribution, pressure distribution, velocity profile in the wake region, the lift coefficient and the drag coefficient are effected parameters by the plasma actuator.

The challenges of the plasma applicators can be listed in Table 1.

Although there are many studies on the flow control with the plasma actuator, the limitations of the plasma actuators are not given comprehensively. In this study, limitations of the flow control with the plasma actuator are examined. While the plasma actuators are effective at very low Reynolds numbers (up to 5×10^4 Re), it becomes insufficient at low Reynolds numbers (higher than 5×10^4 Re). The enhancement of the lift coefficient and the wake region narrowing and shifting to downward are given at varied angles of attack.

EXPERIMENTAL SETUP

In this study, the plasma actuator was driven by a custom-made power supplier. It consists of a signal generator, Mosfet Audio Amplifier to amplify the signal, and coils to raise the output voltage to the desired level. The obtained signal in each step was measured by Tektronix P6015A high voltage probe and Fluke 80i-110s AC/DC current probe and acquired by NI PCIe-7841R model data acquisition card and monitored using Tektronix TDS2012B oscilloscope and Labview interface.

The open low-speed wind tunnel with a square test section of 570 mm × 570 mm × 1000mm which had

lower than 1 % turbulence intensity was used to perform the experiments at Nigde University. It had free stream velocity range of 0-15 m/s and the exhaust of the wind tunnel connected to the open atmosphere to provide safe laboratory conditions. The model in wind tunnel has swept up to 20° angle of attack and the maximum blockage ratio has stayed below 0.1 and it is usually chosen between 0.01 and 0.1 with 0.05 being typical (Barlow et al. 1999). The plasma actuator is placed on NACA2415 airfoil geometry which has 150 mm chord length and 510 mm span length between the end-plates. Two end plates of 280 mm in diameter were used to provide two-dimensional flow around the model.

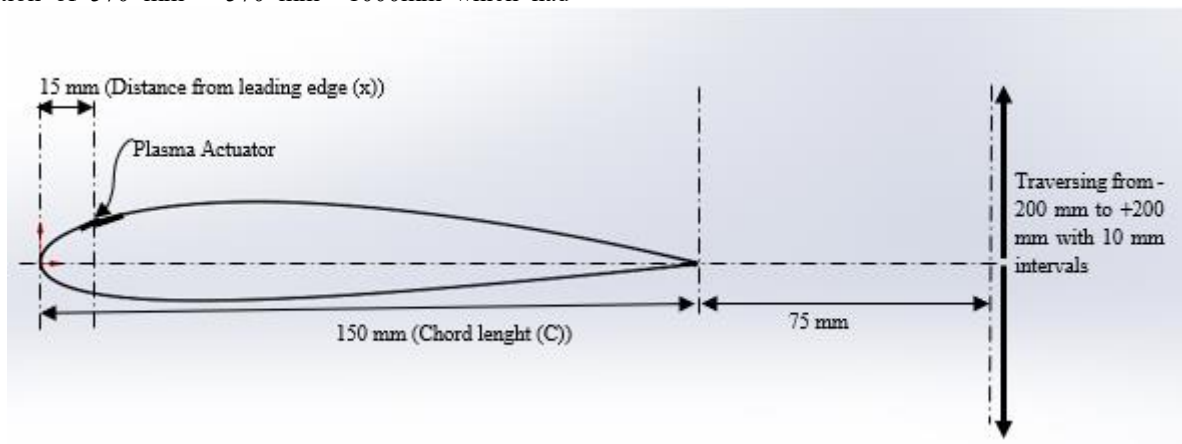


Figure 1. Details of the geometry and the hot wire traversing measurement location

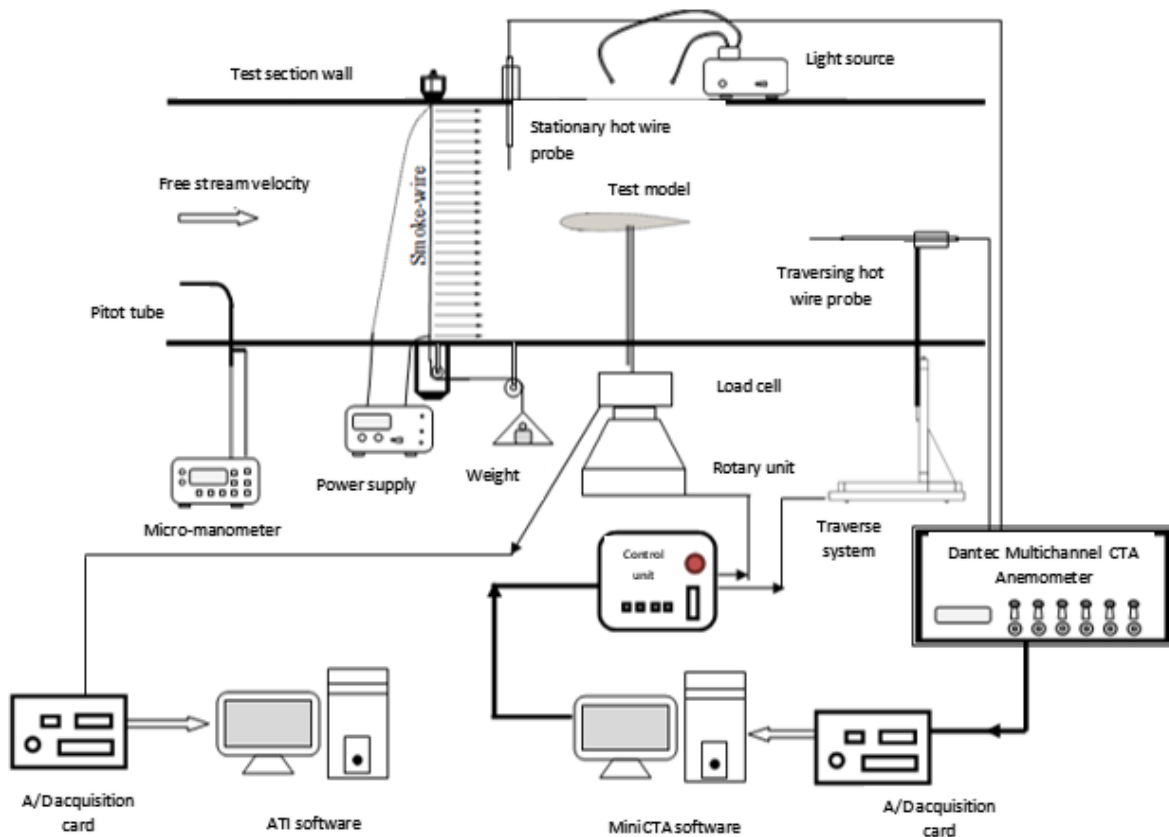


Figure 2. Presentation of the measurement systems

The plasma actuator was located on NACA2415 airfoil at $x/C = 0.1$ as shown in Figure 1. In this configuration, the exposed and grounded electrodes have 5 mm, 12 mm width respectively. It consists of 495 mm grounded and exposed electrodes in length and 3 layers of Kapton dielectric tape between them.

Effect of plasma actuators to flow around airfoil observed by measuring the velocity in the wake region, measuring the aerodynamic forces act on the model and visualizing the flow around the model. The measurement system configuration is given in Figure 2. In the force measurement method, the ATI model load cell measures the 6 components of force, was used to measure the lift component. The attack angle is controlled by the computer-aided rotary unit which connected to load cell. The measurements were conducted at a sampling frequency of 200 Hz and 3000 samples were collected by the data acquisition card. Also, each measurement repeated 2 times to eliminate measurement errors. Then, the lift force acts on the airfoil, projection area of the airfoil, free stream velocity and air density in test section of wind tunnel were measured to calculate the lift coefficient.

The velocity in the wake region of the model and free stream velocity were measured by a hot-wire anemometer. In this method, Dantec 55P11 model probe located at a point which is 210 mm far from the model test section in horizontal direction is used to measure the free-stream velocity. The same probe is also used to measure the velocity in the wake region by locating it downstream of the NACA2415 airfoil model. It was controlled by a traverse mechanism to scan the velocity profile in the wake region. The velocity measurements were taken 75 mm downstream of the airfoil and along the distance ranging from -200 mm to 200 mm with 10 mm intervals as shown in Figure 1. In each interval, 16,384 samples were collected with a sampling frequency of 2 kHz.

Smoke-wire system was used to generate smoke in the wind tunnel test section. It consists of a wire connected to a power supply, light generator, and a camera. To generate the smoke, paraffin injected to the wire which flows through the wire and just small portion of it stay on the wire and when the power supply turned on, the wire heated up and evaporated the paraffin. The top plane of the test section was illuminated by KRUSS OPTRANIC cold light generator to visualize the flow around the airfoil and Fujifilm HS20EXR camera was used to capture the flow visualizations.

RESULTS AND DISCUSSIONS

The NACA2415 airfoil model was compared with the other studies to validate the geometry. In Figure 3, the attack angle versus lift coefficient around the Reynolds number 6×10^4 of compared with the study of Micheal et al. (1996).

In Figure 4, Mueller (2002) expresses the effect of Reynolds numbers to the lift coefficient for Reynolds numbers in the range of $10^4 < Re < 10^7$ for airfoil models. The flow structure and the lift coefficient change with the Reynolds number. Especially, at the low Reynolds number, the lift coefficient gradient increases by the change of Reynolds number. Similar results are observed for NACA2415 airfoil at 10° angle of attack when it is compared with the range of smooth airfoils.

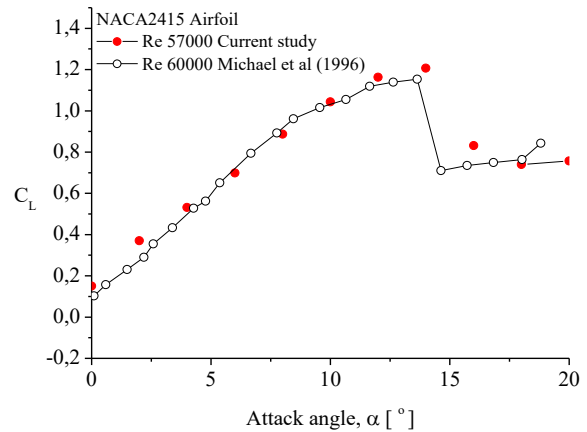


Figure 3. Lift coefficient versus angle of attack for NACA 2415 airfoil

This transition region corresponds to the effective plasma actuation velocities. Plasma actuator generates induced flow on the surface with approximately 2.5 m/s velocity at 8 kV peak to peak voltage and 3.6 kHz frequency in still air. This induced velocity reattaches the separated flow from the airfoil at low Reynolds numbers up to 5×10^4 which corresponds to 6.5 m/s free stream velocity. Because, the induced velocity has the required momentum to reattach the flow on the surface at low Reynolds number.

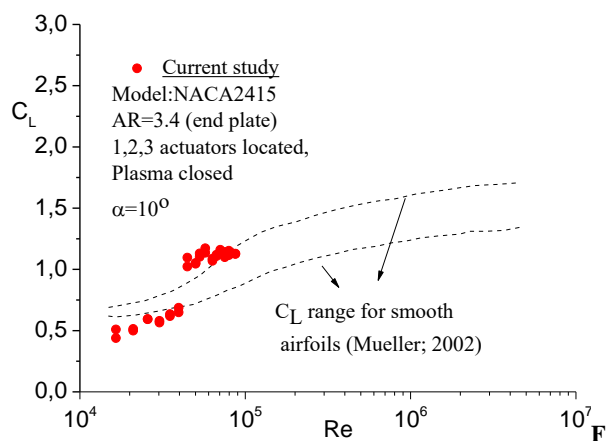


Figure 4. Lift coefficient range of airfoils at low Reynolds numbers

However, the momentum which is generated from the induced velocity of plasma actuator becomes insufficient in higher Reynolds numbers and flow separation occurs. As a result, the flow separation can not be prevented and the plasma actuator becomes insufficient in the flow control at high Reynolds

numbers ($Re > 5 \times 10^5$). In case of separation of flow from the upper surface of the airfoil, the lift coefficient stays lower.

The change of lift coefficient depends on the Reynolds numbers shown in Figure 5 in the case of active and passive plasma actuators. While the lift coefficient enhanced for the value of 5×10^4 Re, the effect of plasma actuator becomes inadequate for the higher Reynolds numbers in the current experimental conditions. At very low Reynolds numbers, a high rate of increment of the lift coefficient is observed. It is because of the high ratio of plasma-induced velocity to free-stream velocity at very low Reynolds number. By increasing the Reynolds number, free stream velocity becomes dominant in the total velocity. The total velocity consists of the plasma induced velocity which was 2.5 m/s in still air for the given operating condition of plasma actuator and the free stream velocity which corresponds to 6.5 m/s for 5×10^4 Re. The plasma actuator was effective till 5×10^4 Re.

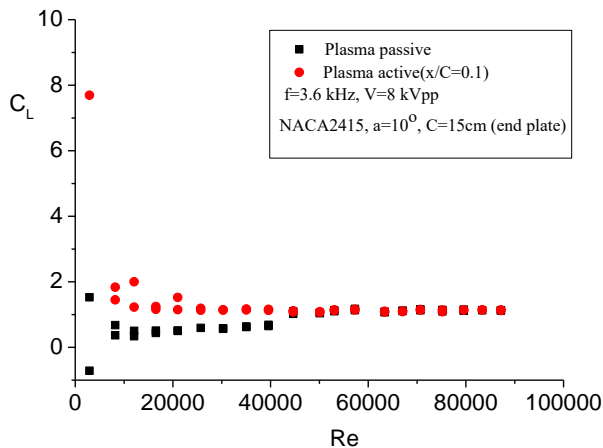


Figure 5. Lift coefficients versus Reynolds numbers in the cases of active and passive plasma actuators

The lift coefficient's dependency on the angle of attack when the plasma actuator is passive at different Reynolds numbers are given in Figure 6. Lift coefficient curves for Re 57200, 75000 and 87000 overlapped. It indicates that the flow structures are approximately the same. On the other hand, lift coefficient curves diverge at very lower Reynolds numbers which indicates the change of flow structure. This could be explained by the stall effect. While the stall effect is uncertain at very low Reynolds numbers, it becomes clear with an increase of the Reynolds number.

Figure 7 presents the lift coefficient's dependency on the angle of attack when the plasma is active and passive. When the plasma actuator is passive, the lift coefficient increased up to 0.6, by increasing the angle of attack up to 6° . By using the plasma actuator, the lift coefficient enhanced to 1.45. The maximum lift coefficient occurs at 14° angle of attack. When the angle of attack increased further, the plasma actuator becomes insufficient to force the flow reattach to the airfoil

surface. The flow boundary layer breaks of the airfoil surface to cause flow separation and the stall effect is observed.

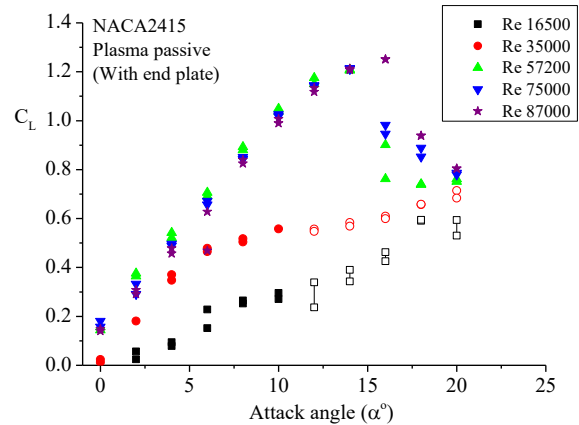


Figure 6. Lift coefficient versus angle of attack at different Reynolds numbers

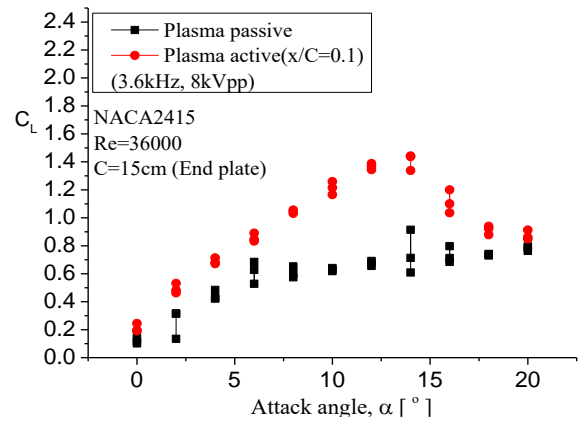


Figure 7. Effects of the plasma actuator on the lift coefficient under variation of angle of attack

The applied voltage, frequency, and the signal type have an influence on the performance of the plasma actuator. Especially, higher applied voltage increases the induced flow which enhances the flow control. The lift coefficient versus Reynolds number is plotted in Figure 8 for the different applied voltages.

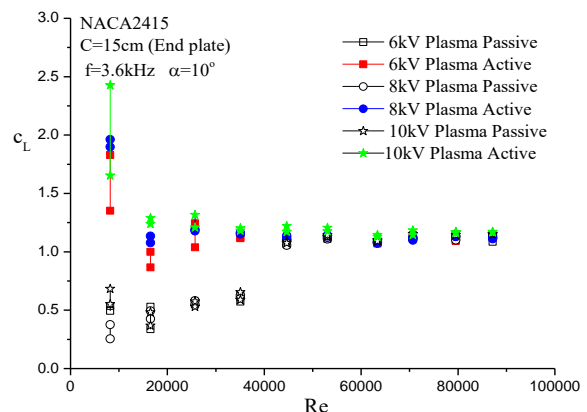


Figure 8. Effect of the plasma actuation voltage to the lift coefficient at different Reynolds number when the angle of attack is 10°

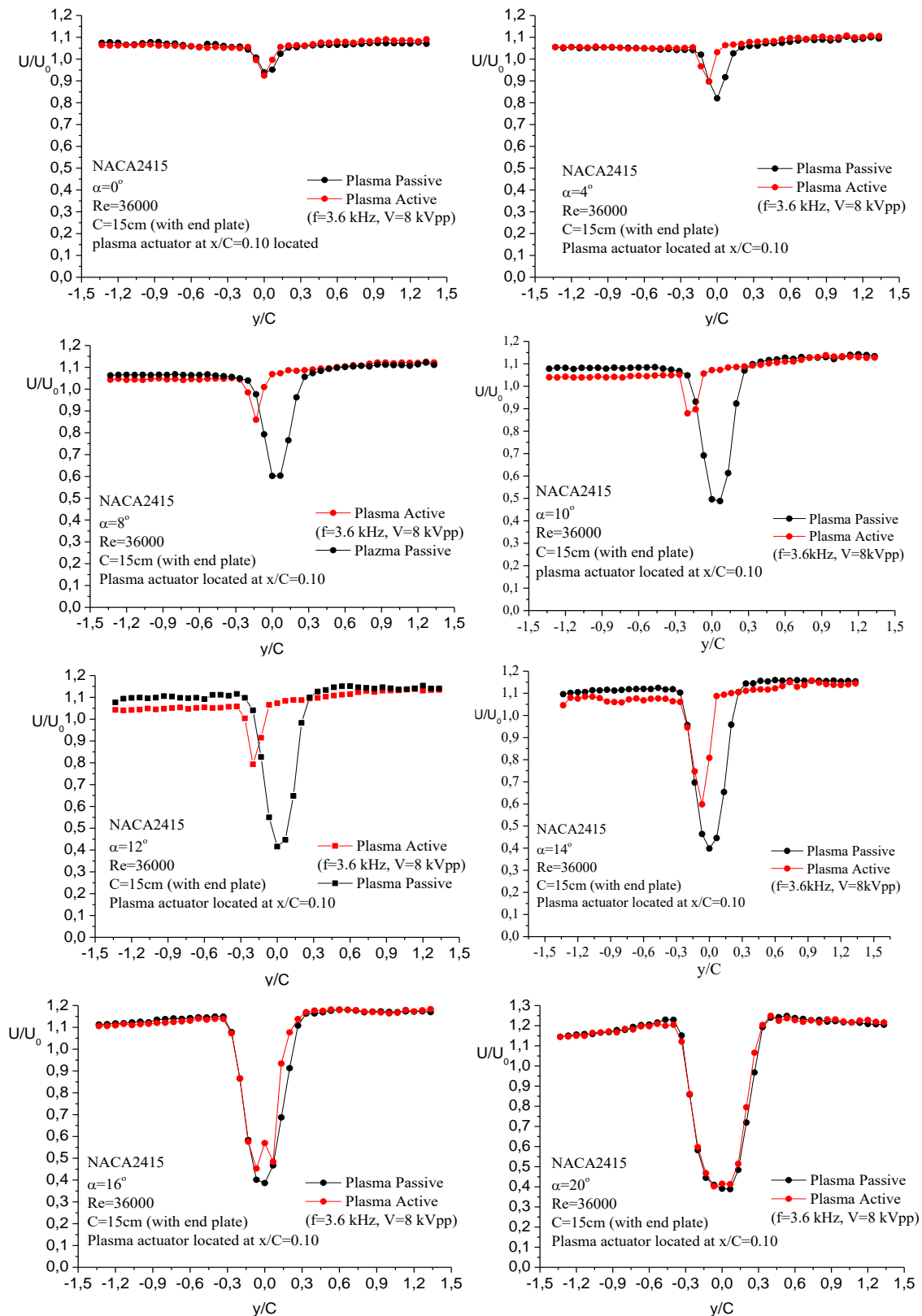


Figure 9. Effect of plasma actuator on the dimensionless velocity over wake region downstream of NACA2415 airfoil at a varied angle of attack

The plasma actuator enhances the lift coefficient up to 5×10^4 Re for all voltage values, after that the plasma actuator becomes inadequate for higher Reynolds numbers. When the plasma-induced flow is sufficiently high, the lift coefficient enhancement occurs. However,

the free-stream velocity is quite bigger than the induced flow at a higher Reynolds number. That is why the plasma actuators become insufficient to control the flow separation around the model at higher Reynolds numbers.

Figure 9 represents the effect of the plasma actuator on the velocity distribution over the wake region at varied angles of attack. According to the Figure 9, the wake region is enlarged by increasing the angle of attack. By using the plasma actuator, the wake region is narrowed essentially. Also, the effect of the plasma actuator on the flow attachment is clearly seen up to 14° angle of attack. The wake region is shifted further downstream because of the flow attachment at the upper surface of the model. When the angle of attack exceeds 14°, the plasma-induced flow becomes insufficient to control the flow separation and hence the wake region is not affected by the plasma actuator.

Figure 10 shows the flow structure around NACA2415 airfoil when the angle of attack and the Reynolds number were 10° and 36000 respectively. It is clearly seen from Figure 10, the applied voltage changes the

induced velocity by the plasma actuator. Changes in the induced velocity attach the flow to the wall. While the plasma actuator is passive, the flow is separated and a wide range of wake occurs. By applying 5 kV voltage to the plasma actuator, the flow separation was prevented partially. Because the plasma-induced flow was insufficient to upgrade the momentum of fluid elements moving in the close vicinity of wing surface to keep attaching the flow on the airfoil totally. By applying 6 kV of voltage, the flow kept on moving close to the airfoil surface. The increase of voltage causes an increment in the induced flow. When the Reynolds number or the angle of attack increases, a higher voltage levels are needed to obtain the flow attachment as shown in Figure 11. However, the power supply or the dielectric material constraints to apply higher voltages.

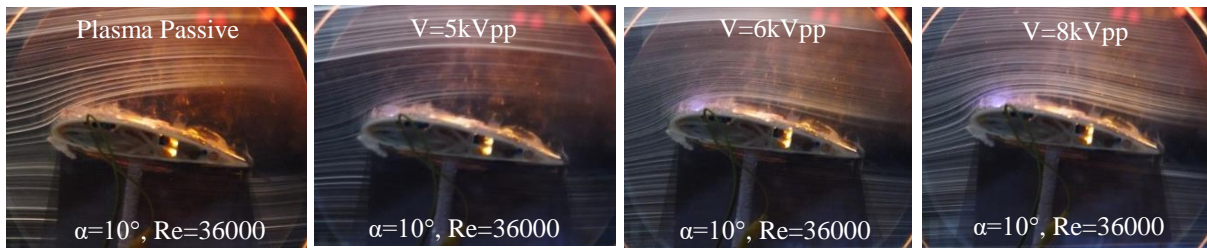


Figure 10: Effect of the applied voltage of the plasma actuator to the flow structure around NACA2415 airfoil

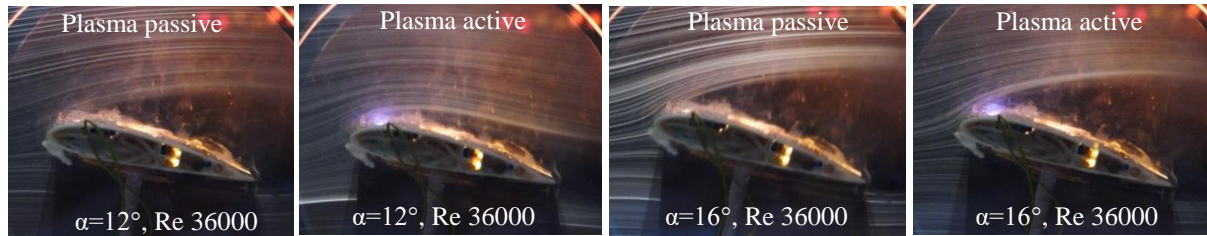


Figure 11: Effect of the angle of attack in passive and active cases of plasma actuator at 8 kV_{pp} voltage and 3.6 kHz frequency to the flow structure around NACA2415 airfoil

Table 2. The uncertainties of the measured and calculated parameters.

| Measured Parameter | Uncertainty (%) |
|----------------------|-----------------|
| Atmospheric pressure | 1.1 |
| Ambient temperature | 0.67 |
| Chord length | 0.66 |
| | |
| Span length | 0.19 |
| Air viscosity | 0.51 |
| Pressure transducer | 9.6 |
| Air density | 1.2 |
| Projected area | 0.68 |
| Hot wire anemometer | 5.44 |
| Lift force | 5.5 |
| Calculated Parameter | Uncertainty (%) |
| Reynolds number | 5.6 |
| Lift coefficient | 12.26 |

The uncertainty of the measured and calculated parameters are calculated according to methodology defined by (Coleman and Steele 2009). The

uncertainties of the measured and calculated parameters are given in Table 2.

CONCLUSION

In this study, limitations of the flow control with a plasma actuator are examined. While the plasma actuators are effective at very low Reynolds numbers (up to 5×10^4 Re), it becomes insufficient at low Reynolds numbers (higher than 5×10^4 Re). The plasma actuator was able to increase the lift coefficient for the range of Reynolds number varied from 0 to 5×10^4 . At very low Reynolds numbers, a high rate of increment of lift coefficients was observed because of the high ratio between plasma-induced flow and free-stream velocity. A rate of increase in the applied voltage caused higher induced velocity. At very low Reynolds numbers, the induced flow could manipulate the flow structure and enhanced the lift coefficient. When the plasma actuator is passive, the lift coefficient increased to its value of 0.6 by increasing the angle of attack up to 6°. When the plasma actuator is activated, the value of lift coefficient

was 1.45 at 14° angle of attack. Also, the stall effect shifted to the higher angle of attack. The wake region was narrowed by the plasma actuators up to 14° angle of attack. In addition, the wake was shifted further downstream because of the flow attachment at the upper surface of the model.

ACKNOWLEDGMENT

The authors would like to acknowledge the financial support of this work by the Scientific and Technological Research Council of Turkey (TUBITAK) under the Contract Number of 110M056. The authors also thank the rest of project team for their assistance in the performing of the study.

REFERENCES

- Abdollahzadeh, M., J. C. Pascoa, and P. J. Oliveira, 2018, Comparison of DBD plasma actuators flow control authority in different modes of actuation, *Aerospace Science and Technology*, 78, 183-96.
- Akansu, Y.E., F. Karakaya, and A. Şanlısoy, 2013, Active Control of Flow around NACA 0015 Airfoil by Using DBD Plasma Actuator, *EPJ Web of Conferences*, 45, 01008.
- Akansu, Yahya Erkan, and Fuat Karakaya, 2013, Elektrohırdınamik Yöntemler ile Aerodinamik Yapılı Cisimler Etrafındaki Akış Kontrolü, In.: TUBITAK.
- Akbıyık, Hürrem, Yahya Erkan Akansu, and Hakan Yavuz, 2017, Active control of flow around a circular cylinder by using intermittent DBD plasma actuators, *Flow Measurement and Instrumentation*, 53, 215-20.
- Barlow, Jewel B., Alan Pope, and William H. Rae. 1999. Low-speed wind tunnel testing (Wiley, New York).
- Benard, N., and E. Moreau, 2010, Capabilities of the dielectric barrier discharge plasma actuator for multi-frequency excitations, *Journal of Physics D: Applied Physics*, 43, 145201.
- Coleman, Hugh W. , and W. Glenn Steele. 2009. Experimentation, Validation, and Uncertainty Analysis for Engineers (John Wiley&Sons, New Jersey).
- Debien, A., N. Benard, L. David, and E. Moreau, 2012, Unsteady aspect of the electrohydrodynamic force produced by surface dielectric barrier discharge actuators, *Applied Physics Letters*, 100, 013901.
- Erfani, Rasool, Hossein Zare-Behtash, Craig Hale, and Konstantinos Kontis, 2015, Development of DBD plasma actuators: The double encapsulated electrode, *Acta Astronautica*, 109, 132-43.
- Feng, Li-Hao, Timothy N. Jukes, Kwing-So Choi, and Jin-Jun Wang, 2012, Flow control over a NACA 0012 airfoil using dielectric-barrier-discharge plasma actuator with a Gurney flap, *Experiments in Fluids*, 52, 1533-46.
- Firat, E., Y.E. Akansu, and M. Hacıaloğulları, 2013, Active control of flow around a square prism by slot jet injection, *EPJ Web of Conferences*, 45, 01029.
- Guler, A. A., M. Seyhan, and Y. E. Akansu, 2018, Effect of signal modulation of DBD plasma actuator on flow control around NACA 0015, *Isi Bilimi Ve Teknigi Dergisi-Journal of Thermal Science and Technology*, 38, 95-105.
- Jolibois, Jérôme, Maxime Forte, and Éric Moreau, 2008, Application of an AC barrier discharge actuator to control airflow separation above a NACA 0015 airfoil: Optimization of the actuation location along the chord, *Journal of Electrostatics*, 66, 496-503.
- Little, Jesse, and Mo Samimy, 2010, High-Lift Airfoil Separation with Dielectric Barrier Discharge Plasma Actuation, *AIAA Journal*, 48, 2884-98.
- Meng, Xuanshi, Haiyang Hu, Xu Yan, Feng Liu, and Shijun Luo, 2018, Lift improvements using duty-cycled plasma actuation at low Reynolds numbers, *Aerospace Science and Technology*, 72, 123-33.
- Micheal, S. Seling, A. L. Christopher, G. Philippe, P. N. Cameron, and J. G James. 1996. Summary of Low-Speed Airfoil Data (SoarTech Publications, USA).
- Roth, J. Reece, Raja Chandra Mohan Madhan, Manish Yadav, Jozef Rahel, and Stephen Wilkinson. 2004. Flow Field Measurements of Paraelectric, Peristaltic, and Combined Plasma Actuators Based on the One Atmosphere Uniform Glow Discharge Plasma (OAUGDP). in, 42nd AIAA Aerospace Sciences Meeting and Exhibit (American Institute of Aeronautics and Astronautics).
- Ryan, Durscher, and Roy Subrata, 2012, Aerogel and ferroelectric dielectric materials for plasma actuators, *Journal of Physics D: Applied Physics*, 45, 012001.
- Sanlısoy, Aytac, 2013, Investigating the Effects of Plasma Actuator on the Flow Control Around NACA2415 Airfoil, Master thesis, Nigde University.
- Song, Huimin, Qiaogen Zhang, Yinghong Li, Min Jia, Yun Wu, and Hua Liang, 2012, Plasma Sheet Actuator Driven by Repetitive Nanosecond Pulses with a Negative DC Component, *Plasma Science and Technology*, 14, 327.
- Sosa, Roberto, and Guillermo Artana, 2006, Steady control of laminar separation over airfoils with plasma sheet actuators, *Journal of Electrostatics*, 64, 604-10.

Taleghani, A. Shams, A. Shadaram, and M. Mirzaei, 2012, Effects of Duty Cycles of the Plasma Actuators on Improvement of Pressure Distribution Above a NLF0414 Airfoil, *IEEE Transactions on Plasma Science*, 40, 1434-40.

Thomas, Flint O., Thomas C. Corke, Muhammad Iqbal, Alexey Kozlov, and David Schatzman, 2009, Optimization of Dielectric Barrier Discharge Plasma Actuators for Active Aerodynamic Flow Control, *AIAA Journal*, 47, 2169-78.

Zito, Justin C., Ryan J. Durscher, Jignesh Soni, Subrata Roy, and David P. Arnold, 2012, Flow and force inducement using micron size dielectric barrier discharge actuators, *Applied Physics Letters*, 100, 193502.



Aytaç ŞANLISOY, received his B.Sc. degree and M.Sc. degree in Mechanical Engineering from Niğde University in 2011 and 2013, respectively. He received his PHD. degree in Mechanical Engineering from Gaziantep University in 2018. He is currently working as Assistant Professor at Yalova University. His research interests include plasma actuators for flow control, plasma gasification systems and thermodynamics.



Yahya Erkan AKANSU, received his B.Sc. degree in Mechanical Engineering from Erciyes University in 1993, M.Sc. degree and Ph.D. degree from Karadeniz Technical University in 1998 and 2004, respectively. He currently works as Professor in Mechanical Engineering Department of Niğde Ömer Halisdemir University. His research interests include active and passive aerodynamic flow control applications.



THEORETICAL ANALYSIS OF A CASCADE REFRIGERATION SYSTEM WITH NATURAL AND SYNTHETIC WORKING FLUID PAIRS FOR ULTRA LOW TEMPERATURE APPLICATIONS

Barış YILMAZ*, Ebru MANÇUHAN** and Deniz YILMAZ***

***Marmara University, Faculty of Engineering, Mechanical Engineering Department
34722, Kadıköy, İstanbul, Turkey,

*byilmaz@marmara.edu.tr (corresponding author), **emancuhan@marmara.edu.tr

***İstanbul Arel University, Faculty of Engineering and Architecture, Mechanical Engineering Department 34295,
İstanbul, Turkey, denizyilmaz@arel.edu.tr

(Geliş Tarihi: 30.01.2019, Kabul Tarihi: 27.02.2020)

Abstract: In this study, a theoretical model is established using Engineering Equation Solver (EES) software in order to investigate the effects of different design and operation parameters on the performance of the cascade systems for Ultra Low Temperature (ULT) between -50 °C and -100 °C. The analysis is performed for natural and synthetic refrigerant pairs to find an environmentally friendly alternative to commercial synthetic refrigerants. Effects of common parameters such as the evaporation temperature of low temperature cycle (LTC), the condensation temperature of high temperature cycle (HTC) and the temperature difference in the cascade heat exchanger (HX) have been investigated with the proposed model. Furthermore, influence of operation parameters including vapor quality of the refrigerant after the expansion valve and the precooler heat exchanger (PCHX) capacity, crucial to reach ULT conditions, on the system performance are examined. This study also contributes to the theoretical evaluation of the feasible natural refrigerant alternatives for ULT applications and the comparison of these refrigerants with synthetic ones in terms of performance and the environmental aspects. It is found that the natural refrigerant R1270/R170 pair results in about 5% better COP and almost half less CO₂ emissions compared to synthetic refrigerant R404A/R508B pair.

Keywords: Ultra-Low Temperature, Cascade Refrigeration System, Natural Refrigerants, COP, TEWI

DOĞAL VE SENTETİK SOĞUTUCU AKIŞKAN ÇİFTLERİ KULLANILAN BİR KASKAD SOĞUTMA SİSTEMİNİN ULTRA DÜŞÜK SICAKLIK UYGULAMALARI İÇİN TEORİK ANALİZİ

Özet: Bu çalışmada, ultra düşük sıcaklık (UDS) (-50 °C ile -100 °C) uygulamalarında farklı dizayn ve çalışma parametrelerinin kaskad sistem performansına etkilerini incelemek için EES yazılımı kullanılarak teorik bir model oluşturuldu. Kaskad sistemlerde kullanılan sentetik soğutucu akışkan çiftine çevre dostu bir alternatif bulmak için doğal ve sentetik soğutucu akışkan çiftleri için analiz yapıldı. Önerilen modelde; yüksek sıcaklık çevrimi (YŞÇ) yoğunlaşma ve düşük sıcaklık çevrimi (DŞÇ) buharlaşma sıcaklıkları ve kaskad ısı değiştiricisi sıcaklık farkı gibi parametrelerinin etkileri incelendi. Ayrıca, UDS uygulamalarında aşırı soğutma şartlarına ulaşabilmek için kritik çalışma parametreleri olan genişleme valfi sonrası soğutucu akışkanın buhar kalitesi ve ön soğutma amaçlı ısı değiştiricisi kapasitesinin sistem performansına etkileri incelendi. Bu çalışmada UDS uygulamalarında kullanılabilecek doğal akışkan alternatiflerinin performans ve çevresel etkileri açısından teorik olarak karşılaştırılmalarına katkıda bulunmaktadır. Yapılan analiz çalışmaları sonucunda soğutma sisteminde R1270/R170 doğal soğutucu çiftinin kullanılması ile, R404A/R508B sentetik soğutucu çiftine kıyasla %5 civarında daha iyi sistem performans katsayısı ve yaklaşık olarak yarısı kadar CO₂ emisyon salımı gerçekleştiği belirlendi.

Anahtar Kelimeler: Ultra Düşük Sıcaklık, Kaskad Soğutma Sistemi, Doğal Akışkanlar, STK, TEWI

NOMENCLATURE

Abbreviations

| | |
|-----|--|
| COP | coefficient of performance |
| EES | engineering equation solver |
| GWP | global warming potential |
| h | specific enthalpy [kJ kg ⁻¹] |
| HTC | high temperature cycle |
| HX | heat exchanger |
| IHX | internal heat exchanger |

| | |
|------------|--------------------------------------|
| LTC | low temperature cycle |
| \dot{m} | mass flow rate [kg s ⁻¹] |
| NBP | normal boiling point |
| ODP | ozone depletion potential |
| P | pressure |
| PCHX | precooler heat exchanger |
| \dot{Q} | heat transfer rate [kW] |
| T | temperature [°C, K] |
| ΔT | temperature difference |
| TEWI | total equivalent warming impact |

| | | | |
|----------------------|--|------|------------------------|
| \dot{W} | power [kW] | E | electric |
| <i>Greek symbols</i> | | Evap | evaporator |
| η | efficiency | FR | freezing |
| α | recycling factor (%) | HP | high pressure |
| β | electrical regional conversion factor (kg CO ₂ /kWh) | HTC | high temperature cycle |
| <i>Subscripts</i> | | in | input |
| C | condensation | LP | low pressure |
| CAS | cascade | LTC | low temperature cycle |
| Cond | condenser | M | mechanical |
| Comp | compressor | out | output |
| CR | critical | p | pump |
| DESUP | desuperheating | S | isentropic |
| | | SUB | subcooling |
| | | SUP | superheating |
| | | tot | total |

INTRODUCTION

Refrigeration systems can be categorized depending on the evaporation temperature aimed to be achieved. The refrigeration processes performed between -50 °C and -100 °C are called Ultra Low Temperature (ULT) applications according to ASHRAE Handbook classification (ASHRAE Handbook, 2010). The refrigeration systems operating at these temperature levels are mostly utilized for the storage of biological samples such as bacteria, bone marrow, cell cultures and DNA. Furthermore, these systems are used to liquify gases in petro chemistry industry. For many medical and industrial applications, the ULT refrigeration has not been accomplished efficiently in single-stage and multistage systems due to the limitations either in the thermo-physical properties of refrigerants or the cascade systems. The essential criteria of the systems operating at these low temperatures are specified in detail in ASHRAE Handbook, 2010.

Synthetic refrigerants consisting of Hydrofluorocarbons (HFCs) and Chlorofluorocarbons (CFCs) are chosen in most industrial refrigeration systems because of their superior cooling properties. In cascade systems, an appropriate selection of refrigerants to operate in the low and high temperature cycles should be made in order to obtain high COP. Generally, the synthetic refrigerants such as R404A, R507A, and R134a are used in HTC whereas the refrigerants such as R23 and R508B are used in LTC of systems in order to reach ULT levels. However, it is known that such compounds have adverse effects on ozone layer and thereby on environment. Recently, natural refrigerants started to be utilized for replacement of the synthetic ones. Among the natural fluids are water, carbon dioxide and various hydrocarbon compounds (propane, ethane, propylene, etc.) (Van Orshoven et al., 1993). Several organic fluids such as R23, R32, R125, R143a, R134a, R218, R170 and ammonia (R717) are also utilized as the working fluid of the power generation systems, especially for low grade energy source applications for instance Organic Rankine Cycle (ORC) (Vidhi et al., 2013; Vijayaraghavan et al., 2005). To achieve an environmentally friendly solution

in ULT applications, the natural refrigerants such as R290 (Propane), R1270 (Propylene) and R717 (Ammonia) may be chosen in HTC, and R170 (Ethane) or R1150 (Ethylene) may be selected in LTC. Moreover, the mixtures of different natural refrigerants can alternatively be used in LTC in order to achieve ULT levels such as nitrous oxide (N₂O) alone and its mixture with CO₂ (Bhattacharyya et al. 2005; Syaka et al. 2011; Bhattacharyya, et al. 2009; Nicola, et al. 2011; Gong et al. 2009).

In literature, there are plenty of theoretical and experimental studies about cascade systems for low evaporation temperature of LTC between -30 °C and -50°C (Lee et al., 2006; Dopazo et al. 2009; Getu and Bansal, 2008; Messineo, 2012; Yilmaz et al., 2014; Bingming et al. 2009; Dopazo et al., 2011; Yilmaz et al. 2018). However, there are few theoretical studies investigating the effects of operation parameters on the COP for different refrigerant pairs in ULT applications. Sarkar et al. (2013), performed a theoretical analysis and optimization study to investigate the effects of operation parameters on the COP for ULTs between -85 °C and -55 °C. In that study; ethane, ethylene and nitrous oxide were used in HTC while the ammonia, propane and propene were used in LTC as working fluids in order to evaluate the refrigeration system performance. They concluded that the COP increased for ethane and ethylene whereas the COP decreased for N₂O. Parekh and Tailor (2011), developed a mathematical model of a cascade system using ozone-friendly refrigerants pair (R507/R23) in order to optimize the design and operating parameters. Model results showed that when the evaporation temperature was decreased from -50 °C to -80 °C and the overall COP reduced from 1.232 to 0.785. Consequently, they stated that the lowest value of evaporation temperature of LTC resulted in the lowest COP. Wadell (2005), analyzed experimentally a cascade system using R134a and R508B refrigerants in high temperature and low temperature cycles, respectively. In experiments, the evaporation temperature of LTC was varied from -86 °C to -79 °C and the studied mass flow rates of refrigerant were between 50-70 g/min. It was concluded that if the evaporator is designed as

microchannel and enhanced surface, better performances may be achieved. Kruse and Russmann (2006), analyzed and compared theoretically trans-critical CO₂/N₂O system and R134a/R23 system. Their results showed that N₂O is a good alternative refrigerant to R23 in LTC with respect to the performance and the environmental trace. Utilization of R134a, R717 and hydrocarbons was proposed in HTC of the cascade system. They also concluded that trans-critical CO₂/N₂O system is more sustainable solution instead of R717 and hydrocarbons. Kılıçaraslan et al. (2010), determined and compared the COP and irreversibility of the cascade system using a large family of environmentally friendly refrigerant pairs. They concluded that the cascade system's COP increases and the irreversibility decreases with rising evaporation temperature of LTC for all selected refrigerant pairs. Mancuhan (2019) theoretically analyzed a refrigeration system with flash intercooling. Modeling of system was done by optimizing the intermediate pressure at given evaporation and condensation temperature values for all medium temperature application's (R717, R134a and R152a) and low temperature application's refrigerants (R290, R404A and R507A). Sun et al. (2019) evaluated the potential of refrigerant and found out which refrigerant couple performs better in cascade refrigeration system. In the considered 28 refrigerant pairs, R161 was suggested for use in HTC, and R41 and R170 were suggested for use in LTC. Babiloni et al. (2019) presented a comprehensive review on available literature on ULT applications. They concluded that the current status of the technology offers the most promising low GWP alternatives, although the existing regulations do not limit high GWP refrigerants used in ULT applications.

The present study proposes a mathematical model for a cascade ULT application with an Internal Heat Exchanger and a precooler heat exchanger in LTC side to determine the optimum design and operating parameters and produce the data for the future experimental applications. Earlier works are mainly focused on the theoretical and experimental analysis of cascade systems operating at evaporation temperatures of LTC between -30 °C and -50 °C (Lee et al., 2006; Dopazo et al. 2009; Getu and Bansal, 2008; Messineo, 2012; Yılmaz et al., 2014; Bingming et al. 2009; Dopazo et al., 2011; Yılmaz et al. 2018). There are limited number of theoretical studies about cascade ULT system in literature. In addition, no study is found on two crucial operation parameters; vapor quality of the refrigerant after the expansion valve of the LTC and the PCHX capacity. These parameters are critical for the LTC subcooling processes which are required to reach ULT levels and affect significantly the system COP. The key contributions of this work can be summarized as follow; performing the theoretical analysis of a unique cascade system operating at ultra-low temperature conditions between -50 °C and -100 °C and evaluating the feasible natural refrigerant alternatives in terms of the increasing the cascade system performance and decreasing the harmful environmental effects.

BACKGROUND

Physical and Environmental Evaluations of Refrigerants

The most convenient refrigerant in a refrigeration application can be decided based on its important characteristics such as Ozone Depletion Potential (ODP), Global Warming Potential (GWP), toxicity, flammability etc. along with the operating and design conditions. Additionally, Total Equivalent Warming Impact (TEWI), a measure of the trace of refrigerants on the environment including both the direct and indirect global warming effects of the refrigeration systems, is calculated. The direct effect represents the release of refrigerant directly to the atmosphere. On the other hand, the indirect effect corresponds to the CO₂ emissions due to fossil fuel consumption for energy production to drive the refrigeration system during its life time. TEWI comparison performed using the following correlation proposed by AIRAH (2012), provides a detailed environmental evaluation of the system.

$$TEWI = GWP_{ref} \left(m_{ref} \times L_{annual} \times N + m_{ref} \times (1-\alpha) \right) + (E_{annual} \times \beta \times N) \quad (1)$$

where N is the system lifetime (year), m_{ref} is the total refrigerant charge (kg), L_{annual} is the refrigerant leakage rate (%), α is the recycling factor, E_{annual} is energy consumed per year (kWh/year) and β is the electricity regional conversion factor (kgCO₂/kWh).

The physical and environmental properties of refrigerants that are subject of this study are given in Table 1.

In this study, one natural and one synthetic refrigerant pairs are used. As the synthetic refrigerant pair, R404A/R508B is chosen. R404A has the evaporation temperature about -40 °C without falling into vacuum pressure. Therefore, it can be used HTC refrigerant in cascade systems. R508B has a very low boiling point of -86.9 °C at 1 atm. Therefore, it can be used LTC refrigerant in ultra-low refrigeration system as these systems operate at just above R508B's boiling point. R508B is also non-toxic and non-flammable. On the other hand, R1270/R170 with negligible GWP offers a natural alternative solution pair for ultra-low refrigeration systems. In a cascade refrigeration system, R1270 is utilized in HTC and R170 is used in LTC. However, they have a safety rating of A3 which shows highly flammable property according to ASHRAE Standard 34 (2016). Hence, using R1270 and R170 requires additional safety measures.

Ultra-low Temperature Refrigeration Systems

Operating at ultra-low temperature levels, i.e. between -50 °C and -100 °C, with a single-stage system is difficult to reach since the parameters such as compression ratio, ambient air temperature and refrigerant properties limit

the system operation. The lowest temperature level that can be reached with single-stage refrigeration system is around $-40\text{ }^{\circ}\text{C}$ to $-45\text{ }^{\circ}\text{C}$ in industrial applications. On the other hand, two-stage cascade systems do not have this limitation as they can efficiently achieve the ULTs between $-45\text{ }^{\circ}\text{C}$ and $-80\text{ }^{\circ}\text{C}$.

Table 1. The physical and environmental properties of refrigerants used in this study (IPCC, Climate Change, 2013)

| Refrigerants | HTC | | LTC | |
|---------------------------------|----------------|-------|----------------|-------|
| | R404A | R1270 | R508B | R170 |
| T_{CR} ($^{\circ}\text{C}$) | 72 | 92 | 14 | 32 |
| P_{CR} (bar) | 37.3 | 44.6 | 39 | 47.6 |
| NBP ($^{\circ}\text{C}$) | -46.4 | -47.7 | -86.9 | -89.3 |
| T_{FR} ($^{\circ}\text{C}$) | Not determined | -185 | Not determined | - |
| ODP | 0 | 0 | 0 | 0 |
| GWP | 3922 | 1.8 | 11698 | 6 |
| Safety Class | A1 | A3 | A1 | A3 |

The schematic diagram of the proposed ULT cascade refrigeration system consisting of high and low temperature cycles is shown in Figure 1. Main components of the HTC are two compressors, an air-cooled condenser, an internal heat exchanger, a primary expansion valve and a secondary expansion valve. HTC compressors are operated between two pressure levels. Low and high pressure compressors sustain a reliable operation if the difference between the evaporation and the condensation pressures is high. An internal heat exchanger of HTC (IHX_{HTC}) provides subcooling effect before entering the primary expansion valve between state 8 and state 11 and protects the compressor from two phase flow as shown in Figure 1. Meanwhile, low quality vapor exits from the secondary expansion valve (state 9) and becomes saturated vapor at state 10. A cascade HX is located between the high and low temperature cycles. In the cascade HX, the refrigerant in the LTC cycle is condensed whereas the liquid phase refrigerant evaporates in the HTC cycle.

The components of the LTC are shown in Figure 1 which are a compressor, an expansion valve, an evaporator, an IHX_{LTC} and a PCHX. The IHX_{LTC} functions as a subcooler and a suction gas heater for compressor of LTC. Therefore, it subcools the refrigerant at the outlet of cascade HX and superheats the refrigerant at the inlet of the compressor. Thus, a more reliable operation for the LTC compressor is achieved. Moreover, the desuperheating of the refrigerant is essential since the exit temperature of LTC compressor is relatively higher than the conventional ULT applications. Minh et al. (2006), stated that utilizing the IHX_{LTC} for subcooling helps to protect the compressor from two-phase flow and provides the low quality of refrigerant entering the evaporator so that it improves the system COP. Desuperheating of the refrigerant is provided by a PCHX located before the cascade HX. The PCHX is assumed to be a water pumped cycle having inlet and outlet temperatures of $10\text{ }^{\circ}\text{C}$ and $35\text{ }^{\circ}\text{C}$, respectively. It lowers

the LTC refrigerant's temperature to 55 K higher than $T_{CAS,E}$.

The desuperheating degree ($\Delta T_{DESUP}=T_1-T_{1a}$) is defined as the difference between the exit temperature of compressor (T_1) and inlet temperature of the cascade condenser (T_{1a}). The subcooling and desuperheating processes let the theoretical model can be applied to the real applications. Figure 2 presents the pressure-enthalpy diagram corresponding to the investigated cascade system.

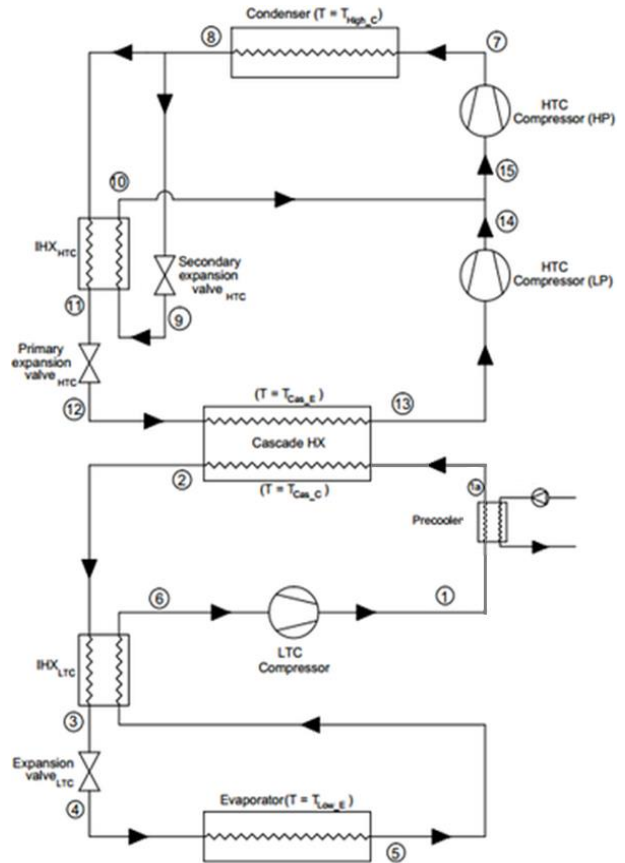


Figure 1. Schematic view of a cascade refrigeration system

Thermodynamic Analysis

The mathematical model of the cascade refrigeration system is developed based on energy and mass conservation equations. Expressions are obtained for each components of both high and low temperature cycles.

The developed model of the system is implemented to the Engineering Equation Solver (EES) software (Klein, 2017). EES software having a high accuracy thermodynamic database involving many of pure substances and mixtures is commonly used for thermodynamic analysis of the cyclic devices.

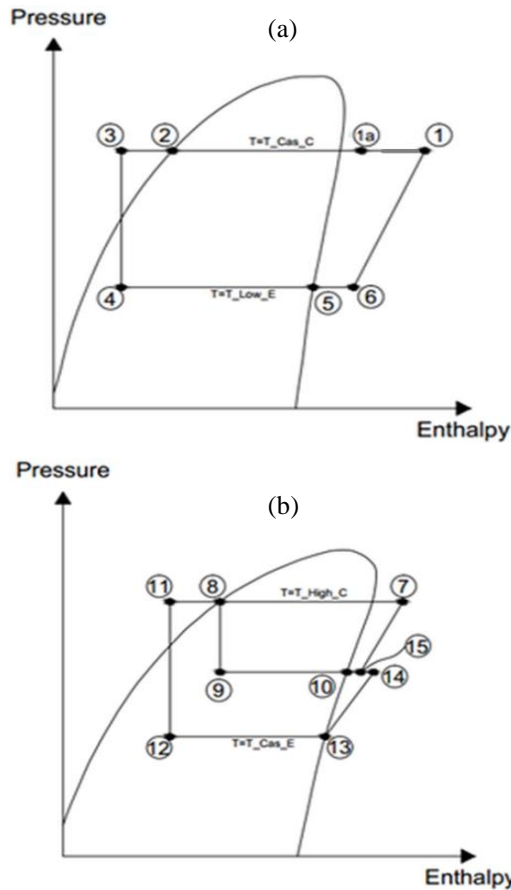


Figure 2. P-h diagrams of the investigated cascade system; for a) LTC, b) HTC

In our system analysis, the following assumptions are taken into account:

- Heat transfer in heat exchangers is performed as isobaric process.
- Refrigerants are expanded with constant enthalpy (isenthalpic) in expansion valves.
- Pressure drops in the system pipes and heat exchangers are neglected.
- The change in potential and kinetic energy is neglected.

In Table 2, we set the variable operating and constant design parameters for our system. In most of the applications, the cascade HX is designed to have 60 K difference, as in the industrial applications, between the $T_{CAS,E}$ and the refrigerant outlet temperature from the PCHX (T_{1a}). Therefore, the maximum temperature difference between the $T_{CAS,E}$ and T_{1a} is assumed to be constant at 55 K as in the reference (SWEP Company, 2016).

The subcooling degree of LTC (ΔT_{SUB_LTC}) is determined depending on the following constraints:

- The vapor quality after the expansion valve should not be lower than 0.10 (Cengel and Boles, 2007) so that it is chosen to be 0.15.
- While the liquid at the cascade condenser outlet (State 2) is cooled, the vapor at the LTC compressor inlet (State 6) is heated by IHX_{LTC} utilization. If the suction gas temperature of the compressor (State 6) gets higher, the discharge temperature (State1) and the desuperheating requirement increases. To prevent the increase in desuperheating, the LTC refrigerant is cooled by a PCHX. The PCHX is chosen to be a water pumped cycle working between 10 °C and 35 °C. The maximum desuperheating capacity of the PCHX is chosen to be 6 kW as a design condition.

Table 2. Design and operating parameters used in the model

| Design parameters | | |
|--|----|--|
| Compressor isentropic efficiency(η_S) (Brunin et al.,1997) | | $\eta_S = 0.874 - 0.0135 \frac{P_H}{P_L}$ |
| Mechanical efficiency (η_M) (Brunin et al.,1997) | | $\eta_M = 0.959 - 0.00642 \frac{P_H}{P_L}$ |
| Compressor electric motor efficiency(η_E) (Brunin et al.,1997) | | 0.90 |
| Compressor Overall Efficiency(η_C) | | $\eta_C = \eta_S \eta_M \eta_E$ |
| Effectiveness of cascade HX | | 1.0 |
| System refrigeration capacity (Q_{EVAP}) | kW | 11 |
| The temperature difference between T_E and T_{Space} | K | 6 |
| The temperature difference in cascade HX (ΔT_{CAS}) | K | 8 |
| The maximum temperature difference between the $T_{CAS,E}$ and T_{1a} (SWEP Company, 2016) | K | 55 |
| Superheating in LTC evaporator | K | 6 |
| Superheating in evaporator side of cascade HX | K | 5 |
| Operating Parameters | | |
| LTC evaporation temperature range (T_E) | °C | -60 to -86 |
| HTC condensation temperature (T_C) | °C | 30 to 55 |
| The evaporation temperature of cascade HX ($T_{CAS,E}$) | °C | -40 to -20 |
| The minimum vapor quality after the expansion valve | - | 0.15 |
| The maximum desuperheating capacity of PCHX | kW | 6 |

- Power consumption of water pump is assumed to be negligible.
- The temperature values of State 11 and State 9 of HTC are set to 8.67 °C and -5 °C, respectively. These values are determined based on the compressor catalog data (GEA Germany, 2016).

Model equations

The cascade system is modelled using Thermodynamics laws. The derived mass and energy equations are presented below for each component of the system. The corresponding schematics and diagrams are given in Figures 1 and 2.

Compressor power consumption of LTC is defined as:

$$\dot{W}_{LTC} = \dot{m}_{LTC,in}(h_1 - h_6) \quad (1)$$

where the mass flow rate of compressor inlet is

$$\dot{m}_{LTC,in} = \dot{m}_6 \quad (2)$$

Total compressor power consumption of HTC is given as:

$$\dot{W}_{HTC} = \dot{m}_{HTC_{LP},in}(h_{14} - h_{13}) + \dot{m}_{HTC_{HP},in}(h_7 - h_{15}) \quad (3)$$

where the mass flow rates inlet to the low pressure and high pressure compressors of HTC are as follows;

$$\dot{m}_{HTC_{LP},in} = \dot{m}_{13} \quad (4)$$

$$\dot{m}_{HTC_{HP},in} = \dot{m}_{15} = \dot{m}_{10} + \dot{m}_{14} \quad (5)$$

Total refrigerant mass flow rate of HTC is

$$\dot{m}_{HTC_{Total}} = \dot{m}_{HTC_{HP},in} \quad (6)$$

The rate of heat is rejected by the condenser of HTC is calculated as:

$$\dot{Q}_{HTC_{Cond}} = \dot{m}_{HTC_{Total}}(h_8 - h_7) \quad (7)$$

The heat transfer rate into the cascade HX is defined as:

$$\dot{Q}_{CAS} = \dot{m}_{HTC_{LP},in}(h_{13} - h_{12}) = \dot{m}_{LTC,in}(h_{1a} - h_2) \quad (8)$$

The refrigeration capacity of LTC evaporator is determined as:

$$\dot{Q}_{LTC_{Evap}} = \dot{m}_{LTC,in}(h_5 - h_4) \quad (9)$$

The heat transfer rate into the IHX of HTC and IHX of LTC are, respectively:

$$\dot{m}_{HTC_{LP},in}(h_8 - h_{11}) = (\dot{m}_{HTC} - \dot{m}_{HTC_{LP}})(h_{10} - h_9) \quad (10)$$

$$\dot{m}_{LTC,in}(h_2 - h_3) = \dot{m}_{LTC,in}(h_6 - h_5) \quad (11)$$

Energy balance for the adiabatic mixing process between the low pressure and the high pressure compressors of HTC:

$$\dot{m}_{HTC_{LP},in}h_{14} + (\dot{m}_{HTC} - \dot{m}_{HTC_{LP}})h_{10} = \dot{m}_{HTC,in}h_{15} \quad (12)$$

Desuperheating capacity of the PCHX of LTC can be defined as:

$$\dot{Q}_{PC_{HX}} = \dot{m}_{LTC,in}(h_1 - h_{1a}) \quad (13)$$

And finally, the overall COP of the cascade system is determined by:

$$COP = \frac{\dot{Q}_{LTC_{Evap}}}{\dot{W}_{LTC} + \dot{W}_{HTC}} \quad (14)$$

RESULTS AND DISCUSSION

The synthetic refrigerant pair of R404A/R508B is reliable choice to be used in ULT operations in a cascade system. However, these refrigerants are not environmentally friendly because of their high GWPs. A natural refrigerant alternative couple may be R1270/R170 having negligible GWPs and satisfactory operation performance for ultra-low applications. In practice, additional safety measures are required for this refrigerant pair since they are highly flammable. If the safety measures are taken in place, R1270/R170 is a convenient alternative. However, the performance of proposed refrigerant pair should be examined in detail and compared with the real applications.

A cascade system using both R404A/R508B and R1270/R170 refrigerant pairs is examined theoretically in order to determine the effects of design and operating parameters for ULT conditions. The mathematical models have been developed and implemented in EES for evaluation. The modelling results include the analysis of operating parameters as in the literature which are T_E , T_C , subcooling and superheating temperatures of LTC, temperature difference (ΔT_{CAS}) in the cascade HX, subcooling and superheating temperatures of HTC (Lee et al., 2006; Dopazo, et al. 2009; Getu, et al. 2008; Yilmaz et al. 2014; Sarkar et al., 2013; Parekh and Tailor; 2011). In addition, the operation parameters such as; the refrigerant vapor quality after the expansion valve of LTC and the PCHX capacity which are crucial to determine the LTC subcooling level and system COP are also considered.

Investigation of Subcooling Degree in LTC

In literature, it is reported that subcooling increases COP whereas superheating decreases it. Therefore, subcooling level should be set as high as possible and superheating value should be set as low as possible. Parekh and Tailor (2011) showed this effect through their cascade system

model. They were determined that increasing the subcooling degree in both LTC and HTC resulted in the increase of the COP. Therefore, the precise determination of the LTC subcooling degree is critical to calculate the maximum overall COP.

The vapor quality at the expansion valve exit is suggested to be selected between 0.10 and 0.20 in the thermodynamics modelling studies of cascade systems (Cengel and Boles, 2007). In this study, the minimum vapor quality of refrigerant is set to the average of the range (0.15). On the other hand, by the utilization of IHX_{LTC} , the condensed refrigerant from the cascade condenser is subcooled while the saturated refrigerant vapor in evaporator of LTC is superheated. If the refrigerant is too much superheated before entering the compressor, the outlet temperature of the compressor will also increase. This causes a very high desuperheating necessity and requires high capacity of PCHX. The maximum capacity of PCHX is assumed to be 6 kW as a constraint in the present study.

The design and operating parameters are shown for both refrigerant pairs R404A/R508B and R1270/R170 in Table 3 and Table 4, respectively. The corresponding performance results are calculated using the mathematical model equations of the system. In Table 3, two cases of the synthetic refrigerant pair are presented to investigate the performance of the system.

In the first case, the vapor quality after the expansion valve (which is a constraint parameter for the system design) is kept constant at 0.15 while the $T_{CAS,E}$ is changed from -40 °C to -35 °C. The highest overall COP is calculated to be 0.73 when the subcooling degree, the capacity of PCHX and the desuperheating degree are set to 33.2 K, 5.42 kW and 76.3 K, respectively. When the

$T_{CAS,E}$ decreases from -35 °C to -40 °C COP decreases from 0.73 to 0.71 correspondingly.

In the second case, the total capacity of PCHX is kept constant at 6 kW while $T_{CAS,E}$ varies from -30 °C to -20 °C. The highest overall COP is calculated to be 0.72 when the subcooling level, the vapor quality after expansion valve and the desuperheating are selected to be 31 K, 0.22 and 77.1 K, respectively. Decreasing $T_{CAS,E}$ within given range increases the COP from 0.63 to 0.72 as seen in Table 3.

In Table 4, similarly, two cases are investigated for the natural pair of refrigerants. In the first case, the vapor quality is kept constant at 0.15 as in the synthetic option. The $T_{CAS,E}$ is varied from -40 °C to -35 °C. The highest overall COP is found to be 0.77 when the subcooling degree, the PCHX capacity and the desuperheating degree are set to 33.2 K, 5.92 kW and 107.3 K, respectively. It is found that the COP decreases slightly from 0.77 to 0.76. In the second case, the PCHX capacity is kept constant at 6 kW similarly while the $T_{CAS,E}$ varies from -30 °C to -20 °C. The highest overall COP is calculated to be 0.76 when the subcooling amount is selected as 31.0 K, the vapor quality after expansion valve is 0.17 and the desuperheating level is 108.9 K. In this case, the $T_{CAS,E}$ decreases from -20 °C to -30 °C and COP increases from 0.70 to 0.76.

Parekh and Tailor (2011) indicated that COP value might be lower than 1 since the difference between T_E and T_C is very high in the ultra-low operational temperatures. From the calculated values given in Table 3 and Table 4, R1270/R170 is found to be a better alternative of R404A/R508B with respect to COP and low environmental trace for ULT conditions.

Table 3. Modeling results of the cascade system with R404A/R508B

| HTC $T_{CAS,E}$ (°C) | LTC $T_{CAS,C}$ (°C) | LTC ΔT_{SUB} (K) | Exp. Valve inlet, T_3 (°C) | Vapor quality x_4 | Q_{PCHX} (kW) | Q_{IHX} (kW) | COP | LTC ΔT_{DESUP} (K) |
|----------------------------|----------------------------|--------------------------------|------------------------------------|---------------------------|--------------------|-------------------|-------------|----------------------------------|
| -40 | -32 | 27.9 | -59.9 | 0.15 | 4.28 | 2.77 | 0.71 | 61.6 |
| -35 | -27 | 33.2 | -60.2 | 0.15 | 5.42 | 3.35 | 0.73 | 76.3 |
| -30 | -22 | 31.0 | -53.0 | 0.22 | 6.00 | 3.46 | 0.72 | 77.1 |
| -25 | -17 | 24.8 | -41.8 | 0.30 | 6.00 | 3.25 | 0.68 | 68.9 |
| -20 | -12 | 17.9 | -29.9 | 0.40 | 6.00 | 2.86 | 0.63 | 57.5 |

Table 4. Modeling results of the cascade system with R1270/R170

| HTC $T_{CAS,E}$ (°C) | LTC $T_{CAS,C}$ (°C) | LTC ΔT_{SUB} (K) | Exp. Valve inlet, T_3 (°C) | Vapor quality x_4 | Q_{PCHX} (kW) | Q_{IHX} (kW) | COP | LTC ΔT_{DESUP} (K) |
|----------------------------|----------------------------|--------------------------------|------------------------------------|---------------------------|--------------------|-------------------|-------------|----------------------------------|
| -40 | -32 | 27.9 | -59.9 | 0.15 | 4.90 | 2.02 | 0.76 | 91.3 |
| -35 | -27 | 33.2 | -60.2 | 0.15 | 5.92 | 2.43 | 0.77 | 107.3 |
| -30 | -22 | 31.0 | -53.0 | 0.17 | 6.00 | 2.43 | 0.76 | 108.9 |
| -25 | -17 | 24.8 | -41.8 | 0.24 | 6.00 | 2.16 | 0.74 | 101.8 |
| -20 | -12 | 17.9 | -29.9 | 0.30 | 6.00 | 1.79 | 0.70 | 92.1 |

The constant vapor quality

Figure 3 (a) and (b) illustrate that increasing the subcooling level from 5 °C to 50 °C reduces the vapor quality after expansion valve when $T_{CAS,E}$ changes between -40 °C and -20 °C. The vapor quality after the LTC expansion valve is examined with respect to desired value of 0.15. The vapor quality value intersects with various $T_{CAS,E}$ values. The LTC operating conditions such as subcooling degree are determined for several temperatures by using these intersection points. It is found that the subcooling degree of LTC (ΔT_{SUB}) varies between 30 °C and 50 °C for R404A/R508B system, on the other hand, ΔT_{SUB} changes between 25 °C and 45 °C for R1270/R170 system for the reliable operation of the cascade system.

The constant PCHX capacity

Subcooling process has to be applied after the cascade HX to reach design evaporation level of T_E (-86 °C). Subcooling degree can be defined as temperature difference between state 2 and state 3 ($\Delta T_{SUB,LTC} = T_2 - T_3$). It is accomplished by an IHX_{LTC} located before the expansion valve.

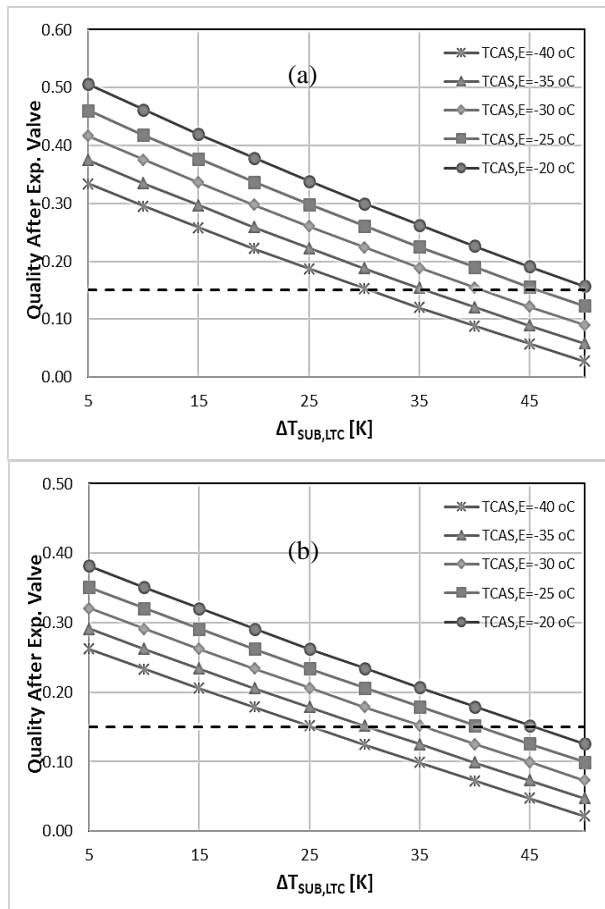


Figure 3. Effect of subcooling of LTC on vapor quality after expansion valve for different $T_{CAS,E}$ (a) R404A/R508B (b) R1270/R170 .

The utilization of IHX_{LTC} both subcools the refrigerant at the outlet of cascade HX and superheats the refrigerant at the inlet of the compressor as mentioned before. Therefore, the necessary capacity of the PCHX is one of the operation parameters. Another operation parameter is the difference between $T_{CAS,E}$ and the refrigerant exit temperature (T_{1a}) from the PCHX. The maximum temperature difference between T_{1b} and $T_{CAS,E}$ is assumed to be constant at 55 K as in the real applications (SWEP Company, 2016). When $T_{CAS,E}$ is chosen to be -40°C, the lowest value of T_{1a} should be 15 °C, if the 6 kW PCHX capacity is considered. The high values of T_1 and T_6 indicate the high subcooling necessity in IHX_{LTC} .

Figure 4 (a) and (b) display that increasing the subcooling level from 5 °C to 50 °C rises the PCHX capacity while $T_{CAS,E}$ changes between -40 °C and -20 °C. The PCHX capacity is chosen to be 6 kW as the desired condition. The PCHX capacity value intersects with various $T_{CAS,E}$ lines so that intersection points correspond to the desired LTC operating conditions such as subcooling degree. The ΔT_{SUB} is found between 18 °C and 50 °C for R404A/R508B system whereas the ΔT_{SUB} is obtained between 14 °C and 45 °C for R1270/R170 system. However, the vapor quality after expansion valve is set to the maximum possible value of 0.20.

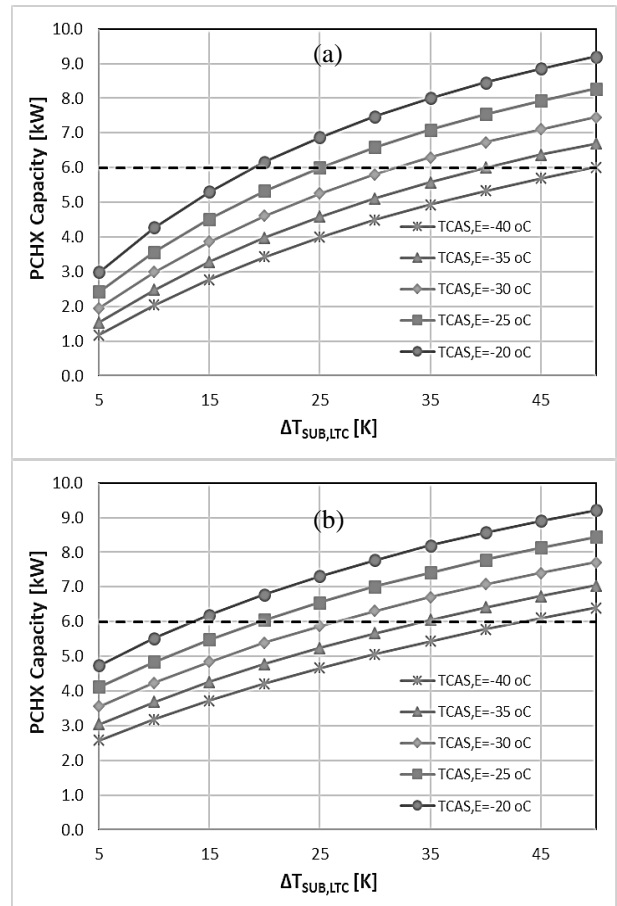


Figure 4.Effect of subcooling of LTC on PCHX capacity for different $T_{CAS,E}$ for (a) R404A/R508B (b) R1270/R170 .

Effect of LTC Subcooling Degree on COP

In Figure 5 (a) and (b), it is observed that increasing the subcooling level from 5 °C to 50 °C promotes the COP for all $T_{CAS,E}$ conditions. In addition, the COP of both systems increases for all values of the LTC subcooling degree while the $T_{CAS,E}$ is decreased from -20 °C to -35 °C.

In this case study, the T_E is kept constant at -86 °C for ULT operation. Decreasing T_E value decreases also the $T_{CAS,E}$ in general. From the calculation results of model equations, it is concluded that the lower value of $T_{CAS,E}$ affects the system COP positively. As a result, the highest COP is calculated (0.73) for the subcooling degree of 33.2 °C at R404A/R508B system along with the selected $T_{CAS,E}$ at -35 °C. Likewise, the highest COP is calculated (0.77) for the subcooling degree about 33.2 °C for R1270/R170 system when $T_{CAS,E}$ is -35 °C.

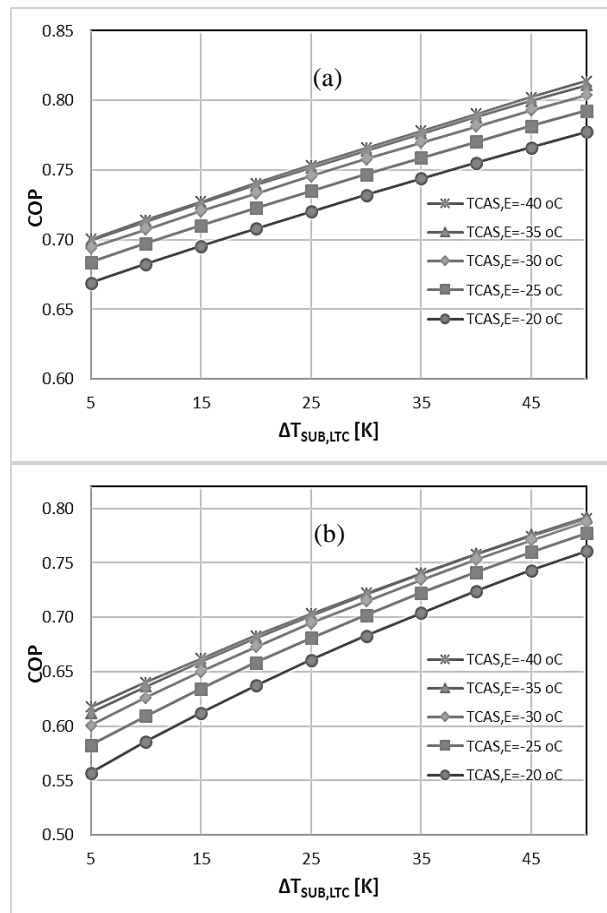


Figure 5.Effect of subcooling of LTC on COP for different evaporation temperature of HTC ($T_{CAS,E}$) for (a) R404A/R508B (b) R1270/R170.

Effect of Evaporation Temperatures of LTC and HTC on the COP

The effect of the operating parameters; T_E of LTC and $T_{CAS,E}$ of HTC on the COP is investigated and compared for two refrigerant pairs.

Figure 6 shows that increasing T_E of LTC results in the increase of COP for both R404A/R508B and

R1270/R170 systems. It is also found that the natural refrigerant pair R1270/R170 results in higher COP than the synthetic refrigerant pair R404A/R508B for all T_E values between -61 °C and -86 °C. In Figure 7, varying the $T_{CAS,E}$ between -40 °C and -20 °C shows a maximum value of COP about -35 °C for both refrigerant pairs.

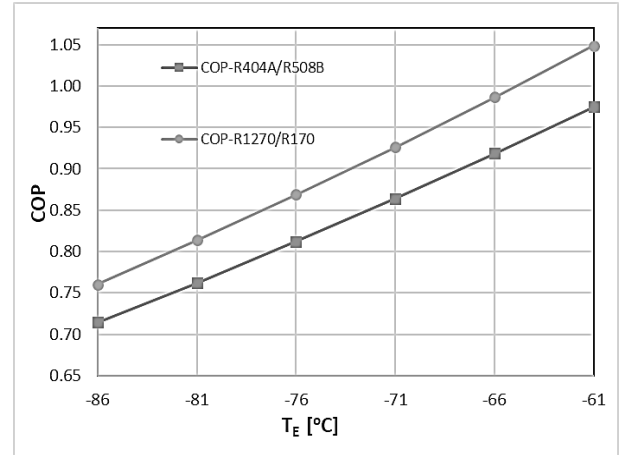


Figure 6. Effect of the LTC side T_E of on COP

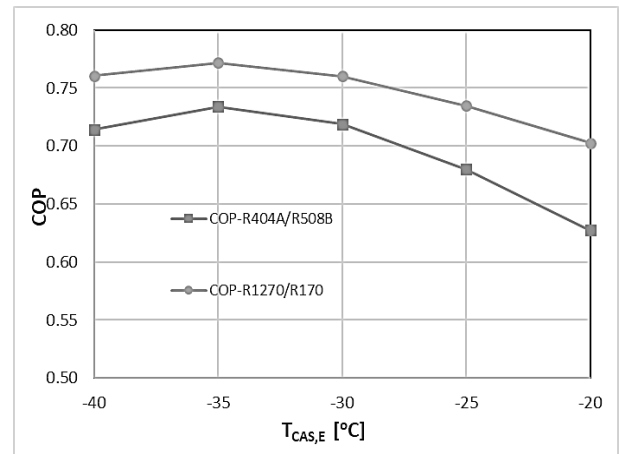


Figure 7. Effect of $T_{CAS,E}$ on COP

Effect of HTC Condensation Temperature (T_c) of HTC on COP

In Figure 8 (a) and (b), it is seen that increasing the T_c from 30 °C to 55 °C, representing the effect of the ambient conditions, reduces the COP values for all $T_{CAS,E}$ values of HTC.

It is observed that the R1270/R170 pair has relatively higher COP values compared to the R404A/R508B pair for all T_c and $T_{CAS,E}$. In addition, it is seen that the increase of the condensation temperature results in decrease in COP for both cases. However, the difference is found higher for R404A/R508B pair.

Impact of the Cascade Refrigerant Pairs on the Environment.

In this section, the effect of using different refrigerant pairs on the system performance and the environment has been examined. Furthermore, TEWI values of two

refrigerant options, R404A/R508B (System 1) and R1270/R170 (System 2), have been investigated for the leakage of the refrigerants to the atmosphere. In this case study, T_C , T_E and $T_{CAS,E}$ are chosen to be 40 °C, -86 °C, and

-35 °C, respectively. The ΔT_{CAS} is assumed to be constant at 8 K, ΔT_{SUB} is 30 °C and ΔT_{SUP} of LTC is 20 °C.

The TEWI analysis assumptions are summarized in Table 5. The corresponding values of the parameters used in Eq. 1 are also listed in the table. The mass flow rate requirements for different refrigerants are initially calculated. Then the total GWP values of each refrigerant is obtained. For the chosen refrigeration capacity of 11 kW, mass flow rates of System 1 refrigerants are found as 0.14 kg/s for R404A and 0.08 kg/s for R508B. On the other hand, the mass flow rates of System 2 refrigerants are calculated as 0.05 kg/s for R1270 and 0.03 kg/s for R170. The amount of the refrigerant charge is estimated according to receiver's volume (Sinar, 2018). In addition, the compressor power consumptions of of System 1 and 2 are given in Table 6.

TEWI analysis plays an important role in the selection of environmentally friendly refrigerant pair of the systems. For comparison between the Systems 1 and 2, the TEWI values are calculated using Equation (1) and the COP_{max} of systems are presented in Table 6.

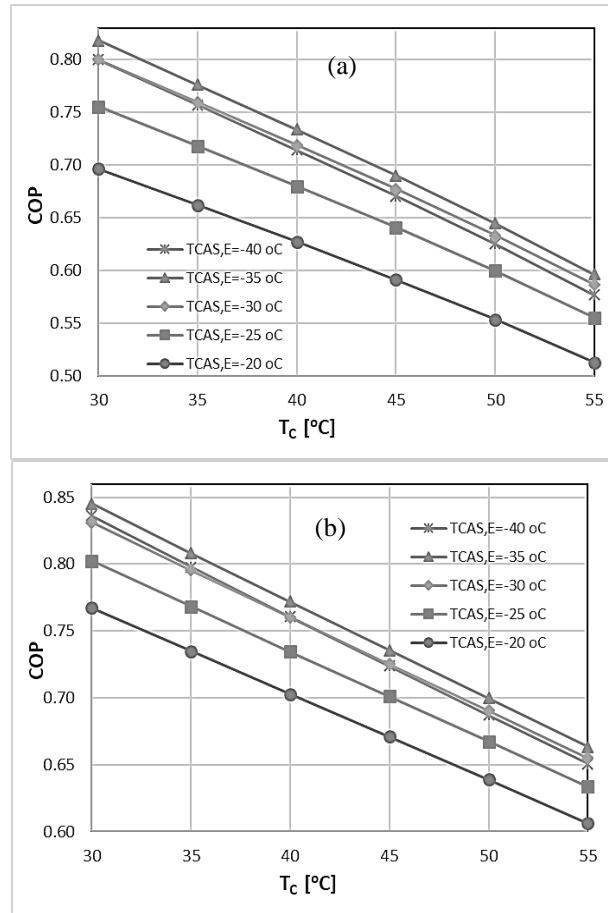


Figure 8. Effect of HTC condensation temperature (T_C) of on COP for different evaporation temperature of HTC ($T_{CAS,E}$) for (a) R404A/R508B (b) R1270/R170.

Table 5. TEWI analysis assumptions (AIRAH, 2012)

| | |
|------------------------------------|--|
| m_{Ref}^* (kg) | $m_{Ref} = \dot{m}_{Ref} \times 240$ |
| L_{annual} (%) | 12.5 |
| N (year) | 15 |
| A (%) | 0.7 |
| β^* (kgCO ₂ /kWh) | 0.65 |
| Operation time (h/year) | 6570 |
| GWP_{Ref} | $GWP_{R404A} = 3922$ $GWP_{R508B} = 11698$ $GWP_{R1270} = 1.8$ $GWP_{R170} = 6$ |

*(Sinar, 2018),**(Horton, 2002)

Table 6. Comparison of TEWI and COP_{max} values for Systems 1 and 2

| | Systems 1 (R404A/R508B) | | Systems 2 (R1270/R170) | |
|---|----------------------------|---------|---------------------------|-------|
| | Refrigerant charge (kg) | 33.6 | 19.92 | 12 |
| Refrigerant leakage rate (%/year) | 0.125 | 0.125 | 0.125 | 0.125 |
| Service life (years) | 15 | 15 | 15 | 15 |
| Recycling factor | 0.7 | 0.7 | 0.7 | 0.7 |
| GWP | 3922 | 11698 | 1.8 | 6 |
| Direct CO ₂ emission of refrigerants (kg CO ₂) | 286,620 | 506,828 | 46.98 | 93.96 |
| Total direct CO₂ emission of refrigerants (kg CO₂) | 793,447.31 | | 140.94 | |
| Power consumption (kW) | 8.71 | 6.96 | 7.81 | 7.09 |
| Operation (h/year) | 6570 | | 6570 | |
| Service life (year) | 15 | | 15 | |
| CO ₂ emission factor | 0.65 | | 0.65 | |
| Indirect CO₂ emission (kg CO₂) | 1,003,781.0 | | 954,456.8 | |
| TEWI equivalent CO₂ emission (kg CO₂) | 1,797,228.3 | | 954,597.7 | |
| COP_{max} | 0.73 | | 0.77 | |

It is found that System 1 with a synthetic refrigerant pair emits considerably higher amounts of greenhouse gases than System 2 during their lifetime. According to the TEWI values, high GWP of System 1 shows the higher contribution to the direct CO₂ emission. On the other hand, the indirect part of TEWI values are found almost the same for both systems. When the total TEWI levels are compared, System 1 shows almost twice more emissions compared to System 2. It is concluded that as well as the natural refrigerant alternative has higher COP (0.77) it also results in the better environmental performance compared to its synthetic counterpart.

CONCLUSIONS

This study evaluates two types of refrigerant pairs, namely R404A/R508B and R1270/R170, corresponding to the synthetic and natural refrigerant options in terms of performance and environmental considerations for a ULT cascade refrigeration system. It is found that the COP of the natural refrigerant pair, R1270/R170, is calculated slightly higher (0.77) than that of the R404A/R508B case (0.73). Furthermore, the TEWI value of the natural refrigerant pair is approximately half of the that of the synthetic refrigerant pair. Thus, R1270/R170 is the better environmentally friendly candidate at ULT applications with higher COP performance.

The proposed ULT cascade system using both refrigerant alternatives, R404A/R508B and R1270/R170, are extensively investigated in order to determine the effects of design and operating parameters on the COP. The following outcomes are obtained from the study:

- The vapor quality after expansion valve is set to 0.15 as the first constraint while the effect of $T_{CAS,E}$ has been evaluated at various temperatures from -40 °C to -20 °C for both refrigerant alternatives. The best COP value is obtained for the $T_{CAS,E}$ value of -35 °C and the optimum ΔT_{SUB} is found to be 33.2 °C for both R404A/R508B and R1270/R170 cases. The COP values are found 0.77 and 0.73 for the natural and the synthetic refrigerant pairs, respectively.
- The PCHX capacity is selected to be 6 kW as the second constraint. The vapor quality after expansion valve is considered to be less than 0.20. In this case, R404A/R508B refrigerant pair satisfies this constraint for $T_{CAS,E}$ at -35 °C and the subcooling degree of LTC at 33.2 °C. On the other hand, R1270/R170 alternative satisfies the design condition at most -30 °C and 31 °C for the $T_{CAS,E}$ and ΔT_{SUB} of LTC, respectively. The replacement of synthetic refrigerant pair with natural refrigerant improves efficiency about 5%.
- It is observed that increasing the T_E results in the increase of COP for both types of refrigerant pairs as expected. The natural refrigerant case results in the higher COP than the synthetic solution for all

evaporation temperatures of LTC between -86 °C and -60 °C.

- Increasing $T_{CAS,E}$ up to about -35 °C increases the COP. For lower values of the $T_{CAS,E}$, less than -35 °C, the COP value decreases. However, it is also revealed that the COP values of the natural refrigerant option are higher than those of the synthetic refrigerant option when the $T_{CAS,E}$ is varied between -40 °C and -20 °C.
- It is found that increasing the T_C from 30 °C to 55 °C reduces the COP values for all $T_{CAS,E}$. It is also observed that the natural refrigerant option has relatively higher COP values compared to the synthetic refrigerant option for all condensation and evaporation temperatures of HTC.
- The environmental trace of both refrigerant options are also evaluated for the leakage of refrigerants scenario in terms of TEWI values. It is found that the system with synthetic refrigerant option causes almost twice more CO₂ emissions than the natural option.

REFERENCES

- AIRAH, Methods of Calculating Total Equivalent Warming Impact (TEWI) 2012, Best Practice Guidelines. The Australian Institute of Refrigeration, Air Conditioning and Heating
- ASHRAE, 2016, "Designation and Safety Classification of Refrigerants," ANSI/ASHRAE, Atlanta, GA, Standard No. 34.
- ASHRAE Handbook—Refrigeration, 2010, "American Society of Heating, Refrigerating and Air-Conditioning Engineers, Inc.," (SI Edition).
- ASHRAE, 2000, "Standard Method of Testing Forced Circulation Air Cooling and Air Heating Coils," ANSI/ASHRAE, Atlanta, GA, Standard No. 33.
- Babiloni, A.M., Joybari, M.M., Esbri, J.N., Cervera, A.B., Albuixech, M.A., Moles, M., 2019, Ultralow-temperature refrigeration systems: Configurations and refrigerants to reduce the environmental impact, *International Journal of Refrigeration*, doi:<https://doi.org/10.1016/j.ijrefrig.2019.11.016>
- Bhattacharyya, S., Mukhopadhyay, S., Kumar, A., Khurana, R.K. and Sarkar, J., 2005, "Optimization of a CO₂-C₃H₈ Cascade System for Refrigeration and Heating," *Int. J. of Refrigeration*, **8**, pp. 1284–1292.
- Bhattacharyya, S., Garai, A., and Sarkar, J., 2009, "Thermodynamic Analysis and Optimization of a Novel N₂O-CO₂ Cascade System for Refrigeration and Heating," *Int. J. of Refrigeration*, **32**, pp.1077–1084.
- Bingming, W., Huagen, W., Jianfeng, L., and Ziwen, X., 2009, "Experimental Investigation on the Performance of NH₃/CO₂ Cascade Refrigeration

System with Twin-screw Compressor,” *Int. J. of Refrigeration*, **32**, pp.1358–1365.

Brunin, O., Feidt, M., Hivet, B., (1997), Comparison of the working domains of some compression heat pumps and a compression-absorption heat pump, *International Journal of Refrigeration*, 20-5, 308-318.
Cengel, Y. A., and Boles, M. A., 2007, “*Thermodynamics: An Engineering Approach*”, Sixth ed. McGraw-Hill, Singapore

Dopazo, J.A., Seara, J. F., Sieres, J., and Uhiá, F.J., 2009, “Theoretical Analysis of a CO₂-NH₃ Cascade Refrigeration System for Cooling Applications at Low Temperatures,” *Appl. Therm. Eng.*, **29**(8-9) pp.1577-1583.

Dopazo, J. A., and Seara, J.F. 2011, “Experimental Evaluation of a Cascade Refrigeration System Prototype with CO₂ and NH₃ for Freezing Process Applications,” *Int. J. of Refrigeration*, **34**, pp. 257-267.

GEA Germany 2016,
<https://vap.gea.com/stationaryapplication/Pages/Product.aspx?ItemObjectID=TS&Size=HGZX7&ProductID=2039>

Getu, H., and Bansal, P., 2008, “Thermodynamic Analysis of an R744-R717 Cascade Refrigeration System,” *Int. J. of Refrigeration*, **31**(1), pp.45–54.

Gong, M., Zhaohu, S., Jianfeng, W., Zhang, Y., Meng, C., and Zhou, Y. 2009, “Performance of R170 Mixtures as Refrigerants for Refrigeration at -80°C Temperature Range,” *Int. J. of Refrigeration*, **32**, pp. 892-900.

Horton, W.T., Modelling of secondary loop refrigeration systems in supermarket applications, Purdue University, PhD thesis, 2002.

IPCC. *Climate Change 2013: The Physical Science Basis*, Cambridge University Press, Cambridge, United Kingdom and New York, USA, 2013.

JP 5 B-A-CVBP - Grundfos Product Center, 2016,
<https://product.selection.grundfos.com/product-detail>
(Accessed 24 December 2016)

Kilicarslan, A., and Hosoz, M., 2010, “Energy and Irreversibility Analysis of a Cascade Refrigeration System for Various Refrigerant Couples,” *Energy Convers. Manag.*, 51 (12), pp.2947-2954.

Klein, S.A., 2017, “Engineering Equation Solver (EES)”, Academic Professional V10.294, F-Chart Software, Madison, WI, USA.

Kruse, H., and Russmann, H., 2006, “The Natural Fluid Nitrous oxide-An option as Substitute for Low Temperature Synthetic Refrigerants,” *Int. J. of Refrigeration* **29** (5), 799-806.

Lee, T., S., Liu, C., H., and Chen, T., W., 2006, “Thermodynamic Analysis of Optimal Condensing Temperature of Cascade-condenser in CO₂/NH₃ Cascade Refrigeration Systems,” *Int. J. of Refrigeration*, **29** (7), pp. 1100–1108.

Mancuhan, E., 2019, “A comprehensive comparison between low and medium temperature application refrigerants at a two-stage refrigeration system with flash intercooling,” *Thermal Science and Engineering Progress*, **13**,
<https://doi.org/10.1016/j.tsep.2019.100357>.

Messineo, A., 2012, “R744-R717 Cascade Refrigeration System: Performance Evaluation Compared with a HFC Two-stage System,” *Energy Procedia*, **14**, pp.56-65.

Minh, N., Q., Hewitt, N., J., and Eames, P. C., 2006, “Improved Vapor Compression Refrigeration Cycles: Literature Review and Their Application to Heat Pumps,” *International Refrigeration and Air Conditioning Conference*, Purdue, USA.

Nicola, D. G., Polonara, F., Stryjek, R., and Arteconi, A., 2011, “Performance of Cascade Cycles Working with Blends of CO₂+Natural Refrigerants,” *Int. J. of Refrigeration*, **34**, pp. 1436-1445.

Parekh, A. D., and Tailor, P.R., 2011, “Thermodynamic Analysis of R507A-R23 Cascade Refrigeration System”, *Int. J. of Mechanical and Mechatronics Eng.*, 5 (9), pp. 1919-1923.

Sarkar, J., Bhattacharyya, S., and Lal, A., 2013, “Performance Comparison of Natural Refrigerants Based Cascade Systems for ULT Applications,” *Int. J. of Sustainable Energy*, **32**(5), pp. 406-420.

Sinar, U., Numerical analysis of a cascade refrigeration system operating at ultra-low temperatures, Marmara University, Master’s Thesis, 2018.

Sun, Z., Wang, Q., Xie, Z., Liu, S., Su, D., Cui, Q., 2019, Energy and exergy analysis of Low GWP refrigerants in cascade refrigeration system, *Energy*, 170, 1170-1180

SWEP Company 2016,
<http://www.swep.cn/refrigerant-handbook/10.-systems/asdf2/>

Syaka, N. D. R. B., and Alhamid, M. I., 2011, “Cascade Refrigeration System Using Mixture of Carbon dioxide and Hydrocarbons for Low Temperature Applications,” *J. of Eng. and Appl. Sci.*, **6** (6), pp. 379-386.

Wadell, R., P., 2005, “Design of Compact Evaporators for ULT Thermal Management of Microprocessors”, MS thesis, Georgia Institute of Technology.

Yilmaz B., Erdönmez N., Sevindir M., and Mancuhan E. 2014, "Thermodynamic Analysis and Optimization of Cascade Condensing Temperature of a CO₂ (R744)/404A Cascade Refrigeration System," 15th International Refrigeration and Air Conditioning Conference, West Lafayette, IN, Paper No. 2958-10.

Yilmaz B., Mancuhan E., and Erdonmez N., 2018, "A Parametric Study on a Subcritical CO₂/NH₃ Cascade Refrigeration System for Low Temperature Applications," J. Energy Resour. Technol., **140**, pp. 1-7.

Van Orshoven, D., Klein, S. A. and Beckman, W. A., 1993, An Investigation of Water as a Refrigerant, J. Energy Resour. Technol **115**(4), pp. 257-263.

Vidhi, R., Kuravi, S., Goswami, D. Y., Stefanakos E., and Sabau, A. S., 2013, "Organic Fluids in a Supercritical Rankine Cycle for Low Temperature Power Generation", J. Energy Resour. Technol **135**(4), 042002.

Vijayaraghavan S., and Goswami, D. Y., 2005, Organic Working Fluids for a Combined Power and Cooling Cycle, J. Energy Resour. Technol **127**(2), pp. 125-130.

Barış YILMAZ graduated from Nuclear Engineering Department of Hacettepe University in 1999. He received his MSc degree from Mechanical Engineering Department of Marmara University in 2002. He received PhD degree from Mechanical Engineering Department of Marmara University and University of Orleans (France) within the frame of the joint PhD program. He is currently working in the Mechanical Engineering Department of Marmara University as an Assistant Professor.

Ebru MANÇUHAN graduated from Mechanical Engineering Department of Uludağ University in 1981. She received her MSc degree from Mechanical Engineering Department of Uludağ University in 1985. She received PhD degree from Mechanical Engineering Department of Yıldız Technical University in 1997. She is currently working in the Chemical Engineering Department of Marmara University as an Associate Professor.

Deniz YILMAZ graduated from Mechanical Engineering Department of Kocaeli University in 2000. She received her MSc degree from Mechanical Engineering Department of Yıldız Technical University in 2003. She received PhD degree from Mechanical Engineering Department of Istanbul Technical University in 2011. She is currently working in the Mechanical Engineering Department of Arel University as an Assistant Professor.



A COMPARISON OF THE THERMAL PERFORMANCE OF A CONVENTIONAL FIN BLOCK AND PARTIALLY COPPER AND ALUMINUM FOAM EMBEDDED HEAT SINKS

S. Kaancan ATAER*, Cemil YAMALI† and Kahraman ALBAYRAK**

*Space Systems Department, Thermal Control Systems, Turkish Aerospace Inc. (TA), Ankara, Turkey
suleymankaancan.ataer@tai.com.tr

†posthumous 13.05.2018

**Mechanical Engineering Department, Faculty of Engineering, Middle East Technical University, Ankara, Turkey
albayrak@metu.edu.tr

(Geliş Tarihi: 02.12.2018, Kabul Tarihi: 05.03.2020)

Abstract: In this research, the metal foams with 4,8,16 pores/cm, an aluminium foam which has 0.93 porosity and a copper foam which has 0.90 porosity that are integrated into a heat sink with a special geometry were designed and tested. During the process of the experiments, the thermal resistances and the pressure losses of the metal foam integrated heat sinks were tested by applying different heat fluxes (10.67, 15.75, 21.33 and 31.50 kW/m²) and two distinct frontal air velocities (4 and 6 m/s) to the specimens. The differences in the thermal performances of the heat sinks were observed by enforcing the custom-made manufactured heaters. The test results demonstrate that the pressure drop of the foam heat sinks is approximately four times more than the fin block; the average convection heat transfer coefficients of foam heat sinks are not dependent to the heater loads and the base plate temperatures of the foam sections were 1 to 1.5 degree lower than the foamless sections. This heat sink design provides lower temperatures on the desired locations of the electrical components than a conventional type fin block.

Keywords: Copper Foam, aluminum foam, soldering method, forced convection, conduction, thermal management

GELENEKSEL KANATÇIKLI BLOK VE KISMİ ALÜMİNYUM VE BAKIR METAL KÖPÜK YERLEŞTİRİLMİŞ ISI ALICILARIN ISIL PERFORMANSLARININ KARŞILAŞTIRILMASI

Özet: Bu araştırmada, 4,8,16 gözenek/cm oranında 0,93 gözenekliliğe sahip alüminyum ve 0,90 gözenekliliğe sahip bir bakır metal köpükler kullanılarak özel bir geometriye sahip ısı alıcı tasarlanmış ve test edilmiştir. Deneyler sırasında, metal köpük entegre edilerek üretilmiş ısı alıcıların ısı dirençleri ve basınç kayıpları, farklı ısı akıları (10.67, 15.75, 21.33 ve 31.50 kW / m²) ve iki ayrı ön hava hızı (4 ve 6 m/s) uygulanarak test edilmiştir. Isı alıcıların ısı performanslarındaki farklılıklar, özel olarak üretilen ısıtıcıların kullanılarak gözlenmiştir. Test sonuçları, köpük ısı alıcılarının basınç düşüşünün kanat bloğundan yaklaşık dört kat daha fazla olduğunu göstermektedir; köpük ısı emicilerinin ortalama konveksiyon ısı transfer katsayıları ısıtıcı yüklerine bağlı değildir ve köpük bölümlerinin taban plakası sıcaklıkları, köpüksüz bölümlerden 1 ila 1.5 derece daha düşüktür. Bu ısı alıcı tasarımı, elektrikli cihazların bileşenlerinin istenen konumlarında geleneksel tip bir kanatçıklı bloktan daha düşük sıcaklıklar sağlamıştır.

Anahtar Kelimeler: Bakır Köpük, Alüminyum Köpük, Lehimleme Yöntemi, Zorlanmış Konveksiyon, İletim, Isıl Yönetim

NOMENCLATURE

| | |
|-----------|--|
| A_{con} | Convection area of the heat sink [m ²] |
| A_{cs} | Cross section area of a duct [m ²] |
| a | Duct channel width [m] |
| b | Duct channel height [m] |
| D_{HF} | Hydraulic dia. of duct for heat sinks [m] |
| \bar{h} | Avg. convection HTC [W/m ² · K] |
| I_f | Fan current [A] |
| I_h | Heater current [A] |
| K | Permeability of the porous zones [m ²] |
| k | Thermal conductivity [W/m · K] |
| l | Length of a fin [m] |

| | |
|-------------|--|
| Nu | Nusselt number |
| P | Pressure of a fluid [Pa] |
| PPI | Number of pore per inch |
| \dot{Q} | Heat transfer rate [W] |
| q | Heat flux [W·m ⁻²] |
| Re | Reynolds number |
| R_{th} | Thermal resistance [°C/W] |
| T_{avgb} | Average base plane temperature [°C] |
| $T_{c,in}$ | Coolant inlet temperature [°C] |
| $T_{c,out}$ | Coolant mean exit temperature [°C] |
| t | Fin thickness of a fin block [m] |
| U | Velocity of a fluid [m·s ⁻¹] |
| V_f | Fan voltage [V] |

| | |
|-----------|---|
| V_h | Heater voltage [V] |
| \dot{W} | Pumping power [W] |
| Δ | Change |
| μ | Viscosity of a fluent [$\text{kg}\cdot\text{m}^{-1}\cdot\text{s}^{-1}$] |
| ν | Kinematic viscosity [$\text{m}^2\cdot\text{s}^{-1}$] |
| ρ | Density of a fluid [$\text{kg}\cdot\text{m}^3$] |

Subscripts

| | |
|---|---------|
| c | Coolant |
| e | Outlet |
| h | Heater |
| i | Inlet |

INTRODUCTION

The miniaturization of the electronic components in the form of integrated circuits (ICs), such as microprocessors, resistors, diodes, plastic leaded chip carriers (PLCCs), etc., increase the geometrical complexity of the electronic devices in restricted spaces. Known as Moore's law, it specifically predicts the doubling of the number of transistors on a given die area every two years. This was later updated as 18 months and it has the validity on the latest semiconductor fabrication technologies as well. At the result of this trend, the compact and small structured electronic box designs require custom-designed cooling systems. The general cooling requirements for the electronic devices require internally generated heat to be spread by optimally arranging the heat flow paths from the source to the sink. Otherwise, the heat cannot be removed away from the surface of the component and an uneven temperature distribution profiles, or hotspot(s) occur. To form near-ideal heat flow paths, the thermal design engineers use all of the three modes of the heat transfer; the conduction, the convection and the radiation. The majority of the applications use both the conduction and the convection to cool the electronic assemblies. At this point, the extensive surface areas, the lower density and the convenience utilization, as well as the open cell metal foam (OCMF) become a considerable material for the heat sink applications. Similar researches, including the OCMF utilization as a heat sink, have been summarized and examined as follows.

In the early studies, Kamath et al. (2013) tested the thermal conductivity and the pressure drops of two different thicknesses, which were the 10 and the 20 PPI aluminum and copper foams. There were two distinct properties of this study. One was locating the testing channel of the foams as vertical and the other was not using any permanent joint method. Screws were used to compress the heater between the foams and the insulating wooden boxes that cover the outer surface of the foams. Kamath also calculated the permeability and the drag coefficient by using Hazen-Dupuit-Darcy approach.

Mancin et al. (2012) calculated heat transfer coefficients of 5, 10, 20 and 40 PPI copper foam blocks whose porosities change between 0.905 and 0.934. In this research, they selected 25, 32.5 and 40 kW/m² thermal

loads with 0.0055 and 0.0125 kg/s air mass flow rates as the testing samples. These test specimens were compared with their mean wall temperatures, pumping power and their interstitial heat transfer coefficient values. Mancin et al. had another study (2010) that evaluated the pressure drop of six distinct pore density aluminum foams during the air flow. The scope of this study was comparing the experimental and the theoretical analysis pressure drops of six samples. Two of Mancin's key researches give extensive data about the metal foam heat sink performance.

Additionally, Dukhan et al. (2005 and 2007) studied thermal performance of 10 PPI and 20 PPI metal foam heat sinks. Both studies measured the temperature from the holes inside of the aluminum foam samples. Researchers provided a model to predict the thermal behaviors of the metal foam heat sinks. The samples were brazed onto the base heating plates to eliminate the contact resistances. A significant difference between the two studies is the directions of the measured temperatures of the samples.

A Turkish researcher, Ateş (2011) compared the thermal and hydrodynamic performances of the microchannel and the aluminum metal foam heat exchangers. In his study, the microchannel heat sinks with four different channel width and the aluminum foam heat sinks with three different pore densities were tested. Some of the aluminum foams were compressed with 2 and 3 compressed factors by using a special jig. The properties of the preferred aluminum foams were 10, 20 and 40 PPI with 92% porosity respectively.

Hernandez (2005) researched the 6101-T6 aluminum foams under three headings: The first one was the fluid flow and the pressure drop, the second was the forced convection and the last one was the thermal management. At the beginning, various porosity and the pore density foams were tested in the air duct. Even though the air velocities were measured from seven different sections of the foams, the pressure values were measured only at the inlet and the outlet of the samples.

Kim Y. (2001) and Calmidi (2000) investigated the convection heat transfer performances of the aluminum foam matrices. In both studies, the changes of the Nusselt numbers with respect to the Reynolds numbers were calculated for all of the aluminum samples. In these studies, Kim S.Y. (2001) tested the convective heat transfer characteristics of the aluminum foam under the asymmetrically heated channel by a hot bath. Calmidi (2000) tested seven distinct aluminum specimens which had various porosity values with three pore densities.

Although Bhattacharya et al. (2002) found and compared the design parameters of the RVC (reticulated vitreous carbon) and the aluminum foam samples in his research, Peak et al. (2000) generated same parameters, the thermal conductivity, permeability and the internal coefficients only for the aluminum foam samples.

The goal of Nawaz et al. (2010) study was the utilization of the 10 PPI aluminum 0.93 porosity foam heat exchangers instead of the conventional aluminum brazed fins. The aluminum foam was joined to the base plane by a polysynthetic thermal compound which had 5 W/m·K for the base plane. This chemical had relatively lower thermal conductivity compared to a Lead-Tin solder paste type joining material ($k = 39 \text{ W/m}\cdot\text{K}$) (Loh et al. 2000) which is used in this research.

Mahjoob and Vafai (2008) categorized the literature researches about the metal foam heat exchangers into three main parts; the micro structural-based correlations for the metal foam heat exchangers, the metal foam tube heat exchangers and the metal foam channel heat exchangers. The purpose of their study was to obtain Nu , Re and the pressure drop correlations for each category. The main inference of this study is that inserting the metal foam into a tube or a channel considerably increased the performance of the metal foams.

Bonet, Topin and Tadrist (2008) studied the flow in porous media and they tested dozens of foam samples from different metals or alloys (Cu, Ni, Ni-Cr). Air and water are used as a working fluid with two distinct velocity ranges; first from 0 to 20 m/s and then from 0 to 0.1 m/s, respectively. Their main concern was investigating the compressibility and the pore size effects on the flow field. The pressure values of various pore sized metal foams were measured by twelve pressure sensors which were located on the top side of the test section, through the main flow axis.

Dukhan and Ali (2012) examined the porous metal foams to determine the wall and the size effects on the pressure disturbances. Fourteen different cylindrical 6-inch *length metal foam specimens* were tested in this study. Seven of the samples had diameter changes which were from 1.27 cm to 8.89 cm, 10 PPI with 89.27% porosity and 20 PPI 90% porosity samples with the same pore diameters. During the experiments, the air velocity changed from 0 to 30 m/s which were sufficient enough to obtain the effect of diameter on the pressure distribution. After merging the empirical data to the Darcy-Weisbach friction factor (f_σ) equation, the coefficients were calculated.

Liu et al. (2006) practiced an experimental study to examine the flow friction characteristics of the aluminum foams. Seven different porosity samples were used in order to find a correlation between the friction factor (f_k) and the Reynolds number.

Another practical study was done by Kim et al. (2000) which had a difference at the metal utilization compared to the others. Instead of a louvered fin, the rectangular section foams were embedded into the plate fin heat exchanger. While the hot water was being circulated into the copper jackets, the air flowed through the aluminium foams with 20 °C inlet temperature. Both the inlet and the outlet air temperatures as well as the entrance and the exit pressures of the air were measured.

Lastly, Antohe et al. (1997) participated in a distinct study that examined the hydraulic characteristics of the nine compressed open-cell aluminum foams. During the study, the specimens were tested by air and Poly-alpha-olefin (PAO) working fluids. Antohe determined the permeability and the inertia coefficients, which were between $1.0 \times 10^{-10} \text{ m}^2 < K < 12 \times 10^{-10} \text{ m}^2$ and $0.3 \text{ m}^{-1} < C < 0.9 \text{ m}^{-1}$. Authors claimed that by obtaining these parameters from a curve fitting was more correct than using a one data point. According to this study, the dependence between the permeability and the inertia coefficients with the velocity range was observed.

In this study, a foam in the form of a staircase is soldered at two different locations as shown in Figure 1. The staircase foam utilization is totally different from the literature geometries and this structure requires a lower pressure difference with respect to a mono-block structure which was examined in Mancin's studies (2010) and (2012). It was observed that the two distinct foam sections simulate the two adjacent excessively heated hotspots situation, which was a possible scenario for the electronic box or the cold plate designs. The reason for using a second foam section at the downstream side is to observe the heat transfer performance of the metal foams when the high temperature air is forced to spread the heat from the surface of the metal foam. The staircase alignment of the foams increase the amount of the metal in the downstream direction which provides a higher heat capacity. Additionally, the length of the foam (at the Z direction) extends to the end of the heat sink that forces the air to pass through the metal foam. After an extensive literature survey, a design for a metal foam embedded electronic box cooling with respect to industrial concerns was not observed. The main goal of the current heat sink design is to catch an optimum pressure difference, the mass and the thermal performance. In this paper, the manufacturing methods of the heat sinks and the test set up will be defined in detail at the beginning. It will be followed by the heat transfer measurements, the pressure drop calculations and the extensive presentation of the performance comparison of the heat sinks.

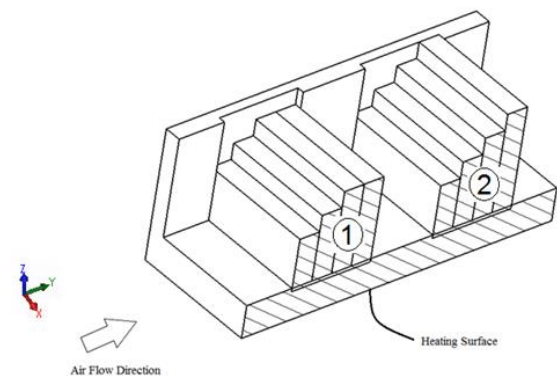


Figure 1. The cross section view of the designed foam embedded heat sink specimens

MANUFACTURING OF THE HEAT SINKS AND THE TEST SPECIMENS

For the current study, a unique heat sink geometry with embedded aluminum and copper foams have been produced. Embedding the foams to aluminum 6061 chassis is achieved by following various steps such as soldering, cutting and coating. An electro discharge cutting process of foams is performed as it is submerged in water.

The thermocouple locations are obtained by a deep-hole drilling process. The machine is used in this step which works like an EDM cutting machine and it has various removable blades. A blade of one millimeter in diameter and thirty millimeters in length are used to drill the heat sink chassis. In this process, the blade caused melting of the aluminum which was then removed from the chassis until the hole reached a depth of thirty millimeters. The six foam chassis and bare fin block were drilled as shown in Figure 2.



Figure 2. The photo of the aluminum fin block heat sink and the thermocouple holes

Both the aluminum foams and their chassis are coated with tin and copper. The reason for the copper coating of all of the foam heat sink chassis is to make them suitable for the soldering operation. A bare aluminum cannot solder itself, so a copper coating is used to create a soldering layer on to the aluminum. After the copper coating operations, all of the foams and their chassis are coated with tin for protection from the effects of corrosion.

Soldering and brazing are the most common joining methods of the metal foams. The most important advantage of these methods is using high thermal conductivity of assistant materials. Both brazing and soldering methods require dissimilar infrastructures. MIKES, a Turkish avionics company, permits usage of its SLC Vapour Phase Soldering Machine for this research. Therefore, soldering methods become applicable for the metal foam joining in extent of this study. The soldering process can be divided in two parts: The Pre-soldering Operations and The Soldering of the Foams to the Chassis of the Specimens in a Vapor Phase Soldering Machine. These are detailed in the following subtitles. The thermal conductivity of the solder, which is composed of 63% tin and 37% lead, is 39 W/m·K (Loh et al. 2000).

The metal foams are inserted into the cream solder that are applied in the pockets of the aluminum chassis which were designed previously. Four different length foams are installed into each pocket. The Lengths of the foams are 16 mm, 21 mm, 26 mm and 31 mm. The SLC 600 Vapor Phase Soldering machine is used for soldering operations of metal foams to the aluminum chassis. This machine commonly solders electrical components on to a bare PCB.

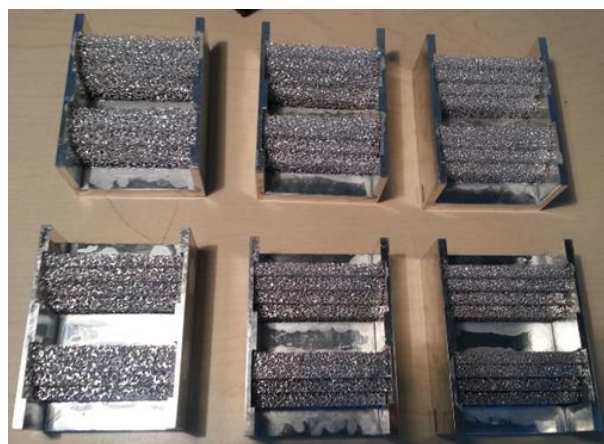


Figure 3. The final form of the soldered metal foam heat sinks

After the soldering operation, the electrical resistivity between the foam and the aluminum chassis is measured with an ohmmeter. The electrical resistivity was measured to be lower than 0.01 mΩ, which means the foams and the chassis behave like a single metal body.

The heat sinks which have identical external dimensions were placed on the testing section of the test rig. The heat sinks are 75 mm wide and 100 mm long with a 10 mm base plate thickness geometries. The aluminum fin block and the external part of the foam-embedded heat sinks were produced from aluminum 6061-T6 alloy. The final forms of the heat sinks are shown in Figure 3.

The external dimensions of the supplied foam plates are 150 mm wide, 150 mm long and 6.35 mm thick. Three particular pore densities were selected for this study through a literature survey. The pore density refers to the number of pores per centimeter or per inch. The pore densities of the samples are 4 pores per cm, 8 pores per cm and 16 pores per cm for both the copper and the aluminum plates. The physical properties of the foam materials are given in Table 1.

Table 1. The physical properties and the geometrical characteristics of the foam plates from literature

| Foam | Avg. Pore Dia. (m) | Porosity | Area Density (m ² /m ³) | Area(m ²) |
|----------|--------------------|----------|--|-----------------------|
| AL 10PPI | 0.00508 | 0.93 | 809.1 | 0.058442 |
| AL 20PPI | 0.0029 | 0.93 | 1240.2 | 0.089581 |
| AL 40PPI | 0.001702 | 0.93 | 1800.8 | 0.130074 |
| CU 10PPI | 0.0050 | 0.905 | 831.0 | 0.060024 |
| CU 20PPI | 0.00254 | 0.905 | 1273.8 | 0.092006 |
| CU 40PPI | 0.00165 | 0.905 | 1849.5 | 0.133595 |

Each heat sink has 2 pieces which are 16 mm long; 2 pieces which are 21 mm long; 3 pieces which are 26 mm long and 1 piece which is 31mm long. Each part was cut from the same foam plate. The heights of the foam layer heat sinks are shown in Figure 4.

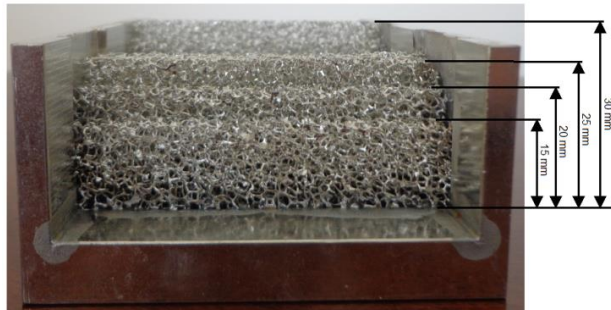


Figure 4. Porous layers of foam embedded heat sink

There are several reasons why the metal foams were used in different heights. The first is to reduce the pressure difference of the heat sink by decreasing the foam thickness. The second is to use the cooling capacity of air efficiently and the last reason is to catch the appropriate heat transfer point between the conduction and the convection heat transfer methods.

TEST SET UP

The primary goal of this experiment was to observe the hydraulic and the thermal behaviour of an aluminium fin block, the open cell copper and the aluminium foam embedded heat sinks. There were fifty-six test cases which were run for seven distinct heat sinks by four separate heaters and two distinct air velocities in total. At the foam embedded heat sinks only the metal foam materials were used to remove the heat from the surface of the heater to the air.

The performance of the heat sinks was evaluated with respect to each other by the inlet and the outlet fluid temperatures, their average base plane temperatures and their pressure drops through the heat sinks. The components of the test rig, their technical properties and the models are shown in Table 2.

The adapter component of the test rig converts the rectangular cross-section exit area of the fan to the cross section area of the test section, so that air can flow through the test specimens. In this study, all the specimens were aimed to be tested under the same conditions such as; the identical air velocities and the thermal loads. The pressure drops of the heat sinks were calculated via the power consumption of the fan.

At the first step of the test rig assembly, item no 5 (see Table 2), the adapter, was attached to the test section (item no 6) with four hexagonal-headed M6 screws by implementing the O-Ring gasket into the hole of test section. Secondly, the honeycombs which prevent the fluctuation of the anemometer AIRFLOW TA2 were placed inside of the adapter.

Following this procedure, in order to install the fan, four hexagonal headed screws and 20 mm long M6 were fastened by pressing the gasket of the adapter part. The subassembly of the test rig was installed to the POM spacers that pressed the insulation materials between the duct assembly and the aluminum plate with fourteen M4 30 mm length screws. Due to the low thermal conductivity, the low thermal expansion co-efficiency and easy machining properties, polyoxymethylene (POM) was ideal to make the test section duct assembly and the adaptor as well as the fan holders and the spacers of the test rig. Despite the low thermal properties of the POM material, negligible heat losses occurred in the experiments.

Two different types of the heater plates were required for two separate heaters. The plates were designed and manufactured by using Pertinax heat-resistant material. The heaters were compressed between the heat plate and the heat sink by six M4 10 millimeter long screws to avoid the thermal resistance. The partial and the whole heaters are illustrated in Figure 5.

Table 2. Component of the test rig

| Item No: | Component: | Properties\Function\Measuring Ranges: |
|----------|----------------------------|--|
| 1 | Fan | AC centrifugal Fan, Max pressure: 330 Pa, Max Vol. rate: 260 m ³ /h |
| 2 | Heaters | Heater capabilities: 60W, 120W, 80W, 160W |
| 3 | Hot Wire Anemometers # 1 | Velocity range: 0-15 m/s, Temperature range: 0- 80 °C |
| 4 | Hot Wire Anemometers # 2 | Velocity range: 0-30 m/s, Temperature range: -30- 200 °C |
| 5 | Adapter | Reduction of air flow area from fan exit to test section inlet. |
| 6 | Test Section Duct Assembly | Providing air flow pass through the heat sinks, locating thermocouples |
| 7 | Heater Plates | Thermal Conductivity: 0.21 W/m·K, Thermal Exp. Coeff.: 1.6×10 ⁻⁴ C ⁻¹ |
| 8 | Fan Holders | Stabilizing fan during the operation. |
| 9 | Insulation Material | Thermal Conductivity: 0.032 W/m·K, Insulating test section from Base Plate |
| 10 | Base Plate | Combining all set-up components on the same plane |
| 11 | Voltmeter of Fan | AC Current range: 0.3 mA - 10 A, AC Voltage range: 30 mV - 1000 V |
| 12 | Ammeter of Fan | AC Current range: 2-400 Ampere, AC Voltage range: 2-600 Volt |
| 13 | Voltmeter of Heater | AC Current range: 10 mA - 10 A, AC Voltage range: 10 mV - 1000 V |
| 14 | Ammeter of Heater | AC Current range: 10 mA - 10 A, AC Voltage range: 10 mV - 1000 V |
| 15 | AC Motor Driver | Output: 750 W, Input Voltage: 200VAC, Input Current: 6.5A, Output Current: 3.6A |
| 16 | Frequency meter | AC Current range: 0.4 mA - 20 A, AC Voltage range: 1000 mV - 1000 V |
| 17 | Thermocouples | Digi-Sense Thermocouple, Wire, TYPE-T, 30-GAUGE, FEP Insulation, |
| 18 | Power Supply | Superior Electric Powerstat 216B Variable Autotransformer, Input Volt: 240V Output Volt: 0-280V Frequency: 50-60 Hz |
| 19 | Data Logger | Up to 120 Channels, 11 function measuring capability, voltage, ampere, and temperature recorder within 1 second's intervals. |
| 20 | Laptop | Collecting & Processing data taken from Data logger |

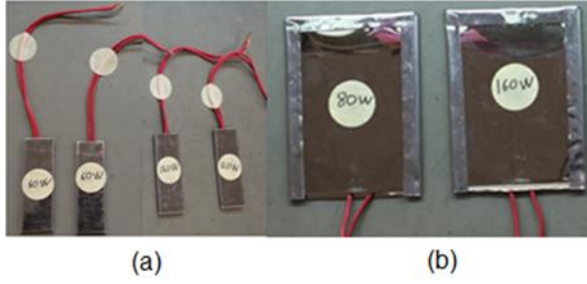


Figure 5. (a) Partial heaters; (b) whole heaters

THE HEAT TRANSFER MEASUREMENTS AND THE PRESSURE DROP CALCULATION

The Pressure Drop

The pressure drops of the test specimens were calculated via the power of the fan as in Equation 1.

$$\Delta P = \frac{\dot{W}}{\dot{Q}} = \frac{Uab}{I_f V_f} \quad (1)$$

The Reynolds numbers of the fin block which were calculated in Equation 2 proved that the flow was in a laminar regime. The pressure drops, the Reynolds numbers of the fin block and their uncertainties are presented in Table 3. The pressure drops of the fin block were lower than all other kinds of the metal foam heat sinks.

$$Re = \rho u \frac{D_{HF}}{\mu} = \frac{u2lt}{(1+t)v} \quad (2)$$

Table 3. The pressure drops of the fin block

| | \dot{m} (kg/h) | ΔP (Pa) | Re |
|-----------------|------------------|-----------------|------|
| Bare Fin | 33 | 36 | 957 |
| | 50 | 70 | 1435 |

Column 2 of Table 4 shows the pressure drops of the foam embedded heat sinks calculated by using the fan power consumption measurement whereas the column 3 shows the pressure drops of the foams which have the same structure were calculated with Hazen-Dupuit-Darcy Equation (Mancin et al. 2010, 2012).

Table 4. Tabulated pressure drop results

| FOAM | \dot{m} (kg/h) | ΔP (Pa) | $\Delta P_{cal.}$ (Pa) | $Re_{cal.}$ |
|---------|------------------|-----------------|------------------------|-------------|
| AL10PPI | 33 | 80 | 199.87 | 131 |
| | 50 | 157 | 436.93 | 196 |
| AL20PPI | 33 | 93 | 256.14 | 87 |
| | 50 | 208 | 547.32 | 130 |
| AL40PPI | 33 | 148 | 379.35 | 76 |
| | 50 | 292 | 815.85 | 114 |
| CU10PPI | 33 | 71 | 181.26 | 105 |
| | 50 | 141 | 388.08 | 158 |
| CU20PPI | 33 | 84 | 244.04 | 70 |
| | 50 | 189 | 504.27 | 105 |
| CU40PPI | 33 | 139 | 356.53 | 61 |
| | 50 | 250 | 743.95 | 92 |

As shown in Equation 3, the Reynolds number of the porous media was calculated where the permeability values of the foam samples were taken from Mancin's studies (2012, 2010). Although the porosity and the pore density of the tested metal foams were similar to the Mancin's study, the heat sink geometries cause different pressure drop from those of Mancin's study. As mentioned in the introduction, the manufacturing sections in the current research have a unique heat sink geometry and a lower metal foam than the mono-block structures. Because of the staircase design, air can pass more easily through the thinner metal foam layers compared to the mono-block metal foams.

$$Re = \frac{\rho U \sqrt{K}}{\mu} \quad (3)$$

For the current study, due to the thickness and the alignment of the foam, the pressure drop values had to be lower than those of Mancin's. The pressure drop data calculated via the power of the fan were approximately 35-40% lower than Mancin's data (see also Figure 6).

Alvarez's (2005) study also confirmed the calculated data with a similar experiment. In Alvarez's study, pressures of the same pore density samples were decreased by reducing the thickness. The staircase alignment of the foams reduced the pressure drops of the specimens as demonstrated in Table 4.

The pressure drop variation versus the pore density is shown in Table 4 and Figure 6. It is obvious that the increase of the pore density and the air frontal velocity enhance the pressure drops of the foam heat sinks. It is known that even though the aluminum foam samples have 93% porosity, the copper ones have 90.5% porosity. The effect of this porosity difference is also seen in Table 4. In fact, the higher porosity aluminum heat sinks have higher pressure drop values compared to the copper heat sinks.

The air velocity directly increases the pressure drops and the Reynolds numbers of all the tested specimens. At the Mancin's study, a rectangular box was selected as the geometry of foams. The effect on the pressure drop of the staircase structure of the heat sinks can be seen in Figure 6.

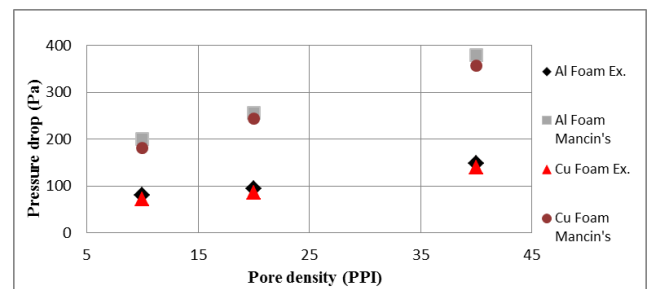


Figure 6. The drop of the tested heat sinks variation and Mancin's results (2012, 2010) with respect to the pore densities

Heat Transfer

In this experiment, the convection coefficients, the Nusselt numbers and the hydraulic diameter of the metal foams were calculated from Equation 4, Equation 5 (Hernández 2005) and Equation 6 (Boomsma, 2002).

$$\bar{h} = \frac{q}{A_{con}(T_{avgb} - T_{c,in})} = \frac{V_h I_h}{A_{con}(T_{avgb} - T_{c,in})} \quad (4)$$

$$Nu = \frac{q D_{HF}}{k_f A_{con}(T_{avgb} - T_{c,in})} = \frac{\rho u c_p 2a^2 b^2 (T_{c,o} - T_{c,i})}{k_f A_{con}(T_{avgb} - T_{c,in})(a + b)} \quad (5)$$

$$D_{HF} = \frac{4A_{cs}}{p} = \frac{4ab}{2(a + b)} \quad (6)$$

$$R_{th} = \frac{\Delta T}{q} = \frac{\Delta T_{avgb} - T_{c,in}}{\dot{m}c(T_{c,out} - T_{c,in})} = \frac{\Delta T_{avgb} - T_{c,in}}{\rho u c a b (T_{c,out} - T_{c,in})} \quad (7)$$

The Nusselt numbers of the fin blocks are calculated with Equation 5 which is shown in Table 5. The Nusselt numbers of the foam embedded heat sinks are higher than the fin block as demonstrated in Table 6 and Table 7. The thermal resistances, Nusselt numbers, the convection coefficients of the tested foam embedded heat sinks are presented in Table 6 and Table 7. While Table 6 shows the results of the foam embedded heat sinks at 4 m/s air inlet velocity, Table 7 shows the results of the foam embedded heat sinks at 6 m/s air inlet velocity. On the one hand, the pore density increases the heat transfer area of the foams and the Nusselt numbers decay with a rising pore density. On the other hand, the increased pore density reduces the thermal resistance of all the heat sinks except for the 20PPI copper foam. Because of the manufacturing defects a specific region of the 20 PPI copper layer, as shown in Figure 7, it does not have a uniform porosity through the whole plate. The reason for this manufacturing defect may be originated from the breaking of the ceramic mold during the investment casting process. Finally, the experimental results show that the thermal resistance of a 40 PPI porous heat sink and a 20 PPI porous one do not go in line with the literature trend, as seen in Table 6 and Table 7.

Table 5. The heat transfer coefficients, Nusselt numbers and the thermal resistances of the fin block for both air velocities 4 m/s and 6 m/s

| | Heater (W) | \dot{m} (kg/h) | R_{th} (K/W) | Nu |
|----------|------------|------------------|----------------|------|
| Bare Fin | 60 | 33 | 0.346 | 5.90 |
| | 80 | | 0.339 | 5.41 |
| | 120 | | 0.365 | 5.13 |
| | 160 | | 0.337 | 5.25 |
| | 60 | 50 | 0.290 | 6.44 |
| | 80 | | 0.242 | 6.51 |
| | 120 | | 0.305 | 6.33 |
| | 160 | | 0.225 | 6.63 |

The 60 W and the 120 W heaters have the same width as the foam sections of the heat sinks, which is 23.4 mm(1"). The 80 W and the 160 W heaters have the same 100 mm width as the heat sink. This can be seen in Figure 5. Although this heater size effects the thermal resistance of the fin block as in Table 5, an increasing thermal resistance trend is seen with the increasing heater power at the foam heat sinks in Table 6 and Table 7. The main reason for the higher thermal resistance values at two partial 1" size 60 W and 120 W heaters is the inadequacy in the fin block heat transfer area. The baseplate temperature of the fin blocks is higher than the foam embedded heat sinks in all of the test cases, which shows the heat accumulation at the base plate of the fin block. Foam metals with a superior property in the excessive heat transfer area solves this heat transfer area inadequacy.

The high thermal conductivity of the copper samples ensured the superior thermal performance of the copper foams. The effects of air velocity can appear when the heat transfer coefficients and the thermal resistances of Table 6 are compared to those of Table 7. The 10 PPI copper embedded heat sinks had the highest heat transfer coefficients. The 10 PPI aluminum embedded heat sinks took the second place.

Table 6. The heat transfer coefficients, Nusselt numbers and the thermal resistances of the metal foam embedded heat sinks at 4 m/s air velocity

| | Heater (W) | \dot{m} (kg/h) | R_{th} (K/W) | \bar{h} (W/m ² ·K) | Nu |
|---------|------------|------------------|----------------|---------------------------------|-------|
| Al10PPI | 60 | 33 | 0.290 | 39.79 | 62.75 |
| | 80 | 33 | 0.324 | 39.94 | 62.99 |
| | 120 | 33 | 0.352 | 38.52 | 60.75 |
| | 160 | 33 | 0.324 | 39.28 | 61.94 |
| Al20PPI | 60 | 33 | 0.287 | 27.35 | 43.13 |
| | 80 | 33 | 0.331 | 26.18 | 41.29 |
| | 120 | 33 | 0.333 | 26.24 | 41.37 |
| | 160 | 33 | 0.266 | 25.81 | 40.71 |
| Al40PPI | 60 | 33 | 0.260 | 18.03 | 28.44 |
| | 80 | 33 | 0.261 | 17.62 | 27.78 |
| | 120 | 33 | 0.250 | 17.30 | 27.27 |
| | 160 | 33 | 0.264 | 17.47 | 27.55 |
| CU10PPI | 60 | 33 | 0.273 | 42.41 | 66.88 |
| | 80 | 33 | 0.241 | 43.86 | 69.16 |
| | 120 | 33 | 0.251 | 42.99 | 67.80 |
| | 160 | 33 | 0.319 | 43.99 | 69.37 |
| CU20PPI | 60 | 33 | 0.105 | 37.08 | 58.47 |
| | 80 | 33 | 0.145 | 32.27 | 50.88 |
| | 120 | 33 | 0.138 | 31.86 | 50.24 |
| | 160 | 33 | 0.141 | 30.92 | 48.76 |
| CU40PPI | 60 | 33 | 0.185 | 24.19 | 38.14 |
| | 80 | 33 | 0.196 | 23.06 | 36.36 |
| | 120 | 33 | 0.217 | 23.44 | 36.96 |
| | 160 | 33 | 0.229 | 23.77 | 37.48 |

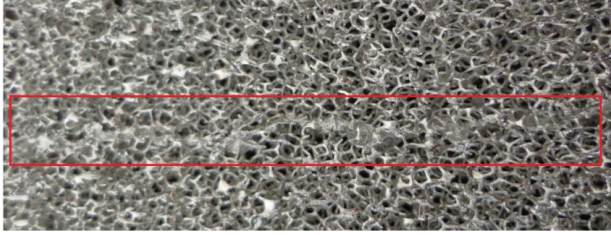


Figure 7. The picture of the closed cells of the copper foam plate

The increase of the pore density impeded the air flow through the metal foam. As a result, the convective heat transfer from the metal foam to air was reduced by the increasing pore density as expected. Finally, it is understood that the thermal resistance is directly dependent on the pore density of the foam samples. All of the thermal resistances, except for the 20PPI copper, were lessened with the pore density. As stated in the results, the Nusselt numbers decline along with the rise of the heat transfer areas falls down. This means that the increase of the pore density increases the conduction heat transfer of the foam metals.

Table 7. The heat transfer coefficients, Nusselt numbers and the thermal resistances of the metal foam embedded heat sinks at 6 m/s air velocity

| | Heater (W) | \dot{m} (kg/h) | R_{th} (K/W) | \bar{h} (W/m ² ·K) | Nu |
|---------|------------|------------------|----------------|---------------------------------|-------|
| Al10PPI | 60 | 50 | 0.207 | 49.50 | 78.06 |
| | 80 | 50 | 0.219 | 59.13 | 93.24 |
| | 120 | 50 | 0.237 | 49.69 | 78.36 |
| | 160 | 50 | 0.207 | 53.40 | 84.21 |
| Al20PPI | 60 | 50 | 0.182 | 34.72 | 54.75 |
| | 80 | 50 | 0.207 | 34.14 | 53.83 |
| | 120 | 50 | 0.220 | 34.75 | 54.80 |
| | 160 | 50 | 0.189 | 34.56 | 54.50 |
| Al40PPI | 60 | 50 | 0.170 | 22.39 | 35.31 |
| | 80 | 50 | 0.220 | 22.34 | 35.23 |
| | 120 | 50 | 0.214 | 22.39 | 35.31 |
| | 160 | 50 | 0.191 | 22.57 | 35.58 |
| CU10PPI | 60 | 50 | 0.178 | 53.68 | 84.64 |
| | 80 | 50 | 0.205 | 56.21 | 88.64 |
| | 120 | 50 | 0.236 | 55.37 | 87.32 |
| | 160 | 50 | 0.203 | 56.56 | 89.19 |
| CU20PPI | 60 | 50 | 0.074 | 42.02 | 66.26 |
| | 80 | 50 | 0.086 | 42.71 | 67.35 |
| | 120 | 50 | 0.084 | 41.15 | 64.89 |
| | 160 | 50 | 0.134 | 41.48 | 65.41 |
| CU40PPI | 60 | 50 | 0.119 | 31.90 | 50.30 |
| | 80 | 50 | 0.171 | 33.60 | 52.99 |
| | 120 | 50 | 0.151 | 32.18 | 50.75 |
| | 160 | 50 | 0.152 | 31.66 | 49.92 |

Figure 8 and Figure 9 show the thermocouple temperatures of the base plane at the stated conditions. Due to the locations of the heaters, the temperatures on the foam sides were higher than TC9 and TC5 in Figure 8. In addition, the metal foam parts in Figure 9 provided the temperature values which get close to one another. The heat transfer coefficients (HTC) of each sample showed similar values at various heaters as mentioned in Mancin's study (2012). In addition, the order of the heat

transfer coefficients with respect to the pore density of the present study and Mancin's study support one another (2012). Another study carried out by Mancin indicated that the 10 PPI aluminum sample had lower mean wall temperature than the 20PPI and the 40 PPI foams which are at the same porosity, as in Figure 10.

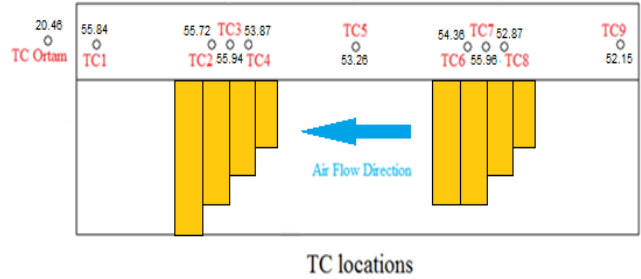


Figure 8. Surface temperatures of CU 20PPI at a 2 section 120 watt heater at 6 m/s air velocity

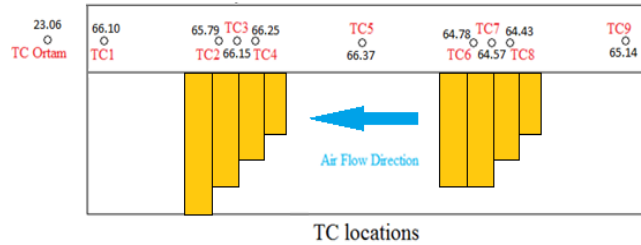


Figure 9. Surface temperatures of CU 20PPI at a whole 160 watt heater at 6 m/s air velocity

At the copper samples, the increase of the pore density decreases the mean wall temperature of the heat sinks as seen in Figure 10. On the contrary, the mean wall temperatures of the aluminum heat sinks increase with pore density. This can be interpreted as, the higher porosity and the lower thermal conductivity of the aluminum foams slowed the heat flow from the foam surface to air.

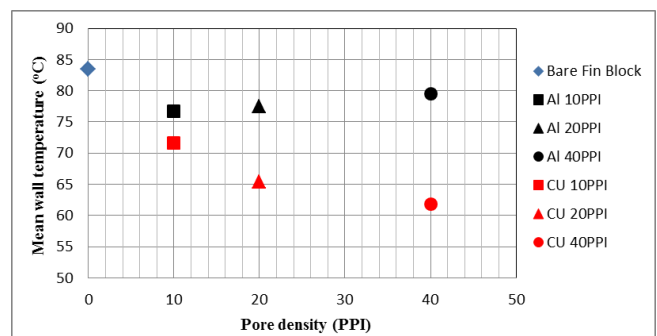


Figure 10. Mean wall temperature as a function of pore density at 160 W heater and 6 m/s frontal air velocity

THE PERFORMANCE COMPARISON OF THE HEAT SINKS

This study has one ultimate goal which is to determine the heat sink that will give the lowest base temperature at a specified heater load and the inlet air temperature with the lowest air pressure drop. Figures 13 was prepared for the evaluation of the heat sinks with the best performance

heat sinks for this goal. The thermal resistances of the heat sinks were calculated by implementing Equation 7.

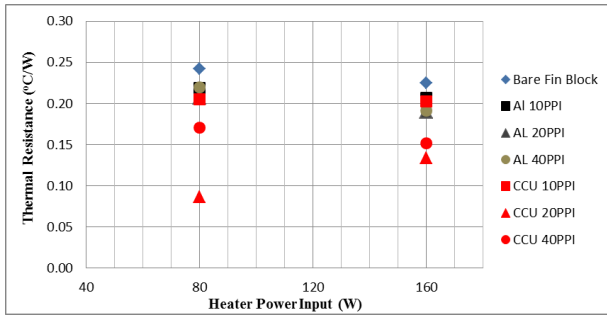


Figure 11. Variation of R_{th} as a function of heater power at 50 kg/h mass flow rate (whole heaters)

As it can be seen in Figure 11, the thermal resistances of the heat sinks drop down at 160 W heater loads. There could be a breakeven point beyond which heat sink works effectively. The effectiveness of the heat sink depends on the heater load and the geometrical configuration of the heat sink, which seems to be worth investigating in further studies. The 20PPI foam embedded heat sinks do not fit in this generalization. The reason for this discrepancy can be originated from the closed cell structure of the copper foam plates. It is clearly understood from the Figure 11 that the fin block has the highest thermal resistances at both heat loads. While the thermal resistances of the aluminium foams are close to each other, the thermal resistances of the copper foams illustrate the differences. The effect of the thermal conductivity of the copper samples is seen in the 20PPI and the 40PPI copper foam embedded heat sinks which have the lowest thermal resistances.

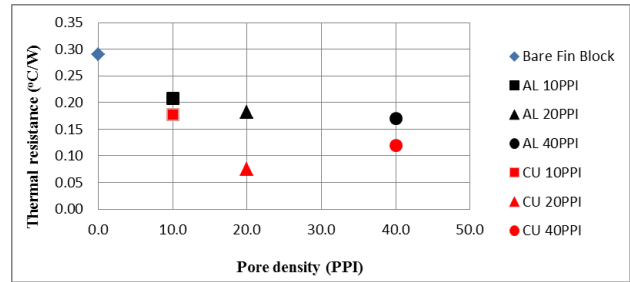


Figure 12. Variation of R_{th} as a function of the pore density at a 60W heater and 6 m/s frontal air velocity

It is observed that the increase of the pore density decreases the thermal resistance of the heat sinks except for the 20 PPI copper sample as seen in Figure 12. Even with the limited usage of the metal foam, the thermal resistance of the metal foam embedded heat sinks are significantly lower than the thermal resistance of the fin block as shown in Figure 12.

Figure 13 demonstrates the base plane temperatures of the samples and the vertical lines indicate the foam boundaries of the heat sinks. It is seen that the temperatures increased in the first foam section while the fresh air provided from a 5 mm gap decreased the second foam section. At the fin block, the temperature continued to increase, which is undesired for the operational life of the electronic components. Finally, the 40PPI copper foam heat sink provided the lowest base plane temperatures. However, the 20PPI copper foam heat sink was the most effective considering the pressure drop and the thermal resistance together. Moreover, the 20PPI foam heat sink produced less noise compared to the 40PPI foam heat sink. The metal foam-structured heat exchangers reduced the thermal resistance by nearly two thirds when compared to a conventional fin block.

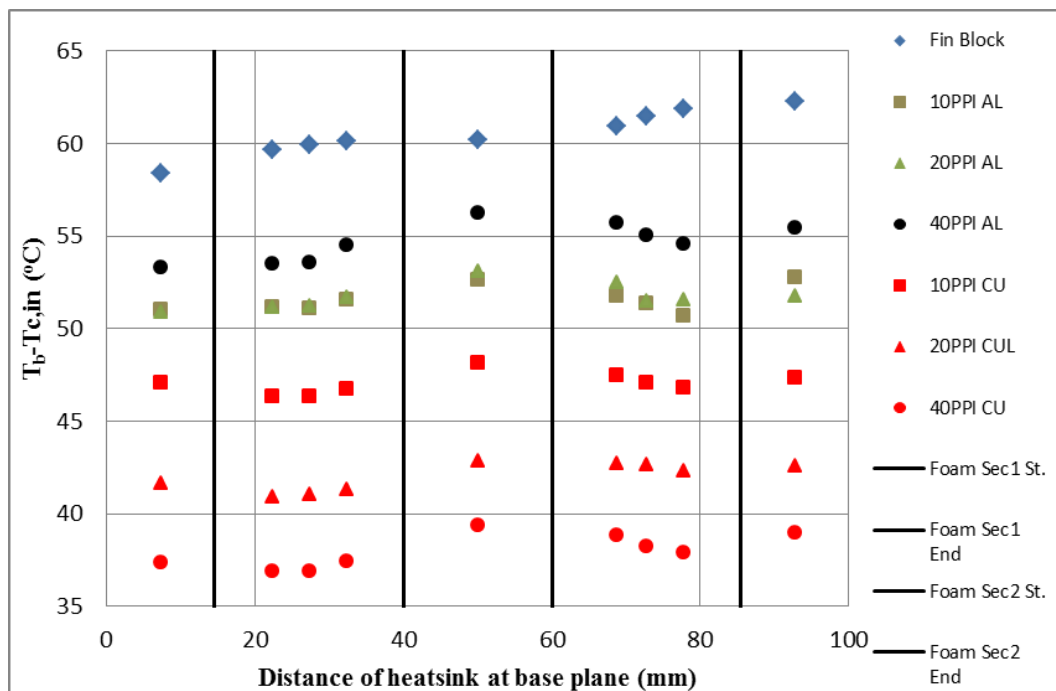


Figure 13. The variation of the base plane temperatures as a function of the distance at 160 W heater

CONCLUSIONS

In this study, an experimental comparison between the thermal and the hydrodynamic characteristics of the partial metal foam embedded heat sinks and those of conventional fin block was presented. The current study not only shows the metal foam embedded heat sink design for the electronic boxes, but also guides the utilization of the metal foams at the industrial heat sinks. The main findings of this study is summarized as follows:

- Both the copper and the aluminum metal foam embedded heat sinks have lower thermal resistance than the aluminum fin block at all heater loads and air velocities. Both the 40 PPI and the 20 PPI copper foam embedded heat sinks are shown convenient to the electronic cooling applications.
- The measured pressure drop of the foam heat sinks increased up to four times more than that of the fin block at 50 kg/h air flow rate, as shown in Table 3 and Table 4. Not only the thermal resistance, but also the pressure difference of the 10 PPI aluminum foam embedded heat sink make it a suitable option among the other aluminum ones.
- The thermal resistance of the foam embedded heat sinks decreased with the increasing pore density as found in the Mancin's study. Only the resistance of the 20 PPI copper foam embedded heat sinks does not fit this trend, which was described under the 'Heat Transfer' subsection. The reasons why Mancin's studies are the guideline researches for the current study are the same pore density foam specimens and the use of the same working fluid.
- At the 80 W and the 160 W larger heater scenarios, the temperature at the foam sections are as low as 1 to 1.5 degree, which is lower than the temperature at the foamless sections. It is clearly observed that locating the metal foam under the equipment that may generate hotspots and it has positive results in terms of equipment performance.

ACKNOWLEDGMENTS

This study was supported by M. Koç, Z.A. Temel, A.H. Erbay, K. Yıldız, M. Kahya, M. Yalçın, S. Gürel and G. Doğan. The authors would like to thank for having a fruitful discussion with Y. Demirtola and A. Ünal. This research did not receive any specific grant from funding agencies in the public, commercial, or not-for-profit sectors.

REFERENCES

Antohe B. V., Lage J. L., Price D. C., Weber R. M., 1997, Experimental Determination of Permeability and Inertia Coefficients of Mechanically Compressed Aluminium Porous Matrices, *Journal of Fluids Engineering*, 119, 404-412.

ATEŞ A. M., 2011, Experimental Comparison of Fluid and Thermal Characteristics of Microchannel and Metal Foam Heat Sinks, *Msc. Thesis, METU*.

Bhattacharya A., Calmidi V.V., Mahajan R.L., 2002, Thermophysical Properties of High Porosity Metal Foams, *International Journal of Heat and Mass Transfer*, 45, 1017-1031.

Bonnet J.P., Topin F., Tadrist L., 2008, Flow Laws in Metal Foams: Compressibility and Pore Size Effects, *Transport in Porous Media*, 73, 233-254.

Boomsma K.S., 2002, Metal Foams as Novel Compact High Performance Heat Exchangers for the Cooling of Electronics, *PhD. Thesis, Swiss Federal Institute of Technology Zurich*.

Calmidi V. V., Mahajan R. L., 2000, Forced Convection in High Porosity Metal Foams, *ASME Journal of Heat Transfer*, 122, 557-565.

Dukhan N., Ali M., 2012, Strong Wall and Transverse Size Effects on Pressure Drop of Flow through Open-Cell Metal Foam, *International Journal of Thermal Sciences*, 57, 85-91.

Dukhan N., Chen K. C., 2007, Heat Transfer Measurements in Metal Foam Subjected to Constant Heat Flux, *Experimental Thermal and Fluid Science*, 32, 624-631.

Dukhan N., Quinones-Ramos P. D., Cruz-Ruiz E., Velez-Reyes M., Scott E. P., 2005, One-Dimensional Heat Transfer Analysis in Open-Cell 10-PPI Metal Foam, *International Journal of Heat and Mass Transfer*, 48, 5112-5120.

Hernández Á. R. Á., 2005, Combined Flow and Heat Transfer Characterization of Open Cell Aluminium Foams, *MSc. Thesis, University of Puerto Rico*.

Kim S.Y., Kang B.H., Kim J.H., 2001, Forced Convection from Aluminium Foam Materials in an Asymmetrically Heated Channel, *International Journal of Heat and Mass Transfer*, 44, 1451-1454.

Kim S.Y., Peak J.W., Kang B.H., 2000, Flow and Heat Transfer Correlations for Porous Fin in a Plate-Fin Heat Exchanger, *ASME Journal of Heat Transfer*, 122, 572-578.

Liu J.F., Wu W.T., Chiu W.C., Hsieh W.H., 2006, Measurement and Correlation of Friction Characteristics of Flow through Foam Matrixes, *Experimental Thermal and Fluid Science*, 30, 329-336.

Loh C.K., Chou Bor-Bin, Nelson Dan and Chou D.J., 2000, Study of Thermal Characteristics on Solder and Adhesive Bonded Folded Fin Heat Sink, *The Seventh Intersociety Conference*, 2, 1-7.

Mahjoob S., Vafai K., 2008, A Synthesis of Fluid and Thermal Transport Models for Metal Foam Heat Exchangers, *International Journal of Heat and Mass Transfer*, 51, 3701–3711.

Mancin S., Zilio C., Cavallini A., Rosetto L., 2010, Pressure Drop During Air Flow in Aluminium Foams, *International Journal of Heat and Mass Transfer*, 53, 3121–3130.

Nawaz K., Bock J., Dai Z., Jacobi A.M., 2010, Experimental Studies to Evaluate the Use of Metal Foams in Highly Compact Air-Cooling Heat Exchangers, *International Refrigeration and Air Conditioning Conference*, 1-11.

Paek J. W., Kang B. H., Kim S. Y., Hyun J. M., 2000, Effective Thermal Conductivity and Permeability of Aluminium Foam Materials, *International Journal of Thermophysics*, 21, 2, 453-464.

Pradeep M. Kamath, C. Balaji, S.P. Venkateshan, 2013, Convection Heat Transfer from Aluminium and Copper Foams in a Vertical Channel - an Experimental Study, *International Journal of Thermal Sciences*, 64 1-10.

Simone Mancin, Claudio Zilio, Andrea Diani, Luisa Rossetto, 2012, Experimental Air Heat Transfer and Pressure Drop through Copper Foams, *Experimental Thermal and Fluid Science*, 36, 224-232.



Süleyman Kaancan ATAER graduated from Mechanical Engineering Department of Gazi University in 2007. Initially, he started his career at MIKES Inc. from September 2010 to March 2014. Secondly, he worked for STM Inc. as a System Engineer for one year. Finally, he has been working as a Space Systems Thermal Design Engineer in Turkish Aerospace Industry, Inc. He received his MSc degree in the year 2014 from the Mechanical Engineering (M.E.) Department of Middle East Technical University. His research interests are Spacecraft Thermal Control and Design, Thermal Mathematical Model Development and Correlation, Space Systems Environmental Testing.



Cemil YAMALI graduated from Mechanical Engineering Department of Middle East Technical University (Ankara, Turkey) in the year 1973. Then, he received his MSc. degree from the same university and his PhD degree from the University of Michigan in 1983. He worked as an Assoc. Prof at METU from 1988 to 2017. His principle research interests were heat transfer, thermodynamics and solar energy.



Kahraman ALBAYRAK graduated from Mechanical Engineering Department of Middle East Technical University (Ankara, Turkey) in the year 1971. He received his MSc. and PhD. degrees from the same department in the years 1974 and 1984, respectively. His research interests are Fluid Mechanics, Fluid Machinery, Boundary Layer, HVAC Systems and Thermo-Fluid Science. He has been supervisor in 38 MSc, 3 PhD researches and has approximately 60 national and international publications. He is currently working for the Mechanical Engineering Department of Middle East Technical University as a lecturer.



RADIOFREQUENCY ABLATION FOR SPHERICALLY-SHAPED HEPATIC TUMORS

Güven Hasret YILMAZ*, Uğur Tuna YAY*, Oğuz TURGUT*, Burak TIĞLI* and Nuri Eren TÜRKOĞLU**

*Gazi University, Faculty of Engineering, Department of Mechanical Engineering
06570 Maltepe, Ankara, Turkey

gvn_yilmaz_06@hotmail.com, tuna2706@gmail.com, oturgut2006@gmail.com, buraktigli@gmail.com

**Politecnico di Milano, Department of Electrical Engineering
Milano, Italy, erenturkoglu12@gmail.com

(Geliş Tarihi: 04.04.2019, Kabul Tarihi: 06.03.2020)

Abstract: The purpose of this study is to destroy spherical shape hepatic tumors using radiofrequency ablation method. Three-dimensional finite elements method has been employed. Five different radiofrequency probes for liver tissue have been used to create a spherical-shaped lesion. Investigated parameters are the electrical voltage, ablation time, geometry and number of electrodes. Results have been given as lesion volume and temperature distribution. Results have been compared with the literature results, and it is seen that present results are in good agreement with the literature results. Results show that a spherical shape hepatic tumor can be destroyed using a hybrid electrode construction consisting of four Christmas-tree and four umbrella-shaped electrodes. It is seen that approximately 20 mm-diameter of lesion can be destroyed using hybrid electrode design after eight minutes. It is hoped that hybrid electrode configuration can be used for treatment of spherical shape hepatic tumors in clinical applications.

Keywords: Electrode, Hepatic tumors, Lesion, Radiofrequency ablation

KÜRESEL ŞEKİLLİ KARACİĞER TÜMÖRLERİ İÇİN RADYOFREKANS ABLASYONU

Özet: Bu çalışmanın amacı radyofrekans ablasyon metodunu kullanarak küresel şekilli karaciğer tümörlerinin yok edilmesidir. Üç boyutlu sonlu elemanlar metodu kullanılmıştır. Karaciğer dokusu için beş farklı radyofrekans prop küresel şekilli lezyonu oluşturmak için kullanılmıştır. İncelenen parametreler elektrik voltajı, ablasyon süresi, geometri ve elektrot sayısıdır. Sonuçlar lezyon hacmi ve sıcaklık dağılımı olarak verilmiştir. Sonuçlar literatür sonuçları ile kıyaslanmış ve sonuçların literatür sonuçları ile uyum içinde olduğu görülmüştür. Sonuçlar bir küresel şekilli karaciğer tümörünün dört elektrotlu yılbaşı ağacı tipi ve dört elektrotlu şemsiye-tipi elektrotlardan oluşan hibrit bir elektrot konstrüksiyonuyla yok edilebileceğini göstermiştir. Yaklaşık 20 mm çapındaki bir lezyonun sekiz dakika sonunda hibrit elektrot dizaynı ile yok edilebildiği görülmüştür. Hibrit elektrot konfigürasyonunun klinik uygulamalarda küresel şekilli karaciğer tümörlerinin tedavisi için kullanılması umulmaktadır.

Anahtar Kelimeler: Elektrot, Karaciğer tümörleri, Lezyon, Radyofrekans ablasyonu

NOMENCLATURE

| | |
|----------|---|
| c | Specific heat [kJ/kg K] |
| c_{bl} | Specific heat of the blood [kJ/kg K] |
| D | Diameter of the trocar tip [mm] |
| E | Electric field intensity [V/m] |
| H | Height of the trocar [mm] |
| J | Current density [A/m^2] |
| k | Thermal conductivity [W/m K] |
| h_{bl} | Heat transfer coefficient of the blood [W/m ³ K] |
| r | Minor radius [mm] |
| R | Major radius [mm] |
| Q_m | Energy generated by the metabolic process [W/m ³] |
| T | Temperature [K] |
| T_{bl} | Temperature of the blood [K] |

| | |
|---------------|---|
| t | Time [s] |
| ρ | Density [kg/m ³] |
| ρ_{bl} | Density of the blood [kg/m ³] |
| σ | Electrical conductivity [S/m] |
| ω_{bl} | Blood perfusion rate [1/s] |

INTRODUCTION

Percutaneous hyperthermia treatments generated with radiofrequency needle electrodes have gained wide popularity in last decades. Primary and secondary tumors could be terminated with no serious complications (Rossi et al., 1998). Also, rehabilitation rates have been increased by the improvement of imaging techniques (Verslype et al., 2012).

Hepatocellular carcinoma (HCC) is the most common primary hepatic tumor in the world (Ferenci et al.,

2010), and the global percentage of HCC increases (Poon et al., 2009). Surgical resection, liver transplantation, and radiofrequency ablation (RFA) treatments are recommended for HCC (Clinical Practice Guidelines, 2012a, 2012b).

RFA is applied primarily to patients instead of surgical resection for unresectable HCC by means of minimally invasive procedure along with highly sensitive necrosis, especially for small HCC (Lin and Lin, 2003). RFA also needs shorter hospitalization, and it has lower complication rates than surgical resection (Ozbek et al., 2016). Some investigators believe that RFA can be used as first option against HCC (Mazzaferro et al., 2009).

RFA has been used first in 1990s and dissipated over in clinics (Livraghi et al., 1999). RFA is applied to 30–40% of HCC patients in Europe and the USA (Clinical Practice Guidelines, 2012a, 2012b). RFA method uses alternative current usually at about 450 kHz–550 kHz to create heat, delivered through a thin instrument known as a probe, to terminate malignant lesions (Chang and Nguyen, 2004; Barajas et al., 2018). Imaging procedures like computed tomography scan, ultrasound or magnetic resonance imaging are used to help guide the probe while the probe enters into the area of the tumor. Depletion of the cells occurs when the temperature reaches about 45°C–50°C (Goldberg et al., 1996; Tungjitkusolmun et al., 2002; Haemmerich et al., 2003a). Guidance of imaging procedures and choice of an appropriate probe are important for successful ablation (Tatli et al., 2012).

In probe designs, there are some parameters such as probe tip temperature, impedance, power output etc. to control the ablation action (Ito et al., 2014).

Stippel et al. (2004) stated that about 60% of tumors encountered in liver tissue are in spherical shape. Literature review has showed that RFA method for liver tumors has been investigated by a number of researchers for different electrode types. Tungjitkusolmun et al. (2002) carried out a study to investigate the three-dimensional finite element analysis for radiofrequency hepatic tumor ablation using four-array umbrella-typed electrode. Haemmerich et al. (2003a) evaluated the effect of different cooling water temperatures on lesion size with cooled-tip electrode. Ito et al. (2014) developed a new expandable bipolar device to get wider coagulation volume. De Baere et al. (2001) experimentally studied the radiofrequency liver ablation for two different types of RFA devices with four-array expandable needle electrode and a triple-cluster cooled-tip needle electrode. McGahan et al. (1990) investigated the RFA method with ultrasound guide for plane electrodes. Rossi et al. (1990) concluded that small tumors whose diameters are less than 20 mm could be destroyed by RFA method using linear needles. Curley et al. (1997) studied the bipolar RFA in pig livers. Livraghi et al. (1997) studied saline-enhanced RFA with a single radiofrequency electrode. Lencioni et al. (1998) evaluated feasibility, safety and effectiveness of RFA by

using cooled-tip electrode needle in hepatic tumors. Hansen et al. (1999) showed that how local vasculature affects the size and shape of a lesion. Haemmerich et al. (2003b) examined the performance of monopolar and bipolar probes for treating lesions. Lee et al. (2004) studied the saline-enhanced hepatic RFA with dual probe bipolar, monopolar and single probe bipolar modes. Mulier et al. (2005) proposed an updated terminology for the electrodes and multiple electrode systems used in radiofrequency processes. Chen et al. (2009) conducted a study to optimize electrode placement for nine times for the tumor of liver with and without vessel. Yang et al. (2010) presented a robotic system for large tumor lesions using overlapping ablations. Audigier et al. (2015) carried out a study to model heat propagation in liver with blood vessel using RFA for multi-tine electrode. Kilic et al. (2015) stated that tumor needle track seeding may occur after RFA for hepatic tumor. Therefore, they suggested performing prophylactic needle track coagulation. Cartier et al. (2016) compared monopolar and multipolar probes. Ahmad (2016) conducted a study for the comparison of monopolar cluster and multipolar electrode systems to treat HCC bigger than 25 mm. Choi et al. (2016) conducted a study to analyze the outcomes of multi-channel switching RFA using a separable cluster electrode in patients with HCC. A probabilistic bio-heating finite element model was proposed by Duan et al. (2016) to predict RFA lesions in liver using RFA probe. The effect of nanoparticle injected into tissue with blood vessels on RFA treatment of liver tumor was investigated by Shao et al. (2017) using RFA probe. Their results showed that using nanoparticles increases ablation efficiency. Givehchi et al. (2018) simulated the liver tumor ablation using radiofrequency ablation.

Literature study showed that the electrodes used in literature do not give realistic sphere lesion. Thus, in this study, RFA method for liver tumors with spherically-shaped has been investigated numerically. Investigated parameters are the electrical voltage, ablation time, geometry, and number of electrodes. Simulations are conducted for three, four, six, and two different types of eight electrodes. A hybrid electrode which creates spherical shape is proposed.

MATERIALS AND METHODS

Simulation of percutaneous treatment has been carried out by using a computer (with 16 GB of RAM and 1 TB of total disk space). Finite element method is used for numerical study. Figure 1 demonstrates the design which is used for analyses. Outer cylinder shows the liver tissue which is hosting the probe. When the probe reaches the tumor location, tines deploy through the tissue. After that, generator utilizes the radiofrequency waves from the probe to the ground pads which are resting on the patient thighs. Probe consisting of electrodes, trocar tip, and trocar base is also seen in Figure 1. Trocar tip and electrodes are made of different materials due to necessity of different thermal conductivity values. Big part of the heating/ablation

process is performed by electrodes where the trocar tip is auxiliary component for this process. Adjustable trocar base is made of polyurethane which does not allow the heat flow.

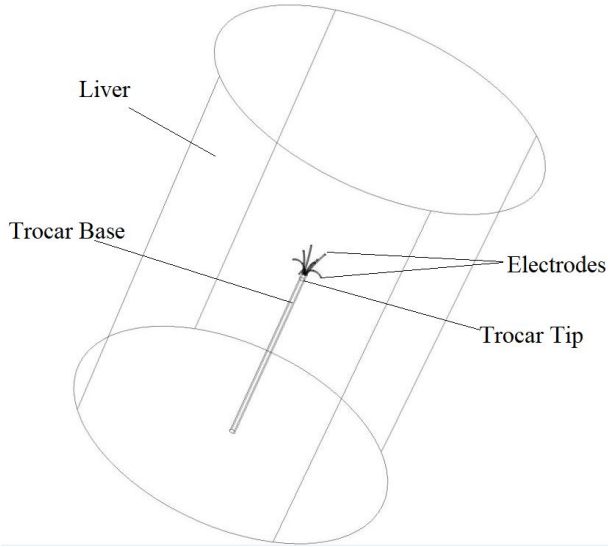


Figure 1. The schematic view of the computational domain.

The five different radiofrequency electrode types used in this study are shown in Figure 2. The electrodes of Case 1 through Case 4 are the Christmas-tree-shaped whereas the electrode given in Case 5 has four Christmas-tree and four umbrella-shaped electrodes. For Case 5, four of eight Christmas-tree-shaped electrodes of Case 4 are changed with four umbrella-shaped electrodes. Thus, the electrode of Case 5 is called as

hybrid. The dimensions of electrodes of Case 5 are shown in Figure 3. In Figure 3, r_1 and r_2 are the minor radii. R_1 and R_2 are the major radii. H_1 and H_2 are the heights of trocar tip and Christmas-tree-shaped electrode, respectively. D is the diameter of the trocar tip. The values of these parameters are: $r_1=0.23$ mm, $r_2=0.2$ mm, $R_1=25$ mm, $R_2=2.75$ mm, $H_1=2$ mm, $H_2=7.962$ mm, $D=1.8288$ mm. The values given in Figure 3 are valid for Case 1 through Case 4. Revolution angle for umbrella-shaped electrodes is 135° . This angle is the most appropriate selection that gives the spherical shape in the best way. However, revolution angle for umbrella-shaped electrodes used in clinical applications is generally 180° . Also, Christmas-tree-shaped electrodes are turned 20° from the vertical axis. There are four main different regions in simulation. These are electrode, trocar tip, tissue, and trocar base. The density ρ (kg/m^3), specific heat c (J/kg K), thermal conductivity k (W/m K), and electric conductivity σ (S/m) of materials of these regions are given in Table 1.

The electrical voltage is chosen between 20-35V. Complete spherical shape is not obtained when electrical voltage is chosen under 30V. In addition, carbonization is observed when electrical voltage is greater than 30V. Thus, 30V is chosen as electrical voltage in this study. The other important values used in the simulation are given in Table 2.

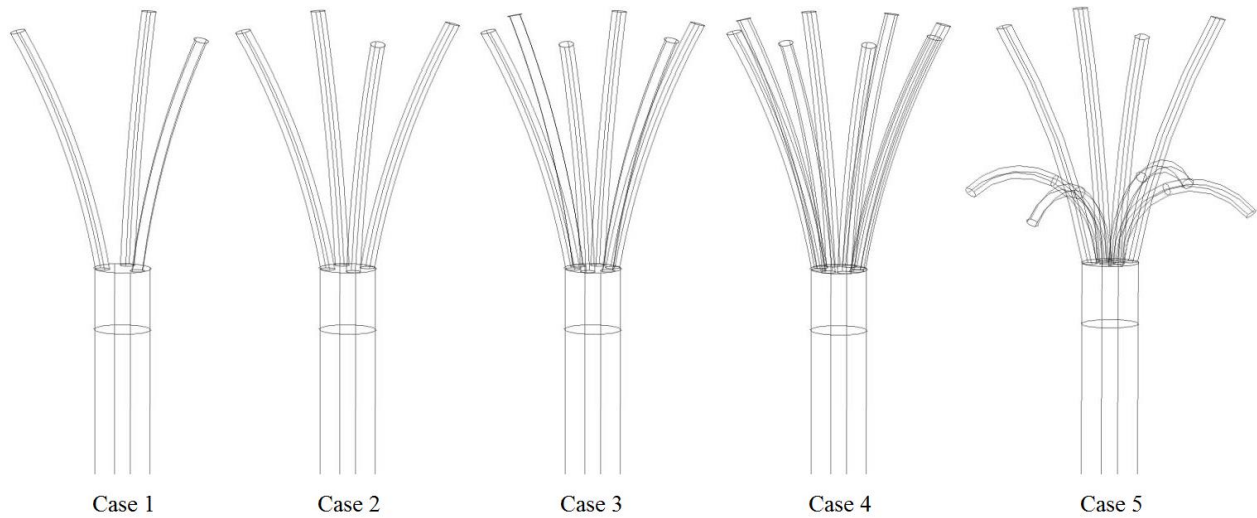


Figure 2. Electrode designs used in this study: Case 1: three-tin, Case 2: four-tin, Case 3: six-tin, Case 4: eight-tin, Case 5: eight-tin (hybrid design).

Table 1. Properties of materials.

| Region | Material | ρ (kg/m^3) | c (J/kg K) | k (W/m K) | σ (S/m) |
|-------------|-----------------|----------------------------|-------------------------|------------------------|---------------------------|
| Electrode | Ni-Ti | 6450 | 840 | 18 | 10^8 |
| Trocar tip | Stainless steel | 21500 | 132 | 71 | 4×10^6 |
| Tissue | Liver | 1060 | 3600 | 0.512 | 0.333 |
| Trocar base | Polyurethane | 70 | 1045 | 0.026 | 10^{-5} |

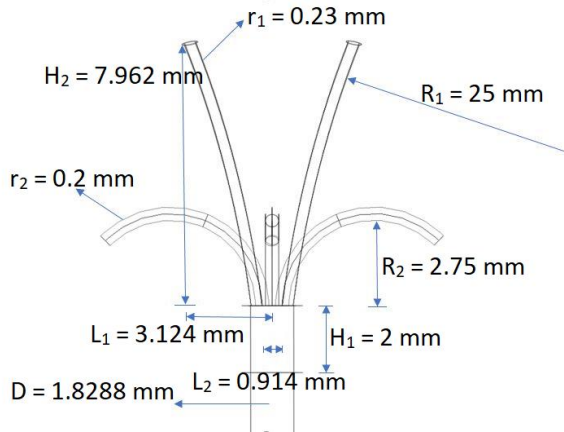


Figure 3. Dimensions of electrodes of Case 5.

Table 2. Parameters used in simulation.

| Parameters | Value | Unit |
|----------------------------------|----------------------|------|
| Blood perfusion rate | 6.4×10^{-3} | 1/s |
| Arterial blood temperature | 37 | °C |
| Initial and boundary temperature | 37 | °C |
| Electrical voltage | 30 | V |
| Ablation time | 8 | min |

Bioheat Equation

Pennes' bioheat equation is a well-known equation and one of the best approaches to simulate RFA in the area of bioheat transfer. Bioheat transfer in radiofrequency tumor ablation occurs between radiofrequency electrode and liver tissue. This type of heating due to electric current flow is called Joule heating. Pennes bioheat transfer equation is given as

$$\rho c \frac{\partial T}{\partial t} = \nabla \cdot k \nabla T + J \cdot E - h_{bl} (T - T_{bl}) + Q_m \quad (1)$$

where ρ is the density (kg/m^3), c is the specific heat (J/kg K), k is the thermal conductivity (W/m K), T is the temperature (K), and t is the time (s). J is the current

density (A/m^2), E is the electric field intensity (V/m), h_{bl} is the convective heat transfer coefficient ($\text{W/m}^3 \text{K}$), and Q_m is the energy generated by the metabolic processes (W/m^3). The convective heat transfer coefficient is given as

$$h_{bl} = \rho_{bl} c_{bl} \omega_{bl} \quad (2)$$

In Eq.1 and Eq.2, the subscript bl designates the blood, and ω_{bl} is the blood perfusion rate (1/s). Pennes' bioheat equation is solved using finite element method for the cases. COMSOL Multiphysics software is used to solve numerically the governing differential equation, i.e. Eq. 1.

Numerical Analysis

COMSOL Multiphysics software is used to simulate the process. It solves the partial differential equations in an integral form. Unknowns are discretized as sums of basis functions defined on finite elements. To perform an accurate simulation of RFA, different mesh numbers have been used. Tetrahedral mesh (cell) has been employed. Fine mesh structure is employed near the probe. Typical three-dimensional mesh distribution is seen in Figure 4a. Mesh optimization study is carried out for the fraction of necrosis which represents the death of cells in living tissue. Because the aim of this study is to destroy the all tumor region in living tissue, i.e., necrosis region, mesh optimization is conducted for the fraction of necrosis. Typical fraction of necrosis at three different points (A, B, C) is given for five different mesh numbers in Table 3 for Case 5 at the end of eight minute. Points A, B and C are at 4 mm, 12 mm and 20 mm from center of probe, and they are shown in Figure 4b. It is seen that the fraction of necrosis does not change significantly when the mesh number changes from 176929 to 743265. Thus, mesh number of 290887 is chosen for the optimum mesh number, and this mesh number is used for the remaining calculations for Case 5. Similar mesh optimization analysis is performed when case is changed.

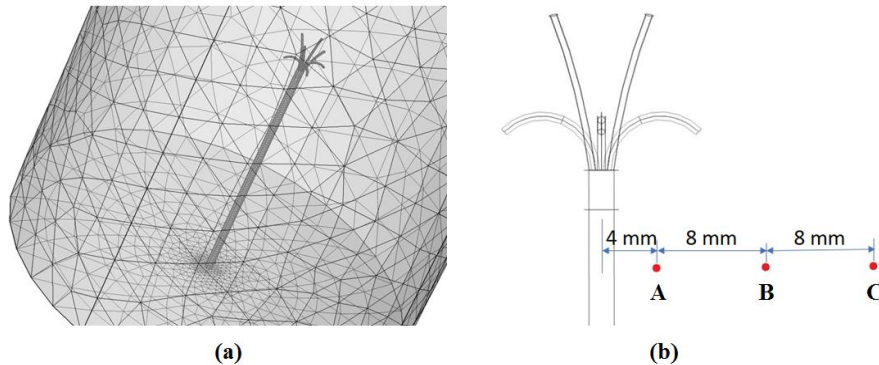


Figure 4. (a) Typical mesh distribution and (b) points used to measure the fraction of necrosis.

Table 3. Fraction of necrosis according to number of mesh elements at three different points at the end of eight minute.

| Points on Tissue | 127874 elements | 139853 elements | 176929 elements | 290887 elements | 743265 elements |
|------------------|-----------------|-----------------|-----------------|-----------------|-----------------|
| Point A | 1 | 1 | 1 | 1 | 1 |
| Point B | 0.4 | 0.3 | 0.332 | 0.329 | 0.327 |
| Point C | 0.173 | 0.168 | 0.163 | 0.163 | 0.162 |

RESULTS

Numerical validation can be done with the results of Tungjitkusolmun et al. (2002), Chen et al. (2009) and Duan et al. (2016). Literature review showed that Tungjitkusolmun et al. (2002) is an accepted article which is highly cited by other researchers. Therefore, Tungjitkusolmun et al. (2002) has been the reason for preference to use it for literature comparison. The study of Tungjitkusolmun et al. (2002) was repeated here to show the accuracy of this numerical study. Three-dimensional finite element analysis for radiofrequency hepatic tumor ablation using four array umbrella-typed electrode was used. Temperature distribution of present study is shown in Figure 5a after eight minute of ablation. Figure 5b shows the temperature regions above than or equal to 50°C. The figure of Tungjitkusolmun et al. (2002) is not given here due to copyright (Please see Figures 4c and 4d in Tungjitkusolmun et al. (2002)). It is seen that the results of present study are in good agreement with the results of Tungjitkusolmun et al. (2002).

After verifying the accuracy of the numerical model, simulations are performed for five cases given in Figure 2. Lesion volumes obtained for Case 1 through Case 5 are seen in Figure 6 after eight minute. Gray area represents regions above than or equal to 50°C. It is seen that the shape of the lesion for Case 1 through Case 4 is nearly similar. It is also seen that the shape of the lesion is nearly spherical for Case 5, i.e., hybrid electrode.

After seeing that spherical lesion is obtained for Case 5 with four Christmas-tree and four umbrella-shaped electrodes, the numerical studies are conducted for Case 5. Evolution of lesion of Case 5 by the end of first, second, fourth, and eight minutes of ablation is seen in Figure 7. As can be seen from Figure 7, the shape is almost a sphere at the last minute, i.e., eight minute, of ablation. It is seen that the shape of lesion changes with time significantly until the end of four minute. However, results show that lesion shape almost remains the same when the time is changed from 4 to 8 minute.

Typical temperature distribution of Case 5 at the end of second, fourth, sixth, and eight minutes is shown in Figure 8. As can be seen in Figure 8, maximum temperature in tissue increases when the time increases. After eight minute of ablation, maximum temperature reaches to 94.2°C. Because of the fact that temperature is less than 100°C, tissue carbonization does not occur within the lesion (Tatli et al., 2012).

In order to see the dimensions of the lesion after the eight minute of ablation, the views of the lesion on *x-y* and *y-z* coordinates are shown in Figure 9. The diameter of the lesion obtained by hybrid design, i.e. Case 5, is approximately 20 mm which is suitable for small-medium tumors. This result agrees with the result of Rossi et al. (1990). It is seen that the shape of the lesion is nearly spherical.

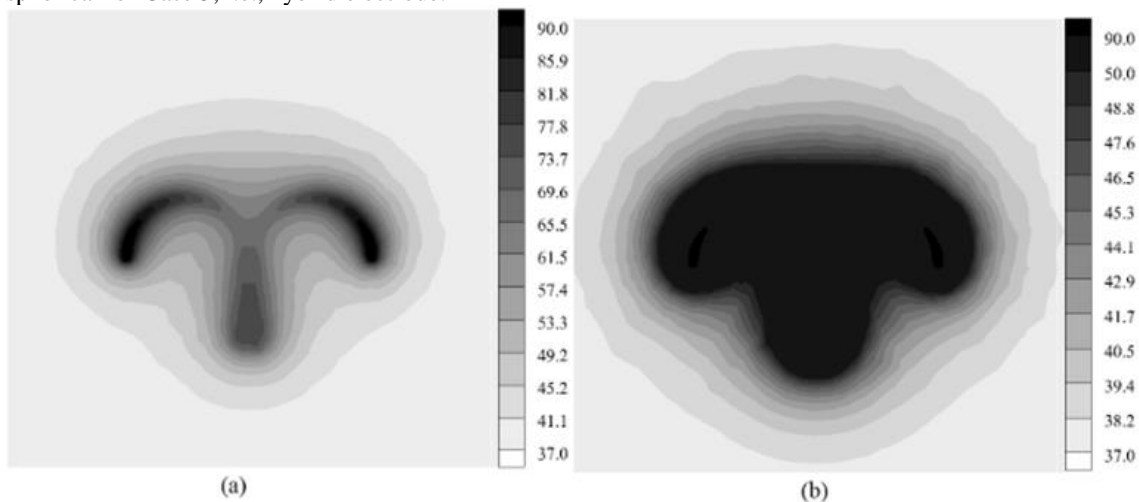


Figure 5. (a) Temperature distribution after eight minute of ablation, and (b) regions greater than or equal to temperature of 50°C.

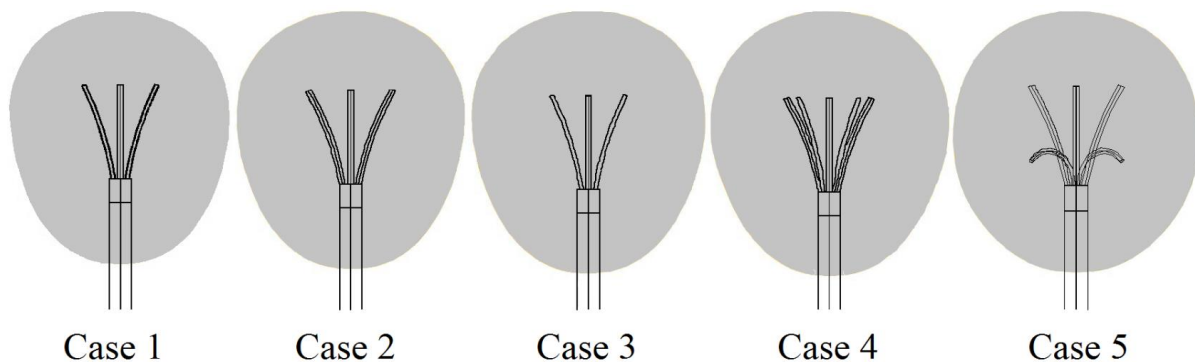
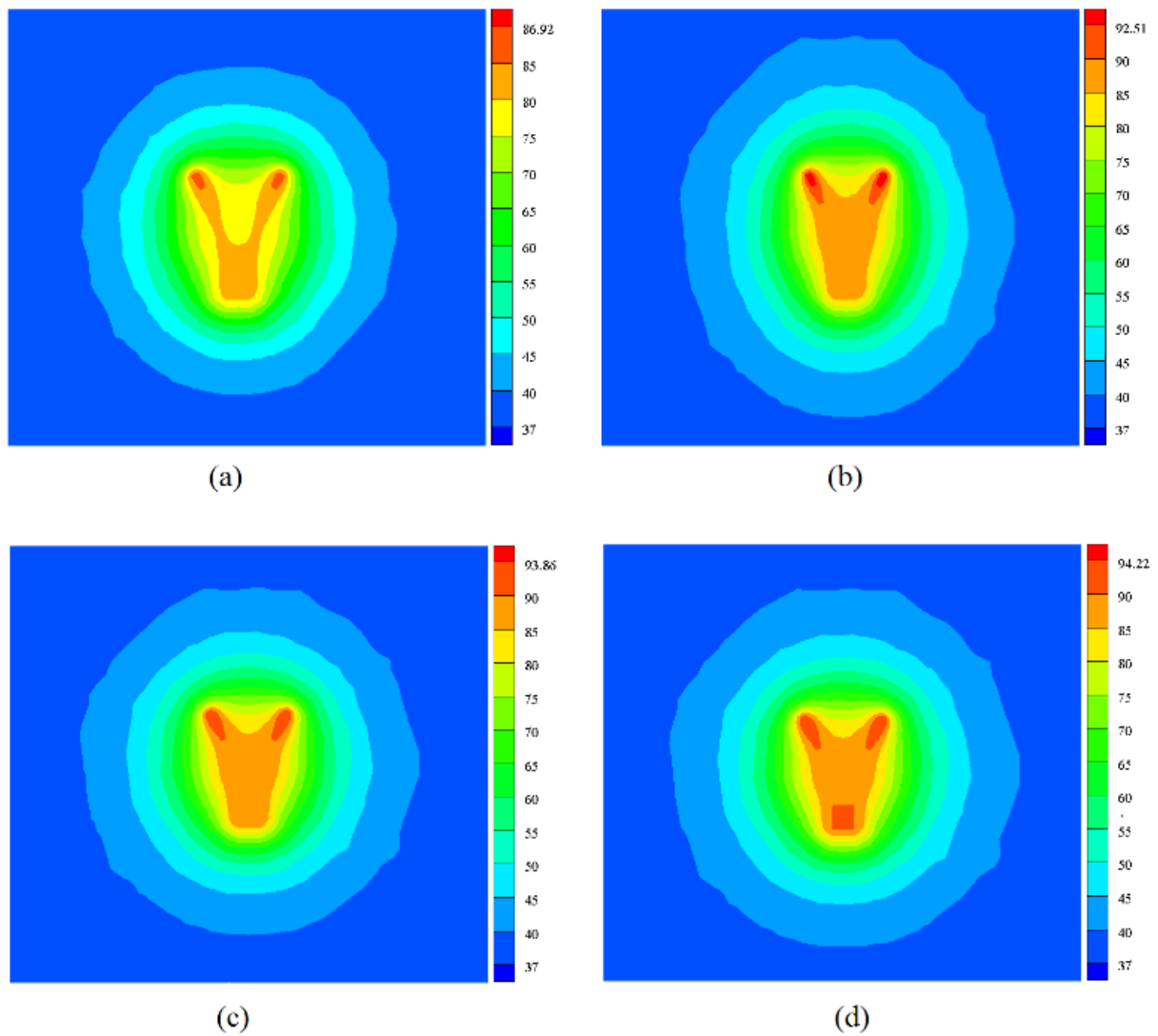
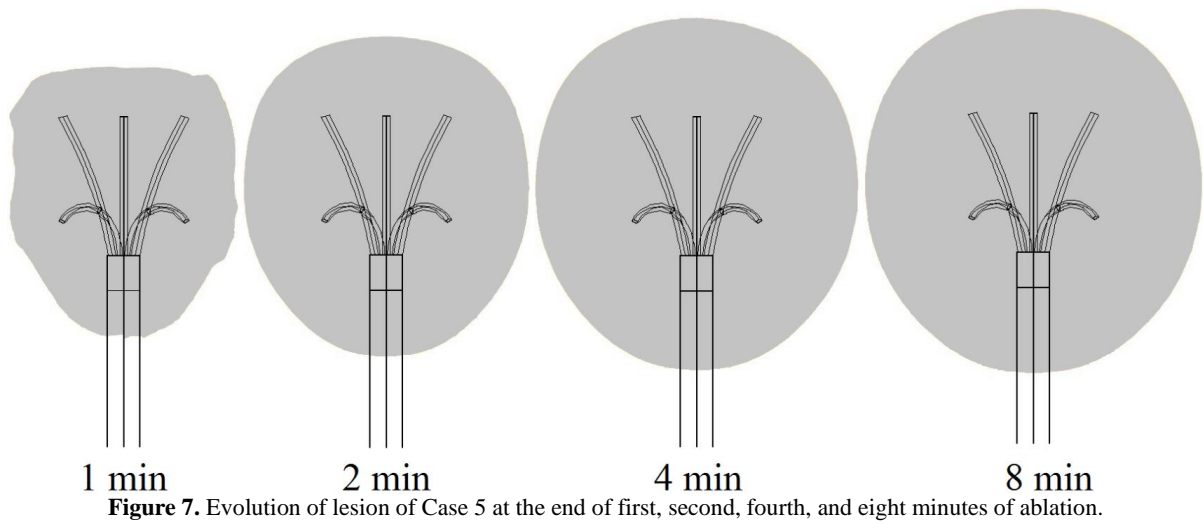


Figure 6. Lesion volumes after eight minute.



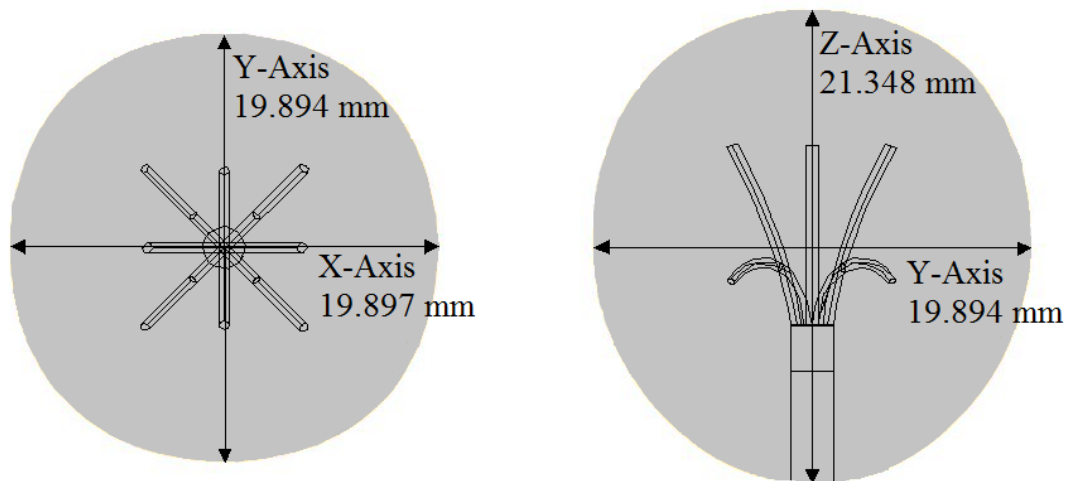


Figure 9. Dimensions of lesion after eight minute of ablation for Case 5.

CONCLUSION

A spherical-shaped lesion is obtained using a hybrid electrode for liver tissue. Three-dimensional finite element method is used. The COMSOL Multiphysics software is employed to simulate the problem. Electrical voltage, ablation time, geometry and number of electrodes are the investigated parameters. Results are presented in the form of lesion volume and temperature distribution. It is seen that present results are in good agreement with the literature results. Hybrid electrode construction consists of four Christmas-tree and four umbrella-shaped electrodes. It is seen that approximately 20 mm-diameter of lesion can be destroyed using hybrid electrode design after eight minutes. Results show that maximum temperature within tissue reaches to 94.2°C after eight minutes of ablation. Spherical lesion is obtained for electrical voltage 30V and at the end of ablation time 8 minute. It is hoped that the hybrid electrode configuration can be used for treatment of spherical shape hepatic tumors in clinical applications.

REFERENCES

- Ahmad M. I. M., 2016, Radiofrequency Ablation with Monopolar Cluster Versus Bipolar Multipolar Electrodes for the Ablation of ≥ 2.5 cm Hepatocellular Carcinoma, *Egypt. J. Radiol. Nucl. Med.*, 47, 1443-1449.
- Audigier C., Mansi T., Delingette H., Rapaka S., Mihalef V., Carnegie D., Boctor E., Choti M., Kamen A., Ayache N. and Comaniciu D., 2015, Efficient Lattice Boltzmann Solver for Patient-Specific Radiofrequency Ablation of Hepatic Tumors, *IEEE T. Med. Imaging*, 34, 1576-1589.
- Barajas M. S., Fraga T. C., Acevedo M. A. E. and Cabrera R. G., 2018, Radiofrequency Ablation: A Review of Current Knowledge, Therapeutic Perspectives, Complications, and Contraindication, *Int. J. Biosen. Bioelectron*, 4, 63-65.
- Cartier V., Boursier J., Lebigot J., Oberti F., Fouchard-Hubert F. and Aubé C., 2016, Radiofrequency Ablation of Hepatocellular Carcinoma: Mono or Multipolar, *J. Gastroenterol. Hepatol.*, 31, 654-660.
- Chang I. A. and Nguyen U. D., 2004, Thermal Modeling of Lesion Growth with Radiofrequency Ablation Devices, *Biomed. Eng.* 3, 1-19.
- Chen C. C. R., Miga M. I. and Galloway R. L., 2009, Optimizing Electrode Placement Using Finite-Element Models in Radiofrequency Ablation Treatment Planning, *IEEE T. Bio-Med. Eng.*, 56, 237-245.
- Choi J. W., Lee J. M., Lee D. H., Yoon J. H., Suh K. S., Yoon J. H., Kim Y. J., Lee J. H., Yu S. J. and Han J. K., 2016, Switching Monopolar Radiofrequency Ablation Using a Separable Cluster Electrode in Patients with Hepatocellular Carcinoma: A Prospective Study, *PLoS One*, 11, 1-17.
- Clinical Practice Guidelines, 2012a, EASL-EORTC Clinical Practice Guidelines: Management of Hepatocellular Carcinoma, *Eur. J. Cancer*, 48, 599-641.
- Clinical Practice Guidelines, 2012b, EASL-EORTC Clinical Practice Guidelines: Management of Hepatocellular Carcinoma, *J. Hepatol.*, 56, 908-943.
- Curley S. A., Davidson B. S., Fleming R. Y., Izzo F., Stephens L. C., Tinkey P. and Cromeens D., 1997, Laparoscopically Guided Bipolar Radiofrequency Ablation of Areas of Porcine Liver, *Surg. Endosc.*, 11, 729-733.
- De Baere T., Denys A., Wood B. J., Lassau N., Kardache M., Vilgrain V., Menu Y. and Roche A., 2001, Radiofrequency Liver Ablation: Experimental Comparative Study of Water-Cooled Versus Expandable Systems, *Am. J. Roentgenol.*, 176, 187-192.

- Duan B., Wen R., Fu Y., Chua K.J. and Chui C.K., 2016, Probabilistic Finite Element Method for Large Tumor Radiofrequency Ablation Simulation and Planning, *Med. Eng. Phys.*, 38, 1360–1368.
- Ferenci P., Fried M., Labrecque D., Bruix J., Sherman M., Omata M., Heathcote J., Piratsivuth T., Kew M., Otegbayo J. A., Zheng S. S., Sarin S., Hamid S. S., Modawi S. B., Fleig W., Fedail S., Thomson A., Khan A., Malfertheiner P., Lau G., Carillo F. J., Krabshuis J. and Le Mair A., 2010, Hepatocellular Carcinoma (HCC): A Global Perspective, *J. Clin. Gastroenterol.*, 44, 239-245.
- Givehchi S., Wong Y. H., Yeong C. H. and Abdullah B. J. J., 2018, Optimal Approach for Complete Liver Tumor Ablation Using Radiofrequency Ablation: A Simulation Study, *Minimally Invasive Therapy & Allied Technologies*, 27, 81-89.
- Goldberg S. N., Gazelle G. S., Halpern E. F., Rittman W. J., Mueller P. R. and Rosenthal D. I., 1996, Radiofrequency Tissue Ablation: Importance of Local Temperature Along the Electrode Tip Exposure in Determining Lesion Size and Shape, *Acad. Radiol.* 3, 212-218.
- Haemmerich D., Chachati L., Wright A. S., Mahvi D. M., Lee Jr. F. T. and Webster J. G., 2003a, Hepatic Radiofrequency Ablation with Internally Cooled Probes: Effect of Coolant Temperature on Lesion Size, *IEEE Trans. Biomed. Eng.*, 50, 493-500.
- Haemmerich D., Wright A. W., Mahvi D. M., Lee Jr. F. T. and Webster J. G., 2003b, Hepatic Bipolar Radiofrequency Ablation Creates Coagulation Zones Close to Blood Vessels: A Finite Element Study, *Med. Biol. Eng. Comput.*, 41, 317-323.
- Hansen P. D., Rogers S., Corless C. L., Swanstrom L. L. and Siperstien A. E., 1999, Radiofrequency Ablation Lesions in a Pig Liver Model, *J. Surg. Res.*, 87, 114-121.
- Ito N., Pfeffer J., Isfort P., Penzkofer T., Kuhl C. K., Mahnken A. H., Schmitz-Rode T. and Bruners P., 2014, Bipolar Radiofrequency Ablation: Development of a New Expandable Device, *Cardiovasc. Intervent. Radiol.*, 37, 770-776.
- Kilic D., Uysal C., Akdur A., Kayipmaz C., Tepeoglu M., and Boyvat F., 2015, Chest Wall Implantation Metastasis Caused by Percutaneous Radiofrequency Ablation for Hepatic Tumor, *Ann. Thorac. Surg.*, 99, 1078–1080.
- Lee J. M., Han J. K., Kim S. H., Lee J. Y., Kim D. J., Lee M. W., Cho G. G., Han C. J. and Choi B. I., 2004, Saline-Enhanced Hepatic Radiofrequency Ablation Using a Perfused-Cooled Electrode: Comparison of Dual Probe Bipolar Mode with Monopolar and Single Probe Bipolar Modes, *Korean J. Radiol.*, 5, 121-127.
- Lencioni R., Goletti O., Armillotta N., Paolicchi A., Moretti M., Cioni D., Donati F., Cicorelli A., Ricci S., Carrai M., Conte P. F., Cavina E. and Bartolozzi C., 1998, Radio-Frequency Thermal Ablation of Liver Metastases with a Cooled-Tip Electrode Needle: Results of a Pilot Clinical Trial, *Eur. Radiol.*, 8, 1205-1211.
- Lin S. M. and Lin D. Y., 2003, Percutaneous Local Ablation Therapy in Small Hepatocellular Carcinoma, *Chang. Gung. Med. J.*, 26, 308-314.
- Livraghi T., Goldberg S. N., Lazzaroni S., Meloni F., Solbiati L. and Gazelle G. S., 1999, Small Hepatocellular Carcinoma: Treatment with Radio-Frequency Ablation Versus Ethanol Injection, *Radiology*, 210, 655-661.
- Livraghi T., Goldberg S. N., Monti F., Bizzini A., Lazzaroni S., Meloni F., Pellicanò S., Solbiati L. and Gazelle G. S., 1997, Saline-Enhanced Radio-Frequency Tissue Ablation in the Treatment of Liver Metastases, *Radiology*, 202, 205-210.
- Mazzaferro V., Llovet J. M., Miceli R., Bhoori S., Schiavo M., Mariani L., Camerini T., Roayaie S., Schwartz M. E., Grazi G. L., Adam R., Neuhaus P., Salizzoni M., Bruix J., Forner A., De Carlis L., Cillo U., Burroughs A. K., Troisi R., Rossi M., Gerunda G. E., Lerut J., Belghiti J., Boin I., Gugenheim J., Rochling F., Van Hoek B. and Majno P., 2009, Predicting Survival after Liver Transplantation in Patients with Hepatocellular Carcinoma Beyond the Milan Criteria: A Retrospective, Exploratory Analysis, *Lancet Oncol.*, 10, 35-43.
- McGahan J. P., Browning P. D., Brock J. M. and Tesluk H., 1990, Hepatic Ablation Using Radiofrequency Electrocautery, *Invest. Radiol.*, 25, 267-270.
- Mulier S., Miao Y., Mulier P., Dupas B., Pereira P., De Baere T., Lencioni R., Leveillee R., Marchal G., Michel L. and Ni Y., 2005, Electrodes and Multiple Electrode Systems for Radio Frequency Ablation: A Proposal for Updated Terminology, *Adv. Exp. Med. Biol.*, 15, 798-808.
- Ozbek O., Keskin F., Kaya H. E., Guler I., Nayman A., and Koc O., 2016, Radiofrequency Ablation of A Rare Pathology: Vertebral Intraosseous Lipoma, *Spine J.*, 16, e155
- Poon D., Anderson B. O., Chen L. T., Tanaka K., Lau W. Y., Van Cutsem E., Singh H., Chow W. C., Ooi L. L., Chow P., Khin M. W. and Koo W. H., 2009, Management of Hepatocellular Carcinoma in Asia: Consensus Statement from the Asian Oncology Summit 2009, *Lancet Oncol.*, 10, 1111-1118.
- Rossi S., Buscarini E., Garbagnati F., Di Stasi M., Quaretti P., Rago M., Zangrandi A., Andreola S., Silverman D. and Buscarini L., 1998, Percutaneous

Treatment of Small Hepatic Tumors by an Expendable RF Needle Electrode, *Am. J. Roentgenol.*, 170, 1015-1022.

Rossi S., Fornari F., Pathies C. and Buscarini L., 1990, Thermal Lesion Induced by 480 kHz Localized Current Field in Guinea Pig and Pig Liver, *Tumori*, 76, 54-57.

Shao Y. L., Arjun B., Leo H. L. and Chua K. J., 2017, Nano-Assisted Radiofrequency Ablation of Clinically Extracted Irregularly-Shaped Liver Tumors, *J. Therm. Biol.*, 66, 101–113.

Stippel D. L., Brochhagen H. G., Arenja M., Hunkemöller J., Hölscher A. H. and Beckurts K. T., 2004, Variability of Size and Shape of Necrosis Induced by Radiofrequency Ablation in Human Livers: A Volumetric Evaluation, *Annals of Surgical Oncology*, 11, 420–425.

Tatli S., Tapan U., Morrison P. R. and Silverman S. G., 2012, Radiofrequency Ablation: Technique and Clinical Applications, *Diagn. Interv. Radiol.*, 18, 508-516.

Tungjitkusolmun S., Staelin S.T., Haemmerich D., Tsai J. Z., Cao H. Webster J. G., Lee F. T., Mahvi D. M. and Vorperian V. R., 2002, Three-Dimensional Finite-Element Analyses for Radio-Frequency Hepatic Tumor Ablation. *IEEE Trans. Biomed. Eng.*, 49, 3-9.

Verslype C., Rosmorduc O. and Rougier P., 2012, Hepatocellular Carcinoma: ESMO-ESDO Clinical Practice Guidelines for Diagnosis, Treatment and Follow-up. *Ann. Oncol.*, 23, 41-48.

Yang L., Wen R., Qin J., Chui C. K., Lim K. B. and Chang S., 2010, A Robotic System for Overlapping Radiofrequency Ablation in Large Tumor Treatment, *IEEE/ASME Trans. Mechatron.*, 15, 887-897.



ENHANCEMENT OF HEAT TRANSFER BY HEAT PIPES WITH PIECEWISE UNIFORM LONGITUDINAL WICK PROFILES

Mehmed Akif PAKSOY * and Salih Özen ÜNVERDİ **
* TÜBİTAK BİLGEM BTE, 41400 Gebze, Kocaeli, makifpaksoy@live.com
** Gebze Technical University Department of Mechanical Engineering
41400 Gebze, Kocaeli, sunverdi@gtu.edu.tr

(Geliş Tarihi: 16.10.2019, Kabul Tarihi: 18.03.2020)

Abstract: An equation (29) is derived to calculate heat transfer rate of a heat pipe evaporator in terms of liquid pressure loss along and temperature difference across the wick and thermo-fluid properties, which shows that various wick profiles transfer same amount of heat under the constraints of pressure loss and temperature difference. It is proved by calculus of variations that among these profiles, wick weight is minimized in case of uniform wick thickness. Case studies are applied for a copper-water heat pipe with a wick of 0.5 porosity, $1.5 \times 10^{-9} \text{ m}^2$ permeability, 8.65 mm outer radius and around 1.96 W/mK thermal conductivity. A case study shows that sum of the pressure losses of the liquid and vapor phases of the adiabatic region is minimized at a certain ratio of vapor core radius to wick outer radius. Finally, 1-D coupled flow and thermal analyses of the wick and vapor core of the heat pipe are performed for two types of designs with piecewise uniform wick thickness profiles which are proposed in this study. Under the constraint of constant total wick volume, heat transfer rate is plotted as function of wick thicknesses for each design. Without the wick volume constraint, increasing the adiabatic zone and condenser wick thicknesses while decreasing wick thickness of the evaporator enhances heat transfer rate up to 6.3%. On the other hand, increasing adiabatic zone wick thickness while decreasing that of the evaporator and condenser improves heat transfer rate up to 26.9% at capillary limit.

Keywords: Heat pipe, wick, optimization, wick thickness, wick profile, wick volume, wick weight, calculus of variations.

PARÇALI ÜNİFORM BOYLAMASINA FİTİL PROFİLLİ ISI BORULARI İLE ISI TRANSFERİNİN ARTTIRILMASI

Özet: Bir ısı borusu evaporatöründe ısı transferini fitildeki aksel basınç kaybı ve radyal sıcaklık değişimi ile termofiziksel özelliklere bağlı olarak hesaplamak amacıyla bir bağıntı (29) çıkarılmış, basınç kaybı ve sıcaklık farkı kısıtları altında farklı fitil profillerinin aynı miktarda ısı transfer ettiği gösterilmiştir. Varyasyonlar hesabı ile fitil ağırlığının farklı fitil profilleri arasında sabit kalınlıkta olan için minimum olduğu ispatlanmıştır. Örnek çalışmalar 0.5 porozite, $1.5 \times 10^{-9} \text{ m}^2$ geçirgenlik, 8.65 mm dış yarıçap ve yaklaşık 1.96 W/mK ısı iletkenliğe sahip bir fitilli olan bakır-su ısı borusu için gerçekleştirilmiştir. Bir örnek çalışmayla adyabatik bölgede, buhar akış yarıçapının fitil dış yarıçapına oranının belirli bir değerinde, sıvı ve buhar fazları basınç kayıpları toplamının minimum olduğu gösterilmiştir. Daha sonra, bu çalışmada önerilen bölgesel olarak sabit kalınlıkta iki farklı fitil tasarımı için ısı borusu fitil ve buhar kolonunun bir boyutlu bağlaşıklık akış ve ısı analizleri gerçekleştirilmiştir. Sabit toplam fitil hacmi kısıtı altında, her iki tasarım için ısı transferi bölgesel fitil kalınlıklarının fonksiyonu olarak çizdirilmiştir. Fitil hacmi kısıtı kaldırıldığında, adyabatik bölge ve kondenser fitil kalınlıkları artırılıp, evaporatör fitil kalınlığı azaltıldığında ısı transferi %6.3'e kadar artmıştır. Öte yandan, adyabatik bölge fitil kalınlığı artırılıp, evaporatör ve kondenser fitil kalınlığı azaltıldığında kapiler limitte ısı transferi %26.9'a kadar artmıştır.

Anahtar kelimeler: Isı borusu, fitil, optimizasyon, fitil kalınlığı, fitil profili, fitil hacmi, fitil ağırlığı, varyasyonlar hesabı.

NOMENCLATURE

| | | | |
|--------|--|----------------------|------------------------------------|
| A | Cross sectional area [m^2] | T_p | Wick outer surface temperature [K] |
| a | Constant defined in Eq. (19) [m] | T_v | Vapor temperature [K] |
| b, c | Constants defined in Eq. (24) [-], [m] | t | Wick thickness [m] |
| C | Thermo-physical properties group, defined in Eq. (31) [$\text{W m}^{-1} \text{Pa}^{-1/2} \text{K}^{-1/2}$] | V | Bulk volume [m^3] |
| C_1 | Thermo-physical properties group, defined in Eq. (49) [$\text{K}^{1/2} \text{Pa}^{-1/2}$] | Greek Symbols | |
| D | Constant defined in Eq. (34) [-] | ΔP | Pressure loss [Pa] |

| | |
|-----------|--|
| f | Darcy friction factor [-] |
| $f(x)$ | Function defining wick thickness profile [m] |
| h_{fg} | Latent heat of evaporation of working fluid [J kg ⁻¹] |
| K | Permeability of the wick [m ²] |
| k | Thermal conductivity [W m ⁻¹ K ⁻¹] |
| k_{eff} | Effective wick thermal conductivity [W m ⁻¹ K ⁻¹] |
| L | Length [m] |
| \dot{m} | Mass flow rate [kg s ⁻¹] |
| Q | Heat transfer rate [W] |
| q'' | Heat flux [W m ⁻²] |
| R | Radial thermal resistance [K W ⁻¹] |
| r | Wick outer radius [m] |
| r_{cap} | Capillary radius [m] |
| T | Temperature [K] |
| T_c | Condenser wick outer surface temperature [K] |
| T_h | Evaporator wick outer surface temperature [K] |

| | |
|--------------|---|
| ΔT | Temperature difference between the pipe side and vapor side of the wick [K] |
| ΔT_v | Vapor temperature drop [K] |
| η | Dummy variable for “ x ” |
| μ | Dynamic viscosity [Pa s] |
| ρ | Density [kg m ⁻³] |
| φ | Wick porosity [-] |
| σ | Surface tension [N m ⁻¹] |

Subscripts

| | |
|--------|----------------------|
| a | Adiabatic zone |
| c | Condenser |
| $diff$ | Differential element |
| e | Evaporator |
| eff | Effective |
| l | Liquid |
| p | Pipe |
| v | Vapor |
| w | Wick |

INTRODUCTION

Heat pipes are becoming increasingly popular in various applications because of their high efficiencies, high heat removal rates, small sizes, compact designs and robust performance (Lin and Wong, 2013; Zohuri, 2016). Number of experimental and mathematical modeling studies on various types of heat pipes are increasing in conformity with the ever-growing application areas of heat pipes. Some researchers focused their attention on very detailed thermo-fluid models and obtained very good agreement between experimental and numerical results (Ranjan et al., 2009; Huang and Chen, 2017; Ranjan et al., 2011). On the other hand, there are many experimental studies which try to understand heat pipes' thermo-fluid characteristics and various limits, and to enhance their thermal performances (Wang et al., 2014; Wong et al., 2017; Deng et al., 2013).

Mono-porous sintered powder wick is one of the most common wick types used in heat pipes. Yet, the effect of various wick parameters like pore structure, particle size and wick thickness on thermal performance of a heat pipe are not investigated comprehensively. Weibel et al., 2010, showed that for a given wick thickness, there is a tradeoff between increased area for heat transfer and increased resistance to vapor flow out of the wick, as the particle size changes. Therefore, an optimum particle size exists which minimizes the thermal resistance. However further study is required since particle size is not only related to thermal resistance, but also to capillary head which is a limiting factor for overall heat pipe performance (Lin and Wong, 2013).

In their study, Hong et al., 2013, experimentally showed that there exists an optimum wick thickness for which effective heat transfer coefficient is maximized when

particle size and type (or porosity) of the wick and other parameters of a heat pipe are fixed. However, in the study it is also noted that experimentally found optimum wick thickness may not be the real optimum since experimental data can be obtained only for discrete wick thickness values.

There are numerous studies suggesting better wick designs. Siddiqui and Kaya, 2016, designed and thermally analyzed an arterial type heat pipe with mesh wick. The study is focused on venting hole diameter and distance between venting holes. They optimized these two geometric parameters considering pressure loss and bubble blockage. Critical venting hole diameter is found by developing a meniscus coalescence criterion which can be defined in terms of the geometrical parameters. Choosing lowest possible hole diameter that satisfies meniscus coalescence criterion yields lowest possible pressure loss. Furthermore, they optimized the distance between venting holes where smaller distance increases number of holes and decreases the clearance time of arteries blocked by bubbles but increases the pressure loss, thereby reducing heat transfer limit of the heat pipe. On the other hand bigger distance between holes increases the clearance time and decreases the pressure loss hence increasing heat transfer limit.

On the modeling side, Zuo and Faghri, 1998, successfully simulated the transient behavior of a heat pipe. Their model is based on a thermal network which results in a set of linear, first order ordinary differential equations, whose solution gives information about the transient thermo-fluid behavior of the heat pipe. Their results were fairly accurate when compared with experimental data. Their findings are also compared with those obtained from both a two-dimensional numerical model and a lumped model and it can be concluded that there are

slight deviations in transient vapor temperatures, but it is observed that the differences among the results are minimal at steady state. Tournier and El-Genk, 1994, developed a two-dimensional numerical model suitable for transient analysis of a heat pipe. Their model involved calculation of radius of curvature of the liquid meniscus which forms at the liquid-vapor interface. Calculated transient and steady-state temperatures were in well agreement with experiments. Kaya and Goldak, 2007, presented a three-dimensional finite element model for simulations of heat pipes at steady state. They showed that vapor flow field remains nearly symmetrical about the heat pipe axis even for a non-uniform heat load. Mwaba et al., 2006, suggested a composite wick which is made from coarse mesh copper screen in condenser and adiabatic region and sintered fine copper powder in evaporator. This design results in lower pressure loss in liquid phase while increasing allowable capillary head in comparison to using sintered wick through the entire heat pipe. They solved the thermo-fluid problem by a commercial CFD software where phase change at the liquid-vapor interface is modeled with momentum and energy sources and sinks. Simulation results showed that wick structure affects heat pipe performance significantly and suggested composite wick can enhance heat pipe performance up to a factor of two.

Most of the modeling studies in the literature and described above tried to model the operational characteristics of heat pipes. One of the few exceptions is the study of Nishikawara and Nagano, 2017. In their study they incorporated the effect of geometrical parameters (i.e. number and size of axial and circumferential grooves) of the wick to evaporator heat transfer coefficient by relating the length of three-phase contact line to groove numbers. They investigated the effect of increasing the length of three-phase contact line and showed that heat transfer coefficient increases up to a point and then starts to decrease because of large distribution of saturation temperature as a result of bigger pressure loss in the grooves. Another study on heat pipe optimization is by Kiseev et al., 2010, where they investigated the effect of capillary structure on heat transfer. They proposed a methodology to calculate capillary structure's effective pores radius which maximizes heat transfer for loop heat pipes.

In this study, a 1-D thermo-fluid model of a conventional heat pipe is developed to investigate the effect of wick profile (i.e. thickness variation) along the heat pipe on heat transfer. To clarify, in Figure 1 (a) longitudinal section of a conventional cylindrical heat pipe with constant wick thickness is presented. Increasing wick thickness profiles along the evaporator which are linear, non-linear (i.e. curved) concave up and concave down are shown in Figure 1 (b), (c), and (d), respectively, while maintaining constant wick thickness along the adiabatic zone and condenser. First, the optimum wick thickness profile along the evaporator that maximizes heat transfer rate is searched under the constraint of a specified pressure loss along the wick. However, it is found that under the constraint of pressure loss, any evaporator wick

profile transfers same amount of heat. So, from this perspective there is not an optimum solution. Then, the optimum wick thickness profile along the evaporator is searched for which minimum evaporator weight is achieved under the constraint of a specified pressure loss along the wick, and by calculus of variations it is found that uniform wick thickness is the solution. The study is extended to the condenser and adiabatic zone to obtain the optimum wick thickness profile for each region. Finally, for two types of designs proposed in this study, under the constraint of overall pressure loss in heat pipe cycle which is imposed by capillary head, piecewise uniform wick thicknesses of evaporator, adiabatic zone and condenser that maximize heat transfer rate are calculated.

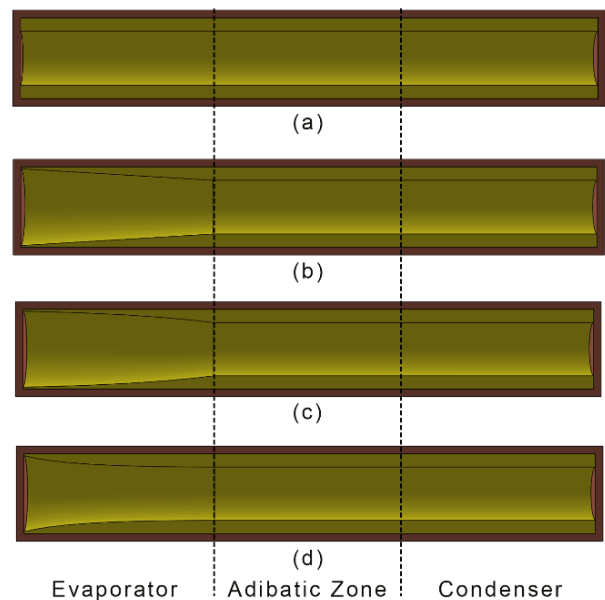


Figure 1. Wick thickness profiles for the longitudinal section of a heat pipe (a: Uniform, b: Linearly increasing, c: Concave up, increasing, d: Concave down, increasing profiles for the evaporator).

THEORY

An analytical model for calculating steady-state heat transfer rate and pressure loss through the evaporator wick of a heat pipe is developed. Then heat transfer rate and pressure loss through the evaporator wick is related using the developed analytical models. Calculus of variations is applied to the developed models in order to minimize volume, therefore weight, of the evaporator wick. Developed models and relations are extended to the condenser wick. Furthermore, steady-state pressure losses are modeled analytically in liquid and gas phases, where both laminar and turbulent regimes are considered for gas flow, of the adiabatic region.

Evaporator Analytical Model

In Figure 2 modeled region, i.e. evaporator wick, is presented with some definitions. Evaporator length, which is measured in x-axis direction, and wick's outer

radius are denoted by L and r , respectively. Evaporator thickness profile is represented with function $f(x)$. T_v is vapor temperature and T_p is the temperature of the wick outer surface which is in contact with heat pipe wall. It is assumed that T_p and T_v are constant throughout the x direction. Therefore, axial heat transfer, in x direction, is neglected since T_p and T_v are assumed to be uniform in axial direction.

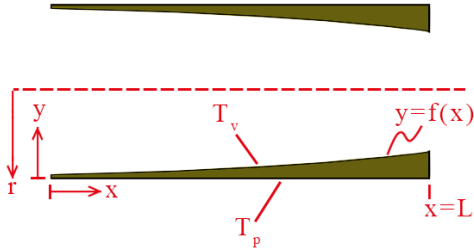


Figure 2. Modeled evaporator wick and notation.

The thermal model is based on conduction through the wick in radial direction using the effective heat transfer coefficient which is defined as (Zuo and Faghri, 1998)

$$k_{eff} = \frac{k_l[(k_l + k_w) - (1 - \phi)(k_l - k_w)]}{[(k_l + k_w) + (1 - \phi)(k_l - k_w)]} \quad (1)$$

in terms of liquid thermal conductivity, k_l , wick material thermal conductivity, k_w , and porosity, ϕ . Definition of effective heat transfer coefficient, k_{eff} , as a parameter facilitates formulation of the problem in terms of wick thickness, $f(x)$.

Assuming a linear temperature profile in radial direction in the wick, heat transfer rate in y direction for a cylindrical differential element with height dx can be expressed as

$$dQ = k_{eff} \frac{T_p - T_v}{f(x)} dx \cdot 2\pi r \quad (2)$$

Therefore, heat transfer rate throughout the evaporator can be calculated as

$$Q = \int_0^L k_{eff} \frac{T_p - T_v}{f(x)} dx \cdot 2\pi r \quad (3)$$

This expression can be simplified by assuming that the factors k_{eff} , $\Delta T = T_p - T_v$ and r are constant and can be taken out of the integral, which results in

$$Q = 2\pi r k_{eff} \Delta T \int_0^L \frac{dx}{f(x)} \quad (4)$$

According to Darcy's Law, pressure loss through a differential element dx in axial direction can be calculated as

$$dP = \frac{\mu_l \dot{m}_l(x)}{\rho_l A_w(x) K} dx \quad (5)$$

where, \dot{m}_l is the liquid mass flow rate in the wick in negative x direction. Considering the integral control volume around the wick of the evaporator shown in Figure 3, mass flow rate entering the volume in liquid

phase and leaving the volume in vapor phase should be equal at steady state.

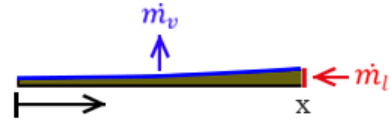


Figure 3. Mass flow rate balance for an integral control volume around the wick of the evaporator.

As the heat transferred to the evaporator from the surroundings should be absorbed by the liquid in the wick as it evaporates at steady state, mass flow rate of the working fluid can be expressed as

$$\dot{m}_l = \dot{m}_v = \frac{2\pi r k_{eff} \Delta T \int_0^x \frac{d\eta}{f(\eta)}}{h_{fg}} \quad (6)$$

where, h_{fg} is the latent heat of evaporation of the fluid. Inserting the mass flow rate (6) into the pressure drop Eq. (5) and integrating along the evaporator results in liquid pressure loss along the evaporator wick as

$$\Delta P = \int_0^L \frac{\mu_l 2\pi r k_{eff} \Delta T \int_0^x \frac{d\eta}{f(\eta)}}{\rho_l A_w(x) K h_{fg}} dx \quad (7)$$

Since heat pipe outer radius is much bigger than the thickness of the wick, i.e. $r \gg f(x)$, cross-sectional area of the wick at axial position x can be approximately calculated as

$$A_w(x) = 2\pi r f(x) \quad (8)$$

Inserting the wick cross-sectional area in Eq. (7), the liquid pressure loss along the evaporator is calculated as

$$\Delta P = \int_0^L \frac{\mu_l k_{eff} \Delta T \int_0^x \frac{d\eta}{f(\eta)}}{\rho_l K h_{fg} f(x)} dx \quad (9)$$

and taking constant factors μ_l , k_{eff} , ΔT , ρ_l , K , h_{fg} out of the integral sign results in

$$\Delta P = \frac{\mu_l k_{eff} \Delta T}{\rho_l K h_{fg}} \int_0^L \frac{\int_0^x \frac{d\eta}{f(\eta)}}{f(x)} dx \quad (10)$$

Relation Between Heat Transfer Rate and Pressure Loss of the Evaporator

Eqs. (4) and (10) are evaporator heat transfer rate and liquid pressure loss along the wick of the evaporator, respectively. Optimum wick profile $f(x)$ can be calculated by either keeping pressure loss constant and maximizing heat transfer rate or by keeping heat transfer rate constant and minimizing pressure loss. In this study, maximization of heat transfer rate throughout the evaporator while keeping the pressure loss along the wick constant, as the wick profile changes, is considered.

First define $g(x)$ as

$$g(x) = \int_0^x \frac{d\eta}{f(\eta)} \quad (11)$$

Taking derivative of both sides with respect to x results in

$$g'(x) = \frac{1}{f(x)} \quad (12)$$

Expressing Eq. (4) in terms of g(L) and Eq. (10) in terms of g(x) and g'(x) results in

$$Q = 2\pi r k_{eff} \Delta T g(L) \quad (13)$$

and

$$\Delta P = \frac{\mu_l k_{eff} \Delta T}{\rho_l K h_{fg}} \int_0^L g(x) g'(x) dx \quad (14)$$

respectively. It is required to select a g(x) that satisfies Eq. (14) for a given ΔP and maximize evaporator heat transfer rate which is given by Eq. (13). Solution of Eq. (14) is

$$\Delta P = \frac{\mu_l k_{eff} \Delta T}{\rho_l K h_{fg}} \left[\frac{g(L)^2}{2} \right] \quad (15)$$

so that,

$$\Delta P = \frac{\mu_l k_{eff} \Delta T}{\rho_l K h_{fg}} \left[\frac{g(L)^2}{2} - \frac{g(0)^2}{2} \right] \quad (16)$$

It can be seen from Eq. (11) that g(0)=0, so pressure drop given by Eq. (16) becomes

$$\Delta P = \frac{\mu_l k_{eff} \Delta T}{2\rho_l K h_{fg}} g(L)^2 \quad (17)$$

Combining Eqs. (13) and (17) evaporator heat transfer rate can be calculated as

$$Q = 2\pi r \sqrt{\frac{2\rho_l K h_{fg} k_{eff} \Delta T \Delta P}{\mu_l}} \quad (18)$$

Eqs. (11) and (17) state that same pressure loss can be obtained with various wick thickness profiles, therefore according to Eq. (18), same heat transfer rate may be achieved with many wick thickness profiles satisfying Eq. (17) with constant g(L) for the prescribed pressure loss.

For example, considering a wick of constant thickness as in Figure 1 (a)

$$f(x) = a \quad (19)$$

Inserting this in Eq. (11) and integrating gives

$$g(L) = \int_0^L \frac{dx}{a} = \left[\frac{x}{a} \right]_0^L = \frac{L}{a} \quad (20)$$

Then, inserting Eq. (20) in Eq. (17) results in pressure loss for the case of uniform wick thickness as

$$\Delta P = \frac{\mu_l k_{eff} \Delta T L^2}{2\rho_l K h_{fg} a^2} \quad (21)$$

from which wick thickness, a, is obtained in terms of evaporator length, permeability of the wick, thermo-fluid properties of the fluid, and pressure and temperature differentials as

$$a = \sqrt{\frac{\mu_l k_{eff} \Delta T L^2}{\Delta P 2\rho_l K h_{fg}}} \quad (22)$$

Heat transfer rate for constant wick thickness that satisfies a given pressure loss can be obtained by inserting (20) and (22) in Eq. (13) as

$$Q = 2\pi r \sqrt{\frac{2\rho_l K h_{fg} k_{eff} \Delta T \Delta P}{\mu_l}} \quad (23)$$

This can be compared with linearly increasing wick profile, Figure 1 (b), where b and c are not known

$$f(x) = bx + c \quad (24)$$

Writing the linear profile in Eq. (11) and integrating gives

$$g(L) = \frac{1}{b} \ln \left(\frac{bL + c}{c} \right) \quad (25)$$

Inserting calculated g(L) in Eq. (17) gives

$$\Delta P = \frac{\mu_l k_{eff} \Delta T}{2\rho_l K h_{fg}} \left[\frac{1}{b} \ln \left(\frac{bL + c}{c} \right) \right]^2 \quad (26)$$

Different b and c combinations can satisfy the above equation for a given pressure loss, ΔP . Eq. (17) can be rewritten to express g(L) in terms of ΔP which is given above, as

$$g(L) = \sqrt{\frac{\Delta P 2\rho_l K h_{fg}}{\mu_l k_{eff} \Delta T}} = \frac{1}{b} \ln \left(\frac{bL + c}{c} \right) \quad (27)$$

Inserting g(L) in Eq. (13) gives the heat transfer rate for linear wick profile that satisfies the pressure loss criterion

$$Q = 2\pi r \sqrt{\frac{2\rho_l K h_{fg} k_{eff} \Delta T \Delta P}{\mu_l}} \quad (28)$$

Comparing Eqs. (23) and (28), it is seen that evaporator heat transfer rate, Q, for any wick profile can be calculated with Eq. (18) in terms of ΔT and ΔP .

By dividing both sides of Eq. (28) with $\sqrt{\Delta P \Delta T}$ and wick outer area, an equation is obtained where right-hand side is a group of constants which is

$$\frac{Q}{2\pi r L \sqrt{\Delta P \Delta T}} = \sqrt{\frac{2\rho_l K h_{fg} k_{eff}}{\mu_l L^2}} \quad (29)$$

Eq. (29) can be simplified as follows:

$$q'' = \frac{Q}{2\pi r L} \quad (30)$$

$$C = \sqrt{\frac{2\rho_l K h_{fg} k_{eff}}{\mu_l}} \quad (31)$$

$$q'' = C \sqrt{\frac{\Delta P}{L}} \times \frac{\Delta T}{L} \quad (32)$$

Eq. (32) relates heat flux to pressure loss along and temperature difference across the evaporator wick. For an evaporator with a chosen wick profile operating at maximum allowable evaporator pressure loss, if the

temperature difference increases dry out occurs as liquid cannot be fed to the tip of the evaporator so that the heat transfer rate cannot be further increased. To increase the heat transfer rate, the entire wick of the evaporator must be wetted which is only possible by increasing its thickness. On the other hand, if the temperature difference decreases, so does the heat flux and therefore pressure loss according to Eq. (32).

Constrained Optimization of the Evaporator Weight

In the previous section it is shown that there is a functional relation, Eq. (29), between evaporator heat transfer rate and liquid phase pressure loss along the wick of the evaporator and temperature difference across the wick of a heat pipe even though wick thickness profile may change. However, the amount of material used for different wick thickness profiles are not the same and there may be an optimum profile for which minimum amount of wick material is used. For a chosen wick material and micro-structure, mass of the evaporator wick is proportional to bulk volume of it which can be expressed based on Eq. (8) as

$$V_w(L) = \int_0^L 2\pi r f(x) dx \quad (33)$$

For a specified heat transfer rate Q , and for any wick thickness profile $f(x)$ that satisfies a specified liquid phase pressure loss ΔP along the wick of evaporator, from Eqs. (17) and (18) one can write

$$g(L) = \int_0^L \frac{dx}{f(x)} = \frac{4\pi r \rho_l K h_{fg} \Delta P}{\mu_l} \frac{1}{Q} = D \quad (34)$$

where D is a constant. Thus, minimization of the evaporator wick volume $V_w(L)$ which is given by Eq. (33) under the constraint (34), which expresses a relation between the chosen liquid pressure loss, ΔP , along the wick and wick thickness profile, $f(x)$, is to be considered. This is an isoperimetric problem in calculus of variations (Lemons, 1997; Gelfand and Fomin, 1963), where wick thickness profile function, $f(x)$, is to be found that minimizes the wick volume functional, $V(f) = \int_0^L F(f) dx$, where $F(f) = 2\pi r f$, while functional $g(f) = \int_0^L G(f) dx$, where $G(f) = 1/f$, satisfying the subsidiary condition or constraint $g(f) = D$ is imposed on admissible curves $f(x)$ as well as two boundary conditions $f(0) = A$ and $f(L) = B$.

According to the theorem for a variational problem with a subsidiary condition, $f(x)$, satisfies the differential equation

$$F_f - \frac{d}{dx} F_{f'} - \lambda \left[G_f - \frac{d}{dx} G_{f'} \right] = 0 \quad (35)$$

where, $F = F(x, f, f')$ and $G = G(x, f, f')$ (Gelfand and Fomin, 1963). In our special case, second and fourth terms of the differential equation drop out, because $F_{f'} = G_{f'} = 0$. Inserting $F_f = 2\pi r$ and $G_f = -1/f^2$ following algebraic equation is obtained

$$2\pi r - \frac{\lambda}{f^2} = 0 \quad (36)$$

Therefore, wick thickness should be a positive constant throughout the evaporator. Inserting this constant wick thickness into Eq. (34) and performing integration results in

$$\frac{f}{L} = \sqrt{\frac{\mu_l k_{eff} \Delta T}{2\rho_l K h_{fg} \Delta P}} = \frac{\mu_l}{4\pi r \rho_l K h_{fg} \Delta P} \frac{Q}{\Delta T} \quad (37)$$

which is the result obtained earlier for a uniform wick thickness in Eq. (22). We conclude that the wick thickness at two endpoints of the evaporator should be equal, i.e. $f(0) = f(L)$, or $A = B$, in order to have a solution to the minimum mass of the wick problem for specified heat transfer rate, Q , and liquid phase pressure loss, ΔP .

This result shows that out of different wick profiles with the same pressure loss and heat transfer rate at the evaporator, the lowest wick mass is obtained with uniform wick thickness, which is given in terms of the length of the evaporator, outer radius and permeability of the wick, thermo-fluid properties of the working fluid, heat transfer rate and pressure loss of liquid phase inside the wick along the evaporator in Eq. (37).

Extending Developed Model to the Condenser

The model developed for the evaporator can be extended to the condenser since the analytical expressions of the physical mechanisms are similar, except that mass and heat fluxes are in opposite directions. Modeled condenser region of the heat pipe is presented in Figure 4.

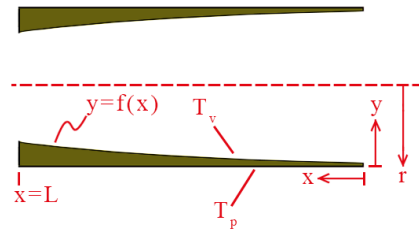


Figure 4. Modeled condenser wick of the heat pipe and the notation.

Heat transfer rate in $-y$ direction for a differential ring element with outer radius, r , thickness, $f(x)$, and height, dx , is

$$dQ = k_{eff} \frac{T_v - T_p}{f(x)} dx \cdot 2\pi r \quad (38)$$

Hence, heat transfer rate throughout the condenser with length, L , is calculated as

$$Q = \int_0^L k_{eff} \frac{T_v - T_p}{f(x)} dx \cdot 2\pi r \quad (39)$$

This expression can be simplified by taking constant quantities out of the integral sign

$$Q = 2\pi r k_{eff} \Delta T \int_0^L \frac{dx}{f(x)} \quad (40)$$

where $\Delta T = T_v - T_p$. Expression given above is the same as the heat transfer rate of the evaporator given in Eq. (4)

except that heat transfer is in opposite direction to that of the evaporator.

Pressure loss along the wick of the evaporator and adiabatic zone and condenser can be expressed by Darcy's Law given in Eq. (5). Mass flow rates through the control surfaces of the integral control volume enclosing the wick of the condenser are shown in Figure 5, where mass flow rate entering the control volume from the vapor phase and leaving the control volume in the liquid phase should be equal in steady state.

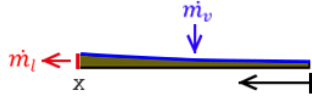


Figure 5. Mass flow rates for the integral control volume enclosing the wick of the condenser.

As the heat rejection rate from the condenser to the surroundings is equal to the mass flow rate times latent heat of condensation of the working fluid at steady state, mass flow rate of the working fluid can be expressed as

$$\dot{m}_l = \dot{m}_v = \frac{2\pi r k_{eff} \Delta T \int_0^x \frac{d\eta}{f(\eta)}}{h_{fg}} \quad (41)$$

Hence, inserting mass flow rate given by Eq. (41) into Darcy's Law, Eq. (5), results in the pressure loss along the condenser wick

$$\Delta P = \int_0^L \frac{\mu_l 2\pi r k_{eff} \Delta T \int_0^x \frac{d\eta}{f(\eta)}}{\rho_l A_w(x) K h_{fg}} dx \quad (42)$$

Assuming the heat pipe radius is much bigger than the wick thickness, i.e. $r \gg f(x)$, the cross-sectional area of the wick, $A_w(x)$, can be calculated by Eq. (8). Inserting the cross-sectional area in Eq. (42) and taking constant quantities out of the integral sign, pressure loss along the wick becomes:

$$\Delta P = \frac{\mu_l k_{eff} \Delta T}{\rho_l K h_{fg}} \int_0^L \frac{\int_0^x \frac{d\eta}{f(\eta)}}{f(x)} dx \quad (43)$$

Mass of the condenser wick is proportional to the bulk volume of the wick which is equal to the integral of the cross-sectional area along the length of the condenser as given in Eq. (33).

Pressure loss expressions for the condenser, Eq. (43), and evaporator, Eq. (10), are identical, therefore the relation, Eq. (18), between heat transfer rate, Q , pressure loss, ΔP , and temperature difference, ΔT , derived for evaporator can be applied to condenser as well. Finally, among these wick profiles, lowest wick mass is attained when the wick thickness is uniform along the condenser which may be calculated by Eq. (37).

Reducing Pressure Losses in the Adiabatic Zone

Consideration of the entire wick in a heat pipe including the evaporator, adiabatic zone and the condenser is necessary to apply the findings of this study. Modeling

and optimization of the adiabatic section is simpler in comparison to evaporator and condenser since heat transfer and phase change phenomena can be neglected so only pressure loss needs to be considered. For the adiabatic zone, uniform wick thickness results in the minimum pressure loss among various wick profiles, because excessive pressure losses due to constriction and expansion are avoided. A case study comparing pressure losses for uniform and non-uniform wick profiles in the adiabatic zone, for both laminar and turbulent vapor flows, is presented in the appendix.

The modeled adiabatic region is shown in Figure 6. For the adiabatic region, mass flow rate of both phases should be equal according to conservation of mass principle at steady state

$$\dot{m} = \dot{m}_l = \dot{m}_v \quad (44)$$

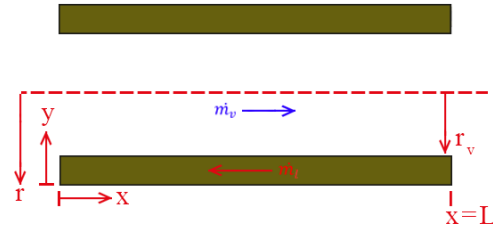


Figure 6. Modeled adiabatic zone and notation.

Pressure loss of vapor flowing along the axis of the heat pipe (vapor column) can be calculated by Poiseuille-Hagen and Darcy-Weisbach formulas for fully developed laminar and turbulent flows in a tube, respectively. On the other hand, pressure loss of liquid flowing along the porous wick of the adiabatic zone can be calculated by Darcy's law as in the case of evaporator and condenser. If the vapor flow is laminar, sum of the pressure losses in vapor and liquid phases along the length of the adiabatic zone, L_a , is

$$\Delta P_a = \frac{8\mu_v L_a \dot{m}}{\pi \rho_v r_v^4} + \frac{\mu_l \dot{m}}{\pi(r^2 - r_v^2)\rho_l K} L_a \quad (45)$$

whereas for turbulent vapor flow, it becomes

$$\Delta P_a = f \frac{L_a}{4} \frac{\dot{m}^2}{\pi^2 r_v^5 \rho_v} + \frac{\mu_l \dot{m}}{\pi(r^2 - r_v^2)\rho_l K} L_a \quad (46)$$

Adiabatic zone pressure loss curves for liquid flow in the porous wick and for vapor flow as well as their sum calculated by Eqs. (45) and (46) are plotted in Figure 7 as functions of ratio of vapor column radius to wick outer radius r_v/r while keeping wick outer radius, r , constant. Note that, Figure 7 is plotted for typical parameters of a conventional water-copper heat pipe existing in the literature which are given in Table 1 (Tournier and El-Genk, 1994), while changing r_v/r .

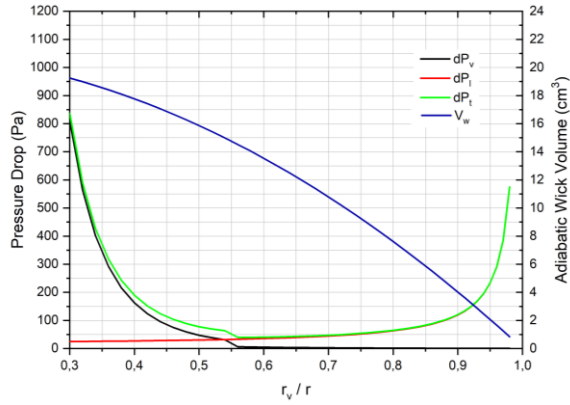


Figure 7. Pressure losses vapor in the adiabatic zone of the heat pipe as functions of vapor column radius to wick outer radius ratio, r_v/r (dP_l : liquid pressure loss, dP_v : vapor pressure loss, dP_t : total pressure loss, V_w : wick bulk volume).

Table 1. Typical water-copper heat pipe parameters for case studies.

| Parameter | Value | Unit |
|-----------|----------------------|---------------|
| L_e | 600 | mm |
| L_a | 90 | mm |
| L_c | 200 | mm |
| r | 8.65 | mm |
| r_v | 7.90 | mm |
| r_{cap} | 54 | μm |
| φ | 0.5 | % |
| K | 1.5×10^{-9} | m^2 |
| \dot{m} | 0.188 | gr/s |

In Figure 7, at small values of r_v/r vapor flow is turbulent and pressure loss of vapor column is greater than that of the liquid flow in the porous wick. Around $r_v/r = 0.55$ vapor flow becomes laminar and pressure loss of liquid exceeds that of the vapor henceforth, i.e. for bigger

Table 2. Heat transfer rates and pressure losses.

| Case | Parameter | Unit | Present Model | Tournier and El-Genk, 1994 exp. | num. | Schmalhofer and Faghri, 1992 exp. | El-Genk and Huang, 1993 exp. |
|------|------------|------|---------------|---------------------------------|------|-----------------------------------|------------------------------|
| #1 | Q | W | 432 | 443 | 455 | - | - |
| #2 | | | 144 | - | - | 150 | - |
| #3 | | | 547 | - | - | - | 570 |
| #1 | ΔP | Pa | 707 | - | 769 | - | - |
| #2 | | | 286 | - | - | - | - |
| #3 | | | 920 | - | - | - | - |

RESULTS AND DISCUSSION

Various Evaporator Wick Thickness Profiles

Heat pipe evaporators for which fundamental geometric and physical parameters are presented in Table 1 operating under typical conditions are analyzed by the developed analytical models. In the analyses, temperature difference over the wick thickness, ΔT , is assumed to be 5.51 K as used in the study of Tournier and El-Genk, 1994, which is a typical operating value. Effective wick thermal conductivity, k_{eff} , is calculated as 1.93 W/mK by Eq. (1). Functions of different wick

thickness profiles studied for the evaporator are given in Table 3. Heat transfer rates, pressure losses and wick volumes presented in Table 3 are calculated by Eqs. (4), (7) and (33), respectively. Heat transfer rates and corresponding pressure losses are found to be equal for diversity of evaporator wick thickness profiles considered where slight differences in heat transfer rates and corresponding pressure losses are due to round-off errors. It should be noted that for wick profiles presented $g(L)$ is constant since it is a pre-requisite for constant pressure loss which also results in constant heat transfer rate as deduced from Eqs. (17) and (18).

Model Validation

A 1-D model is built using the Eq. (4) and (40) for heat transfer rate and Eq. (45) and (46) for liquid and vapor pressure losses. Details of the 1-D model are presented under section “1-D Analysis of Flow and Heat Transfer for a Heat Pipe”. Developed models are validated with the experimental and numerical studies from the literature, and the results are presented in Table 2. Validation studies are carried out by using wick thermo-physical properties and wick outer surface temperature values obtained from the related studies as inputs while heat transfer rates and pressure losses are the outputs of the model (Tournier and El-Genk, 1994; Schmalhofer and Faghri, 1992; El-Genk and Huang, 1993). Good agreement between heat transfer rates are observed where deviations between the predictions of the present model and the measurements are less than 5%. On the other hand, the difference between the pressure losses calculated by the present model and the numerical model of Tournier and El-Genk, 1994, is around 10%. Deviations among the present 1-D model predictions and those of more sophisticated numerical simulations and experimental findings are reasonable since some assumptions and simplifications have been done for the present model to be analytically solvable.

Table 3. Functions defining different wick profiles over evaporator.

| Profile No | Wick profile (mm) | Value of constants | Q (W) | ΔP (Pa) | Wick volume (cm ³) |
|------------|----------------------|---------------------------|--------|-----------------|--------------------------------|
| 1 | $y = c$ | $c=0.75$ | 463.57 | 416.58 | 24.46 |
| 2 | $y = bx + c$ | $b=3.326, c=0.15$ | 463.53 | 416.50 | 37.43 |
| 3 | | $b=2.024, c=0.30$ | 463.51 | 416.47 | 29.58 |
| 4 | | $b=1.184, c=0.45$ | 463.61 | 416.64 | 26.26 |
| 5 | $y = ax^2 + bx + c$ | $a=21.36, b=0, c=0.15$ | 463.59 | 416.61 | 88.48 |
| 6 | | $a=13.21, b=1, c=0.15$ | 463.60 | 416.63 | 66.37 |
| 7 | | $a=0.555, b=1, c=0.45$ | 463.60 | 416.62 | 26.63 |
| 8 | $y = ax^b + c$ | $a=1.363, b=0.50, c=0.15$ | 463.59 | 416.62 | 27.84 |
| 9 | | $a=2.119, b=0.75, c=0.15$ | 463.59 | 416.61 | 31.81 |
| 10 | $y = -ax^2 + bx + c$ | $a=2, b=3.816, c=0.15$ | 463.60 | 416.62 | 34.40 |

Reference uniform wick with 0.75 mm thickness and linearly increasing wick profiles (profiles 2 to 4) for which pressure loss in axial direction and resulting heat transfer rate is the same are plotted in Figure 8 over evaporator length. As can be seen from the figure, as the slope increases, wick thickness at the tip of the evaporator, $x=0$ m, decreases, while it increases at the end, $x=0.6$ m. It is also noted that as the slope decreases volume occupied by the wick decreases reducing wick material usage and allowing more space for vapor flow.

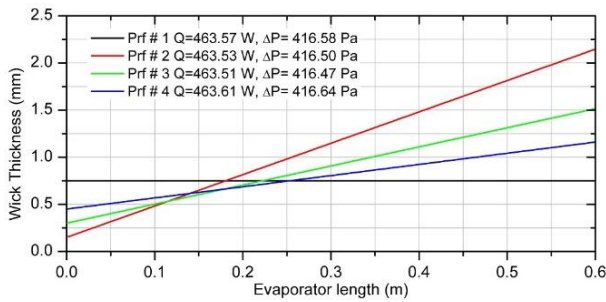


Figure 8. Linearly increasing wick profiles over evaporator.

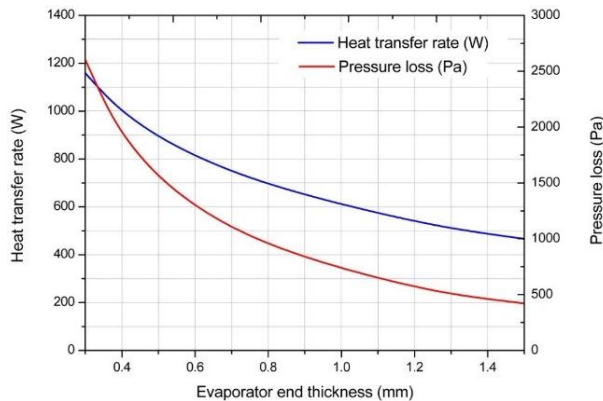


Figure 9. Change of heat transfer rate and pressure loss by evaporator end thickness.

Heat transfer rate and pressure loss along the evaporator are plotted in Figure 9, for 0.3 mm wick thickness at the tip, $x=0$ m, as the slope of the wick is increased which results in wick thickness at evaporator end, $x=0.6$ m,

change from 0.3 mm to 1.5 mm. Pressure loss and heat transfer rate both decrease with increasing slope of the wick profile. On the other hand, wick volume increases as heat transfer rate decreases in this case (Figure 10).

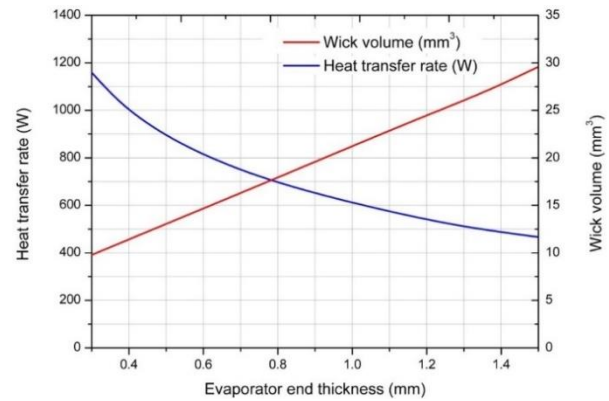


Figure 10. Change of heat transfer rate and wick volume by evaporator end thickness.

Parabolic wick thickness profiles which result in the same axial pressure loss and heat transfer rate given in Table 3 are plotted in Figure 11. As the wick thickness at the tip of the evaporator is decreased significantly below the uniform thickness, e.g. parabolic wick Profile # 5 in Figure 11, thickness at evaporator end, $x=0.6$ m, approaches to the pipe centerline to compensate the excessive pressure losses nearby the tip. Wick volume increases up to 360% in comparison to reference uniform wick profile where still pressure loss and heat transfer rate are the same. Increased wick thickness at evaporator end allows keeping fluid velocity thus pressure loss lower even though fluid flow rate is the highest at evaporator end. On the other hand, increased wick thickness decreases heat transfer rate locally, thereby balancing excessive heat transfer near the tip. The increased sensitivity of heat transfer rate and pressure losses to wick thickness as the thickness gets smaller can also be deduced if one notices Profile # 5 is slightly under Profile # 6 near the tip. These two wick thickness profiles are nearly the same between $x=0$ m and $x=0.15$ m where Profile # 6 is slightly higher than Profile # 5. Between $x=0.15$ m and $x=0.60$ m Profile # 5's wick thickness is

significantly higher resulting in 30% more wick volume in comparison to Profile # 6.

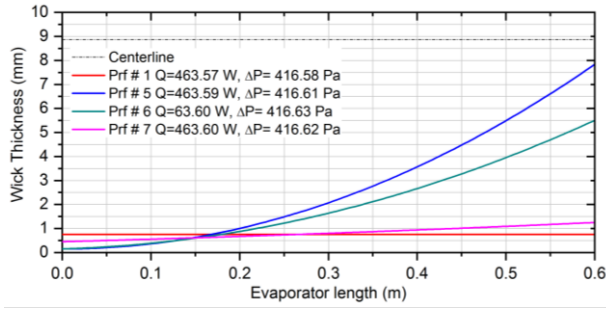


Figure 11. Concave up, increasing wick profiles over evaporator.

Concave down, increasing wick profiles, Figure 12, has lower thickness at evaporator end, $x=0.6$ m, in comparison to linear increasing and concave up, increasing wick profiles. For the concave down case, the higher the slope at $x=0$ m, the less the wick thickness at $x=0.6$ m is, if heat transfer rate remains equal to that of the reference uniform wick profile.

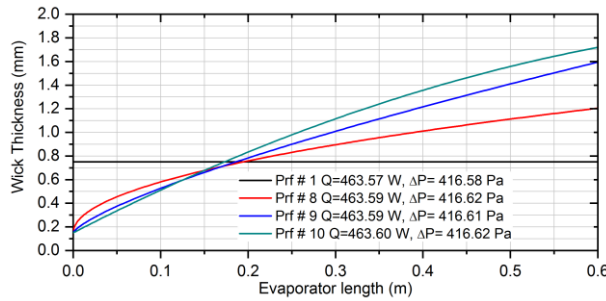


Figure 12. Concave down, increasing wick profiles over evaporator.

Effect of Pressure Loss and Temperature Difference on Heat Transfer Rate

According to Eqs. (29) and (32) heat transfer rate and heat flux are proportional to the square root of pressure loss, ΔP , and temperature difference, ΔT , along and across the wick, respectively. Heat flux given by Eq. (32) as a function of $\Delta P/L$ and $\Delta T/L$ is plotted in Figure 13 for various thermo-physical group values, “C”. An evaporator with a specified value of “C” operates on the relevant surface drawn in Figure 13, whether or not it operates at the design or an off-design, e.g. at a lower temperature difference or heat flux, point. This is because if actual heat flux is lower than the design-point value, fluid flow thus pressure loss reduces and the operating condition stays on the specified surface.

Figure 13 is applicable for uniform and non-uniform evaporator and condenser wick profiles. In case of uniform wick profile heat flux can be expressed as:

$$q'' = k_{eff} \frac{\Delta T}{t} \quad (47)$$

By combining Eqs. (32) and (47)

$$k_{eff} \frac{\Delta T}{t} = C \sqrt{\frac{\Delta P}{L}} \times \frac{\Delta T}{L} \quad (48)$$

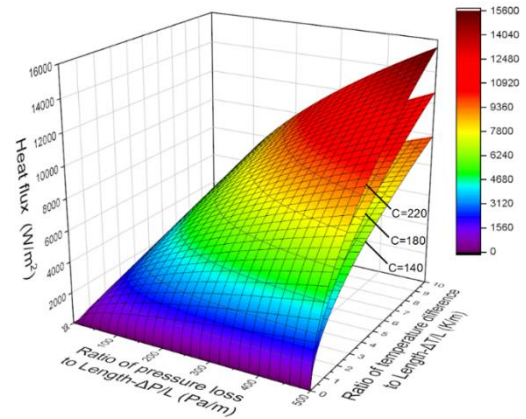


Figure 13. Heat flux as a function of $\Delta P/L$ and $\Delta T/L$ for various thermo-physical group values, “C”.

Equation (48) can be simplified as follows, to obtain an equation for dimensionless wick thickness, t/L , in terms of $\Delta T/L$ and $\Delta P/L$

$$C_1 = \frac{C}{k_{eff}} = \sqrt{\frac{2\rho_l K h_{fg}}{\mu_l k_{eff}}} \quad (49)$$

$$\frac{t}{L} = \frac{1}{C_1} \sqrt{\frac{\Delta T/L}{\Delta P/L}} \quad (50)$$

Dimensionless wick thickness t/L as a function of $\Delta P/L$ and $\Delta T/L$ is plotted in Figure 14 for various thermo-physical group values, “C₁”. Given a specified pressure loss and temperature difference for an evaporator or condenser with uniform wick profile; wick thickness, heat flux and heat transfer rate can be calculated by using Figure 13 and Figure 14. In case of an over designed heat pipe actual temperature difference, heat transfer rate and pressure loss is lower than those at the design point. Pressure loss for an operating condition can be found for a given wick thickness and actual temperature difference using Figure 14. Using the found operating pressure loss and the temperature difference, heat flux and thus heat transfer rate can be calculated from Figure 13.

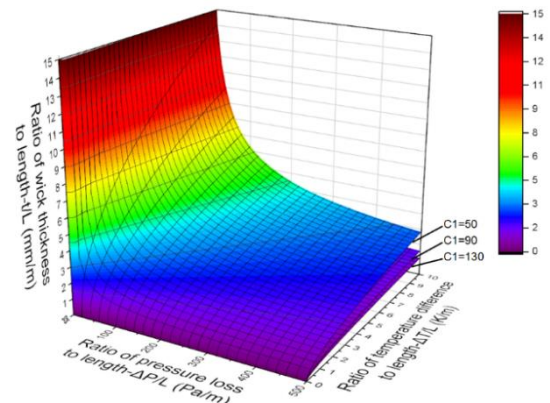


Figure 14. Ratio of wick thickness to length for various thermo-physical group values.

For a wick of 8.65 mm outer radius, heat transfer rate is plotted as a function of pressure loss and temperature difference in Figure 15, where C is 179.3 according to the parameters given in Table 1. It can be concluded that as the pressure loss raises heat transfer rate increases for a given temperature difference. Similarly, as the temperature difference increases, so does the heat transfer rate for a given pressure loss.

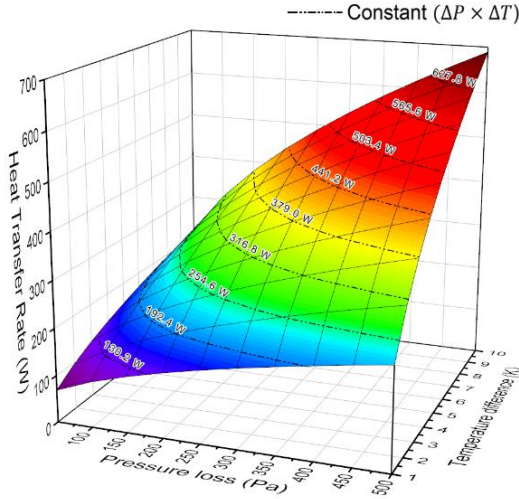


Figure 15. Change of evaporator heat transfer rate with pressure loss and temperature difference.

There exist a hidden variable in Figure 15 which is the wick thickness. Wick thickness should be increased to keep pressure loss along the wick constant if the temperature difference increases as a consequence of increased heat transfer rate and thus the flow rate. Uniform evaporator wick thickness values corresponding to heat transfer rates presented in Figure 15 over the same range of pressure loss and temperature difference values are plotted in Figure 16.

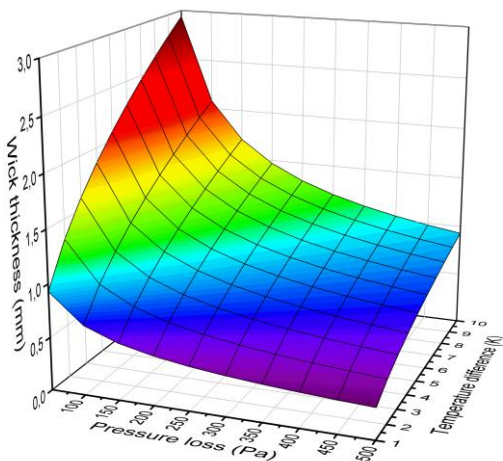


Figure 16. Change of evaporator wick thickness with pressure loss and temperature difference.

1-D Analysis of Flow and Heat Transfer for a Heat Pipe

Analysis of different wick profiles for heat transfer, pressure loss and mass over evaporator and condenser

results in a uniform profile as optimal solution. It is also noted that lower the evaporator and condenser wick thickness the higher the heat transfer rate. These insights together with analysis of r_v/r in adiabatic zone for reduced pressure loss leads to two types of designs shown in Figure 17. Increasing adiabatic zone wick thickness up to a critical value of r_v/r results in lower pressure loss as shown in Figure 7, thus higher heat transfer rate at capillary limit. However, it also results in increased vapor pressure loss at the adiabatic zone causing an increase in vapor temperature drop which in turn has a decreasing effect on the heat transfer rate. For this reason, consideration of the entire wick and vapor in a heat pipe including the evaporator, adiabatic zone and the condenser is necessary to apply the findings.

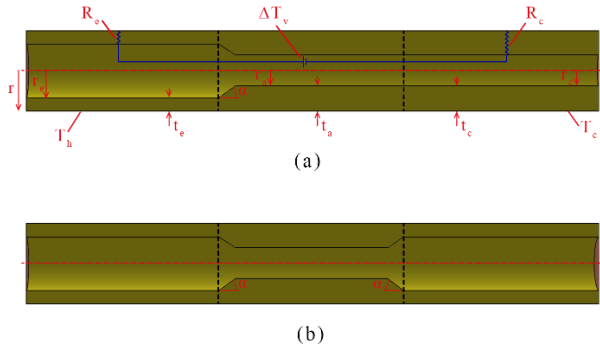


Figure 17. Suggested wick profiles for a heat pipe (a: $t_e < t_c = t_a$, b: $t_e = t_c < t_a$).

To investigate overall wick and vapor system a 1-D model is built which consists of two radial resistances and a potential difference to represent vapor temperature drop in axial direction as shown in Figure 17. Axial heat transfer through the wick is neglected since it is very low in comparison to radial heat transfer rate. Radial thermal resistances of evaporator, R_e , and condenser, R_c , which are obtained from Equations (4) and (40) for uniform wick thickness are

$$R_e = \frac{t_e}{k_{eff} 2\pi r L_e} \quad (51)$$

$$R_c = \frac{t_c}{k_{eff} 2\pi r L_c} \quad (52)$$

Axial vapor temperature drop, ΔT_v , i.e. potential difference in Figure 17 is related to vapor pressure loss since vapor at evaporator and condenser are both saturated at different pressures the difference of which drives the vapor flow. Vapor temperature drop is found using saturation data in thermodynamic tables. Then, heat transfer rate is calculated as follows:

$$Q = \frac{T_h - T_c - \Delta T_v}{R_e + R_c} \quad (53)$$

Liquid and vapor pressure losses in evaporator, adiabatic zone and condenser are calculated by Equations (45) and (46) where adiabatic zone length, L_a , is replaced by evaporator and condenser effective lengths, $L_{eff,e}$, and $L_{eff,c}$, respectively, for evaporator and condenser, which are defined as follows (Zohuri, 2016):

$$L_{eff,e} = \frac{L_e}{2} \quad (54)$$

$$L_{eff,c} = \frac{L_c}{2} \quad (55)$$

If turbulence occurs at any region in the vapor core, pressure loss is calculated by turbulent formulation otherwise laminar approach is applied. The location of laminar to turbulent transition is determined if turbulent flow exists in evaporator due to increased mass flow rate caused by evaporation and thus vapor speed based on Reynolds number criterion ($Re > 2300$). Same method is applied to the condenser to determine the location of turbulent to laminar transition due to condensation.

Change of wick thickness along the transition regions between evaporator and adiabatic zone and adiabatic zone and condenser is also of scientific interest. In this study, linear wick thickness profile for both transition regions (gradual contraction and expansion) is assumed with $\alpha=20^\circ$. Local vapor pressure losses due to gradual expansion and contraction are calculated by the semi-empirical formulas from the literature (Crane, 2009; Idelchik, 1994).

In the analyses capillary limit is also considered. For circulation of working fluid, capillary pressure difference, ΔP_{cap} , should be higher than the sum of the liquid pressure loss, ΔP_l , and vapor pressure loss, ΔP_v .

$$\Delta P_{cap} \geq \Delta P_l + \Delta P_v \quad (56)$$

Capillary pressure difference is calculated by Young-Laplace equation as follows:

$$\Delta P_{cap} = \frac{2\sigma}{r_{cap}} \quad (57)$$

Results for Overall Heat Pipe Wick

Using the developed 1-D model for transport phenomena at the wick and vapor, effect of wick thicknesses of

evaporator, adiabatic zone and condenser on heat transfer and capillary limit are investigated parametrically. Wick parameters, r , r_{cap} , ϕ , K , which are kept constant in case studies are given in Table 1. Evaporator, adiabatic zone and condenser lengths are kept equal to each other for convenience as 200 mm. In the analysis, temperature difference, which is the driving potential for heat transfer, between evaporator and condenser wick outer surfaces, $T_h - T_c$, is kept constant at 20°C , where $T_c = 25^\circ\text{C}$.

Under the constraint of constant total, i.e. sum of evaporator, adiabatic zone and condenser, wick volume, and therefore weight, effect of wick thicknesses on heat transfer rate and overall pressure loss are studied for the case depicted in Figure 17 (a) and results are presented in Figure 18. Similarly, under the constraint of constant total wick volume, the design shown in Figure 17 (b) is studied by increasing adiabatic zone wick thickness and results are given in Figure 19. In both cases heat transfer rate and overall pressure loss increases as wick is thickened in the adiabatic zone. However in case of Figure 17 (a) evaporator wick thickness reduces more rapidly than the case presented in Figure 17 (b) to compensate for increased adiabatic zone and condenser wick volumes. This fact results in a rapid increase of overall pressure loss and capillary limit is reached at 349 W, as opposed to gradual increase of overall pressure loss thus higher heat transfer rate which is 742 W in case of Figure 17 (b).

When the performance of the two designs are evaluated by removing the constant overall wick volume constraint following results are obtained. In Figure 20, heat transfer rate is plotted for the case presented in Figure 17 (a) where adiabatic zone and condenser wick thicknesses are equal to each other and higher than that of the evaporator. Increasing adiabatic zone and condenser wick thicknesses up to a certain value enhances heat transfer rate at capillary limit up to 620 W, beyond which heat transfer deteriorates, while it is 583 W in case of uniform wick thickness throughout the heat pipe.

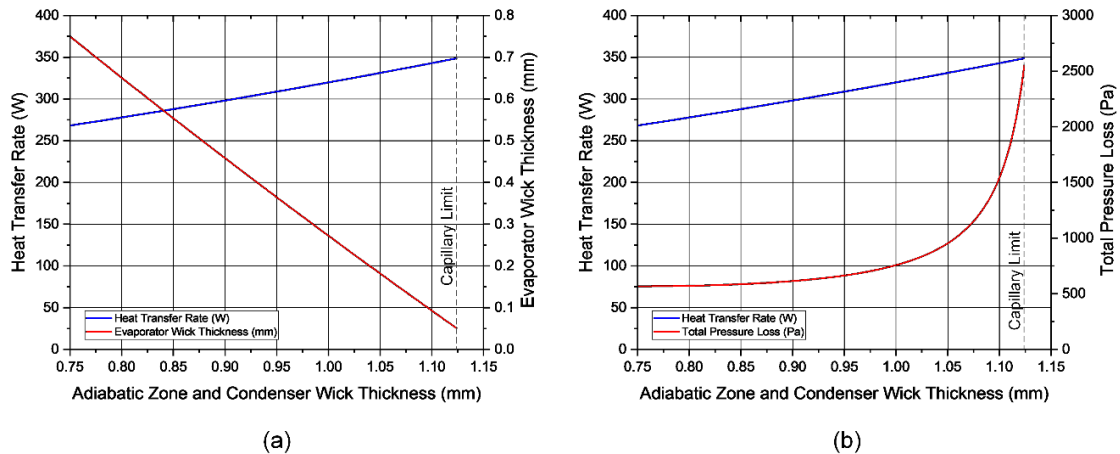


Figure 18. Heat transfer rate with evaporator wick thickness (a) and overall pressure loss (b) as functions of $t_a = t_c$ under constant wick volume constraint for the design shown in Figure 17 (a).

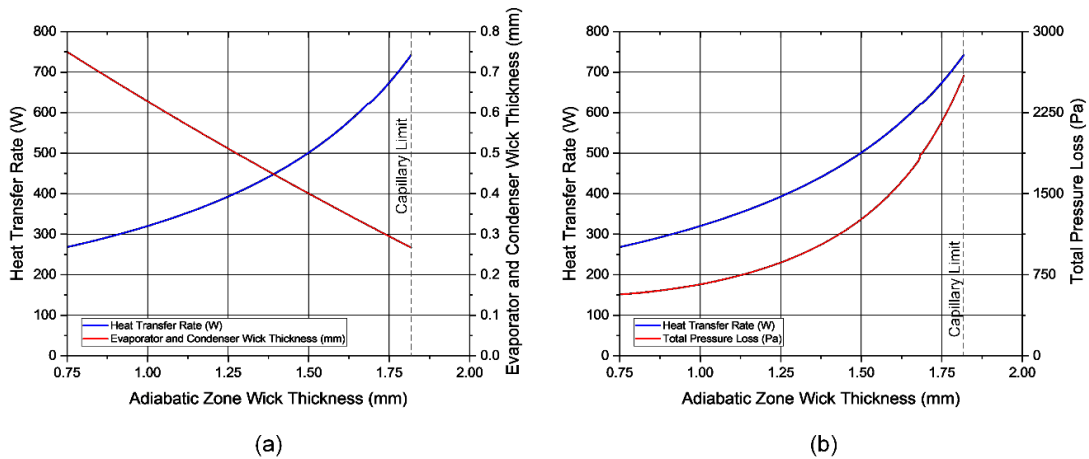


Figure 19. Heat transfer rate with evaporator and condenser wick thickness (a) and overall pressure loss (b) as functions of t_a under constant wick volume constraint for the design shown in Figure 17 (b).

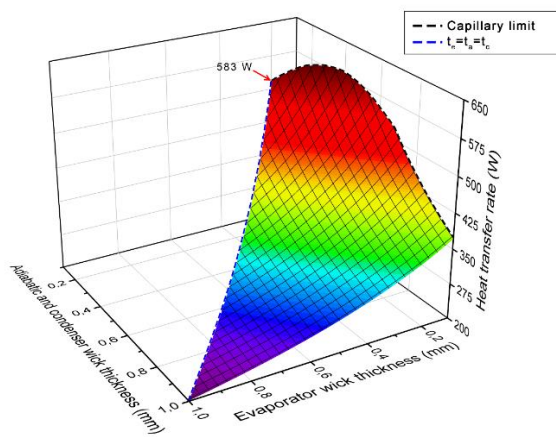


Figure 20. Change of heat transfer rate by wick thicknesses ($t_a=t_c$).

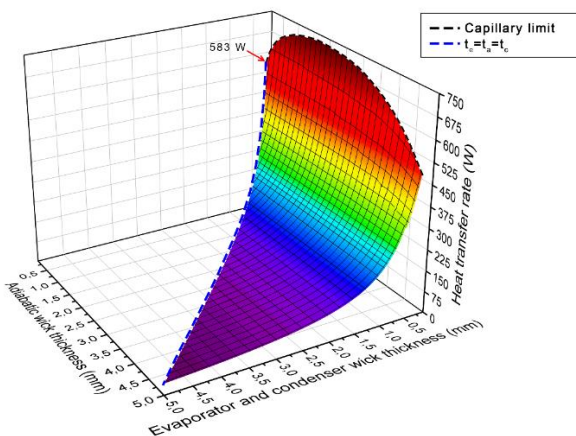


Figure 21. Change of heat transfer rate by wick thicknesses ($t_e=t_c$).

In Figure 21, evaporator and condenser wick thicknesses kept equal to each other and lower than adiabatic zone wick thickness as shown in Figure 17 (b). Decreasing evaporator and condenser wick thickness increases heat transfer rate rapidly. As stated before, for uniform wick thickness throughout the heat pipe, capillary limit is 583 W. Increasing adiabatic zone wick thickness up to a

certain value results in increased capillary limit which reaches 744 W, thereafter it deteriorates. Increase of capillary limit with increasing adiabatic zone wick thickness is due to resulting lower pressure loss in the adiabatic zone which allows higher pressure loss thus lower wick thickness and consequently increased heat transfer rate in evaporator and condenser.

At capillary limit, evaporator and condenser wick thickness and heat transfer rate as functions of adiabatic zone wick thickness are plotted in Figure 22 (a). Increasing adiabatic zone wick thickness above approximately 2 mm decreases maximum heat transfer rate which is due to increased vapor temperature drop as a result of increased vapor pressure loss along the adiabatic zone. Also plotted at the capillary limit is total volume of the wick, Figure 22 (b). As seen from the figure, total wick weight increases as adiabatic zone wick thickness increases. On the other hand, heat transfer rate increases, rapidly between 0.36 mm to 1 mm, at a moderate rate between 1 mm to 1.5 mm and very slowly between 1.5 mm to 2 mm interval of the adiabatic zone wick thickness. This result is significantly important, especially for weight critical applications, since increase of weight has high positive impact on heat transfer rate up to a certain value of adiabatic zone wick thickness. Further increase of weight up to a critical value for which peak value of heat transfer is achieved enhances heat transfer at a reduced rate. Beyond the critical value of weight heat transfer deteriorates at increasing rates as the wick weight is further increased.

As seen from Figure 20 and Figure 21, increasing only adiabatic region wick thickness while lowering that of evaporator and condenser facilitates higher heat transfer rate at capillary limit in comparison to increasing the adiabatic zone and condenser wick thickness while lowering the evaporator wick thickness. This is because of heat transfer rate being inversely proportional to evaporator and condenser wick thicknesses since heat is primarily transferred by conduction in radial direction there.

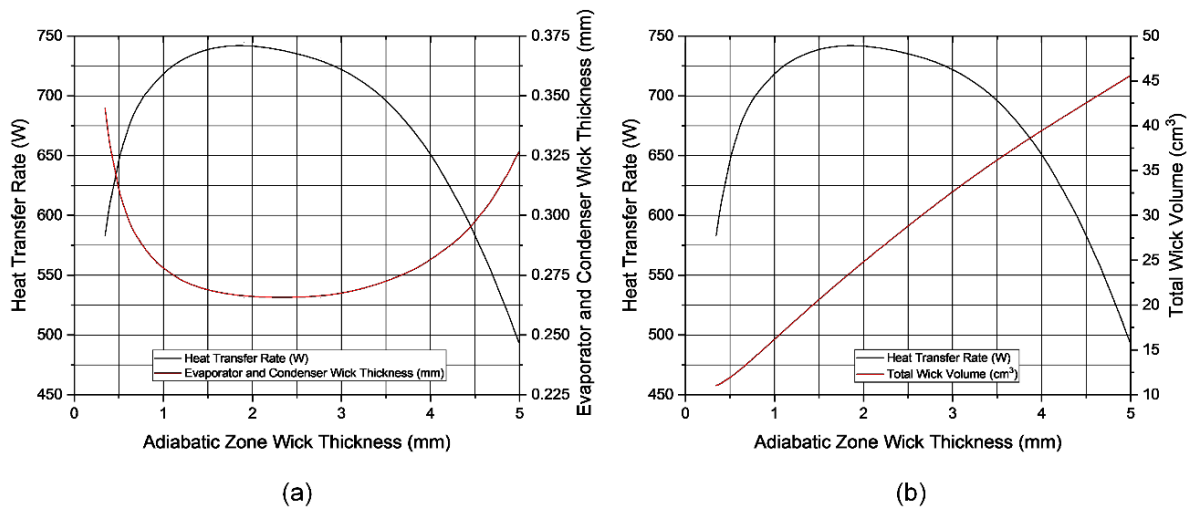


Figure 22. Heat transfer rate, wick thicknesses (a) and total wick volume (b) as a function of adiabatic zone wick thickness at capillary limit.

Lower liquid pressure loss could be obtained for the case in Figure 17 (a) due to higher cross-sectional area of the condenser wick as compared to case in Figure 17 (b). This design results in reduced pressure loss in the adiabatic zone and condenser, while it increases in the evaporator. On the other hand, resistance to radial heat transfer decreases at the evaporator and increases at the condenser. Decrease of radial thermal resistance of the evaporator is higher than increase of that of the condenser so that heat transfer rate is higher as compared to uniform wick thickness case.

Another discussion is real-life application of proposed wick designs. First discussion is the production method for the proposed optimal wick profiles in Figure 17. Normally mono-porous sintered wicks are produced by inserting a rod inside the copper tube, Figure 23 (a), and filling the empty space between the rod and copper tube wall by copper powder. After sintering the copper powder the rod is pulled out leaving the space for vapor flow. However suggested wick profile in Figure 17 (b) does not allow for a rod to be pulled out so it is suggested to use two rods as in Figure 23 (c). One of the rods are inserted from the bottom and another one is inserted from the top side. Then, copper powder is filled from top side and sintered. After the sintering procedure rods are being pulled out from top and bottom avoiding undercut. However by keeping the adiabatic and condenser section wick thicknesses equal, it is possible to produce the wick with a single rod as seen in Figure 23 (b). In this case, heat pipe performance is enhanced without changing the classical heat pipe production method.

In the literature few studies, e.g. (Zohuri, 2016), on variable thickness wicks exist which are aimed at managing non-uniform heat flux at evaporator. Full wetting of variable thickness wick is possible for heat pipes for which axial length is much bigger than pipe radius. For such heat pipes axial pressure loss is much bigger than that across the wick. Typical capillary pumping capacity of heat pipes are quite high so that full wetting in radial direction is guaranteed.

In the literature, variable thickness wick is proposed for thermal management of evaporators subject to non-uniform heating (Zohuri, 2016).

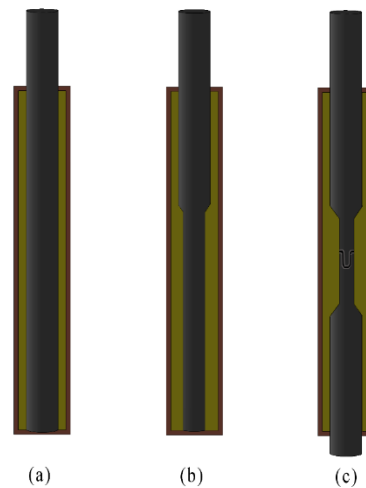


Figure 23. Single rod (a), (b) and suggested two rod (c) production methods.

CONCLUSIONS

In this study, first, one-dimensional thermo-fluid model of the transport phenomena in the wick of the evaporator of a heat pipe is developed analytically to study the effect of longitudinal wick profiles on heat pipe performance. Based on the developed model, an analytical relation between pressure loss along and temperature difference across the wick of the evaporator of a heat pipe is derived by one-dimensional analyses based on Darcy's Law of pressure loss of liquid flow in a porous medium and Fourier's Law of Heat Conduction, see Equation (17). In this expression both thermo-fluid properties of the working fluid and porous wick and integral of the reciprocal of thickness profile of the wick along the evaporator appear. Furthermore, heat transfer rate is expressed in terms of outer radius and permeability of the wick, thermo-fluid properties of the working fluid, liquid pressure loss along the wick and temperature difference

across the wick, for any wick thickness profile, see Equation (18). It is found that same pressure loss and heat transfer rate can be obtained with different evaporator wick profiles. It is shown that the ratio of the evaporator heat transfer rate to the square root of the liquid axial pressure loss in the wick of the evaporator times the temperature difference across the evaporator wick is constant for a chosen working fluid and wick micro-structure, see Equation (29).

Secondly, an isoperimetric problem of calculus of variations is solved to find the evaporator wick thickness profile that minimizes evaporator wick volume, thus weight, under the constraints of fixed heat transfer rate and admissible wick thickness profiles satisfying a chosen liquid pressure loss along the wick, see Equation (34), which results in a uniform wick thickness along the evaporator. Uniform wick thickness as given by Equation (37) is expressed in terms of the length of the evaporator, outer radius and permeability of the wick, thermo-fluid properties of the working fluid, as well as the liquid pressure and temperature differences along and across the evaporator wick.

Then, the thermo-fluid model and the results of the optimization problem are extended to the condenser section of the heat pipe. As in the case of evaporator, condenser heat transfer rate can be calculated in term of outer radius and permeability of the wick, thermo-fluid properties of the working fluid, and liquid pressure and temperature differences along and across the condenser wick, respectively, for any wick thickness profile. For a given heat transfer rate, among the wick thickness profiles that satisfy a specified liquid pressure drop along the wick of the condenser, as in the case of evaporator, minimum material use is achieved by keeping the wick thickness uniform, which can be calculated by Equation (37).

Finally, the uniform wick thickness that minimizes the sum of the pressure losses along the wick and the central vapor column of the adiabatic zone of the heat pipe is calculated based on Darcy's Law for liquid flow in porous wick and Poiseuille-Hagen and Darcy-Weisbach formulas for laminar and turbulent vapor flows, respectively. It is concluded that wick thickness in evaporator and condenser may need to be less than that of the adiabatic zone in order to enhance heat transfer rate while keeping sum of the liquid and vapor phase pressure losses in the adiabatic zone at minimum value.

Under the constraint of overall pressure loss in heat pipe cycle which is imposed by capillary head, the wick thicknesses of evaporator, adiabatic zone and condenser should be selected in such a way that heat transfer rate is maximized. Therefore, two novel piecewise uniform wick thickness profiles, one with bigger wick thickness in adiabatic zone as compared to that of the evaporator and condenser, and the other with common wick thickness of the adiabatic zone and condenser being bigger than that of the evaporator are proposed to realize the target mentioned above.

Coupled flow and thermal analyses in the wick and vapor core showed that for a conventional heat pipe, i.e. uniform wick thickness throughout the heat pipe, of specified length, radius and wick porous structure operating at a specified temperature difference heat transfer rate is 268 W. Under constant total wick volume constraint, when adiabatic zone and condenser wick thicknesses are increased by keeping them equal to each other and evaporator wick thickness is lowered, heat transfer rate is found to increase up to 349 W when capillary limit is reached. On the other hand, under the same constraint, if evaporator and condenser wick thicknesses are equal to each other and adiabatic zone wick thickness is higher, calculations show that heat transfer rate can be increased up to 742 W when capillary limit is reached.

In case of the design where adiabatic zone wick thickness is higher than that of evaporator and condenser, when the constant wick volume constraint is removed heat transfer rate can be increased up to 27.6% at capillary limit which is achieved for total wick volume increase of 136% in comparison to conventional heat pipe. On the other hand, if adiabatic region and condenser wick thicknesses are equal and higher than that of evaporator heat transfer rate increases up to 6.3% at capillary limit where total wick volume increases 6.9%.

Since developed model is kept simple to make it analytically solvable, future work may focus on evaluation of the performance of suggested designs by more-sophisticated multi-dimensional models such as an axisymmetric thermo-fluid model incorporating pressure losses in radial direction, pressure jump at liquid vapor interface due to capillarity, interfacial resistance to heat transfer and axial heat transfer in the wick.

It is well known that sum of the pressure losses in the heat pipe should be less than the capillary head. Designs suggested in this study modify distribution of pressure loss among various wick zones to enhance heat transfer rate at capillary limit. However, in the analyses, evaporator, condenser and adiabatic zone lengths are kept equal to each other which may not be the case in real applications. Also wick thicknesses in the analyses changed in pairs, i.e. wick thickness of the condenser is kept equal to that of the adiabatic zone, or wick thickness of the condenser is kept equal to that of evaporator, but the influence of different wick thickness for each zone on the performance is not evaluated in this study. Therefore, it is necessary to derive optimal ratios of evaporator, adiabatic zone and condenser wick thicknesses for a heat pipe with various lengths of the three zones.

ACKNOWLEDGEMENTS

Authors gratefully acknowledge suggestions and support of Dr. İsmail Teke of Yıldız Technical University, Istanbul and Dr. İlyas Kandemir of Gebze Technical University, Gebze-Kocaeli. Authors also deeply appreciate assistance of Muhammed Said Gündoğan of Bilkent University, Ankara.

REFERENCES

- Crane Co., 2009, Flow of Fluids Through Valves, Fittings and Pipe, Technical Paper No. 410.
- Deng D., Liang D., Tang Y., Peng J., Han X. and Pan M., 2013, Evaluation of capillary performance of sintered porous wicks for loop heat pipe, *Exp. Therm. Fluid Sciences*, 50, 1-9.
- El-Genk M. S. and Huang L., 1993, An experimental investigation of the transient response of a water heat pipe, *Int. J. Heat Mass Transfer*, 36, 3823-3830.
- Gelfand I. M. and Fomin S. V., 1963, Calculus of variations, Prentice-Hall.
- Hong, F.J., Cheng P., Wu H.Y. and Sun Z., 2013, Evaporation/boiling heat transfer on capillary feed copper particle sintered porous wick at reduced pressure, *Int. J. Heat Mass Transfer*, 63, 389-400.
- Huang Y. and Chen Q., 2017, A numerical model for transient simulation of porous wicked heat pipes by lattice Boltzmann method, *Int. J. Heat Mass Transfer*, 105, 270-278.
- Idelchik I. E., 1994, Handbook of Hydraulic Resistance, CRC Begell House.
- Kaya T., Goldak J., 2007, Three-dimensional numerical analysis of heat and mass transfer in heat pipes, *Heat Mass Transfer*, 43, 775-785.
- Kiseev V.M., Vlassov V.V. and Muraoka I., 2010, Optimization of capillary structures for inverted meniscus evaporators of loop heat pipes and heat switches, *Int. J. Heat Mass Transfer*, 53, 2143-2148.
- Lemons D.S., 1997, Perfect Form: Variational Principles, Methods and Applications in Elementary Physics, Princeton University Press.
- Lin K.T. and Wong S.C., 2013, Performance degradation of flattened heat pipes, *Appl. Therm. Engineering*, 50, 46-54.
- Mwaba M.G., Huang X. and Gu J., 2006, Influence of wick characteristics on heat pipe performance, *Int. J. Energy Research*, 30, 489-499.
- Nishikawara M. and Nagano H., 2017, Optimization of wick shape in a loop heat pipe for high heat transfer, *Int. J. Heat Mass Transfer*, 104, 1083-1089.
- Ranjan R., Murthy J.Y. and Garimella S.V., 2009, Analysis of the wicking and thin-film evaporation characteristics of microstructures, *J. Heat Transfer*, 131, 1-11.
- Ranjan R., Murthy J.Y., Garimella S.V. and Vadakkan U., 2011, A numerical model for transport in flat heat pipes considering wick microstructure effects, *Int. J. Heat Mass Transfer*, 54, 153-168.
- Schmalhofer J. and Faghri A., 1992, A study of circumferentially- heated and block- heated heat pipes-I. Experimental analysis and generalized analytical prediction of capillary limits, *Int. J. Heat Mass Transfer*, 36, 201-212.
- Siddiqui A. and Kaya T., 2016, Design and thermal analysis of a segmented single-artery heat pipe, *Appl. Therm. Engineering*, 96, 652-658.
- Tournier J.M. and El-Genk M.S., 1994, A heat pipe transient analysis model, *Int. J. Heat Mass Transfer*, 37, 753-762.
- Wang Q., Hong J. and Y. Yan, 2014, Biomimetic capillary inspired heat pipe wicks, *J. Bionic Engineering*, 11, 469-480.
- Weibel J.A., Garimella S.V. and North M.T., 2010, Characterization of evaporation and boiling from sintered powder wicks fed by capillary action, *Int. J. Heat Mass Transfer*, 53, 4204-4215.
- Wong S.C., Cheng H.S. and Tu C.W., 2017, Visualization experiments on the performance of mesh-wick heat pipes with differing wick wettability, *Int. J. Heat Mass Transfer*, 114, 1045-1053.
- Zhu N. and Vafai K., 1999, Analysis of cylindrical heat pipes incorporating the effects of liquid-vapor coupling and non-Darcian transport - a closed form solution, *Int. J. Heat Mass Transfer*, 42, 3405-3418.
- Zohuri B., 2016, Heat pipe design and technology: Modern applications for practical thermal management (2nd Ed.), Springer.
- Zuo Z.J. and Faghri A., 1998, A network thermodynamic analysis of the heat pipe, *Int. J. Heat Mass Transfer*, 41, 1473-1484.

APPENDIX - CALCULATION OF ADIABATIC ZONE PRESSURE LOSSES FOR VARIOUS WICK PROFILES

If vapor flow is laminar, sum of the pressure losses in vapor and liquid phases, in differential form, can be expressed as

$$dP_a = \frac{C_1}{(r-f(x))^4} dx + \frac{C_2}{[r^2 - (r-f(x))^2]} dx \quad (1)$$

If vapor flow is turbulent, sum of the pressure losses in vapor and liquid phases, in differential form, becomes

$$dP_a = \frac{C_3}{(r-f(x))^5} dx + \frac{C_2}{[r^2 - (r-f(x))^2]} dx \quad (2)$$

where constants C_1 , C_2 and C_3 are defined as follows:

$$C_1 = \frac{8\mu_v \dot{m}}{\pi \rho_v} \quad (3)$$

$$C_2 = \frac{\mu_l \dot{m}}{\pi \rho_l K} \quad (4)$$

$$C_3 = \frac{f \dot{m}^2}{4\pi^2 \rho_v} \quad (5)$$

Vapor column radius is presented as $r_v=r-f(x)$ since different adiabatic zone wick thickness profiles, $f(x)$, are to be considered.

Table 1. Typical water-copper heat pipe parameters for the case studies.

| Parameter | Value | Unit |
|-----------|----------------------|-------------------|
| L_a | 90 | mm |
| μ_v | 1.1×10^{-5} | Pa s |
| μ_l | 4.7×10^{-4} | Pa s |
| ρ_l | 983.2 | kg/m ³ |
| ρ_v | 0.13 | kg/m ³ |
| r | 8.65 | mm |
| ϕ | 0.5 | % |
| K | 1.5×10^{-9} | m ² |
| f | 0.13 | - |
| \dot{m} | 0.188 | gr/s |

Adiabatic zone pressure loss is found by integrating Equations (1) and (2) over the adiabatic zone length.

$$\Delta P_a = \int_0^L \left(\frac{C_1}{(r-f(x))^4} + \frac{C_2}{[r^2 - (r-f(x))^2]} \right) dx \quad (6)$$

Table 2. For laminar vapor flow, pressure losses for various adiabatic zone wick thickness profiles.

| Profile No | Wick profile (mm) | Vapor pressure loss (Pa) | Liquid pressure loss (Pa) | Total pressure loss (Pa) | Wick volume (cm ³) |
|------------|-----------------------|--------------------------|---------------------------|--------------------------|--------------------------------|
| 1 | $f(x) = 0.75$ | 0.927 | 137.141 | 138.068 | 3.51 |
| 2 | $f(x) = 3.99x + 0.57$ | 0.928 | 139.821 | 140.749 | 3.51 |
| 3 | $f(x) = 8.95x + 0.35$ | 0.936 | 151.845 | 152.781 | 3.51 |
| 4 | $f(x) = 0.93 - 3.99x$ | 0.928 | 139.821 | 140.749 | 3.51 |
| 5 | $f(x) = 1.16 - 8.95x$ | 0.936 | 151.845 | 152.781 | 3.51 |

$$\Delta P_a = \int_0^L \left(\frac{C_3}{(r-f(x))^5} + \frac{C_2}{[r^2 - (r-f(x))^2]} \right) dx \quad (7)$$

Values of C_1 , C_2 and C_3 are calculated by parameters given in Table 1. Friction factor f in Equation (5) is calculated for $Re=3161$ which is reached at $r_v=3.46$ mm. Friction factor is assumed to be constant throughout the adiabatic zone in the following analyses.

Pressure losses calculated by Equation (6) for constant, linearly increasing and linearly decreasing wick thickness profiles under the constraint of constant wick volume are presented in Table 2 for laminar vapor flow. In Figure 1 wick thickness profiles given in Table 2 are plotted.

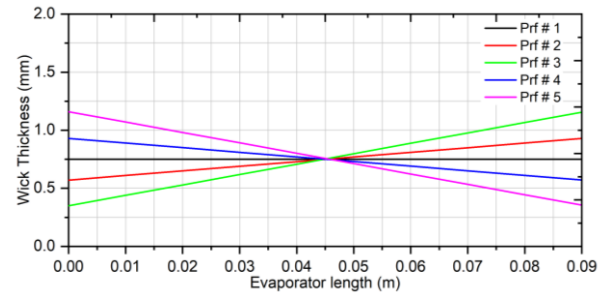


Figure 1. Wick thickness profiles given in Table 2 over adiabatic zone length.

As seen from Table 2 and Table 3, uniform wick thickness results in the lowest pressure drop in comparison to linearly increasing and decreasing wick profiles. Under constant wick volume constraint, pressure losses in both phases increase along with the absolute value of the slope of the wick profile, for both flow regimes.

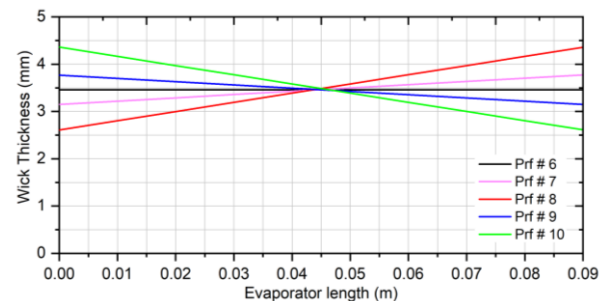


Figure 2. Wick thickness profiles given in Table 3 over adiabatic zone length.

Table 3. For turbulent vapor flow, pressure losses for various adiabatic zone wick thickness profiles.

| Profile No | Wick profile (mm) | Vapor pressure loss (Pa) | Liquid pressure loss (Pa) | Total pressure loss (Pa) | Wick volume (cm ³) |
|------------|------------------------|--------------------------|---------------------------|--------------------------|--------------------------------|
| 6 | $f(x) = 3.46$ | 21.37 | 35.55 | 56.92 | 13.54 |
| 7 | $f(x) = 6.92x + 3.15$ | 21.79 | 35.62 | 57.41 | 13.54 |
| 8 | $f(x) = 19.43x + 2.61$ | 25.28 | 35.99 | 61.27 | 13.54 |
| 9 | $f(x) = 3.77 - 6.92x$ | 21.79 | 35.62 | 57.41 | 13.54 |
| 10 | $f(x) = 4.36 - 19.43x$ | 25.28 | 35.99 | 61.27 | 13.54 |



Mehmed Akif PAKSOY was graduated from Middle East Technical University, Ankara, Turkey in 2012. He received his Masters degree in Mechanical Engineering from Gebze Technical University, Kocaeli, Turkey in 2014. He worked as design and analyses engineer for public and private companies. He is currently working as a senior researcher for The Scientific and Technological Research Council of Turkey. His research interests include heat pipes, computational fluid dynamics, heat transfer and mechanical design.



Salih Özen ÜNVERDİ was graduated from Istanbul Technical University, Istanbul, Turkey in 1982. He received his Ph.D. degree from University of Michigan, Ann Arbor, Michigan, USA in 1990. He is one of the pioneers of the front-tracking method for direct numerical simulations of multi-phase flows. He worked for several global and local automotive companies as design and analyses engineer. He is currently lecturing and researching in Mechanical Engineering Department of Gebze Technical University. His research interests include computational fluid dynamics, heat transfer, thermodynamics and combustion.

ISI BİLİMİ VE TEKNİĞİ DERGİSİ İÇİN MAKALE HAZIRLAMA ESASLARI

Isı Bilimi ve Tekniği Dergisi'nde, ısı bilimi alanındaki özgün teorik ve deneysel çalışmaların sonuçlarının sunulduğu makaleler ve yeterli sayıda makaleyi tarayarak hazırlanmış olan literatür özeti makaleler yayınlanmaktadır. Makaleler, Türkçe veya İngilizce olarak kabul edilmektedir. Makaleler ilk sunumda serbest formatta hazırlanabilir. Ancak yayın için kabul edilmiş olan makaleler dergimizin basım formatına tam uygun olarak yazarlar tarafından hazırlanmalıdır. Aşağıda, ilk sunuş ve basıma hazır formatta makale hazırlamak için uyulması gereken esaslar detaylı olarak açıklanmıştır.

İLK SUNUŞ FORMATI

İlk sunuşta, makale A4 boyutundaki kağıda tek sütun düzeninde, 1.5 satır aralıklı ve sayfa kenarlarından 25'er mm boşluk bırakılarak yazılmalıdır. Yazı boyutu 11 punto olmalı ve **Times New Roman** karakter kullanılmalıdır. Şekiller, tablolar ve fotoğraflar makale içinde **olmaları gereken yerlere** yerleştirilmelidir. Makale, elektronik olarak editörün e-posta adresine gönderilmelidir.

BASIMA HAZIR MAKALE FORMATI

Hakem değerlendirmelerinden sonra, yayın için kabul edilmiş olan makaleler, dergimizin basım formatına tam uygun olarak yazarlar tarafından hazırlanmalıdır. Makaleler yazarların hazırladığı haliyle basıldığı için, yazarların makalelerini basım için hazır formatta hazırlarken burada belirtilen esasları titizlikle takip etmeleri çok önemlidir. Aşağıda, basıma hazır formatta makale hazırlamak için uyulması gereken esaslar detaylı olarak açıklanmıştır.

Genel Esaslar

Makaleler genel olarak şu başlıklar altında düzenlenmelidir: Makale başlığı (title), yazar(lar)ın ad(lar)ı, yazar(lar)ın adres(ler)i, özet (abstract), anahtar kelimeler (keywords), semboller, giriş, materyal ve metod, araştırma sonuçları, tartışma ve sonuçlar, teşekkür, kaynaklar, yazarların fotoğrafları ve kısa özgeçmişleri ve ekler. Yazılar bilgisayarda tek satır aralıklı olarak, 10 punto Times New Roman karakteri kullanılarak Microsoft Office Word ile iki sütun düzeninde yazılmalıdır. Sayfalar, üst kenardan 25 mm, sol kenardan 23 mm, sağ ve alt kenarlardan 20 mm boşluk bırakılarak düzenlenmelidir. İki sütun arasındaki boşluk 7 mm olmalıdır. Paragraf başları, sütunun sol kenarına yaslanmalı ve paragraflar arasında bir satır boşluk olmalıdır.

Birinci seviye başlıklar büyük harflerle kalın olarak, ikinci seviye başlıklar bold ve kelimelerin ilk harfleri büyük harf olarak ve üçüncü seviye başlıklar sadece ilk harfi büyük olarak yazılır. Bütün başlıklar sütunun sol kenarı ile aynı hizadan başlamalıdır ve takip eden paragrafla başlık arasında bir satır boşluk olmalıdır. Şekiller, tablolar, fotoğraflar v.b. metin içinde ilk atıf

yapılan yerden hemen sonra uygun şekilde yerleştirilmelidir. İlk ana bölüm başlığı, Özetten (Abstract'tan) sonra iki satır boşluk bırakılarak birinci sütuna yazılır.

Başlık, Yazarların Adresi, Özet, Abstract ve Anahtar Kelimeler

Yazılar Türkçe veya İngilizce olarak hazırlanabilir. Her iki durumda da makale özeti, başlığı ve anahtar kelimeler her iki dilde de yazılmalıdır. Eğer makale Türkçe olarak kaleme alınmışsa, Türkçe başlık ve özet önce, İngilizce başlık ve Özet (Abstract) sonra yazılır. Eğer makale İngilizce olarak kaleme alınmışsa önce İngilizce başlık ve özet (abstract) sonra Türkçe başlık ve özet yazılır. Başlık, sayfanın üst kenarından 50 mm aşağıdan başlar ve kalın olarak 12 punto büyüklüğünde, büyük harflerle bütün sayfayı ortalayacak şekilde yazılır. Yazar(lar)ın adı, adresi ve elektronik posta adresi başlıktan sonra bir satır boşluk bırakılarak yazılmalıdır. Yazarların adı küçük, soyadı büyük harflerle yazılmalı ve bold olmalıdır. Yazarların adresinden sonra üç satır boşluk bırakılarak, Özet ve Abstract 10 punto büyüklüğünde bütün sayfa genişliğinde yazılır. Özet ve Abstracttan sonra anahtar kelimeler (Keywords) yazılır.

Birimler

Yazılarda SI birim sistemi kullanılmalıdır.

Denklemler

Denklemler, 10 punto karakter boyutu ile bir sütuna (8 cm) sığacak şekilde düzenlenmelidir. Veriliş sırasına göre yazı alanının sağ kenarına yaslanacak şekilde parantez içinde numaralanmalıdır. Metin içinde, denklemlere '**Eş. (numara)**' şeklinde atıfta bulunulmalıdır.

Şekiller

Şekiller 8 cm (bir sütun) veya 16 cm (iki sütun) genişliğinde olmalıdır ve makale içerisinde olmaları gereken yerlere bilgisayar ortamında sütunu (veya bütün sayfa genişliğini) ortalayacak şekilde yerleştirilmelidir. Şekil numaraları (sıra ile) ve isimleri şekil **altına, 9 punto büyüklüğünde** yazılmalıdır.

Tablolar

Tablolar 8 cm (bir sütun) veya 16 cm (iki sütun) genişliğinde olmalıdır. Makale içerisinde olmaları gereken yerlere bilgisayar ortamında sütunu (veya bütün sayfa genişliğini) ortalayacak şekilde yerleştirilmelidir. Tablo numaraları (sıra ile) ve isimleri tablo **üstüne, 9 punto büyüklüğünde** yazılmalıdır.

Fotograflar

Fotograflar, siyah/beyaz ve 8 cm (bir sütun) veya 16 cm (iki sütun) genişliğinde olmalıdır. Fotograflar digitize edilerek, makale içinde bulunmaları gereken yerlere bilgisayar ortamında sütunu (veya bütün sayfa genişliğini) ortalayacak şekilde yerleştirilmelidir ve şekil gibi numaralandırılmalı ve adlandırılmalıdır.

Yazar(lar)ın Fotoğraf ve Kısa Özgeçmişleri

Yazarların fotoğrafları digitize edilerek, makalenin en sonuna özgeçmişleri ile birlikte uygun bir şekilde yerleştirilmelidir.

SEMBOLLER

Makale içinde kullanılan bütün semboller alfabetik sırada Özetten sonra liste halinde tek sütun düzeninde yazılmalıdır. Boyutlu büyüklükler birimleri ile birlikte ve boyutsuz sayılar (Re, Nu, vb.) tanımları ile birlikte verilmelidir.

KAYNAKLAR

Kaynaklar metin sonunda, ilk yazarın soyadına göre alfabetik sırada listelenmelidir. Kaynaklara, yazı içinde, yazar(lar)ın soyad(lar)ı ve yayın yılı belirtilerek atıfta

bulunulmalıdır. Bir ve iki yazarlı kaynaklara, her iki yazarın soyadları ve yayın yılı belirtilerek (Bejan, 1988; Türkoğlu ve Farouk, 1993), ikiden çok yazarlı kaynaklara ise birinci yazarın soyadı ve "vd." eki ve yayın yılı ile atıfta bulunulmalıdır (Ataer vd, 1995). Aşağıda makale, kitap ve bildirilerin kaynaklar listesine yazım formatı için örnekler verilmiştir.

Ataer Ö. E., Ileri A. and Göğüş, Y. A., 1995, Transient Behaviour of Finned-Tube Cross-Flow Heat Exchangers, *Int. J. Refrigeration*, 18, 153-160.

Bejan A., 1998, *Advanced Engineering Thermodynamics* (First Ed.), Wiley, New York.

Türkoğlu H. and Farouk B., 1993, Modeling of Interfacial Transport Processes in a Direct-Contact Condenser for Metal Recovery, *Proc. of 73rd Steel Making Conference*, Detroit, 571-578.

Türkoğlu H., 1990, *Transport Processes in Gas-Injected Liquid Baths*, Ph.D. Thesis, Drexel University, Philadelphia, PA, USA.

İnternet, 2004, Türkiye İstatistik Kurumu, *Atıksu İstatistikleri*, <http://www.tuik.gov.tr/HaberBulteni>.

DIĞER HUSUSLAR

Hakem değerlendirmesinden sonra kabul edilen makaleler, yukarıda açıklandığı şekilde dizilerek basıma hazırlandıktan sonra, bir elektronik kopyası editöre gönderilmelidir. Makalenin basıma hazır kopyası ile birlikte, "Telif Hakkı Devri Formu" da doldurularak gönderilmelidir. Telif Hakkı Devri Formu'na ve bu yazım klavuzuna www.tibt.org.tr adresinden ulaşılabilir.



TÜRK ISI BİLİMİ VE TEKNİĞİ DERNEĞİ
ÜYELİK BAŞVURU FORMU

FOTOĞRAFINIZ

A. Adınız Soyadınız :
Ünvanınız :
Doğum yeri : : Doğum tarihi: / / 19 T.C. Kimlik No:
İş Adresiniz :
Ev adresiniz :
Telefonunuz : İş Ev Cep
E-posta :

B. *Derneğe Asil üye Fahri üye olmak istiyorum.

1. Sizi tanıyan dernek üyesi (Üyelik için) :

2. Mezun olduğunuz
Yüksek Okullar Yıl Branşınız Ünvanınız

3. İlgilendiğiniz konular :

2015 yılı aidatı olarak toplam 25 YTL (Yirmibeş Milyon TL) derneğin

İş Bankası Maltepe Şubesi Hesap No: 42120867567
IBAN: TR08 0006 4000 0014 2120 8675 67

hesabına yatırılmıştır.

Tarih :

İmza :

* Asil üye olmak için beş yıllık deneyim gereklidir.
Fahri üyelik için yüksekokul mezunu olma şartı yoktur.

Türk Isı Bilimi ve Tekniđi Derneđi
Gazi Üniversitesi
Mühendislik Fakültesi
Makina Mühendisliđi Bölümü
06570 Maltepe/ ANKARA

İÇİNDEKİLER / CONTENTS

| | |
|--|-----|
| A Life Cycle Costing Approach to Determine the Optimum Insulation Thickness of Existing Buildings <i>Yaşam Dönemi Maliyetlemesi Yaklaşımı İle Mevcut Binalarda Optimum Yalıtım Kalınlığının Belirlenmesi</i> Semih ÇAĞLAYAN, Beliz OZORHON, Gülbin ÖZCAN-DENİZ and Sadık YİĞİT | 1 |
| The Effects of CO₂, H₂O, and N₂ Dilutions on Pollutants of Shale Gas Combustion <i>Şeyl Gaz Yanmasının Kirlenmeleri Üzerinde CO₂, H₂O ve N₂ Dilüsyonlarının Etkileri</i> Suat ÖZTÜRK | 15 |
| Prediction of the Annual Heat Load of an Articulated Electric Urban Bus <i>Bir Elektrikli Körüklü Şehir İçi Otobüsün Yıllık Isı Yükü Kestirimi</i> M. Nicem TANYERİ and S. Çağlar BAŞLAMİŞLİ | 27 |
| Improving Performance and Thermoeconomic Optimization of an Existing Binary Geothermal Power Plant: A Case Study <i>Mevcut Bir Binary Jeotermal Santralin Performans Geliştirilmesi ve Termodinamik Optimizasyonu: Bir Vaka Çalışması</i> Ceyhan YILMAZ | 37 |
| Validation of Aerodynamic Heating Prediction Tool <i>Aerodinamik Isınma Kestirim Aracının Doğrulanması</i> Buğra ŞİMŞEK, Sıtkı USLU and Mehmet Ali AK | 53 |
| Performance Evaluation for Thermal Architectures of Flue-Gas Assisted Organic Rankine Cycle Systems <i>Baca Gazı Destekli Organik Rankine Çevrimlerinin Termal Mimarileri İçin Performans Değerlendirmesi</i> Burak TURKAN and Akın Burak ETEMOĞLU | 65 |
| CFD Investigation of the Near-Surface Streamline Topology On a Simple Nonslender Delta Wing <i>Hesaplamalı Akışkanlar Dinamiği Kullanılarak Basit Üçgen Kanat Modelinde Yakın Yüzey Akış Yapısının İncelenmesi</i> Haci SOGUKPINAR, Serkan CAG and Bulent YANIKTEPE | 77 |
| Yapay Sinir Ağları ve Uyarlamalı Sinirsel Bulanık Çıkarım Sistemi ile Francis Tipi Türbinler İçin Verim Tahminlemesi <i>ANN and ANFIS Performance Prediction Models For Francis Type Turbines</i> Ece AYLI ve Oğuzhan ULUCAK | 87 |
| Flow and Forced Heat Transfer from Tandem Square Cylinders Near a Wall <i>Duvar Yakınında Art Arada Yerleştirilmiş Kare Kesitli Silindirler Etrafında Akış ve Zorlanmış Taşınım İle Isı Geçişi</i> Özge YETİK and Necati MAHİR | 99 |
| A Novel Thermal Analysis for Cooking Process in Bulgur Production: Design Considerations, Energy Efficiency and Wastewater Diminution for Industrial Processes <i>Bulgur Üretiminde Pişirme İşlemine Yönelik Özgün Bir Isıl Analizi: Endüstriyel Süreçler İçin Tasarım Önerileri, Enerji Verimliliği ve Atıksu Azaltımı</i> İbrahim Halil YILMAZ and Mehmet Sait SÖYLEMEZ | 113 |
| Investigating the Effects of Plasma Actuator On the Flow Control Around NACA2415 Airfoil <i>Plazma Aktüatörün NACA2415 Airfoil Etrafında Akış Kontrolüne Etkilerinin Araştırılması</i> Aytaç SANLISOY and Yahya Erkan AKANSU | 131 |
| Theoretical Analysis of a Cascade Refrigeration System with Natural and Synthetic Working Fluid Pairs for Ultra Low Temperature Applications <i>Doğal ve Sentetik Soğutucu Akışkan Çiftleri Kullanılan Bir Kaskad Soğutma Sisteminin Ultra Düşük Sıcaklık Uygulamaları İçin Teorik Analizi</i> Barış YILMAZ, Ebru MANÇUHAN and Deniz YILMAZ | 141 |
| A Comparison of the Thermal Performance of a Conventional Fin Block and Partially Copper and Aluminum Foam Embedded Heat Sinks <i>Geleneksel Kanatçıklı Blok ve Kısmi Alüminyum ve Bakır Metal Köpük Yerleştirilmiş Isı Alıcıların Isıl Performanslarının Karşılaştırılması</i> S. Kaancan ATAER, Cemil YAMALI and Kahraman ALBAYRAK | 155 |
| Radiofrequency Ablation for Spherically-Shaped Hepatic Tumors <i>Küresel Şekli Karaciğer Tümörleri İçin Radyofrekans Ablasyonu</i> Güven Hasret YILMAZ, Uğur Tuna YAY, Oğuz TURGUT, Burak TİĞLİ and Nuri Eren TÜRKOĞLU | 167 |
| Enhancement of Heat Transfer by Heat Pipes with Piecewise Uniform Longitudinal Wick Profiles <i>Parçalı Üniform Boylmasına Fital Profilli Isı Boruları ile Isı Transferinin Arttırılması</i> Mehmed Akif PAKSOY and Salih Özen ÜNVERDİ | 177 |